Zhixiang Hou

Editor

Measuring Technology and Mechatronics Automation in Electrical Engineering

Springer

Lecture Notes in Electrical Engineering

Volume 135

Zhixiang Hou
Editor

Measuring Technology and Mechatronics Automation in Electrical Engineering

Springer

Zhixiang Hou
Deptartment of Automobile and Mechanical Engineering
Changsha University of Science and Technology
Chiling Road, Tianxin District 45
410014 Changsha, Hunan
People's Republic of China

Printed on acid-free paper

Preface

Measuring Technology and Mechatronics Automation are the combination of Mechanical engineering, Electronic engineering, Detecting Techniques, Computer engineering, Software engineering, Control engineering, and Systems Design engineering in order to design, and manufacture useful products. Mechatronics is a multidisciplinary field of engineering, that is to say it rejects splitting engineering into separate disciplines. Originally, mechatronics just included the combination between mechanics and electronics. On the other hand, electrical engineering is a field of engineering that generally deals with the study and application of electricity, electronics and electromagnetism. The field first became an identifiable occupation in the late nineteenth century after commercialization of the electric telegraph and electrical power supply. It now covers a range of subtopics including power, electronics, control systems, signal processing and telecommunications.

This book focus on the research of measuring technology and mechatronics automation in electrical engineering field. In modern technology, the products of automobile, aerotechnics, medicine, robotic and other innovative manufacture reflect increasingly the feasibility and potential of mechatronics automation in electrical engineering. A mechatronics engineer unites the principles of mechanics, electronics, and computing to generate a simpler, more economical and reliable system. Mechatronics is centered on mechanics, electronics, computing, control engineering, molecular engineering, and optical engineering, which, combined, make possible the generation of simpler, more economical, reliable and versatile systems.

Firstly, this book discusses the mechatronics engineering cybernetics which deals with the question of control engineering of mechatronic systems. It is used to control or regulate such a system (see control theory). Through collaboration, the mechatronic modules perform the production goals and inherit flexible and agile manufacturing properties in the production scheme. Modern production equipment consists of mechatronic modules that are integrated according to a control architecture. The most known architectures involve hierarchy, polyarchy, heterarchy, and hybrid. The methods for achieving a technical effect are described by control algorithms, which might or might not utilize formal methods in their design.

Hybrid systems important to mechatronics include production systems, synergy drives, planetary exploration rovers, automotive subsystems such as anti-lock braking systems and spin-assist, and every-day equipment such as autofocus cameras, video, hard disks, and CD players.

In addition, the book is also concerned the intelligent systems, which entered the video game industry as a one-man team, named toru narihiro, who was hired by nintendo to port over famicom disk software into the standard rom-cartridge format that was being used by the nes outside japan. the team soon became an auxiliary program unit for nintendo (like hal laboratory originally) that provided system tools and hired people to program, fix, or port nintendo-developed software. thus much of the team's original discography contains minuscule contributions to several big nintendo r&d1 and nintendo ead titles.

Beside, as the third part of this book, power electronic converters can be found wherever there is a need to modify a form of electrical energy (i.e. change its voltage, current or frequency). The power range of these converters is from some milliwatts (as in a mobile phone) to hundreds of megawatts (e.g. in a HVDC transmission system). With "classical" electronics, electrical currents and voltage are used to carry information, whereas with power electronics, they carry power. Thus, the main metric of power electronics becomes the efficiency. The first very high power electronic devices were mercury arc valves. In modern systems the conversion is performed with semiconductor switching devices such as diodes, thyristors and transistors. In contrast to electronic systems concerned with transmission and processing of signals and data, in power electronics substantial amounts of electrical energy are processed. An AC/DC converter (rectifier) is the most typical power electronics device found in many consumer electronic devices, e.g. television sets, personal computers, battery chargers, etc. The power range is typically from tens of watts to several hundred watts. In industry the most common application is the variable speed drive (VSD) that is used to control an induction motor. The power range of VSDs start from a few hundred watts and end at tens of megawatts.

Moreover, as an important component of this book, computer software, or just software, is a collection of computer programs and related data that provide the instructions for telling a computer what to do and how to do it. In other words, software is a conceptual entity which is a set of computer programs, procedures, and associated documentation concerned with the operation of a data processing system. We can also say software refers to one or more computer programs and data held in the storage of the computer for some purposes. In other words software is a set of programs, procedures, algorithms and its documentation. Program software performs the function of the program it implements, either by directly providing instructions to the computer hardware or by serving as input to another piece of software. The term was coined to contrast to the old term hardware (meaning physical devices). In contrast to hardware, software is intangible, meaning it "cannot be touched"[1]. Software is also sometimes used in a more narrow sense, meaning application software only. Sometimes the term includes

data that has not traditionally been associated with computers, such as film, tapes, and records.

Finally, as the Editor of this book, I thank Springer Publication, IEEE Instrumentation and Measurement Society, City University of Hongkong and Changsha University of Science and Technology. I wish to express our heartful appreciation to Editors Alex Greene and Michael Luby hard work for the best papers publication.

Zhixiang Hou

Contents

Chapter 1
Adoption of Mobile Content Service in 3G Era: An Empirical Analysis in China

Hao Huang, Yide Liu and Wei Xing

Abstract In 3G era, mobile network operators and content providers must provide mobile content service accepted by consumers to obtain more profits. It is crucial to investigate the antecedents of adoption of mobile content service and the way they interact. In this paper, we explore how customers perceive and adopt mobile content service in China. We first extend the technology acceptance model (TAM) by integrating innovation of consumer, external influence, and perceived financial cost. Then some hypotheses are raised and tested using structural equation modeling. We find that the TAM is also correct in the situation of mobile commerce. In addition, innovation of consumer, external influence, and perceive financial cost have influence on the intention of adopting mobile content service. Managerial insights are generated in the last part of this paper.

Keywords Mobile content service · Technology adoption · Technology accepted model (TAM) · Structural equation modeling

H. Huang (✉)
Institute of Finance and Trade Economics,
Chinese Academy of social science, 100836 Beijing, China
e-mail: huanghao98@sina.com

Y. Liu
Faculty of Management and Administration,
Macau University of Science and Technology,
999078 Macau, China
e-mail: g.liuyide@gmail.com

W. Xing
School of Management, Qufu Normal University Rizhao,
276826 Shandong, China
e-mail: xingweimail@gmail.com

1.1 Introduction

Mobile commerce (henceforth, M-commerce) refers to commercial transactions conducted through a variety of mobile equipment over a wireless telecommunication network in a wireless environment [1]. M-commerce applications can be broadly divided into two categories: content delivery (i.e., reporting, notification) and transactions (i.e., purchasing, promotions) [2].

With rapid development of mobile services, research on the adoption of mobile services is becoming an important topic. The current study attempts to extend the scope of innovation adoption research to an emerging class of mobile telephone innovations that we refer to as mobile content services. Mobile content services are designed to provide their users with various types of information: data, video, images, etc. Recognizing the increasingly diversified usage contexts of information appliances, we further define mobile content services as that (1) have a one-to-one binding with the user, (2) offer ubiquitous services and access, and (3) provide a suite of utilitarian and hedonic functions.

Although an abundance of studies have been conducted to extend the scope of user adoption of technology, none of them was conducted on mobile content services by extending the well-established technology acceptance model (TAM). With the rapid rise of the number of global telecom groups that offer and improve mobile content services, it is an opportunity to study the users' adoption of mobile content services. Such a study will be interesting to both the academics and the telecom executives in China. This paper investigates individuals' perception of the adoption of mobile content services for corporate purposes.

1.2 Theoretical Foundations and Hypotheses Development

TAM is one of the most widely used models for information technology (IT) adoption. According to TAM, an individual's IT adoption is influenced by perceived usefulness and perceived ease of use. Perceived usefulness is defined as the degree to which a person believes that using a particular system would enhance his or her job performance [3]. Perceived ease of use refers to the degree to which a person believes that using a particular system would be free of effort. The perceived ease of use influences the user intention indirectly through the perceived usefulness. These two perceptions help shape the user's attitude toward usage and intention to use. Davis's scale items for measuring the two independent variables, perceived usefulness and perceived ease of use, have shown high internal validity. TAM is a parsimonious and robust model, consistently validated by numerous studies across different settings and technologies. Beyond IT applications for corporate use, recent studies have also established the model's applicability for user adoption of mobile ticketing [4], mobile payment systems

for e-commerce merchants [5]. Some studies have extended the TAM model by identifying antecedent attributes to the user's perceived usefulness and perceived ease of use. Lederer et al. validated that perceived ease of use can be explained by usability characteristics, and perceived usefulness by characteristics of useful information, task environment, and functional needs to perform jobs [6]. The role of perceived ease of use in TAM, however, remains controversial because some studies show that perceived ease of use directly affects either self-reported use or intended ICTs use, whereas other studies have not found a direct linkage between perceived ease of use and ICTs adoption. Gefen and Sträubfound that the nature of the task may influence the perceived ease of use [7]. Their empirical evidence showed that perceived ease of use and perceived usefulness affect intended use when a Web site is used for an inquiry task and where ICTs is intrinsic to the task and interface design is critical. Wireless technology is one type of ICTs. We argue TAM is also correct for mobile content services. Therefore, we wish to investigate the following four hypotheses.

H1. Attitude of use will have a positive effect on the behavioral intention to use mobile content services.
H2. Perceived usefulness will have a positive effect on the attitude of using mobile content services.
H3. Perceived ease of use will have a positive effect on the attitude of using mobile content services.
H4. Perceived ease of use will have a positive effect on the Perceived usefulness of mobile content services.

Personal innovativeness (PI) as a construct that is important to the study of individual behavior toward innovations has had a long-standing tradition in innovation diffusion research in general and the domain of marketing in particular [8, 9]. Rogers (1995) conceptualize this construct in terms of its operational definition, i.e., individuals are characterized as "innovative" if they are early to adopt an innovation [8]. Consistent with the emphasis in the marketing literature on the construct of PI, we argue that PI is an important concept for examining the acceptance of information technology innovations also. However, as noted above, it has not been included in any of the dominant technology acceptance models, although there is considerable theoretical as well as empirical support from other disciplines for its role as a key variable in innovation adoption. As recommended in prior research, we focus attention on domain-specific as opposed to global innovativeness. We define PI in the domain of information technology, henceforth PI, as "the willingness of an individual to try out any new information technology." This definition is derived from the work of Flynn and Goldsmith (1993). We argue that the effects of PI are manifest in technology acceptance behavior through its relationships with beliefs or perceptions. Indeed, Midgley and Dowling note that the "trait-behavior" model is an inadequate representation of innovation adoption behavior as several

variables potentially intervene between trait and behavior [10]. We propose that PI serves as a key variable for the antecedents. Therefore, we wish to investigate the following two hypotheses.

H5. Personal innovativeness will have a positive effect on the attitude of using mobile content services.
H6. Personal innovativeness will have a positive effect on the behavioral intention to use mobile content services.

External influence is driven by social values that define normal behavior for the group or society to which an individual belongs [11]. In the current study, External influence is defined as the extent to which users believe that "important others" would approve or disapprove of their performing a given behavior [12]. The external influence from peers, superiors, and family members has been found to affect consumer behavior as well as IT adoption decisions at home [13, 14]. According to the consumer behavior literature, when usage of an innovation is seen as a form of public consumption, such usage is significantly influenced by friends and colleagues [15]. In a survey of young people, Carroll et al. found that those who do not use mobile technology (e.g., SMS, chatting, and e-mail) appear to struggle to maintain their social links [16]. Thus, using mobile services that are widely accepted by group members can often be a way to maintain membership and secure support through increased interactions within the group. In turn, the assured membership could be instrumental in achieving a valued outcome, such as improved status within a social group. The external influence that leads an individual to use a technology has been found to affect adoption attitude directly [17]. Therefore, we wish to investigate the following hypothesis.

H7. External influence will have a direct positive influence on adoption attitude.

One does not need to consider the cost of information systems if he or she uses the IS for work purpose because his/her employers will bear the cost. The cost of information systems based on the wired Internet is relatively low. In contrast, the cost associated with wireless services are relatively high and many wireless users have to bear the cost themselves. Therefore, cost should be considered in m-commerce user acceptance. Wu and Wang found that cost factor is negatively related with user's intent to use in m-commerce [18]. We think that cost is user's assessment of the object world or reality, not his/her perception. Cost factor should thus directly affect the users' adoption behavior. We believe that cost factor will significantly affect m-commerce user's acceptance. Therefore, we hypothesize that:

H8. Financial cost will have a negative effect on the behavioral intention to use mobile content services.

The research model is shown in Fig. 1.1

Fig. 1.1 Research model
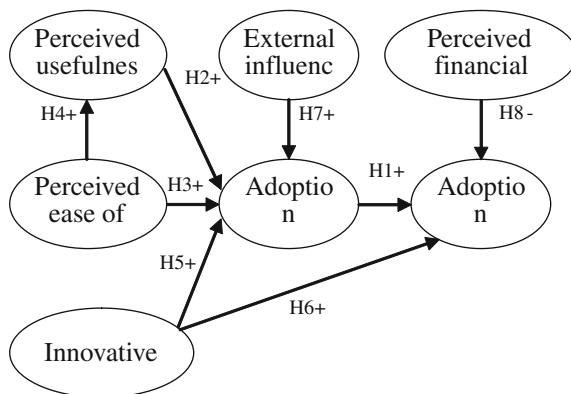
1.3 Research Design and Method

Regarding instrument construction, the items used to operationalize the constructs of each investigated variable are mostly adopted from relevant previous studies, with necessary validation and wording changes being made. Specifically, items measuring perceived usefulness and ease of use are adapted from Davis (1989), whereas items measuring personal innovativeness, external influence are taken from Hee-woong (2006) [19]. Moreover, constructs shared by different investigated models were measured using the same items. All items were measured using a five-point Likert type scale with anchors ranging from 'strongly agree' to 'strongly disagree'. To ensure the desired balance and randomness in the questionnaire, half of the items were worded with proper negation and all items in the questionnaire were randomly sequenced to reduce the potential ceiling (or floor) effect, which induces monotonous responses to the items for measuring a particular construct. Furthermore, to ensure data validity and reliability, this study first pre-tested the questionnaire by having several consumers and telecommunication professionals review it. Of the 188 returned questionnaires from Beijing, Dalian, Hangzhou, and Fujian, 29 were excluded because of incomplete answers, leaving 159 usable responses. The response rate thus reached 84.6% (Table 1.1).

This study used structural equation modeling (SEM) for hypotheses testing. Following the two stage approach, analysis of data from 159 samples was conducted through two stages. First, the measurement model was estimated using confirmatory factor analysis to test whether the constructs possessed sufficient validation and reliability. To ensure data validity and reliability, internal consistency, convergent validity, and discriminate validity were demonstrated. Second, the structural model that best fitted the data was identified, and the hypotheses were tested between constructs using this model.

Table 1.1 Research variables

Latent variable	No. of investigated variable	Name of investigated variable	Source
Perceived usefulness (PU)	4	PU1, PU2, PU3, PU4	Davis [3] Davis et al. [20] Elizabeth [21]
Attitude (ATTI)	5	ATTI1, ATTI2, ATTI3, ATTI4, ATTI5	
Intention (INTE)	2	INTE1, INTE2	
Perceived ease of use (PE)	4	PE1, PE2, PE3, PE4	
Innovativeness (INOV)	4	INOV1, INOV2, INOV3, INOV4	Hung et al. [22] Kenneth C [23]
External influence (INFU)	4	INFU1, INFU2, INFU3, INFU4	Hung et al. [22] Pedersen [24]
Perceived financial cost (COST)	4	COST1, COST2, COST3, COST4	Pin Luarn et al. [25] Kim et al. [19]

Table 1.2 Reliability test

Variable	Item number	Cronbach's α
PU	4	0.795
ATTI	5	0.853
INTE	2	0.807
PE	4	0.812
INOV	4	0.746
INFU	4	0.804
COST	4	0.706

1.4 Statistical Analyses

Regarding reliability, the survey had strong internal consistency with all multiple-item constructs. The Cronbach's alpha coefficients range from 0.706 to 0.853 that exceed recommended value of 0.50 [26]. These values show good internal consistency among scales employed for the present study. These alphas equal 0.795, 0.812, 0.746, 0.804, and 0.706 for PU, PEOU, innovativeness, external influence, and financial cost, respectively. The results of reliability tests are presented in Table 1.2.

Additional assessment of discriminant validity was conducted by comparing the average variance extracted from each construct with its communal variances shared with other constructs. Result shows that the square root of the average variance extracted for all first-order factors was higher than their shared variances. This reaffirmed the discriminant validity of the model constructs.

Table 1.3 Standard path coefficients

Hypothesis	H1	H2	H3	H4	H5	H6	H7	H8
Path coefficients	0.74*	0.51**	0.14*	0.62*	0.26*	0.09*	0.09**	−0.32*

*, ** denote significance at the 0.05 and 0.01 level respectively

The structural model shown in Fig. 1.1 was tested using LISREL8.7. The overall fit of the model was assessed using the typical statistics, both incremental and absolute fit indices. The incremental fit indices(e.g., CFI, IFI, NNFI) were all >0.90 and the absolute fit indices (e.g., RMSEA) were <0.08. $\chi 2/df = 2.52 < 3$. Thus, results of the structural model analysis suggest a good fit of the proposed model to the data (Table 1.3).

1.5 Discussions

The industry of mobile content services is growing in China. In order to foster the acceptance of these services, it is important to understand the underlying motives of user behavior. Our study enhanced understanding of the interaction of users with mobile content services and provided valuable insights for industry professionals.

We empirically validated the existing theories within the context of mobile content services. We also investigated the direct and indirect effects of perceived financial cost, personal innovativeness, external influence, and perceived usefulness on customer's adoption attitude. The integration of these perspectives, and the empirical examination of the factors that affect customer's adoption in a mobile content service context, advanced the understanding of these constructs and their linkage to user's mobile content adoption behavior in China.

According to the path coefficients, perceived usefulness exhibits the strong direct effect on adoption attitude (0.51), and it will affect adoption intention through attitude. The positive effect of perceived ease of use on attitude also is validated, but its most effects on attitude are works through perceived usefulness ($0.62 \times 0.51 = 0.32$). The relationships between perceived usefulness, perceived ease of use, attitude and intention are validated in this research, and it shows that TAM is also correct in the mobile content services context. In addition, this study introduced external influence to explain consumer's adoption behavior. The slight positive effect (0.09) which external influence exert on attitude shows that consumers are becoming more and more rational in china. Consumers give more attention to practicality of mobile content service, and publicity has little contribution for consumer's adoption. Personal innovativeness affects on both adoption attitude and adoption intention, but it gives more influences to attitude than to adopt intention.

Base on analysis above, we provide some management suggests for China's practitioners of mobile content service. First, mobile content providers should develop more pragmatic services to ensure requirements from different costumer group are satisfied. Moreover, operation of mobile content service must become convenience for most consumers. Second, because the innovativeness of young people is higher than others, more mobile content services should be developed for young people. Third, since China's consumers are sensitive to price of mobile content service, mobile content providers can attract consumers with preferential price, and foster consumption habit of mobile content service. Last, mobile content providers should not put much fund into the external publicity, because our empirical study has shown consumers' attitude are not easy controlled from external influence.

This empirical study has two limitations. One limitation is the positive effect of perceived usefulness exerting on adoption intention is not validated because of inaccuracy of measurement. It will be tested by the further research. Another limitation is the Cronbach's α of trust lower than 0.5, so latent variable trust is excluded in the phrase of data analysis. Future researches should reveal some other factors affecting consumers' adoption of mobile content service from a more wide scope.

References

1. Coursaris C, Hassanein K (2002) Understanding M-commerce a consumer-centric model [J]. Q J Electron Commer 3(3):247–271
2. Balasubramanian S, Peterson RA, Jarvenpaa SL (2002) Exploring the implications of M-commerce for markets and marketing [J]. J Acad Mark Sci 30:348–361
3. Davis F (1989) Perceived usefulness, perceived ease of use, and user acceptance of information technology [J]. MIS Q 13:319–340
4. Mallat N, Rossi M, Tuunainen VK (2009) The impact of use context on mobile services acceptance: the case of mobile ticketing [J]. Inf Manag 46:190–195
5. Au YA, Robert J (2008) The economics of mobile payments: understanding stakeholder issues for an emerging financial technology application [J]. Electron Commer Res Appl 7:141–164
6. Lederer AL, Maupin DJ, Sena MP, Zhuang YL (2000) The technology acceptance model and the World Wide Web [J]. Decis Support Syst 29:269–282
7. Gefen D, Sträub DW (1997) Gender differences in the perception and use of e-mail: an extension to the technology acceptance model [J]. MIS Q 21:389–400
8. Rogers EM (1995) Diffusion of Innovations, 4th edn. The Free Press, New York
9. Flynn LR, Goldsmith RE (1993) A validation of the goldsmith and hofacker innovativeness scale [J]. Educational Psychol Meas 53:1106–1116
10. Midgley DF, Dowling GR (1978) Innovativeness: the concept and its measurement [J]. J Consumer Res 4:229–242
11. Engel J, Blackwell R, Miniard P (2001) Consumer Behavior [M]. Dryden Press, Orlando

12. Ajzen I (1991) The theory of planned behavior [J]. Organ Behav Hum Decis Process 50:179–211
13. Lowry PB, Vance A, Moody G, Beckman B, Read A (2008) Explaining and predicting the impact of branding alliances and web site quality on initial consumer trust of E-commerce web sites [J]. J Manag Inf Syst 24:199–224
14. Venkatesh V, Brown S (2001) A longitudinal investigation of personal computers in homes: adoption determinants and emerging challenges [J]. MIS Q 25:71–102
15. Fisher RJ, Price L (1992) An investigation into the social context of early adoption behavior [J]. J Consumer Res 19:477–486
16. Carroll J, Howard S, Vetere F, Peck J, Murphy J (2002) Just what do the youth of today want? Technology appropriation by young people [C]. In: 35th annual Hawaii international conference on system sciences (HICSS'02)-vol 5, p 131
17. Venkatesh V, Morris M, Davis G, Davis F (2003) User acceptance of information technology: toward a unified view [J]. MIS Q 27:425–478
18. Wu J, Wang S (2005) What drives mobile commerce? An empirical evaluation of the revised technology acceptance model [J]. Inf Manag 42:719–729
19. Kim H-W, Chan HC, Gupta S (2007) Value-based adoption of mobile internet: an empirical investigation [J]. Decis Support Syst 43(1):111–126
20. Davis F, Bagozzi R, Warshaw P (1989) User acceptance of computer technology: a comparison of two theoretical models [J]. Manag Sci 35:982–1003
21. Grandon EE, Pearson JM (2004) Electronic commerce adoption: an empirical study of small and medium US businesses [J]. Inf Manag 42:197–216
22. Hung S-Y, Chang C-M, Yu T-J (2006) Determinants of user acceptance of the e-Government services: the case of online tax filing and payment system [J]. Gov Inf Q 23:97–122
23. Yang KCC (2005) Exploring factors affecting the adoption of mobile commerce in Singapore. Telematics Inform 22:257–277
24. Pedersen PE (2005) Adoption of mobile internet services: an exploratory study of mobile commerce early adopters [J]. J Organ Comput Electron Commer 15:203–222
25. Luarn P, Lin H-H (2005) Toward an understanding of the behavioral intention to use mobile banking [J]. Comput Hum Behav 21:873–891
26. Hair JF, Anderson RE, Tatham RL, Black WC (2005) Multivariate Data Analysis with Readings [M]. Prentice-Hall, New Jersey

Chapter 2
A Game Analysis on Multi-Level Emergency Management for Construction Accident

Renhui Liu

Abstract This paper analyzes the framework of multi-level emergency management conducted by government, company and project managers. There exists the fact that sometimes, in the construction market, construction accidents are not reported, and information asymmetry is a main factor that causes ethical risk for emergency management. Using modern information asymmetry theory in economics, this paper studies the dynamic game process of emergency management behaviors with incomplete information when construction accident happens. As the sector entity undertaking project management has more information and is responsible for the accident, moral hazard and adverse selection may happen during emergency management of construction accident. This paper suggests that a system should be established to encourage integrity behaviors and to prevent discreditable behaviors. Effective emergency management system should be able to solve the problem that information about project construction accident is prevented from reporting.

Keywords Construction project · Construction accident · Emergency management · Game theory

2.1 Introduction

The feature, that construction project needs lots of money, requires good cooperation of every profit related participant so as to finish it very well, for example, participation of owner, designer, contractor, government and user. Thus, how to

R. Liu (✉)
School of Management, Harbin Institute of Technology, 150001 Harbin, China
e-mail: Irh@hit.edu.cn

coordinate the relationship between each other is an important condition to complete a construction project successfully. As the profit relationship between each other is complicated, most crisis and construction accidents result from bad coordination of relationships between profit related entities, and information can't be passed or communicated as well as misunderstanding between project members.

Game theory research on complicated problems in construction project management is becoming more and more mature. Many scholars do detailed study on client-agent issue during construction project management using game theory and get a lot of achievements. Game theory refers to the methodology that studies decisions made by decision makers when their behaviors are affecting each other and the balance of those decisions. Game theory proves the fact that decision behaviors of people are interacted. When one party is making decisions, he will be affected by other decision makers and will also has an influence on balance problem and making decisions by them. Secondly, such a series of decisions forms a strategy profile, and there exists an equilibrium, which is made up of best strategies of all participants [1]. Game theory was put forward in two papers established in 1928 and 1937 by J.von Neumann, who is a famous mathematician, for the first time. However, the symbol of establishment of game theory is a book called The Theory of Games and Economic Behavior, which is written by J.von Neumann and O. Morgenstem together. This book mainly introduces the typical character of economy entities and puts forward some game theory models such as strategy model, normalized model and extended model. It lays a foundation for theory and methodology of game theory. After that, game theory develops very fast and is widely used [2]. For example, Rapoport and Fuller (1998) did a research on the coordination of relationship during game playing between three disoperative parties based on different information structures [3]. Putterman and Skillman (1988) analyzed influence of supervision on how hard people work using different supervision methods and compensation systems [4]. Holmstrom and Milgrom (1987, 1991) studied client-agency issue under multiple tasks, including incentive contract, asset ownership and contract design [5]. Stanley Baiman (2000) studied function of contract information and motivation to the control of quality and cost of product, and he put forward equation deduction of the theory [6]. Abdulaziz (2003) studied the meaning and function of motivation mechanism and motivation contract to project cost control, schedule control and reaching project goals from the perspective of practice [7].

2.2 Working Process of Hydraulic Variable Pitch System

Hydraulic variable pitch system [6] is shown in Fig. 2.1. When the wind turbine generator operates above wind speed, it needs to regulate pitch angle to keep rated power. When output power of generator is higher than rated power, blade angle

will be turned down to reduce wind energy capture. Under the case, the working process of hydraulic system is as follows: when pump is driven by electric motor, hydraulic oil will through the one-way valve (11.1) flow into the system and pressure oil will through electromagnetic ball valve (1), electro-hydraulic proportional directional valve (4), one-way valve (22), electromagnetic ball valve (2) flow into rod cavity (24) to push piston rod right. At the same time, oil will from rod-less cavity (25) through operated check valve (23), electro-hydraulic proportional directional valve (4) flow back pressure pipeline. When power control need to increase pitch angle, electro-hydraulic proportional directional valve will reverse direction and oil will make piston rod move left.

2.3 Multi-Layer Emergency Management Structure

Construction accident is complex, and emergency management is conducted in a complex environment. Project management parties and related companies, government and non-governmental organizations participate in the process and mechanism of construction project emergency management. As a new emergency management, it emphasizes diversification of the subjects. To conduct effective emergency management not only requires a big revolution of ways how administrative department of construction conduct supervision but also need the owner, contractor and supervisor to improve their emergency management abilities and effectively integrate various levels of resources, which will enhance the emergency management ability of construction projects. This is also the basic goal of building a multi-level system of emergency management.

Project level involves the project department of construction company, representatives of the owner, designers in charge from design company, the project supervision department of supervisor company and related personnel from equipment and material suppliers. But the project department of construction company gets the most sufficient information and bear most responsibility in emergency management, so it should play the most important role. Company level refers to companies that relevant project management departments belong to, which mainly consists of construction enterprise, owner, supervisor enterprise and design company, etc. During emergency management, according to the level of construction accident, emergency management for construction project will involve administrative department of construction, county government, and provincial government.

Multi-level emergency management is helpful to fully understand emergency management for construction accident and to effectively organize and reasonably solve all contradictions and problems during emergency management for construction accident. It is also helpful to adjust the working pattern while construction accident is changing constantly in order to keep up with development of society better.

2.4 Dynamic Game Analysis on Emergency Management Behaviors With Incomplete Information

When construction accident happens, it will bring influence on both project, enterprises and government, what's worse, they even need bear legal responsibility. As project management units have more information and they must bear legal responsibility if any accident happens, ethic risk and adverse selection exist during emergency management for construction accident.

2.4.1 Participant

The two participants in dynamic game are "construction administration department" and "project manager" during emergency management for construction accident. The "construction administration department" generally refers to the entity sector that need to make administrative decisions and conduct supervision behaviors when construction accident happens; The "project managers" refers to relevant participants who are involved in project construction, including owner, construction company, supervision company, design company and subcontractors. And "project manager's emergency behaviors" refers to measures and behaviors taken by the owner or construction company to conduct emergency management for construction accident.

2.4.2 Strategy Space

The strategy space of "construction administration department" consists of administrative action plans, that of "project manager" strategy is emergency management measures taken by project participants in a certain condition of emergency. Assuming that there are n kinds of possible emergency actions of "project manager", "project managers' emergency behaviors" chooses action i with probability of pi and changes from emergency situation i to j with probability of pij. The "construction administration department" will choose to undertake relevant plans according to different emergency situation j and its dynamic changes of situation.

2.4.3 Variable Definition

During the process of emergency management for construction accident, assuming that there is a dynamic game between emergency behaviors of "construction

administration department" and "project manager", variables are defined as follow:

CM (Cost of Monitoring)—the cost that construction administration department spends on monitoring whether project manager is hiding accident information;
CH (Chastisement)—the punishment on project manager by construction administration department for hiding construction information;
D (Damage)—damage utility for hiding information;
ΔR—difference of the benefit to project manager between different degrees of hiding information;
π—probability that construction administration department checks whether construction entities are hiding some information;
η—probability that project manager hides true accident information.

Among the variables mentioned before, CM, CH, D, ΔR ≥ 0, 0 ≤ π,η ≤ 1. Assuming that:

1. f : Θ → Ω is already known, and it is relatively stable within a limited duration of construction accident situation. Θ refers to collection of the information that is reported by project manager and can be seen by construction administration department, Ω refers to collection of all information about emergency management situation of project manager. The information that can represent emergency management of project manager consists of emergency rescue plans, emergency rescue organizations, qualification of the general contractor and all kinds of risk management situations.
2. Project managers who hide accident information, besides construction administration department and owner, can be the contractor, supervision company, design company, consulting company and insurance company, etc., including construction workers, management and technical personnel and so on.
   According to the theory, these parties have their own utility curves which are different from each other, which represents different interests when they are hiding accident information. But for the sake of simplicity, it assumes that the interests of construction administration department and other profit related parties are the same. It will monitor the behavior of hiding accident information of construction project as the interest representative of construction workers, insurance companies and other profit related parties.
3. D ≥ CM, CH ≥ ΔR, according to the rational man hypothesis, it is known that construction administration department is not rational if the cost is larger than the loss brought to construction market because of untruthful information; And if the marginal benefit because of hiding information is bigger than possible punishment, the punishment by construction administration department is not trustful.

2.5 One Stage Game Theory

During emergency management in a sudden accident, the construction administration department's strategic is to choose to always "monitor" the whole process of construction accident that actually happens during project construction or completely "not to monitor", here M (Monitoring) represents choosing to monitor and NM (No Monitoring) refers to choosing not to monitor; The strategies in the situation of construction accident is to hide information (using F as False) or timely, accurately report information (using R as Real); Among them, (NM, R) represents cooperative behaviors. Obviously, The construction administration department doesn't have pure strategy Nash equilibrium on whether monitoring or not in the situation of construction emergency, but mixed strategy Nash equilibrium can be found.

If π is given, expected benefits for project managers to choose to hide real information about the accident ($\eta = 1$) and timely, accurately report information ($\eta = 0$) are:

$$U_{b1}(\pi, 1) = -C_H \cdot \pi + \Delta R \cdot (1 - \pi) = \Delta R - (C_H + \Delta R) \cdot \pi \qquad (2.1)$$

$$U_{b1}(\pi, 0) = 0 \cdot \pi + 0 \cdot (1 - \pi) = 0 \qquad (2.2)$$

Make $U_{b1}(\pi, 1) = U_{b1}(\pi, 0)$, then $\pi^* = \Delta R/(\Delta R + C_H)$, namely, project manager need to estimate the probability π that construction administration department may conduct monitoring, if $\pi < \Delta R/(\Delta R + C_H)$, project manager will choose to hide information; if $\pi > \Delta R/(\Delta R + C_H)$, project managers will choose to timely, accurately report information; if $\pi = \Delta R/(\Delta R + C_H)$, project manager will choose to hide or timely, accurately report real information randomly. Further, $\partial(\pi^*)/\partial(\Delta R) > 0$, which means that if the difference of the benefit to project manager between different degrees of hiding information is bigger, it is more possible for construction project subjects to hide information, then construction administration department should pay more efforts on monitoring them.

If η is given, expected benefits for construction administration department to choose to conduct monitoring ($\pi = 1$) and find no problems ($\pi = 0$) are:

$$U_{m1}(1, \eta) = (-C_M + C_H) \cdot \eta + (-C_M) \cdot (1 - \eta) = \eta \cdot C_H - C_M \qquad (2.3)$$

$$U_{m1}(0, \eta) = -D \cdot \eta + 0 \cdot (1 - \eta) = -D \cdot \eta \qquad (2.4)$$

Make $U_{m1}(1, \eta) = U_{m1}(0, \eta)$, then $\eta^* = C_M/(C_H + D)$. If $\eta > C_M/(C_H + D)$ then construction administration department will choose to conduct monitoring; on the contrary, the best decision for construction administration department is not to conduct monitoring temporarily or to choose randomly. Further, $\partial(\eta^*)/\partial(C_M) > 0$ means that if the cost of monitoring for construction administration department is bigger, it is more possible for construction project subjects to hide information.

It can be seen that the effectiveness of mechanism of information disclosure, which is about construction accident for projects depends on the four factors: the

benefit to project management entities by hiding information, the punishment from construction administration department for hiding information, capacity and responsibility of supervisor. If the construction administration department is antagonistic to hiding information behavior more strongly, the capacity of supervisor is stronger. If law defines more responsibilities for construction administration department, the motivation for construction project subjects to hide information in the situation of emergency is smaller, which means that it is more possible for them to provide reliable information. Conversely, if it can bring obvious benefit to the construction project subjects by hiding information, and the construction administration department disregard the behavior and the responsibility of supervisor is very small, then it is quite possible for construction project subjects to hide information.

2.6 Conclusion

In repeated game with limited times, the equilibrium of every stage is the equilibrium result of one stage game, which means that mixed strategy equilibrium of one stage game will appear, However, with the assumption that all participants obey in repeated game with limited times, the equilibrium result will be got eventually, but the premise is that probability of project managers to be rational is big enough. Then, the assumption of repeated game with limited times can provide behavior rules for establishing the mechanism of monitoring construction accident.

In the situation of emergency, malicious behaviors are very common and serious between project subjects, companies as well as enterprises and the government. And we should also pay more efforts on monitoring the evaluation of construction project contracts and build an public environment of being proud of keeping one's words and being ashamed of being dishonest. During key procedures such as construction market access, biding evaluation and registration review of all kinds of personnel who are qualified, we should set up evaluation index of enterprise credit and individual credit and intensify the economic punishment on enterprises and individuals for being dishonest, as well as gradually establishing and developing the system that encourages credible behaviors and prevent discreditable behaviors.

References

1. Xie S (2003) Economy game theory [M]. Fudan University Press, Shanghai, pp 17–18
2. Zhang W (1996) Game theory and information economy [M]. Shanghai Sanlian Book Store, Shanghai Renming Press, Shanghai, pp 76–82
3. Rapoport A, Fuller MA (1998) Coordination in noncooperative three-person games under different information structures. Kluwer Academic Publishers, Dordrecht

4. Putterman L, Skillman G (1988) The incentive effects of monitoring under alternative compensation scheme. Int J Ind Econ. 6:109–119
5. Holmstrom B, Milgrom P (1991) Multi-task principal-agent analyses: incentive contracts. Asset ownership and job design. J Law Econ Organ 7:24–52
6. Stanley B (2000) Information, contracting, and quality costs. Manag Sci 46(6):776–789
7. Bubshait AA (2003) Incentive disincentive contracts and its effects on industrial projects. Int J Project Manag 21:128–131

Chapter 3
Agent-Based Modeling of Water Bloom Formation Mechanism in Lakes and Reservoirs

Shuo-Qi Dong, Xiao-Yi Wang, Zai-Wen Liu, Ji-Ping Xu, Xiao-Ping Zhao and Xiao-Kai Wang

Abstract Based on Agent simulation technology, water bloom formation mechanism model in lakes and reservoirs is described by concept model design. Key factors of water bloom formation mechanism model are determined by experiments. And then there is an in-depth study of the relationship between key factors and algal growth and death mechanisms to determine the behavior rule of each Agent. In this series of constraints, the entities, Agent and the interactive cooperation of Agent are built to dynamically describe water bloom forming process and effectively analyze the energy and material flow state of the algal growth trends and water systems. It provides an effective conceptual modeling method for the further study of water bloom formation mechanism.

Keywords Water bloom · Formation mechanism · Agent · Modeling

3.1 Introduction

With the development of economy and society, the problem of eutrophication in lakes and reservoirs is becoming more and more serious. Under appropriate circumstances, algae can easily become the dominant species of phytoplankton and form water bloom. As a consequence, the structure of Lake Ecosystem changes with the function degeneration, and the water quality trapped into a rapid decline. According to the report on China's 2009 Environmental Status, in 26 key state-

S.-Q. Dong · X.-Y. Wang (✉) · Z.-W. Liu · J.-P. Xu · X.-P. Zhao
College of Computer and Information Engineering, Beijing Technology
and Business University, 100048, Beijing, China
e-mail: sdwangxy@163.com

X.-K. Wang
School of Physics and Electronic Engineering, Shanxi University, 030006, Shanxi, China

controlled lakes (reservoirs), class V accounts for 19.2%, class inferior V 34.6%, providing favorable conditions for the growth of algae. Therefore, digging into water bloom formation mechanism and simulating the outbreak of water bloom is of great importance to the promotion of environmental protection and technological progress.

In recent years, Agent-based modeling and simulation (ABMS) is gradually being concerned in the field of complex system modeling [1], make modelers more clearly understanding and grasping the relationship and interactions of entities and Agent in the system. The water bloom formation in lakes and reservoirs is a complex evolutionary dynamic process [2] along with the external environment and water internal evolution. ABMS is an effective means of studying complex system. On the base of the growth and death mechanism characteristics, the collaborative environment of eutrophication block entities is built to better simulate the entity modeling, behavior control and interaction collaboration in the process of water bloom forming.

3.2 Determine the Collection of Water Bloom Agent

In lakes and reservoirs water bloom forming process is essentially the process that autotrophic organisms (mainly phytoplankton) establish superiority in the water. In order to study the main factors affecting water bloom, a simulation training experimental platform is built in outdoor. Water samples from Yuyuantan are put into the sun room simulating the cultivation of water bloom.

It is needed to determine the collection of Agent $A = \{a_1, \ldots, a_i, \ldots, a_n\}$, in which $a_i \in \{♀|♀$ is (active && can_send_ms && can_receive_ms && can perceive && can react && can adaptive)$\}$, active represents initiative, can_send_ms represents sending messages, can_receive_ms represents accepting message, can perceive represents sensing the outside world, can react represents creating a feedback loop with the outside world, can adaptive represents self-adaption.

Chlorophyll a is the most direct indicator characterizing algae standing crops and the comprehension index reflecting phytoplankton biomass in water [3]. When the concentration of chlorophyll a >40 µg/L, it shows a good linear relationship between chlorophyll a and algal density whose correlation coefficient is above 0.8705, shown in Fig. 3.1a and b. Therefore Knowledge base and function modules all directly connect to the concentration of chlorophyll a.

Algal growth rate in lakes and reservoirs depends on three factors that are water temperature, light intensity and nutrient concentrations [4]. Among them, the water temperature is an important factor closely related to algal growth and death succession, it not only affects the physiological and biochemical responses of algae cells, but also the nutrient absorption and utilization rate of algae directly or indirectly by changing the water quality parameters related; light intensity is also an important environmental factor [5] affecting algal growth and toxin production, it is been used for photosynthesis by phytoplankton in water composing cellular material and storing energy, once algae photosynthesis is strengthened with other
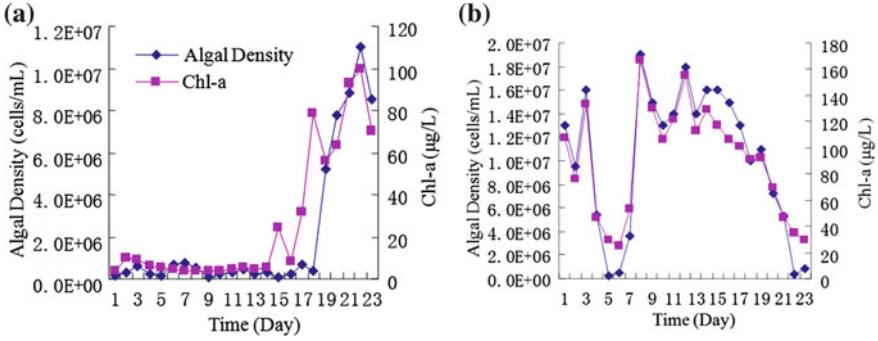
Fig. 3.1 Correlation analysis of algal density and chlorophyll a. (**a**) Comparable result of experiment one. (**b**) Comparable result of experiment two

factors appropriate, it is easy to outbreak water bloom; Phosphorus is an important element needed for biological growth, the concentration of total phosphorus is always the most important factor to limit phytoplankton growth, taken it as the main limiting factor in nutrient cycling of lakes and reservoirs.

Ultimately determine chlorophyll a, water temperature, light intensity and total phosphorus as the key Agent elements of water bloom Agent model. Each water bloom Agent element has its own knowledge, beliefs, memory strategies, goals and ability. While solving its own sub problem, Agent element obtains suggestions from others and responds to the changes in the environment so as to combine the qualitative and quantitative methods in system running process organically [6].

3.3 Knowledge Base of Water Bloom Agent Model

Algae is always experiencing the growth and death which are two opposite comprehensive processes through the ways of respiration, sedimentation, decomposition, predation, and etc. Therefore, the increment of chlorophyll a is closely related to algal growth rate, death rate and the net loss rate [7], the formula is as follows.

$$\frac{dc_a}{dt} = (G_p - D_p - m_p)c_a \tag{3.1}$$

In which, c_a is the concentration of chlorophyll a (mg/L), G_p is algal growth rate $(1/d)$, D_p is algal death rate $(1/d)$, and m_p represents the net loss rate $(1/s)$.

According to the water bloom formation mechanism and influenced conditions, algal growth rate G_p depends on three factors that are light intensity, water temperature and the concentrations of nutrient. By analysis and experiment, Di-Toro and other researchers believe that the combined effect these factors act on is equal to the product of every individual factor's influence, that is,

$$G_p = G(T) \times G(I) \times G(P) \tag{3.2}$$

Table 3.1 The calibrating parameter values

Parameter	Unit	Constraint	Calibrating value
G_{max}	$1 \cdot d^{-1}$	0.01–20	5.71
K_I	$w \cdot m^2$	0.01–10	0.01
K_p	$mg \cdot L^{-1}$	0.01–2	0.34
D_{max}	$1 \cdot d^{-1}$	0.01–30	0.20
m_p	$1 \cdot s^{-1}$	0.01–0.3	0.1

where $G(T)$, $G(I)$ and $G(P)$ are water temperature, light and phosphorus functions affecting algal growth rate. The functions can be expressed as

$$G(T) = G_{max} \times 1.066^{(T-20)}, \quad G(I) = \frac{I}{I + K_I}, \quad G(p) = \frac{TP}{TP + K_P} \tag{3.3}$$

Here, T is water temperature (°C), I is light intensity ($w \cdot m^2$), TP is the concentration of total phosphorus (mg/L), G_{max} is the maximum algal growth rate $(1/d)$, K_I is the half-saturation constant of light ($w \cdot m^2$), K_p is the half-saturation constant of phosphorus (mg/L).

Algal growth rate D_p can be obtained from the maximum algal growth rate D_{max}, that is,

$$D_p = D_{max} 1.08^{(T-20)}. \tag{3.4}$$

Solving the above formula, the formula of chlorophyll a changing with time is

$$
\begin{aligned}
c_a(t+1) = c_a(t) \\
+ \left[G_{max} \cdot 1.066^{(T-20)} \frac{TP}{TP + K_p} \cdot \frac{I}{I + K_I} - D_{max} \cdot 1.08^{(T-20)} - m_p \right] \\
\cdot c_a(t).
\end{aligned}
\tag{3.5}
$$

Select a section of data from the sun room with algal highest value, calibrate the parameter values using nonlinear optima model [8], and the results are shown in Table 3.1.

In the biochemical reaction process of TP, algae absorbs phosphorus when in growth, and releases phosphorus at the time of algal death. Therefore, the changes of TP are opposite to chlorophyll a, the formula can be expressed as

$$\frac{dTP}{dt} = (D_p + m_p - G_p) \cdot c_a \cdot A_{pp} + Q_{IP} - Q_{OP}. \tag{3.6}$$

In which, A_{pp} is the content of TP in algal cells (mg/mg), generally taking 0.22%; respectively, Q_{IP} and Q_{OP} are the inflow and outflow of phosphorus. Agent model is built on the basis of experiment with no inflow and outflow. To simulate the real situation, they are added in the model and given random values in an appropriate range.

Fig. 3.2 Construction of Agent simulation model for water bloom formation mechanism

3.4 Simulation Model of Water Bloom Formation Mechanism

After determining the collection of water bloom Agent and the behavior rules in knowledge base, the simulation model of water bloom formation mechanism is structured completely and shown in Fig. 3.2. The simulation model mainly consists of four modules, namely management module, decision module, monitoring module and implementation module.

Figure 3.2 shows that management module controls monitoring module and decision module, which is responsible for the selection of water bloom Agent, the adjustment of their initial values and the communication to decision module; monitoring module is responsible for regular collection of water bloom Agent data from the system, and feed back the changes of data to decision module by analyzing and processing; based on the received information from the management and monitoring module about Agent, decision module gives orders to implementation module, according to analyzing the impact relationship between Agent from the growth and death model of algae in lakes and reservoirs and knowledge base; implementation module receives the command and changes the behavior of water bloom Agent, thus achieving the interaction and communication between each Agent in the formation of water bloom.

Set the initial value of the water bloom Agent, run the dynamic simulation model of water bloom formation mechanism, and the concentration curve of

Fig. 3.3 Simulation result of water bloom Agent model. **a** Concentration curve of chlorophyll a. **b** Water bloom Agent dynamic model diagram

chlorophyll a and water bloom Agent dynamic model diagram can be obtained which are shown in Fig. 3.3a and b.

There are some differences between the simulation result and the actual data, but the overall trend is consistent. It is indicating the rational design for the knowledge base of water bloom formation mechanism, and the running result is credible.

3.5 Conclusion

Compared to other modeling methods, Agent-based modeling and simulation method has a higher level of abstraction and the ability to dynamically describe the autonomy of water bloom Agent. It achieves intelligent behavior modeling of water bloom Agent so as to make water bloom forming process more vivid, the simulation system more realistic and the entities, Agent and the interactive cooperation of Agent clearer. This method breaks the single-level and single-view limitations of the traditional mathematical modeling, provides a more realistic and effective way to describe and study water bloom forming process in lakes and reservoirs, and enhances the ability of awareness, management and control about the water bloom ecological disaster formation mechanism.

References

1. Li C, Xu L et al (2008) Multi-agent interaction and cooperation simulation using swarm of inter-basin water transfer [J]. J Syst Simul 20(8):2146–2151
2. Peng Z, Yang T et al (2006) Water environment mathematical model and application [J]. Chemical Industry Press, Beijing, pp 134–137
3. Liu Z, Lv S et al (2008) Forecast methods for algal bloom in rivers and lakes [J]. Water Resour Prot 24(5):42–47
4. Wu T, Gao G et al (2009) Analysis on factors inducing algal bloom in reservoir based on basin eutrophication model [J]. Shuili Xuebao 40(4):391–397
5. Gao T, Xin Q et al (2010) Effect of climate, hydrological and ecological processes on Yanghe Reservoir's Eutrophicaiton [J]. J Hydroecology 3(3):28–31
6. Saqalli M, Gerard B et al (2010) Testing the impact of social forces on the evolution of Sahelian farming systems: a combined agent-based modeling and anthropological approach [J]. Ecol Model 221(22):2714–2727
7. Hense I (2010) Approaches to model the life cycle of harmful algae [J]. J Mar Syst 83(3–4):108–114
8. Liu Z, Wu Q et al (2008) Algae growth modeling based on optimization theory and application to water-bloom prediction [J]. J Chem Ind Eng 59(7):1869–1873

Chapter 4
A Hardware-in-the-Loop System for Development of Automotive Battery Management System

Haifeng Dai, Xuezhe Wei, Zechang Sun and Jiayuan Wang

Abstract Battery management system (BMS) plays a vital role in the development of hybrid electric vehicles (HEVs), plug-in hybrid electric vehicles (PHEVs) and pure electric vehicles (PEVs). The vehicle management relies highly on the information transmitted from BMS. In this study, a battery pack-level hardware-in-the-loop (HIL) system is developed to verify the functions of BMS, including the cell voltage and temperature monitoring, battery voltage and current measurement, State of Charge (SOC) estimation, power relay and cooling fan control etc. By emulating different types of input signals to BMS, and at the same time detecting the output signals from BMS, the HIL system could verify and evaluate the BMS before it goes to mass-production, and thereby accelerate the BMS development and reduce the development costs.

Keywords Hardware-in-the-Loop · Battery pack-level · Battery management system · Function verification

4.1 Introduction

Driven by the wish for fuel saving technologies and sustainability of energy resources, it may be expected that new battery systems will be used in future automotive vehicles. In order to meet the high requirements regarding safety and reliability, the operation of the battery cells is monitored and managed by an electronic and electric system called battery management system, which typically has the functions to estimate and predict the SOC and available power of the

H. Dai (✉) · X. Wei · Z. Sun · J. Wang
School of Automotive Studies, Tongji University, 201804 Shanghai, China
e-mail: tongjidai@tongji.edu.cn

battery system, to prevent failures of the battery system due to external and internal conditions like short-circuit or due to imbalance of the battery cells.

To develop a BMS with high efficiency and reliability, the BMS could be done with a V-model [1] based process, where testing of hardware and software is already considered during the development. As one of the most important steps in V-model, the hardware-in-the-loop (HIL) has been extensively used in the automotive industry for component development and rapid prototyping [2]. With system-level requirements taken into consideration, HIL testing significantly reduces the time and cost of system-level integration and trouble-shooting later in the development cycle.

A few researches have been reported on the topic of HIL testing system development for BMS. Yongsheng He et al. [3, 4] developed a HIL system to verify the battery algorithm including the State of Charge estimation and power capability prediction for lithium-ion battery cells, especially for lithium iron phosphate battery cells. In this study, a cell-level HIL system is used to verify and develop the algorithms for various vehicle applications. Testing results indicate that the HIL testing provides valuable data and critical guidance to evaluate the accuracy of the developed battery algorithms, to accelerate battery algorithm future development and improvement, and to reduce hybrid/electric vehicle system development time and cost. Plett et al. [5] designed and implemented a HIL system to validate the BMS algorithm for hybrid electric vehicles. This study developed a validation strategy based in part on a data synthesis system to provide the missing "truth" data. The advantages and limitations of such a HIL system and how the HIL system works were also presented. This paper concluded that the HIL system can help to minimize the amount of testing that is required if a careful design-of-experiments approach is taken. Stefan Butzmann et al. [6] developed an integrated battery simulator (IBS) for development of automotive battery management systems. The presented IBS simulates the behavior of a real li-ion battery with up to 120 in series connected cells for the purpose of BMS testing. The IBS thus allows testing of the cell voltage monitoring functions, the charge balancing functions and of the software of the BMS. Li [7] and Wang et al. [8] have also been proposed a system-level and cell-level HIL system for BMS respectively.

This paper developed a battery pack-level HIL system to verify and test several functions of the BMS, including the cell voltage and temperature monitoring, battery voltage and current measurement, SOC estimation, power relay and cooling fan control etc. To get the target mentioned above, the HIL system emulates different types of input signals to BMS, and at the same time detects the output signals from BMS. This will allow the battery pack manufactures to accelerate the BMS development and reduce the development costs.

4.2 Battery Management System

Batteries employed in the EVs are often operated under arduous conditions, being subjected to both large dynamic transients in current and power demand over wide
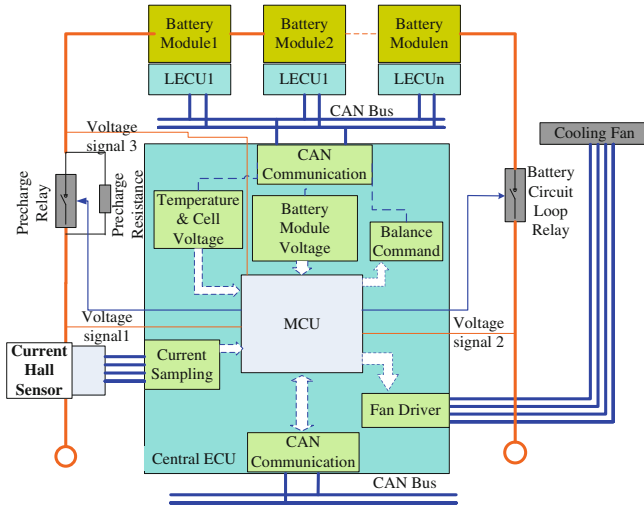
Fig. 4.1 Basic architecture of BMS

temperature range. The accommodation of such operation conditions requires a battery management system for the battery packs. Figure 4.1 shows the basic architecture of a typical level-based battery management system for lithium-ion batteries [9].

The voltage and current of the battery pack should be monitored to determine the SOC, State of Health (SOH) and calculate the maximum available power and/or energy. Those functions are realized in an Electronic Control Unit (ECU) called Central Electronic Control Unit (CECU). Besides, the CECU is also responsible for the power relay control and cooling fan control. Furthermore, since the battery pack is made up of up to hundreds of individual battery cells-often connected in series, the voltage of each individual cell has to be monitored for purpose of protection the cells from over-charge or over-discharge. For purpose of cell voltage and temperature monitoring, the battery is usually divided into several modules, each consisting of a specific number of cells, where the voltages and temperatures of the cells in the module are monitored by an ECU called Local Electronic Control Unit (LECU).

The LECU also has the task to provide charge balancing functionality. State of the art today includes the resistive charge balancing, where the cell voltages are adapted to each other by discharging of highly charged cells to the values of lower charged cells, and inductor/capacitor based energy shifting balancing, where the cell voltages are adapted to each other by discharging the highly charged cells and charging the lower charged cells. In most cases, the resistive charge balancing has a limited balancing effect (usually the balancing current is lower than 200 mA) due to thermal power dissipation, and the energy shifting balancing has a higher efficiency in cell balancing (normally the balancing current could be as high as 2A) [10].
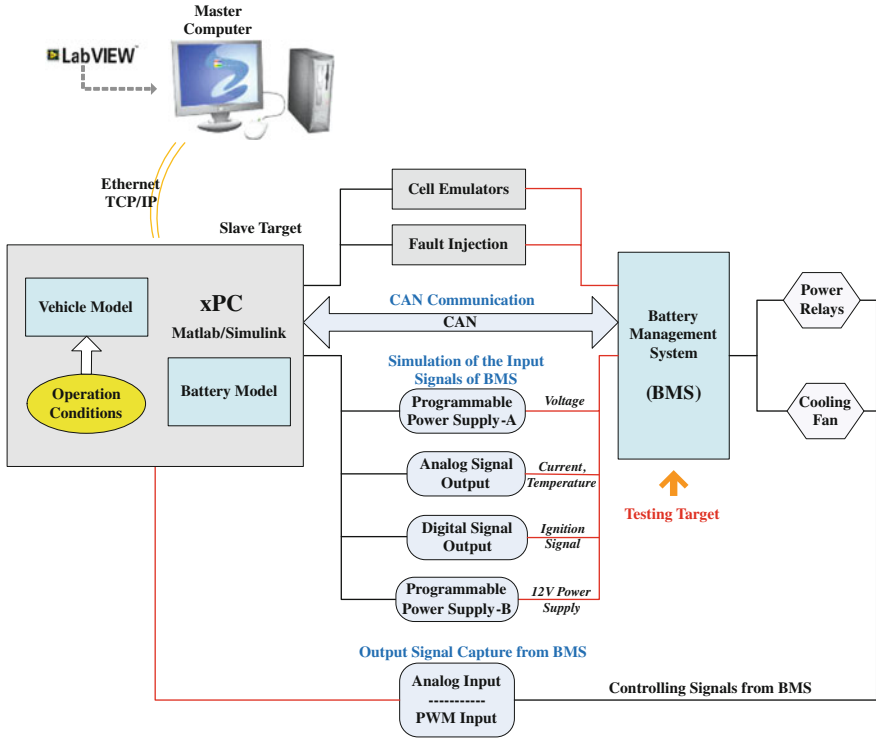
Fig. 4.2 Architecture of the HIL system

The BMS contains the microcontrollers including the periphery for controlling other functional blocks of the battery pack and for communicating both with external functional blocks in vehicle, like the vehicle management system (VMS) and within the internal BMS units (CECU and LECUs), as shown in Fig. 4.1. The microcontroller of the CECU triggers sampling of battery voltage and current and calculates the state of battery in order to determine all relevant parameters necessary for battery operation. For calculation of these parameters, a highly sophisticated battery state estimation/prediction algorithm is used [11]. In case of detection of a failure condition, the microcontroller also releases the power relays and thus disconnect the battery from the vehicle high voltage supply net.

4.3 HIL System Hardware Development

According to the evaluation target, the HIL system was designed with architecture and some key components as shown in Fig. 4.2 [7].

The programmable power supply-A (PPS-A) was recruited to emulate the high voltage of the battery pack, normally, the output voltage range is 48–400 V. The

cell emulator [8] was used to emulate the cell dynamics of a battery module, which could be connected in series. The fault injection unit (FIU) was used to generate some failure conditions to evaluate the performance and reliability of the BMS. The analog signal output unit was designed to emulate the temperature signal and current signal. The digital signal output unit was designed to generate ignition signal from the vehicle to control the working states of BMS. The programmable power supply-B (PPS-B) was used to provide the 12 V power supply to the BMS. The analog input and PWM input unit, together with power relays and cooling fans, are used to test the controlling functions of the BMS.

This system obviously was developed based on an xPC target-master computer architecture. The vehicle model, battery model and hardware drivers of the xPC target are designed and programmed in the Matlab/Simulink environment in the master computer. The models are at last compiled and downloaded into the xPC target, which offers a real-time environment for the model running. The slave xPC target controls the programmable power supply-A and -B, the analog signal output unit, which is designed with a PCI programmable board PCI-6733 by NI Co., and the digital signal output unit, which is designed with a PCI programmable board PCI-6528 by NI Co., to generate different voltage, current and temperature signals as the input signals of BMS, at the same time, it detects the output signal from BMS by the analog input and PWM input unit, which is composed of a PCI-6025 and PCI-6733 boards, and exchanges information with BMS by CAN communication.

Except for the designing and programming Matlab/Simulink models, the master computer has another important function-monitoring and operation interface. The monitoring and operation interface is developed with the LabVIEW platform. The interaction between the master computer and slave target is realized through Ethernet with TCP/IP protocols. The master computer sends different commands to the slave target to start different test programs, the slave target then runs corresponding models to generate the emulated signals to BMS, get key information from BMS and send to master computers to display and record.

4.4 Software of the HIL System

The software system includes the software for master computer and software for the xPC based real-time slave target. The software of the master computer is mainly responsible for test monitoring, data recording and other interaction with the slave target. And the software in the slave target is composed of several real-time models, including the power battery model, the vehicle model, and other models controlling and communicating with the peripheral testing modules, i.e. the cell emulators module, the analog input and PWM input unit, the power supply units, the analog signal output unit etc.
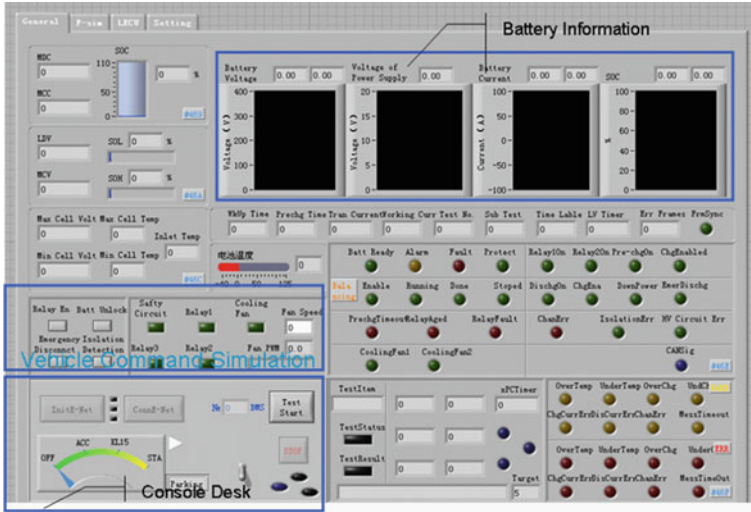
Fig. 4.3 General testing interface

4.4.1 Control and Display Panel

The software system of the master computer was developed in LabVIEW environment, which is a graphical program language released by NI Co. Software developed in LabVIEW is composed of two parts, one is the front panel, which is more like a human machine interface (HMI) with the function of display, operation etc., and the other is the program panel, which is the actual functional code of the software system. The general testing interface of the software of master computer is shown in Fig. 4.3.

4.4.2 Automatic Testing Design

To implement a more efficient test, the HIL system also supports an automatic testing process. An automatic testing configuration sub-program was inserted into the software system of the HIL. The principle of the automatic testing process is shown in Fig. 4.4.

By a test configuration file, one can predefine each sub-test and the orders, then the HIL software system will read the test configuration file. Once the automatic test was enabled, the software will start the test process from the very first one defined in the configuration file and end until all pre-defined tests finished.

Fig. 4.4 Automatic testing
schedule
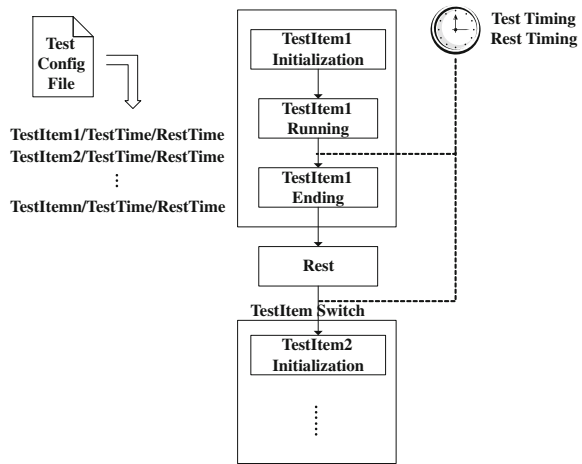
Fig. 4.5 Software structure
of xPC target
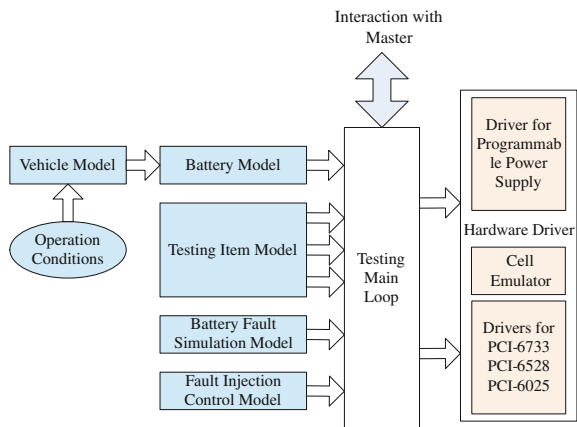
4.4.3 Software Architecture of xPC Target

Software in the xPC target is mainly composed of several real-time models,
including the vehicle model, battery model, the testing item model, battery fault
simulation model and fault injection control model. The software architecture of
the xPC slave target is shown in Fig. 4.5.

In this software system, the testing main loop is responsible for the scheduling
of the different models, and responsible for the interaction with master and the
base hardware. The battery model, embedded into the vehicle model, and com-
bined with the operation conditions, calculates the current and power of the battery
system, and transmits the values to the testing main loop which interacts with the
base hardware to convert the values to electric signals. The battery model also is
used to generate target voltage for the cell emulators. The testing item model is
responsible for the schedule of different testing tasks with a specific rule. The

Fig. 4.6 Current emulation and measurement results
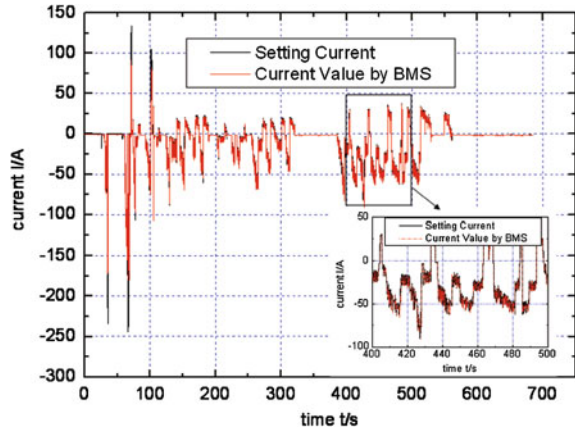
Fig. 4.7 Voltage emulation and measurement results
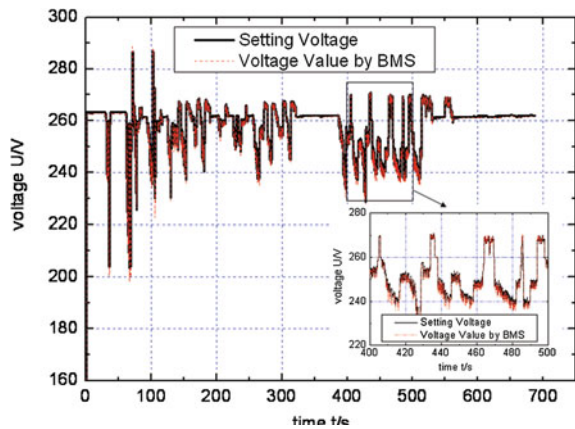
battery fault simulation model generates some cell faults like cell over-charge, over-discharge, over-temperature etc., to test the fault detection functions of the BMS, and fault injection control model is responsible to simulating different faults to test the fault-tolerance of the BMS. Hardware drivers are responsible for the controlling of the base hardware, including the PPS units, the PCI boards and cell emulators.

4.5 Initial HIL Experimental Results

Figure 4.6 shows the emulated current of the battery system, and the current measurement value sent from BMS is also plotted in this figure, which could evaluate the current measurement accuracy of the BMS, and at the same time, the

Fig. 4.8 SOC estimation result from BMS under test
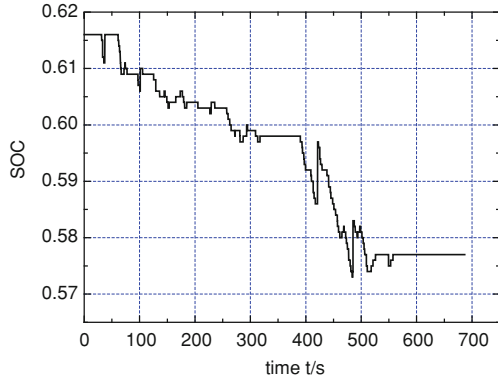
Fig. 4.9 Emulated cell voltage variation under balancing
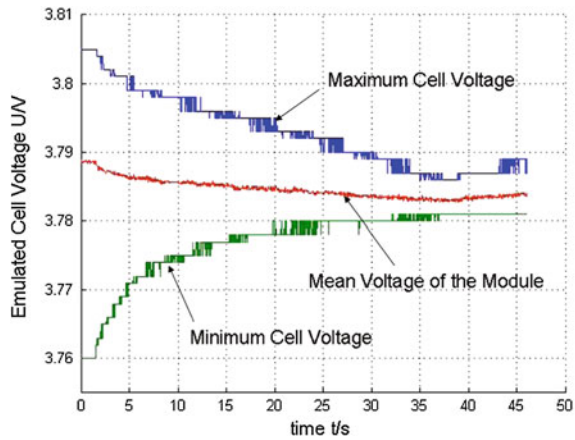
voltage emulated and measured by BMS are shown in Fig. 4.7. Figure 4.8 shows the SOC variation during the testing sent from BMS, which could evaluate the SOC estimation function of the BMS.

In Fig. 4.9, two channels with different output voltage are taken as the example to show the voltage variation and balancing effects when the balancing function of LECU is under test. The balancing is implemented with an inductor based energy shifting method [12]. The testing results indicated the effectiveness of the cell emulator on the balancing test.

4.6 Summary

A battery pack-level HIL system was developed and implemented to validate and evaluate the battery management system for power batteries, especially for lithium-ion batteries used on EVs. Thereby a systematic verification and evaluation

methodology has been formulated to verify the functions of BMS and evaluate the reliability of BMS under different working conditions.

The HIL system is mainly composed of several critical units, which emulate different types of input signals to BMS, and at the same time detect the output signals from BMS. This system allows not only the HIL tests of BMS under considerable working conditions, but also fast ageing simulations of battery cells as well as testing of BMS operation in conditions of failures.

The HIL testing system could help to provide critical testing data which guides for the further development and improvement of the BMS, although the testing system will not be substitute for actual testing of real working conditions. Therefore, with the HIL system introduced here, the battery pack manufactures could accelerate the BMS development and reduce the development costs.

References

1. Pankiewitz C, Cois O, Heubner A, Soboll S (2009) Model based development of lithium-ion battery systems. In: Proceedings of 9th stuttgart international symposium on automotive and engine technology. March, pp 333–343
2. Bullock D, Johnson B, Wells RB, Kyte M, Li Z (2004) Hardware-in-the-loop simulation. Trans Res Part C: Emerg Technol 12:73–89
3. He YS, Liu W, Koch BJ (2010) Battery algorithm verification and development using hardware-in-the-loop testing. J Power Sources 195:2969–2974
4. He YS, Liu W, Koch BJ (2010) Power capability testing of a lithium-ion battery using hardware in the loop. SAE 2010 World congress and exhibition, 2010-01-1073
5. Plett GL, Billings R, Klein MJ (2007) Desktop and HIL validation of hybrid-electric vehicle battery-management-system algorithms. SAE 2007 World congress and exhibition, 07AE-304
6. Butzmann S (2009) Integrated battery simulator for development of automotive battery management systems. In: Proceedings of 9th stuttgart international symposium on automotive and engine technology, pp 345–353
7. Li YH, Sun ZC, Wang JY (2009) Design for battery management system hardware-in-loop test platform. In: Proceedings of ICEMI, pp 399–402
8. Wang Q, Wei XZ, Dai HF (2010) Hardware-in-loop test platform for electric vehicle cell battery management system. Appl Mech Mater: Appl Mech Mech Eng 29:2398–2403
9. Sun ZC, Wei XZ, Dai HF (2008) Battery management systems in the China-made "Start" series FCHVs. In: Proceeding of IEEE vehicle power and propulsion conference, 978-1-4244-1849-7/08
10. Moore SW, Schneider PJ (2001) A review of cell equalization methods for lithium ion and lithium polymer battery systems. SAE 2001 World congress and exhibition, 2001-01-0959
11. Dai HF, Wei XZ, Sun ZC (2007) Model based SOC estimation for high-power li-ion battery packs used on FCHVs. High Technol Lett 13:322–326
12. Wei XZ, Zhu B (2009) The research of vehicle power li-ion battery pack balancing method. In: Proceedings of IEEE Electronic Measurement and Instruments, pp 498–502

Chapter 5
A Master–Slave System for Intelligent Visual Surveillance

Bin Xiong and Xiaoqing Ding

Abstract In developing intelligent visual surveillance systems, the wide monitoring range and close-up view of target place conflicting constrains on the system configurations and camera parameters. This paper proposed a master–slave solution. The system consists of a static camera, which detects the moving targets in its wide view, and a Pan-Tile-Zoom (PTZ) camera, which recognize the corresponding target and tracks it for close-up view. Result of an indoor experiment demonstrates that the proposed method is quite effective.

Keywords Visual surveillance · Master–slave · Pan-tile-zoom camera

5.1 Introduction

Visual surveillance system is more and more prevalent in our lives, especially in airports, banks, parking lots, and so on. Most of the practical applications of visual surveillance are just the recorder systems, which only provide the recorded video, and users can only review them afterwards. Therefore, intelligent visual surveillance system based on computer vision is attracting growing interest.

In the past years, researchers have developed various kinds of intelligent visual surveillance systems [1]. Pfinder system [2] uses a static camera to detect and track indoor single human target, and also can analysis its posture. VSAM system [3, 4]

B. Xiong (✉) · X. Ding
Department of Electronic Engineering, Tsinghua University,
100084 Beijing, China
e-mail: xiongbin@ocrserv.ee.tsinghua.edu.cn

D. Xiaoqing
e-mail: dingxq@tsinghua.edu.cn

aims at outdoor targets of pedestrian or vehicle, and builds a multi-camera network to monitor activities in a cluttered environment. W4 system [5] is a real-time surveillance system to detect and track human and their body parts.

Generally, visual surveillance systems prefer to get wide monitoring range. So cameras with wide field-of-view are preferred. In some researches, multi-camera network is used, in order to cover wider area. Meanwhile, close-up views of specified objects are required for further identification or analysis. In these cases, cameras with narrow field-of-view are preferred. Therefore, these place conflicting constraints on the system configurations and camera parameters.

In this paper, a solution using a master–slave configuration is proposed. A static camera with wide field-of-view is used as the master camera and a Pan-Tile-Zoom (PTZ) camera is used as the slave camera in the system. Similar solutions are mentioned in [6–11]. In most of these researches, a calibration of cameras is needed in order to build the corresponding relations of the cameras. But in the proposed solution, no calibration process is needed, and the correspondence of the targets is only based on their appearances. Firstly we detect and track the moving target in the video of the master camera by background subtracting. Then we apply the image matching method based on key-points to detect the corresponding target in the video of slave camera. Finally, we control the motion of PTZ camera to track the target and zoom into obtain the close-up images.

5.2 Master Camera Process

Since the master camera is static, the targets of interest would be the moving objects against the stationary background in the video stream. Therefore, we use the background subtracting method to detect the moving targets. Considering the complexity of various scenarios, including the lighting changes, scene changes and moving objects, we model the background of video using the Mixture of Gaussians (MOG) [12], which is one of the commonly used methods, and detect the moving targets by subtracting the modeled background.

Figure 5.1 demonstrates the results of the background subtraction. The images of the first row are original images from the master camera, and the images of the second row are the binary images of results, where highlight represents the foreground.

Based on these foreground images, a blob detection approach based on connected regions and contour analysis is introduced to locate the targets. Relatively, the areas of targets in the master images are very small because of the wide field-of-view. Thus, we just obtain the locations of the targets and track them individually by Kalman Filtering [13] in order for continuously labeling.

Though the master process is able to handle multiple targets simultaneously, the slave process can only focus on one target at one time, because of its narrow field-of-view. So, after detecting and tracking, one of the targets will be specified for a

Fig. 5.1 Examples of background subtracting

close-up view for further identification or analysis. This selecting process could be done automatically or manually according to the different purposes of the applications.

5.3 Slave Camera Process

Firstly, at the initial stage, we set the slave camera aiming at the center of the scenario as the master camera, and zoom the lens to make the field-of-view as close to the master camera as possible. Then, the view of slave camera is very similar to the view of master camera, though there may be differences in scale, rotation, lighting, viewpoint, or other imaging conditions.

After specifying the interesting target in the view of master camera, we use an image matching method based on SIFT [14] to recognize the corresponding target. This key-point based method is very robust to the differences in imaging conditions.

Figure 5.2 shows an example of recognizing result. The left image is from master camera, and the rectangle box indicates the location of interesting target. The right image is from slave camera, and the rectangle box, which indicates the location of corresponding target, is estimated by the matching key-points.

Secondly, after recognizing the target in the view of slave camera, we use a classifier based method [15] for tracking. Since the slave camera is a PTZ camera, the viewing angle and the zooming of the camera are not stationary. Therefore, general tracking methods that only use spatial features, such as location and size, would not be effective. The introduced algorithm makes full use of the appearance of the target and the background, and integrate generative and discriminative model in both offline and online learning. Also, it can deal with the condition of few samples in the early stage of tracking which is a central issue of the classifier based tracking approaches. The biggest drawback of this method is that once the tracking deviates from the true target, it will be hard to correct itself because of the online learning. To overcome this problem, the matching process
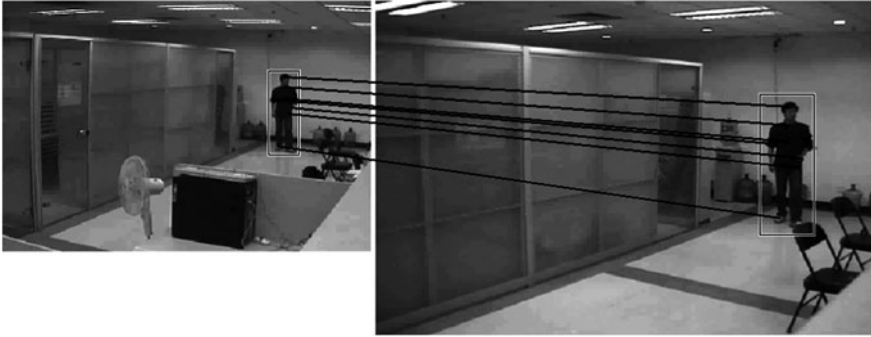
Fig. 5.2 Recognition of specified target using matching method based on SIFT. *Left* is from master camera, and *right* is from slave camera. *Rectangle boxes* indicate the targets, and *lines* between the two images indicate the matching key-points

with the view of master camera could be repeated after some period of time to check and correct the result of tracking.

Thirdly, while tracking the target, we control the mechanical motion part of the PTZ camera to rotate the angle of view in order to center the target, and control the zooming part of the PTZ camera to gradually get the proper field-of-view in order to obtain the close-up view of the target.

Finally, when the tasks of identification or analysis have been completed, the motion and zooming part of the PTZ camera will be reset to the initial position, and the next specified target of interest will be treated as the same process.

5.4 Result of Experiment

We take an experiment of an indoor scenario for example. Figure 5.3 shows the results. It can be seen that, the master–slave system performance great for intelligent visual surveillance task. While the master camera cover the wide range of scenario, the slave camera can rotate and zoom to "catch" the interesting target and obtain the close-up images.

From the results of experiment, the proposed solution of master–slave configuration is quite effective for the task of intelligent visual surveillance. The field-of-view of the master camera is much wider than the slave camera, so that it can guarantee the detection rate of the target in a wide monitoring rage. Meanwhile, the slave camera is very flexible. Though its field-of-view is very narrow, it can move its view angles to continually tracking the target, and can zoom into obtain the close-up images. The resolution of slave camera is much higher than the master camera, so that the face detection methods can performance great for the slave images, and that is very important to the surveillance system. Other processes of recognition and behavior analysis for the targets will greatly benefit from the close-up images, while not sacrificing the wide surveillance range.
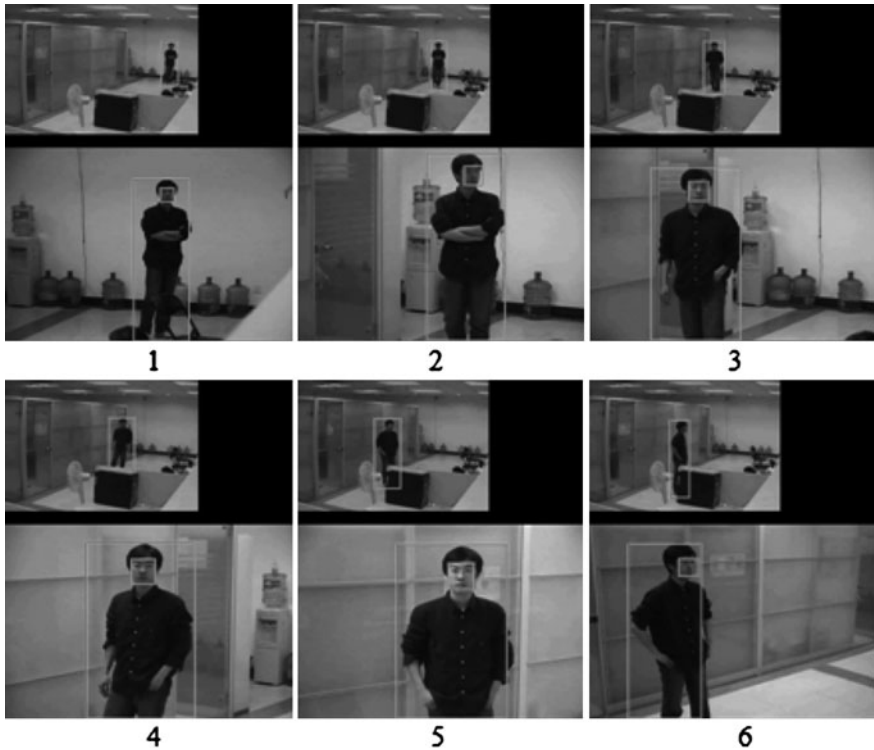
Fig. 5.3 Examples of the result. The upper one of each result image indicates the view from the master camera, with detected targets marked by *rectangle boxes*. The lower one indicates the view from the slave camera, where the corresponding targets are marked by *rectangle boxes* too. Besides, there are *small boxes* in the slave images that indicate the face detecting results

5.5 Conclusion

In this paper, we proposed a solution for intelligent visual surveillance, using a master–slave configuration. For the view of master camera, we use a background subtracting method based on Mixture of Gaussians (MOG) model to detect the moving targets. For the view of slave camera, we use a matching algorithm of SIFT to recognize the corresponding target. Then we track the target with a classifier based method, and control the rotating and zooming part to "catch" the target. It provided one of the solutions to the conflict between wide surveillance range and close-up images of targets. The two parts of the system have got their respective focuses, and matching algorithms connect them together with the objects' features. Result of experiment shows that this solution is quite effective.

References

1. Hu W, Tan T, Wang L, Maybank S (2004) A survey on visual surveillance of object motion and behaviors. IEEE Trans Syst Man Cybern Part C: Appl Rev 34:334–352
2. Wren CR, Azarbayejani A, Darrell T, Pentland AP (1997) Pfinder: real-time tracking of the human body. IEEE Trans Pattern Anal Mach Intell 19:780–785
3. Collins RT, Lipton AJ, Kanade T, Fujiyoshi H, Duggins D, Tsin Y, Tolliver D, Enomoto N, Hasegawa O, Burt P, Wixson L (2000) A system for video surveillance and monitoring: VSAM final report
4. Lipton AJ, Fujiyoshi H, Patil RS (1998) Moving target classification and tracking from real-time video. In: Proceedings of the fourth IEEE workshop on applications of computer vision
5. Haritaoglu I, Harwood D, Davis LS (2000) W4: real-time surveillance of people and their activities. IEEE Trans Pattern Anal Mach Intell 22:809–830
6. Jain A, Kopell D, Kakligian K, Wang Y-F (2006) Using stationary-dynamic camera assemblies for wide-area video surveillance and selective attention. IEEE Comput Soc Conf Comput Vis Pattern Recognit 1:537–544
7. Horaud R, Knossow D, Michaelis M (2006) Camera cooperation for achieving visual attention. Mach Vis Appl 16:331–342
8. Peixoto P, Batista J, Araújo H (2000) Integration of information from several vision systems for a common task of surveillance. Robot Auton Syst 31:99–108
9. Senior AW, Hampapur A, Lu M (2005) Acquiring multi-scale images by pan-tilt-zoom control and automatic multi-camera calibration. In: Proceedings of the seventh IEEE workshops on application of computer vision, pp 433–438
10. Zhou X, Collins RT, Kanade T, Metes P (2003) A master–slave system to acquire biometric imagery of humans at distance. In: Proceedings of 1st ACM workshop on video surveillance
11. Badri J, Tilmant C, Lavest J-M, Pham Q-C, Sayd P (2007) Camera-to-camera mapping for hybrid pan-tilt-zoom sensors calibration. Scandinavian conference on image analysis
12. Stauffer C, Grimson W (1999) Adaptive background mixture models for real-time tracking. IEEE Conf Comput Vis Pattern Recognit 2:246–252
13. Kalman RE (1960) A new approach to linear filtering and prediction problems. J Basic Eng 82:35–45
14. Lowe DG (1999) Object recognition from local scale-invariant features. International conference on computer vision
15. Lei Y, Ding X, Wang S (2008) Visual tracker using sequential bayesian learning: discriminative, generative and hybrid. IEEE Trans Syst Man Cybern Part B 38:1578–1591

Chapter 6
A Method of Detection and Tracking for Laser Spot

Yanpeng Sun, Bo Wang and Yingshuo Zhang

Abstract A method of target tracking based on fractional Fourier transform is proposed by using the time–frequency information of target image, in order to improve the accurate performance of target recognition and tracking. Firstly, removing the Gaussian noise from target image using the repeated fractional Fourier domain filtering algorithm. And then the edge of target image is extracted making use of the continuity of FRFT. Finally, calculating the Hausdorff matched distance between the point set of edge of the target template and the region which is going to be matched, and making the target be searched and locked stably to complete the tracking of moving targets. The simulation results show that, under the precondition of real-time, the method which based on FRFT tracking have more precision on the track of the target than kalman filtering tracking and mean-shift tracking.

Keywords Target tracking · Fractional Fourier transform · Edge detection

6.1 Introduction

The detection and tracking technology for Moving object is one of an important content in computer vision research. It is widely used in range of applications such as navigation on Robot vision, monitoring for public scene, guidance for military visual, intelligent traffic and so on [1, 2]. In recent years, the algorithm of target tracking research has had great progress, as it is used in different occasions, there

Y. Sun · B. Wang (✉) · Y. Zhang
School of Electronics Information Engineering, Shenyang University of Aerospace, 110136
Shenyang, China
e-mail: wangbo881112@163.com

are significant differences on the content of the algorithms. Generally speaking, the algorithm may be divided into several methods, based on template matching, characteristic, motion and the detection of the tracking method. The accuracy of target detection can directly affect the follow-up tracking, so it is a key issue whether we can detect goal accurately.

In order to detect the goal accurately, the first, it is to take feature extraction of target. The discontinuity gray of image can be reflected by image edge information, it make a performance for the strength of the mutation. With the feature of relative stability and not sensitive to light conditions change, the image edges can be used for the important characteristics of identification and tracking. At p resent the image edge detection mainly apply in the airspace such as Roberts, Sobel, Canny [3, 4], Fourier transform domain and the wavelet transform domain.

A new method of edge detected based on fractional Fourier domain is proposed in this paper, and it may do target identification and tracking. FRFT is a kind of generalized form Fourier transform and a new kind of time–frequency analysis tools in rapid development phase of recent years [5]. FRFT is applied in the field of target tracking, and uses the method of image feature analysis on fractional Fourier domain and the relationship between FRFT and the optical image. The edge of target can be detected accurately in using this method on time–frequency domain, and it has higher precision compared to traditional airspace edge detection.

6.2 Fractional Fourier Transform (FRFT)

FRFT is a kind of generalized form Fourier transform. It can be considered as a rotation by an angle α in the time–frequency and therefore there exists an order of transformation in which such signals are compact. The FRFT is also defined with the help of the transformation kernel K_α as

$$K_\alpha(t,u) = \begin{cases} \sqrt{\frac{1-j\cot\alpha}{2\pi}}\exp\left(j\frac{t^2+u^2}{2}\cot\alpha - tu\csc\alpha\right), & \alpha \neq n\pi \\ \delta(t-u), & \alpha = 2n\pi \\ \delta(t+u), & \alpha \neq (2n\pm1)\pi \end{cases} \tag{6.1}$$

The FRFT is defined using this kernel as

$$X_\alpha(u) = \{F^\alpha[x(t)]\}(u) = \int_{-\infty}^{\infty} x(t)K_\alpha(t,u)dt \tag{6.2}$$

For angle α varying from 0 to p, the value of $p(\alpha = p\pi/2)$ lies from 0 to 4 and it can be shown that the transform kernel is periodic with a period 4. While FRFT for two-dimensional signal can be defined with the help of the transformation kernel $K_{p1,p2}(s,t,u,v)$ as

$$K_{p1,p2}(s,t,u,v) = \frac{1}{2\pi}\sqrt{1-j\cot a}\sqrt{1-j\cot \beta} \times e^{\left[j(s^2+u^2)/2\cot \alpha - jsu\csc \alpha\right]}$$
$$\times e^{\left[j(t^2+v^2)/2\cot \beta - jtv\csc \beta\right]} \tag{6.3}$$

The FRFT is defined using this kernel as

$$X_{p1,p2}(u,v) = F_{p2}^{y\to v}\left\{F_{p1}^{s\to u}[x(s,t)]\right\} = \int_{-\infty}^{\infty}\int_{-\infty}^{\infty}x(s,t)K_{p1,p2}(s,t,u,v)dsdt \tag{6.4}$$

where $\alpha = p_1\pi/2$, $\beta = p_2\pi/2$ are the rotation angle of FRFT, both can be the same or different. After discretization, the two-dimensional FRFT can also be used to calculate by digital method. Some two-dimensional single change has been applied in signal processing, such as discrete cosine transform, discrete Walsh transform. The Single discrete fractional Fourier transform for matrix of $M \times N$ can be expressed with the help of the transformation kernel $\psi_{\alpha,\beta}$ as

$$X_{\alpha,\beta}(m,n) = \sum_{p=0}^{M-1}\sum_{q=0}^{N-1}x(p,q)\psi_{\alpha,\beta}(p,q,m,n) \tag{6.5}$$

With inverse transformation is

$$x(p,q) = \sum_{p=0}^{M-1}\sum_{q=0}^{N-1}X_{\alpha,\beta}(m,n)\psi_{-\alpha,-\beta}(p,q,m,n) \tag{6.6}$$

Unpack format can be defined as

$$\psi_{\alpha,\beta} = \psi_a \otimes \psi_\beta \tag{6.7}$$

where ψ_a, ψ_β are the transformation kernel of one-dimensional DFRFT, $\otimes$ is tensor product, α, β in their two-dimensional is the order of fractal dimension.

When $\alpha = \beta = \pi/2$, the two-dimensional DFRFT transforms into the traditional DFT;

When $\alpha = \pi/2$ and $\beta = 0$, the two-dimensional DFRFT proceed row DFT;

When $\alpha = 0$ and $\beta = \pi/2$, the two-dimensional DFRFT proceed column DFT [6–8].

So the numerical calculation for two-dimensional DFRFT can be calculated through row and column on the base of one-dimensional DFRFT.

6.3 The Method of Target Trackingtarget tracking on FRFT

The process of target tracking can be divided into such five parts: the acquisition of moving target, image filtering, image enhancement, target detection and target tracking [9].
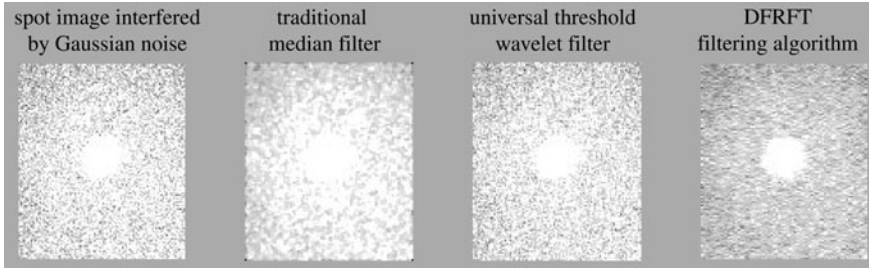
Fig. 6.1 The comparison of filter result

(1) *Image Filtering*. The signal spectrum and noise spectrum have strong coupling, and the spectrum is almost always a distribution throughout the frequency domain. The traditional filtering methods are difficult to realize signal–noise separation effectively. In this kind of situation, filtering method on fractional Fourier domain can be used. Using MSE minimum estimate algorithm to estimate parameters of the noising image and to receive fractional orders (p_1, p_2) of those rows and columns [10]. The rows and columns contain high content signal components. The aim is to identify the distribution of signal energy in the time–frequency plane, to obtain the corresponding filter parameters. Choose the type of Gaussian filter function h, because we want to remove the Gaussian noise from spot image, using two-dimensional DFRFT to make the chosen filter function switch to the ranks p_1, p_2. Then multiply with noisy images in this fractional domain. Use two-dimensional fractional Fourier inverse transform to restore to the time domain, to obtain the filtered noise images.

The Fig. 6.1 shows the results of the traditional median filter, universal threshold wavelet filter and DFRFT filter. From the image contour of filtering results we find the DFRFT filtering algorithm can better improve the quality of the image, compared with the traditional median filter and universal threshold wavelet filtering method. It can restore flare image from strong noise background and lay a good foundation for the follow-up target identification and tracking.

(2) *Target Detection*, focusing on the detection of image edge.

Do series FrFT on target image. According to the definition of FRFT, do FRFT on the image, and the result is a rotation of the original image in α domain. It is equivalent to do tiny mobile for the plane of images if tiny order time on FrFT is choosed (Fig. 6.2). It is difficult to discern the difference with naked eye between the original image and the transformed image, when the order time on FrFT is very small; But as the order time on FrFT increasing, compared with the edge of original image, it has small changes for the transformation of the image, and compared with the part of similar size of image pixels, the changes are not abvious. It can be concluded that the low contrast of the image will change slow, and the high contrast part such as image edge will change fast in the process of the fractional order time gradually increasing.
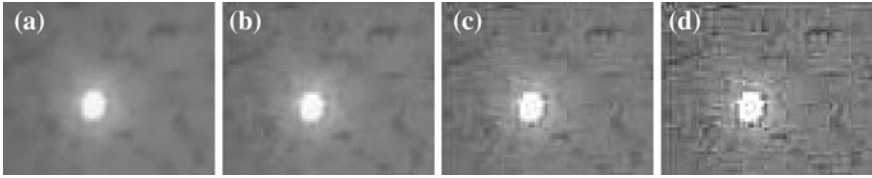
Fig. 6.2 FRFT of spot image with small order
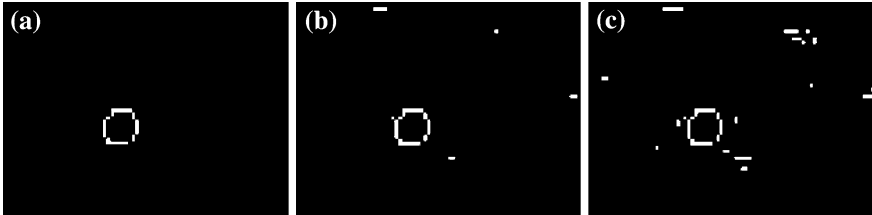
Fig. 6.3 The edge detection of spot image based on FRFT

In Fig. 6.2, (a) is the original image, (b) is the frft with order 0.01 on original image, (c) is the frft with order 0.02 and (d) is the frft with order 0.03. when p = 0.01, it has a little difference between transformed image and original image, with the increase of order, the changes of image edge is more and more obvious.

You will get image edges after the subtraction of transformed image and the original image. $f(x, y)$ is used to represent the transformed image and $h(x, y)$ represents the original image, so the edges of image can be represented as $g(x, y) = f(x, y) - h(x, y)$. Subtraction plays an important role in enhancing the differences between the two images. See Fig. 6.3a–c correspond to the subtractions of Fig. 6.2b–d and original image.

(3) *Target tracking*. The feature points of the target are extracted as a template, and Hausdorff is used to calculate the distance between edge points and the point set of template matching area. The most direct thought is whether the edge points data can be reduced effectively, if yes, the whole amount of algorithm can be reduced. The last step of edge detection on FRFT can set a higher threshold, and it can reduce the number of point set of the edge significantly. When do the followed matching operation of a frame image edge, in order to avoid repeated computation, an area of the matched image is applied, the position of calculated edge point of image can be saved to the next frame matching directly. The optimum method can improve execution speed greatly.

6.4 The Experimental Results and Performance Analysis

In order to validate the effectiveness of this method, it also needs to be validated and analyzed. The edge matching method itself should be proved, then the

| Frame 5 | Frame 25 | Frame 55 | Frame 75 |
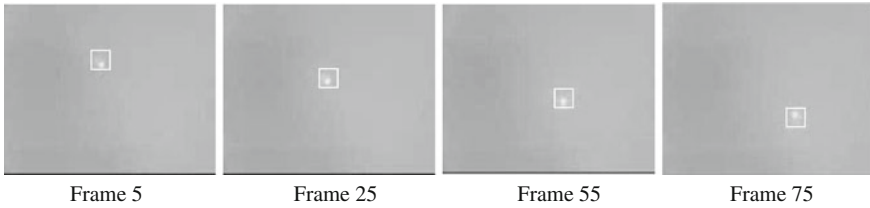
Fig. 6.4 Results figure on target tracking

effectiveness of tracking is verified. The sport laser flare images are researched as experiment in this paper. In initial selection, the size of the goals flare image is 13×13, and make it as a template image, the point of pixel [66, 32] is the center of target. Edge template matching method is used to do the follow-up tracking. The experimental results of edge template matching tracking are shown in Fig. 6.4, the frames of target image respectively are 5, 25, 55 and 75. From the graph, a clear and reliable tracking process can be obtained making use of our algorithm.

Some other methods of image tracking can also be used for the experiment of the laser flare movement, then the results of the experiment are given and analyzed. Kalman filtering and Mean-shift target tracking method are used respectively to get the movement of the target real trajectories, then the real trajectory and the results of tracking trajectory by three tracking method are compared and analyzed. The orbit curves through three methods and the position of the real target tracking point are shown in Fig. 6.5, the high position of target is shown as (a–c) are given as width position of target and comprehensive position of Target.

In the figure, compared with the method of Kalman filter and the target tracking based on mean-shift, using the method of tracking based on FRFT can get a closer position to real target in each frame, relative to the location of the real object coordinates, it is same or it has a small change, which explains that the tracking of this method is stronger on accuracy. This can also be confirmed by the actual data, the accuracy of edge tracking on FRFT is about 97.94%, the Kalman filter is about 95.56% and the mean-shift is about 96.86%. About real-time, on the same operation environment and for a frame video, the matching time based on edge of FRFT is 899.58 ms, and based on kalman filter and mean-shift are respectively 169.45 and 225.52 ms. Although it consumes some time to do FRFT transform on image, but its real-time can also be guaranteed basically.

6.5 Conclusion

A new method of target tracking is proposed in this paper, by using the analysis of image feature on FrFT and the relationship between FRFT and the optical imaging. FrFT is taken to the field of target tracking, it can remove the noise of the time–frequency coupling effectively and be able to detect the target image edge
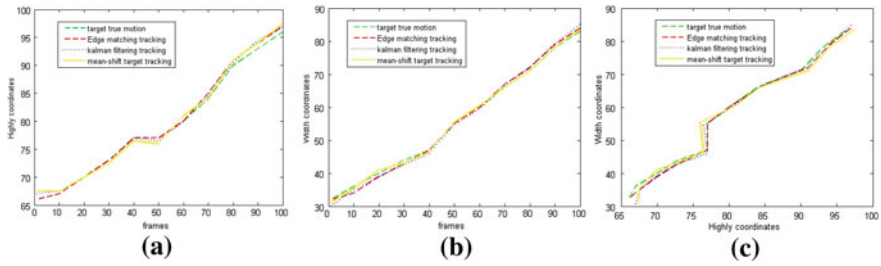
Fig. 6.5 The track curve of tracking point position and real target position. **a** High position of target. **b** Width position of target. **c** Comprehensive position of target

accurately, it take a great contribution to the subsequent target tracking. The laser flare movement images are selected to do the experimental research, and FRFT is used for filter and edge detection. Targets can be locked stably through Hausdorff distance matching calculations of the edge of point set. The simulation results show that, compared with the method of Kalman filter and the target tracking based on mean-shift, using the method of tracking based on FRFT can track the target more accurately.

References

1. Xiao W, Sen Z, Lin J (2010) Energy-efficient adaptive sensor scheduling for target tracking in wireless sensor networks. J Control Theory Appl 8:86–92
2. Zhang J, Pan J, Wu Y (2009) Target tracking and measuring of sports based on binocular vision. Comput Eng Appl 45(25):191–194
3. Chen R (2011) Early fire detection of large space combining thresholding with edge detection techniques. Appl Mech Mater 44:2060–2064
4. Tello Alonso M, Lopez-Martinez C, Mallorqui JJ, Salembier P (2011) Edge enhancement algorithm based on the wavelet transform for automatic edge detection in SAR images. IEEE Geosci Remote Sens Soc 49(11):222–235
5. Rajesh K, Rajiv S (2010) A novel FRFT beamformer for Rayleigh faded channels. Wirel Pers Commun 52:693–707
6. Ran T, Deng B, Wang Y (2009) Fractional fourier transform and its application. Tsinghua university press, BeiJing, pp 12–49
7. Tao R, Deng B, Zhang WQ et al (2008) Sampling and sampling rate conversion of band limited signals in the fractional Fourier transform domain. IEEE Trans Signal Process 56(1):158–171
8. Tao R, Zhang F, Wang Y (2008) The research progress of the discrete fractional Fourier transform. J Chin Sci 38
9. Zhang K, Liu Z (2008) The research of edge template matching tracking algorithm on Ir seeker. J Northwest Polytech University 26(3):303–307
10. Chen X, Yu S, Guan J, He Y (2010) A method about moving object detection based on FRFT in sea clutter adaptive. Signal Process 26(11):1613–1620

Chapter 7
Analysis of Starting Process for Medium-Sized Induction Motors With High-Voltage

Yunyan Xia, Dawei Meng, Yongming Xu and Yufeng Lu

Abstract In order to more accurately analysis the starting process of medium-sized motors with high-voltage, the dynamic model of three-phase induction motor was established. The starting characteristics of the new medium-sized motors with high-voltage were calculated, based on this, the stator and rotor temperature rise was calculated, combined with the heat dissipation mode the amount of time for motors to reach thermal equilibrium was calculated. Compared with the steady-state characteristic curve, the dynamic characteristic curve is much closer to the practical situation and the temperature rise is in accord with the experimental value.

7.1 Introduction

The medium-sized motor with high-voltage is one of the electrical industry leading products. Its starting process has been the concerns of people. The most important problem is the starting characteristics and temperature rise. Compared with small motors, high-voltage motor starting process has a greater impact on the grid. The motor starting process is a dynamic process, the research on this process can not adopt steady-state characteristic curve [1]. The paper [2] and [3] calculates the starting process of the induction motor, but the load torque change is given by

Y. Xia (✉) · D. Meng · Y. Xu · Y. Lu
College of Electrical and Electronic Engineering,
Harbin University of Science and Technology,
150080 Harbin, China
e-mail: yunyan_x@163.com

the approximate formula, and the starting time is calculated using the steady-state curve, which has difference with the actual situation. This paper establishes the dynamic equation of asynchronous motor based on the M–T coordinate system. Combined with the actual load and the heat dissipation mode, this paper calculates the starting characteristics and the motor temperature rise, improves the accuracy.

7.2 Dynamic Equation of the Induction Machine

Due to the rotor speed changing in the starting process, using M–T coordinate system of the synchronous constant speed rotation is good. According to the paper [4], the state equation can be established as follows:

$$
P \begin{bmatrix} i_{M1} \\ i_{T1} \\ i_{M2} \\ i_{T2} \end{bmatrix} = \begin{bmatrix} L_{ss} & 0 & L_m & 0 \\ 0 & L_{ss} & 0 & L_m \\ L_m & 0 & L_{rr} & 0 \\ 0 & L_m & 0 & L_{rr} \end{bmatrix}^{-1} \left\{ \begin{bmatrix} u_{M1} \\ u_{T1} \\ 0 \\ 0 \end{bmatrix} \right.
$$
$$
+ \begin{bmatrix} -r_1 & L_{ss} & 0 & L_m \\ -L_{ss} & -r_1 & -L_m & 0 \\ 0 & L_m & -r_2 & L_{rr} \\ -L_m & 0 & -L_{rr} & -r_2 \end{bmatrix} \begin{bmatrix} i_{M1} \\ i_{T1} \\ i_{M2} \\ i_{T2} \end{bmatrix} + \omega \begin{bmatrix} 0 & 0 & 0 & 0 \\ 0 & 0 & 0 & 0 \\ 0 & -L_m & 0 & -L_{rr} \\ L_m & 0 & L_{rr} & 0 \end{bmatrix} \left. \begin{bmatrix} i_{M1} \\ i_{T1} \\ i_{M2} \\ i_{T2} \end{bmatrix} \right\}
$$
$$
\tag{7.1}
$$

where r_1, r_2 are per phase resistances of the stator and the rotor; u_{M1}, u_{T1} are the two-phase voltage of the stator; $i_{M1}, i_{T1}, i_{M2}, i_{T2}$ are the two-phase current of the stator and rotor; $\Psi_{M1}, \Psi_{T1}, \Psi_{M2}, \Psi_{T2}$ are the fluxes of the stator and rotor in the two-phase coordinate system; P is the differential operator; ω is the speed of the rotor angle; L_{ss}, L_{rr}, L_m are the self inductances of the stator and the rotor and the mutual inductances of the stator and the rotor.

Due to $H = \pi^2 \frac{GD^2}{P_N} \left(\frac{n_s}{60} \right)^2$, the motion equation of the rotating system is transformed and expressed with the per-unit(pu) system as follows [5]:

$$
H \frac{d\omega}{dt} = T_e - T_m \tag{7.2}
$$

where GD^2 is the flywheel torque; P_N is the rated power; T_e, T_m are the per-unit of the electromagnetic torque and Load torque; H is the inertia constant.

Electromagnetic torque T_e can be expressed with the per-unit system as follows:

$$
T_e = X_m (i_{T1} i_{M2} - i_{M2} i_{T2}) \tag{7.3}
$$

The Equations (7.1), (7.2), (7.3) are the dynamic fundamental equation of the three-phase induction motor in the M–T coordinate system. It is very easy to calculate the starting characteristics of the three-phase induction motor with the three equations.

7.3 Temperature Rise Equation of the Motor

In the starting process the stator current generate heat, assume the resistance temperature coefficient is α at 15°C, the adiabatic temperature rise of stator winding when the time is t can be expressed as follows [3]:

$$\theta_{s1} = \frac{A}{B} e^{j_s^2 \cdot B \cdot t} - \frac{A}{B} \tag{7.4}$$

where $A = \frac{\rho[1+(\theta_0-15)\alpha]}{\rho_s C_s}$; $B = \frac{\rho\alpha}{\rho_s C_s}$; θ_0 is the Environment temperature; j_s is the current density of stator winding; ρ, ρ_s are the stator winding resistivity and density; C_s is the specific heat of stator winding.

When the motor starts, slip changes from s_1 to s_2,M_m is the load torque and M_e is the electromagnetic torque. Then the rotor winding heat is expressed as follows:

$$Q_2 = \frac{GD^2}{4} \omega_1^2 \int_{s_2}^{s_1} \frac{s}{1 - \frac{M_m}{M_e}} ds \tag{7.5}$$

According to the paper [6], the equivalent resistance of rotor bar R_B and the equivalent resistance of end ring R_K in the starting process can be calculated. The calorific value of rotor bar and end ring, Q_B, Q_K are expressed as follows:

$$Q_B = R_B \cdot Q_2 \quad Q_K = R_K \cdot Q_2 \tag{7.6}$$

For the motor of radial ventilation structure, heat between the stator windings and core is transferred by the stator insulation and the heat between the rotor bar and core is transferred by conduction. In the ventilation channel and the end, the heat of stator winding and the rotor bar is transferred by convection with air. Stator insulation thermal resistance R_{s1}, thermal resistance R_{s2} of the stator end, thermal resistance R_{s3} of the windings in the radial ventilation channel can be calculated [7], the heat emission of stator winding when the time is t is expressed as follows:

$$Q_1 = \left(\frac{\Delta\theta_{s1}}{R_{s1}} + \frac{\Delta\theta_{s2}}{R_{S2}} + \frac{\Delta\theta_{s3}}{R_{S3}} \right) \cdot t \tag{7.7}$$

where $\Delta\theta_{s1}$,$\Delta\theta_{s2}$,$\Delta\theta_{s2}$ are the temperature difference between the stator windings and the core, the stator windings and ending air, the stator windings and the ventilation channel gas.

Actual temperature rise is expressed when the time is t as follows:

$$\theta_s = \theta_{S1} - \frac{Q_1}{C_s M_s} \tag{7.8}$$

The thermal resistance of rotor bar and the heat emission Q_{B1} can be calculated when the slip changes from S_1 to S_2 in time t_1, so actual temperature rise of the rotor bar is expressed as follows:

$$\theta_B = \frac{Q_B - Q_{B1}}{C_B M_B} \tag{7.9}$$

where C_B is specific heat of the bar; M_B is the weight of the bar.

The end ring dissipates the heat by convection with the air, so the heat which is transferred between the rotor bar and the end ring can not be considered. The heat emission of the end ring Q_{K1} in time t_1 can be calculated. The actual temperature rise of the end ring in time t_1 is expressed as follows:

$$\theta_K = \frac{Q_K - Q_{K1}}{C_K M_K} \tag{7.10}$$

where C_K is specific heat of the end ring; M_K is the weight of the end ring.

7.4 The Calculation Process and the Results Analysis

The starting characteristics of the medium-sized induction motor with high-voltage can be calculated with the (7.1), (7.2), (7.3) equations. As the motor speed ω in the starting process is not constant, (7.1) is nonlinear differential equations, we use the fourth order Runge–Kutta method to solve the Equation (7.1) and use the first order Euler to solve (7.2). The continuous time is discredited during the calculation and the speed ω is considered as the constant in each time step. Electromagnetic torque is calculated according to (7.3). Because the current component of the stator and the rotor in (7.3) is given by the solution of (7.1), so (7.2) and (7.1) need simultaneous solution. When the current component of the stator and the rotor is obtained, the starting current per unit value can be expressed as follows:

$$I_{st} = \sqrt{i_M^2 + i_T^2} \tag{7.11}$$

According to the time step h and the calculating times n when the motor reaches steady state, the motor start-up time can be determined: $t = n \cdot h$.

Usually the initial value of the starting process is zero. According to the initial conditions, the current component of the stator and rotor in the two-phase coordinate system is calculated in a step by the formula (7.1). By the formula (7.2) and (7.3), the electromagnetic torque and speed in a step are calculated. According to the formula (7.4) and (7.7), adiabatic temperature rise of the stator winding and the heat emission are calculated. At last the actual temperature rise of the stator winding is obtained in the step by the formula (7.8). According to the changing value of the slip, the calorific value and the heat emission of the rotor bar and end ring in the step are also obtained. Then their actual temperature rise can be

Table 7.1 Relationship between load torque and speed (per unit)

T_m	0.0669	0.0784	0.1130	0.1706	0.2512	0.3549	0.4816	0.6314	0.8402	1
ω	0	0.1	0.2	0.3	0.4	0.5	0.6	0.7	0.8	0.9

Fig. 7.1 Dynamic characteristic of motor
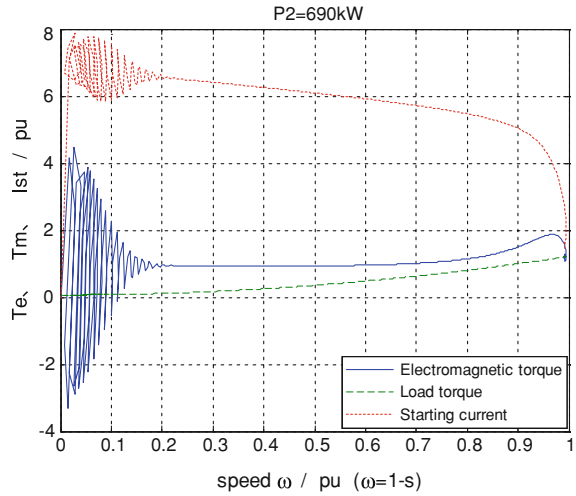
calculated by the formula (7.9) and (7.10). This step starting characteristics and temperature rise results is considered as the initial value and the process is repeated into the next step calculation. Each step temperature rise is accumulated and the motor temperature rise is obtained in the calculation time. When the motor current and electromagnetic torque reaches the stable value, the calculation of the starting characteristics is over. The motor is in the steady state. When the temperature rise reaches stability, the calculation ends.

In order to obtain the temperature rise of the stator windings and the rotor bar, first the temperature rise of the core needs to be calculated. Besides the heat which is transferred by the stator winding and rotor bar, there is their own loss in the cores of the stator and rotor. The core convects and dissipates heat with the air by the ventilation channel and air gap. The temperature rise of the core is calculated by heat relationship.

According to the calculation method in this paper, the starting characteristic and temperature rise of the medium-sized and radial ventilation motors with high-voltage in Y series and in YKK series are calculated, which achieves good results. Now this paper takes a 6 kV and six poles motor in Y series whose power is 690 kW for example to analyze calculation result. Table 7.1 is the load data of the motor.

Figures 7.1 and 7.2 are the starting characteristics calculated by the method of dynamic and steady-state calculation. In low-speed section, the dynamic characteristic curves are included in the strong pulsating component. That is because the

Fig. 7.2 Steady-state characteristic curve
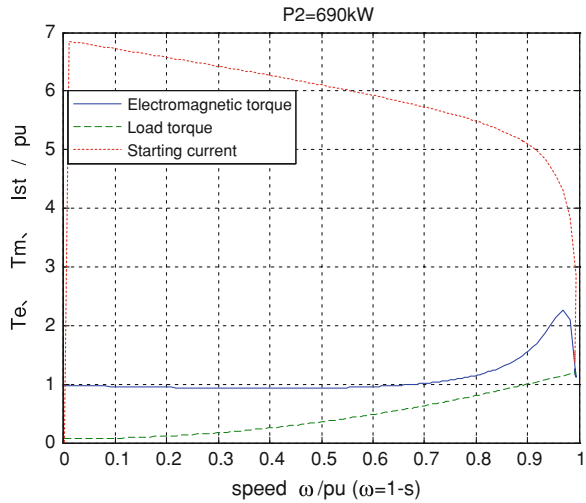
Fig. 7.3 Temperature rise curve of motor
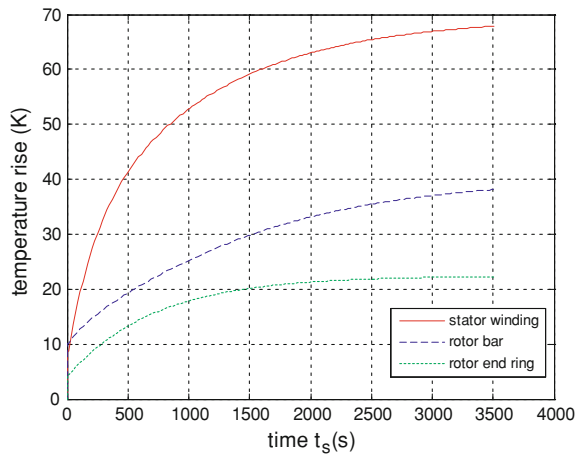
stator current has low frequency alternating component and non-periodic component. Since the three-phase fundamental frequency current produces the rotating magnetic field at synchronous speed and the non-periodic component produces static magnetic field, the frequency of the induced current in the rotor windings is sf_1 and $(1-s)f_1$. The stator winding current and rotor current whose fundamental frequency issf_1 produce a rotating magnetic field which is a relatively stationary in space, and produce one-direction torque. However the static magnetic field produced by the non-periodic stator current and rotor current at the frequency of $(1-s)f_1$ interacts with the synchronous rotating magnetic field, which produces an alternating electromagnetic torque [8]. The alternating torque component

appears when the transient is taken into account. It can decrease to zero with the attenuation of the non-periodic current.

Figure 7.3 is the temperature rise of the stator and rotor windings from start to thermal equilibrium. As can be seen from the figure, when the motor starts to reach 3,500 s, the stator and rotor windings temperature rise tends to balance. By calculating, the average temperature rise of the stator winding is 69 K. The value which is measured with resistance method by experiment is 73.9 K. The method is verified to meet the precision of the engineering by a variety of the motors.

7.5 Conclusions

This paper calculates the starting characteristics of the medium-sized motors with high-voltage. The phenomenon that is unknown in the steady-state theory is explained by the dynamic theory. It proves that the dynamic characteristics correspond with the practical situation. Based on the starting characteristics, this paper calculates the stator and rotor temperature rise of radial ventilation motor. The calculation result is much closer to the experimental value. The calculation results of the starting characteristics and temperature rise have great significance to the motor design and the safe operation of the power system.

References

1. Zhang LZ (1997) Transient analysis of induction machines and its application. Electr Mach Control 1(1):18–22
2. Gao JD, Zhang LZ, Huang LP (1984) Research on starting process of induction machines. Electrotech J 5(1):1–6
3. Fu FL (1993) Engineering calculation of the starting temperature rise for the asynchronous motor. Electr Mach Technol 14(2):9–11
4. Wang JY (2003) AC variable speed. Higher Education Press, Beijing, pp 101–111
5. Gao JD, Wang XH, Li FH (2005) Ac motor and system analysis. Tsinghua University Press, Beijing, pp 327–330
6. Sheng ZW (2005) Calculation of temperature rise of rotor bars and end rings of squirrel cage induction motors during starting. Explosion-proof Electr Mach 40:12–14
7. Wei YT, Meng DW (1998) Heat exchanges in the motor. China Machine Press, Beijing, pp 270–305
8. Zhang AJ (2006) The research on the dynamic process of induction motors considering skewed rotor, North China Electric Power University, pp 6–40

Chapter 8
An Epipolar Rectification Algorithm for Uncalibrated Images

Peizhen Wang, Ping Chen, Dailin Zhang and Mengdi Wang

Abstract Traditional epipolar rectification algorithms require stereo images captured with binocular parallel stereo camera, and the requirements for the image acquisition system are high. In this paper an epipolar rectification algorithm for uncalibrated images which are not from binocular camera is proposed. Firstly, Minimum Enclosing Rectangle (MER) is calculated according to matching points, which are from Scale Invariant Feature Transform (SIFT); then image pairs adjustment is implemented with four vertex points parameters of MER; lastly, combining Hartley algorithm with Francesco algorithm epipolar rectification is realized. The experimental results show that the proposed algorithm is invariant to translation, rotation and scaling transformation to a certain extent.

Keywords Epipolar rectification · Coke microscopic images · SIFT · MER

8.1 Introduction

Epipolar rectification refers to projective transformation for stereo images, the epipolar lines of matching points are made parallel with the horizontal axis and located at the same vertical axis, the search range of matching algorithm is mapped to one-dimensional scan lines from two-dimensional image plane, so that the speed

P. Wang (✉) · P. Chen · M. Wang
School of Electrical and Information, Anhui University of Technology,
243002 Ma'anshan, China
e-mail: pzhwang@ahut.edu.cn

D. Zhang
Anhui Key Laboratory of Clean Conversion and Utlization,
Anhui University of Technology, 243002 Ma'anshan, China

and precision of matching algorithm is improved. In essence it is to implement the mechanical deviation rectification through software algorithm and to satisfy the ideal geometry assumption of parallel binocular stereo matching algorithm.

Traditional epipolar rectification algorithms require stereo images captured with binocular parallel stereo camera, the requirements for the image acquisition system are high, and are rarely applied for monocular images captured existing rotation and scaling, the rectification algorithm of reference [1, 2] depends on the parameters of camera calibration, and the requirements for system are high, the rectification algorithm of reference [3] is only applied for stereo images with rotation, but without scaling.

In this paper coke microscopic images are captured through adding a 90° polarizing device to HD microscope photometric with certain rotation. Due to spatial clearance, they follow with certain translation in the process of rotation. Meanwhile, scaling may change when microscope focuses. In this situation, it is difficult to realize epipolar rectification through the traditional epipolar rectification algorithms.

For the reason mentioned above, in this paper combining Hartley algorithm [4, 5] with Francesco algorithm [6] an epipolar rectification algorithm for uncalibrated images is proposed. It mainly includes following two steps: (1) Through image pairs adjustment, image pairs are represented with parallel binocular characteristics, and the corresponding homography matrix is obtained; (2) Combining Hartley algorithm with Francesco algorithm, epipolar rectification for uncalibrated images is realized, and the eventual homography matrix is obtained.

8.2 Epipolar Geometry of Stereo Vision

8.2.1 Epipolar Geometry

Suppose that m_1 and m_2 are two corresponding points of a point M in R^3 in image pairs I_1 and I_2. F is a 3×3 matrix with rank 2, called fundamental matrix. Hence, the epipolar line equation between two corresponding points is defined as

$$m_2^T F m_1 = 0 \tag{8.1}$$

All of the epipolar lines in the same image intersect at the epipole. Suppose that e_1 is the epipole of image I_1, and e_2 is the epipole of image I_2. The epipoles are related by fundamental matrix as follows:

$$F e_1 = F^T e_2 = 0 \tag{8.2}$$

8.2.2 Epipolar Geometry After Epipolar Rectification

After epipolar rectification, the epipolar lines of image pairs parallel to each other and remain level. Two corresponding points exist only horizontal parallax, and the epipoles are located in the horizontal direction at infinity. Therefore, the epipoles of image pairs rectified are given as

$$e_1 = e_2 = \begin{bmatrix} 1 & 0 & 0 \end{bmatrix}^T \tag{8.3}$$

The fundamental matrix of image pairs rectified has the form

$$\hat{F} = \begin{bmatrix} 0 & 0 & 0 \\ 0 & 0 & -1 \\ 0 & 1 & 0 \end{bmatrix} \tag{8.4}$$

After epipolar rectification, the corresponding points of image pairs still satisfy Eq. 8.1. Suppose that H_1 and H_2 are the homography matrices for epipolar rectification, the epipolar line equation is defined as

$$(H_2 m_2)^T \hat{F} H_1 m_1 = 0 \tag{8.5}$$

8.3 Image Pairs Adjustment

Through image pairs adjustment, the homography matrix is obtained by Minimum Enclosing Rectangle (MER), image pairs are performed as parallel binocular characteristics. It mainly includes the steps of feature parameters acquisition and parallel binocular adjustment.

8.3.1 Feature Parameters Acquisition

Scale Invariant Feature Transform (SIFT) algorithm [7, 8] is invariant with the changing of illumination, translation, rotation and scaling, and has good stability, when to solve the image color differences caused by polarization changing. Therefore, feature points of coke microscopic images are extracted, nearest neighbor and next-nearest neighbor feature points are searched based on SIFT feature description, the ratio of nearest neighbor to next-nearest neighbor is computed for matching, RANSAC algorithm is employed to eliminate the mismatching points.

In this paper MER can be acquired through the following steps:
Calculate the convex hull of matching points after SIFT feature matching;
Calculate the area, length, width and vertex coordinates of external rectangle;
Rotate counterclockwise of 2°, repeat step (2), rotate counterclockwise until 90°, turn to step (4);
Statistics the parameters of external rectangle, acquire the length a, width b and vertex coordinates (x_i, y_i) corresponding to the rectangle of minimum area, $i = 1 \sim 4$.

The aspect ratio of MER is calculated by its parameters. In this case the optical axis of the camera capturing the coke microscopic images keeping perpendicular to coke surface, the movement process of its surface appears as similitude transformation, and in this transformation the aspect ratio has good invariance, so as to determine the accuracy of MER obtained, defined as the below equation:

$$|a_1/b_1 - a_2/b_2| < \eta$$
$$\text{for } 0 < \eta < 0.05.$$

$$(8.6)$$

8.3.2 Parallel Binocular Adjustment

The movement process of coke surface is similitude transformation, and which contains translation, rotation and scaling transformation, includes two types: One is transforming image I_1 into image I_1', the other is transforming image I_2 into image I_2', the transformation is performed based on the size of images:

If $(a_1+b_1) > (a_2+b_2)$, then transform image I_1 into image I_1';
If $(a_1+b_1) < (a_2+b_2)$, then transform image I_2 into image I_2';
If $(a_1+b_1) = (a_2+b_2)$, then select any one transformation above.

Suppose that transformation is transforming image I_1 into image I_1', it chooses four vertex coordinates $x_i = (x_i, y_i)$ and $x_i' = (x_i', y_i')$ of MER as the parameters of parallel binocular transformation, then the following equation can be obtained from $x_i' = H_1 x_i$:

$$\begin{bmatrix} x_i & y_i & 1 & 0 & 0 & 0 & -x_i'x_i & -x_i'y_i \\ 0 & 0 & 0 & x_i & y_i & 1 & -y_i'x_i & -y_i'y_i \end{bmatrix} \boldsymbol{h} = \begin{bmatrix} x_i' \\ y_i' \end{bmatrix}$$

$$(8.7)$$

for $i = 1 \sim 4$, $h = [h_{11} \ h_{12} \ h_{13} \ h_{14} \ h_{15} \ h_{16} \ h_{17} \ h_{18}]^T$.

At this time, image I_1 is transformed into image I_1' based on the homography matrix H_1 through image pairs adjustment, image pairs I_1 and I_2 is appeared as parallel binocular characteristics.

8.4 Epipolar Rectification Transformation

Through epipolar rectification transformation, epipolar rectification transformation decomposition matrix is obtained based on epipolar geometry, then combining Hartley algorithm with Francesco algorithm the homography matrix is estimated, It mainly includes the steps of epipolar rectification transformation decomposition and homography matrix estimation.

8.4.1 Rectification Transformation Decomposition

In view of parallel binocular image pairs, the process of epipolar rectification decomposition includes the following steps:

(1) Translation transformation

The coordinate axis of origin images are moved to the center of images, suppose that the size of image pairs are the same, then the center of image pairs are the same, and the translation transformations are the same, the corresponding translation transformation is as follows:

$$T = \begin{bmatrix} 1 & 0 & -x_0 \\ 0 & 1 & -y_0 \\ 0 & 0 & 1 \end{bmatrix} \tag{8.8}$$

for $x_0 = w/2$, $y_0 = h/2$, w is the width of images, h is the height of images.

(2) Rotation transformation

After epipolar rectification, the epipoles are located in the horizontal direction at infinity. Thus, the coordinate axis are rotated about θ degrees, the epipoles are located in the horizontal x axis, the coordinate of the epipoles is [f, 0, 1]T, the corresponding rotation transformation is as follows:

$$R = \begin{bmatrix} \cos\theta & \sin\theta & 0 \\ -\sin\theta & \cos\theta & 0 \\ 0 & 0 & 1 \end{bmatrix} \tag{8.9}$$

(3) Projective transformation

Through projective transformation, the epipoles [f, 0, 1]T located in the horizontal x axis is mapped to the epipoles [f, 0, 0]T located in the horizontal direction at infinity, then all of the epipolar lines in the image pairs parallel with the x axis, the corresponding projective transformation is as follows:

$$K = \begin{bmatrix} 1 & 0 & 0 \\ 0 & 1 & 0 \\ -1/f & 0 & 1 \end{bmatrix} \tag{8.10}$$
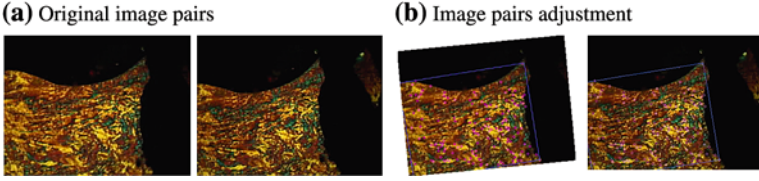
Fig. 8.1 Original image pairs and image pairs adjustment

Then the homography matrices after epipolar rectification are $H_2 = KRT$ and $H_2' = K'R'T$.

8.4.2 Homography Matrix Estimation

For estimating the homography matrices, suppose that there are N pairs of matching points after SIFT feature matching, the purpose of identifying the homography matrices H_2 and H_2' is to minimize the objective function shown as the following equation.

$$E(H_2, H_2') = \sum_{i=1}^{N} \left((H_2' x_i')^T \hat{F} H_2 x_i \right)^2 \tag{8.11}$$

By Eq. 8.4 knowable, the first raw of $\hat{F}$ is null vector, Eq. 8.11 includes only the second and third rows of H_2 and H_2', then the first row of H_2 and H_2' cannot be recovered by the minimization of the objective function Eq. 8.11. Therefore, it is necessary to introduce new constraint to identify the first row elements, here with, it is implemented by minimizing the Euclidean distance between the pairs of matching points, shown as Eq. 8.12.

$$d(H_2, H_2') = \sum_{i=0}^{N} \left(||H_2 x_i - H_2' x_i'||^2 \right) \tag{8.12}$$

Combining Eq. 8.11 with Eq. 8.12, it can be identified the homography matrix H_2 and H_2' by minimizing the objective function Eq. 8.13.

$$F(H_2, H_2') = \eta E(H_2, H_2') + (1 - \eta) d(H_2, H_2') \tag{8.13}$$

Suppose that the transformation is transforming image I_1 into image I_1', it can be identified the eventual homography matrix as follows:

$$\begin{cases} H = H_1 H_2 \\ H' = H_2' \end{cases} \tag{8.14}$$
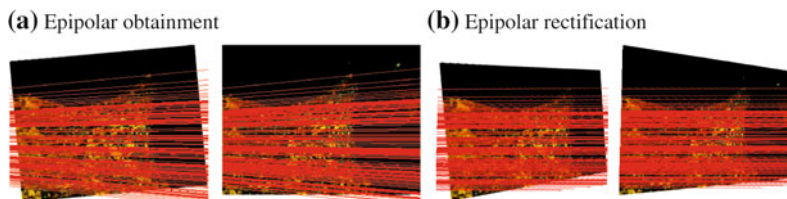
Fig. 8.2 Image pairs before and after epipolar rectification transformation

8.5 Experimental Results

To test the validity of the proposed algorithm, in this paper we used coke microscopic images captured with HD microscope photometric as experimental samples, shown as chart (a) in Fig. 8.1. After parallel binocular transformation, image pairs are performed as parallel binocular characteristics, shown as chart (b) in Fig. 8.1. From the left chart it is not difficult to find that there are certain rotation and scaling. The red points are expressed as matched points obtained by SIFT, and the blue rectangle is expressed as the MER.

After image pairs adjustment, the epipolar lines can be obtained based on matching points, shown as chart (a) in Fig. 8.2. Then combining Hartley algorithm with Francesco algorithm epipolar rectification is implemented, there is only horizontal parallax existed in image pairs, shown as chart (b) in Fig. 8.2.

8.6 Conclusions

In this paper, an epipolar rectification algorithm for uncalibrated images is proposed, which can be used to solve dense matching problem. With feature points from SIFT algorithm and its MER, uncalibrated image pairs are rectified to obtain characteristics of parallel binocular. By combining Hartley algorithm with Francesco algorithm, epipolar rectification is implemented, and the synthesis of two algorithm constraints make the parameter solution more perfect. The proposed algorithm has been tested for rectifying pairs of coke microscopic images. It can be found from the experiments that the proposed algorithm is suitable for image pairs with translation, rotation and scaling transformation to a certain extent.

References

1. Zhang Z (1998) Determining the epipolar geometry and its uncertainty:a review [J]. Int J Comput Vis 27:161–195
2. Charles L, Zhang Z (1999) Computing rectifying homographies for stereo vision [J]. Proc IEEE Conf Comput Vis Pattern Recognit 1:94–99
3. Lin G, Zhang W (2006) An effective robust rectification method for stereo vision [J]. J Image Graph 11(2):203–209
4. Hartley R (1999) Theory and practice of projective rectification [J]. Int J Comput Vision 35(2):1–16
5. Isgro F, Trucco E (1999) On robust rectification for uncalibrated images [J]. Proc Int Conf Image Anal Process 160:297–302
6. Hartley R, Zisserman A (2000) Multiple view geometry in computer vision [M]. Cambridge University Press, UK
7. Lowe DG (2004) Distinctive image features from scale-invariant keypoints [J]. Int J Comput Vis 60(2):91–110
8. Chen P,Wang P, Zhou F, Wang X (2010) Research on feature extraction and matching method of plant image [J]. Proc Chin Conf Image Graph 1:430–434

Chapter 9
A New Approach for Multi-Objective-Optimization-Based Fuzzy-PID Control

Wang Hong-ru and Wang Jianzhong

Abstract A parameter self-tuning PID controller based on genetic optimization is proposed in this paper. A mathematical model of the fuzzy-PID controller, which parameters are tunable and can be updated timely, is set up. Membership function, fuzzy control rules and parameters of the PID controller are optimized by improved GA. And self-adaptive crossover and mutation operators are used to improve the performance of global searching and converging. Therefore, the proposed controller avoids disadvantages of conventional fuzzy-PID controller with invariable inference rules, and has higher accuracy. Experiments indicate that the proposed controller has better performance than that the conventional one, and can meet with requirements of the given servo system.

Keywords PID control · Fuzzy inference · GA · Multi-objective optimization

9.1 Introduction

With the development of intelligent control technology, fuzzy-PID control algorithm [1, 2] has been presented in recent years. It integrates advantages of both PID control [3, 4] and fuzzy control [5, 6], so it has better performance. Therefore, fuzzy-PID control algorithm is more and more extensively used in industrial

H.-r. Wang (✉)
School of Mechanical Engineering, Jiangsu University of Science
and Technology, 212003 Zhenjiang, China
e-mail: wanghrr@126.com

J. Wang
School of Mechanics, Beijing Institute of Technology, 100081 Beijing, China
e-mail: cwjzwangg@bit.edu.cn

Fig. 9.1 Structure of fuzzy-PID controller
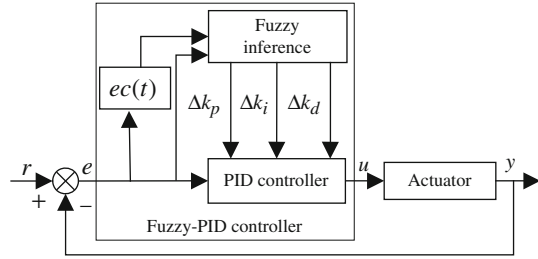
control applications. However, because conventional fuzzy-PID control algorithm is often used with fixed inference rules and expert's experiences, its accuracy can be improved further.

To deal with the above-mentioned problems, a parameter self-tuning fuzzy-PID control algorithm is proposed. In this method, a mathematical model of fuzzy-PID controller is set up, and is optimized by multi-objective genetic algorithm. Apex and width of trigonometric membership function, fuzzy logic rules and parameters of PID controller are taken as unknown, and are tuned automatically by GA. And to improve the performance of global searching and converging speed of conventional GA, self-adaptive operators of crossover and mutation are introduced. Simulation experiments verify validity of the proposed algorithm.

9.2 Design of Fuzzy-PID Controller

Fuzzy-PID controller integrates fuzzy control and conventional PID control, and tunes parameters of PID controller online by fuzzy inference with errors or derivation of errors. Aiming at the two-freedom servo system with low-speed motion, a fuzzy-PID controller (shown in Fig. 9.1) is developed in this paper.

$$R_{ij} : \begin{matrix} if \ e(t) \ is \ A_i \ and \ ec(t) \ is \ B_j \\ then \ k_P = k_P^{ij}, k_I = k_I^{ij}, k_D = k_D^{ij} \end{matrix} \quad (9.1)$$

where A_i and B_j are labels of fuzzy sets in X and Y, respectively, $i = 1, 2, \cdots n$ and $j = 1, 2, \cdots, m$. k_P^{ij}, k_I^{ij} and k_D^{ij} are real numbers which needed be determined.

From Fig. 9.1, the overall output $u(t)$ of the fuzzy-PID controller, which is also the input of the actuator, can be formulated as:

$$u(t) = k_P e(t) + k_I \int e(t) dt + k_D ec(t) \quad (9.2)$$

Therefore, fuzzy control rules described by Eq. (9.1) can be rewritten as:
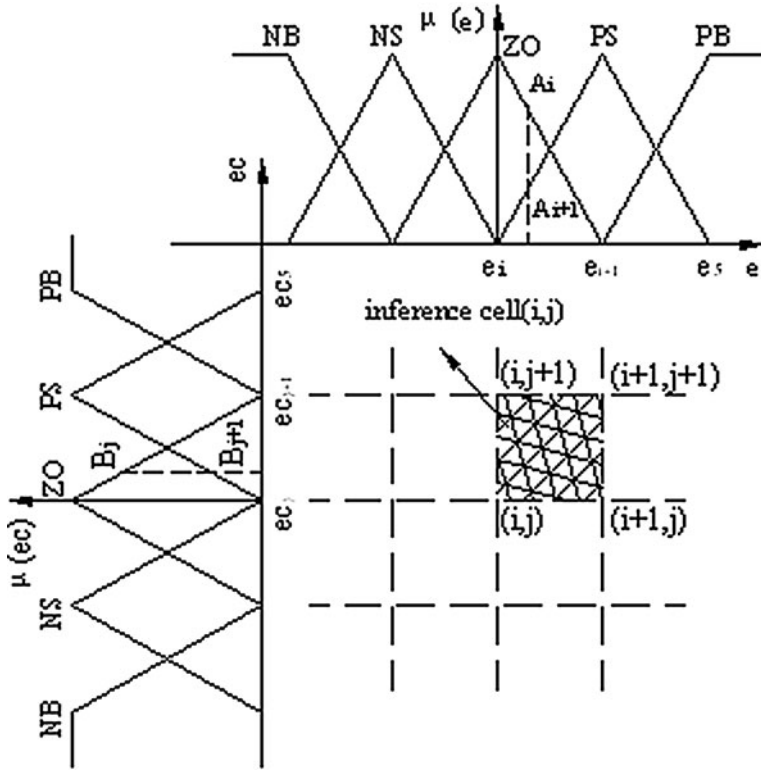
Fig. 9.2 Membership function of input variables

$$R_{ij} : \begin{array}{l} \textit{if } e(t) \textit{ is } A_i \textit{ and } ec(t) \textit{ is } B_j \\ \textit{then } u^{ij}(t) = k_P^{ij} e(t) + k_I^{ij} \int e(t)dt + k_D^{ij} ec(t) \end{array} \qquad (9.3)$$

Fuzzy inference can be implemented by:

$$\begin{array}{l} R_{ij} = (A_i \quad \textit{and} \quad B_j) \rightarrow C_{ij} \\ R = \bigcup_{i=1}^{n} \bigcup_{j=1}^{m} R_{ij} \end{array} \qquad (9.4)$$

where C_{ij} is label of fuzzy set for overall output in Z.

Single-point fuzzy set is used to fuzzify output variables, and centroid [6] is employed to defuzzify the fuzzy variables. So, the overall output of the proposed fuzzy-PID controller can be defined as:

$$u(t) = \sum_{i=1}^{n} \sum_{j=1}^{m} w_{ij} u^{ij} / \sum_{i=1}^{n} \sum_{j=1}^{m} w_{ij} \qquad (9.5)$$

where $w_{ij} = A_i(e) \wedge B_j(ec)$ is activation coefficient of R_{ij} by the input of (e, ec). Trigonometric membership function has good performance of computation and sensitivity, so all input variables are described by trigonometric membership function with fifty percent overlap, which is shown in Fig. 9.2, where $n = m = 5$. e_i and ec_j are apexes of fuzzy sets $\{A_i\}$ and $\{B_j\}$, respectively, and exist $e_1 < e_2 < e_3 < e_4 < e_5$ and $ec_1 < ec_2 < ec_3 < ec_4 < ec_5$. $\{A_i\}$ and $\{B_j\}$ can be computed by Eqs. 9.6 and 9.7. Base plane of fuzzy control rules can be divided into sixteen inference cells, and fuzzy control rules of output lies at four corners of the corresponding inference cell (shown in Fig. 9.2). And fuzzy inference is operated on these cells.

$$A_i = \begin{cases} \dfrac{e - e_{i-1}}{e_i - e_{i-1}}, & e \in [e_{i-1}, e_i], \quad i = 2, 3, 4, 5 \\ \dfrac{e_{i+1} - e}{e_{i+1} - e_i}, & e \in [e_i, e_{i+1}], \quad i = 1, 2, 3, 4 \\ 1, & e < e_1 \ or \quad e > e_5 \end{cases} \tag{9.6}$$

$$B_j = \begin{cases} \dfrac{ec - ec_{j-1}}{ec_j - ec_{j-1}}, & ec \in [ec_{j-1}, ec_j], \quad j = 2, 3, 4, 5 \\ \dfrac{ec_{j+1} - ec}{ec_{j+1} - ec_j}, & ec \in [ec_j, ec_{j+1}], \quad j = 1, 2, 3, 4 \\ 1, & ec < ec_1 \ or \quad ec > ec_5 \end{cases} \tag{9.7}$$

Let e_i and e_{i+1} be two adjacent apexes in $\{A_i\}$, and ec_j and ec_{j+1} be two adjacent apexes in $\{B_i\}$. As a result, $e_i < e < e_{i+1}$ and $ec_j < ec < ec_{j+1}$ form one inference cell named IC (i, j) in input space $X \times Y$. The output of fuzzy-PID controller is computed with dual-split interpolation [7] in IC (i, j):

$$u(t) = [\sum_{k=i}^{i+1} \sum_{l=j}^{j+1} w_{kl} k_P^{kl}] e(t) + [\sum_{k=i}^{i+1} \sum_{l=j}^{j+1} w_{kl} k_I^{kl}] \int e(t) dt + [\sum_{k=i}^{i+1} \sum_{l=j}^{j+1} w_{kl} k_D^{kl}] ec(t) \tag{9.8}$$

Equation (9.8) is the mathematical model of the proposed fuzzy-PID controller, and is obviously parametric. That is to say, parameters including e_i, ec_j, k_P^{ij}, k_I^{ij} and k_D^{ij} can all be tuned online. In this paper, multi-objective-optimization-based improved GA is employed to tune those parameters.

9.3 Optimization of the Proposed Fuzzy-PID Controller

GA is very fit for optimization of fuzzy-PID controller, because it is free of local information about optimized objects and can works only with fitness function. In this paper, fuzzy control rules set and membership function is optimized simultaneously by the following steps.

A. Encoding

Based on symbol symmetry of linear systems and the given application, the number of parameters that need to be encoded can be simplified into four as "positive small" apex e_4 and "positive big" apex e_5 of error, "positive small" apex ec_4 and "positive big" apex ec_5 of derivation of error. Through this simplification, the total number of parameters need to be encoded is forty-nine. Because of symbol symmetry of PID controller, there exists:

$$\begin{cases} k_P^{ij} = k_P^{(6-i)(6-j)} \\ k_I^{ij} = k_I^{(6-i)(6-j)} \qquad (i = 1, 2, \cdots, 5; j = 1, 2, \cdots, 5) \\ k_D^{ij} = k_D^{(6-i)(6-j)} \end{cases} \qquad (9.9)$$

Real number encoding [8, 9] occupies smaller space, and has advantages of higher computation accuracy and speed, when compared with binary encoding. Therefore, real number encoding is used in this paper, and the kst chromosome in the lst generation can be encoded by:

$$p_k^l = [e_{4k}^l, e_{5k}^l, ec_{4k}^l, e_{5k}^l, k_{Pk}^{ij\,l}, k_{Ik}^{ij\,l}, k_{Dk}^{ij\,l}] = [p_{k1}^l, p_{k2}^l, \cdots, p_{k49}^l] \qquad (9.10)$$

Chromosome $p_{ki}^l(i = 1, 2, \cdots, 49)$ is corresponding to the tunable parameter.

B. Initialization of Population

Size of the population needs to be determined before genetic operation. In this paper, initials of all tunable parameters are gotten by repeated experiments.

C. Design of Fitness Function

Performance of GA is influenced deeply by fitness function. All conventional GA use monotonic fitness function, and can not satisfy for some individuals in a population. That is to say, monotonic functions cannot provide good performance. Therefore, in order to get good dynamic performance, a nonmonotonic fitness function is adopted in this paper. And overrun, rising time, adjustable time, absolute value of error and square of the control input are regarded as evaluation items, so the fitness function can be defined as:

$$f = \frac{1}{\int_0^\infty (\omega_1 u^2(t) + \omega_2 |e(t)|)dt + (1 - e^{-\omega_3})\sigma + (1 - t_r/t_s)e^{-\omega_3}} \qquad (9.11)$$

where $u(t)$, σ, $e(t)$, t_s and t_r stand for actuator's input, overrun, error of the actuator, adjustable time with five percent error allowance, and rising time, respectively. ω_i ($i = 1, 2, 3$) is weight coefficient, which is selected on the base of the control system's requirements, such as promptness, exactness and stability.

With proper values of ω_i ($i = 1, 2, 3$), the fitness function can not only avoid excessive control input, but also make the control system have good performance.

Table 9.1 Parameters of trigonometric membership by 15 times optimization

	$e(t)$ Apex	Breadth	$\underline{ec}(t)$ Apex	Breadth
NB	−0.003485	0.001679	−2.528	2.717
NS	−0.001321	0.003485	−1.283	2.528
ZO	0	0.002642	0	2.566
PS	0.001321	0.003485	1.283	2.528
PB	0.003485	0.001679	2.528	2.717

Table 9.2 Parameters P obtained by 15 times optimization

k_P^{ij}		$e(t)$ NB	NS	ZO	PS	PB
$ec(t)$	NB	11.4227	11.5345	11.4672	12.1983	12.4027
	NS	11.5345	12.2154	12.4007	12.7419	11.9053
	ZO	11.4672	12.4007	12.1210	12.7061	11.2809
	PS	12.1983	12.7419	12.7061	11.3515	12.3876
	PB	12.4027	11.9053	11.2809	12.3876	12.5278

Table 9.3 Parameters I obtained by 15 times optimization

k_I^{ij}		$e(t)$ NB	NS	ZO	PS	PB
$ec(t)$	NB	0.01673	0.02162	0.01487	0.01590	0.02471
	NS	0.02162	0.01296	0.02583	0.02059	0.02645
	ZO	0.01487	0.02583	0.02377	0.02492	0.01294
	PS	0.01590	0.02059	0.02492	0.01371	0.02078
	PB	0.02471	0.02645	0.01294	0.02078	0.02401

Table 9.4 Parameters D obtained by 15 times optimization

K_D^{ij}		$e(t)$ NB	NS	ZO	PS	PB
$ec(t)$	NB	0.3453	0.4917	0.2472	0.2398	0.3541
	NS	0.4917	0.2675	0.3067	0.8794	0.3950
	ZO	0.2472	0.3067	0.7611	0.1139	0.6981
	PS	0.2398	0.8794	0.1139	0.3106	0.2477
	PB	0.3541	0.3950	0.6981	0.2477	0.4013

D. Selection

Selection operator of conventional GA is based on the "survival of the fittest" principle, and cannot guarantee global optimum. In order to overcome that, papers of [10] and [11] give improved methods. However, they result in declination of computation efficiency because of mass computation. To avoid the above defects, this paper exploits selection operator that only need fitness values of offspring individuals. The principle is: do crossover and mutation in parent generation and
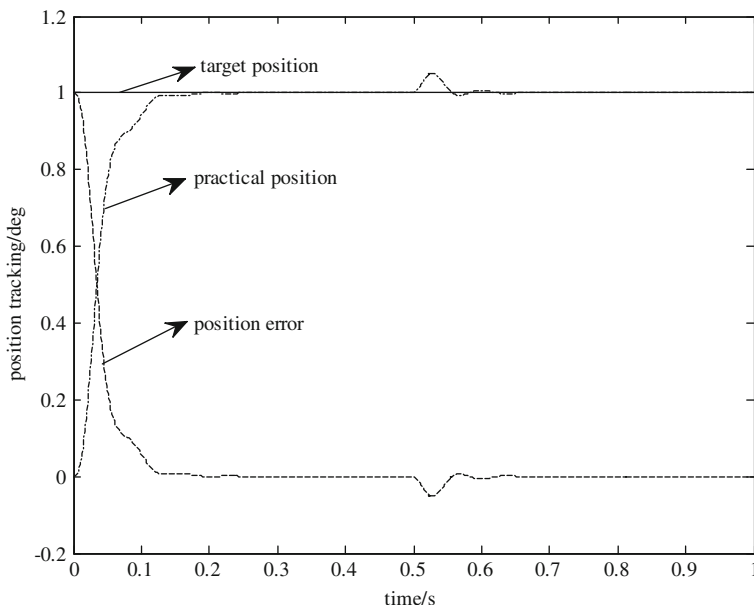
Fig. 9.3 Position tracking with conventional fuzzy-PID controller

reproduce optimum individuals of parent generation to next generation; then compute fitness value of each individual and rank them from the bigger to the smaller; finally, reproduction probability by (Eq. 9.12) is assigned to each offspring individual. By this way, superior individuals and inferior individuals in offspring generation have much opportunity to survive into the next generation, and the rest is eliminated.

$$P_s(k) = \begin{cases} 1 - \frac{k}{l}, & 0 \leq k \leq l \\ \frac{k-1}{n-l-1}, & l < k \leq n-1 \end{cases} \tag{9.12}$$

where n denotes population size, and $l = \mathrm{int}(n/2)$.

E. Crossover and Mutation

To optimize functions with multi-apexes, GA should have the following two characteristics. One is converging on optimum individuals in search space containing optimum individuals; the other is having the ability of searching new solution space during global search. Self-adaptive operators of crossover and mutation are exploited to compromise the above qualifications in this paper, and are defined respectively as:
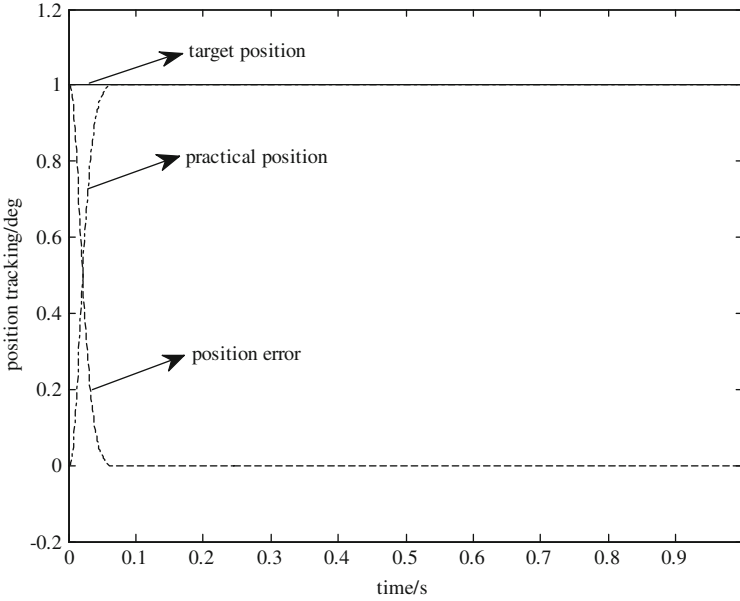
Fig. 9.4 Position tracking with optimized fuzzy-PID controller

$$
P_c = \begin{cases} \dfrac{k_c}{(f_{\max} - f_{avg})} + P_{c1}e^{-\frac{c}{\tau_c}(f_c - f_{avg})}, & f_c \geq f_{avg} \\[3mm] \dfrac{k_c}{(f_{\max} - f_{avg})} + P_{c2}, & f_c < f_{avg} \end{cases} \tag{9.13}
$$

$$
P_m = \begin{cases} \dfrac{k_m}{(f_{\max} - f_{avg})} + P_{m1}e^{-\frac{c}{\tau_c}(f_m - f_{avg})}, & f_m \geq f_{avg} \\[3mm] \dfrac{k_m}{(f_{\max} - f_{avg})} + P_{m2}, & f_m < f_{avg} \end{cases} \tag{9.14}
$$

where $f_{\max}$ and f_{avg} are maximum and average fitness values in current population, respectively. f_c denotes bigger fitness value between two crossover individuals. f_m denotes fitness value in mutation operation. k_c, P_{c1} and P_{c2} are all crossover coefficients, and satisfy $(k_c, P_{c1}, P_{c2}) \in [0, 1]$ and $P_{c1} > P_{c2}$. k_m, P_{m1} and P_{m2} are all mutation coefficients, and satisfy $(k_m, P_{m1}, P_{m2}) \in [0, 1]$ and $P_{m1} > P_{m2}$. $\tau_c = (f_{\max} - f_{avg})/\ln(P_{c1}/P_{c2}).\tau_m = (f_{\max} - f_{avg})/\ln(P_{m1}/P_{m2})$

Equations (9.13), (9.14) indicate that the modified GA takes diversity of population as control variables and use individual's fitness values to tune probability of crossover and mutation.

9.4 Experiments

Based on the given servo system, comparison experiments between conventional fuzzy-PID controller and GA-optimization-based fuzzy-PID controller are carried out to verify the proposed method. Both controllers have the same experimental conditions, they are initial control rules, membership function, parameters' intervals, inserting a step signal with the amplitude of two at 0.5 s as a disturbance, and taking gaussian white noise signal with mean value of 0 and variance of 0.01 as measurement noise. Table 9.1, 9.2, 9.3, 9.4 give parameters of trigonometric membership function and PID controller obtained by fifteen generation GA optimization. Figures 9.3 and 9.4 are unit step responses with the two control schema.

From Figs. 9.3 and 9.4, we can conclude that the proposed fuzzy-PID controller can not only shorten rising time and reduce tracking error, but also have better performance of disturbance rejection. Therefore, the proposed method is promising.

9.5 Conclusion

In order to improve the control accuracy of fuzzy-PID controller, this paper proposes a new approach for multi-objective-optimization–based fuzzy-PID control. This method combines the advantages of fuzzy control and PID control, and makes design of controller independent of the controlled target. Meanwhile, fuzzy control rules and membership function are all optimized and self-adaptive operators of crossover and mutation are adopted, so computation speed and control accuracy are highly raised. Simulations of the given two-freedom servo system show the good performance of the proposed controller, and sequentially verify the validity of this paper.

References

1. Tao CW, Taur JS (2004) Robust fuzzy control for a plant fuzzy linear model [J]. IEEE Trans Fuzzy Syst 13:30–41
2. Deng X, Gong X et al (2010) Hydraulic servo-sewing vibration testing machines hardware-in-the-loop simulation using fuzzy-PID controlPID control algorithm [J]. Modul Mach Autom Manuf Tech 10:67–69
3. Cong S, Li Z (2006) Practical motion control techniques [M]. Publishing House of Electronics Industry, Beijing

 4. Tao Y, Yin Y et al (2003) Novel PID control and its application [M]. China Machine Press, Beijing
 5. Spatti DH, da Silva IN et al (2010) Fuzzy control system for voltage regulation in power transformers [J]. IEEE Lat Am Trans 8:51–57
 6. Li G (2005) Intelligent control and its MATLAB implementation [M]. Publishing House of Electronics Industry, Beijing
 7. Ren Z, Ren G (2004) Interpolation models of typical fuzzy controllers [J]. Fuzzy Syst Mat 18(1):67–75
 8. Tomioka S, Nisiyama S, Enoto S (2007) Nonlinear least square regression by adaptive domain method with multiple genetic algorithms [J]. IEEE Trans Evol Comput 11:1–16
 9. Roy R, Ghoshal S.P, Bhatt P (2009) Evolutionary computation based four-area automatic generation control in restructrured environment [C]. In: Third Internal Conference on Power System(ICPS 09), [s.n.], pp 1–6
10. Kuo T, Hwang SY (1996) A genetic algorithm with disruptive selection [J]. IEEE Trans Syst, Man Cybern 26:299–307
11. Liu Z, Zhou J, Lai S (2003) New adaptive genetic algorithm based on ranking [C]. In: Proceedings of the Second Internal Conference on Machine Learning and Cybernetics, Xi'an, China, vol 3, pp 1841–1844

Chapter 10
A New Naïve Style Possibilistic Network Classifier

Jianli Zhao, Jiaomin Liu, Zhaowei Sun and Yan Zhao

Abstract This paper proposes a new approach of classification under the possibilistic network (PN) framework with Tree Augmented Naïve Bayes Network classifier (TAN), which combines the advantages of both PN and TAN. The classifier is built from a training set where instances can be expressed by imperfect attributes and classes. A new operator, the possibilistic mean is designed to estimate the conditional possibility distributions of each attribute with imperfection, and the weight between two attributes given the class is determined by the conditioning specificity gain. Experiment has shown the efficiency of the new classifier in imperfect cases.

Keywords Tree augmented naïve bayes network · Possibility theory · Possibilistic classifier · Imperfect cases

J. Zhao (✉) · J. Liu
School of Electrical Engineering, Hebei University of Technology,
300130 Tianjin, China
e-mail: zhaojianli2005@126.com

Z. Sun
Hebei Education Department, Student Information and Employment Center,
050061 Shijiazhuang, China
e-mail: sunzhaowei@126.com

Y. Zhao
Hebei University of Science and Technology, 050018 Shijiazhuang, China
e-mail: zhaoyaner@126.com

10.1 Introduction

Tree Augmented Naïve Bayes (TAN) provided by Friedman [1] is widely used in Machine Learning and Data Mining with excellent performance. It permits each attribute node to have no more than one dependent attribute through tree structure to decompose the conditional probability, in which the class is the condition. In recent years, many scholars have proposed some improved TAN for higher classification accuracy and lower complexity of structure learning. The typical ones [2] are WAODE (weightily averaged one dependence estimator), HANB (hidden augmented naïve bayes classifiers). Nevertheless, the attribute values of all the TAN should be precise in the learning algorithms, while in some industrial practice some values are unable to get [3]. So, TAN as most probabilistic approaches runs into problems when faced with imperfection that may pervade datasets.

Possibilistic networks (PN) recently gained some attentions to handle uncertain as well as imprecise information for its close structural resemblance to probabilistic ones. While possibilistic propagation remains a NP—complete problem and this makes such networks unsuitable to the classification task due to the amount of data that has to be manipulated. Several attempts in the development of possibilistic classifiers construct the possibilistic framework with naive bayes classifiers, such as NBSPC [4] and NPC [5]. As the NB classifier, the independence assumption between attributes of NBSPC and NPC restricts their application in some fields. This fact has given us the idea to design a new classifier to take the benefits from the better classification performance of TAN classifier, and use possibility theory to handle imperfection.

10.2 Basic Theory

TAN classifier supposes that the structure of Bayesian network composed of attribute nodes $X_1, X_2, \ldots, X_n$ is a tree, that is to say each attribute variable has no more than one attribute parent except the class parent. So the classification formula of TAN is

$$c(x) = \arg \max_{c \in C} P(c) \prod_{j=1}^{n} P(x_j | parent(x_j), c), \ (parent(x_j) \text{ is the parent of } X_j).$$

$$(10.1)$$

Among the improved models for TAN, HANB (Hidden augmented naïve bayes classifier) [6] creates a hidden parent for each attribute which combines the influences from all the other attributes. This model can not only avoid the intractable computational complexity for learning an optimal Bayesian network, but also take the influences from all attributes into account.

Possibility theory was initiated by Zadeh as an approach to uncertainty induced by vague linguistic information [7]. Let $V = (X_1, X_2, \ldots, X_n)$ be a set of discrete variables. We denote by $\Omega^{(i)} = dom(X_i)$, $i = 1, \ldots, n$, the domain associated with

the X_i. $\Omega = \Omega^{(1)} \times \cdots \times \Omega^{(n)}$, which denotes the universe of discourse. The possibilistic network on is (G, Π_0), where (1) $G = (V, E)$ is a DAG over V, where V is the set of nodes and E is the set of edges. X_i is called the parent of X_j only if there is a directed edge from X_i to X_j. $par_G(X_j)$ is all the parent node of X_j. (2) $\Pi_0 = \{\pi(X_i)|par_G(X_i) \in [0, 1]|X_i \in V\}$ is a set of conditional possibilistic distribution.

Just as the demotion of Joint probability distribution of Bayes Network, the joint possibilistic distribution of V for $\forall x_{i_1}^{(1)} \in \Omega^{(1)}, \cdots, x_{i_n}^{(n)} \in \Omega^{(n)}$ is:

$$\pi(X_1 = x_{i_1}^{(1)}, \cdots, X_n = x_{i_n}^{(n)}) = \min_{k=1}^{n} \pi(X_k = x_{i_k}^{(k)}| \bigcap_{X_j \in par_G(X_k)} X_j = x_{i_j}^{(j)}). \qquad (10.2)$$

PN (Possibilistic Network) are well suited to represent and process imprecise information, while the possibilistic propagation remains an NP–complete problem, which makes such networks unsuitable to the classification task due to the amount of data we have to deal with. Some attempts in the development of possibilistic classifiers are NBSPC (Naïve Bayes Style Possibilistic Classifier) and NPC (Naïve Possibilistic network Classifier) and they are all under the assumption that all the attributes are conditionally independent given the class label. For more information, you can refer to [4, 5].

As the role specificity gain plays in possibility theory is similar to that of Shannon entropy in probability theory. We use specificity gain to measure the dependency between two nodes. Given the variable A, B and possibility distribution π, the specificity gain between A and B

$$S_{gain}(A, B) = nsp(\pi_A) + nsp(\pi_B) - nsp(\pi_{AB}). \qquad (10.3)$$

$$\pi_A = \sum_{a \in dom(A)} [\pi_A]_\alpha(a), \ \pi_B = \sum_{a \in dom(B)} [\pi_B]_\alpha(b), \ \forall a \in dom(A), \ \forall b \in dom(B).$$
$$(10.4)$$

$\pi_A(a)$ is the possibility degree of the variable A valued a, which is induced from the database, so as to the $\pi_B(b)$. $\pi_{A,B}(a, b)$ is the joint possibility degree of A and B, and you can refer to [8] for the detail computation method. π_A is the possibility distribution composed of all the degree of possibility $\pi_A(a)$. $nsp(\pi)$ is the nonspecificity of π, and $nsp(\pi_A) = \int_0^{\sup(\pi)} \log_2 |[\pi_A]_\alpha|d\alpha$, which is used to measure the conditioning dependency between two attributes given a class.

10.3 Tree Augmented Naïve Possibilistic Network Classifier

10.3.1 Building Procedure

We adopt the ideas of HANB to construct a TANPC, and the structure of TANPC
is shown in Fig. 10.1. C is the class node, and is also the parent of all attribute
nodes. Each attribute A_i has a hidden parent $A_{hpi}, i = 1, 2, \ldots, n$, represented by a
dashed circle.

The joint possibility distribution represented by a TANPC is defined as follows.

$$\pi(A_1, \cdots, A_n, C) = \min_{i=1}^{m} \pi(A_i | A_{hpi}, C),$$

$$\pi(A_i | A_{hpi}, C) = \sum_{j=1, j \neq i}^{m} W_{ij}^* \pi(A_i | A_j, C), \quad \sum_{j=1 \wedge j \neq i}^{m} W_{ij} = 1. \tag{10.5}$$

Here, we consider the case where this imperfection is represented by means of
possibility distributions, which expresses partial ignorance. We propose to cal-
culate a new value which better represents the plausibility of belonging of an
instance to a given class. To introduce our possibilistic classifier, we must estimate
the conditional possibility distributions at first. We call the new value possibilistic
mean (π_{P_m}), which is based on the one dependence assumption of attributes in
TAN and is only defined in product-based setting. Let Tr be a training set com-
posed of P instances characterized by K symbolic attributes and a possibility
distribution π reflecting the uncertainty over instance classes. We define the
following equation.

$$\pi_{P_m}(c_i) = \frac{1}{P} \sum_{j=1}^{P} \pi(I_j | c_i). \tag{10.6}$$

where $\pi_{P_m}(c_i)$ is called the possibilistic mean of the given the class c_i, computed
over Tr and $\pi(I_j | c_i)$ is the possibility distribution of the class c_i of the jth instance.

$$\pi_{P_m}(a_i | a_j, c_k) = \underset{Tr(a_i, a_j, c_k)}{mean} \alpha_i \beta_i \alpha_j \beta_j \pi(I_s | c_k). \tag{10.7}$$

where $\pi_{P_m}(a_i|a_j, c_k)$ is called the possibilistic mean of the attribute value a_i given the class c_k and attribute value a_j computed over Tr and $\pi(I_s|c_k)$ is the possibility distribution of the attributes values (I_s such the a_i and a_j belong to I_s) of instance s given the class c_k. α is scaled [0, 1] uncertainty factor that reflects the degree of belief of the set S contains the actual attribute value. Elements of the set S are supposed equipossible to be the real attribute value, thus we assign a possibility distribution $\beta = 1/n$ to each of them, and n denotes the cardinal of S. For the sake of simplicity we use $\pi(a_i|a_j, c_k)$ instead of $\pi_{P_m}(a_i|a_j, c_k)$ in the rest of this paper.

The approach to determine the weights W_{ij} is crucial for learning an TANPC, and we use the *conditioning specificity gain* between two attributes A_i and A_j as the weight of $\pi(A_i|A_j, C)$. The definition is in Eq. (10.8).

$$W_{ij} = \frac{S_{gain}(A_i, A_j|C)}{\sum\limits_{j=1 \wedge j \neq i}^{n} S_{gain}(A_i, A_j|C)}. \tag{10.8}$$

where $S_{gain}(A_i, A_j|C)$ is the *conditioning specificity gain* defined in Eq. (10.9).

$$S_{gain}(A_i, A_j|C) = \sum_{c \in dom(C)} \frac{\pi_C(c)}{\sum\limits_{c' \in dom(C)} \pi_C(c')}$$
$$\times \int_0^{sup(\pi)} \log_2 \frac{(\sum\limits_{a_i \in dom(A_i)} [\pi_{A_i|C}]_\alpha(a|c))(\sum\limits_{a_j \in dom(A_j)} [\pi_{A_j|C}]_\alpha(a_j|c))}{\sum\limits_{a_i \in dom(A_i)} \sum\limits_{a_j \in dom(A_j)} [\pi_{A_i, A_j|C}]_\alpha(a_i, a_j|c)} d\alpha. \tag{10.9}$$

TANPC need not to learn the structure of the PN, and it's time complexity about $O(nm^2 + n_c m^2 v^2)$, where m denotes the number of attributes, n denotes the number of the classes, $v = \frac{1}{m}\sum\limits_{j=1}^{n} n_j$ denotes the mean of the numbers of each attribute values.

10.3.2 Classification Procedure

In this section, we will present a classification method for perfect testing set. Base on the product-based definition of the possibilistic conditioning, a given instance is assigned to the most plausible class c^* defined as

$$c^* = \arg\max_{c_i} \pi_{P_m}(c_i) \prod_{j=1}^{m} \pi(a_j|A_{hpi}, c_i). \tag{10.10}$$

Just like the NPC, each of the attributes of the imperfect instance maybe described by a set S of values which has an uncertainty degree α to express the possibility of the assigned set S to contain the true value of the attribute.

Table 10.1 Description of datasets

Dataset	#Training	#Testing	#Attributes	#Classes
Congressional	448	49	16	2
Nursery	675	75	8	5
Solar flare	832	93	10	2

Table 10.2 Experimental results

Datasets	NBC		NPC		HANB		TANPC	
	PCC (%)	SD_WC	PCC (%)	SD_WC	PCC (%)	SD_WC	PCC (%)	SD_WC
Congressional voting	86.04	0.17	84.03	0.25	91.25	0.13	89.47	0.07
Nursery	73.59	0.25	76.6	0.36	83.74	0.22	80.66	0.25
Solar flare	78.74	0.27	82.19	0.17	87.62	0.18	85.79	0.11
Mean	*79.46*	*0.23*	*80.94*	*0.26*	*87.54*	*0.18*	*85.31*	*0.14*

A given instance is assigned to the most plausible class c^* defined as

$$c^* = \arg\max_{c_i} \prod_{j=1}^{m} mean_{k=1, \alpha_{jk} \neq 0}^{cardinal(A_j)} \alpha_{jk} \pi(A_{jk} \mid A_{hpj}, c_i). \qquad (10.11)$$

where $cardinal(A_j)$ denotes the numbers of value of attribute A_j, and α_{jk} is the possibility degree of attribute value α_{jk} in $\vec{i}_1$, and A_{jk} is the kth possible value of attribute A_j.

10.4 Experimental Results

Available dataset are perfect, thus we have to artificially introduce imperfection. We assign a normalized random set of possibility distributions to each imperfect attribute, so that the actual value receives the highest possibility distribution (equals to 1). We have applied NPC, NBC, HANB and TANPC to three real databases obtained from the UCI repository of Machine Learning databases [9] using 5-fold-cross validation, and all the datasets are given in Table 10.1, where #Training, #Testing, #attributes, and #classes denote, respectively, the number of training instances, the number of testing instances, the number of attributes and the number of classes.

We have provided two measures to evaluate the performance of the four classifiers. One is percent of correct classification (PCC) defined as Eq. (10.12). For each instance to classify, we choose the class which has the highest degree of possibility. If more than one class is obtained, then one which has the highest initial possibility distribution is chosen. For further comparing the classification accuracy of the four classifier, we have proposed another measure, called Standard

deviation of well classification (SD_WC) defined as Eq. (10.13) especially for the well classified instances.

$$PCC = \frac{number(well\ classified\ instances)}{number(total\ classified\ instances)} * 100.\qquad(10.12)$$

$$SD\_WC = \sqrt{\frac{\sum_{i=1}^{K}(1-\Psi(i))^2}{K}}.\qquad(10.13)$$

where K is the number of the well classified instances.

In NBC and HANB, $\Psi(i)$ is $P'(c_i)$, which denotes the computed probability of the ith instance belonging to the class c. while in NPC and TANPC, $\Psi(i)$ is $\pi'(c_i)$, which denotes the computed possibility degree of the ith instance assigning to the class c. Table 10.2 shows the comparison results.

From the experiments result we can know that the TANPC maintains computational complexity of TAN and at the same time displays better accuracy. But its PCC is little lower than HANB.

10.5 Conclusion

In this paper, we have addressed the problem of constructing a classifier from imperfect data. The proposed classifier, named TANPC is a possibilistic counterpart of the TAN ones and it is built from a training set where instances can be expressed by imperfect attributes and classes. Furthermore, TANPC is able to classify new instances that may have imperfect attributes. Unfortunately, we could not get hold of any real world dataset containing "true" imperfect attribute values, while artificial introduction of imperfection will influence the accuracy of classification. In the nearly future, if anyone can direct us to such a dataset, we are confident that the TANPC will prove successful when applied to true imprecise data. Another improvement is that we will extend our TANPC to handle numeric attributes.

References

1. Friedman N, Geiger D, Goldszmidt M (1997) Bayesian network classifiers. Mach Learn 29:131–163
2. Jiang L, Zhang H, Cai Z (2009) A novel Bayes model: hidden naive Bayes. IEEE Trans Knowl Data Eng 21(10):1361–1371
3. Sun Z, Finnie GR (2007) A fuzzy logic approach to experience-based reasoning. Int J Intell Syst 22(8):867–889

4. Borgelt C, Gebhardt J (1999) A naïve Bayes style possibilistic classifier. In: Proceedings of seventh European Congress on intelligent techniques and soft computing, Germany, pp 556–565
5. Haouari B, Ben Amor N, Elouedi Z et al (2009) Naïve possibilistic network classifiers. Fuzzy Sets Syst 160(22):3224–3238
6. Zhang H, Jiang L, Su J (2005) Hidden naive Bayes. In: Proceedings of twentieth national conference on artificial intelligence (AAAI '05), pp 919–924
7. Ben Amor N, Benferhat S, Dubois D et al (2003) Anytime propagation algorithm for min-based possibilistic graphs, Soft computing, A fusion of foundations. Methodologies and Applications, vol 8. Springer, Berlin, pp 150–161
8. Borgelt C (2000) Data mining with graphical models [D]. Otto-von-Guericke-University of Magdeburg, Germany
9. Frank A, Asuncion A (2010) UCI machine learning repository. University of California, School of Information and Computer Science, Irvine [http://archive.ics.uci.edu/ml]

Chapter 11
An Improved Ant Clustering Algorithm Based on Habitation-Searching

Yu-bo Duan, Zhong Dai, Qin Chen, Ke-yong Shao and Shuang-shuang Xu

Abstract An Improved Ant Clustering Algorithm based on habitation-searching is proposed to solve the clustering problem in data mining. In this algorithm, each ant stands for one data object, and the ants search suitable places to stay according to the probability function for ants becoming active and the clustering rules, which are given in the paper. The ants affect each other in the process, in this way the clustering will be formed by dynamic self-organization for the ants. Besides, in order to improve the quality and speed of the clustering, the activation threshold changes adaptively as the algorithm runs. The achieved results are compared with those obtained by LF algorithm, showing that significant improvements are obtained by the proposed method, and demonstrating the effectiveness of the algorithm.

Keywords Ant clustering algorithm · Habitation model · Probability activation function · Data mining

11.1 Introduction

Proposed by Italian scholar M. Dorigo in the early 20th century for the first time, Ant Colony Algorithm [1] is an evolutionary algorithm which is applied to combinatorial optimization. It possesses a number of properties such as intelligent

Y.-b. Duan (✉) · Q. Chen · K.-y. Shao · S.-s. Xu
Electrical and Information Engineering College, Northeast Petroleum University, 163318, Daqing, China
e-mail: duanyubo2011@163.com

Z. Dai
Natural Gas Branch of Daqing Oilfield, 163318 Daqing, China

search, global optimization, robustness, positive feedback and distributed parallel computing.

Inspired by the behaviors of ants such as food hunting and corpses piling, a series of ant colony algorithms have been designed and successfully applied to the areas of combinational optimization [1–4], network routing [5] and robotics [6]. Some researchers have made achievements in data mining by simulating swarm intelligence. Deneubourg et al. [7] proposed a basic model (*BM*) and simulated in clustering successfully. Based on *BM*, Lumer and Faieta [8] presented a similarity measure between two data objects and designed the *LF* algorithm for data clustering. Recently, a large number of authors have developed more sophisticated models based on *BM* and *LF* models. But all separate ants from the being clustered data objects, which brings a large amount of extra information storage and more computation time caused by ants' large amount of random idle moves before they pick up or drop corpses and large amount of repetition occurs during the random idle moves.

In order to overcome the aforementioned problems and get a higher quality in clustering, we propose an Ants Habitation Model (*AHM*) and an Improved Ant Clustering Algorithm (*IACA*) based on the phenomenon that ants tend to stay with fellows with similar features. In *IACA*, each ant represents an individual data object. Ants move according to the probability activation function and clustering rules, form into groups eventually and hence the corresponding data items are clustered. Besides, the activation threshold changes adaptively in the process of clustering to ensure the quality.

11.2 Ants Habitation Model

Ant nests are close to each other, so they can take care of each other and resist the invasion of outsiders. However, ant nests are grouped rather than distributed evenly, those have similarly features live relatively close and those have different features are far away from each other. For the need of security, ants are inclined to choose more comfortable and secure environment to stay. This makes ants to group with those that have similar features. Even within an ant group, they like to have familiar fellows in the neighborhood. This is the inspiration for us to design the Ants Habitation Model (*AHM*). In the *AHM*, the ant searches for a comfortable position to stay, and his behavior is simple and repetitive: when he is not satisfied with his current position, he becomes active to search for a suitable place to stay. The further details of *AHM* can be shown by follows:

In *AHM*, each ant represents one data object, which is closer to the nature of clustering problem. For convenience, we use q_i to stand for the state of ant_i, where $q_i = (x_i, c_i)$, $(1 \leq i \leq n)$, and n is the number of data set, c_i is the label of cluster. When calculating the fitness of ant_i, we take into consideration the ants that are both in the neighborhood of γ and with same label. Then we define $f(ant_i)$ as follow to describe the current fitness of ant_i

$$f(ant_i) = \sum_{j=1}^{n_1} \exp\left[\frac{-\|x_i - x_j\|^2}{(0.5\gamma)^2}\right] \tag{11.1}$$

where x_j represents the ants in the surrounding area of γ and those have the same label with x_i, and n_1 is the number of x_j. The less similarity with neighbors an ant is, the lower the fitness is, and more bigger probability of activation is needed, so the ant is easier to be waken up to be active, and searches for the best place to stay. That is to say, the activation probability decreases with high fitness, therefore, the probability function of activation can be expressed as follow:

$$p(ant_i) = e^{-\alpha \cdot f(ant_i)} \tag{11.2}$$

In the above, α is a parameter, and can be called ant's activation threshold. At the beginning of clustering, letting the value of α be equal to the mean distance of all ants. In order to improve the quality of clustering, the value of α is adjusted adaptively during the process of clustering. We use

$$\overline{f(t)} = \frac{1}{n}\sum_{i=1}^{n} f(ant_i) \tag{11.3}$$

to express the average fitness of ants in the tth iteration. To a certain extent, $\overline{f(t)}$ indicates the quality of the clustering. The value of α can be modified adaptively using the following function

$$\alpha = \alpha + k'\Delta\overline{f(t)} \tag{11.4}$$

k' is a constant. When the value of $f(ant_i)$ is determined, the value of $p(ant_i)$ decreases if α is increased. This means the ant has less chance to be activated with large α. Generally, ants can form a rough clustering quickly in the initial stage of clustering with smaller α, while at the latter stage when the whole quality is high, increase α so that the ants in the proper places have less chance to be activated, which can retain the whole high quality. In order to avoid updating α too frequently, we can update α every 20 iterations. The labels of clusters update by the following rules: (a) if an ant becomes active, his label changes to the label of the ant which has the smallest distance with him; (b) if the state is unchanged, the label remains unchanged.

During iterations, we can calculate the cluster centers by the following expression:

$$\overline{v_k} = \frac{1}{H}\sum_{i=1}^{H} x_i \tag{11.5}$$

where x_i belongs to cluster k, and H corresponds to the sum of data belong to cluster k.

Both in *BM* and *LF* models, ants are separated from the being clustered data objects, since the clustered data objects can hardly move automatically and directly, movements of the being clustered data have to be executed by the ants' movements, which brings a large amount of extra information storage. Moreover, in *LF* ants carrying isolated data will make continuous movements since they will never find a suitable location to drop down the isolated data which increases the running time, and for ants' idle movements when carrying no data object consume considerable computational time. While in *AHM*, things are different, and ants directly represent the being clustered data objects, therefore, no such problem exists. Further more, ants move according to a very little local neighborhood information and the parameters are adjusted adaptively, the cluster is formed dynamically through ant's cooperation. Besides, the results are given by the labels, so it is more direct and easier than *BM* and *LF*.

11.3 Improved Ants Clustering Algorithm

According to the above explanation, the *IACA* can be described as follows: initialize the parameters; label every ant; calculate ant's fitness $f(ant_i)$ and activation probability $p(ant_i)$ according to (1) and (2); for each ant, if $p(ant_i) \geq p_0$, ant_i becomes active, then searches for a suitable place and changes his label; update the labels of clusters, and calculate cluster centers according to (5); with a certain probability, reactivate those categories which are very close and the one only have one datum to find suitable places and change the category number; update the labels of clusters and cluster centers once again;

calculate the *k*th cluster's deviation error $D_k = \sum_{i=1}^{H} (\sum_{j=1}^{m} (x_{ij} - v_{kj})^2)^{1/2}$ and the whole error $\varepsilon = \sum_{k=1}^{c} D_k$, if $\varepsilon \leq \varepsilon_0$, end the iteration and output the results. Otherwise, continue; if it is necessary to update α, then modify α according to (4);

$t = t + 1$, if $t > t_{max}$, break and output the results, else return to c.

11.4 Experimental Results

In order to evaluate the performance of the proposed approach, we choose the famous Iris and Wine data set to experiment, and for comparison, *LF* and *IACA* will be applied respectively. In the test, abundance of experimental results show that the *IACA* clustering results after 3 000 iterations are mostly better than those of *LF* after 1 000 000 iterations. We adopt the maximum iterations of *LF* algorithm as 1 000 000, and those for *IACA* as 3 000 in all experiments. We choose the parameters $k_1 = 0.10$, $k_2 = 0.15$ in *LF* [8], and also initialize α value of *IACA* as

Table 11.1 Test results of *IACA* and *LF* on Iris and Wine

Data set	Iris		Wine	
Algorithm	LF	AHC	LF	AHC
Maximum iterations	1 000 000	3 000	1 000 000	3 000
Average running times (s)	56.81	5.66	62.37	7.44
Average errors	6.68	4.56	8.65	5.82
Percentage of the errors (%)	4.45	2.84	4.52	2.61

Fig. 11.1 The first two properties' projection of Iris data set
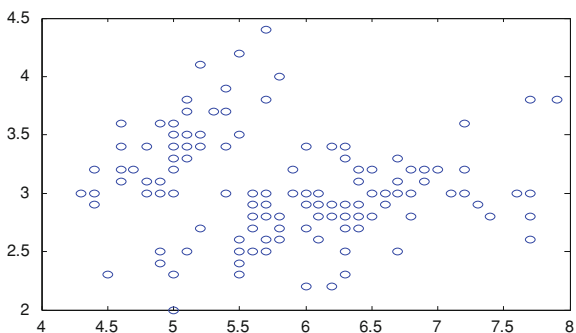
Fig. 11.2 The clustering results of IACA
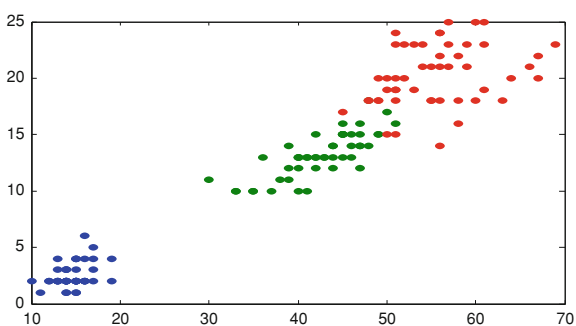
0.1. Results of 150 trials of both algorithms on Iris and Wine data set are described in Table 11.1. The first two properties' projection of Iris data set is shown in Fig. 11.1, and the clustering results of *IACA* depict in Fig. 11.2.

It can be observed that *IACA* is superior to *LF*, the quality of the clustering of *IACA* is better than *LF*, and *LF* algorithm costs much more computation time than *IACA*, because *LF* algorithm spends much time on searching for the proper location to pickup or drop down the data objects, what's more, in *LF* algorithm, ants make mass idle move and the parameters are not adaptively selected, it takes quite a lot of time to cluster and affects the quality of clustering results. On the contrary, in our algorithm, ants or the being clustered data move effectively and the parameters are selected and adjusted adaptively, so it costs less time and can obtain better clustering quality.

11.5 Conclusion

An Ants Habitation Model (*AHM*) and An Improved Ant Clustering Algorithm (*IACA*) are presented to solve the clustering problem in data mining by simulating the behaviors of gregarious ant colonies. In *AHM*, each data object is represented by an ant. The ants gradually find suitable places to rest according to the probability function for ants becoming active and the clustering rules, and then change their labels dynamically. The movement of an ant influences the fitness of his neighbors. With the number of iterations increase, such movements gradually increase, eventually making similar ants gathered within a small area and different types of ants located in separated areas. Thus, the corresponding data objects are clustered. In *IACA*, the ants can form into high-quality clusters by making simple moves according to little local neighborhood information and the parameters are selected and adjusted adaptively. Experimental results demonstrate *AHM* and *IACA* cost less times and are more efficient than *BM* and *LF*.

References

1. Dorigo M, Maniezzo V, Colorni A (1996) Ant system: optimization by a colony of cooperative learning approach to the traveling agents. IEEE Trans Syst Man Cybernet 26(1):29–41
2. Gutjahr WJ (2002) ACO algorithms with guaranteed convergence to the optimal solution [J]. Inform Process Lett 82(3):145–153
3. Hongjian C, Ling C, Ling Q et al (2003) Application of genetic algorithms based on the strategy of gene reconfiguration [C]. The processing of the second asian workshop on foundations of Software. Southeast University Press, pp 89–92
4. Watanabe I, Matsui S (2003) Improving the performance of ACO algorithms by adaptive control of candidate set. Proc 2003 Congress Evol Comput 2:1355–1362
5. Liu LG, Feng GZ (2007) Simulated annealing based multi-constrained QoS routing in mobile ad hoc networks. Wirel Pers Commun 41:393–405
6. Liu S, Mao L, Yu J (2006) Path planning based on ant colony algorithm and distributed local navigation for multi-robot systems. In: Proceedings of 2006 IEEE international conference on mechatronics and automation pp 1733–1738
7. Deneubourg JL, Goss S, Franks N et al (1991) The dynamics of collective sorting: robot- like ant and ant- like robot [C]. In: Proceedings of the first conference on simulations of adaptive behavior: from animals to animats. MIT Press, Cambridge, pp 356–365
8. Lumer E, Faieta B (1994) Diversity and adaptation in populations of clustering ants [C]. In: Proceedings of the third international conference on simulation of adaptive behavior: from animals to animats. MIT Press, Cambridge, pp 499–508

Chapter 12
An Optimal Model of Full Postponement Strategy in a Two-Stage Supply Chain

Yanhong Qin and Guangxing Wei

Abstract We set stackelberg-game model and centralized model of full postponement strategy in a two-stage supply chain made up of one manufacture and one distributor in the first place, and then we study the impact of decision variables, i.e. customization service price and promised customization time of distributor, final customized product price and promised delivery time of manufacture on the profit of manufacture, distributor and supply chain.

Keywords Postponement · Stackelberg game · Mass customization · Centralization

12.1 Introduction

Postponement is the capability of a supply chain to delay product differentiation or customization until closer to the time that demand for the product is known [1], and the product is kept in the generic form in the upstream of supply chain with lower inventory cost until to the point of differentiation closer to final customer. As well known to us, the most important problem of postponement of mass customization is the response time and price of customized product, which will influence the customer choose between the customized product and standard products and thus the profit of manufacture and supply chain. If the price of customized product is too high or the delivery time is too long exceeding the specified waiting time of customer, then the customer will abandon purchasing

Y. Qin (✉) · G. Wei
School of Management of Chongqing Jiaotong University, 400074 Chongqing, China
e-mail: qinyanhong24@163.com

customized product or turn to buy the standard product on the shelf or the more competitive product of other manufacture of supply chain. That is to say, various customer in mass customization is some sensitive to the price and response time of customized product, so the manufacture must provide the competitive combination of price and delivery time of customized product in the supply chain, especially after the customer order decoupling point (CODP) where the manufacture activity is driven by customized demand. In this paper, we consider the impact of price and promised delivery time of customized product on the manufacture and the distributor under the full postponement strategy which is different from the full postponement strategy in Yeung et al. [2] but relative to the postponement strategy in Graman [3], and the full postponement strategy here means the manufacture produce only the generic product and the final customization activity is completed at distributor. The customer sends order to manufacture who will provide the final product price and promised delivery time of supply chain for customer based on the customization service price and time of distributor. So the decision sequence is that the distributor makes decision on the customization price and promised customization time firstly, and then the manufacture makes decision on the final product price and promised response time of supply chain, which form a Stackelberg game relation, i.e. the distributor is leader and manufacture is follower in the supply chain.

12.2 Assumption and Notation

Assumptions:

(1) The number of basic or common product is equal to the final product, i.e. each final product contains one unit of the common item and the difference among products is cosmetic, such as color, interface, appearance, and so on, so the price of each customized product is same.
(2) Once the common product finished by manufacture, they will be conveyed to distributor, so there is no inventory at manufacture.
(3) The market demand is linear and negative to product price and promised delivery time, but there is no relation between product price and promised delivery time. Besides, in unit time, there are always same orders for the customized products in certain market, so the distributor serve for the same number customers in each time, and the problem can be regarded as the M/M/1 model in queuing theory.

For the manufacture adopt the mass production mode, so the manufacture time and efficiency of common product is stable and constant. Besides, from the supply chain, the work of conveying common product and the customized products is outsourced and the transportation time is stable and can be regarded as constant for the professional logistics.

Notation:

P: The price of final customized product, i.e. the price of unit product quoted for customer by manufacture;

P_c: The price of customized service quoted for manufacture by distributor;

T_c: The time of customization promised by distributor;

T_{sc}: The delivery time promised by manufacture to customer;

D: According to assumption (4), the market demand $D = \alpha - \beta_1 P - \beta_2 T_{sc}$ $(\alpha, \beta_1, \beta_2 \geq 0)$();

q: The orders in unit time for the customized products in certain market;

t_c: The actual time of customization performed by distributor, $F(t_c)$ denotes the distribution function, and $f(t_c)$ is the corresponding density function;

π_m^d, π_r^d, π_{sc}^d: The expected profit obtained by manufacture, distributor and supply chain where the manufacture dominates the supply chain and both manufacture and distributor make decision independently;

π_m^c, π_r^c, π_{sc}^c: The expected profit obtained by manufacture, distributor and supply chain where both manufacture and distributor make decision collaboratively from maximizing the profit of whole supply chain, and this decision mode is called centralized decision model

α: The maximal demand for the final product in the unit time of supply chain;

β_1: The price elasticity of customized demand;

β_2: The elasticity of response time of supply chain;

γ_c: The penalty cost of unit time and unit product paid for the customer by manufacture when the customized product is delivered in postponed way, i.e. the delivery time exceeds the specified waiting time of customer;

γ_m: The penalty cost of unit time and unit product paid for the manufacture when the distributor can't delivery customized product;

T_m: The total time of manufacture and transportation between manufacture and distributor and delivery between distributor and customer;

C_m: The cost of unit common product produced by manufacture;

C_r: The cost of unit product customization happened in distributor

As above, the market demand function is

$$D = \alpha - \beta_1 P - \beta_2 T_{sc} (\alpha, \beta_1, \beta_2 \geq 0) \tag{12.1}$$

The response time of supply chain is

$$T_{sc} = T_m + T_c \tag{12.2}$$

For the assumption (7), the promised response time of supply chain T_{sc} is linear to customization time, so we can translate the decision problem of T_{sc} to the optimal decision of T_c. As a result, the total orders in unit time is

$$Q = D(P, T_c) \tag{12.3}$$

As the assumption (6), the distributor serve for the q customers, the problem can be reduced as the M/M/1 model in queuing theory, i.e. one service desk

(it means the distributor in this paper) serves for the q customers, and the reach time between each batch follows the negative exponential distribution. Similarly, t_c follows the negative exponential distribution with the parameter λ, and $1/\lambda$ denote the average time of customization performed by distributor, so the density function is:

$$f(t_c) = \begin{cases} \lambda e^{-\lambda t_c} & t_c > 0 (\lambda > 0) \\ 0 & else \end{cases} \tag{12.4}$$

The distribution function is

$$F(t_c) = 1 - e^{-\lambda t_c}, \quad (\lambda > 0) \tag{12.5}$$

12.3 The Profit Model in Stackelberg Game

When the common product is produced by manufacture, there are three relative cost: manufacture cost of common product, the service cost paid to distributor to finish the final customization by manufacture, the penalty cost paid to customer as a result of delayed delivery. Besides, the manufacture can obtain revenue in product sale and penalty expense from the distributor for the excess customization time. So the expected profit of manufacture is:

$$\pi_m^d(P) = [P - C_m - P_c - r_c \int_{T_c}^{\infty} (t_c - T_c)f(t_c)dt_c + r_m \int_{T_c}^{\infty} (t_c - T_c)f(t_c)dt_c]Q \tag{12.6}$$

The profit model of distributor is

$$\pi_r^d(P_c, T_c) = [P_c - C_r - r_m \int_{T_c}^{\infty} (t_c - T_c)f(t_c)dt_c]Q \tag{12.7}$$

In this model, the manufacture and distributor share the demand information, i.e. when the manufacture obtains order and sends the customized demand information to distributor, the distributor will provide the customization price and time, and then the manufacture will provide the product price and promised response time of supply chain for customer. So the decision sequence is the distributor makes decision firstly, and then the manufacture makes decision, which form a game relation of Stackelberg. The backward induction method is adopted to solve the problem, given the decided customization time and price of distributor. Take the Eqs. (12.1), (12.2) into (12.6), and then

$$\pi_m^d(P) = [P - C_m - P_c - r_c \int_{T_c}^{\infty} (t_c - T_c)f(t_c)dt_c + r_m \int_{T_c}^{\infty} (t_c - T_c)f(t_c)dt_c]$$
$$(\alpha - \beta_1 P - \beta_2 T_m - \beta_2 T_c) \tag{12.8}$$

The first order derivation and second order derivation is $d^2\pi_m^d/dp = -2\beta_1 < 0$.

Obviously, the profit function is concave in decision variable P, when P change in $[0, \infty)$, the manufacture can obtain the maximal profit at the optimal solution P^* given P_c and T_c. Let $d\pi_m^d/dp = 0$:

$$P^* = \frac{\alpha - \beta_2 T_c - \beta_2 T_m}{2\beta_1} + \frac{1}{2}[C_m + P_c + (\gamma_c - \gamma_m) \int_{T_c}^{\infty} (t_c - T_c)dt_c] \tag{12.9}$$

The distributor can forecast P^*, so the distributor can maximize the profit by

$$\max \pi_r^d(P_c, T_c) = [P_c - C_r - r_m \int_{T_c}^{\infty} (t_c - T_c)f(t_c)dt_c]Q \tag{12.10}$$

Take Eqs. (12.1), (12.2) and (12.9) into (12.3), then

$$Q = \frac{1}{2}\{[\alpha - \beta_2(T_c + T_m)] - \beta_1[C_m + P_c + (\gamma_c - \gamma_m) \int_{T_c}^{\infty} (t_c - T_c)f(t_c)dt_c \tag{12.11}$$

The Hessian matrix is $H = \begin{bmatrix} -\beta_1 & F(T_c) - 1 - \beta_2 \\ 0 & -\gamma_c f(T_c) \end{bmatrix}$. So the profit function of distributor is joint concave in T_c and P_c. There exist optimal $T_c^* P_c^*$ to maximize the profit of distributor, let $\frac{\partial \pi_r^d}{\partial P_c} = 0$, $\frac{\partial \pi_r^d}{\partial T_c} = 0$, and then

$$P_c^* = \frac{\alpha - \beta_2(T_c + T_m)}{2\beta_1} + \frac{1}{2}[C_r - C_m + (2\gamma_m - \gamma_c) \int_{T_c^*}^{\infty} (t_c - T_c^*)f(t_c)dt_c \tag{12.12}$$

$$T_c^* = F^{-1}(1 - \frac{\beta_2}{\gamma_c \beta_1}) \tag{12.13}$$

When we take Eq. (12.5) into the above equation, then $T_c^* = \frac{1}{\lambda}\ln(\frac{\gamma_c \beta_1}{\beta_2})$.

12.4 The Profit Model in Centralized Mode

For more and more supply chains are adopting the centralized decision mode to meet the various customer requirement and maximize the profit of supply chain, so there are two variables, i.e. the response time of supply chain and the customization time of distributor. The profit of supply chain is

Table 12.1 The optimal results in stackelberg-game model

Decision variable	Requirement	The distributor			The manufacture			Supply chain
	D	P_c	T_c	Profit	P	T_{sc}	Profit	Profit
Result	60.7	945.63	2.23	19,894	1552.3	6.35	99,743	119,637

Table 12.2 The optimal results in centralized model

Decision variable	Requirement	The supply chain		
	D	P	T_{sc}	Profit
Result	114.5	1357.8	6.35	119,637

$$\pi_{sc}^c = [P - C_m - C_r - \gamma_c \int_{T_c}^{\infty} (t_c - T_c)f(t_c)dt_c]D \qquad (12.14)$$

Similar to the analysis above, take Eqs. (12.1), (12.2) and (12.3) into (12.15)

$$\pi_{sc}^c = [P - C_m - C_r - \gamma_c \int_{T_c}^{\infty} (t_c - T_c)f(t_c)dt_c] \times [\alpha - \beta_1 P - \beta_2(T_m + T_c)] \qquad (12.15)$$

Obviously, the profit function is concave in decision variable P, when P change in $[0, \infty)$, the manufacture can obtain the maximal profit at the optimal solution P^* given P_c and T_c. Let $\frac{d\pi_m^d}{dP} = 0$:

$$P^* = \frac{\alpha - \beta_2 T_c - \beta_2 T_m}{2\beta_1} + \frac{1}{2}[C_m + P_c + \gamma_c \int_{T_c}^{\infty} (t_c - T_c)dt_c] \qquad (12.16)$$

$$T_c^* = F^{-1}(1 - \frac{\beta_2}{\gamma_c \beta_1}) \qquad (12.17)$$

So, the optimal customization time of distributor in stackelberg-game model and centralized model is same, and then the response time of supply chain is same.

12.5 Numerical Analysis

The operation data of supply chain in some location is as following:

$\alpha = 420$, $\beta_1 = 0.2$, $\beta_2 = 1.0$, $C_m = 750$, $C_r = 380$, $\gamma_c = 40$, $\gamma_m = 50$, $T_m = 10$, $\lambda = 4$.

Then we compare the Tables 12.1 and 12.2, we can get some important conclusions: (1) The optimal customization time and then the optimal response time of supply chain in stackelberg-game model and centralized model is same; (2)

The price of final product of supply chain in centralized model is lower than that in stackelberg-game model, but the market requirement scale and the total profit in centralized model is bigger than that in stackelberg-game model.

12.6 Conclusion

For various customers in mass customization is sensitive to the price and promised response time of customized product, so the manufacture must provide the competitive combination of price and delivery time of customized product to some extent, especially in the downstream of the CODP in the supply chain. Given a supply chain is made up of one manufacture and one distributor in stackelberg game condition and centralized decision model, we can compute the optimal combination of decision variables, i.e. customization price, customization time and final product price to maximize the profit of manufacture and distributor under the full postponement strategy, i.e. the manufacture produce only the generic product and the final customization activity is completed at distributor. Besides, we analyzed the impact of different decision variable on the customization cost and profit of whole supply chain between stackelberg-game model and centralized decision model.

References

 1. Gattorna J (2006) Living supply chains. Prentice Hall, Harlow
 2. Yeung JHY, Seles W, Deming Z (2007) Postponement strategy from a supply chain perspective: cases from China. Int J Phys Distrib Logist Manag 37(4):331–356
 3. Graman GA (2010) A partial-postponement decision cost model. Eur J Oper Res 201:34–44
 4. Danuta KM, Artur S (2010) The selected determinants of manufacturing postponement within supply chain context: an international study. Int J Prod Econ 133(1):192–200
 5. Lee HL, Tang CS (1997) Modeling the costs and benefits of delayed product differentiation. Manag Sci 43:40–53
 6. Li S, Ragu-Nathan B, Ragu-Nathan TS (2007) The impact of supply chain management practices on competitive advantage and organizational performance. Omega 34(3):107–124
 7. Wong H, Potter A, Naim M (2010) Evaluation of postponement in a soluble coffee supply chain: a case study. Int J Prod Econ 131(1):355–364
 8. Yang J, Zhao SG (2005) Study on postponement in customization supply chain. Ind Eng Manag 23(4):5–41
 9. Mason R, Lalwani C (2008) Mass customized distribution. Int J Prod Econ 114(2):71–83
10. Luck R, Ray A (1990) An observer based compensator for distributed delays. Automatica 26(5):903–908

Chapter 13
Application of an Improved Watershed Algorithm in Craniocerebrum MRI Image

Mingquan Wang

Abstract In light of the fuzziness of craniocerebrum MRI image and the requirement in practical application, an improved watershed algorithm is proposed. In consideration of the structure information of image, the valley-bottom value produced by noise is very small. However, the minimum valley-bottom of each area will have a very big dynamic value corresponding to real area, which is close to the valley-bottom dynamic value when there is no noise. Hence, the valley-bottom produced by noise can be filtered, thusly effectively restraining the over-segmentation, provided that a threshold is simply given. Experimental results show that the algorithm can quickly and accurately obtain the segmentation result of medical image, possessing higher noise-resistant capability.

Keywords Watershed · Over-segmentation problem · Dynamics combination rule · Craniocerebral MRI image

13.1 Introduction

The image segmentation technology is the key technology in medical image processing and analysis. It is also a necessary and important procedure for extracting special histological information from medical images. There are many methods of medical image segmentation [1]. However, Owing to complexity of human anatomy structure, irregularity of human organs and tissue, individual

M. Wang (✉)
Key Laboratory of Instrumentation Science and Dynamic Measurement,
Ministry of Education, North University of China, Taiyuan, China
e-mail: wangmq@nuc.edu.cn

varieties and different characteristics of medical image modes, the effect of general image segmentation algorithm is not idealistic. Because method of medical-image segmentation has better pertinence, it is realized that no segmentation algorithm can satisfy all image patterns [2].

The shortage of watershed consists in over-segmentation. The image is segmented to too many small areas to appear the interested target [3]. The purpose of watershed transform is to seek watershed-line of gradient image. Therefore, the segmentation method which is based on watershed depends on the algorithm that counting gradient of inactive segmenting image. But, for image segmentation based on watershed transform, because traditional morphologic gradient algorithm has a serious shortage, which is influenced by noise and quantization error, produced many local valley-bottom within the equal and consistent area. Moreover, each valley-bottom of gradient image will introduce a catchment basin during the watershed transform. Therefore, the gradient operator will bring on over-segmentation ultimately. That is to say an equal and consistent area may be divided into multi-areas so as to bring a great deal illusory edge and unable to affirm which is the real edge.

In summary, we have proposed an improvement watershed algorithm, carried on the method through the dynamic combination rule which divides while merges, effective suppression over-segmentation phenomenon. Because we considered the picture structure information, the value of valley-bottom which was due to the background, the noise, the edge and the internal tiny change in the picture was very small, but corresponds to the genuine region, in each region smallest valley of valley-bottom had a very great value, which was similar to dynamic value of valley-bottom which did not happen the tiny change. The method was used to divide some CT pictures. The experimental result indicated the method may obtain the better division result.

13.2 Improved Method of Watershed

13.2.1 Summary

The method of watershed [4] is provided with lighter calculate burden and higher segmentation precision; Usually, proceed watershed transform for morphologic gradient signal of the inactive segmenting image, Namely, gradient images are regarded as fictitious landform surface, moreover, gradient of each pixel represent height of the spot; because edge pixel of the inactive segmenting image usually have biggish gradient, the gradient correspond to watershed-line of the earth's surface; Pixels within each region usually have smaller gradient, therefore, corresponding to catchment basin of the earth's surface; Such watershed-line segment gradient image into some different catchment basins which correspond the equal and consistent area of inactive segmenting image separately.

13.2.2 Improved Method

Dynamic combination rule is an otherness concept and a sort of measuring for gray difference and the measuring is based on definite structure information. It is not measuring extreme point or drainage area that corresponds to extreme point, but measuring structure which include the extreme point. In consideration of structure information, thus, remove excess valley-bottom. The information of shape and size is not available in the calculation of dynamic combination rule. Therefore, needn't know prior knowledge. It is provided with great versatility [5].

First, define dynamic value of a path between two spots. The dynamic value is the height difference between tiptop and low-water mark, i.e.

$$D(P(x,y)) = sup|f(x_i) - f(x_j)| \quad x_i x_j \in P(x,y) \tag{13.1}$$

P(x, y) indicates the path which joins x and y. sup indicates least upper bound, f(x) indicates gray of X spot.

In order to restrain over-segmentation, need to remove unimportant valley-bottoms, therefore, calculate the dynamic value of valley-bottom. Dynamic value of valley-bottom M equal to the least dynamic value in all path that link M and another spot whose gray is less than M, h(M), h(N) indicate height of valley-bottom. In this way:

$$D(M) = inf(D(P(x,y))) \quad x \in M, y \in N, h(M) > h(N) \tag{13.2}$$

D(M) indicates dynamic value of valley-bottom M, inf indicates infimum.

Figure 13.1 indicates an image included noise, actually, M, N is the real valley-bottom without noise. The image only contains two areas, but due to the influence of the noise we can see many small valley-bottoms from the figure, valley-bottom will bring a small area on condition that it is segmented by watershed directly, thus, emerge phenomena of over-segmentation. Now, calculate dynamic value of each valley-bottom separately, and label calculated value in the figure, In consideration of the structure information, It can be see from the figure that those valley-bottom value produced by noise is very small, for real area, there is a prodigious dynamic value in the least valley-bottom of each area, The value is close to dynamic value of valley-bottom without noise [6], therefore, only provide a threshold simply to sieve valley-bottom that is produced by noise, thereby restrain over-segmentation.

13.2.3 Detailed Steps

Obtaining of gradient image

The morphologic method is fit for describing image structure and geometric character. Thus, adopt the method of getting morphology-gradient in the algorithm. The definition of morphology-gradient is that the result of dilated image

Fig. 13.1 Suppression of over-segmentation by way of dynamic merge

M   N
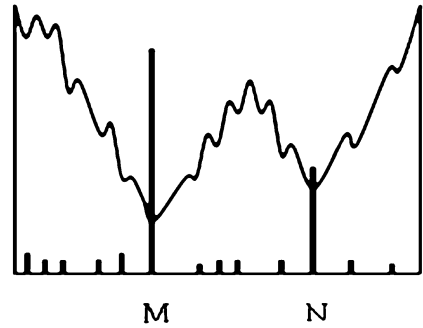
subtract the result of eroded image, if f indicates input gray image, b indicates structure element, morphology-gradient image is marked g

$$g = (f \oplus b) - (f \odot b) \tag{13.3}$$

Rearrangement of gradient image

Reset pixel according to the pixel value in the experiment, Paint cumulative histogram of the former image. In consideration of visiting the pixel's neighborhood frequently in the course of calculation, therefore, storage eight neighborhood pixels information in the course of reset. The course of segmentation can carry through orderly in the resetting image, furthermore, visit neighborhood information of pixels directly, and quicken operation speed.

Segmentation, combination

Only deal with a small part of pixel other than entire image in one step of segmentation, for example, when gradient rise to h, only deal with those pixel whose gradient is h, other one are not managed [7]. Thus, it is not necessary to scan the entire image during any step. It is necessary to have a storage structure which storage the found inactive pixel and flip quickly, use queue structure in the program, quicken management course by means of queue.

The course of algorithm is the course of rising gradient, provided that already deal with gradient of h level, that is too say that gradient which is less than h or equal to h have been managed, suppose the pixel combination is M, now considering the relation of pixel with h + 1 gradient and managed pixel, suppose it is N, There are three cases (i) N and M is non-intersect, it means that there is a lack of pixel whose gradient is lower than N around N, by all appearances, N should turn into valley-bottom of a new drainage area, (ii) N and M is intersecting and connectivity, return N to valley-bottom which is corresponding to M spot. (iii) N and M is intersecting but not connectivity, it means that N belongs to different drainage area [8]. Calculate distance with different valley-bottom, and put them return to corresponding drainage area, concrete steps as follows:

Pixel queue

There is a processing queue in the course of executing program, the queue take charge putting pixel enter into queue, and come out from the queue when needed.

When handling h gradient grade, put spots with h gradient and managed spots existing in the neighborhood enter into queue. When once course of entering queue finished, put out the spot, manage them separately.

Take out pixel spot one by one from queue, suppose p is extracting-spot, and calculate the number of drainage area within the neighborhood of P spot which is indicated as Num B. Num W indicates the number of watershed.

According to Num B and Num W to identify the output of P

If Num B = 1, there is only one drainage area which is border upon P, so P is endowed with output of the spot.

If Num B = 0, Num W > 0, the watershed is endowed with output of P spot.

If Num B > 1, there is many drainage area bordering upon P spot, if take no account of combination restrain over-segmentation, P spot is supposed to watershed. Restrain over-segmentation by dynamic combination in the algorithm. First, find the deepest valley-bottom, which is bordering upon P spot as combination mother-area. Towards other drainage area, calculate difference value between P spot and bottom. The value is the dynamic value of valley-bottom, if the value is less than setting threshold, merges all pixels of the drainage area into mother-area. Towards P spot, if all non-mother area is merged, P spot is endowed with output of mother-area. Otherwise P spot is endowed with watershed.

Identify whether new valley-bottoms come forth or not

Corresponding to the number one relation between M and N that is described formerly, spots with h gradient are not available around some pixels with gradients of h + 1. Actually, those pixels correspond to valley-bottom of a new drainage area, therefore, need to re-scan the image in the algorithm, identify whether new valley-bottoms come forth or not.

Binary-valued of outcome

Binary-valued of outcome distinguish boundary from non-boundary.

13.3 Experimental Result and Analysis

Choose the craniocerebrum MRI image. Adopt traditional watershed and improved-watershed segmentation method, experimental result of the two as follows:

Figures 13.2 and 13.3 are two different pictures. Figures 13.4 and 13.5 are the result of watershed without adding over-segmentation after withdrawing the outline to use the district adaptive threshold algorithm. It can be seen that the ordinary watershed can not directly manifest the difference between the two images. Figures 13.6 and 13.7 are the result of restrained the over-segmentation occurrence by means of combination whilst segmentation, Over-segmentation occurrence is improved clearly, in the figures each part mutually divides. The boundary of each segment keeps closure, Moreover it can be seen obviously the differences between peripheral tissue of lobus occipitalis through the improved watershed algorithm.

Fig. 13.2 Craniocerebrum a
existing over segmentation
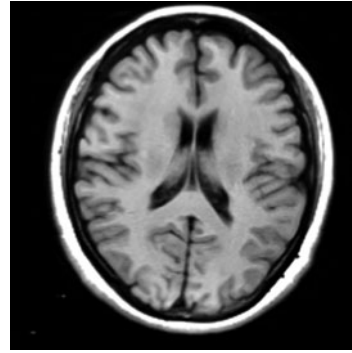
Fig. 13.3 Craniocerebrum b
existing over segmentation
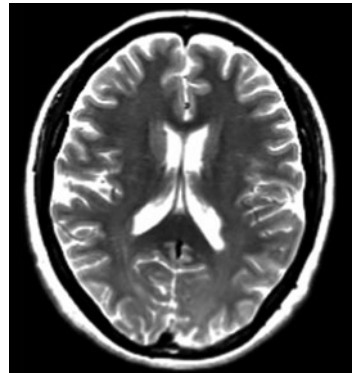
Fig. 13.4 Craniocerebrum a
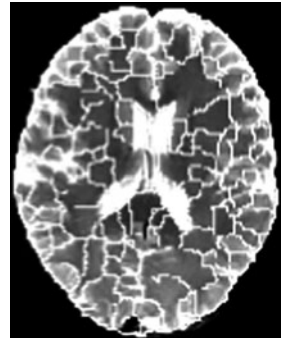
In addition, in order to compare resist-noise capability of algorithm, adding
noise to former image—Fig. 13.2, than segment the image with noise. The result
of experiment is showed as Figs. 13.8 and 13.9. It can be seen from the figure that
segmentation quality of tradition method is influenced after adding noise, and
much noise is remained. Moreover, in the improved method, the result of seg-
mentation is not influenced, and noise is eliminated easily.

Fig. 13.5 Craniocerebrum b
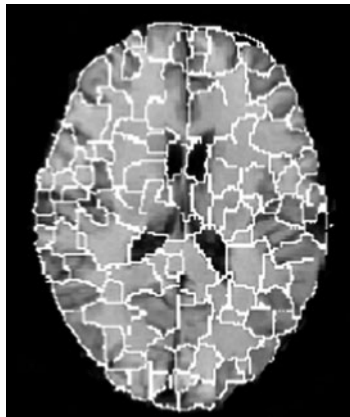
Fig. 13.6 Craniocerebrum a
segmentation result

Fig. 13.7 Craniocerebrum b
segmentation result

Table 13.1 is the data of algorithm evaluation and comparison, 0 is the target object, B is the background, err is the error dividing result that the object is segmented the background. Through to compare the two different craniocerebral pictures, on account of the existence of over-segmentation and difference of

Fig. 13.8 Traditional watershed
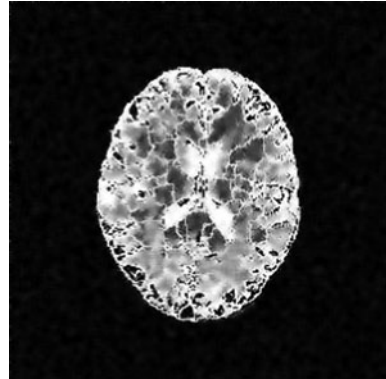
Fig. 13.9 Segmentation method addressed in this paper

Table 13.1 Relevant data for calculation of error categorization probability

	$p(O)$	$p(B)$	$p(O|B)$	$p(B|O)$	$p(err)$
Traditional method	0.473	0.521	0.311	0	0.170
Improved method	0.473	0.521	0	0.032	0.016

segmented regions between the two methods after improved, the probability of wrong-segmentation is one tenth of traditional method. Hence, the textual method is better than traditional method.

13.4 Conclusion

This paper presents an improved method based on the watershed algorithm, from algorithm thought, algorithm implement and segmentation result. Watershed method based on the dynamic combination rule has many excellences.

First, algorithm execution process is the course of area growth, in which the area grows outward in a whole and remains the boundary closed all the time, thus,

the algorithm is not so necessary as the edge detection method to connect the edge after the edge is detected.

Secondly, most of the area growth segmental algorithms, including some certain algorithms of watershed, need to identify the seed of area growth, selection of which is of great significance to the result of segmentation. However, correct selection of seed right requires lots of future knowledge of the image and execution of the present algorithm doesn't require so much to the future knowledge.

Finally, due to sufficient consideration of the whole structural information of the image, over-segmentation is thusly effectively restrained. Experimental results show that the algorithm can accurately segment cerebral CT images. Furthermore, it has higher ability in resisting noise.

References

1. Pal NR, Pal SK (1993) A review on image segmentation techniques. Pattern Recognit 26:1277–1294
2. Zhang Y-J (2002) Fundamentals of Image Processing and Analysis. Tsinghua University Press, Beijing
3. Luo HT, Zhang YJ (1997) An example of image segmentation evaluation and related discussion. J Data Acquis Process 12(1):18–22
4. Gong TX, Peng JX (2003) Color image segmentation based on watershed transform. Huazhong Univ Sci Tech 31(9):74–76 (Nature Science Edition)
5. Yang XY, Liu J (2001) Unsupervised texture segmentation with one-step means shift and boundary Markov random fields. Pattern Recognit Lett 22(10):1073–1081
6. Bieniek A, Moga A (2000) An efficient watershed algorithm based on connect components. Pattern Recognit 33(6):907–916
7. Bandera A, Urdiales C, Arreblole F, Sandoval F (2001) Scale-dependent hierarchical unsupervised segmentation of texture images. Pattern Recognit Lett 22(2):170–175
8. Bieniek A, Moga A (2000) An efficient watershed algorithm based on connect components. Pattern Recognit 3:907–916

Chapter 14
Application of Data Fusion in Ecological Environment Monitoring System

Xiao Jiang, Liyan Huang, Junguo Zhang, Yuzhu Li and Yang Kai

Abstract In this dissertation, the principle and value of data fusion are studied, and the existent typical touting protocol for Wireless Sensor Network (WSN). A kind of wireless sensor network data fusion algorithm based on the routing protocol LEACH is proposed, which is combines LEACH agreement with the hierarchical structure of the adaptive weighting combination. The hierarchy structure of each cluster design for an adaptive weighted model, through the adaptive weighted method from the sensor node of raw data acquisition to extract characteristic data, then will feature the data sent to converge node. We show by simulation that the algorithm has good data fusion efficiency, especially suitable for periodic report types of wireless sensor network.

Keywords Multi-sensor data fusion · LEACH · Self-Adoption Weighting

14.1 Introduction

The construction of ecological environment with monitoring and warning system is of far-reaching significance for timely obtaining the information, rational use of environmental resources, protecting and improving the ecological environment, scientific planning and construction of ecological environment protection. In the monitoring system based on WSN, sensor nodes continuously collect data according to a certain period. So it is not necessary to have all data collected transmitted to the sink node. Because: (l) there are a lot of redundancy. Every

X. Jiang (✉) · L. Huang · J. Zhang · Y. Li · Y. Kai
Mechanical and Electronic Engineering, Beijing Forestry University, Beijing, China
e-mail: xiaojiang56@gmail.com

sensor node may continuously gather the same data, and neighborhood nodes collect the similar data; (2) Sending all collected data to the aggregation node will spend a lot of energy, which will seriously affect the life of the network. Therefore, the original redundant data information fusion, only the results of effective transmission to sink node, the use of data fusion technology can greatly reduce the transmission of WSN data, which can effectively save energy costs, play a role in extending the network lifetime.

14.2 System Description

14.2.1 Overview of Leach Protocols

The basic idea of LEACH algorithm is: randomly select cluster head nodes in a cycle, the energy of the entire network load evenly distributed to each sensor node. Energy model used in LEACH protocol is the first order model [1, 2], as shown in Fig. 14.1.

The energy consumption of a sensor node sending k-bit packet to d meters away is:

$$E_{Tx}(k, d) = E_{Tx-elec}(k) + E_{Tx-amp}(k, d) = kE_{elec} + k\varepsilon_{amp}d^n \tag{14.1}$$

The energy consumption of a sensor node receiving k-bit packet is:

$$E_{Rx}(k) = E_{Rx-elec}(k) + kE_{elec} \tag{14.2}$$

where E_{elec}: The energy dissipated per bit to run the transmitter or the receiver circuit, because it is not difference between the two in actual application, here assume both are equal; n: The constant determined by radio channel; ε_{amp}: The gain of the Tx amplifier, whose value depend on the channel model used.

Free space channel model assumes the signal only spread in the ideal medium, without any interference, and there is only the loss of wave energy diffusion. At this point, $n = 2$, $\varepsilon_{amp} = \varepsilon_{fs} = 10$ pJ/bit/m^2. The multipath fading channel model takes all kinds of interference encountered in the signal propagation process and the resulting dramatic changes in the received signal amplitude, which is fading, into account. Then $n = 4$, $\varepsilon_{amp} = \varepsilon_{mp} = 0.013$ pJ/bit/m^4. In practical applications, according to d, we can take the decision to adopt what the specific model. If this distance is less than the threshold d_0, then free space channel model; if greater than or equal to d_0, the multi-path fading channel model. Therefore, equation (14.1) can be written as follows:

$$E_{Tx}(k, d) = E_{Tx-elec}(k) + E_{Tx-amp}(k,d) = \begin{cases} kE_{elec} + k\varepsilon_{amp}d^2, d < d_0 \\ kE_{elec} + k\varepsilon_{amp}d^4, d \geq d_0 \end{cases} \tag{14.3}$$
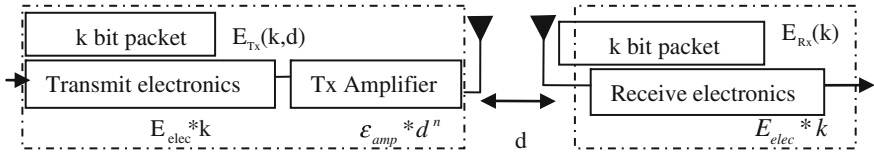
Fig. 14.1 The first order radio energy dissipation model

Fig. 14.2 Integration model
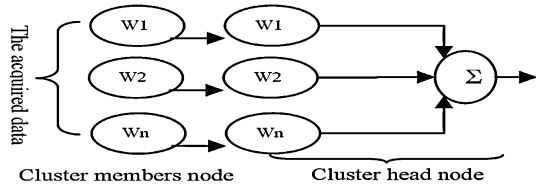
14.2.2 Presentation of Algorithm

LEACH agreement using "clumping thought" reflects the importance of data fusion, but it just processes the data from the cluster members simply in the packing and compression, without real meaning of fusion. Based on literatures [3], this paper introduces data-level fusion to cluster head node—similar multisensor adaptive weighted fusion. The preliminary treatment, rejecting data without significant differences, is made based on acquired data, and then the data is transponded to base station after treatment with the adaptive Weighting fusion. Its model is shown in Fig. 14.2.

14.2.3 Fusion Algorithm for Cluster Members Nodes

We use two main formulas for each cluster members. Formula (14.4) is used to judge whether to record the data collected, record only when the absolute value of the difference between the collected data and the last recorded data is more than a certain threshold, otherwise default it no significant differences and eliminate the data. Formula (14.5) is used to decide whether to send the collected data in the cluster to cluster head node. Send data only when the difference value between the collected data and the recorded is greater than or equal to threshold. Otherwise, just status word is sent for informing cluster head node.

$$a(t) = \begin{cases} a(t-1), & |a(t-1) - p| < \theta_1 \\ p, & |a((t-1) - p| \ge \theta_1 \end{cases}. \tag{14.4}$$

$$\text{Send}(t) = \begin{cases} a(t) & |a(t-1) - p| < \theta_1 \\ \text{Status Word}, & |a(t-1) - p| \ge \theta_1 \end{cases}. \tag{14.5}$$

In essence, it is a kind of simple and common data fusion method that a single sensor node according to the change of the collected data decides whether to send the data to sink node, which can prevent to send a lot of repetitions and highly similar. This simple data fusion method already has applied in many sensor networks.

14.2.4 Fusion Algorithm for Cluster-Head Node

The basic idea of adaptive weighted fusion algorithm is: on the base of the Minimum Mean-Square Error principle [4], the optimal weighting factor corresponding to each sensor is calculated adaptively, and the optimal merged result is achieved.

The optimal weighting factor W_p^* is decided by the variance of each sensor σ_p^2, σ_p^2 is not known in ordinary circumstances, but we can get them according to the measurements provided by each sensor via corresponding algorithm.

Suppose two different sensors p, q, respectively, the measured values are X_p, X_q, and observational error V_p, V_q, namely: $X_p = X + V_p$, $X_q = X + V_q$. Here V_P, V_q is Gaussian white noise process with zero mean, irrelevant. So the cross correlation coefficient R_{pq} between X_p and X_q, the autocorrelation coefficient R_{pp} of X_p satisfies:

$$R_{pq} = E\left[X_p X_q\right] = E\left[X^2\right] \qquad R_{pp} = E\left[X_p . X_p\right] = E\left[X^2\right] + E\left[V_p^2\right] \qquad (14.6)$$

$$\sigma_p^2 = E\left[V_p^2\right] = R_{pp} - R_{pq} \quad (p = 1, 2 \ldots n) \qquad (14.7)$$

We can get R_{pp}, R_{pq} through it own estimated value in the time domain. Suppose the member of the data is k, the estimated value in the time domain of R_{pp} is $R_{pp}(k)$, so

$$R_{pp}(k) = \frac{1}{k} \sum_{i=1}^{k} X_p(i) X_p(i) = \frac{1}{k} \left[\sum_{i=1}^{k-1} X_p(i) X_p(i) + X_p(k) X_p(k) \right]$$
$$= \frac{k-1}{k} R_{pp}(k-1) + \frac{1}{k} X_p(k) X_p(k) \qquad (14.8)$$

$R_{pq}(k)$ is secured after the correlative operation between q and p has been performed. The mean $\overline{R}_p(k)$ of $R_{pq}(k)$ is used in further estimation of R_{pq}. Then,

$$R_{pq} = \overline{R_p}(k) = \frac{1}{n-1} \sum_{q=1, q \neq p}^{n} R_{pq}(k) \quad (q \neq p, q = 1, 2 \ldots n) \qquad (14.9)$$

Thus we can estimate σ_p^2, relying on the estimated value in the time domain of R_{pp}.

14.3 The Theoretical Analysis and Simulation Comparisons

14.3.1 The Theoretical Analysis

The method, adaptive weighted fusion algorithm, is analyzed comparatively with transferring the raw data directly, or the average value. That transmission the mean value instead of the original data is "transferring the average value".

First, assuming each sensor node gathers m data and compress in a packet to deliver to cluster-head node, and those data within adaptive data fusion algorithm can also be compressed into a packet to send, and the size of data package is k bits. Secondly, assume these three methods are based on the LEACH agreements, i cluster members belong to a cluster head, and data packet get to the destination after passed through j nodes from the cluster-head node. In order to simplify the formula, presuppose that the distance of each node are approximately equal, which is d, then $E_{Tx}(k, d)$, $E_{Rx}(k)$ are known. In different data sending methods, every member node of this cluster sending a data to gathering node cost total communication energy P, (note: not including gathering node receiving energy) and cluster head node energy cost P_c. which are as follows:

(1) Raw data transmitted directly

$$P = i^*((j + 1)^* E_{Tx}(k, d) + j^* E_{Rx}(k)) \qquad P_c = i(E_{Tx}(k, d) +\ E_{Rx}(k)) \quad (14.10)$$

(2) Average transmission after calculating

$$\begin{aligned} P &= i^*(E_{Tx}(k, d) +\ E_{Rx}(k)) + j^*(E_{Tx}(k, d) +\ (j - 1)E_{Rx}(k) \\ P_c &= i^* E_{Tx}(k, d) +\ E_{Rx}(k) \end{aligned} \qquad (14.11)$$

Communication energy consumption reaches maximum, when there are significant differences between the data every member collected, all members send data to the head. Meanwhile, average method and adaptive data fusion, they are all compressed n packet into one to sink node. We may safely draw the communication energy consumption of average method is equal to the maximum of data fusion method.

14.3.2 The Presentation and Simulation of Cluster-head Data Fusion Algorithm

We here define the measures and contrast analysis the maximum energy consumption of adaptive weighted model with direct transmission original data to evaluate the performance of clustering protocols.

1) Total communication energy each round each cluster cost on average: low consumption is the basic of network requirements. The simulation only

Fig. 14.3 Number of live
nodes over time
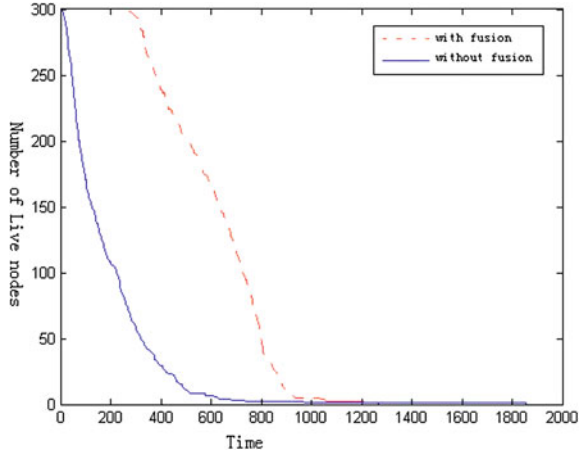
Fig. 14.4 energy
consumption over time
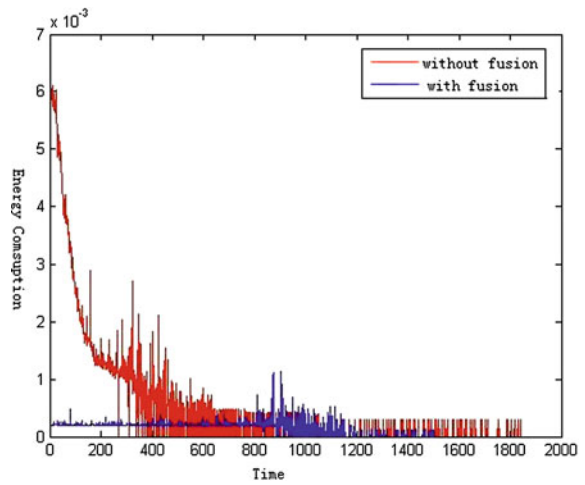
computing energy consumed of wireless transceiver module by sending and
receiving data, not including the energy consumption of other hardware and
module when leisure.

2) Number of alive nodes per round: This instantaneous measure reflects the total
number of nodes and that of each type that has not yet expended their all
energy.

Combined with the ecological environment monitoring system, this paper sets
up network scene 200 m × 200 m size: the number of sensor nodes 300, sink node
in the external 50 m in network. The following two graphs are obtained using
MATLAB.

It can be seen from the Fig. 14.3 that after adopting data fusion, the rate of node
death reduced significantly, and it is a very good prolongation of the network

Fig. 14.5 Output plots of
adaptive weighted fusion
estimate algorithm
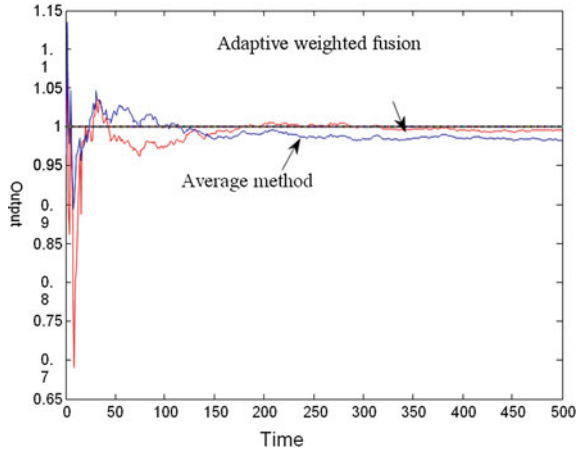
lifetime. In Fig. 14.4, we know that adopting data fusion can reduce the energy
consumption.

14.3.3 Simulation and Analysis of the Results

Three groups of sensor measurements are imitated and get the output curves by
means of adaptive weighted fusion and average method. And we also get the
weight curve corresponding to the sensors, as shown Figs. 14.5, 14.6.

It can be seen from the Fig. 14.5, estimation results by adaptive weighted fusion
estimation algorithm is far superior to the traditional average estimation algorithm
results. And, with the increase of measuring frequency, finally the results more and
more close to true value, namely the mean square deviation is smaller and smaller.

From Fig. 14.6 we can come to the conclusion that the larger in variance, the
smaller in weights, which verify that the adaptive weighted fusion is correct.

14.3.4 The Testing of Anti-Interference Ability

Following the above method expect for one faulted sensor imitated, we can get
Figs. 14.7 and 14.8. From Fig. 14.7, we can see when sensor is at fault, the result
by traditional average algorithm owns a lot of concussion; it is difficult to estimate
the measurement correctly by the mean method. But the result by the fusion
algorithm can still converges to true value; this explains it has very strong fault-
tolerant characteristics. And from Fig. 14.8, we can see the weights of variance 2
(fault sensor) is small, almost to zero, very little impact to estimate results, this just

Fig. 14.6 Distribution of
weights of three sensors
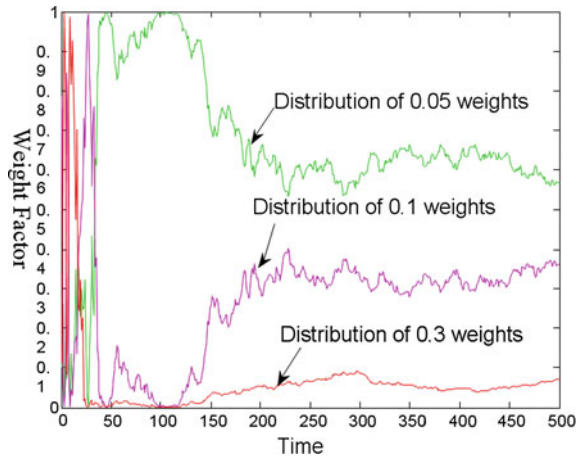
Fig. 14.7 Outputs plots of
fusion with faulted sensor
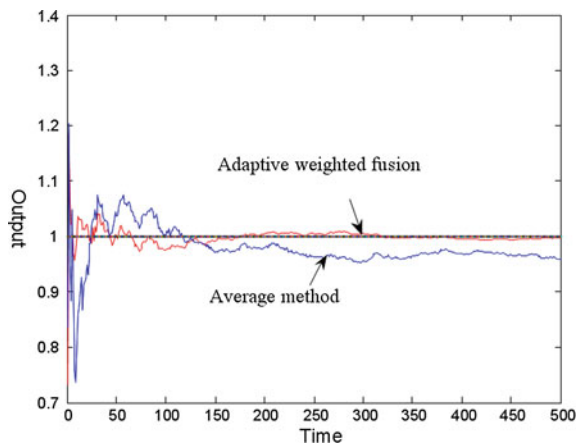
Fig. 14.8 Distribution of
weights of three sensors
involving faulted sensor
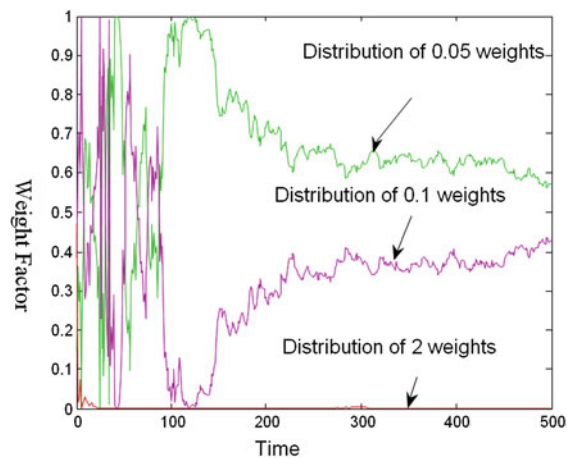
prove that the adaptive weighted fusion estimation algorithm is correct and has strong fault-tolerant performance.

14.4 Conclusions

Because the routine reporting of environment monitoring system is cyclical, collected data with high redundancy, therefore, we put forward adaptive weighted used in the hierarchical structure of the application and the LEACH agreement. The results show that the algorithm has good data fusion efficiency, especially suitable for periodic report types of wireless sensor network applications.

References

1. Gu X (2009) Search of low energy consumption and clumps routing protocol of wireless sensor network. Hefei Technology University, Hefei
2. Ke H (2005) The key technologies and research challenges of Wireless sensor network. J Telecom Sci 6:9–12
3. Dai Y (1994) Weak signal detection methods and instruments. National Defense Industry Press, Beijing
4. Zhang Y, Xu B et al (2008) Analysis and processing algorithm for images compressing and data fusion. In: Proceedings of DCABES 2008, Dalian, China, July, 2008, pp 290–294

Chapter 15
A Skew Detection Algorithm for PDF417 in Complex Background

Jian-Hua Li, Ping Li, Yi-Wen Wang and Xiao-Dan Li

Abstract The automatic identification of 2D (two dimensional) bar code PDF417 is very sensitive to skew angle. However, the common skew angle detection methods have shortcomings such as weak performance in time complexity. This paper mainly introduces an algorithm that utilizes Mathematics Morphology to extract the PDF417 code area from the complex background and then get skew angle of PDF417 bar code image using the least square method based on the properties of PDF417 character code and the extraction of feature points. Experiments show that this algorithm has virtue of less computation and high accuracy.

Keywords PDF417 · Skew angel · Least square method

J.-H. Li (✉) · P. Li · Y.-W. Wang
Key Laboratory of Electronic Thin Films and Integrated Devices,
University of Electronic Science and Technology of China,
610054 Chengdu, China
e-mail: jianhua703@163.com

P. Li
e-mail: pli@uestc.edu.cn

Y.-W. Wang
e-mail: yiwen@uestc.edu.cn

X.-D. Li
College of Computer Science and Technology,
Southwest University for Nationalities,
610041 Chengdu, China

15.1 Introduction

PDF417 (portable data file) is a 2D stacked bar code which was invented by Symbol Company in 1991. The composition of the bar code symbol character consists of 4 bars and 4 blanks and the total width is 17, so we call it 417 or PDF417. Figure 15.1 shows the composition of PDF417, it mostly consists of left blank area (a), start pattern (b), left row indicator (c), codeword (d), right row indicator (e), stop pattern (f), and right blank area (g), The broadband ratio of the combination list of start character bar and space is 8111113, and the broadband ratio of the combination list of terminator bar and space is 711311121 [1].

Bar code recognition is a major component of the barcode system, which determines the superiority of the 2d bar code. On account of the skew and offset that occurred during printing and scanning, we need to rotate the image to the horizontal after obtaining the bar code image in order to get accurate information from bars and blanks. Currently, the main methods for getting skew angle of the image are: Hough transform, projection method, Fourier transform, Connected component analysis. Hough transform algorithm, including the basic and the improved, is the most commonly algorithm for angle detection, which flawed in giant calculating cost [2]. Fourier transform method will transform the form of the image into frequency domain in which the direction with highest density of frequency domain space is the exact skew angle. But, high computational complexity does humiliate its performance [3]. Projection method obtains the angle by calculating the cost function of the image Projection histogram in different angles, which still has high calculation and complexity [4]. Connected components analysis detects the angle by analyzing the trait of the connected components, but the method is susceptible to noise [5]. As a result of the requirement of cost and size, current bar-code identification system is invariably designed as handheld devices which mostly driven by ARM or DSP. Thus, a skew-angle detection algorithm with less computation, lower time-complexity and better performance in anti-interference is of indispensability.

With comprehensive consideration on the current implementing algorithms and features of PDF417 itself, this paper present a new algorithm for skew-angle detection. Tests show that the algorithm has advantages in speed and accuracy.

15.2 PDF417 Angle Detection Algorithm

To get the skew angle of two-dimensional bar code PDF417, this paper uses its two characteristics: the start pattern parallel to each other and the width maintain the corresponding ratio of 8111113. The highlights of this algorithm include four key steps: Preprocessing, image distinguish, finding character points, linear fitting.

Fig. 15.1 The composition
of the PDF417 bar code
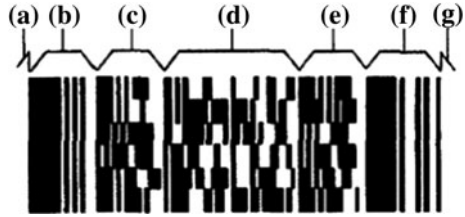
Fig. 15.2 Flow chart of
PDF417 angle detection
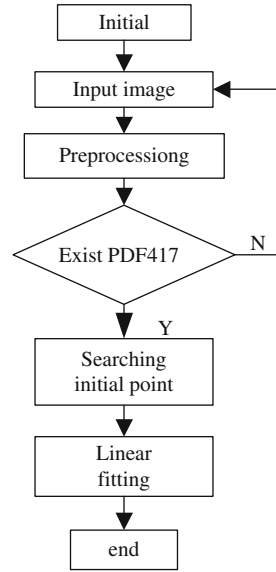
15.2.1 Image Preprocessing

The pre-processing includes Grayscale, Morphological Segmentation, filtering, image binaryzation of the collected color image. After graying process, our algorithm utilizes Mathematical Morphology to segment the image. Then we apply OTSU on the image for binaryzation, which followed by median filter operation.

Mathematical Morphology, which mainly contains corroding, dilating, opening and closing operations, is a graphic analyzing method that utilizes structuring element with specific shapes to extract target object for image recognizing. PDF417 code area can be isolated due to its information and the background area [6].

For an image f and structuring element B the opening is defined as:

$$\gamma_B(f) = \delta_{\check{B}}[\varepsilon_B(f)] \tag{15.1}$$

Fig. 15.3 Source image
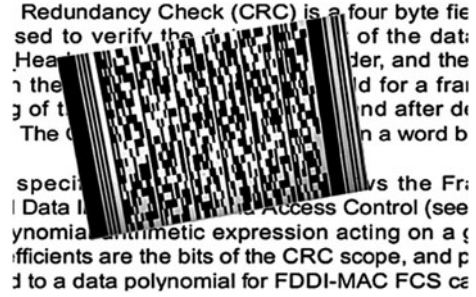
In the above equation, $\delta_{\underset{B}{\vee}}$ and ε_B are dilation and erosion operations, which are defined respectively as:

$$\delta_B f(x) = \max_{b \in B} f(x+b) \tag{15.2}$$

$$\varepsilon_B f(x) = \min_{b \in B} f(x+b) \tag{15.3}$$

We can adopt opening operation of Morphology on filtering the source image while regarding code-area as segmenting target and others as noises. With the fact that corroding utilizes the same structuring element as dilating operation, opening operation can provide a splendid performance on filtering the noises and preserve the valid information while the target contains much bigger connected area than the noises. However, considering the mere fact that the connected area of the PDF417 edge would probably not be invariably much bigger than the noises', we would get so many edge information lost so that the image could not be segmented correctly if we directly employ opening operation of Morphology to process the source image.

Therefore, we define a generalized opening operation, namely; apply corroding and dilating operation sequentially with different structuring elements on the image.

To segment a PDF417 source image, three steps would be employed as follows:

Firstly, adopting a 6×6 structuring element to corrode the PDF417 image (as Fig. 15.3 shows) for filtering the noises. For the reason that the valid information must be preserved, we shall not pick up structuring elements with too large size while corroding. Consequently, the noises cannot be eradicated completely and some edge information will be messed up as well. Therefore, we then employ an 18×18 structuring element to dilate the image for restoring the valid information. The processing result has been shown in Fig. 15.4.

Secondly, we utilize a 24×24 structuring element to employ classical opening operation on the current image for filtering. Thus, the code area can be marked (as Fig. 15.5 shows).

Find out the convex vertexes of the marked area generated by step 2, such as from A to H in Fig. 15.5. We can draw 4 lines through AE, DH, BC and GF from

Fig. 15.4 Image after
generalized opening
operation
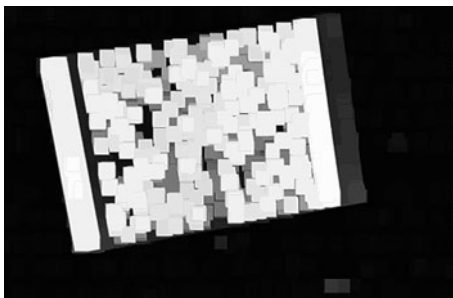
Fig. 15.5 Image after
filtering with classical
opening

Fig. 15.6 Image after
segmenting
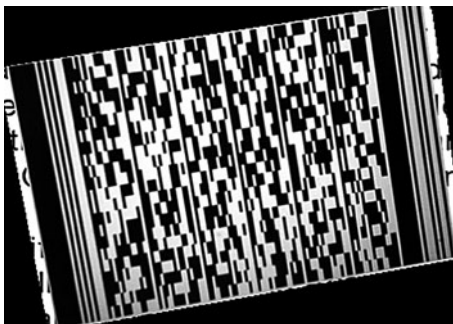
which the closure area contains exactly the PDF417 code information (as Fig. 15.6
shows).

15.2.2 Feature Points Extraction

The PDF417 broadband ratio of the combination list of start character bar and
space is 8111113, and the broadband ratio of the combination list of terminator bar
and space is 711311121. Moreover, in PDF417, the feature points confined in the
two broadband ratios are unique and could be detected by line scanning. However,

Fig. 15.7 Marked the feature points
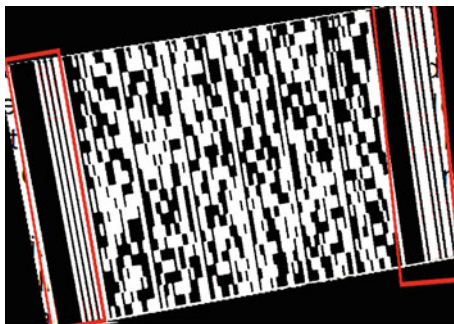
if using sequential scanning to trace the feature points, amount of the points complied with requirements will be detected, which will not contribute to improve the accuracy of algorithm for image skew angle, On the contrary, the whole image recognition time will be immensely increased by adopting the sequential scanning method. Therefore, this paper utilizes two kinds of stepping to scan the image to search the feature points. The line by line method will be adopted from the initial row until the first feature point be detected. Then the next scanning line shifts to the 5th line to the current one. Figure 15.7 illustrates the process of searching feature points by using the method proposed by this paper. Then the points complied with requirements constitute the corresponding array $H_1[], H_2[]\ldots H_9[], H_{10}[]$.

15.2.3 Calculating Skew Angle by Fitting a Straight Line

As Fig. 15.1 show, the skew angle of one specific PDF417 code can be represented by the slopes of the start and end characters' border lines in ideal condition. Yet, because of the environmental interference or the man-made noises during scanning, deformation would probably occurred on the start and end characters. Meanwhile, under the aim to obtain larger visual angle, wide-angle lens has always been chosen for collecting the source image, which would almost certainly leads to deformation. However, in the gathered image, the pixels in the principle optical axis are not anamorphic and other pixels will shrink radically to the centre. As the distance between the start character space and stop character space becomes broader, the possibility of image deformation is bigger during the image collection process so that the differences between angles in the two spaces are larger than those in the each space. (The differences exactly reflect the tendency of image deformation.) Therefore a straight line in the start character space or the stop one should not determine the skew angle of bar code. Taking advantage of the feature points in Fig. 2.2, and according to the least square method, this paper respectively

Table 15.1 The results of these three algorithms

Parameter (°)	Hough	Fast hough	Ours
Max. error	1.2	0.5	0.32
Min. error	0.2	0.1	0.08
Mean error	0.8	0.3	0.2

Table 15.2 Performance comparison results

Actual skew angle	Resolution	Fore-ground (Pixels)	Hough		Fast hough		Ours	
			Angle (°)	Time (s)	Angle (°)	Time (s)	Angle (°)	Time (s)
0	640 × 480	20016	0.55	6.859	0.31	0.75	0.22	0.313
5.54	640 × 480	27070	6.12	9.14	5.12	0.97	5.41	0.317
5.62	640 × 480	24006	6.22	8.125	5.22	0.77	5.54	0.319
5.79	640 × 480	27070	6.19	9.14	6.29	0.97	5.54	0.334
11.63	960 × 720	193028	12.53	65.16	11.93	4.23	11.31	0.325
21.94	640 × 480	34035	23.14	14.7	22.14	3.2	21.82	0.314
40.5	640 × 480	115069	41.62	38.55	39.7	3.05	40.3	0.325
44.75	960 × 720	211062	44.55	70.95	44.65	6.53	44.55	0.315

literates the information in the 10 arrays $H_1[], H_2[]\ldots H_9[], H_{10}[]$. Therefore, skew angle can be derived according to the formula:

$$\beta = \tan^{-1} a \qquad (15.4)$$

Get the 10 angles $\beta_1, \beta_2\ldots\ldots\beta_9, \beta_{10}$ respectively, and calculate the average:

$$\beta = \frac{\beta_1 + \beta_2 + \ldots + \beta_9 + \beta_{10}}{10} \qquad (15.5)$$

Then we calculate the absolute deviation of $\beta_1, \beta_2\ldots\ldots\beta_9, \beta_{10}$ relative to β_r respectively, abandon the 5 measured angle with bigger deviation. Regard the average of the remains as the skew angle of the PDF417 image.

15.3 The Analysis of Accuracy and Time Complexity of the Algorithm

Classical Hough transform, fast Hough transform (the Hough transform after the row-difference projection transform of the image) and ours method are compared in terms of their processing time and accuracy to the same images containing PDF417 code. Table 15.1 shows the results of these three algorithms; Table 15.2 lists the performance comparison results. From the data of Table 15.1, we might

conclude that, the time required for Hough transform and fast Hough transform is closely related to the amount of foreground pixels.

Generally, the higher resolution a image has, the more pixels in its foreground. Hence, it takes fast Hough transform less time than Hough transform to the same image. Image resolution and foreground pixels' number have little impact on the algorithm we proposed in this paper. The time we spend in algorithm Processing is very little and it keeps to about only 0.314 s for different images. That time can be negligible when comparing with Hough transform and fast Hough transform.

As shown in Table 15.2, the accuracy error of Hough transform algorithm 0.5° and Fast Hough transform algorithm maintain around 0.15° the precision of algorithm we proposed is basically around 0.1°.

15.4 Conclusion

The authors propose an algorithm for PDF417 skew-angle detection by applying least square method on points that obtained by utilizing the feature of the PDF417 code that all characteristic codes are parallel with specific proportion. Serial comparisons between our algorithm, Hough transform and fast Hough transform by applying images with different skew-angle and resolution shows that our algorithm have better performance on time complexity and accuracy.

References

1. State Standard of the People's Republic of China GB/T17172—1997, China Standard Press, 1998.8
2. Gatos B, Perantonis SJ, Papamarkos N (1996) Accelerated Hough transform using rectangular image decomposition. Electron Lett 32(8):730–732
3. Ohbuchi E, Hanaizumi H, Hock LA (2004) Barcode readers using the camera device in mobile phones. In: Proceedings of the 2004 international conference on cyber worlds (CW'04), pp 260–265
4. Smith R (1995) A simple and efficient skew detection algorithm via text row accumulation. Proceedings of third international conference on document analysis and recognition. IEEE, Montreal, pp 1145–1148
5. Hinds SC, Fisher JL (1990) A document skew detection method using run-length encoding and the hough transform. In: Proceedings of tenth international conference on pattern recognition. IEEE Computer Society, Atlantic City, pp 464–468
6. Shih FY, Pu CC (1995) Analysis of the properties of soft morphological filtering using threshold decomposition. IEEE Trans Signal Process 43(2):539–544

Chapter 16
A Study of Cancelling the Leakage Signal With a RPC for Single Antenna LFMCW Radar Altimeter

Feng Zhang, Guo-qi Zeng and Zhi-mian Wei

Abstract To fulfill the practical demands of airborne equipment's miniaturization and integration, topic around single antenna radar altimeter become one hot topic. But the problem of leakage signal greatly limits its applied scope. To solve this problem, first, carry out qualitative analysis on the leakage single of the single antenna altimeter; secondly, apply the Reflected Power Canceller(RPC) to the receiver of the altimeter system, and then propose the optimized design; then, a detailed analysis and deduction of the RPC's working process is given; finally, simulation of the cancellation performance is carried out, and the results indicate that the effect on cancelling is significant.

Keywords Radar altimeter · Single antenna · LFMCW · RPC

16.1 Introduction

A radar altimeter is an altimeter device that extracts altitude information from echo signal. The information it provides plays a crucial role to the safety of an aircraft [1]. They are generally divided into two categories, pulse and continuous.

F. Zhang (✉)
School of Electronics and Information Engineering, Beihang University,
Beijing 100191, China
e-mail: zhangfeng_3399@163.com

G. Zeng · Z. Wei
Research Institute of UAV, Beihang University,
Beijing 100191, China
e-mail: zengguoqi@buaa.edu.cn

Z. Wei
e-mail: zhimianw@sina.com

LFMCW (Linear Frequency Modulation Continuous Wave) radar altimeter has shown to contain the advantages of small radiated power, high-range accuracy and low probability intercept etc.

However, due to continuous wave system sending and receiving signals continuously, there is no separate period of time. Therefore different with a pulse radar which eliminates the transmitter leakage signal by closing the receive channel, there is no temporal discrimination for transmitter channels and receive channels to operate in separate time periods. How to solve the leakage signal problem is one of the keys to expand continuous wave radar's scope of application.

Nowadays, a dual antenna is commonly used in FMCW altimeter systems to provide adequate isolation. This approach is no longer practical when space constraints or large objects exist near the antennas. Furthermore, with the developing of aerospace and military technology, various of aircraft external devices increased, positioning antennas is also difficult, let alone aircrafts as small UAVs. Therefore single antenna system greatly expands the application scope of the radio altimeter.

While single antenna radar altimeter does save space, there are problems of low transmitter–receiver isolation and reflecting issue of the antenna port. As an effective solution of signal leakage problems, canceller, with PIN diode, is applied to a single antenna FMCW Radar PILOT successfully as early as 1988 [2]. This article mainly researches of using a Reflected Power Canceller (RPC) to resolve the issue of leakage signals for single antenna LFMCW radar altimeter, and proposed implementation scheme, and then carried out the simulation of the optimized design.

16.2 Analysis of Leakage Signal

According to actual systems, the leakage signal is largely due to low circulator isolation and impedance mismatch between transmission line and load [3]. To sum up, the receiver will receive four kinds of signals:

(a) The leakage signal from circulator varies with the circulator isolation.
(b) Because of the impedance mismatch between transmission line and load, signals spread as moving standing wave, thus part of them reflect back to the receiver.
(c) The normal echo signal which is carrying height information.

The signal needs to be processed contain from small echo signals to relatively larger leakage signal, that's why the receiver's dynamic range ought to be big, otherwise the large leakage power can saturate the receiver, and lead to the system working disability by blocking the receive channel.

Since reflected power canceller has been proved to be durable, stable, easy to install, and the most important thing is the remarkable eliminative effect. RPC can easily cancel the power by nearly 30 dB [4]. This article will make some improvement for single antenna radar altimeter system by way of applying RPC to it.

Fig. 16.1 Single antenna altimeter with RPC
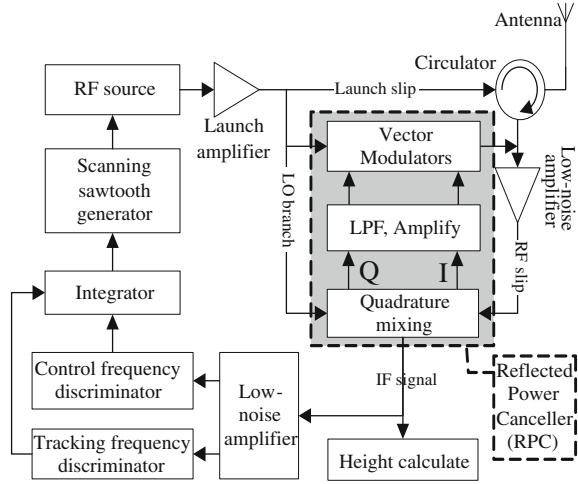
Fig. 16.2 Scanning sawtooth waves
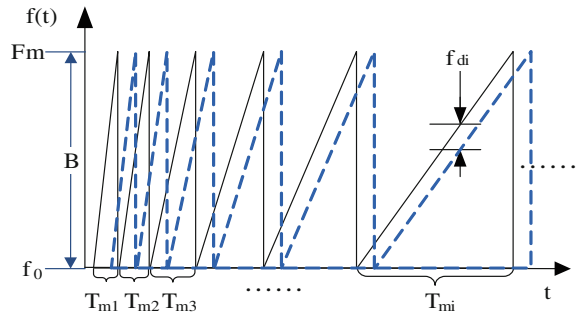
16.3 Implementation of Optimizing Single-Antenna Radar AltimeterRadar altimeter

To solve the leakage problem referred above, RPC is applied to the traditional single antenna altimeter for improvement. Its basic structure as shown in Fig. 16.1:

There are two work statuses while measuring height, search and track. In state of search, system produces a set of modulation sawtooth wave whose modulation period search from small to large as shown in Fig. 16.2. Based on similar principles we know:

$$\Delta F / T_{mi} = f_{di} / \tau. \tag{16.1}$$

s: ΔF—The maximum frequency deviation; T_{mi}—A single ramp cycle; f_{di}—Beat frequency in the ith sawtooth cycle; τ—Delay. At different actual height ΔF—, τ keep constant, and T_{mi} changes in ascending, therefore f_{di} varies from large to small with T_{mi}. While beat spectrum of a cycle within the range of the threshold frequency of control frequency discriminator, its output signal switches system to tracking state. Correction circuit continuously rectifies the modulation slope of the

Fig. 16.3 Diagram of the fundamental idea of the cancellation rectangular coordinate system
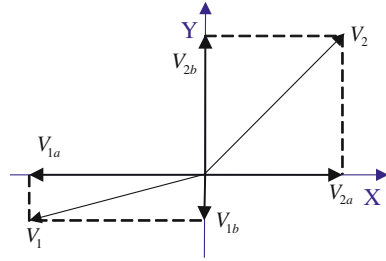
sawtooth until the beat frequency locked to the rating. Meanwhile, the single sawtooth cycle is T_{m0}. And the current height can be calculated by formula (16.2).

$$H = cf_b T_{m0}/(2\Delta F). \tag{16.2}$$

16.4 Reflected Power Canceller

16.4.1 Fundamental Idea of Cancellation

Here gives a brief introduction to the fundamental idea of cancellation. Assuming that the orthogonal signal I and Q to form a rectangular coordinate system. V_2 is synthetized by V_{2a} on X-axis and V_{2b} on Y-axis, and the leakage signal could be in any quadrant of the coordinate system, its projection on the X-axis and Y-axis are V_{1a} and V_{1b}, as shown in Fig. 16 3. To change voltage amplitude of V_{2a} and V_{2b}, as long as adjusting the attenuators of I, Q branch, then the two components V_{1b}, V_{1b} of the leakage signal can be cancelled and achieve the goal of elimination.

16.4.2 Implementation Scheme

Taking into account the actual demand for the cancellation of the system, use the closed-loop analog reflected power canceller. The key component of the canceller is the vector modulator, and the best solution approach is using bi-phase modulators (BPM) [3] as the variable attenuator to deal with the orthogonal signals. Considering the RPC separately in despite of the whole system, detailed it in the form of components first, and get the detailed block diagram as shown below.

There are two separate branches in RPC, I and Q. The leakage signal which is not eliminated can be detected by quarter mixer in working conditions. After processed by amplifier and low-pass filter respectively, I and Q two -way signal are provided to the vector modulator as modulating signal. Then the vector modulator adjust amplitude and phase of the RF signal, coupling from the transmitter, to ensure the cancellation signal's amplitude is same as the leakage signal, while the

phase difference is 180°, so as to achieve the purpose of cancellation. Due to the decrease of leakage signal energy, the problems of lowering receiver sensitivity, receiver saturation and other issues can be avoided. The following is detailed analysis of its work process.

16.4.3 Work Process Analysis

Signals are defined as shown above in Fig. 16.4. The LO input of the quarter mixers is divided into two routes, I and Q. One is coupled from the transmitter and the other's phase is shifted by 90°, they are expressed as follows:

$$U_{0DI} = A_{0D}\cos(2\pi f_0 t + \theta_0). \tag{16.3}$$

$$U_{0DQ} = -A_{0D}\sin(2\pi f_0 t + \theta_0). \tag{16.4}$$

Where: $\theta_0 = \varphi(t) = 1/(2 \cdot K_i t^2)$, K_i is the same as above. Based on the above analysis, the impact of leakage signal on receiver depends on the size of its energy; moreover, although different kinds of leakage signals' phase shift are different, they are not much difference. As a matter of convenience for analyzing the working process of the system, phase shift is unified set to θ_0, and the leakage signal entering into receiver is:

$$U_{RL} = A_{RL}\cos(2\pi f_0 t + \theta_{RL}). \tag{16.5}$$

Where: A_{RL} is leakage signal amplitude, θ_{RL} is leakage signal phase.

Substituting the formula (16.3), (16.4), (16.5) into the formula as follows, we can get two channels signal outputs of quarter mixers:

$$U_{DOUTI} = U_{0DI} \cdot U_{RL} = A_{0D}A_{RL}[\cos(2 \cdot 2\pi f_0 t + \theta_0 + \theta_{RL}) + \cos(\theta_0 - \theta_{RL})]/2. \tag{16.6}$$

$$U_{DOUTQ} = U_{0DQ} \cdot U_{RL} = -A_{0D}A_{RL}[\sin(2 \cdot 2\pi f_0 t + \theta_0 + \theta_{RL}) + \sin(\theta_0 - \theta_{RL})]/2. \tag{16.7}$$

The frequency detector outputs are processed by DC amplifier and low-pass filter, and the outputs are expressed as follows:

$$U_{DI} = K_{DC}A_{0D}A_{RL}\cos(\theta_0 - \theta_{RL})/2 = K_{DC}A_{0D}A_{RL}\cos\theta_d/2. \tag{16.8}$$

$$U_{DQ} = -K_{DC}A_{0D}A_{RL}\sin(\theta_0 - \theta_{RL})/2 = -K_{DC}A_{0D}A_{RL}\sin\theta_d/2. \tag{16.9}$$

The formula (16.8), (16.9) are orthogonal frequency discriminator outputs which are related to the phase difference between the leakage signal and the LO signal. They are the vector modulator two channels modulation signal input, I and Q. The RF inputs are just the same with quarter mixers except that the amplitude is A_{0V}. Substituting the formula (16.8), (16.9) U_{0VI} and U_{0VQ} into the formula as follows, we can get the cancellation signal which is the vector modulator output:
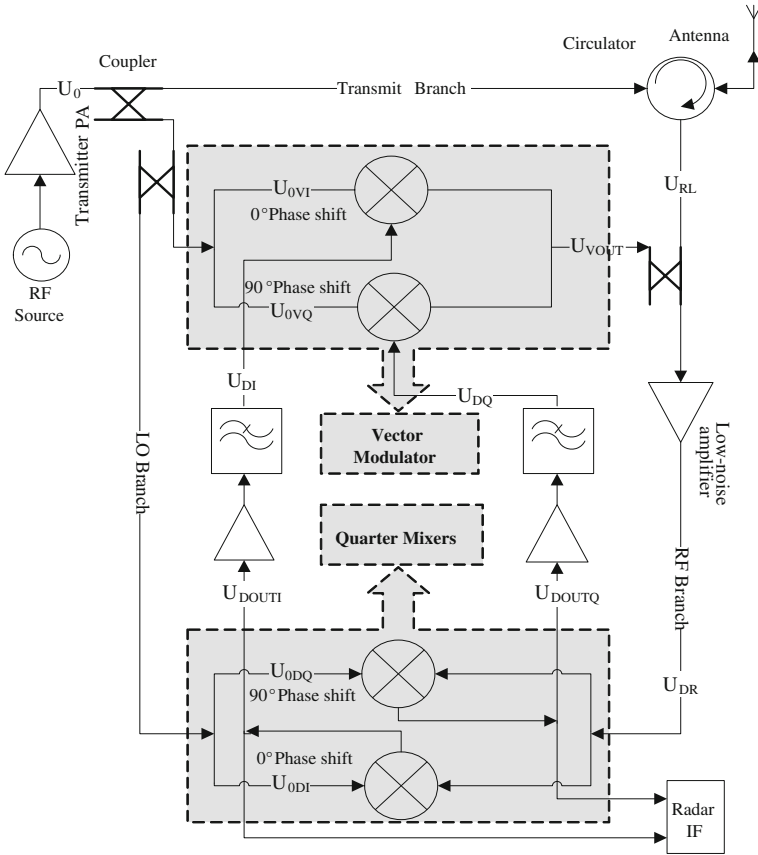
Fig. 16.4 Analog reflected power canceller system detailed design

$$U_{VOUT} = U_{DI} \cdot U_{0VI} + U_{DQ} \cdot U_{0VQ} = K_{DC}A_{0D}A_{RL}A_{0V}\cos(2\pi f_0 t + \theta_0 - \theta_d)/2.$$
(16.10)

According to the above formula, the LO signal phase is amended by θ_d. Under the perfect condition, by means of adjusting the amplifier coefficient to ensure the amplitude of U_{VOUT} is equal to the leakage signal, and is of the opposite phase from the leakage signal. Ultimately, come up to the purpose of cancellation.

16.5 System Workflow

By above knowable, there are two basic operating statuses for system known as searching and tracking states. After setting the initialization parameters, it is consented to go into the searching state, emitting frequency modulated continuous

Fig. 16.5 LFMCW radar
altimeter simulation
flowchart
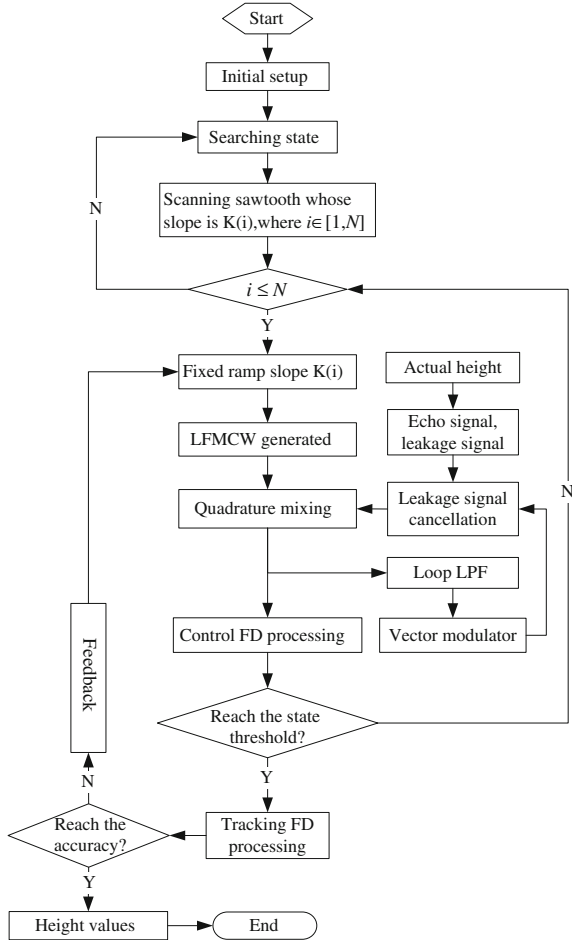
Fig. 16.6 Before using RPC
the output signal spectrum of
the mixer
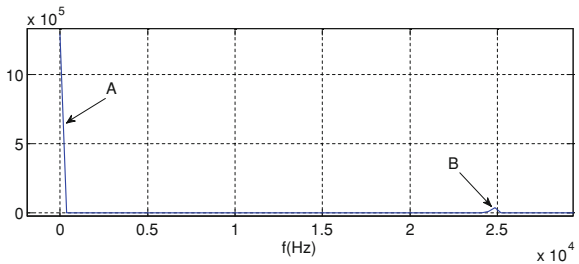
wave. At this point the signal has been leaking into the receiver. RPC starts to
process the leakage signals and won't stop untill the simulation ends.

First of all, the echo signal is processed by RPC while it is received. After
treated by quarter mixers, the output is divided into two routes. One is filtered by

Fig. 16.7 After using RPC the output signal spectrum of the mixer
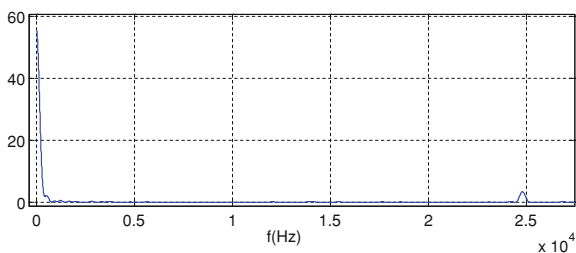
Fig. 16.8 The tracking process of the system when the actual height is 1.5 km
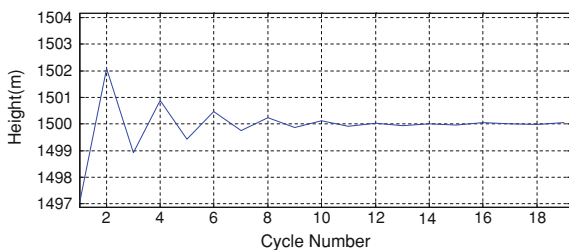
the loop filter before getting into the vector modulator to generate the cancellate signal. The other enters the control frequency detector after treated by a low-pass filter. And the output signal switches the servo loop into track status as soon as it hit the state switching threshold. In tracking state, the slope of sawtooth is keeping modified until the beat frequency is close to the rated frequency. Finally, the height values can be calculated by formula (16.2), Its work flow chart is as shown in Fig. 16.5:

16.6 Simulation Results

Under the conditions that FM bandwidth of 100 MHz, rated beat frequency is 25 kHz, scanning sawtooth cycle value in the range of tens of microseconds to tens of milliseconds, and the condition $T_{mi} \geq 10\,\mu s$ must be satisfied. Before and after using RPC the output signal spectrum of mixer is shown in Fig. 16.6.

A point represents the output of leakage signal after processed by mixer, all focus on the lower frequency band. B point represents the beat frequency signal carrying height information, compared to A, its frequency band is higher so that it can be selected by a band-pass filter, as the input of control frequency discriminator and be processed the next step (Fig. 16.7).

For the actual system, the estimated vector and leakage vector can't be completely satisfy the conditions of equal amplitude and opposite phase equal, which means that the cancellation is not complete. Specific to this simulation results, the ratio of leakage power and leakage signal power left after cancellation is about

43 dB. Finally after many calibrations, system reaches steady state. The output is current height (Fig. 16.8).

16.7 Conclusion

In this paper, the leakage signal of single antenna altimeter is calculated and analyzed in detail. On the basis of traditional framework of single antenna LFMCW radar altimeter, we introduced the RPC and a detailed analysis and deduction of the RPC's working process is carried out. It is not only implements the cancellation of leakage signal and achieves the purpose of optimizing the system, but also fulfill the practical demands of airborne equipment's miniaturization and integration. The application of RPC is of great significance in expanding the scope of application of single antenna altimeters.

References

1. Wen H (2006) Methods of improving the precision of height measurement in LFMCW radar altimeter [D], Xi'an:Master thesis, Xi'an University of Electronic Science and Technology
2. Barrett M, Reits BJ, Stove AG (1987) An X band FMCW navigation radar [C]. In: Proceedings of IEEE international conference Radar-87, London, p 448
3. Beasley L et al (1990) Solving the problems of a single antenna frequency modulated cw radar [C]. In: Proceedings of IEEE international radar conference, Radar 90, pp 391–395
4. Yang Yi, Han Yu, Liu J-X (2009) Design of FMCW radar altimeter digital signal processor based on FFT and constant beat-frequency [J]. Inf Electron Eng (1):48–51
5. Guo L-H, Wang D-J (2004) Carrier feed-through nulling in millimeter wave continuous wave radar. Mod Radar 4:41–45
6. Stove AG (1992) Linear FMCW radar techniques [J], IEE Proc Radar Signal Process 139(5):343–350
7. Beasley PDL, Stove AG (1991) Pilot—an example of advanced FMCW techniques [J], IEE Colloquium high time-bandwidth product waveforms. In: Radar and Sonar, pp 10/1–10/5

Chapter 17
A VCO Nonlinearity Correction Method Based on BP Network

Zhengjun Mo, Yaqing Tu, Wei Xiao and Yanlin Shen

Abstract Voltage Controlled Oscillator (VCO) nonlinearity correction is one of the key technologies for the high resolution linear frequency modulated continuous wave (LFMCW) radar. For the closed-loop correction methods are complex to realize and high-cost, a VCO nonlinearity correction method based on BP network is proposed. Through reverse training the back propagation (BP) network, the control voltage that linear frequency modulated signal needed is gained. And the timing correction policy is introduced to track the change of the frequency-voltage curve caused by elements' aging and environment changes. Simulation results show the high corrected precision and easier realization of the proposed method.

Keywords Nonlinearity correction · VCO · BP network

17.1 Introduction

Voltage Controlled Oscillator (VCO) is an adjustable signal source which applied in radar, sonar, radio communication and other fields widely. As a typical application,VCO in the linear frequency modulated continuous wave (LFMCW) radar desires its frequency changed linearly by time. However, due to the influence of the varactor's inherent nonlinearity and other reasons,the nonlinearity of VCO is only several percent or even more worse [1]. Therefore various correction methods have been used to improve the linearity of the VCO. For example, reactance

Z. Mo (✉) · Y. Tu · W. Xiao · Y. Shen
Department of Information Engineering, Logistical Engineering University,
401311 Chongqing, China
e-mail: mzj07_007@163.com

compensation methods [2–5] correct the nonlinearity by adjusting the structure of resonance loop. Though this kind of method will not aggravate the output noise or limit the modulating speed, it's complex and not precise. Opened-loop methods [6–8] achieve the correction purpose by correcting the control voltage through predetermined nonlinearity correction table. This kind of method is easy to application and costs less, but could aggravate the output noise and cannot correct timely. Closed-loop methods are introduced in literature [9–14], reverse feedback and phase-locked loop technologies are adopted to track the nonlinearity. This kind of method has high corrected precision but is complex and costs a lot.

Artificial neural network (ANN) is a sort of abstract mathematical model based on the research of modern neuroscience [15]. It has many advantages, such as self-learning, self-organizing, self-adaptive and parallel processing. It provides a way to approximate any nonlinear continuous function by any precision, especially some uncertain nonlinear problems. The frequency-voltage curve of VCO is an uncertain nonlinear function, so this paper corrects VCO nonlinearity by ANN.

The remainder of this paper is organized as follows: Sect. 17.2 describes the principle of the VCO nonlinearity correction. Section 17.3 introduces the BP network. Section 17.4 gives the details of the proposed method. Section 17.5 presents simulation results. Finally, Sect. 17.6 concludes the paper.

17.2 The Principle of the VCO Nonlinearity Correction

The frequency of VCO transmitted signal will change nonlinearly without correction, and it can be expressed as:

$$f(v) = f_0 - \frac{B}{2} + \frac{B}{T}(v - v_0) + e(v) \quad v_0 \leq v \leq v_0 + v_m \tag{17.1}$$

Where f_0 is the middle frequency of the transmitted signal, B is the modulation bandwidth, T denotes the sweeping period and $e(v)$ is the nonlinear part. In general, the control voltage of VCO is a sawtooth or triangular wave. This paper takes the sawtooth wave for example, it is defined as:

$$v(t) = v_0 + \frac{v_m}{T}t \quad 0 \leq t \leq T \tag{17.2}$$

Where v_0 and v_m are the minimum and the maximum value of the control voltage respectively, substituted Eq. 17.2 into Eq. 17.1 to give:

$$f(t) = f[v(t)] = f_0 - \frac{B}{2} + \frac{Bv_m}{T^2}t + e[v(t)] \quad 0 \leq t \leq T \tag{17.3}$$

It's clear that the $f(t)$ will be nonlinear under a sawtooth control voltage as the $e(v)$ is not zero generally. How to eliminate or minimize the nonlinear is to seek a
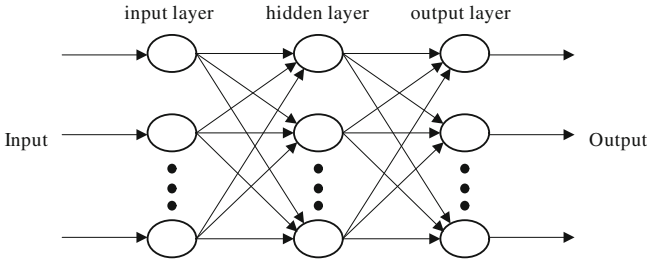
Fig. 17.1 The structure of 3-layer BP network

$\Delta v(t)$, and take $v_1(t) = v(t) + \Delta v(t)$ as new control voltage to replace $v(t)$, then $f(t)$ meets:

$$f(t) = f[v_1(t)] = f_0 - \frac{B}{2} + \frac{Bv_m}{T^2}t + \frac{B}{T}\Delta v(t) + e[v_1(t)] = f_0 - \frac{B}{2} + \frac{Bv_m}{T^2}t \quad (17.4)$$

In fact, the $\Delta v(t)$ in Eq. 17.4 is hard to solve directly as it depends on $e[v_1(t)]$ while $e[v_1(t)]$ is time-varying. However, $\Delta v(t)$ or $v_1(t)$ can be gained by all sorts of approximation ways such as the ANN method.

17.3 The BP Network

BP network is also called error back propagation neural network as the most popular network widely used in pattern recognition, image process and control field. BP network generally adopts the three-layer network structure(input layer, hidden layer and output layer) as shown in Fig. 17.1.

Hecht-Nielsen has demonstrated that any continuous function defined in closed interval can be approached by a three-layer BP network precisely. Let x_i ($i = 1, 2, \ldots, m$) denotes the input of the BP network, y_k ($k = 1, 2, \ldots, p$) denotes the output of the BP network, ω_{ji} ($j = 1, 2, \ldots, n$) denotes a connecting weighted value between the hidden layer j-node and the input layer i-node, ω_{kj} denotes a connecting weighted value between the output layer k-node and the hidden layer j-node and b_j denotes a hidden layer threshold of the j-node. In general, the function of hidden layer is S-type:

$$O_j = f(I_j) = \frac{1}{1 + e^{-I_j}} \quad (17.5)$$

Where I_j and O_j are the input and output of hidden layer j-node neuron, I_j defines:

$$I_j = \sum_{i=1}^{m} x_i \omega_{ji} + b_j \tag{17.6}$$

The output layer's function is selected as the linear-type, the output of the BP network is:

$$y_k = \sum_{j=1}^{n} \omega_{kj} O_j \tag{17.7}$$

The connecting weighted values and thresholds could be gained through network training.

17.4 A VCO Nonlinearity Correction Method Based on Neural Network

17.4.1 Main Idea

BP network could approach continuous functions in closed interval with any precision, especially suitable for dealing with nonlinear problems. As the frequency-voltage curve of the VCO during a sweeping period is a continuous function, the BP network could be utilized to correct VCO nonlinearity. Firstly, getting enough data from the curve by sampling during the whole period; secondly, using the obtained data to train the BP network; finally, the control voltage that linear frequency modulated signal needed can be generated by the trained network.

17.4.2 Steps of the Method

The implementation steps of the proposed method are as follows:

(1) Collecting 'frequency-voltage' data. Firstly, calculating the instantaneous frequency of the output signal of the VCO in a sweeping period; then the 'frequency-voltage' curve could be gained; Finally, collecting the data by choosing enough points from the curve.
(2) Training the BP network. Constructing a three-layer BP network and setting the network's parameters. Then training the network with the data from step (1)–let the frequencies as the input of the network while the voltages as the output. Considering the result is different after training each time even under the same data and the same parameters, the proposed method constructs n BP networks to train and choose the best trained network.
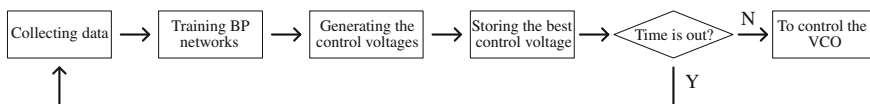
Fig. 17.2 The flow chart of the method

(3) Generating the corrected control voltages. Inputting the ideal linear FM (frequency modulation) data to the n trained networks, their outputs will be the corrected voltages. Loading the n control voltages sequences to the VCO and detecting nonlinearities, the control voltage sequence according to the smallest nonlinearity will be stored in a storage unit.
(4) Reading the control voltage from the storage unit and loading it to the VCO. Then the VCO will output FM signal with tiny frequency modulated nonlinearity.
(5) Timing correction strategy is implemented to eliminate the random small changes that arosed by vibration, aging and environment changes which means repeating step (1) to (3) periodicity.

17.4.3 The Flow of the Method

Summarizing the detailed steps introduced above, the flow chart of the proposed method is shown in: (Fig. 17.2).

17.5 Simulation Results

500 times Monte-Carlo experiments were run in MATLAB to test the proposed method. The frequency of the VCO's output signal varies from 21.0 to 21.6 GHz, and the control voltage changes between 0.5 and 1.5 V. In the simulation 1000 points are collected and the nonlinearity which simulated by sine frequency modulated is 5%. What's more the nonlinear of the VCO meets the endpoints unbiased principle. BP network's parameters are set as follow: the number of neuron in the hidden layer is 30 and its transfer function is tansig, the transfer function of the output layer is purelin, the reverse transfer function of the network is trainlm. In the experiments, 5 BP networks are constructed to train each time.

Figure 17.3 shows the change of the control voltage and frequency-time curve before and after correction in one experiment. It's clear that the linear control voltage turns to nonlinear while the nonlinear frequency modulated by the VCO turns to linear after correction. The nonlinearity of the VCO bacomes 0.0143%
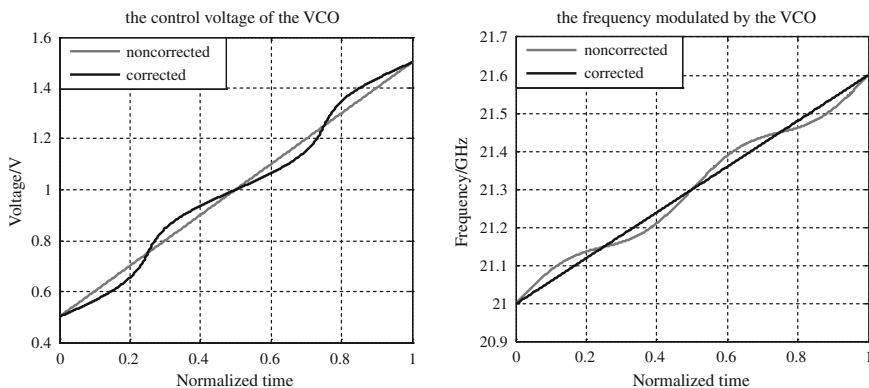
Fig. 17.3 The result of one experiment
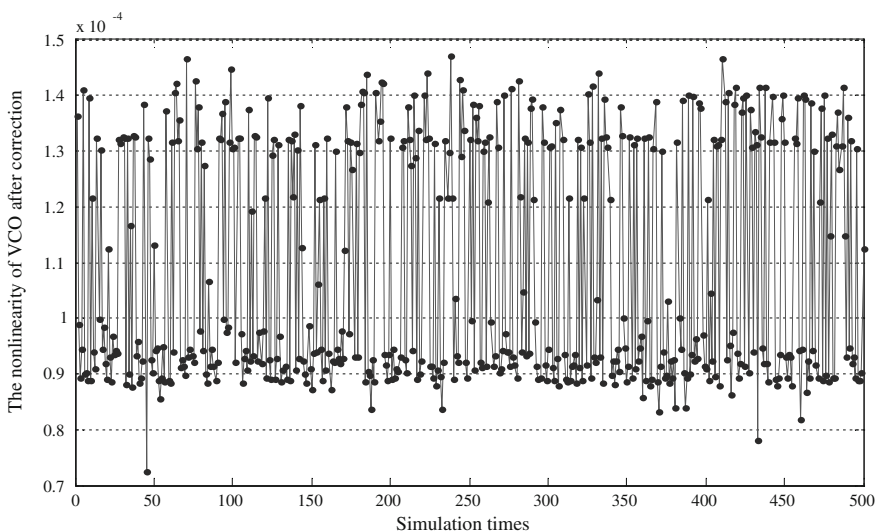
Fig. 17.4 The results of the 500 times Monte-Carlo experiments

after correction that reduced two orders of magnitude from 5%, while the nonlinearity corrected by fine delay phase-locked loop could just achieve 0.02% [13].

The results of the 500 times Monte-Carlo experiments are shown in Fig. 17.4. From the figure, it could draw a conclusion that the nonlinearities of the VCO after correction are all below 0.015%, which shows that the proposed method is stable.

17.6 Conclusion

A VCO nonlinearity correction method based on BP network is proposed to improve the linearity of VCO. The control voltage that linear changed frequency needed is obtained by inverse training the BP network. High corrected precision can be achieved through setting the parameters of the network reasonably and adopting appropriate correction strategy. Compared with the present methods, the proposed method has a simple principle and holds the advantages of both the opened-loop methods and the closed-loop methods. The proposed method has a good application prospect.

References

1. Zheng W, Lu G, Chen W, Liu F (2005) Novel method for linearity correcting and system application. Fire Control Radar Technol 34:12–15
2. Lockyear WH (1980) Linearize VCOs by reactance compensation. Microwave 23(2):60–68
3. Xie L, Yu H (2007) New investigation of the reactance compensation method for linearity correcting, In: Proceeding of the academic exchanges of graduates in Beijing on Information and Communications Technology, vol 2. pp 1040–1045
4. Ma J, Chen A (2006) A method of extending the VCO's bandwidth. Electron Packag 6(8):30–32
5. Kwon H, Kang B (2005) Linear frequency modulation of voltage-controlled oscillator using delay-line feedback. IEEE Microw Wirel Compon Lett 15(6):120–123
6. Feng Z, Li Y, Liang L, et al (2000) Requirement analysis of linearity for FMCW source using open-loop correction. Microw Millim Wave Technol, 2nd International Conference on 2000. ICMMT, pp 679–682
7. Chen Z, Ding Y, Xiang J (2001) A method on nonlinear correction of broadband LFMCW signal utilizing its relative sweep nonlinear error. Syst Eng Electron 23(2):16–18
8. Huang R, Zong C (2004) Research into the method of the nonlinear compensation for VCO. Control Instrum Chem Ind 31(3):50–51
9. Williams DA (1988) A highly linearised mm-wave voltage controlled oscillator for FMCW radar applications. Solid State Compon Radar, IEEE Colloq 6(1):615
10. Yun X, Yun C, Zhou B, Zhang G (1996) mm-Wave wide-band ultralinear sweep source. Chinese J Electron 24(2):100–102
11. Wang X, Feng J, Xiang J (1996) Linearity correction for linear FM sweep signals. Chinese J Electron 24(10):120–122
12. Musch T (2003) A high precision 24-GHz FMCW radar based on a fractional-N ramp-PLL instrumentation and measurement. IEEE Trans 52(2):324–327
13. Sun P, Chen W (1996) Analysis of LFMCW delay phase-locked linearization loop. Syst Eng Electron 26(10):1348–1352
14. Sun P, Chen W (2004) A nonlinear analysis of closed-loop linearizer employing delay-difference method. In: Proceedings of 4th international conference on microwave and millimeter wave technology, pp 1023–1025
15. Fu Y, Zhao H et al (2010) Application design of neural network in MATLAB. China Machine Press, Beijing, pp 83–97

Chapter 18
Blood Skeleton Extraction Approach for Retinopathy Images

Xing-yu Shang and Dong-bo Zhang

Abstract Few existing blood vessel extraction methods regard to retinopathy images. Due to the interference of the lesions border, it is difficult to correctly extract the vasculature. In this paper, We propose a operator for non-vessel structure inhibition, and achieve blood vessel skeleton extraction by combining with non-maxima suppression and hysteresis multi-thresholding technique. The experiment results show that our method achieves good performance.

Keywords Retinal fundus image · Blood vessel extraction · Gabor filter

18.1 Introduction

The lesions of retinal fundus tells us the diabetics, hypertension, obesity, arteriosclerosis and retinal retinopathy, etc. So, the accurate extraction of blood vessels in retinal images will help ophthalmologist locate and determine the lesions area. Chaudhuri [1] proposed a vessel segmentation method using 2-D Gaussian filter. Qin Li [2] proposed a method which included a multi-scale analytical scheme based on Gabor filters and a threshold probing technique used in [3] to segment vessels. All those methods rely on local information of blood vessels, such as color, shape, gradient and contrast, etc. But these information are not enough to distinguish non vessel pixels, e.g., boundary of optic disk and lesions area, narrow and dark gap between bright areas. So, we propose a non-vessel

X.-y. Shang (✉) · D.-b. Zhang
School of Information Engineering, Xiangtan university, Xiangtan, China
e-mail: shangcao@126.com

inhibition method for retinopathy images based on Gabor filter. Then we use non-maxima suppression technology, and get the binary vessel skeleton image by hysteresis multi-thresholds technology. Experiments prove that our method achieves good performance.

18.2 Gabor Filter-Based Vessel Skeleton Extraction Algorithm

18.2.1 Gabor Filter

Here we use the following two-dimensional Gabor filter [4] as the kernel function.

$$g_{\lambda,\delta,\theta,\phi}(x,y) = e^{-\frac{\tilde{x}^2+\gamma^2\tilde{y}^2}{2\delta^2}}\cos(2\pi\frac{\tilde{x}}{\lambda}+\phi) \qquad (18.1)$$

$$\tilde{x} = x\cos\theta + y\sin\theta \quad \tilde{y} = -x\sin\theta + y\cos\theta$$

Where γ is spatial aspect ratio, λ is the wavelength. The standard deviation δ determines the size of the receptive field. The ratio δ/λ determines the spatial frequency bandwidth. The angle parameter θ_i, $\theta_i \in [0, \pi)$ specifies the orientation of the normal to the vascular strip. The parameter φ ($\varphi \in (-\pi, \pi]$) is a phase offset in the cosine factor. The function gives a maximum response at excitatory stripe zones when $\varphi = 0$ and a maximum response at inhibitory stripe zones when $\varphi = \pi$. And when $\varphi = +\pi/2$ the function gives a maximum response at object edges. we select 12 different filter templates to achieve feature detection. The response $r_{\lambda,\delta,\theta,\varphi}(x,y)$ of Gabor filter is the convolution of $g_{\lambda,\delta,\theta,\varphi}(x,y)$ with input image $f(x,y)$ as follows.

$$r_{\lambda,\delta,\theta,\varphi}(x,y) = \int\int f(u,v)g_{\lambda,\delta,\theta,\varphi}(x-u,y-v)dudv \qquad (18.2)$$

Where $\gamma = 0.5$ and $\delta/\lambda = 0.56$. At each pixel only the maximum of their responses is retained.

$$r^{AH}_{\lambda,\delta,\phi}(x,y) = \left|\max\{H(r_{\lambda,\delta,\theta_i,\phi}(x,y))|\theta_i = 0, \pi/12, 2\pi/12, \ldots, 11\pi/12\}\right| \qquad (18.3)$$

Where, $H(z)$ correspond to half-wave rectification function, if the value $r_{\lambda,\delta,\theta,\varphi}(x,y)$ below zero will be set to zero, otherwise, it is retained.

Figure 18.1b shows the result of using Gabor filter to Fig. 18.1a. The edge of lesions and bright yellow exudates have similar property of vessel, the response of Gabor filter to them is even much higher than most of real vessel pixels. To solve those problems, we propose non-vessel structure inhibition to suppress the edge of object. The operator $v_{\lambda,\delta}(x,y)$ as follows:

$$v_{\lambda,\delta}(x,y) = H(r^{AH}_{\lambda,\delta,\pi}(x,y) - \alpha_1 r^{AH}_{\lambda,\delta,0}(x,y) - \alpha_2 r^{AH}_{\lambda,\delta,\pi/2}(x,y)) \qquad (18.4)$$

Where $r^{AH}_{\lambda,\delta,\pi}(x,y)$, $r^{AH}_{\lambda,\delta,0}(x,y)$ and $r^{AH}_{\lambda,\delta,\pi/2}(x,y)$ represent the response of Gabor function with phase offset $\varphi = \pi$, 0 and $\pi/2$, respectively. The factor α_1 and α_2
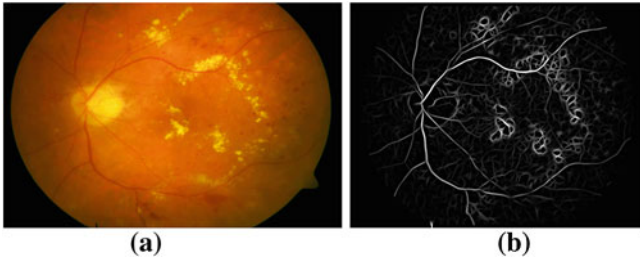
Fig. 18.1   **a** Retinal fundus images with lesions. **b** Result of application of Gabor filter to the image
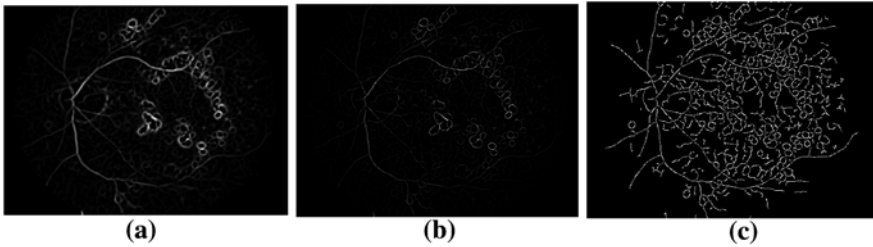
Fig. 18.2   **a** Result using Gaussian matched filter. **b** Result of non-maxima suppression after using Gaussian matched filter. **c** Result of standard hysteresis thresholding after thinning by non-maxima suppression

control the strength of inhibition to bright stripes and object edge, by much tests, we get a better effect when parameter value $\alpha_1 = 0.5$, $\alpha_2 = 1$ were used (Fig. 18.2).

18.2.2 Binarization Using Hysteresis Multi-threshold Technology

Before using Hysteresis Multi-threshold Technology, we thin the blood vessels into one pixel width by the Non-maxima Suppression [5]. However, there are still lots of non-vessel pixels appear as scattered dot or short lines (Fig. 18.3c) when we use standard hysteresis threshold techonlogy. So, we propose a hysteresis multi-threshold technique based on standard hysteresis threshold [5] which use a pair of threshold values t_l and t_h to classify pixels. In standard hysteresis threshold technology, we select $t_l = 0.05 * \text{max\_I}$ and $t_h = 0.1 * \text{max\_I}$, where max_I specifies the maximum response of candidate pixels. In hysteresis multi-threshold technology, we define multi-pairs of thresholds t_l^i and t_h^i, $i \in \{1, \ldots, N_i\}$, $t_l^i < t_l^{i+1}$, $t_h^i < t_h^{i+1}$. The classification rule is same with standard hysteresis threshold [5]
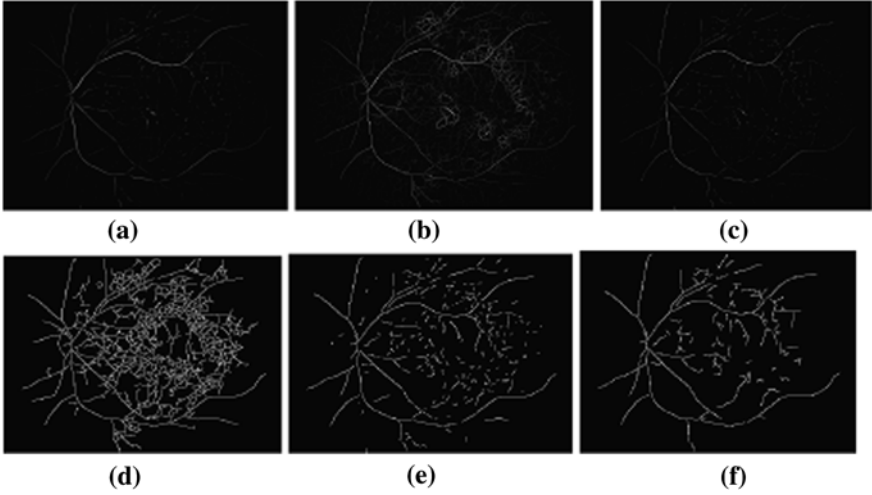
Fig. 18.3 **a** Responses of non-vessel structure inhibition to Fig. 18.1b **b** Result of non-maxima suppression to Fig. 18.1b **c** Result of non-maxima suppression to **a**. **d** Result of standard hysteresis thresholding process to **b**. **e** Result of standard hysteresis thresholding process to **c**. **f** Result of hysteresis multi-thresholding process to **c**

under threshold pair i. Binary output $b^i_{\lambda,\delta}(x, y)$ under threshold pair i can be obtained by (18.5) and (18.6).

$$t_{\lambda,\delta}(x, y) = nMST(v_{\lambda,\delta}(x, y)) \tag{18.5}$$

$$b^i_{\lambda,\delta}(x, y) = HT^i(t_{\lambda,\delta}(x, y)), \, i \in \{1, \ldots, N_i\} \tag{18.6}$$

Where, *HT* is hysteresis thresholding operator. nMST is non maxima suppression thinning operation. Let $C^{i,k}_{\lambda,\delta}$ be the connected components of binary output $b^i_{\lambda,\delta}$

$$b^i_{\lambda,\delta} = \bigcup_k C^{i,k}_{\lambda,\delta} \tag{18.7}$$

Where, $C^{i,k}_{\lambda,\delta}$, $k = 1, \ldots, N^i_c$ represent the kth connected component under threshold pair i. By morphological dilation operation with a 2×2 square structuring element is applied in $C^{i,k}_{\lambda,\delta}$.

$$D^{i,k}_{\lambda,\delta} = C^{i,k}_{\lambda,\delta} \oplus q_2 \tag{18.8}$$

The final vessel skeleton structure $V_{\lambda,\delta}$ can be achieved by following sequent operation. Then we delete lines less than 10 pixels. Following pairs of thresholds are used, i.e., {(0.03,0.06) *max_I,(0.04, 0.07)*max_I,(0.05, 0.08)*max_I,(0.06, 0.1)*max_I}.

$$B_{\lambda,\delta}^{(N_t,N_t-1)} = \bigcup_{(b_{\lambda,\delta}^{N_t} \oplus q_2) \cap D_{\lambda,\delta}^{N_t-1,k} \neq \phi} (b_{\lambda,\delta}^{N_t} \cup C_{\lambda,\delta}^{N_t-1,k}) \tag{18.9}$$

$$B_{\lambda,\delta}^{(N_t-1,N_t-2)} = \bigcup_{(B_{\lambda,\delta}^{(N_t,N_t-1)} \oplus q_2) \cap D_{\lambda,\delta}^{N_t-2,k} \neq \phi} (B_{\lambda,\delta}^{(N_t,N_t-1)} \cup C_{\lambda,\delta}^{N_t-2,k}) \tag{18.10}$$

$$V_{\lambda,\delta} = B_{\lambda,\delta}^{(2,1)} = \bigcup_{(B_{\lambda,\delta}^{(3,2)} \oplus q_2) \cap D_{\lambda,\delta}^{1,k} \neq \phi} (B_{\lambda,\delta}^{(3,2)} \cup C_{\lambda,\delta}^{1,k}) \tag{18.11}$$

18.3 Experiment Analysis and Results

The Gaussian filter [1] is compared with our method. Both Gaussian filter and Gabor filter are consist of a widows with 15×15 pixels and 12 orientations. The parameter α_1 and α_2 are assigned to 0.5 and 1. Figure 18.2a shows the result of Fig. 18.1a using Gaussian filter. Figure 18.1b) shows the result of Gabor filters. We can see that the response of Gabor matched filter is more smooth and clear. In our method, the non-vessel structure can be greatly suppressed, after thinning, the main vascular skeleton is completely retained (Fig. 18.3c). And by hysteresis multi-thresholding binarization, scattered dots or short lines are deleted. (Figure 18.3f). But using Gaussian filter, the non-vessel structures is difficult to be excluded (Fig. 18.2b). After computation of standard hysteresis thresholding, the real vessel structure is hardly to be identified (Fig. 18.2c). Figure 18.3b shows the result using the non-maxima suppression directly to (Fig. 18.1b). Figure 18.3c shows the result of non-maxima suppression after non-vessel inhibition process (Fig. 18.3a). Most non-vessel structures are excluded in (Fig. 18.3c). The results of standard hysteresis thresholding to Fig. 18.3b, c are shown in Fig. 18.3d, e. The vascular skeleton in Fig. 18.3e is much more distinguishable. The result of hysteresis multi-thresholding to Fig. 18.3c is shown in Fig. 18.3f. In comparison with Fig. 18.3d, lots of scattered dots or short lines are deleted.

18.4 Conclusion

We introduce a non-vessel structure inhibition operator to extract vasculature in retinopathy images. By combining with non-maxima suppression and hysteresis multi-thresholding technique, the method achieves good performance. But some small vessels and vessel bifurcations are lost because of excessive inhibition and there are still residual non-vessels structures in final result images. Further work is required in this area.

References

1. Chaudhuri S, Chatterjee S, Katz N, Nelson M, Goldbaum M (1989) Detection of blood vessels in retinal images using two-dimensional matched filters. IEEE Trans Med Imag 8:263–269
2. Li Q, You J, Zhang L, Zhang D (2006) A new approach to automated retinal vessel segmentation using multiscale analysis. In: 18th International Conference on Pattern Recognition, 2006, vol 4. IEEE, pp 77–80
3. Hoover A, Kouznetsova V, Goldbaum M (2000) Locating blood vessels in retinal images by piecewise threshold probing of a matched filter response. IEEE Trans Med Imag 19(3):203–210
4. Grigorescu C, Petkov N, Westenberg MA (2003) Contour detection based on nonclassical receptive field inhibition. IEEE Trans Image Proc 12(7):729–739
5. Grigorescu C, Petkov N, Westenberg MA (2004) Contour and boundary detection improved by surround suppression of texture edges. Image Vis Comput 22(8):609–62

Chapter 19
Calculation and Analysis of Temperature and Fluid Fields in Water-Cooled Motor for Coal Cutters

Dawei Meng, Liying Wang and Yongming Xu

Abstract To study the temperature distribution of the water-cooled motor for coal cutters, with the aid of the theory of hydromechanics and finite volume method, the authors set up three-dimensional partial physical and mathematical models for the stators and rotors. Under the basic assumptions and boundary conditions, by the numerical analysis and computation, the temperature distributions of stators, rotors and water-cooled jackets are worked out. Considering the fact that the water is cooled in turn and the circumferential temperature distribution is uneven, the authors calculate the temperature field for the whole motor. Under the condition of same flow and heat sources, the influence of water-cooled jacket to the motor temperature is studied. The result shows that the highest temperature is lower than the maximum permissible temperature; the better cooling effect can be acquired by selecting the jacket structure reasonably. The study provides the theoretical basis for optimized design of water-cooled motor.

Keywords Water-cooled motor · Temperature field · Three-dimensional · Finite volume method

19.1 Introduction

The water-cooled motor is an essential part of the coal cutters for the thin seam, its development trend is toward the increasement of the power density [1]. But the more the power density is, the more the loss per unit volume is, and thus, its work

D. Meng · L. Wang (✉) · Y. Xu
Department of Electrical Engineering, Harbin University of Science and Technology, No. 52, Xuefu Road, Harbin, Heilongjiang, China
e-mail: wangliying0615@163.com

Table 19.1 Basic motor parameters

Parameters	Values	Parameters	Values (mm)
Rated power	100 KW	Partition thickness	10
Rated voltage	1,140 V	Axial length of jacket	510
Outer diameter of stator	324 mm	Water jacket height	11
Inner diameter of stator	213 mm	Water jacket width	60.2575
Diameter of rotor	90 mm	Internal shell thickness	11
Gap length	0.5 mm	External shell thickness	5

efficiency will get lower and local overheating will occur. And meanwhile, the worse working conditions also lower the reliability and shorten the motor life. So calculating the motor temperature in the all parts accurately is necessary for the motor designs and operation. Based on the theory of hydromechanics, a water-cooled motor of YBCM190-4 type is used to calculate the temperature field by the finite volume method. Because the whole model is too great to deal with, a method from the part to the whole is used. First the partial model for two water-cooled jackets is set up, and then the distribution of temperature field is calculated, the next partial model is solved by changing boundary conditions on the basis of the previous calculation; this process is repeated until the temperature distribution of the whole motor is calculated.

19.2 Set-up of Physical Model

Limited in the installation space, the sizes of motor and cooling structure are shown in Table 19.1. The cooling system is composed of 16 water jackets flowing axially inside the shell. The cooling water flows from the inlet, then through all water jackets, and finally to the outlet, the whole motor, thus, is cooled, as shown in Fig. 19.1.

The partial model set up in the paper includes two water jackets, one is for water in, and the other is for water out, i.e. 1/8 of the motor, as shown in Fig. 19.2.

19.2.1 Basic Assumptions

1. The distribution of heat sources is even in their respective areas and the penetrated depth of the surface loss on the stators and rotors is 1.5 mm;
2. The turbulence model is used to solve the fluid field because of large fluid Reynolds number in the water jackets;
3. The fluid in the jackets is incompressible and the flow type is steady flow [2, 3];
4. The heat radiation is unconsidered, and heat is transferred only by air gap between stators and rotors;
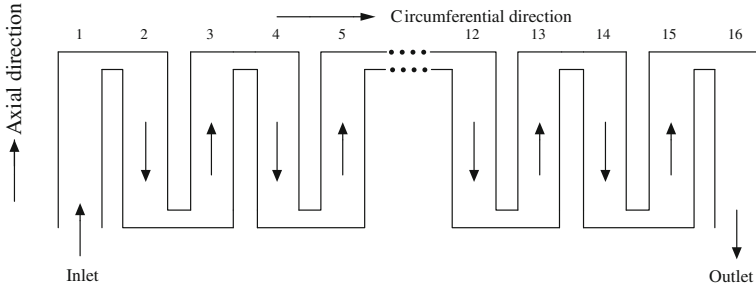
Fig. 19.1 Expansion plot of water-cooled jacket

Fig. 19.2 Physical model of temperature field calculation
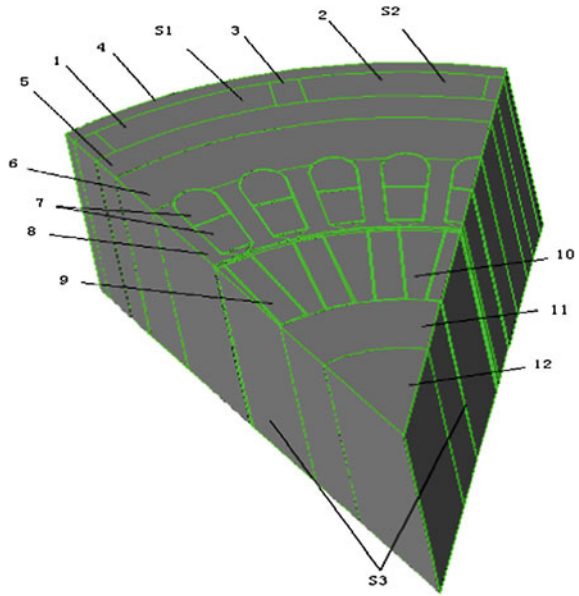
5. That the water temperatures in adjacent inlets and outlets are assumed to be equal when the whole motor is solved;
6. No heat transfer between adjacent partial models, and no heat transfer between the straight-line parts and winding ends of stators and rotors.

19.2.2 Mathematical Model and Boundary Conditions

The rated velocity in the jacket inlet *S1* is 0.384 m/s, the jacket outlet *S2* is that of free flow, and *S3* is adiabatic surface [4]. The flow type of the fluid in the jacket is

Table 19.2 Losses in each part

Parameters	Values (W)	Parameters	Values (W)
Copper loss of stator	2,698	Copper loss of rotor	1,200
Iron-core loss of stator yoke	605	Surface loss of rotor	600
Iron-core loss of stator tooth	449	Loss of rotor tooth	200

turbulent flow, the fluid is incompressible, the field area meets Mass Conservation Equation, Momentum Conservation Equation and Turbulent Transport Equation.

The standard $\kappa - \varepsilon$ equation is a semi-empirical formula based on the turbulent energy and dissipation rating, as seen in the following:

$$\frac{\partial(\rho\kappa)}{\partial t} + \frac{\partial(\rho\kappa\mu_i)}{\partial x_i} = \frac{\partial}{\partial x_i}\left[\left(\mu + \frac{\mu_t}{\sigma_\kappa}\right)\frac{\partial\kappa}{\partial x_j}\right] + G_\kappa - \rho\varepsilon. \tag{19.1}$$

$$\frac{\partial(\rho\varepsilon)}{\partial t} + \frac{\partial(\rho\kappa\mu_i)}{\partial x_i} = \frac{\partial}{\partial x_j}\left[\left(\mu + \frac{\mu_t}{\sigma_\kappa}\right)\frac{\partial\varepsilon}{\partial x_j}\right] + \frac{C_{1\varepsilon}\varepsilon}{\kappa} - C_{2\varepsilon}\rho\frac{\varepsilon^2}{\kappa}. \tag{19.2}$$

where: κ—turbulent energy; ε—dissipation rating of turbulent energy; μ_i—velocity along the direction of i; μ—dynamic viscosity; G_κ—generated term of turbulent energy by the mean velocity gradient; μ_t—turbulent velocity.

The heat transfer in the motor fluid and solid areas meets the equation of heat conduction [5]:

$$\frac{\partial}{\partial x}\left(\lambda_x\frac{\partial T}{\partial x}\right) + \frac{\partial}{\partial y}\left(\lambda_y\frac{\partial T}{\partial y}\right) + \frac{\partial}{\partial z}\left(\lambda_z\frac{\partial T}{\partial z}\right) = -q. \tag{19.3}$$

where: T is the temperature of solid; λ_x, λ_y, λ_z are the coefficients of the heat conduction in the direction of x, y and z; q is the density of heat source.

19.2.3 Heat Sources in the Motor

In order to calculate the temperature distribution of the motor, it is important to calculate the losses accurately [6], the losses of the stator and the rotor are calculated by the electro-magnetic analysis and shown in Table 19.2.

19.3 Calculation and Analysis of Temperature and Fluid Fields

By solving the model with the finite volume method, the temperature distributions of cooling water under the first partial models acquired and shown in Fig. 19.3.

The highest temperature of the motor is on the rotor bars from the Fig. 19.3, and the whole of rotor bars is all but isothermal body; the highest temperature of the
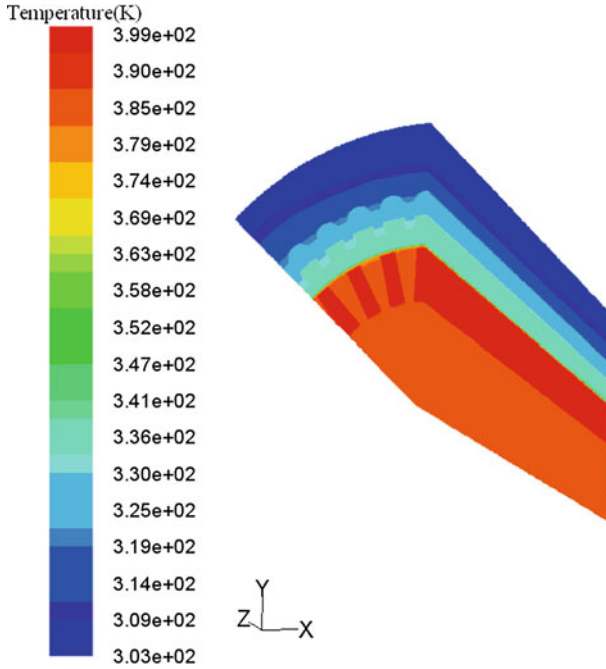
Fig. 19.3 Temperature distribution in the motor

Fig. 19.4 Temperature of water-cooled jacket
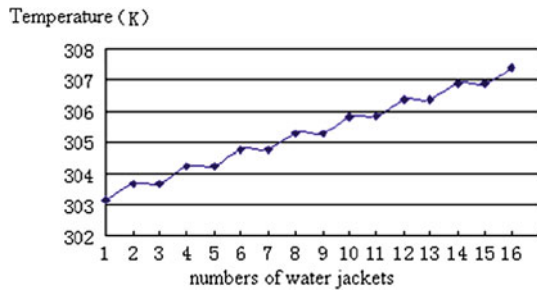
stator is on the upper winding close to slot wedge. This is consistent with cooling structure and the way of heat dissipation. From the temperature distribution of insulating layer, it is seen that the peak temperature rise is lower than permissible temperature rise (H-class insulation). The average temperature of water in the inlet is 303.15 K, and then increases by 0.5255 K after the water flows through the first set jackets.

It is seen from Fig. 19.4 that the fluid temperature in the water jackets rises from 303.15 to 307.5 K with the water flowing. The temperature difference is 4.25 K. This is consistent with the measurement on the field.
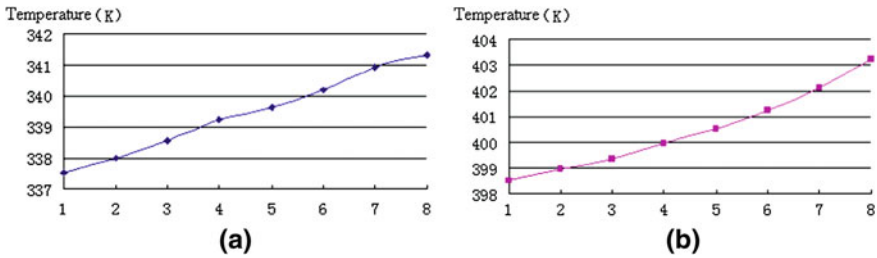
Fig. 19.5 Circumferential temperature distribution of stator winding and rotor bars. **a** Stator winding; **b** rotor bars
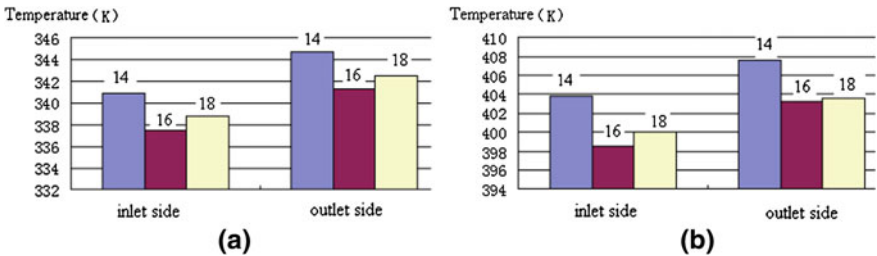
Fig. 19.6 Temperature contrast of winding and bars with different water-cooled jacket structures. **a** Stator winding; **b** rotor bars

The Fig. 19.5 is the highest temperature curves of stator winding and rotor bars in each partial model. It is seen that the temperature of stator winding rises from 337.549 to 341.3307 K and the circumferential temperature difference is 3.78 K, the temperature of rotor bars rises from 398.5232 to 402.637 K and the circumferential temperature difference is 4.11 K.

19.4 Calculation of Temperature Field After Changing Structure of Water Jacket

With the same flow and heat sources, the cooling structure determines the temperature distribution of motor. So improving the cooling system has an important significance.

In order to verify that the design of cooling system is reasonable, the pression check of the cooling system is done under the same water flow [7]. The cooling system consists of 16 water jackets. When the water jackets are changed into 14 or 18, the water pressures are all lower than the technical requirements of 3 MPa. This proves the design is reasonable. Based on this, the temperature and fluid fields are calculated for the motors with 14 and 18 water jackets.

   The temperature difference of cooling water is 3.90 K for 14 water jackets, 4.1 K for 18 ones, and 4.25 K for 16 ones, respectively. The temperature difference in 16 water jackets is greater than that of 14 and 18 ones. Under the same water flow, the greater the temperature difference of the cooling water is, the more the heat taken is, and the better the cooling effect is. Moreover, from the temperature contrast curves in the Fig. 19.6, it is seen that the design of the cooling systems with 16 water jackets is more reasonable.

19.5 Conclusions

By the calculation and analysis to the temperature and fluid fields of water-cooled motor, the following conclusions are acquired:

1. The highest temperature of the motor is lower than the maximum permissible temperature, this makes the motor safe and stable;
2. the structure of water jackets has a greater effect on the cooling effect. And the design of cooling system of 16 water jackets is more reasonable;
3. the calculation method from a part to the whole leads to some error for the ignorance of heat transfer between partial models during the calculation, so the model in this paper needs to be improved further.

References

1. Feng JR, Yang QP, Liu JG (2005) The technical actuality and development trend of electric traction shearers for thin seam. Electro Mechanic Coal Mine 11:11–13
2. Jiang F, Huang P (2004) Fluent advanced application and example analysis. Tsing Hua University Press, Beijing
3. Zhou JJ, Xu GQ, Zhang HJ (2010) Fluent engineering technology and example analysis. China Water Resources and Hydropower Press, Beijing
4. Li WL, Yang XF (2009) Calculation and analysis of temperature and fluid fields of stator ends in the large air-cooled turbine generator, vol 29. Proc CSEE 36:80–87
5. Li WL, Fu M, Zhou F (2000) Calculation of stator 3D Temperature field in the large and medium-sized asynchronous motor based on fluid similarity theory and the finite element method, vol 20. Proc CSEE 5:14–17
6. Wei YT, Meng DW, Wen JB (1998) Heat exchange of electric machine. Mechanical Industry Publishing Company, Bejing
7. Tuztas M, Egrican AN (2002) Mathematical model of finned tube heat exchangers for thermal simulation software of air-conditioners, vol 29. Int Commun Heat Mass Transf 4:547–556

Chapter 20
Combined Genetic Algorithm Control for Bearingless Motor Suspended System

Weiran Wang, Xianxing Liu, Zhu Xin and Yuxin Sun

Abstract Genetic algorithm is an efficient global optimal searching algorithm. It is based on the natural selection and the heredity theory, and combined the principle of the fittest survival with the stochastic exchange of community internal chromosome. This paper takes bearingless motor as control object, makes the simulation in Matlab and use real-time emulation system dspace to experiment about the bearingless motor suspended system. The result demonstration that as increase iterative number of times the result parameter get more and more perfect to the suspension control. With the end of evolution, the algorithm finds the best control parameters. The algorithm is optimal globally, effect significantly to the suspension system, so it fitted for complex and non-linear bearingless motor about the suspension control.

Keywords Genetic algorithm · Bearingless motor · Parameter optimization for the suspended system · Dspace

W. Wang (✉) · X. Liu · Y. Sun
Department of Electrical and Information Engineering, Jiangsu University,
Zhenjiang, China
e-mail: 16959377@qq.com

X. Liu
e-mail: liuxianxing@ujs.edu.cn

Y. Sun
e-mail: syx4461@ujs.edu.cn

Z. Xin
Jiangsu Zhenjiang Installation Group, Zhenjiang 212003, Jiangsu, China
e-mail: zlebr@qq.com

(a)

(b)
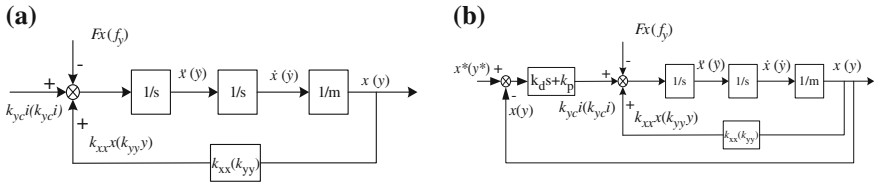
Fig. 20.1 Rotor suspension system. **a** The diagram of rotor suspension system. **b** The diagram of rotor suspension system with adjuster

20.1 Introduction

Bearingless induction motor is one kind of new motor which combined motor with magnetic bearings in one stator windings [1, 2]. Compared with traditional magnetic motors, the axial space of bearingless induction motor is short and with the high speed. Bearingless motor make the rotating magnetic field of itself as the bias magnetic field, so magnetic power greatly reduced, with the advantage of high quality energy-saving. Bearingless motor use two sets of different windings on stator to produces a radial magnetic field force (Maxwell force) which will make the rotor suspended in space, so there will be no contaction between the rotor and the stator. There are many kinds of bearingless motor, but the structure and working principles are general similar.

20.2 The Basic Principle and Mathematical Model of Bearingless Motor

20.2.1 The Mathematical Model of Suspension

The movement of the rotor of motor radial suspension in two degrees of freedom

$$m\ddot{x} = k_{xc}i + k_{xx}x - f_x \qquad (20.1)$$

$$m\ddot{y} = k_{yc}i + k_{yy}y - f_y \qquad (20.2)$$

$k_{xc}i$, $k_{yc}i$ is control pull force which produces by the suspending control winding [3]; $k_{xx}x$, $k_{yy}y$ is magnetic pull force which produces by the rotor displacement, This magnetic pull force is proportional to rotor's displacement and the direction is same to the direction of rotor's displacement. So accelerate the movement of rotor along the direction of displacement. f_x, f_y is the load force which is respectively along the x–y axis. The diagram is as shown in Fig. 20.1a.

Such as shown in the Fig. 20.1a, the magnetic pull force of displacement eccentric $k_{xx}x$, $k_{yy}y$ is a positive feedback. So the system is unstable. The rotor's mass is m = 2.85 kg

$$k_{yy} = k_{B2}^2 \frac{9\mu_0 r l N_2^2 I_{2m}^2}{16\pi\delta_0^3}$$

$$= 0.9^2 \times \frac{4\pi \times 10^{-7} \times 9 \times 57.3 \times 10^{-3} \times 120 \times 10^{-3} \times 100^2 \times 3^2}{16\pi \times 0.35^3 \times 10^{-9}}$$

$$= 2630500$$

So the Open-loop transfer function is:

$$G(s) = \frac{1}{ms^2 - k_{yy}} = \frac{1}{2.85s^2 - 2630500} \tag{20.3}$$

As the same, we can get the transfer function along the x-axis, but only some x-axis component of external disturbance force in the x-axis direction generally. Rotor's gravity mainly decomposed along the y-axis.

20.3 The Design of PID Controller for Rotor Suspension System

PID controller is a linear controller [1, 4]. It is based on the control deviation e between the given value with the actual output value, and got the control volume by linearly composed the proportional, integral and differential of the deviation. Figure 20.1b shows the suspension control system with the PID correction. Its open-loop transfer function is:

$$G(s)H(s) = \frac{K_d s + K_p}{ms^2 - k_{yy}} = \frac{K(s - z)}{ms^2 - k_{yy}} = \frac{K(s - z)}{2.85s^2 - 2630500} \tag{20.4}$$

The open-loop pole are 960.72, -960.72, we should increases zero spot in left side of the pole which in left half axis, supposes the increased zero spot is $s = z = -1000$, the origin of coordinates is the critical stable point, the critical stability gain is $k_{xx} = 2630500$. If make the closed-loop characteristic root in the left plane, so the open-loop gain should be greater than the critical stability gain $K_p > k_{xx}$, $K_p = 4.65 \times 10^6$, $K_d = 1000$.

So the closed-loop transfer function is:

$$\frac{K_d s + K_p}{ms^2 - k_{yy} + (K_d s + K_p)} = \frac{1000s + 4.65 \times 10^6}{2.85s^2 - 2630500 + 1000s + 4.65 \times 10^6}$$

$$= \frac{1000s + 4.65 \times 10^6}{2.85s^2 + 1000s + 2019500}$$

20.4 Combined Adapted Genetic Algorithm to Improve Suspension Controller

① Optimal selection operator

Optimal selection operator combined best retention and proportional selection. First, find the highest and lowest fitness value of the individual in current groups, while allow the two best individuals do not participate in crossover, mutation and direct into the next generation. Second, arrange the remained individual's fitness. In the end, operate proportional selection. The selection ideas no only ensure the best individual's fitness in the group does not be decreased but also increase the average value of fitness in the population.

② Adaptive crossover operator and mutation operator

When individual's fitness in the population tends to same or local optimum, P_c need increase; when individual's fitness in the population tends to scattered, P_c need decrease. Meanwhile the individual corresponds to the lower P_c when the individual fitness higher than the average value of the group. That sends the better solution to the next generations. And the individual corresponds to the high P_c when the individual fitness lowers than the average value. That solution should be eliminated. Similar to the above adaptive mutation operator, the adaptive crossover operator and mutation operator is:

$$P_c = \begin{cases} k_1 \frac{(f_{\max}-f')}{f_{\max}-f_{avg}}, \; f' \geq f_{avg} \\ k_2, \; f < f_{avg} \end{cases} \quad P_m = \begin{cases} k_3 \frac{(f_{\max}-f)}{f_{\max}-f_{avg}}, \; f \geq f_{avg} \\ k_4, \; f < f_{avg} \end{cases} \tag{20.5}$$

Which f_{max} is the largest fitness value of the population; f_{avg} is the average fitness value of each population; f' is the larger fitness value in two individuals which want to crossover; f is the fitness of the individual which want to mutate. $k_1, k_2, k_3, k_4 \in (0,1)$.

20.5 The Simulation and Experiment by Dspace About the Suspension Control Combined the Adaptive Genetic Algorithm

Get the open-loop transfer function of bearingless motor's suspension system according to the conventional engineering design methods [5]. $G(s)H(s) = \frac{K_d s + K_p}{ms^2 - k_{yy}}$. Closed-loop transfer function is $\frac{K_d s + K_p}{ms^2 - k_{yy} + (K_d s + K_p)}$, when $K_p > k_{yy}$, and got the error function of displacement err(s) is: $err(s) = \frac{f(s)}{ms^2 - k_{yy} + (K_d s + K_p)}$ Choose the parameters of PI controller that making the error function is minimal and making it accord with the above transfer function.

(a)

(b)

(c)

(d)

(e)

(f)
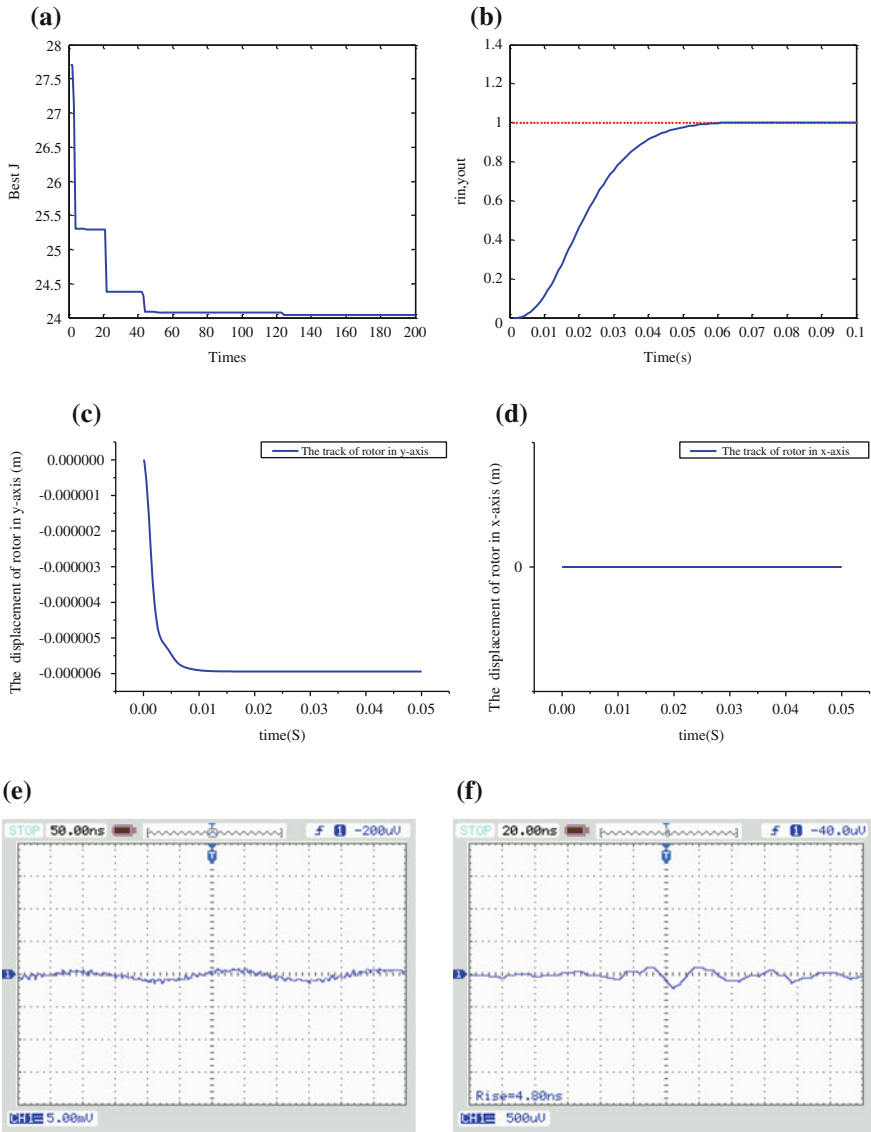
Fig. 20.2 The results of adaptive genetic algorithm to improve the bearingless motor rotor position control. **a** The process of genetic algorithms to find the optimal parameters. **b** The response of optimal parameters under step function. **c** The rotor position response of y-axis after genetic algorithm found optimum parameters, the load of y-axis is 12 N. **d** The rotor position response of x-axis after genetic algorithm found optimum parameters, the load of x-axis is 0 N. **e** The response of rotor position (0 cm) about y-axis by dspace. **f** The response of rotor position (0 cm) about y-axis by genetic algorithm improved

The initial PID parameters: $K_p = 4.65 \times 10^6$, $K_i = 0$, $K_d = 1000$. Set the adaptive genetic algorithm parameters: the population $M = 40$, the evolution number is 200, the coefficient $w_1 = 0.999$, $w_2 = 0.001$, $w_3 = 2$, $w_4 = 100$, the best value is min(abs(input function-closed-loop transfer function))).

As shown in Fig. 20.2, it is the results of adaptive genetic algorithm to improve the bearingless motor rotor position control. Figure 20.2a shows the evolution process of adaptive genetic algorithm find the best parameters. As the increase of evolution, the index reduced and close to the best parameters gradually; Fig. 20.2b shows that after find the optimal PID parameters, the response under step function; Fig. 20.2c shows bearingless motor suspension control system's suspension response in y-axis after find the best PID parameters ($K_p = 5.5169 \times 10^6$, $K_i = 516.7658$, $K_d = 3845.5693$) and the load of y-axis is 12 N. And the rotor can stable suspension under the condition of set y-axis stable position is 0 m, the place of rotor in y-axis ultimate stability in -5.6×10^{-6} m, this is an acceptable error; Fig. 20.2d shows bearingless motor suspension control system's suspension response in x-axis after find the best PID parameters and the load of x-axis is 0N and there is no error almost. Figure 20.2e is the experiment by dspace, the range of A/D, D/A is 10 v, the rate of D/A data and signal is 1:10, oscilloscope is set to $\times$ 10. When the load of y-axis is 12 N and set stable position of y-axis is 0m. We can see the output of the oscilloscope is -200 uv. According to the proportion of above, we know that rotor displacement in y-axis is -2×10^{-6} m in this moment (it is -2 mm). The fluctuations and err is also small; Fig. 20.2f is the response of rotor position about y-axis by genetic algorithm improved in same data. We can see the output of the oscilloscope is -40 uv so the rotor displacement in y-axis is -2×10^{-6} m (it is -0.4 mm). Compared to the Fig. 20.2e, the accuracy of rotor displacement combined genetic algorithm control is improved about 500%.

References

1. Wang B (2003) Study on magnetic suspension principles and control methods of bearingless motors, Shenyang University of Technology
2. Zhang H, Zhang H, Pei J (2010) Suspension control of bearingless induction motors based on current model. Electr Mach Control 03:73–76
3. Qiu Z, Deng Z, Wang X, Meng L (2007) Study on the modeling and control of a permanent-magnet-type bearingless motor considering rotor eccentricity and Lorenz force. Proc CSEE 03:64–70
4. Liu J (2005) Advanced PID control and the simulation of MATLAB, Electronic Industry Press, 10
5. Long J (2010) Permanent brushless dc motor speed control system's optimal design based on the MATLAB. China Comp Commun 08:30

Chapter 21
Corner Detection via Two-Layer Threshold Method

Zhihui Yang and Xiaolan Han

Abstract This paper presents a two-layer threshold method for the corner detection. The method is inspired by the classical Susan corner detection model, and the improvement is two-fold. One is the choice of the self-adaptive threshold, which can be used to detect the possible corner areas. However, since a corner has an arbitrary orientation and sometimes is disturbed by noises, we provide a series of rotate coordinate systems, the second improvement, to enhance the accuracy of our method. Experiment results show that the improved algorithm is robust and is of high efficiency.

21.1 Introduction

The corner is an important local feature of image, which contains much important shape information, and can be widely used in many fields such as image segment, image matching, 3D reconstruction, etc. [1]

There is no unified mathematical definition for corner, but it is generally believed that corner is a point where brightness of pixels changes violently [2], or a point with local maximum value of edge curvature [3]. In recent 30 years, many corner detectors have been proposed in the literature. Usually they are required to gain accurate and stable result and be easy to carry out for practical requirements

Z. Yang (✉) · X. Han
Institute of Image Processing and Pattern Recognition,
North China University of Technology,
100041 Beijing, People's Republic of China
e-mail: zhyang@ncut.edu.cn
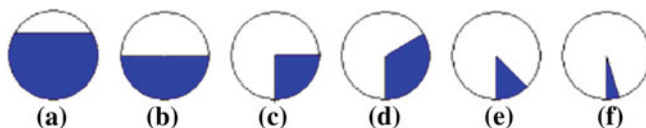
Fig. 21.1 Six kinds of the general USAN areas. **a** The nucleus is in the USAN area. **b** The nucleus is on the edge. **c, d, e** The nucleus is a corner. **f** The nucleus is a noisy point

[4]. The corner detectors of gray scale images can be divided into three types which are based on gradient, mask or the combination of them [2, 5, 6]. One of classic corner detectors is Susan algorithm which is proposed by Smith and Brady [7]. Since the algorithm adopts a circular mask and concerns every direction, it is more accurate and insensitive to noises.

The paper proposes a new corner detector based on an improved Susan model. The detector introduces a self-adaptive two-layer threshold to judge the univalue segment assimilating nucleus (USAN) area and introduces a rotate coordinate system to filter the candidate points to improve the detection ability by avoiding missing and error detection. Experiments show that our algorithm is robust with high efficiency and accuracy.

The paper is organized as follows. Section 21.2 introduces the classic Susan algorithm and describes the improved algorithm in detail. Then some experimental results compared with Harris detector and classic Susan detectors are given in Sect. 21.3. Finally, the conclusion is presented in Sect. 21.4.

21.2 The Improve Susan Algorithm

First we will give a brief account of the classical Susan model described in [7].

The intrinsic idea of the classical Susan model lies in the definition of the nucleus similar area, which is used for the judgment of corners. The Susan model adopts a 7×7 circular mask whose centre pixel is called a nucleus. Then the neighborhood of the nucleus is divided into two sub- regions: the region where the pixels are equal or similar to the nucleus, which is called a univalue segment assimilating nucleus (USAN) area, and the region where the pixels are not similar to the nucleus. The number of the similar pixels is defined as the size of the USAN area. Susan model believes that the USAN area of the corner should be smaller than that of half of all the mask pixels. In addition, from the definition, we may observe that the smaller the USAN is, the more possible the point is a corner. However, some points with extremely small USAN are considered as noises. Based on the principle, The Susan model sets up a corner detection framework, with which a point satisfying above conditions is considered as a corner. The mask moves over all the pixels of the possible regions to detect all corners.

The following figure shows six cases to determine whether a nucleus is a corner (Fig. 21.1)

Compared with some other detectors, the classical Susan model works faster and is of stronger anti-noise ability. However, its drawback is also apparent: it strongly depends on the threshold. Furthermore, under some circumstances, such as the contrast of the target and background changes sharply, the result is poor and contains false corners.

To avoid above-mentioned drawbacks, we first introduce a self-adaptive threshold to distinguish all kinds of USAN areas, and then present a series of rotate coordinate systems to enhance the accuracy and anti-noise ability of the improved algorithm.

Before presenting the improved algorithm, we first give a mathematical model to find the self-adaptive threshold. Consider a 7×7 circular mask, which contains 37 pixels, and then assume the initial threshold $T = 25$ [7]. Then we choose a 3×3 small mask and set

$$\begin{cases} \tau = \lambda \cdot \sqrt{\dfrac{\sum\limits_{i=1}^{8} (I(r)-I(r_i))^2}{8}} \\ T' = \min(T, \tau) \end{cases} \tag{21.1}$$

where $\lambda = 0.8 \in (0, 1)$ is a regulation parameter. Notice that $\sqrt{\dfrac{\sum\limits_{i=1}^{8} (I(r)-I(r_i))^2}{8}}$ is the standard deviation of a 3×3 grid window, which reflects the similarity for nearby points of the nucleus. Combined with the initial threshold, T' can be applied to find the corners from the local feature of the image and avoid the effect of noises.

Now we can state main steps of the proposed algorithm.

Step 1: Define a possible corner area. For a general gray scale image, there are many flat areas, which is defined by

$$\begin{cases} |I(x + w) - I(x - w)| < Threshold \\ |I(y + w) - I(y - w)| < Threshold \end{cases} \tag{21.2}$$

where w is the size of the window with the default value 3 and the *Threshold* usually takes 30. From above definition we can see that Eq. (21.2) implies areas with smooth intensity. Thus we may neglect those areas in order to speed up calculations.

Step 2: Find those candidate Corners by using the self-adaptive Susan algorithm in the non-plat areas.

Step 3: Suppress error detection caused by noises. Take any candidate corner point as the origin and set up a coordinate system, as shown in Fig. 21.2.

Fig. 21.2 A coordinate system centered at a candidate corner, where $U^+ = (\omega, 0)$, $V^+ = (0, \omega)$, $U^- = (-\omega, 0)$, $V^- = (0, -\omega)$.
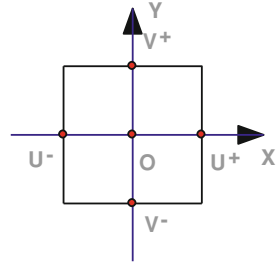
Fig. 21.3 Revolve the coordinate system by 45°
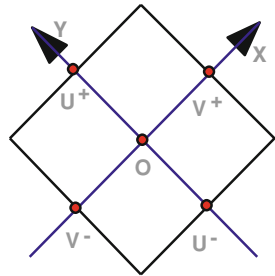
In order to avoid the error detection, we define the corner response function (CRF) as follows:

$$CRF = 2^2 \cdot |I(V^-) - I(O)| + |I(V^+) - I(O)| + 2 \cdot (|I(U^+ - I(V^-)| + |I(U^-) - I(V^-)|) \tag{21.3}$$

Next we will explain why, in Eq. (21.3), every term contributes to the CRF with different weight. In fact, $I(V^-) - I(0)$ is inside the corner area and influences the location accuracy of the corner greatly, so its weight is the biggest. $I(U^+) - I(V^-)$ and $I(U^-) - I(V^-)$ are across both-side of the corner, so their weights are in medium. $I(V^+) - I(0)$ is outside the corner area and its influence is the least, so its weight is the smallest. Here we adopt terms $I(U^+) - I(V^-)$ and $I(U^-) - I(V^-)$, not $I(U^+) - I(0)$ and $I(U^-) - I(0)$, because those terms will reduce the noise effect possibly occurring in the center.

According to the *Susan* model, here the CRF value should be larger than 125 and smaller than 1,350. In addition, we need to rotate the coordinate system to find a corner in different directions. Here we first revolve the system by 45°, and repeat the step at most eight times (Fig. 21.3). If the USAN size is beyond the scope, we may identify the corresponding nucleus as a false corner and remove it.
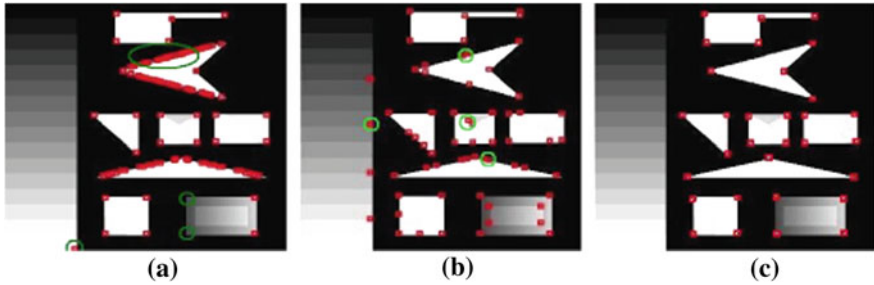
Fig. 21.4 Comparison of detection effects by three algorithms for a standard image **a** Harris algorithm. **b** Classic Susan algorithm. **c** The proposed algorithm

21.3 Experiment Results

In this section some experimental results are presented and discussed. The performance of the proposed corner detector is compared with *Harris* detector and classic *Susan* detector. The goal of the experimental test is to analyze the accuracy, stability and anti-noise abilities of the proposed technique.

According to the improved corner detection algorithm, related experimental schemes are designed as follows by using Matlab 7:

(1) Comparison of the corner detection results by using *Harris* algorithm, classic *Susan* algorithm and the improved algorithm for standard images.

From the results, we can see that the missed detection and error detection by *Harris* algorithm are relatively serious. As the blue markers show in Fig. 2.14a, there are two missed corners in the bottom right corner of the image, while there are many redundant corners in the middle of the edges of the image. As shown in Fig. 21.4b, classic *Susan* algorithm works better, but it still has many error detected corners. Figure 21.4c demonstates much better performance, which contains no error detection and missed detection

(2) Comparison of corner detection results through *Harris* algorithm, *Susan* algorithm and the improved algorithm for standard images with Gaussian noises.

To verify the anti-noise ability of the algorithm, we add the Gaussian noise in the stardard image and then compare the detection result by three algorithms (See Fig. 21.5).

From Fig. 21.5, we can see that the results given by *Harris* algorithm and classic *Susan* algorithm are poor. By contrast, the result by the new algorithm is almost insensitive to the noises.
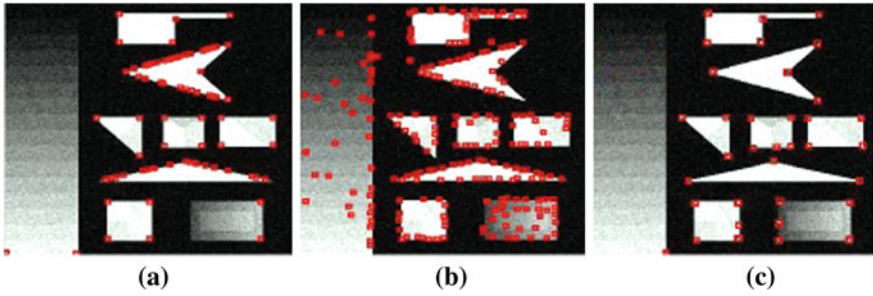
Fig. 21.5 Comparison of three algorithms for a standard image with Gaussian noise. **a** Harris algorithm. **b** Classic Susan algorithm. **c** The proposed algorithm
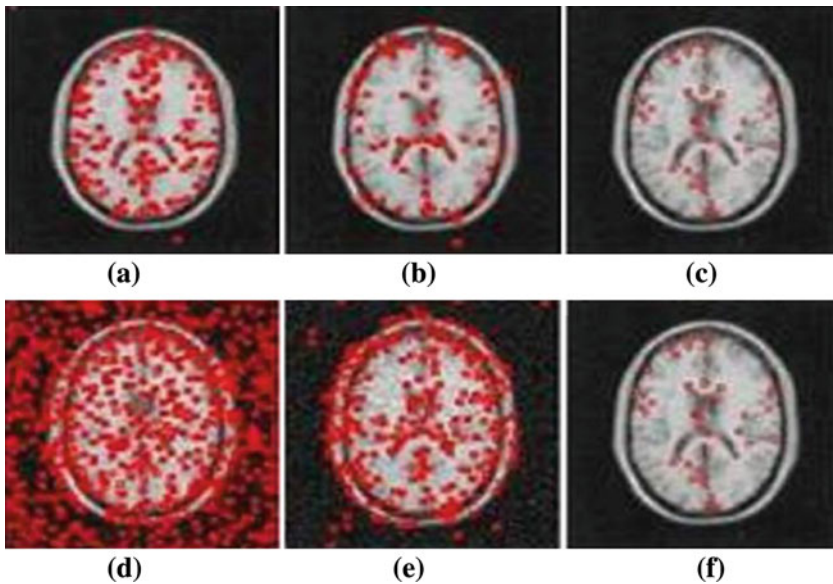
Fig. 21.6 Comparison of detection effects by three algorithms for a cell image. **a** Harris result. **b** classic Susan result. **c** the proposed method result. **d** Harris result with Gaussian noise. **e** classic Susan result with Gaussian noise result. **f** the proposed method result with Gaussian noise

(3) Medical images are usually complicated due to noises and other interference of tissues. Therefore, the paper chooses a cell image to verify the efficiency of our algorithm (Fig. 21.6).

We can see the similar result as shown in Figs. 21.4 and 21.5.

21.4 Conclusions

Following the basic idea of classical Susan algorithm, we present a novel algorithm to find all possible corners. The intrinsic difference between our algorithm and the classical one lies in the choice of the threshold and the rotated coordinate systems. We adopt a self-adaptive mechanism through comparing the standard deviation of a smaller 3×3 grid window with a default threshold of a 7×7 mask. Furthermore, in order to avoid the effect of noises, we may remove those false corners in virtue of a series of rotated coordinate systems. The experiment results show that our algorithm is stable and accurate. Finally, the proposed algorithm is of computational complexity $O(N \log N)$, thus it runs with less time.

References

1. Zhang X, Wang H (2009) Robust image corner detection based on scale evolution difference of planar curves. Pattern Recogn Lett 30:449–455
2. Trajkovic M, Hedley M (1998) Fast corner detection. Image Vis Comput 16:75–87
3. Mokhtarian F, Suomela R (1998) Robust image corner detection through curvature scale space. IEEE Transa Pattern Anal Mach Intell 20:1376–1381
4. Yeh C (2003) Wavelet-based corner detection using eigenvectors of covariance matrices. Patter Recognit Lett 24:2797–2806
5. Kitchen L, Rosenfeld A (1982) Gray-level corner detection. Pattern Recogn Lett 1:95–102
6. Harris C, Steven MA (1988) Combined corner and edge detector. In: Proceeding of 4th Alvey vision conference, Manchester, pp 189–192
7. Stephen M, Smith J, Brady Michael (1997) SUSAN-a new approach to low level image processing. Int J Comp Vis 23:45–78

Chapter 22
DC Transformer Based on Two Dual Switches Push–Pull DC Converters

Xianjin Zhang and Yongxian Song

Abstract This paper presents a novel DC transformer based on two dual switches push–pull DC converters, whose output voltage is not regulated. It has no output filter and runs under near 100% duty ratio. Zero voltage switching (ZVS) conditions and higher efficiency may be easily got, and the bridge arm shoot-through problem is not exist. In this paper, the principle of the transformer is analyzed in detail including output-input characteristics and ZVS conditions. At last, the experiment results are done to verify the performance of the proposed transformer in laboratory.

22.1 Introduction

The DC transmission and distribution generation system have become more and more interesting than the AC transmission system especially in renewable sources. An new type of DC converter-DC transformer, with a simple topology, soft switch mode and higher efficiency, has been presented and studied, which runs in open-loop mode for eliminating the stability problems of closed-loop control [1–14]. The DC transformer was used as a connector between two different AC grids which have different frequencies and voltage level, and the power maybe easily exchanged between them [1–5]. It can also be applied in different DC power

---

X. Zhang (✉) · Y. Song
Department of Electronic Engineering, Huaihai Institute of Technology,
222005 Lianyungang, China
e-mail: zxjb0703113@yahoo.cn

applications with different voltage level for exchanging power [6–9], and can be used in distributed generation systems, such as distributed LED lighting systems (PFC+ DC transformer+ LED lighting) and communication systems (PFC+ DC transformer+ VRM) [10–13].

The bridge arm shoot-through problem in half bridge and full bridge topology is a very serious problem. In order to resolve it and according to the characteristic of DC transformer, a novel DC transformer based on tw o dual switches push–pull DC converters is proposed in this paper. The switches voltage stress is clamped at input voltage by two primary clamped diodes, ZVS conditions can be easily achieved respectively for high efficiency. The voltage stress of secondary rectifier diodes is also clamped by output voltage. The proposed DC transformer operation principle is particularly analyzed. The output characteristics and ZVS conditions will be discussed in detail. The experimental results verify the performance of the proposed DC transformer.

22.2 The Proposed Topology and Operational Principle

22.2.1 The Proposed Topology

The proposed DC transformer is shown in Fig. 22.1. Where the high frequency transformer is magnetic integrated transformer made up of four windings: two primary windings N_{P1}, N_{P2} and two secondary windings N_{S1}, N_{s2}. The inductors L_{r1} and L_{r2} are resonant inductances including the transformer leakage inductance. The diodes D_1 and D_2 are freewheeling diodes and can clamp switches voltage. The capacitors C_{D3} and C_{D4} are parasitic capacitors of the rectified diodes D_3 and D_4. Because the DC transformer is made up of two dual switches push–pull converters, the problem of shoot-through of the switches does not exist.

22.2.2 The Operational Principle

Switches S_1–S_4 are driven by the interleaved PWM signals as shown in Fig. 22.2. The operation behavior in each half of switching period can be divided into five operation modes. The equivalent circuits of each mode are given in Fig. 22.3. Before the analysis, some assumptions are made: the switches parasitic capacitors $C_1 = C_2 = C_3 = C_4 = C_s$; the diode parasitic capacitors $C_{D3} = C_{D4} = C_d$; the inductor $L_{r1} = L_{r2} = L_r << L_m$, where L_m is the magnetizing inductance; the turn ratio of primary-secondary turns $N_{P1}/N_{S1} = n$.

Mode 1 ($t_0 < t < t_1$): The equivalent circuit is presented in Fig. 22.3a. Before the time t_0, S_1 and S_2 are on, S_3 and S_4 are off. The power is sent to secondary side via D_3, primary-secondary windings N_{P1}, N_{S1}. At time t_0, S_1 and S_2 are turned off under zero voltage because of the capacitors C_1, C_2. The L_{r1} and L_{r2} are

Fig. 22.1 The proposed DC transformer
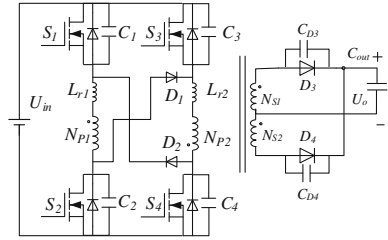
Fig. 22.2 The key waves
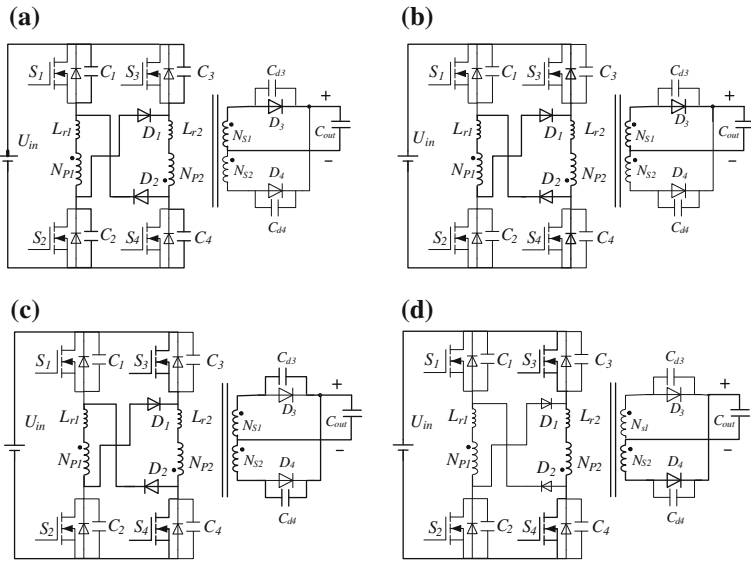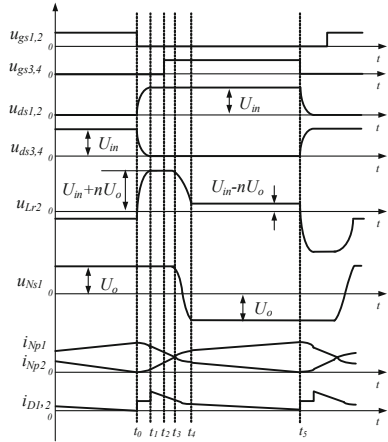
Fig. 22.3 The equivalent circuits

respectively resonant with C_1, C_2 and C_3, C_4. The C_1 and C_2 are charged, C_3 and C_4 are discharged. This mode ends at the time t_1 when the voltages ($u_{ds1,2}$) drain-source of S_1 and S_2 increase to input voltage U_{in} and the voltages ($u_{ds3,4}$) drain-source of S_3 and S_4 drop to zero.

In this mode, ($U_{in}-nU_o$) is neglected because it is very small. The current i_{Lr1} and i_{Lr2} are described as followed.

$$i_{Lr1}(t) = \frac{I_p}{2}(1 + \cos \omega_{r1}(t - t_0)) \tag{22.1}$$

$$i_{Lr2}(t) = \frac{I_p}{2}(1 - \cos \omega_{r1}(t - t_0)) \tag{22.2}$$

The voltages $u_{ds1,2}$, $u_{ds3,4}$ of the switches are given below.

$$u_{ds1,2}(t) = \frac{I_p Z_{r1}}{4} \sin \omega_{r1}(t - t_0) \tag{22.3}$$

$$u_{ds3,4}(t) = U_{in} - U_{ds1,2} = U_{in} - \frac{I_p Z_{r1}}{4} \sin \omega_{r1}(t - t_0) \tag{22.4}$$

Where $\omega_{r1} = \sqrt{\frac{2}{L_r C_s}}$, $Z_{r1} = \sqrt{\frac{L_r}{2C_s}}$ and I_p is the current value of primary winding N_{P1} current i_{NP1} at time t_0.

Mode 2 ($t_1 < t < t_2$): Figure 22.3b gives the equivalent circuit. At time t_1, the body diodes of S_3 and S_4 are conduction. The i_{Lr1} decreases and the i_{Lr2} increases linearly under the voltage U_{in} and U_o. The voltages $u_{ds1,2}$ are equal to input voltage U_{in} and the voltages $u_{ds3,4}$ of S_3 and S_4 is zero. The current i_{Lr1} and i_{Lr2} is obtained by Eqs. (22.5) and (22.5).

$$i_{Lr1}(t) = i_{Lr1}(t_1) - \frac{U_{in} + nU_o}{L_r}(t - t_1) \tag{22.5}$$

$$i_{Lr2}(t) = i_{Lr2}(t_1) + \frac{U_{in} + nU_o}{L_r}(t - t_1) \tag{22.6}$$

Mode 3 ($t_2 < t < t_3$): The equivalent circuit is Fig. 22.3b. At time t_2, S_3 and S_4 are turned on. Because their body diodes have been conduction, S_3 and S_4 are ZVS. The i_{Lr1} and i_{Lr2} will decrease and increase respectively linearly. The body diodes of S_3 and S_4 will not be continuous conduction, when the i_{Lr1} is equal to the i_{Lr2} at the time t_3. At the same time, secondary winding N_{S1} current i_{NS1} will also go to zero, and D_3 will be turned off. In this mode, the i_{Lr1} and i_{Lr2} are achieved in Eqs. (22.7) and (22.8).

$$i_{Lr1}(t) = i_{Lr1}(t_2) - \frac{U_{in} + nU_o}{L_r}(t - t_2) \tag{22.7}$$

$$i_{Lr2}(t) = i_{Lr2}(t_2) + \frac{U_{in} + nU_o}{L_r}(t - t_2) \tag{22.8}$$

Fig. 22.4 The equivalent resonant circuits.
a. Equivalent resonant circuit in mode 1. **b**. Equivalent resonant circuit in mode 4

(a) (b)
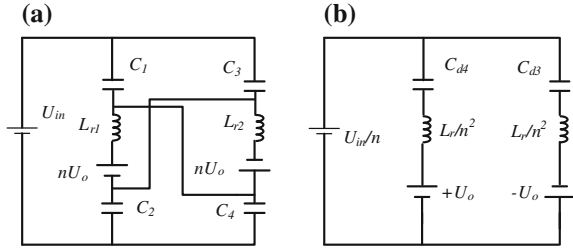
Mode 4 ($t_3 < t < t_4$): The equivalent circuit is Fig. 22.3c. Before the time t_3, the voltage (u_{NS1}) across the secondary windings is U_o because of D_3 being on. At time t_3, because D_3 is turned off, the voltage u_{NS1} polarity begins to change. The L_{r1} and L_{r2} are resonant with the captors C_{D3} and C_{D4}. So the resonant current will charge C_{D3} and discharge C_{D4}. This mode will end at time t_4, and the voltage u_{NS1} will be $-U_o$. In this mode, ($U_{in}/n - U_o$) is also neglected. The winding N_{S2} current i_{NS2} and the voltages (u_{Cd3}, u_{Cd4}) across the rectified diodes D_3 and D_4 are listed below.

$$u_{Cd3}(t) = 2U_o(1 - \cos \omega_{r2}(t - t_3)) \tag{22.9}$$

$$u_{Cd4}(t) = 2U_o \cos \omega_{r2}(t - t_3) \tag{22.10}$$

$$i_{NS2}(t) = \frac{2U_o}{Z_{r2}} \sin \omega_{r2}(t - t_3) = I_S \sin \omega_{r2}(t - t_3) \tag{22.11}$$

where $\omega_{r2} = \sqrt{\frac{n^2}{4L_r C_d}}$, $Z_{r2} = \sqrt{\frac{L_r}{n^2 C_d}}$ and I_s is the winding N_{S2} current i_{NS2} at time t_4.

Mode 5 ($t_4 < t < t_5$): The equivalent circuit is seen Fig. 22.3d. After the time t_4, the voltage across the diode D_4 drops to zero, the power is sent to secondary side via the D_4, primary-secondary windings N_{P2} and N_{S2}. The i_{Lr1} and i_{Lr2} will also decrease and increase linearly respectively. This mode ends when S_3 and S_4 are turned off at the time t_5. In this mode, the inductor current i_{Lr1} and i_{Lr2} is expressed.

$$i_{Lr1}(t) = i_{Lr1}(t_4) - \frac{U_{in} - nU_o}{L_r}(t - t_4) \tag{22.12}$$

$$i_{Lr2}(t) = i_{Lr2}(t_4) + \frac{U_{in} - nU_o}{L_r}(t - t_4) \tag{22.13}$$

After the time t_5, the proposed DC transformer will begin next half period operation (Figs. 22.4, 22.5).

22.3 The Input–Output Characteristics

Each dual switches push–pull DC converter operates under above 100% duty ratio. The simplified circuit and current wave is shown in Fig. 22.6 when the S_1 and S_2

Fig. 22.5 The equivalent
circuit and current waveform
under S_1 and S_2 on

(a)   **(b)**   **(c)**
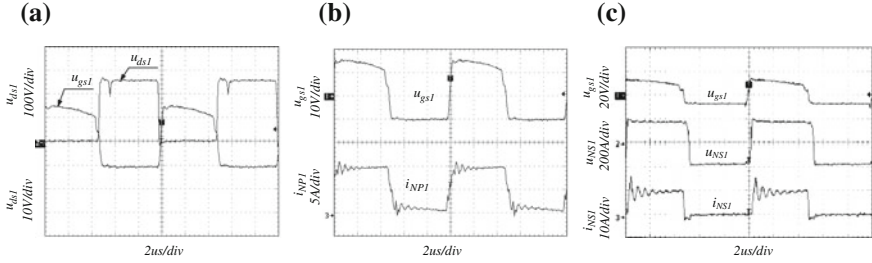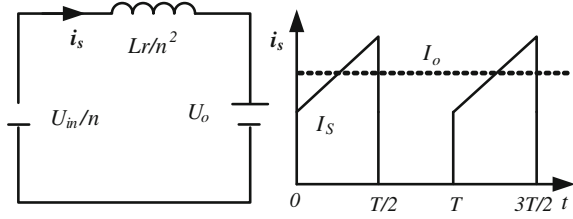
Fig. 22.6 The main experimental waveforms under full load

are conduction. In order to simply analysis, resonant process will be neglected.
The output voltage U_o will be described from the Fig. 22.6.

$$U_o \approx \frac{U_{in}}{n} - L_r \frac{2(I_o - I_s)}{n^2 T/2} \tag{22.14}$$

Where I_o is the output current, I_S is secondary winding N_{S2} current at time t_4,
and T is period of the switches. From Eq. (22.11), I_S related to U_o, L_{r1}, L_{r2}, C_{D3},
and C_{D4}. In order to achieve hard output characteristics, the L_{r1} and L_{r2} must be as
small as possible from Eq. (22.14).

22.4 ZVS Conditions

In order to achieve ZVS, for example S_3 and S_4, the energy stored in L_{r1} and L_{r2}
must be larger enough at time t_0. The voltage $u_{ds3,4}$ must be resonant to zero before
S_3 and S_4 is turned on. At the same time, the voltage $U_{ds3,4}$ will go to zero. The
Eq. 22.15 must be maintained, which is achieved from Eq. (22.4).

$$\frac{1}{4} I_p Z_{r1} \geq U_{in} \tag{22.15}$$

The Eq. (22.16) is also maintained, which is from Eq. (22.11) and Fig. 22.3b.

$$L_r \geq \frac{(2U_{in}\sqrt{C_s} + U_o\sqrt{2C_d})^2}{2n^2 I_o^2} \tag{22.16}$$

From Eq. 22.16, the L_{r1} and L_{r2} must be as large as possible in order to achieve ZVS, and S_3, S_4 must be turned on between t_1 and t_3 from Fig. 22. 2. So the time T_{off} of S_3, S_4 not conduction must meets

$$(t_1 - t_0) \leq T_{off} \leq (t_3 - t_0) \tag{22.17}$$

From Eqs. 22.4 and 22.11 and Fig. 22.3b, T_{off} is calculated.

$$T_{off} \geq t_1 - t_0 = \frac{1}{\omega_{r1}} \arcsin \frac{2U_{in}}{nZ_{r1}(I_o - U_o/Z_{r2})} \tag{22.18}$$

In order to achieve as maximum duty ratio as possible, T_{off} is only a little larger than the time $(t_1 - t_0)$ because of not needing to consider shoot-through problem in a dual Push–Pull converter.

According to above analysis, the inductance L_{r1} and L_{r2} must be small enough from Eq. 22.14 to get good output characteristics, but the inductance must be large enough to maintain ZVS conditions.

22.5 Experimental Results

The measured results of the proposed DC transformer are provided to verify the performance. The parameters are listed: U_{in} = 180 V, $L_{r1} = L_{r2}$ = 25 µH, n = 11:13, P_o = 2 kW, f = 100 kHz, D = 0.48, S_1–S_4:IRF460, D_1–D_4:DSEI30-06A. Main experimental waveforms are shown in Fig. 22.6 under full load and 1/4 load, where u_{gs1}, u_{ds1}, u_{NS1}, i_{NP1} and i_{NS1} respectively are the gate voltage and drain-source voltage, the voltage and current of secondary winding N_{S1} and primary winding N_{P1}.

It can be concluded that the voltage u_{ds1} is clearly zero when the S_1 is turned on and turned off from Fig. 22.6a. It means that the ZVS is achieved. Because of having no output filter inductor, the voltage of the output capacitor Cout has ability of clamping the voltage peak of the secondary winding N_{S1} and the voltage caused by the reverse recovery voltage of D_3 and D_4. So the voltage u_{NS1} peak obviously is very small in Fig. 22.6c and Fig. 22.7b.

From Fig. 22.7a, the primary and secondary windings current of i_{NP1} and i_{NS1} begin to fall when the switches are on under light load. This is that the secondary current i_{NS1} is higher than the load current under light load. In order to maintain the average value of the secondary current equal to load current, the primary and secondary current must fall, and it means that the primary winding voltage, which is referred to the output voltage U_o, is higher than the input voltage U_{in}.

The efficiency of the proposed DC transformer under full load shows in Fig. 22.8. Because the switching loss is small under ZVS and the losses of the reverse recovery of the rectified diodes are also small under the clamping capability of output capacitor Cout, the proposed DC transformer has a high efficiency from the Fig. 22.8.

Fig. 22.7 The main experimental waveforms under 1/4l load

(a)   **(b)**
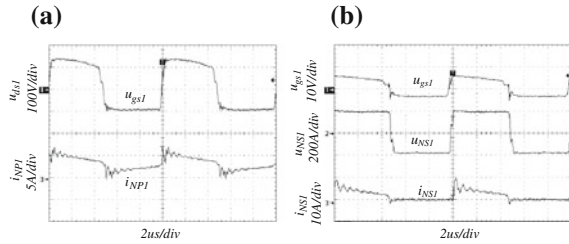
Fig. 22.8 The efficiency and output power
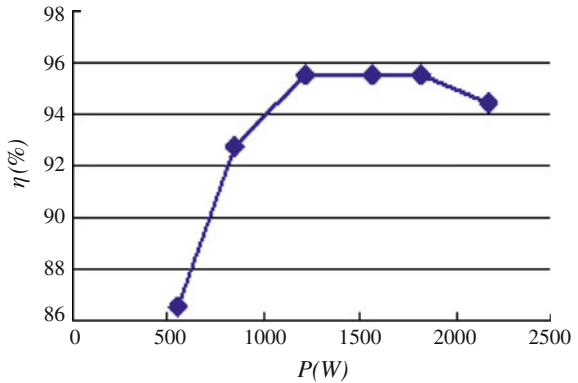
22.6 Conclusions

The proposed DC transformer based on two dual switches push–pull converters is presented in this paper. It is made up of two dual switches push–pull converters and the high frequency transformer consists of magnetic integrated transformer and two flywheel diodes are only needed in primary, so the bulk and lost of the proposed DC transformer will be reduced. Because power switches has no shoot-through problem, it has higher reliability. The DC transformer easily achieves zero-voltage switching. Power switches losses will also be cut down under ZVS. Because of the clamping function of output capacitor Cout, the voltage of secondary winding has not voltage peak and the reverse recovery of the rectified diodes has been very well restrained. Under the above conditions the proposed DC transformer may have a higher efficiency under higher switching frequency.

References

1. Manjrekar MD, Kieferndorf R, Venkatarnmanan G (2000) Power electronic transformers for utility applications. IEEE IAS Ann Meet 4:2496–2502
2. Marchesoni M, Novaro R, Savio S (2002) AC locomotive conversion systems without heavy transformers: is it a practicable solution. Int Sympos Industr Electron 4:1172–1177

3. Chengxiong M, Shu F, Dan W (2003) Theory of power electronic transformer and its applications. High Volt Eng 29(10):4–6
4. Chengxiong M, Shu F, Dan W (2003) Theory of power electronic transformer and its applications part 2 applications and control. High Volt Eng 29(12):1–3
5. EPRI Report (1995) Proof of the principle of the solid-state transformer the AC/AC switch mode regulator, EPRI TR-105067, research project 8001–8013, final report August 1995
6. Hui zhen W, Sai jun M (2006) A ZVSZVS dual switch push-pull DC/DC transformer for high input voltage application. Proc CSEE 16(6):49–54
7. Harada K, Anan F, Yamasaki K et al (1996) Intelligent transformer. In: Proceedings of the PESC, pp. 1337–1341
8. Chengren Y, Xu M, Yao G et al (2002) A novel simple and high efficiency DC/DC transformer. In: Proceedings of the CPES, pp. 173–177
9. Ronan ER, Sudhoff SD, Glover SF et al (2002) A power electronic-based distribution transformer. IEEE Trans Power Deliv 17(2):537–543
10. Kang M, Enjeti PN, Pitel IJ (1999) Analysis and design of electronic transformers for electric power distribution system. IEEE Trans Power Elect 14(6):1133–1141
11. Alou P, Cobos JA, Prieto R et al (2003) A two stage voltage regulator module with fast transient response capability. IEEE PESC 29:l38-143
12. Ivensky G, Abramovitz A, Gulko M et al (1992) A resonant DC-DC transformer. Proc APEC 4:731–737
13. Chengren Y, Xu M, ShanLe C et al (2004) A family of high power density bus converters. Proc PESC 13: 527–532
14. Zhang X, Chen J, Gong C (2010) Input-series output-parallel DC transformer. J Nanjin Univ Aeronaut Astronut 42(1):30–36

Chapter 23
Design and Implementation of Embedded File System Cache Management

Jinhai Zhang

Abstract With the rapid development of embedded systems, embedded operating system has also been more widely used, is provided for in the embedded file system to support demand is also increasing. Such as mobile music, image storage, etc., and now the hard disk can be recorded TV there, all of which need to have embedded file system support. The embedded file system not only will be widely used in digital and entertainment product, but also has good outlook in system software represented by GUI system.

Keywords Embedded file system · FAT · Cache · LRU algorithm

23.1 Introduction

Cache is a memory or disk access speed up the technology, mainly used to improve system responsiveness. The principle of operation is to use a faster storage device to keep a slow storage device from the data in the read, when the need to re-read or write, the first completed in the fast storage devices, and then write according to different strategies to the real slow storage device [1, 2]. For example, RAM memory access speed is much faster than disk drives, so you can be part of the space opened up into a high-speed RAM cache, disk access when there is demand, put the data read into this part of the high-speed cache, when the next time there is this part of the data access requirements, the system can operate to save the data in RAM in order to improve the system response speed [3].

J. Zhang (✉)
Marine College of Shandong Jiaotong University, Weihai, China
e-mail: zhangjinhai76@163.com

You can also use caching to improve the portability of the system, because access operation to carry out high-speed cache, users do not have to worry about with the hardware devices such as data alignment issues are closely related. Cache can be used to reduce the number of disk access, improve the system capacity and reduce the average response time [4]. Especially when a small amount of data transfer for the data retained in the cache until the system when it is deemed appropriate for data transmission, thus improving system performance.

Cache usually written in two ways. Write-through, each time a write cache, but also a real memory to write data to cache and memory to ensure data consistency, This approach is simple and reliable, but because each update must be on a real high-speed cache memory for writing, its speed will be greatly affected. Write-back, data is only written to the cache, and also sets a flag to indicate the need for write-back, When write-back conditions are met, then the real memory is written. These approaches improve system performance, but bear the sudden power-down and the risk of data loss.

23.2 Summary of Embedded File System

With the computer technology and a wide range of products to penetrate other sectors, application-centric classification has become more realistic, which is in accordance with the embedded computer applications and embedded applications will be divided into non-embedded computers and general purpose computers [5]. General-purpose computer with the computer's standard form, by assembling different applications to similar features in all aspects of society, its typical products for PC, and embedded computer is based on embedded systems in the form of hidden in a variety of devices! products and systems.

Embedded computer far exceeds the number in the application of a variety of general-purpose computer, a general purpose computer, the external device includes a 5–10 on the embedded microprocessor, keyboard, mouse, floppy drive, hard drives, monitors, graphics cards, network cards, sound cards, printers, scanners, digital cameras, hubs, etc. are controlled by the embedded processor [6, 7]. In the industrial pipeline control, communications, instrumentation, automotive, marine, aerospace, military equipment, consumer products and other fields is the embedded computer world. Embedded systems is the advanced computer technology, semiconductor technology and electronic technology and specific applications of various industries after the combination of the product. Decided that it must be a technology-intensive, capital-intensive, highly decentralized and innovative knowledge integration system.

The first embedded file system, are made with the corresponding embedded operating system, such as the Windows CE file system and embedded Linux operating system version µCLinux the file system.

Windows CE operating system is mainly used in FAT file system family, FAT file system is the general term FAT12/16/32 file system, which was first in the PC

for the Windows operating system on a machine equipped [8]. The original version is FAT12, it is accompanied by the birth of the DOS file system. Using 12-bit file allocation table, and hence the name, you can manage the disk capacity is 8 M, mainly for the early floppy disk. Windows 95 operating system solved by VFAT format does not support long file name issues, but because the allocation of disk files to the cluster as a unit, a cluster assigned only to a file using, regardless of the file using the entire capacity of the number of clusters, even if a have to take a small file cluster, all remaining unused cluster space has led to inefficient use of large-capacity disk. To solve this problem, Microsoft introduced a new disk partition format FAT32, FAT is the last line of the file system product, Windows 95 OSR2 and later Windows versions support.

In the Linux operating system, the first file system is Minix, it is very limited and poor performance. The file name can not exceed 14 characters maximum and the maximum file size is 64 M bytes. The first designed specifically for the Linux file system called the Extended File System or Ext. It appeared in April 1992, even though it can solve some problems but the performance is still bad. Extension 1993, Second Edition, or Ext2 file system was designed and added to Linux. It is the Linux community to design the most successful file system. Ext3 file system is developed from Ext2 file system is to promote version of Ext2 file system, it has high availability, data integrity protection, fast read, convert and convenient.

VxWorks operating system, file system support: DosFS file system, TrueFFS file system, RawFS file system, TapeFS file systems. VxWorks operating system and device driver file system used between a standard I/O user interface, which makes a single operating system can run multiple same or different types of file systems. Based on these standard interface protocols, the user can write your own operating system Vxworks file system, and can be written into their device drivers, to achieve the free combination of both. Have greater flexibility and scalability. However, VxWorks is a commercial operating system, although very suitable for embedded applications, while the cost of its use is also very high.

Embedded file system for the domestic research, is relatively small, most of them are directly embedded operating system file system, but there are some companies or research institutions launched its own file system, such as ZLG MCU Ltd. ZLG/FS, it is a relatively independent form of embedded FAT-compatible file system, support multi-task, can be easily ported to other operating systems. In addition, domestic Hopen embedded operating system is also mentioned in the "File System Management component" concept.

23.3 Cache Replacement Algorithm

In the cache management, the most important item is the cache replacement algorithm, there are optimal page replacement algorithm, the least recently used algorithm, FIFO algorithm, The most frequently used is LRU (Least Recently Used) algorithm, which is based on the locality principle: are frequently used in

the previous block may be also used frequently in the future, In turn, the block is no longer used for a longer period of time in the future may not be used. The LRU algorithm there is several different approaches:

First, while most likely to think of the most simple method: timing method. Each cache entry is defined in a variable time devoted to the storage of signs, used to record the cache entry is accessed since the last time that has elapsed since. Cache entry is accessed every time, time cleared. To assign a new cache entry, selected from all entries to a transfer out of the longest, while the all clear sign of the timing re-starts.

If you could make a little change in the timing method to be counting method: when the cache entry is accessed, the count flag is cleared, all other cache entries counter increases 1; to allocate new cache item, select one of the largest count transferred out, while all the counters.

Both of these methods is really quite simple, but the efficiency is not good, because in each moment, or a cache entry for each allocation, you need to access all cache entries to record and update the situation is very cumbersome and quite expensive.

There is another way to achieve the list method. Each node records list a cache entry. Access to a cache for each item, put the removed from the list, put end of the chain; to allocate new cache entry, put the chain transfer out of the first node, and then into the end of the chain. List method can be regarded as simple improved timing and counting, because the maintenance of a list, relatively speaking, than the maintenance of all cache entries in the flag should be simple and easy.

23.4 Cache Implementation

The HFS file system, the structure of the cache module shown in Fig. 23.1, including the initialization of the cache entry, access, release, hit the check, write-back capabilities. System uses a write-back cache operation, cache management module may be to determine whether items can be configured to enable, if you do not use the cache in each sector of operation, read and write directly to disk, but when the data is written, still need a common buffer for temporary storage of data to be written.

ZLG MCU's embedded file system ZLG/FS list method is used, by operating a one-way linked list, to complete the replacement of cache entries, and then hit the query cache entries, but also one-way linked list by traversing the same time, Comparison of the cache for each drive letter, and sector indexes are the same for the specified sector.

23.4.1 Cache Management Strategy

System uses a hash table with LRU algorithm with the approach to the management of the cache, the cache can take the low number of sectors for the 8-bit hash
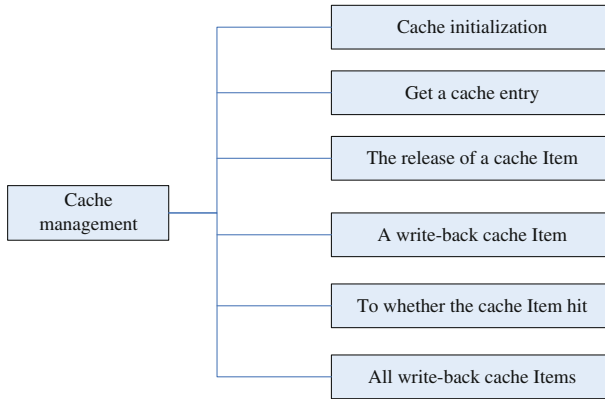
Fig. 23.1 Cache module structure

code, if the hash code is k, then this to exist in Kazakhstan Xi k-table point to a single item in the list, the system first starts, all the elements of the hash table are empty, the table does not exist in any single list. Once when the cache entry needs to be made, this will be added to the appropriate list, in the cache entry is released for various reasons, and from the list to be removed.

Used by the file system cache management strategy shown in Fig. 23.2.

At the same time, all the cache entries and exists in another LRU table, it is a non-circular two-way linked list, the system first starts, all of the cache entry pointer is the order through links, and each has a table pointer and the tail pointer to the list ends. Every time a cache entry is used or accessed, it was moved to the end of LRU table, and inserted into the hash table corresponding to the chain, when the cache entry is released; they are inserted into LRU table header. Thus, LRU table header element is always the least recently used items or the most suitable to be allocated out of the item. In the allocation of the cache item, the direct access to the header element to LRU.

DiskCache in every element of the array, a sector of the contents of the cache, the actual data stored in the buf structure members, it is an array, the size and sector of the same size.

During the write-back cache, the members need to _Disk_Cache the Flag set as write-back, and then call the appropriate hardware drivers for writing. Use write-back cache can improve system performance though, but it must bear the sudden loss of power or other failures of the risk of data loss, in order to minimize this risk, HFS file system uses T-Kernel operating system, process cycle, each after a certain time interval, we call the write-back function to write data back to disk, and write in the usual process, the only way to use write-back, data is only written to the cache, and to some extent, this approach can reduce the above risks.

Cache management module are configurable, as different storage media, such as hard drives and FLASH compared to the hardware read and write speeds vary widely, in order to improve the hard drive file access speed, you can use the cache,
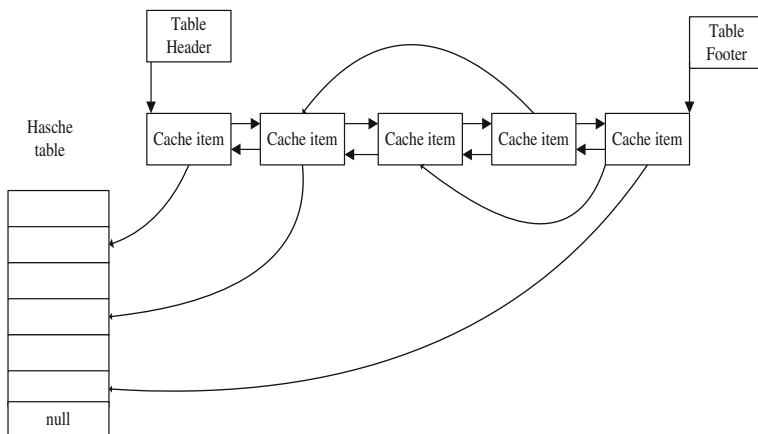
Fig. 23.2 Cache management strategy

while the FLASH is not necessary, forced to use but will affect the cache read and write speed.

23.4.2 Cache Management Algorithm Performance Analysis

With the ZLG/FS taken in compared to the cache management algorithm, HFS system to increase the cache hash table entries hit query, and replace the one-way two-way linked list, so HFS system has a higher response rate.

The bidirectional link will increase the system's memory footprint, is more typical practice space for time, embedded system memory now than before, there had been substantial increases, so using this method, the cost of the system worth it. At the same time, because the hash table used in the hit query, hash table lookup time complexity typically o (1), compared ZLG/FS by one-way linked list o (n), can save a lot of traversing the linked list time.

For the system in the actual application process also proves the judge read the same in the size of a 10 M file, if only one-way linked list, the average read time of 16 s, while the use of HFS system cache management algorithm, only 12 s or so, the performance can be improved about 25%.

23.5 Cache Implementation

The file system is implemented in the embedded reading and writing of data, and image display or audio and video decoding module function, resulting in a rich audio–visual effects, it can be used to preserve some important system and process

information. Also, because the system is compatible with FAT format, can exchange data with the PC, and greatly improves the performance of embedded products.

In the system development process, the layered system architecture design, and through standardized call interface between modules in order to make the system easy to transplant; the system was proposed based on the hash table lookup cache management strategy, disk space cluster second search strategy, optimization algorithms, multi-character reading and writing and put into practice to improve the system in real time; processing procedures through the use of periodic write-back cache to improve data security system.

References

1. Q. Li (2004) Embedded systems, real-time concept. 9:12. (Wangan Sheng translation)
2. Satyanarayanan M (2009) A survey of distributed file systems. Annu. Rev. Comput. Sci. 4:73–104
3. Sandberg R (2007) Sun network filesystem protocol specification, Technical report. Sun Microsystems, Inc, USA
4. T-Engine Forum (2008) T-Format (3): global symbol naming rule in C language. T-Engine Forum Specification, pp 6–8
5. Micrium Technologies Corporation (2008) User's & reference manual for μC/FS. pp 7–9
6. Woodhouse D (2009) JFFS: the journalling flash file system. Red Hat, Inc, USA
7. Denning PJ (2005) The locality principle. Commun. ACM 48(7):19–24
8. Min Z, Gay J (2006) Concept of subsytem. T-Engine Application Development Centre (TEADEC), pp 3–4

Chapter 24
Differential Evolution Using Second Mutation for High-Dimensional Real-Parameter Optimization

Youyun Ao

Abstract High-dimensional global optimization is usually a difficult task in optimization domains. Due to its simplicity and efficiency, differential evolution (DE) is an ideal method for global optimization. This paper proposes an enhanced DE for high-dimensional real-parameter optimization, which is called SMDE. In SMDE, on the one hand, in order to utilize the different characteristics and strengths of different mutation variants, two mutation variants are employed during evolution process; on the other hand, in order to effectively exploit and explore the search space, respectively, second mutation based on improved non-uniform mutation and opposition-based learning is employed after performing each generation evolution. Experimental studies indicate that SMDE has the ability of optimizing high-dimensional real-parameter optimization problems.

Keywords Differential evolution · Evolutionary algorithm · Global optimization · Second mutation

24.1 Introduction

Conventional evolutionary algorithms, including genetic algorithm (GA) [1], evolution strategy (ES) [2], genetic programming (GP) [3], and evolutionary programming (EP) [4], have been widely applied to both numerical and combinational optimization problems. In the past two decades, some new kinds of evolutionary

Y. Ao (✉)
School of Computer and Information, Anqing Teachers College,
Anqing, 246011 Anhui, China
e-mail: youyun_ao@tom.com

algorithms, including differential evolution (DE) [5] and particle swarm optimization (PSO) [6], etc., have been proposed. Usually, evolutionary algorithms can show the excellent search performances when used to optimize the low-dimensional optimization problems, while their search performances can deteriorate quickly as the dimensions of problems to be optimized increase. This is because as the dimensions of problems to be optimized increase, the size and complexity of the search space increase exponentially, which affects the search ability of evolutionary algorithms [7].

DE has become a popular method for global optimization and can perform better than or not worse than GA and PSO [8]. In the past, most reported studies on DE are preformed on the low-dimensional optimization problems. Recently, some studies have shown that DE also is an ideal method for high-dimensional global optimization [9, 10]. Opposition-based learning [9] has been proven to be an effective search technique in DE for low-dimensional or high-dimensional global optimization [9, 11]. And, non-uniform mutation [12], also called dynamic mutation and initially employed in real-coded GA, can improve the search precision. This paper proposes an enhanced DE for high-dimensional real-parameter optimization (SMDE). SMDE employs two mutation variants "DE/rand/1/bin" and "DE/best/1/bin" to enhance the search ability during evolution process and uses second mutation based on improved non-uniform mutation and opposition-based learning to effectively exploit and explore the search space, respectively after performing each generation evolution. SMDE is tested on several high-dimensional real-parameter optimization problems, and experimental results show that SMDE is promising.

24.2 Proposed Algorithm

Usually, DE [5] first randomly initializes population within the bounds of decision variables, then repeatedly performs three operators (i.e., mutation, crossover, and selection) successively to generate the next generation population till the termination criterion is achieved. The details of SMDE are described in the following.

24.2.1 Two Mutation Variants

Classical DE only uses one mutation variant. However, in order to make the best of cooperative advantages of different mutation variants. In SMDE, two mutation variants "DE/rand/1/bin" and "DE/best/1/bin" are randomly chosen to generate the new vector $v_i(t)$ as follows:

$$v_i(t) = \begin{cases} x_{r_1}(t) + F \times (x_{r_2}(t) - x_{r_3}(t)), & \text{if } rand[0, 1] \leq 0.5 \\ x_b(t) + F \times (x_{r_1}(t) - x_{r_2}(t)), & \text{otherwise} \end{cases} \quad (24.1)$$

where $rand[0,1]$ is a uniformly distributed random number in the range [0,1]. "DE/rand/1/bin" and "DE/best/1/bin" can explore and exploit the search space by random search and learning from the best individual, respectively. After mutation, if one or more variable $v_{ij}(t)$ of $v_i(t)$ is beyond the corresponding boundary, the violated variable $v_{ij}(t)$ is either reflected back from the violated boundary or set to the corresponding boundary value according to the following formula [13]:

$$v_{ij}(t) = \begin{cases} (L_j + v_{ij}(t))/2, & \text{if}(r \leq 1/3)\&(v_{ij}(t) < L_j) \\ L_j, & \text{if}(1/3 < r \leq 2/3)\&(v_{ij}(t) < L_j) \\ 2L_j - v_{ij}(t), & \text{if}(r > 2/3)\&(v_{ij}(t) < L_j) \\ (U_j + v_{ij}(t))/2, & \text{if}(r \leq 1/3)\&(v_{ij}(t) > U_j) \\ U_j, & \text{if}(1/3 < r \leq 2/3)\&(v_{ij}(t) > U_j) \\ 2U_j - v_{ij}(t), & \text{if}(r > 2/3)\&(v_{ij}(t) > U_j) \end{cases} \tag{24.2}$$

where r is a uniformly distributed random number in the range [0,1], and $[L_j, U_j]$ is the range of the jth decision variable.

24.2.2 Improved Opposition-Based Learning

The basic idea of opposition-based learning is to calculate its opposite point simultaneously when evaluating a point, which can provide another chance to find a point closer to the global optimum.

Definition 1 [11]   Suppose that $x_i(t)$ denotes the ith point of the tth generation population $P(t)$, the opposite point $o_i(t)$ of $x_i(t)$ is completely defined by its jth component $x_{ij}(t)$ as follows:

$$\forall i \leq NP, \forall j \leq n : o_{ij}(t) = L_j + U_j - x_{ij}(t) \tag{24.3}$$

where NP is the population size, n is the number of decision variables, L_j and U_j are the lower and upper of the jth decision variable, respectively. In SMDE, in order to explore the search space more effectively, the search technique of opposition-based learning is improved as follows:

$$o_{ij}(t) = \begin{cases} L_j + U_j - x_{ij}(t), & \text{if } j \in S \\ x_{ij}(t), & \text{otherwise} \end{cases} \tag{24.4}$$

where S is a random integer set, non-empty and $S \subseteq \{1, 2, \ldots, n\}$.

24.2.3 Improved Non-Uniform Mutation

Originally, the aim of introducing non-uniform mutation is to improve the search precision in real-coded genetic algorithm [12]. For any given point

$x_i(t) = [x_{i1}(t), x_{i2}(t), \ldots, x_{ij}(t), \ldots, x_{in}(t)]$, its jth component $x_{ij}(t)$ is randomly chosen to mutate, the mutated component $x_{ij}(t)'$ and other components consist of the mutated point $x_i(t)' = [x_{i1}(t), x_{i2}(t), \ldots, x_{ij}(t)', \ldots, x_{in}(t)]$ as follows:

$$x_{ij}(t)' = \begin{cases} x_{ij}(t) + \Delta(t, U_j - x_{ij}(t)), & \text{if } rand[0, 1] \leq 0.5 \\ x_{ij}(t) - \Delta(t, x_{ij}(t) - L_j), & \text{otherwise} \end{cases} \qquad (24.5)$$

where $rand[0, 1]$ is a uniformly distributed rand number in the range [0,1], L_j and U_j are the lower and upper bounds of the jth variable, respectively. The function $\Delta(t, y)$ returns a value in the range $[0, y]$, such that $\Delta(t, y)$ approaches to zero as t approaches to T, and it is defined as follows:

$$\Delta(t, y) = y \times r \times (1 - t/T)^b \qquad (24.6)$$

where r is a uniformly distributed random number in the range [0,1], t and T are the generation number and the maximum generation number, respectively. The parameter b determining the degree of dependency on the generation number is often set to 2 or 3, and b is set to 3 in SMDE. The function $\Delta(t, y)$ causes non-uniform mutation to search uniformly at early stage when t is small and very locally at later stage when t approaches to T, respectively. The property of non-uniform mutation can increase the probability of finding the global optimum. In SMDE, in order to exploit the search space more effectively, non-uniform mutation is improved as follows:

$$x_{ij}(t)' = \begin{cases} x_{ij}(t) + \Delta(t, U_j - x_{ij}(t)), & \text{if } j \in S \ \& \ rand[0, 1] \leq 0.5 \\ x_{ij}(t) - \Delta(t, x_{ij}(t) - L_j), & \text{if } j \in S \ \& \ rand[0, 1] > 0.5 \end{cases} \qquad (24.7)$$

where S is a random integer set, non-empty and $S \subseteq \{1, 2, \ldots, n\}$.

24.2.4 Second Mutation

Based on the above ideas, in SMDE, the procedure of second mutation is described as follows:

- Step 1   Based on the objective function values of individuals, the offspring population $P(t + 1)$ of population $P(t)$ is divided into two subpopulations $P_1(t + 1)$ and $P_2(t + 1)$ (with the same population size), and the individuals of $P_1(t + 1)$ are superior to or not worse than those of $P_2(t + 1)$.
- Step 2   The subpopulation $P_1(t + 1)$ uses improved non-uniform mutation to generate the subpopulation $M_1(t + 1)$, while the subpopulation $P_2(t + 1)$ uses improved opposition-based learning to generate the subpopulation $M_2(t + 1)$.
- Step 3   The new population $M(t + 1)$ is obtained by the union of $M_1(t + 1)$ and $M_2(t + 1)$.

24.2.5 The Framework of SMDE

Based on the above details, the framework of SMDE is outlined as follows:

- **Step 1** Randomly initialize the starting population $P(0)$ with population size NP.
- **Step 2** Set $t = 0$ (t the generation number).
- **Step 3** Perform DE operations and generate the offspring population $P(t + 1)$ of population $P(t)$, and let $Q(t + 1)$ (temp population) duplicate $P(t + 1)$.
- **Step 4** The offspring population $P(t + 1)$ treats improved non-uniform mutation and opposition-based learning as second mutation to generate the new offspring population $M(t + 1)$.
- **Step 5** Select NP individuals from the union of $M(t + 1)$ and $Q(t + 1)$ as the next population $P(t + 1)$.
- **Step 6** If (the termination criterion is achieved) then stop, and go to Step 7; else let $t = t + 1$, and go to Step 3.
- **Step 7** Output the best individual of $P(t + 1)$.

24.3 Experimental Studies

24.3.1 Benchmark Functions and Experimental Setup

In order to investigate the performance of SMDE, SMDE is validated on six shifted and scalable high-dimensional functions 1–6 [7, 9]. The details of six benchmark functions 1–6 are described in Table 24.1. The parameter setup of SMDE is as follows: the scaling factor $F = 0.5$, the crossover rate $CR = 0.2$, and the population size $NP = 100$, respectively; for functions 1–6 with $n = 100, 500, 1000$, the maximum generation number T is set to 2.5e+3, 1.25e+4, 2.5e+4, and the corresponding number of the fitness evaluations (FES) is equal to 5.0e+5, 2.5e+6, 5.0e+6, respectively.

24.3.2 Experimental Results and Discussion

The experimental results are listed in Table 24.2. For functions 1–6 with $n = 100, 500, 1000$, Table 24.2 gives the 1st (best), 7th, 13th (median), 19th, and 25th (worst) error values over 25 runs, where error value is the difference of the objective and optimal objective function values $(f(x) − f(x^*))$.

For functions 1–6 with $n = 100$, Table 24.2 shows that F_1, F_5 and F_6 are optimized quite well, and SMDE can find the global optimum of F_1 after 5.0e+5 FES. We can conclude that SMDE has the ability to optimize the shifted and

Table 24.1 Benchmark functions 1–6

Function	Decision space	Objective function	n	Global optimum	Properties
F_1/ Shifted Sphere Function	$x \in [-100, 100]^n$	$F_1(x) = \sum_{i=1}^{n} z_i^2 + f\_bias_1, z = x - o,$ $x = [x_1, x_2, \ldots, x_n], o = [o_1, o_2, \ldots, o_n]$: the shifted global optimum	100/500/1000	$x^* = o,$ $F_1(x^*) = f\_bias_1 = -450$	unimodal, shifted, separable, scalable
F_2/ Schwefel's Problem 2.21	$x \in [-100, 100]^n$	$F_2(x) = \max_i\{|z_i|, 1 \le i \le n\} + f\_bias_2,$ $z = x - o, x = [x_1, x_2, \ldots, x_n],$ $o = [o_1, o_2, \ldots, o_n]$: the shifted global optimum	100/500/1000	$x^* = o,$ $F_2(x^*) = f\_bias_2 = -450$	unimodal, shifted, non-separable, scalable
F_3/ Shifted Rosenbrock's Function	$x \in [-100, 100]^n$	$F_3(x) = \sum_{i=1}^{n-1}\{100(z_i^2 - z_{i+1})^2 + (z_i - 1)^2\} + f\_bias_3,$ $z = x - o + 1,$ $x = [x_1, x_2, \ldots, x_n], o = [o_1, o_2, \ldots, o_n]$: the shifted global optimum	100/500/1000	$x^* = o,$ $F_3(x^*) = f\_bias_3 = 390$	multi-modal, shifted, non-separable, scalable, having a very narrow valley from local optimum to global optimum
F_4/ Shifted Rastrigin's Function	$x \in [-5, 5]^n$	$F_4(x) = \sum_{i=1}^{n}\{z_i^2 - 10\cos(2\pi z_i) + 10\} + f\_bias_4,$ $z = x - o, x = [x_1, x_2, \ldots, x_n],$ $o = [o_1, o_2, \ldots, o_n]$: the shifted global optimum	100/500/1000	$x^* = o,$ $F_4(x^*) = f\_bias_4 = -330$	multi-modal, shifted, separable, scalable, local optima's number is huge
F_5/ Shifted Griewank's Function	$x \in [-600, 600]^n$	$F_5(x) = \sum_{i=1}^{n}\frac{z_i^2}{4000} - \prod_{i=1}^{n}\cos(\frac{z_i}{\sqrt{i}}) + f\_bias_5,$ $z = x - o, x = [x_1, x_2, \ldots, x_n],$ $o = [o_1, o_2, \ldots, o_n]$: the shifted global optimum	100/500/1000	$x^* = o,$ $F_5(x^*) = f\_bias_5 = -180$	multi-modal, shifted, non-separable, scalable
F_6/ Shifted Ackley's Function	$x \in [-32, 32]^n$	$F_6(x) = -20\exp(-0.2\sqrt{\frac{1}{n}\sum_{i=1}^{n}z_i^2})$ $-\exp(\frac{1}{n}\sum_{i=1}^{n}\cos(2\pi z_i)) + 20 + e + f\_bias_6,$ $z = x - o, x = [x_1, x_2, \ldots, x_n],$ $o = [o_1, o_2, \ldots, o_n]$: the shifted global optimum	100/500/1000	$x^* = o,$ $F_6(x^*) = f\_bias_6 = -140$	multi-modal, shifted, separable, scalable

Table 24.2 Error values achieved for functions 1–6

n	FES	Status	1	2	3	4	5	6
n = 100	5.0e+5	1st (best)	0	5.2744e+00	9.3119e+01	4.0793e+01	5.6843e−14	1.6236e−09
		7th	0	5.5932e+00	9.3119e+01	4.4773e+01	5.6843e−14	3.0017e−09
		13th (median)	0	5.6929e+00	9.3164e+01	4.5768e+01	5.6843e−14	3.3125e−09
		19th	0	6.4540e+00	9.3193e+01	5.0743e+01	5.6843e−14	3.3968e−09
		25th (worst)	0	9.6420e+00	9.3500e+01	5.1738e+01	8.5265e−14	3.8591e−09
		Mean	0	6.5313e+00	9.3219e+01	4.6763e+01	6.2528e−14	3.0387e−09
		Std	0	1.7920e+00	1.6029e−01	4.5049e+00	1.2711e−14	8.4855e−10
n = 500	2.5e+6	1st (best)	5.6843e−14	3.9531e+01	8.5630e+02	5.9782e+02	2.2737e−13	6.6180e−10
		7th	1.1369e−13	4.0897e+01	1.0004e+03	6.0898e+02	2.2737e−13	8.0396e−10
		13th (median)	1.1369e−13	4.1483e+01	1.3972e+03	6.1198e+02	2.2737e−13	8.4162e−10
		19th	1.7053e−13	4.3309e+01	1.9785e+03	6.2603e+02	2.2737e−13	9.1256e−10
		25th (worst)	1.7053e−13	4.4209e+01	2.1637e+03	6.4054e+02	2.5580e−13	9.2530e−10
		Mean	9.0949e−14	4.1886e+01	1.4792e+03	6.1707e+02	2.3306e−13	8.2905e−10
		Std	6.4811e−14	1.8779e+00	5.7917e+02	1.6530e+01	1.2711e−14	1.0606e−10
n = 1000	5.0e+6	1st (best)	1.0800e−12	6.0628e+01	2.3872e+03	1.6658e+03	5.1159e−13	1.2024e+00
		7th	1.2506e−12	6.1869e+01	2.4125e+03	1.7353e+03	6.1411e−13	1.2139e+00
		13th (median)	1.5348e−12	6.2680e+01	2.5529e+03	1.8026e+03	7.1000e−13	1.2967e+00
		19th	2.7853e−12	6.2803e+01	2.8785e+03	1.9315e+03	7.4300e−13	1.3283e+00
		25th (worst)	2.7853e−12	6.3333e+01	3.3190e+03	1.9630e+03	7.6739e−13	1.6700e+00
		Mean	1.8872e−12	6.2262e+01	2.7100e+03	1.8197e+03	6.6922e−13	1.3423e+00
		Std	8.3581e−13	1.0536e+00	3.9262e+02	1.2662e+02	1.0563e−13	1.9089e−01

Fig. 24.1 Convergence graph for functions 1–6 with $n=1000$
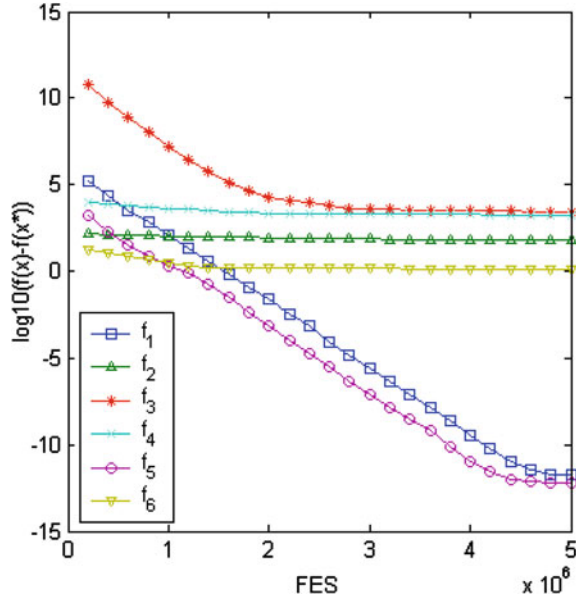
scalable functions whether unimodal or multi-modal as well as separable or non-separable. For F_2, SMDE can find such solutions that are near to the global optimum. However, SMDE has failed to get close enough to the global optimum of F_3 or F_4, it is likely to be the properties of local optima that affect the search ability of SMDE. For functions 1–6 with $n = 500, 1000$, the optimized results of F_1, F_5 and F_6 are still near to their optima, while those of F_3 and F_4 gradually depart from their global optima as the dimensions increase. In addition, we also note that the performance of F_6 drops fast from $n = 500$ to 1000. On the whole, the performance of SMDE is relatively stable. For the same function to be optimized, it requires more FES to be optimized and the performance of SMDE can drop to some extent as the dimensions increase.

For more intuitively comprehending the evolution process of each function 1–6 with $n = 1000$, the corresponding evolution process curves ($\log 10(f(x) - f(x^*))$) vs. FES) are given in Fig. 24.1.

24.3.3 Comparison with Other Evolutionary Algorithms

In order to further compare the relative performance of SMDE with DEwSAcc [10] and EPUS-PSO [14] in terms of solution precision, Table 24.3 presents the mean results of error values over 25 runs. For each run, all algorithms are terminated at 5.0e+5, 2.5e+6, and 5.0e+6 FES for functions 1–6 with $n = 100, 500, 1000$, respectively. Best results are highlighted in bold. For F_1, F_2, F_3 and F_5 with $n = 100$, the mean results of SMDE are better than or not worse

Table 24.3 Mean results of different algorithms for functions 1–6

F	n = 100			n = 500			n = 1000		
	SMDE	DEwSAcc	EPUS-PSO	SMDE	DEwSAcc	EPUS-PSO	SMDE	DEwSAcc	EPUS-PSO
1	**0**	5.6843e−14	7.47e-01	**9.0949e−14**	2.0958e−09	8.45e+01	**1.8872e−12**	8.7874e−03	5.53e+02
2	**6.5313e+00**	8.2500e+00	1.86e+01	**4.1886e+01**	7.5737e+01	4.35e+01	6.2262e+01	9.6058e+01	**4.66e+01**
3	**9.3219e+01**	1.4463e+02	4.99e+03	**1.4792e+03**	1.8130e+03	5.77e+04	**2.7100e+03**	9.1498e+03	8.37e+05
4	4.6763e+01	**4.3778e+00**	4.71e+02	6.1707e+02	**3.6403e+02**	3.49e+03	**1.8197e+03**	1.8239e+03	7.58e+03
5	6.2528e−14	**3.0695e−14**	3.72e-01	**2.3306e−13**	6.9013e−04	1.64e+00	**6.6922e−13**	3.5826e−03	5.89e+00
6	3.0387e−09	**1.1255e−13**	2.06e+00	**8.2905e−10**	4.8041e−01	6.64e+00	**1.3423e+00**	2.2956e+00	1.89e+01

than those of DEwSAcc and EPUS-PSO, while for F_4 and F_6, DEwSAcc outperforms SMDE and EPUS-PSO. For functions 1–6 with $n = 500, 1000$, the search ability of SMDE is better than or similar to that of DEwSAcc or EPUS-PSO. On the whole, SMDE outperforms DEwSAcc and EPUS-PSO.

24.4 Conclusions and Future Work

Through employing two mutation variants during evolution process and using second mutation after performing each generation evolution, this paper gives an enhanced DE for high-dimensional global optimization (SMDE). Numerical results show that SMDE is feasible and effective. However, there is some possible work to do in the future. First testing parameters of SMDE, including the population size, the scaling factor, and the crossover rate, can be one work. Second, in order to further improve the solution precision, some heuristic search techniques can be introduced into SMDE during evolution process. In addition, in the process of second mutation, both improved non-uniform mutation and improved opposition-based learning randomly select some variables of an individual to operate, in order to improve the efficiency, some adaptive selection strategies must be made.

References

1. Holland JH (1975) Adaptation in natural and artificial systems. University of Michigan Press, Ann Arbor
2. Rechenberg I (1973) Evolution strategy: optimization of technical systems by means of biological evolution, Fromman-Holzboog
3. Koza JR (1992) Genetic programming: on the programming of computers by means of natural selection. The MIT Press, Cambridge
4. Fogel DB (1993) Applying evolutionary programming to selected traveling salesman problems. Cybern Syst 24:27–36
5. Storn R, Price K (1997) Differential evolution—a simple and efficient heuristic for global optimizationglobal optimization over continuous spaces. J Glob Optim 11(4):341–359
6. Kennedy J, Eberhart RC (1995) Particle swarm optimization, In: Proceedings of the 1995 IEEE international conference on neural networks, vol 4, pp 1942–1948
7. Tang K, Yao X, Suganthan PN, MacNish C, ChenYP, Chen CM, Yang Z (2007) Benchmark functions for the CEC'2008 special session and competition on large scale global optimizationglobal optimization, Technical report, Nature Inspired Computation and Applications Laboratory, USTC, China, 2007, http://nical.ustc.edu.cn/cec08ss.php
8. Vesterstrom J, Thomsen RA (2004) Comparative study of differential evolution, particle swarm optimization, and evolutionary algorithm evolutionary algorithms on numerical benchmark problems, 2004 IEEE congress on evolutionary computation (CEC2004), vol 2, 2004, pp 1980–1987
9. Rahnamayan S, Gary Wang G (2008) Solving large scale optimization problems by opposition-based differential evolution differential evolution (ODE). World Sci Eng Acad Soc Trans Comput 7(10):1792–1804

10. Zamuda A, Brest J, Bošković B, Žumer V (2008) Large scale global optimizationglobal optimization using differential evolutiondifferential evolution with self-adaptation and cooperative co-evolution. In: Proceeding of IEEE world congress on computational intelligence, pp 3718–3725
11. Rahnamayan S, Tizhoosh HR, Salama MMA (2008) Opposition-based differential evolution differential evolution. IEEE Trans Evol Comp 12(1):64–79
12. Michalewicz Z (1996) Genetic algorithms+data structures=evolution programs, 3rd edn., Springer Hidelberg
13. Ao Y, Chi H (2010) Dynamic differential evolution differential evolution for constrained real-parameter optimization. J Adv Inf Technol 1(1):43–51
14. Hsieh ST, Sun TY, Liu CC, Tsai SJ (2008) Solving large scale global optimization global optimization using improved particle swarm optimizer, In: Proceeding of IEEE world congress on computational intelligence, pp 1777–1784

Chapter 25
Dynamic Multi-objective Optimization Algorithm Based on GEP and Virus Evolution

Weihong Wang, Yanye Du, Qu Li and Zhaolin Fang

Abstract Dynamic Multi-objective Optimization (DMO) is a hot research direction in the field of evolutionary computation nowadays. As Gene Expression Programming (GEP) has a powerful search capability, a new algorithm for DMO called Virus-GEP Dynamic is proposed. The algorithm is designed on the classic multi-objective optimization algorithm NSGA-II to make it suitable for DMO, while using GEP for encoding and virus evolution for evolution mechanism. With the infection operation of virus population, the diversity of the host population is increased. Experiments on test problems of three different types have shown that the algorithm has better performance on convergence, diversity and the breadth of the distribution.

25.1 Introduction

25.1.1 Dynamic Multi-Objective Optimization

In the real world, many optimization problems have multiple objectives, and constrained by time factors. Many systems need to consider the dynamic scheduling problems, consider the constraints caused by time, and these constraints are

W. Wang (✉) · Y. Du · Z. Fang
College of Computer Science, Zhejiang University of Technology, Hangzhou, China
e-mail: wwh@zjut.edu.cn

Q. Li
College of Computer Science, Zhejiang University, Hangzhou, China

called dynamic constraints. The mathematical models abstracted from problems with multiple objectives and related with time factors are Dynamic Multi-objective Optimization (referred to as DMO) [1, 2].

25.1.2 Gene Expression Programming

Gene Expression Programming (GEP) [3] was invented by Candida Ferreira, based on the Genetic Algorithm (GA) and the Genetic Programming (GP). A GEP gene is the basic unit of a GEP genome and consists of head and tail parts. The gene is then mapped into an Expression Tree (ET) [4] by following a width-first fashion. And the ET is easy to be converted into a mathematical expression.

25.1.3 NSGA-II Algorithm

NSGA-II algorithm proposed by Deb et al. in 2002 is one of the best evolutionary multi-objective optimization algorithms. The specific evolutionary process of NSGA-II is described as follows [5–7].

(1) Randomly generate the initial population P_0, do non-dominated sorting of the population, and assign ranks for the individuals. Then take selection and genetic operators on the initial population to get the new population Q_0, and set $t = 0$.
(2) Generate the new population $R_t = P_t \cup Q_t$, and do non-dominated sorting of R_t to get the non-dominated fronts $F_1, F_2, \cdots$.
(3) For all F_i, do sorting according to the Crowded-Comparison Operator, and choose the N best individuals to compose the population P_{t+1}.
(4) Take copy, crossover and mutation operators on the population P_{t+1} to generate the population Q_{t+1}.
(5) End the process if the termination condition holds, or else, set $t = t + 1$, go to (2).

25.1.4 Virus Evolutionary Mechanism

As a major component of the biological immune system, virus system [8] has many information processing mechanisms and functional features. Virus Evolutionary Genetic Algorithm (VEGA) is a theory based on the virus evolution to improve the performance of the traditional genetic algorithm [9]. According to the virus evolutional mechanism, there are two populations during the evolutional process [10, 11]: the host population and the virus population. Corresponding to
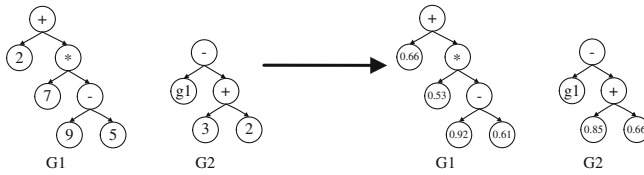
Fig. 25.1 Expression Tree 1

the solution space, the host population takes GA's genetic operations, transfers evolutional information between the former and next generation individuals, and implements the global search of the solution space. On the other hand, the virus population is the set of sub-strings drew out of the host individuals, takes the infection operation, transfers the evolutional information between the same generation individuals, and implements the local search of the solution space.

25.2 New DMO Algorithm Virus-GEP Dynamic

25.2.1 Coding and Genetic Operators

Each individual (chromosome) are composed of n genes, where n is equal to the number of decision variables of the multi-objective optimization problem. Each gene is responsible for one decision variable's assignment.

Each gene still consists of head and tail parts. The head elements are from the function set and terminal set, and the tail elements are only from the terminal set. The function set consists of simple arithmetic operators, $F = \{+, -, *, /\}$, and the terminal set consists of constants and values of other genes. Suppose the genes $\{G_1, G_2, \cdots, G_n\}$, the corresponding terminal set for each gene $G_i(i = 1, 2, \cdots, n)$ is $T_i = \{0, 1, \cdots, 9, g_1, g_2, \cdots, g_{i-1}\}(i = 1, 2, \cdots, n)$, where figures $0, 1, \cdots, 9$ show its location in the constants filed C. For example, the constants field C is $C = \{0.25, 0.31, 0.66, 0.85, 0.19, 0.61, 0.78, 0.53, 0.38, 0.92\}$, then 0 represents the constant 0.25, 1 represents the constant 0.31,..., 9 represents the constant 0.92. And $g_1, g_2, \cdots, g_{i-1}$ represent the values of $G_1, G_2, \cdots, G_{i-1}$ respectively.

For example, consider the following gene:

$$G_1 : + 2 * 7 - 9\,\vdots\,5037881\, G_2 : - g_1 + 320\,\vdots\,6863958$$

Then its corresponding expression tree is shown in Fig. 25.1, and the corresponding expression and value are show in Eq. 25.1.

$$g_1 = 0.66 + 0.53 * (0.92 - 0.61) = 0.8243\, g_2 = g_1 + (0.85 + 0.66)$$
$$= 0.8243 + 1.51 = 2.3343. \tag{25.1}$$

Genetic operators are same with basic GEP, only increases the constant mutation. Constants mutation: each component of the constants field is changed according to the constants mutation rate, replace it with a randomly generated value.

25.2.2 Flow of Virus-GEP Dynamic Algorithm

25.2.2.1 Initialization

(1) Initialization of the host population. According to the host population's coding scheme, randomly generate N host individuals to compose the initial host population $hostPop(t)$, and evaluate the fitness function $fitnessHost_i$ of each individual i in $hostPop(t)$.
(2) Initialization of the virus population. According to the virus coding scheme, take copy operation, generate M virus individuals from $hostPop(t)$ with the probability of P_{copy}, to compose the initial virus population $virusPop(t)$, and set $\alpha_{i,t} = 0, life_{i,t} = 0$ for each individual i in $virusPop(t)$.

25.2.2.2 Generate the Subpopulation S by the Host Population P

Keep the host population, set $P = hostPop(t)$.

(1) Genetic operations on the host population

Take mutation, transposition and recombination operations on the host population. Then take selection operation to gain the new next host population $hostPop(t+1)$, composed with N host individuals.

(2) Virus infection operation on the host population

For each virus individual i in $virusPop(t)$, take virus-infection operation on each host individual in $hostPop(t+1)$ with the probability of $P_{\inf ect} = \min\left\{(1 + \alpha_{i,t})P_{initInfect}, P_{\max Infect}\right\}$, and the host individuals infected by the virus individual i composes the set U.

(3) Update the host population

For each host individual k in U, evaluate its fitness function $fitnessHost'_k$, suppose the fitness function of k before infection is $fitnessHost_k$, and compute $\Delta fitnessHost_k = fitnessHost'_k - fitnessHost_k$. The fitness function of individual k is calculated as follows:

$$fitnessHost_k = \sum_{j=1}^{m} f_j. \tag{25.2}$$

where $f_j(j = 1, 2, \ldots, m)$ are the objective functions. If $\Delta fitnessHost_k < 0$, then replace the corresponding host individual in $hostPop(t + 1)$ with individual k.

Set the subpopulation S = $hostPop(t + 1)$.

(4) Update the virus population
(a) For each virus individual i in $virusPop(t)$, evaluate its fitness function $fitnessVirus_i = \sum_{k \in U} (fitnessHost_k' - fitnessHost_k)$. If $fitnessVirus_i > 0$, then

take copy operation on virus individual i with the probability of P_{copy}, by the randomly selected host individual from U; or else, take cut operation on virus individual i with the probability of P_{cut}. Add virus individual i into $virusPop(t + 1)$.
(b) For each virus individual i in $virusPop(t + 1)$, evaluate its life force $life_{i,t+1} = r \times life_{i,t} + fitnessVirus_i$. If $life_{i,t+1} < 0$, then take copy operation on virus individual i with the probability of P_{copy}, by the randomly selected host individual from $hostPop(t + 1)$, to generate a new virus individual to replace virus individual i in $virusPop(t + 1)$, and set $\alpha_{i,t+1} = 0, life_{i,t+1} = 0$.

25.2.2.3 Generate the Next Host Population P' by P and S

(1) Generate the new population $R = P \cup S$, and do non-dominated sorting of R to get the non-dominated fronts $F_1, F_2, \cdots$.
(2) For all F_i, do sorting according to the Crowded-Comparison Operator, and choose the N best individuals to compose the population P'.

25.3 Experiments and Analysis

25.3.1 Convergence Measure and Test Problems

In order to describe the performance of the DMO algorithm, we must take into account the convergence and diversity of the obtained solution. In this paper, we use the measure of the objective space used in [1], which is shown in Eq. 25.3.

$$e_f(t) = \frac{1}{np} \sum_{j=1}^{np} \min_{i=1:nh} \left\| S_{P,i}(t) - X_j^{sol} \right\|. \tag{25.3}$$
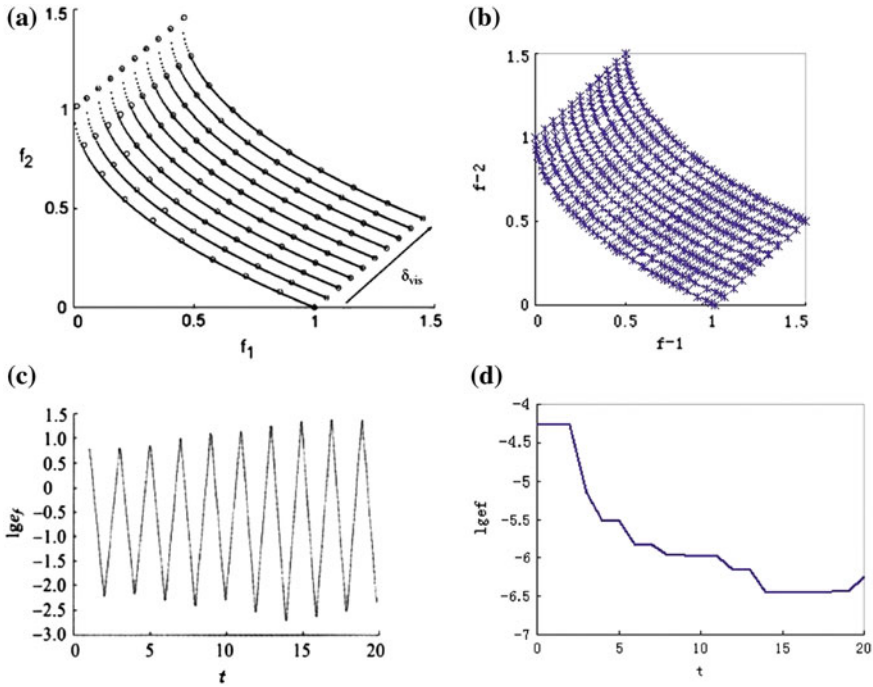
Fig. 25.2 Result of FDA1. **a** Results of DBM [1]. **b** Results of D-GEP Chaotic NSGA-II.
c Results of DBM [1]. **d** Results of D-GEP Chaotic NSGA-II

Where, nh is used to mark the number of samples of known S_P, np is the number of
the obtained non-dominated solutions, X_j^{sol} is the solution calculated in the
objective space, and operator $\|\cdot\|$ is the Euclidean distance. The above parameters
assess the convergence of the obtained solutions in S_P. For the diversity mea-
surement, we use the distribution of the optimal solutions obtained in the objective
space to describe the diversity of the solutions.

We use FDA1, FDA2 and FDA3 as test problems to study the dynamic multi-
objective optimization problems of Type 1, Type 2 and Type 3, respectively
(see [1]).

25.3.2 Analysis of the Experimental Results

We compared the results obtained by the new algorithm with those obtained by the
DBM(direction-based method) algorithm which was proposed in [1].
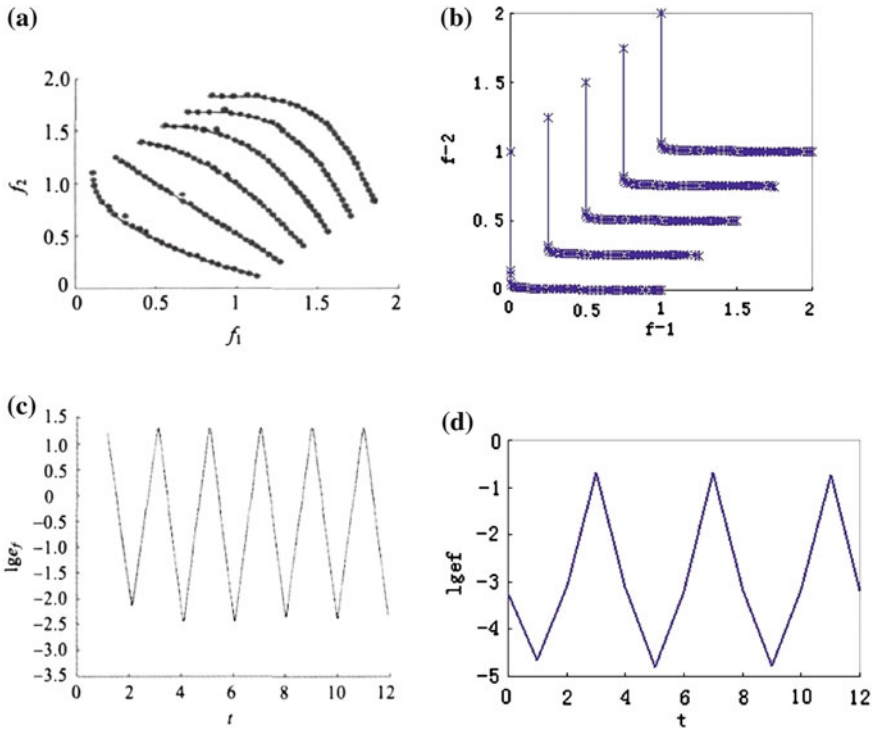
Fig. 25.3 Result of FDA2. **a** Results of DBM [1]. **b** Results of D-GEP Chaotic NSGA-II. **c** Results of DBM [1]. **d** Results of D-GEP Chaotic NSGA-II

25.3.2.1 FDA1 Test Problem

Compare Fig. 25.2a with Fig. 25.2b, we find that, the new algorithm can find the optimal solutions in a wide range at each time step, that is, distribution of the obtained solutions is broader and uniform in the objective space. On the other hand, compare Fig. 25.2c with Fig. 25.2d, we can see that, convergence of the new algorithm is much better than DBM, the value of $lg(e_f)$ can keep change in the range of $[-6.4, -4.3]$.

25.3.2.2 FDA2 Test Problem

Compare Fig. 25.3a with Fig. 25.3b, we can see that, uniformity of the new algorithm is poor, but to maintain a good diversity. On the other hand,, compare Fig. 25.3c with Fig. 25.3d, convergence of the new algorithm is much better than DBM, the value of $lg(e_f)$ can keep change in the range of $[-4.8, -0.7]$.
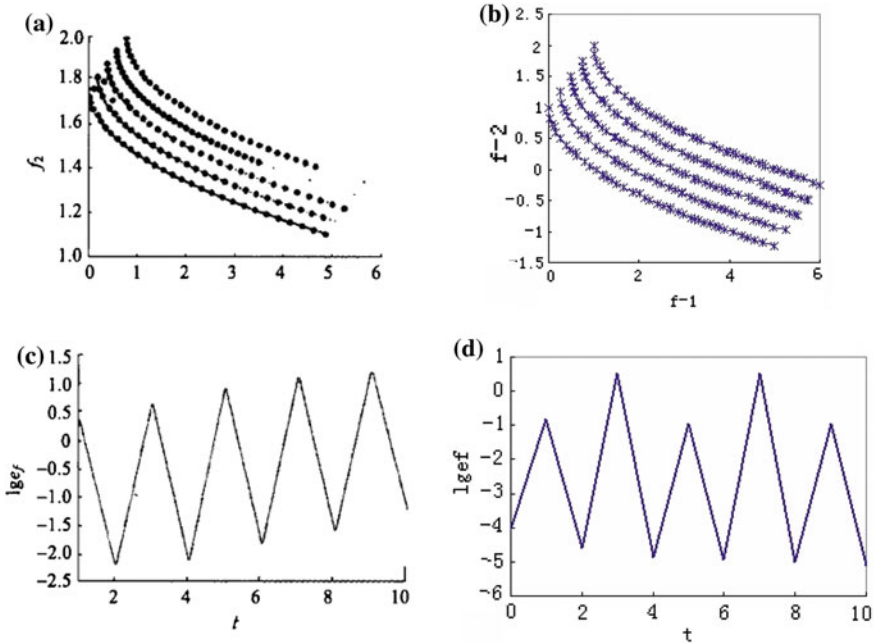
Fig. 25.4 Result of FDA3. **a** Results of DBM [1]. **b** Results of D-GEP Chaotic NSGA-II. **c** Results of DBM [1]. **d** Results of D-GEP Chaotic NSGA-II

25.3.2.3 FDA3 Test Problem

Compare Fig. 25.4a with Fig. 25.4b, we can see that, uniformity of the new algorithm is poor, but to maintain a good diversity. On the other hand, compare Fig. 25.4c with Fig. 25.4d, convergence of the new algorithm is much better than DBM, the value of $lg(e_f)$ can keep change in the range of $[-5.0, 0.5]$.

25.4 Conclusions

To take full advantage of GEP, we transformed its coding structure and genetic operators, and proposed a new algorithm Virus-GEP Dynamic based on GEP and virus evolution to solve DMO problems. Through the horizontal infection operation, this algorithm increases the diversity of the host population during the evolutional process, and make it's easier to jump out of the local optimum, resulting in faster search for better solution. We took experiments on test problems of three different types, and the results shown that the algorithm has better performance on convergence, diversity and the breadth of the distribution.

References

1. Farina M, Deb K, Amato P (2002) Dynamic multiobjective optimization problems: test cases, approximations, and applications. IEEE Trans Evolut Comput 8(5):425–442
2. Shang R, Jiao L, Gong M et al (2007) An immune clonal algorithm for dynamic multi-objective optimization [J]. J Softw 18(11):2700–2711 In Chinese
3. Ferreira C (2001) Gene expression programming: a new adaptive algorithm for solving problems. Complex Syst 13(2):87–129
4. Yuan C, Peng Y, Tan X et al (2010) Theories and applications of gene expression programming algorithms [M]. Science Press, Beijing In Chinese
5. Gong M, Jiao L, Yang D et al (2009) Evolutionary multi-objective optimization algorithms [J]. J Softw 20(2):271–289 In Chinese
6. Deb K, Pratap A, Agarwal S et al (2002) A fast and elitist multi-objective genetic algorithm: NSGA-II. IEEE Trans Evolut Computat 6(2):182–197
7. Lei D, Yan X (2009) Intelligent multi-objective optimization algorithm and its applications [M]. Science Press, Beijing In Chinese
8. Xianbin C, Bennian W, Xufa W (2001) A virus evolutional genetic algorithm. J Mini-micro Syst (01)
9. Kubota N, Shimojima K, Fukuda T (1996) The role of virus infection in a virus-evolutionary genetic algorithm. J Appl Math Comput Sci 6(3):415–429
10. Shicheng H, Xiaofei X, Xiangyang L (2004) A virus co-evolution genetic algorithm for project optimization scheduling. J Softw (01)
11. Shicheng H, Xiaofei X, Dechen Z (2003) A virus evolutionary genetic algorithm for large product structure optimization problem. J Comput Integrated Manufact Syst (03)

Chapter 26
Dynamics Analysis of a Linear Shale Shaker in Considering Forces of Solids

Weibing Zhu, Heshun Wang and Lin Dong

Abstract Based on principle of machine dynamics, the kinematic terms of sliding backward and forward, free flight, remaining in contacting with the screen and staying stationary on the screen for solid particles are obtained. By translating the nonlinear acting forces of solid particles into inertial force and damping force, the nonlinear vibration equations for the shaker are established. The equivalent linearization method is used to get the first order approximate solution of the vibration equations. The calculating formulas of combination coefficient and equivalent damp coefficient of solid particles are obtained.

Keywords Drilling fluid · Linear shale shaker · Solid particle · Nonlinear vibration equation · Dynamics analysis

26.1 Introduction

A drilling fluid shale shaker is a vibrator used for solid/liquid separation. The purpose of using a shaker is to recover drilling fluid and remove large solids as most as possible. With rapid development of drilling new technology, the demand

W. Zhu (✉) · H. Wang · L. Dong
School of Mechanical Engineering and Automation, Xihua University,
610039 Chengdu, China
e-mail: qazzwb@sohu.com

H. Wang
e-mail: wangheshun@sohu.com

L. Dong
e-mail: donglin@mail.xhu.edu.cn

Fig. 26.1 The sketch of a
linear shale shaker
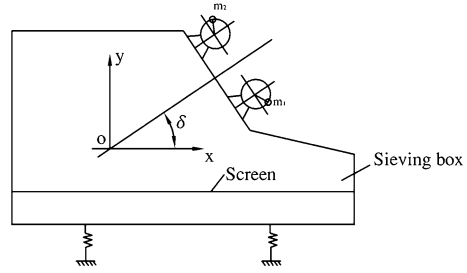
for drilling fluid solids control is getting higher and higher. Much research work on vibration principle, vibration pattern, kinematics, dynamics, screen selection and vibration testing of a shale shaker has been done by many researchers [1–5]. When drilling fluid containing drilled solids flows onto the vibrating screen, the liquid/solid separation process begins. The drilling fluid gradually passes through the screen, the solids convey toward the discharge end. The liquid along the screen disappears through the screen cloth as it reaches a point, called liquid endpoint. At first, the solid particles are submersed by drilling fluid, then gradually become uncovered, at last, drier solids will be conveyed off the screen. From academic analysis and experimental research [6, 7], in submersed condition, the height of free flight motion of solids is not larger than the thickness of drilling fluid. After the solids pass the liquid endpoint, they have four types of kinematic modes, sliding backward or forward, free flight motion, remaining in contacting with the screen and staying stationary. During the working of a shale shaker, solids will produce various nonlinear acting forces such as inertial force, impacting force, frictional force. These nonlinear acting forces will influence the dynamic performance and lifetime of a shaker, this paper will address this problem.

26.2 Motion of Solid Particles

The SDZS type shaker of bi-axial self-synchronous with translation linear trace is shown in Fig. 26.1, it is composed of vibration exciter, sieving box and supporting devices. The two vibrating electric motors are installed on the sieving box directly. Two eccentric blocks with same mass moment are installed on each vibrating axis, when the axes rotate, they will produce inertia forces. When the force center of the vibrating forces coincides with the quality center of the vibrating system, the translation linear trace will be realized.

$$m_1 = m_2 = m \quad m_1 r_1 = m_2 r_2 = mr. \tag{26.1}$$

Where m_1, m_2 are masses of eccentric blocks, respectively; $m_1 r_1$, $m_2 r_2$ are mass moments of eccentric blocks, respectively; δ is vibration angle.

Strictly speaking, the motion of solid particles should be discussed on the whole screen surface. But, once a steady state is achieved, the solids conveying

Fig. 26.2 After the liquid endpoint, the acting forces of solids
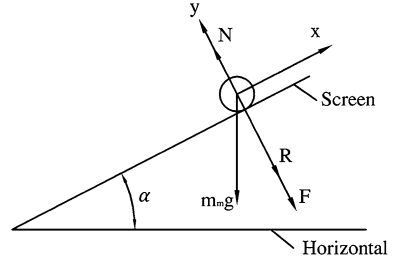
velocities before and after the liquid endpoint are matched [8, 9]. For sake of simplicity, we only discuss the motion of solid particles after they pass the liquid endpoint.

After the solids pass the liquid endpoint, they have four types of kinematic modes, sliding backward or forward, free flight motion, remaining in contacting with the screen and staying stationary. As shown in Fig. 26.2, the forces acting on the solids are, gravity, adhesive force of drilling fluid, force of inertia, counterforce of screen.

$$F = m_m(\ddot{y} + \Delta\ddot{y}). \tag{26.2}$$

Where F is force of inertia, m_m is mass of solid, $\ddot{y}$ is acceleration component of screen normal to screen surface, $\Delta\ddot{y}$ relative acceleration between screen and solid, g is acceleration of gravity, α is screen angle, R is adhesive force of drilling fluid, N is counterforce of screen.

26.2.1 Sliding Backward

When a solid remains in contacting with the screen and stays stationary, it has the same kinematic trail as the vibrating screen. When it begins its sliding backward motion, the direction of friction force is contrary to that of relative velocity. Solids enter sliding backward mode as soon as the following expression is satisfied:

$$-m_m g \sin\alpha + f_d N < m_m\ddot{x}. \tag{26.3}$$

Where f_d is dynamic friction coefficient, $\ddot{x}$ is acceleration component of screen parallel with screen.

When a solid particle slides backward, its parallel velocity is not equal to that of the screen, and it has a personal acceleration component. At the beginning of sliding backward, its dynamic equation in x direction is:

$$-m_m g \sin\alpha + f_d N = m_m a_{hx}. \tag{26.4}$$

Where a_{hx} is acceleration component of solid parallel with screen.

26.2.2 Term of Flight Motion

If $N = 0$, solids will leave the screen cloth, and enter a flight mode. At the beginning, $\Delta \ddot{y} = 0$, so the term of flight motion for solids is:

$$N = -m_m \ddot{y} + m_m g \cos \alpha + R \leq 0. \qquad (26.5)$$

After entering a flight motion mode, a solid has a free fall motion.

26.2.3 Remaining in Contacting with Screen and Staying Stationary

If the following expression is satisfied, a solid will remain in contacting with screen and stay stationary:

$$|-m_m g \sin \alpha - m_m \ddot{x}| \leq f_S N. \qquad (26.6)$$

Where f_S is static friction coefficient.

26.2.4 Sliding Forward

When a solid enter a sliding forward mode, the direction of friction force is contrary to that of relative sliding velocity. The solids enter the sliding forward mode as soon as the following expression is satisfied:

$$-m_m g \sin \alpha - f_d N > m_m \ddot{x}. \qquad (26.7)$$

When a particle slides forward, it has a personal acceleration component parallel with screen surface:

$$-g \sin \alpha - f_d \left(g \cos \alpha + \frac{R}{m_m} - \ddot{y} \right) = a_{zx}. \qquad (26.8)$$

Where a_{zx} is acceleration component of solid parallel with screen.

26.3 Dynamics Equations of the Shale Shaker

In order to make a precise analysis of the linear shale shaker, we should consider the effect of solid particles on the vibrating system. When a solid enter a flight motion mode, it will produce various nonlinear acting forces such as inertial force, impacting force, frictional force:

$$F_y = \begin{cases} 0 & (\varphi_d < \varphi < \varphi_z) \\ m_m(\ddot{y} + g\cos\alpha) & (\varphi_z - 2\pi + \Delta\varphi \le \varphi \le \varphi_d) \\ m_m(\dot{y}_m - \dot{y}_z)/\Delta t & (\varphi_z \le \varphi \le \varphi_z + \Delta\varphi) \end{cases}. \tag{26.9}$$

$$\dot{y}_m = \dot{y}_d - g(\varphi_z - \varphi_d)/\omega \quad \Delta\varphi = \omega\Delta t. \tag{26.10}$$

Where F_y is nonlinear acting force of solid normal to screen surface, $F_y(\ddot{y}, \dot{y}, y, t)$; $\dot{y}$ and y are velocity and displacement components of sieving box normal to screen surface, respectively; $m_m(\ddot{y} + g\cos\alpha)$ is acting force of solid when having same motion as screen; $m_m(\dot{y}_m - \dot{y}_z)/\Delta t$ is instantaneous impacting force of solid when touching screen; φ is phase angle of sieving box; φ_d and φ_z are phase angles of initializing flight and ending flight, respectively; $\dot{y}_m$ and $\dot{y}_z$ are velocity components of solid and screen normal to screen surface when solid touching screen, respectively; $\dot{y}_d$ is velocity component of screen normal to screen surface when solid departing from screen; ω is circular frequency of vibration; Δt is time of impacting.

Nonlinear acting forces of a solid parallel with screen surface:

$$F_x = \begin{cases} 0 & (\varphi_d < \varphi < \varphi_z) \\ m_m\ddot{x} & (\varphi'_{1i} \le \varphi \le \varphi''_{1i}, i = 1, 2) \\ \mp f_d m_m(\ddot{y} + g\cos\alpha) & \left(\varphi'_{2j} \le \varphi \le \varphi''_{2j}, j = 1, 2, 3\right) \\ f_d m_m(\dot{y}_m - \dot{y}_z)/\Delta t & (\varphi_z \le \varphi \le \varphi_z + \Delta\varphi) \end{cases}. \tag{26.11}$$

Where F_x is nonlinear acting force of solid parallel with screen surface, $F_x(\ddot{x}, \dot{x}, x, t)$; $\dot{x}$ and x are velocity and displacement components of sieving box parallel with screen surface, respectively; $m_m\ddot{x}$ is acting force of solid when having same motion as screen; $\mp f_d m_m(\ddot{y} + g\cos\alpha)$ are acting forces of solid when sliding forward or backward (sliding forward adopt minus, sliding backward adopt positive sign); $f_d m_m(\dot{y}_m - \dot{y}_z)/\Delta t$ is impacting friction force of solid when touching screen; φ'_{1i} is initializing phase angle of solid when moving with screen; φ''_{1i} is ending phase angle of solid when moving with screen; φ'_{2j} is initializing phase angle of solid when sliding forward or backward; φ''_{2j} is ending phase angle of solid when sliding forward or backward.

$$\varphi'_{11} = \varphi_m \quad \varphi''_{11} = \varphi_q. \tag{26.12}$$

$$\varphi'_{12} = \varphi_z \quad \varphi''_{12} = \varphi_k + 2\pi. \tag{26.13}$$

$$\varphi'_{21} = \varphi_k \quad \varphi''_{21} = \varphi_d. \tag{26.14}$$

$$\varphi'_{22} = \varphi_z \quad \varphi''_{22} = \varphi_m. \tag{26.15}$$

$$\varphi'_{23} = \varphi_q \quad \varphi''_{23} = \varphi_t. \tag{26.16}$$

Where φ_k and φ_m are initializing and ending phase angles of sliding forward, respectively; φ_q and φ_t are initializing and ending phase angles of sliding backward, respectively.

Nonlinear vibrating equations for the vibrating box are:

$$\begin{cases} M\ddot{y} + c_y\dot{y} + k_y y + F_y = 2m\omega^2 r \sin\delta \sin\omega t \\ M\ddot{x} + c_x\dot{x} + k_x x + F_x = 2m\omega^2 r \cos\delta \sin\omega t \end{cases}. \tag{26.17}$$

Where M is mass of sieving box; k_y and k_x are stiffness coefficient components of spring normal to and parallel with screen surface, respectively; c_y and c_x are damp coefficient components normal to and parallel with screen surface, respectively.

26.4 Solution of the Dynamics Equations

Equation (26.17) is complicated nonlinear differential equations with two freedoms. According to the theory of nonlinear vibration, as for the problem of weak nonlinear, we can perform equivalent linearization treatment on the nonlinear acting forces [10, 11]. Suppose the first order approximate solutions of Eq. (26.17) are:

$$\begin{cases} y = \lambda_y \sin(\omega t - \varphi_y) \\ x = \lambda_x \sin(\omega t - \varphi_x) \end{cases}. \tag{26.18}$$

Where λ_y and λ_x are vibration amplitudes of sieving box normal to and parallel with screen surface, respectively; φ_y and φ_x are phase differences between sieving box and exciting force normal to and parallel with screen surface, respectively.

According to the Fourier series, expand the nonlinear acting forces, ignore static force and force of quadratic harmonic wave and upwards, so the nonlinear acting forces may be written as:

$$\begin{cases} F_y \approx a_{1y} \cos\varphi + b_{1y} \sin\varphi \\ F_x \approx a_{1x} \cos\varphi + b_{1x} \sin\varphi \end{cases}. \tag{26.19}$$

According to Euler-Fourier formula [10], the Fourier coefficients of a_{1y}, b_{1y}, a_{1x} and b_{1x} may be expressed:

$$a_{1y} = \frac{\omega}{\pi} \int_{-\frac{\pi}{\omega}}^{\frac{\pi}{\omega}} F_y \cos\varphi\, dt \quad b_{1y} = \frac{\omega}{\pi} \int_{-\frac{\pi}{\omega}}^{\frac{\pi}{\omega}} F_y \sin\varphi\, dt. \tag{26.20}$$

$$a_{1x} = \frac{\omega}{\pi} \int_{-\frac{\pi}{\omega}}^{\frac{\pi}{\omega}} F_x \cos\varphi\, dt \quad b_{1x} = \frac{\omega}{\pi} \int_{-\frac{\pi}{\omega}}^{\frac{\pi}{\omega}} F_x \sin\varphi\, dt. \tag{26.21}$$

$$\theta = \varphi_z - \varphi_d. \tag{26.22}$$

When get the values of a_{1y}, b_{1y}, a_{1x} and b_{1x}, substitute Eq. (26.19) into Eq. (26.17), then the vibration amplitudes and phase differences may be expressed:

$$\lambda_y = \frac{2m\omega^2 r \sin\delta \cos\varphi_y - b_{1y}}{k_y - M\omega^2} \qquad \varphi_y = \arctan\frac{c_y\omega + a_{1y}/\lambda_y}{k_y - M\omega^2 + b_{1y}/\lambda_y}. \tag{26.23}$$

$$\lambda_x = \frac{2m\omega^2 r \cos\delta \cos\varphi_x - b_{1x}}{k_x - M\omega^2} \qquad \varphi_x = \arctan\frac{c_x\omega + a_{1x}/\lambda_x}{k_x - M\omega^2 + b_{1x}/\lambda_x}. \tag{26.24}$$

So the combination coefficients and equivalent damp coefficients of solid particles are obtained:

$$k_{my} = -\frac{b_{1y}}{m_m\omega^2\lambda_y} \qquad c_{my} = \frac{a_{1y}}{\omega\lambda_y}. \tag{26.25}$$

$$k_{mx} = -\frac{b_{1x}}{m_m\omega^2\lambda_x} \qquad c_{mx} = \frac{a_{1x}}{\omega\lambda_x}. \tag{26.26}$$

Where k_{my} and k_{mx} are combination coefficients of solid particles normal to and parallel with screen surface, respectively; c_{my}, c_{mx} are equivalent damp coefficients of solid particles normal to and parallel with screen surface, respectively.

26.5 Calculating Example

The SDZS type linear shale shaker, operates with 101.5 rad/s circular frequency of vibration, 4.5 mm double vibrating amplitude, 30°vibration angle. Assume that, screen angle $\alpha = 0°$, $f_d = 0.7$, k_y and k_x are far less than $M\omega^2$. Because the dynamic coefficient of friction is small, the solids will slide forward for a while, then enter flight motion mode. According to the kinematic terms of solids, $\varphi_k = 3.5°$, $\varphi_m = 333.5°$, $\varphi_d = 22.8°$, $\varphi_z = 290.8°$, $\varphi_q = 334.6°$, $\varphi_t = 350.2°$, $\theta = 268°$, and put these values into Eq. (26.20) and Eq. (26.21), $a_{1y} = 0.7m_m\lambda_y\omega^2$, $b_{1y} = -0.35m_m\lambda_y\omega^2$, $a_{1x} = 0.01m_m\lambda_x\omega^2$, $b_{1x} = -0.01m_m\lambda_x\omega^2$. So, $k_{my} = 0.35$, $k_{mx} = 0.01$, $c_{my} = 0.7m_m\omega$, $c_{mx} = 0.01m_m\omega$.

26.6 Conclusions

After the solids pass the liquid endpoint, they have four types of kinematic modes, sliding backward or forward on the screen, free flight motion, remaining in contacting with screen and staying stationary. During the working process of a shale shaker, solid particles will produce various nonlinear acting forces such as inertial

force, impacting force, frictional force. These nonlinear acting forces will influence the dynamic performance and lifetime of the shaker.

By the method of translating nonlinear acting forces into inertial force and damping force, the nonlinear vibration equations for the linear shale shaker are established. The equivalent linearization method is used to get the first order approximate solutions of the equations. The calculating formulas of combination coefficient and equivalent damp coefficient of solid particles are obtained.

Combination coefficient and equivalent damp coefficient of solid particles are important parameters for dynamics analysis of a shale shaker. From the actual calculating results of the linear shale shaker, the values of a_{1x} and b_{1x} are smaller than those of a_{1y} and b_{1y}, so they can be ignored.

References

 1. Cagle WS, Wilder LB (1978) Layered shale shaker screens improve mud solids control. World Oil 186:89–94
 2. Hoberock LL (1981) Modern shale shakers are key to improved drilling. Oil Gas J 79:107–113
 3. Dehn C (1999) Novel screening unit provides alternative to conventional shale shaker. Oil Gas J 97:40
 4. Zhao GZ, Zhang MH, Li JY (1996) Working theory and testing technology of drilling fluid shaker. Petroleum Industry Press, Beijing
 5. Ren CG, Zhu WB, Shu M (2010) Dynamics analysis of dual-motor excitation self-synchronization balanced elliptical drilling shale shaker. Drill Prod Technol 33:79–82
 6. Zhao GZ (1988) Research on throwing index of a shale shaker. Oil Field Equip 17:22–28
 7. Zhu WB, Zhang MH (2000) Analysis on solids conveyance dynamics of drilling fluid shaker. Petroleum Mach 28:37–39
 8. Hoberock LL (1980) A study of vibratory screening of drilling fluids. J Petroleum Technol 32:1889–1902
 9. Lal M, Hoberock LL (1985) Solids conveyance dynamics and shale shaker performance. SPE14389:1–11
10. Wen BC, Liu SY (2001) Theory and dynamic design method of a vibrating machine. Machine Industry Press, Beijing
11. Wen BC, Li YN, Han QK (2000) Analytic method and engineering application of nonlinear vibrating theory. Northeastern University Press, Shenyang

Chapter 27
$(\in, \in \vee q)$-Fuzzy *LI*-Ideals in Lattice Implication Algebras

Jiayin Peng

Abstract By using the concept of quasi-coincidence of a fuzzy point with a fuzzy set, the notions of $(\in, \in \vee q)$-fuzzy *LI*-ideals, which is generalization of ordinary fuzzy *LI*-ideal in lattice implication algebras, is defined, and their related properties and equivalent descriptions are discussed. The product and the projections of $(\in, \in \vee q)$-fuzzy *LI*-ideals are investigated. How to deal with the lattice implication homomorphic image and inverse image of $(\in, \in \vee q)$-fuzzy *LI*-ideals are studied.

Keywords Lattice implication algebra · $(\in, \in \vee q)$-fuzzy *LI*-ideal · Product · Projection · Lattice implication homomorphism

27.1 Introduction

Lattice implication algebra is the algebraic structures for the lattice valued logical system. After it was proposed by Y. Xu in paper [1], the lattice implication algebra have been playing an important role in the study of many-valued logical system. In classical logic and many-valued logic, Modus Ponences rule (MP rule) is very useful for a formal deduction. Xu, Qin and Jun [2–6] discussed a special kind of substructures in lattice implication algebra-filters, and given various kinds of filters and their properties. It is shown that filter is a kind of abstract of MP rule. The

J. Peng (✉)
Key Laboratory of Numerical Simulation of Sichuan Province,
Neijiang Normal University, Neijiang 641112, China
e-mail: pengjiayin@njtc.edu.cn

concept of *LI*-ideal is dual to filter of lattice implication algebra. Jun et al. [7] introduced the concept of *LI*-ideal in lattice implication algebras and studied their properties. In 1965, Zadeh [8] introduced the concept of fuzzy subset. At present these ideas have been applied to other algebraic structures such as semigroups, groups, rings ideas,modules, vector spaces, and so on. Jun, Qin and Xu [9, 10] fuzzified the concepts of filters and implicative filters and discussed their basic ptoperties. A new type of fuzzy subgroup, that is, $(\in, \in \vee q)$-fuzzy subgroup, was introduced in an earlier paper of Bhakat and Das [11] by using the combined notions of "belongingness" and "quasi-coincidence" of fuzzy points and fuzzy sets, which was introduced by Pu and Liu [12]. In fact, the $(\in, \in \vee q)$-fuzzy subgroup is an important generalization of Rosenfeld's fuzzy subgroup. In this paper, the $(\in, \in \vee q)$-fuzzy *LI*-ideals of lattice implication algebras are consider, and some related properties are investigated.

27.2 Preliminaries

Let $(L, \vee, \wedge, ', O, I)$ be a bounded Lattice with an order-reversing involution $'$, I and O the greatest and the smallest element of L respectively, and $\rightarrow: L \times L \rightarrow L$ be a mapping. $(L, \vee, \wedge, ', \rightarrow, O, I)$ is called a lattice implication algebra if the following conditions hold for any $x, y, z \in L$:

(I1) $x \rightarrow (y \rightarrow z) = y \rightarrow (x \rightarrow z)$;
(I2) $x \rightarrow x = I$;
(I3) $x \rightarrow y = y' \rightarrow x'$;
(I4) $x \rightarrow y = y \rightarrow x$ implies $x = y$;
(I5) $(x \rightarrow y) \rightarrow y = (y \rightarrow x) \rightarrow x$;
(I6) $(x \vee y) \rightarrow z = (x \rightarrow z) \wedge (y \rightarrow z)$;
(I7) $(x \wedge y) \rightarrow z = (x \rightarrow z) \vee (y \rightarrow z)$.
In a lattice implication algebra L, the following hold for any $x, y, z \in L$:

(1) $x \leq y \Leftrightarrow x \rightarrow y = I$.
(2) $O \rightarrow x = I = x \rightarrow I$, $x \rightarrow O = x'$, $I \rightarrow x = x$.
(3) $x \vee y = (x \rightarrow y) \rightarrow y$.
(4) $x \rightarrow y \leq (y \rightarrow z) \rightarrow (x \rightarrow z)$.
(5) $x \leq y$ implies $x \rightarrow z \geq y \rightarrow z$ and $z \rightarrow x \leq z \rightarrow y$.

A lattice implication algebra $(L, \vee, \wedge, ', \rightarrow, O, I)$ is said to be a lattice H implication algebra if for any

$$x, y, z \in L, \ x \vee y \vee ((x \wedge y) \rightarrow z) = I.$$

Let L_1 and L_2 be lattice implication algebras, $f : L_1 \rightarrow L_2$ a mapping from L_1 to L_2, if $f(x \rightarrow y) = f(x) \rightarrow f(y), f(x \vee y) = f(x) \vee f(y), \ f(x \wedge y) = f(x) \wedge f(y)$ and $f(x') = (f(x))'$ hold for any $x, y \in L_1$, then f is called a lattice implication homomorphism from L_1 to L_2.

Let L be a lattice implication algebra. An $LI-$ideal J is a non-empty subset of L such that for any $x, y \in L$,

(1) $O \in J$;
(2) $(x \rightarrow y)' \in J$ and $y \in J$ imply $x \in J$.

A mapping $\mu : L \rightarrow [0,1]$ is called a fuzzy set of L, and the set $\mu_t = \{x \in L | \mu(x) \geq t\}$ is said to be a level subset of a fuzzy set μ. A fuzzy set μ of L of the form

$$\mu(y) = \begin{cases} t(\neq 0), & y = x, \\ 0, & y \neq x \end{cases}$$

is said to be a fuzzy point with support x and value t and denoted by x_t. A fuzzy point x_t is said to be belong to (resp. is quasi-coincident with) a fuzzy set μ, written as $x_t \in \mu$ (resp. $x_t q \mu$) if $\mu(x) \geq t$ (resp. $\mu(x) + t > 1$). If $x_t \in \mu$ or (resp. and) $x_t q \mu$, then we write $x_t \in \vee q \mu$ (resp. $x_t \in \wedge q \mu$). The symbol $\overline{\in \vee q}$ will mean that $\in \vee q$ does not hold.

27.3 ($\in, \in \vee q$)-Fuzzy *LI*-Ideals of Lattice Implication Algebras

We begin with considering the generalized fuzzification of *LI*-ideals of lattice implication algebras. In what follows, L, L_1 and L_2 denote the lattice implication algebras unless otherwise specified, and $F(L)$ denotes the set of all fuzzy sets in L.

Definition 27. 1 $\mu \in F(L)$ is called an ($\in, \in \vee q$)-fuzzy *LI*-ideal of L if for any $x, y \in L$ and $t, r \in (0, 1]$,

(F1) $x_t \in \mu$ implies $O_t \in \vee q \mu$;
(F2) $(x \rightarrow y)'_r \in \mu$ and $y_t \in \mu$ imply $x_{\min(t, r)} \in \vee q \mu$.

Theorem 27. 1 μ is an ($\in, \in \vee q$)-*fuzzy LI-ideal of L if and only if for any $x, y \in L$,

(F3) $\mu(O) \geq \min(\mu(x), 0.5)$ *and*
(F4) $\mu(x) \geq \min(\mu((x \rightarrow y)'), \mu(y), 0.5)$.

Proof Suppose that μ is an ($\in, \in \vee q$)-fuzzy *LI*-ideal of L. If $t \triangleq \min(\mu(x), 0.5) > \mu(O)$ for some $x \in L$, then $t \in (0, 0.5]$ and $x_t \in \mu$, but $O_t \overline{\in \vee q} \mu$, this is a contradiction. Thus $\mu(O) \geq \min(\mu(x), 0.5)$ for all $x \in L$.

Similarly, we can prove
$\min(\mu(y), \mu((x \rightarrow y)'), 0.5) \leq \mu(x)$ for all $x, y \in L$.

Conversely, assume that (F3) and (F4) hold for all $x, y \in L$ and let $(x \rightarrow y)'_r \in \mu$ and $y_t \in \mu$. Then $\mu(y) \geq t$ and $\mu((x \rightarrow y)') \geq r$. Now we prove that (F1) is true: by (F3) we have $\mu(O) \geq \min(t, 0.5)$. If $t \leq 0.5$, then $\mu(O) \geq t$, i.e., $O_t \in \mu$, hence $O_t \in \vee q \mu$. If $t > 0.5$, then $\mu(O) \geq 0.5$ and so $\mu(O) + t \geq 0.5 + t > 1$, i.e., $O_t q \mu$, thus $O_t \in \vee q \mu$. Therefore (F1) holds. Similarly, we can prove that (F2) holds.

Theorem 27. 2 *μ is an $(\in, \in \vee q)$-fuzzy LI-ideal of L if and only if for any $t \in (0, 0.5]$, the non-empty level subset μ_t of μ is an LI-ideal of L.*

Proof Assume that μ is an $(\in, \in \vee q)$-fuzzy *LI*-ideal of *L* and let $t \in (0, 0.5]$ and $y, (x \rightarrow y)' \in \mu_t$. Then $\mu(y) \geq t$ and $\mu((x \rightarrow y)') \geq t$. It follows that $\mu(O) \geq t$ and $\mu(x) \geq t$. So $O \in \mu_t$ and $x \in \mu_t$. Therefore μ_t is an *LI*-ideal of *L*.

Conversely, suppose that non-empty set μ_t is an *LI*-ideal of *L* for any $t \in (0, 0.5]$. If $\mu(x) < \min(\mu(y), \mu((x \rightarrow y)'), 0.5) \triangleq t$ for some $x, y \in L$, then $t \in (0, 0.5]$, $y \in \mu_t$ and $(x \rightarrow y)' \in \mu_t$, but $x \notin \mu_t$, this is a contradiction. Thus (F4) holds. Similarly, we can prove that (F3) holds. Therefore μ is an $(\in, \in \vee q)$-fuzzy *LI*-ideal of *L*.

Now, we consider that the level subset $\mu_t (\neq \emptyset)$ of μ is an *LI*-ideal of *L* for $t \in (0.5, 1)$.

Theorem 27. 3 *Each non-empty level subset μ_t, $t \in (0.5, 1]$, of μ is an LI-ideal of L if and only if for any $x, y \in L$,*

(F5) $\max(\mu(O), 0.5) \geq \mu(x)$,
(F6) $\max(\mu(x), 0.5) \geq \min(\mu(y), \mu((x \rightarrow y)'))$.

Proof Suppose that $\mu_t (\neq \emptyset)$ is an *LI*-ideal of *L* for all $t \in (0.5, 1]$. If $\mu(x) > \max(\mu(O), 0.5)$ for some $x \in L$, then choose $t \in \mathbb{R}$ such that $\max(\mu(O), 0.5) < t < \mu(x)$, and so $t \in (0.5, 1]$ and $x \in \mu_t$, but $O \notin \mu_t$, this is a contradiction. Hence $\max(\mu(O), 0.5) \geq \mu(x)$ for all $x \in L$. Similarly, we have that $\max(\mu(x), 0.5) \geq \min(\mu(y), \mu((x \rightarrow y)'))$ for any $x, y \in L$.

Conversely, assume that (F5) and (F6) hold for all $x, y \in L$ and let $y \in \mu_t$ and $(x \rightarrow y)' \in \mu_t$ for $t \in (0.5, 1]$. Then $\mu(y) \geq t$ and $\mu((x \rightarrow y)') \geq t$, i.e., $\max(\mu(O), 0.5) \geq t$ and $\max(\mu(x), 0.5) \geq t$. Hence $\mu(O) \geq t$ and $\mu(x) \geq t$, i.e., $O \in \mu_t$ and $x \in \mu_t$. Therefore $\mu_t (\neq \emptyset)$ is an *LI*-ideal of *L*.

Theorem 27. 4 *Let μ be an $(\in, \in \vee q)$-fuzzy LI-ideal of L. If $x, y \in L$ and $y \leq x$, then $\mu(y) \geq \min(\mu(x), 0.5)$.*

Proof By $y \leq x$, we have $(y \rightarrow x)' = I' = O$, and so

$$\mu(y) \geq \min(\mu((y \rightarrow x)'), \mu(x), 0.5)$$
$$= \min(\mu(O), \mu(x), 0.5)$$
$$\geq \min(\mu(x), 0.5).$$

Definition 27. 2 $\mu \in F(L)$ is called an $(\in, \in \vee q)$-fuzzy lattice ideal of *L* if for any $x, y \in L$ and $t, r \in (0, 1]$,

(F7) if $y \leq x$, then $x_t \in \mu$ implies $y_t \in \vee q \mu$;
(F8) $x_r \in \mu$ and $y_t \in \mu$ imply $(x \vee y)_{\min(t,r)} \in \vee q \mu$.

Similar to Theorem 1, 2, and 3, we have

Theorem 27. 5 μ *is an* $(\in, \in \vee q)$*-fuzzy Lattice ideal of L if and only if for any* $x, y \in L$,

   (F9) $\mu(y) \geq \min(\mu(x), 0.5)$ *whenever* $y \leq x$;
   (F10) $\mu(x \vee y) \geq \min(\mu(x), \mu(y), 0.5)$.

Theorem 27. 6 μ *is an* $(\in, \in \vee q)$*-fuzzy lattice ideal of L if and only if for any* $t \in (0, 0.5]$, *the non-empty level subset* μ_t *of* μ *is a lattice ideal of L*.

Theorem 27. 7 *Each non-empty level subset* μ_t, $t \in (0.5, 1]$, *of* μ *is a lattice ideal of L if and only if for any* $x, y \in L$,

   (F5) $\max(\mu(y), 0.5) \geq \mu(x)$ *whenever* $y \leq x$;
   (F6) $\max(\mu(x \vee y), 0.5) \geq \min(\mu(x), \mu(y))$.

Theorem 27. 8 *Each* $(\in, \in \vee q)$*-fuzzy LI-ideal of L is an* $(\in, \in \vee q)$*-fuzzy lattice ideal*.

Proof Theorem 27. 4 shows that $\mu(y) \geq \min(\mu(x), 0.5)$ if $y \leq x$. By

$$((x \vee y) \rightarrow y)' = ((x \rightarrow y) \wedge (y \rightarrow y))'$$
$$= (x \rightarrow y)'$$
$$\leq x,$$

we get

$$\mu(x \vee y) \geq \min(\mu(((x \vee y) \rightarrow y)'), \mu(y), 0.5)$$
$$= \min(\mu((x \rightarrow y)'), \mu(y), 0.5)$$
$$\geq \min(\mu(x), \mu(y), 0.5).$$

Theorem 27. 9 *In a lattice H implication algebra L, every* $(\in, \in \vee q)$*-fuzzy lattice ideal is an* $(\in, \in \vee q)$*-fuzzy LI-ideal*.

Proof Let μ be an $(\in, \in \vee q)$-fuzzy lattice ideal of L. Since $O \leq x$, it follows that $\mu(O) \geq \min(\mu(x), 0.5)$ for all $x \in L$. Let $x, y \in L$, we have

$$\mu(x) \geq \min(\mu(x \vee y), 0.5)$$
$$= \min(\mu(y \vee (x' \vee y)'), 0.5)$$
$$= \min(\mu(y \vee (x \rightarrow y)'), 0.5)$$
$$\geq \min(\min(\mu(y), \mu((x)'), 0.5), 0.5)$$
$$= \min(\mu(y), \mu((x)'), 0.5).$$

Hence μ is an $(\in, \in \vee q)$-fuzzy *LI*-ideal of L.

References

1. Xu Y (1993) Lattice implication algebra. J Southwest Jiaotong University 28(1):20–27
2. Xu Y, Qin KY (1993) On the filters of lattice implication algebras. J Fuzzy Math 1(2):251–260
3. Qin KY, Xu Y (1999) On the super filters of lattice implication algebras. J Southwest Jiaotong University 34(1):52–54
4. Jun YB (1997) Implication filter of lattice implication algebras. Bull Korean Math Soc 34(1):193–198
5. Jun YB, Xu Y, Qin KY (1998) Positive implicative and associative filter of lattice implication algebras. Bull Korean Math Soc 35(1):51–61
6. Jun YB (2001) The prime filters theorem of lattice implication algebras. Int J Math Sci 25(2):115–118
7. Jun YB, Roh EH, Xu Y (1998) *LI*-ideals in lattice implication algebras. Bull Korean Math Soc 34:13–24
8. Zadeh LA (1965) Fuzzy sets. Inf Control 8:338–353
9. Jun YB (2001) Fuzzy positive implicative and fuzzy associative filters of lattice implication algebras. Fuzzy Sets Syst 121:353–357
10. Qin KY, Xu Y (1999) On some properties of fuzzy filters of lattice implication algebras. In: Liu YM (eds) Fuzzy Set Theory and its Application. Press of Hebei University, Baoding, China, vol 28, no 1, p 179–182 (in Chinese)
11. Bhaka SK, Das P (1996) ($\in$, $\in \vee q$)-fuzzy subgroup. Fuzzy Sets Syst 80(3):359–368
12. Pu PM, Liu YM (1980) Fuzzy topology. I. Neighborhood structure of a fuzzy point and Moore- Smith convergence. J Math Appl 76(2):571–599
13. Yuan B, Wu W (1990) Fuzzy ideals on a distributive lattice. Fuzzy Sets Syst 35:231–240

Chapter 28
Face Detection of AdaBoost Fast Training Algorithm Based on Characteristic Reduction

Xinchun Wang, Yuminm Liu, Qing Ye and Kaihua Yue

Abstract To resolve the problem that AdaBoost face detection training is very time consuming, the paper put forward a new approach of reducing training time by removing characteristics with little category effect. The main characteristic of the approach is that it can reduce characteristics according to the detection accuracy. Experiments prove that the improved approach can greatly reduce training time in the case of nearly no influence on detection.

Keywords Adaboost · Face detection · Face characteristic

28.1 Introduction

Face detection is a branch of biometrics, whose main purpose is to find the face location in an image. As biometric facial characteristic is easily accessible and it bears high value of practical application and theoretical research, it has been concerned widely in recent years. However, for face is non-grid and is easily affected by face figure, skin color, expression and illumination and other factors, face detection has a certain difficulty. Face detection algorithms are many, such as those based on skin color, those based on PCA and those based on template matching and so on. However, the above algorithms are poor in real time relatively [1].

In 2001 AdaBoost [2] algorithm, proposed by Violia based on the characteristic of Class Harr, promoted face detection technology greatly. The algorithm is the

X. Wang (✉) · Y. Liu · Q. Ye · K. Yue
Department of Physical and Electronics, Chuxiong Normal University, Chuxiong, China
e-mail: wxch@cxtc.edu.cn

Fig. 28.1 Four common
homologous Harr
characteristics
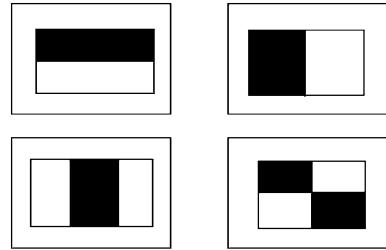
turn point of face detection, which makes face detection achieve real time at high
detection rate. However, the disadvantage of the algorithm is to take a long time
for training. The paper analyzes various reasons of long time training in depth, and
improves it so as to achieve reduction of training time with nearly little effect on
detection rate.

28.2 Description of AdaBoost

28.2.1 Ideas of AdaBoost

AdaBoost is a kind of classification algorithm, whose idea is to utilize a large
number of common classifiers with general classification ability together to con-
stitute a classifier with very strong classification ability by a certain method.
Theory proved that as long as each simple classifier is better than random
guessing, and when the number of weak classifiers tends to infinity, classification
error rate of the strong classifier will tend to zero [3]. To classify two types of
samples with the AdaBoost algorithm main work is selecting the most effective
weak classifiers as simple classifiers, and then increasing weights of misclassified
samples and decreasing the weight of correctly classified samples according to
classification results of simple classifiers. Consequently, during the next round of
training, the main is focused on the previous misclassified samples. And select
weak classifier with least classification error after updating the weight. Then,
linearly combine weak classifiers into a strong classifier with strong classification
ability.

28.2.2 Characteristic Calculations

To classify two types of samples well, characteristic selection is vital. We should
select favorable characteristics to classify samples. Four common homologous
Harr characteristics are illustrated in Fig. 28.1.

Fig. 28.2 Calculate eigenvalues by integral graph
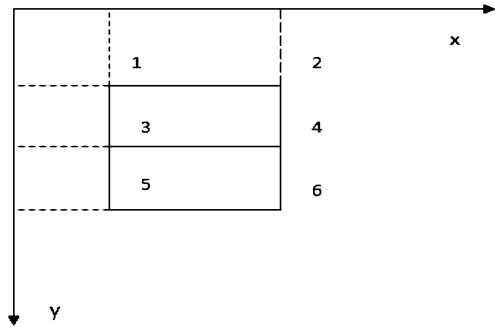
According to the above method of calculation we can know that change of the location or the size of the rectangle will lead to the change of the eigenvalue; even for a 19 × 19 image there will be tens of thousands of characteristics. When calculating the eigenvalue, the same pixel value will be repeated to calculate different eigenvalues, which will spend a lot of time in the calculation of eigenvalues. So, in order to improve the speed of calculating eigenvalues the method of integral graphs is introduced. The integral graph of an image I(u,v) denotes the sum of all pixels upper left the pixel (u, v), which means $I(u, v) = \sum_{i \le u, j \le v} f(i, j)$. To calculate Harr eigenvalue becomes convenient. That is illustrated in Fig. 28.2.

The numbers in Fig. 28.2 denote the value of integral graph corresponding to the positions. So, only to perform addition and subtraction over these values simply can work out eigenvalues. For instance, the eigenvalue of the image is $1 + 4 - 2 - 3 - (3 + 6 - 5 - 4)$. Therefore, regardless of the size of the same rectangular calculation time of characteristic required is the same. As long as an integral figure on the calculation of the image, and then when calculating characteristics only need to query graph and perform simple addition and subtraction operations on it.

28.2.3 AdaBoost Algorithm

Given a training set $(x_i, y_j), \cdots, (x_L, y_L)$, where x_i is an input training sample and y_i is a type sign of classification. $y_i = \in (1, 0)$ denotes genuine sample or not. Specific steps are as follows.

First. Known to have a training set composed of n training samples $(x_i, y_j), \cdots, (x_n, y_n)$, where $y_i = \in (0, 1)$ $(i = 1, 2, \cdots, n)$ corresponds to veritable sample or pseudo sample. There are m veritable samples and l pseudo ones in the training samples. And samples to be classified have k simple characteristics, which are expressed as $f_j(x), 1 \le j \le k$. One rectangle characteristic j corresponds to one a weak classifier h_j. Weak classifier function is as follows.

$$h_j(x) = \begin{cases} 1 & p_j f_j(x) \ge p_j \vartheta_j \\ 0 & others \end{cases}. \tag{28.1}$$

Where $p_j = \pm 1$, which is used to determine the direction of the inequality and θ_j is a threshold.

Second. Assume $\omega_{t,i}$ is the weight of the i_{th} sample in the t_{th} cycle. First, initialize weights of the samples. For samples of $y_i = 0$, $\omega_{ij} = 1/2m$ while for samples of $y_i = 1$, $\omega_{ij} = 1/2l$.

Last. *for $t = 1, \cdots T$*

a. Weight normalization, $\omega_{t,i} = \omega / \sum\limits_{j=1}^{n} \omega_{t,i}$;

b. For each characteristic j, train to get weak classifier. That means to determine θ_j and offset p_{ij} to make objective function $\varepsilon_j = \sum\limits_{i=1}^{n} \omega_{ii} |h_j(x_i) - y_i|$ minimum.

c. Find a weak classifier with minimal error ε_t from a weak classifiers in (b).

d. Update the corresponding weight $\omega_{t+1,i} = \omega_{t,i} \beta_{t,i}^{1-e_i}$ of each sample. Determination method of e_i is: if the ith sample is classified correctly, $e_i = 0$, or $e_i = 1$, where $\beta_t = \varepsilon_t / (1 - \varepsilon_t)$.

e. Formed strong classifier

$$h_j(x) = \begin{cases} 1 & \sum\limits_{t=1}^{T} \alpha_t h_t(x) \ge 0.5 \sum\limits_{t=1}^{T} \alpha_t \\ 0 & others \end{cases}. \tag{28.2}$$

Where $\alpha_t = \log(1/\beta_t)$.

28.3 Time Consumption Analysis and Improvement of Adaboost

If to reduce training time under the circumstance of remaining the same number of samples and characteristics we only can optimize the algorithm when training simple classifiers [4]. From the above analysis the most time consuming part of the algorithm is the training of simple classifiers. The key to reduce training time is to improve simple classifier training. Training simple classifier is just to find the optimal threshold θ_j and the offset p_i so as to make classification error of all samples minimum. However, it is not easy, for all samples must be traverse time after time. If traverse all samples directly without saving the results of the last traversal, all samples must be traversed once again when calculating new error using the new threshold every time. As the number of samples is numerous, calculation amount is huge if traverse all samples from the beginning every time.

Besides algorithm efficiency large number of samples and characteristics are the main causes that affect the training time. The training time can decrease greatly if we can reduce the number of samples and characteristics. The following will introduce the two approaches respectively.

28.3.1 Improving Traversal Method to Calculate Threshold and Offset of Simple Classifier Quickly

For each characteristic f calculate all characteristic value of the training samples and sort them. Scanning over sorted characteristics can determine the optimal threshold for the characteristic, which can train an optimal simple classifier. Specific method [5] is: for each sorted elements in the table calculate the four values. According to the analysis training time mostly spends on calculation of eigenvalue and threshold and sort. In fact, during the process of iteration the eigenvalues of samples do not change; change only happen to weights. For each characteristic the sort corresponding to samples does not change. Therefore, when first calculate eigenvalues and sort eigenvalues they can be storaged temporarily. So there is no need to repeat of calculation and sort of eigenvalues when every training, which can further save time. The above treatment can decrease training time, but the cost is the need for larger memory space to improve the training speed.

28.3.2 Decrease Training Time by Characteristic Reduction

As shown in Fig. 28.3, some characteristics can easily distinguish the two types of samples with the help of some threshold, which are good classification performance characteristics. As shown in Fig. 28.4, some characteristics can not distinguish the two types of samples in any case, which are not good classification performance characteristics.

From Figs. 28.3 and 28.4 for characteristics easy to classify two kinds of samples, eigenvalues are close and distance between categories is great. For those hard to classify two kinds of samples, eigenvalues are dispersed within respective category, or the distance between categories is close. So, we can define a criterion: if standard deviation of some eigenvalue in the category is small, we believe that characteristic is effect to 2 kinds of samples. Define the following function.

$$F_j = \frac{\left| \bar{f}_j^+ - \bar{f}_j^- \right|}{\frac{1}{n}\sum_{i=0}^{n}(f_{j,i}^+ - \bar{f}_j^+)^2 + \frac{1}{l}\sum_{i=0}^{l}(f_{j,i}^- - \bar{f}_j^-)^2}. \tag{3}$$

Fig. 28.3 Good
classification performance
characteristics
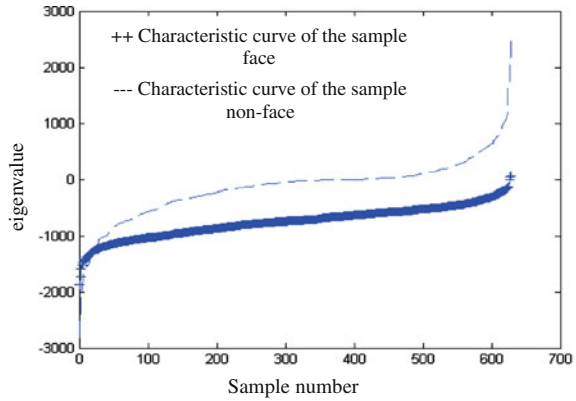
Fig. 28.4 Bad classification
performance characteristics
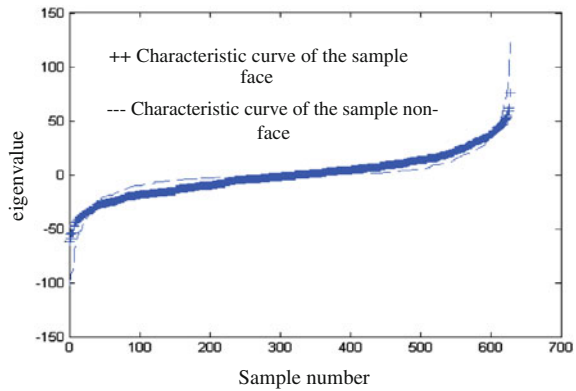
Where, $\bar{f}_j^+$ and $\bar{f}_j^-$ denote the eigenvalue mean of the j_{th} positive and negative sample respectively, $j \in (1, 2 \cdots k)$, k is the total number of characteristics; i is the sample number; n, l are the sum of positive and negative samples respectively. FunctionF_j can reflect ability of Characteristic$j$ to classify two kinds of samples. A relatively large value ofF_j means characteristic$j$ is easy to classify two kinds of samples, else not.

28.3.3 Experiment Results and Analysis

Training samples used in this paper is MIT CBCL database. The training samples in the database include 3,429 face samples and 4,554 non-face samples and the samples size is 19 × 19. For taking into account that the large number of samples will take a lot of memory space the paper used only 1,000 face images from the database, including 1,000 face images and 2,000 non-face images. As the face images in the database are from abroad the paper collected 500 domestic face

Table 28.1 Comparison of detection results under the circumstance of different characteristic number

Chosen characteristics rate (55,860)	Number of weak classifiers	Detection rate in face image set	False detection rate in non-face image set	Training time (min)
1	55	0.9942	0.0210	789.3524
1/3	55	0.9839	0.0205	267.2777
1/5	55	0.9859	0.0395	172.9666
1/7	55	0.9920	0.0425	127.8333
1/8	55	0.9839	0.0335	114.7849

images moreover and standardized the images to the size of 19×19. So, there are 1,500 face images and 2,000 non-face image in all. For a image of 19×19 there are 55,860 Harr characteristics if not perform characteristic reduction. The experiment environment is P4 2.8G, memory 512M, OS Windows XP, and MATLAB 7.0.

Before training, calculate the classification capability of 1,500 face images and 2,000 non-face images of the size 19×19 first, that is to say calculate F_j according to Function (3) and sort the results. After sorting, according to different proportions, the ratio of reserved characteristics number and the total number, we choose the fore characteristics corresponding to F_j. Then, train classifiers by the method of rapid traverse. Under the circumstance that the number of reserved characteristics is different the paper compared the face detection rate in face set, non-face false detection rate in non-face set. Where, face set in the test set includes 1,000 standardized, different colors, different expression, different shapes face images. And non-face set includes 2,000 standardized different scenes non-face images. The experimental results are following.

From Table 28.1 for adopting rapid traverse and characteristic reduction training time is much less than the traditional approach. And with the characteristic reduction training time almost decreased proportionally. Furthermore, even if the total number of features reduced to 1/8, the detection rate and false detection rate of trained strong classifiers have no obvious difference compared with no characteristic reduction. The paper only trained 55 samples, but they formed a strong classifier of high detection rate. The results are basically consistent with the expected results, as means effective characteristic reduction removes a great number of weak classifiers so as to decrease training time almost without affecting detection rate and false detection rate. Although choosing characteristic takes some time it is once and for all, is much less than training time and has less effect on total training time. The more times the training is, the less effect it has on.

We can reduce characteristics further in the case of meeting the requirement to further reduce training time. For the paper only compares the detection effect after characteristic reduction it doesn't train more weak classifiers. We can train more weak classifiers to form strong classifiers to improve detection rate. For color images we can combine with complexion for further verification at the later stage.

For grey images we can further verify to achieve high detection rate according to global eigenvalues, such as mean, variance, and etc. In practice, we can cascade multiple strong classifiers to become hierarchical classifier for the detection of human faces, which can locate the face image from the complex ground.

28.4 Conclusion

The paper analyzes time consuming of AdaBoost face image detection algorithm from different aspects and improves it in algorithm itself and number of characteristics. It pays more emphasis on characteristic reduction so as to reduce training time nearly without affecting detection rate. The approach of the paper applies not only to the field of face detection, can also be extended to other detection field using AdaBoost algorithm.

References

1. Lu-Hong L, Hai-Zhou A, Guagn-You X et al (2002) A survey of human face detection. Chin J Comput 25(5):449–458
2. Viola P, Jones M (2001) Robust real time object detection. In: 8th IEEE international conference on computer vision(ICCV), 2001. IEEE Computer society Press, Vancouver
3. Freund Y, Schapire RE (1995) A decision-theoretic generalization of on-line learning and an application to boosting. Computational learning theory: eurocolt95, 1995. Springer, Barcelona Spain, Germany
4. Hai-cuan W, Li-Ming Z (2004) A novel fast training algorithm for Adaboost. J Fudan Univ(Nat Sci) 43(1):27–32
5. Z Nan, Face detection based on AdaBoost algorithm physics. Physics college of Peking University

Chapter 29
Fast Haze Removal Algorithm for Surveillance Video

Bin Xie, Fan Guo and Zixing Cai

Abstract In this paper, we present a new approach to remove haze from surveillance video sequences. The approach first extracts the background image through frames differential method, and then estimates the atmospheric light and transmission map from the background image, finally renders haze-free video according to the haze image model. The main advantage of the proposed approach is its speed since this approach adopts a 'universal strategy' that is applying the same atmospheric light and a single pseudo-transmission map to a series of video frames. Experiments and performance analysis demonstrate that a good haze-free video can be produced effectively and efficiently.

Keywords Video haze removal · Image haze model · Atmospheric light · Transmission map

29.1 Introduction

Most outdoor vision applications such as surveillance camera system require robust detection of image features. Under foggy weather conditions, the contrast and color of images are drastically altered or degraded. Hence, it is imperative to remove weather effects from video in order to make vision system more reliable. So far, there have been many works to remove fog from a single image [1–3], but only a few researches focus on video. These fog removal methods for video sequence mainly use frame by frame strategy. For this kind of methods, the basic idea of most

B. Xie (✉) · F. Guo · Z. Cai
School of Information Science and Engineering, Central South University,
Changsha 410083, China
e-mail: xiebin@csu.edu.cn
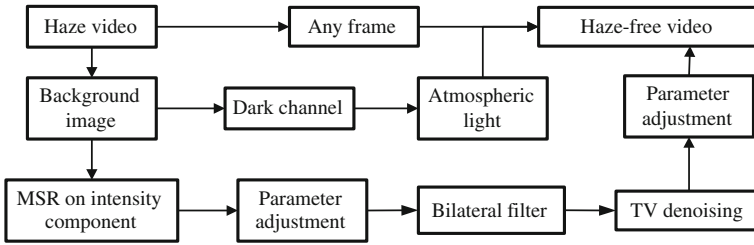
Fig. 29.1 Haze removal process for video

approaches lies in depth-like map computation by using multiple images under different weather conditions [4, 5]. Although the results are satisfactory, strict requirement on the inputs, that two reference images captured in different weather conditions are needed in these methods, limits their applications. Other approaches separate the foreground and background images, and then combined two results to get the haze-free video sequences. For example, John and Wilscy [6] applied the wavelet fusion method on background and foreground pixels separately which reduces the computation time. Xu et al. [7] remove fog from the foreground and background images by using a contrast limited adaptive histogram equalization (CLAHE)-based method. However, these existing algorithms have high complexity with a long computation time. In order to solve these problems, we consider adopting a 'universal strategy' to estimate a depth-like map by only using the background image of video, and then applying this map to a series of video frames. Compared with the existing frame by frame methods, our method calculates transmission map only once, so the fog removal speed is much faster.

29.2 Proposed Approach

Given a video that has haze, mist or fog, we first extract the background image, and then estimate the atmospheric light value using the dark channel prior proposed by He et al. [1]. Then, the transmission map is calculated on the intensity component of the background image, through a process of multi-scale Retinex (MSR), parameter adjustment, bilateral filter and total variation (TV) denoising filter. Finally, output haze-free video can be gained according to the haze image model. This process is also depicted in Fig. 29.1.

29.2.1 Haze Image Model and Atmospheric Light Estimation

Haze image model (also called image degradation model), proposed by McCartney [8] in 1975, consist of direct attenuation model and air light model. Direct attenuation model describes the scene radiance and its decay in the medium, while

air light results from previously scattered light. The formation of a haze image model is as following:

$$I(x) = J(x)t(x) + A(1 - t(x)) \qquad (29.1)$$

Where I is the observed intensity and also the input haze image, J is the scene radiance and also the restored haze-free image, A is the global atmospheric light, and t is the transmission map describing the portion of the light that is not scattered and reaches the camera. Theoretically, the goal of haze removal is to recover J, A, and t from I.

For surveillance camera systems, the primary interest is to enhance the visibility of the entire video (not single image). For this purpose, the haze removal approach for video should adopt different strategy against that for a single image. Here we adopt a universal strategy to deal with video defog problem, that is to restore video according to the haze image model, only with the same atmospheric light value and a single transmission map. For universal usage consideration, dark channel is used to estimate A in our previous dehazing algorithm [9]. We first pick the top 0.1% brightest pixels in the dark channel. The pixel with highest intensity in the first frame is then selected as the atmospheric light.

According to the haze image model, only the value of atmospheric light A and the transmission map t are both known, can we gain the final recovered result. Thus, in the following part, we will present our pseudo-transmission map estimation approach in details.

29.2.2 Pseudo-Transmission Map Estimation

The transmission map of haze image model is obtained through the following three stages:

(1) Background extraction.

Our research considers an outdoor surveillance video camera capturing a scene (with moving objects) over an extended period of time. We would like to process it in real-time to obtain a haze-free video. Transmission map is only calculated for the background part of the video, in order to apply the universal transmission map to more frames with tolerable error. For simplicity, we define the static part of the scene as the background part and the moving objects in the scene as the foreground part. The background image can be obtained by using frame differential method [10]. For example, the background image of Fig. 29.2a is shown in Fig. 29.2b.

(2) Initial transmission map extraction.

Transmission map is calculated based on the assumption that the intensity of an image reflects the amounts of photons received by every position of the image.

Fig. 29.2 Background extraction example: **a** the first original haze frame from video. **b** Background image obtained by frame differential method

The farer distance between the scene points and camera, the fewer photons are received by the sensor, which leads to darker intensity in the image. Thus, the depth information reflected by the transmission map can be measured by intensity, in other words, the transmission map can be obtained by the intensity component of an image. So our objective is to obtain the transmission information from the intensity component of an image. For this purpose, MSR, bilateral filter are used on the intensity component of the background image. Detailed process can be referred to our previous work [9].

(3) Universal pseudo-transmission map estimation.

For surveillance camera system, the camera is fixed and often positioned high in the air, so the background of each frame is unchangeable and the difference in transmission between a foreground object and the background behind it is usually small. Although the haze removal result obtained by using bilateral filter to obtain transmission map is good for a single image, using the filter to calculate transmission map for each frame is surely time-consuming. In order to make the pseudo-transmission map calculated once and used for all, the map should only contain scene outlier. Therefore, the moving foreground object and image details can be regarded as noise. As the total variation based on Rudin-Osher-Fatemi (ROF) model proved to be quite efficient for denoising and regularizing images without smoothing the boundaries of the objects [11], we use the total variation algorithm to calculate the pseudo-transmission map obtained by bilateral filter. This pseudo-transmission map is applied to all video frames without creating significant errors in the enhanced video.

Figure 29.3 shows our video results with pseudo-transmission map. From Fig. 29.3 we can see that the pseudo-transmission map Fig. 29.3e does not induce significant artifacts into enhanced frame. Furthermore, the main advantage of our approach is its speed since the atmosphere light and the transmission map is estimated only using background image, and applied to all frames.
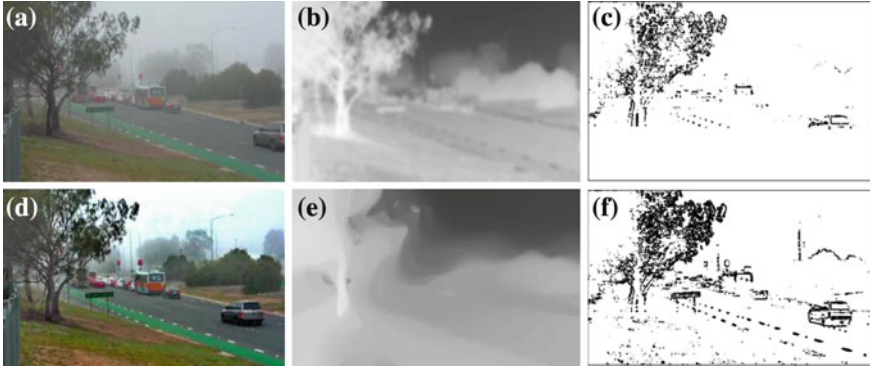
Fig. 29.3 Our video defogging example: **a** One arbitrarily selected original frame from the foggy video. **b** The initial transmission map estimated using bilateral filter. **c** The original visible edges. **d** The haze removal result of the video. **e** The universal transmission map estimated using total variation denoising filter. **f** The visible edges of frame **d**

29.2.3 Scene Radiance Restoration

According to the haze image model we can recover the scene radiance of each frame with the same transmission map obtained by the algorithm presented above. Because the direct attenuation term $J(x)t(x)$ can be very close to zero, so the transmission map $t(x)$ is restricted to a lower bound t_0, which means that a small amount of haze are preserved in very dense haze regions. A typical value of t_0 is 0.1. The final scene radiance $J(x)$ is then recovered by:

$$J(x) = \frac{I(x) - A}{\max(t(x), t_0)} + A \qquad (29.2)$$

Since from the first frame, the transmission map $t(x)$ and the atmospheric light A can be estimated, so we can apply Equation (29.2) to each frame of the original video in order to obtain the final haze-free result.

29.3 Experimental Results and Analysis

Here we present a set of results using videos that captured in foggy weather conditions. We first extract the background image using frame differential method, and then the universal transmission map can be obtained. Figure 29.3 shows the procedure of our approach. As can be seen in the figure, the initial transmission map obtained by using bilateral filter on the intensity component of the background image contains too much 'noise' for video processing, such as the moving foreground object and image details (Fig. 29.3b). Thus, we use total

variation denoising filter to get our universal video transmission map (Fig. 29.3e). Finally, we apply the obtained atmospheric light and our final transmission map to each frame of the original video.

So far there is a lack of widely accepted methodology to assess the performances of the defog algorithm, or to compare them with one another. Unlike image quality assessment or image restoration areas, it is not easy (sometimes even impossible) to have a fully reference image. For performance analysis, the definition of meteorological visibility distance proposed in Ref. [12] is considered here. In order to be consistent with the definition, the set of edges which have a local contrast above 5% is computed as to obtain the visible edges under foggy weather. To implement the definition, Kohler's segmentation method that based on Logarithmic Image Processing (LIP) model [13] is used here. The visible edges in the video frames before and after haze removal are selected by a 5% contrast thresholding, the computation results of visible edges are also given in Fig. 29.3. From Fig. 29.3c and f, we can see that the frames after haze removal have more visible edges than before. Since the performance analysis is based on the meteorological visibility distance, the result coincides with the visual evaluation of human eyes.

29.4 Conclusion

This paper proposes a fast video defogging approach using haze image model with the same atmospheric light and transmission map. The proposed method is applicable under the situation that the camera is fixed and positioned high above the ground. Given a haze video, continuous haze-free video can be produced through haze image model with universal estimated atmospheric light and transmission map. The experiment results show that our method is effective and efficient.

References

1. He K, Sun J, Tang X (2009) Single image haze removal using dark channel prior [C]. In: Proceedings of the IEEE computer society conference on computer vision and pattern recognition (CVPR), Piscataway, U S A, pp 1956–1963
2. Tan R (2008) Visibility in bad weather from a single image [C]. In: Proceedings of the IEEE computer society conference on computer vision and pattern recognition (CVPR), Piscataway, U S A, pp 1–8
3. Fattal R (2008) Single image dehazing [J]. ACM Trans Graph 27(3):72–79

4. Narasimhan SG, Nayar SK (2003) Contrast restoration of weather degraded images [J]. IEEE Trans Pattern Anal Mach Intell 25(6):713–724
5. Chen G, Zhou H, Yan J (2007) A novel method for moving object detection in foggy day [C]. In: 8th ACIS international conference on software engineering. Artificial intelligence, networking, and parallel/distributed computing, pp 53–58
6. John J, Wilscy M (2008) Enhancement of weather degraded video sequences using wavelet fusion [C]. Cybernetic intelligent system, 2008. CIS 2008. In: 7th IEEE international conference on London, Sept 2008, pp 1–6
7. Xu Z, Liu X, Chen X (2009) Fog removal from video sequences using contrast limited adaptive histogram equalization [C]. Computational intelligence and software engineering, international conference on 2009, pp 1–4
8. McCartney EJ (1976) Optics of atmosphere: scattering by molecules and particles [M]. Wiley, New York, pp 23–32
9. Xie B, Guo F, Cai Z (2010) Improved single image dehazing using dark channel prior and multi-scale retinex [C]. In: International conference on intelligent system design and engineering application, pp 848–851
10. Haritaoglu I, Harwood D, Davis LS (2000) W4: Real-time surveillance of people and their activities [J]. IEEE Trans Pattern Anal Mach Intell 22(8):809–830
11. Chambolle A (2004) An algorithm for total variation minimization and applications [J]. J Math Imaging Vis 20(1):89–97
12. CIE (1987) International lighting vocabulary. No. 17.4
13. Kohler R (1981) A segmentation system based on thresholding [J]. Comput Graph Image Process 15:319–338

Chapter 30
Genetic Algorithm and Fuzzy Based Combustion Temperature Control Model of MSW Incinerators

Hairui Wang, Wen Xie and Ya Li

Abstract In this paper, we develop a fuzzy controller for improving the waste combustion control effect according to fuzzy theory. On the strength of the above mentioned, we adopt the Genetic Algorithm (GA) to generate fuzzy rules in waste combustion process. We expect to improve the control effect while control system parameter is unstable and to develop a GA based fuzzy controller to optimize the control. By using fuzzy methods, it solves a temperature control model that consists of four inputs and two outputs. GA (Genetic Algorithm) is used to construct the learning algorithm, which is able to find the optimum rule base. The simulation and field application results show that the GA-based fuzzy model can adapt to the complex incineration process. It is an appropriate way to solve the incineration temperature control problem.

Keywords Municipal solid waste incinerator · PID · Genetic algorithm · Fuzzy control

30.1 Introduction

MSW incineration process is usually complex, nonlinear, time delay, load disturbance and noise. System variable is inaccurate when controller component is ware and torn by any interference [1]. This is very difficult to create a mathematics

H. Wang (✉) · W. Xie · Y. Li
Yunnan Computer Technology Application Key Lab,
Kunming University of Science and Technology,
650093 Kunming, China
e-mail: hrwang88@163.comsherly2001@sina.com

H. Wang · W. Xie · Y. Li
School of Information Engineer and Automation,
Kunming University of Science and Technology,
650093 Kunming, China

module. Traditional automation control system always use experience or intuition by setting to acquire a good efficiency. Generally, the conventional waste incineration control system usually provides automation control such as logic control and sequence functions, and linearized process control is performed by PID (proportional integral-derivative).

In the absence of knowledge of the underlying process, a PID controller is the best controller. By tuning the three parameters in the PID controller algorithm, the controller can provide control action designed for specific process requirements. The response of the controller can be described in terms of the responsiveness of the controller to an error, the degree to which the controller overshoots the setpoint and the degree of system oscillation. Note that the use of the PID algorithm for control does not guarantee optimal control of the system or system stability.

The well-known fuzzy theory, developed by Zadeh in 1965 [2], used in widespread use. The general characteristic of the fuzzy control is the IF–THEN fuzzy rules. By the late 1970s, the interest of fuzzy systems had grown rather explosively, Still most of the work was theoretical. At the same time, there also emerged some important applications. One of these was fuzzy logic control (FLC). The genesis of FLC was a 1972 paper by Chang and Zadeh [3]. The PID formulas are simple and can be easily adopted to corresponding to different controlled plant but it can not yield a good control performance if controlled system is highly-order or nonlinear. It is well know that FLC have emerged as one of the most active and useful research areas in fuzzy control theory. FLC can improve control performance especially for high-order or non-linear system, one of the fundamental problems in fuzzy control technology is that need experience for rule base constructed.

As a mature technology for waste incineration process, waste incineration has obtained a wide range of applications; MSW incineration technology is advanced waste disposal technology. After crushing solid waste roughly, mix it with limestone, soda and other additives, and then put it into the incinerator via hopper, and auxiliary fuel is also added from the hopper at regular adherence; the air or oxygen-rich (temperature of 100–300°C) preheated via the flue gas's heat will be blown into the incinerator through the air supply tube. Solid waste in the incinerator go through preheated warm-dry zone from top to bottom, it's temperature will be heated to 100–200°C, and water in the waste is vaporized. Dried solid waste will be descended to the middle of the incinerator, and be heated to 200–600°C. The organic components in the solid waste begin to gasify, combustible gas and noncombustible material will be produced at simultaneously. Gasification residues will be put into the burning zone. There the combustible material is burning and release amount of heat to maintain the incinerator's temperature at 600–1250°C. When the noncombustible material reach the melting zone with high temperatures (1250–1450°C), the noncombustible material will be molten into molten slag. The combustible gas and smoke generated by gasification enter the secondary combustion chamber and begin to combust. A lot of heat energy may be produced and may be used to generate electricity. The incineration process keeps reducing atmosphere let during the whole process of burning waste,

the molten slag and metal are discharged through the slag port, the metal can be recycled and utilized by the magnetic power, the molten ash can be used as construction materials [4].

A great deal of research work focused on the process of waste incineration at domestic and abroad, the emphasis of research is to establish the waste incinerator numerical model [5] and establish grate material thickness prediction model [6] by using fuzzy approach. Chen et al. [7] studied the influence of incineration process on generation of NOx and CO based on genetic algorithm of fuzzy neural network.

In this paper, the focus is mainly concentrated on the fuzzy control rules which is auto-generated by genetic algorithms (GA) and two temperatures [8] .

In MSW's process, the steam evaporation of waste heat boiler are considered to be equal to the heat of the combustible gas of the secondary combustion chamber in the waste combustion process, in theory, the combustible gas in the secondary combustion chamber is pyrolyzed from the combustion incinerator. Because the first combustion chamber is in restorable atmosphere, the gas heat of pyrolyzed gasification is almost not lost, and the coke is to ensure the melting temperature of the melting zone, waste feed speed is an important adjustable input in combustion control logic, so ACC regular automatic combustion control system can stabilize the evaporation of steam in waste combustion process via adjusting waste feed speed and the combustion-supporting air flow. In addition, the quality of tail gas from chimney can be adjusted via the feedback control system inject the dosage into the air purification equipment. Once the combustion system of MSW incinerator is in a stable state of combustion, there exists much relation between the added quantity of the secondary combustion air and the quality of tail gas, automatic control logic is not only be able to let the exhaust quality meet the country exhaust standard, but can be able to maximize heat recovery.

30.2 The Structure of Fuzzy Controller of the MSW Incinerator

In the practical operation control of the MSW incinerator, in order to ensure the temperature control accuracy of melting zone and the second combustion chamber and avoid the primary air and secondary air-conditioning sector non-linear effects, we can ascertain the corresponding relationship between secondary damper opening and the amount of secondary air. To capture the main factors and to give up a secondary factor as the implemental principle, the fuzzy controller of the process of MSW has four input variables and two output variables, they are melting zone temperature deviation (TCP1), change rate of melting zone temperature deviation (DTCP1), the second combustion chamber temperature deviation (TCP2) and the change rate of second combustion chamber temperature deviation (DTCP2), which constitute the four input variables of fuzzy controller. To use feed quantity and secondary air flow as the two fuzzy controller's output variables. To control the combustion process of MSW incinerator through adjusting feed quantity and secondary air amount. The primary air amount is

controlled by the changes of oxygen amount, the chamber negative pressure (Pf) adjustment method is applied with the tone control.

The system use fuzzy controller to control the two temperatures of the process of MSW. From the technical process of MSW, we can obtain some information, after the solid waste enter the MSW incinerator, under the high temperature radiation of melting zone, the solid waste goes through drying and gasification of pyrolysis from top to bottom, the part which can't be gasificated will enter melting zone with high temperature, where remains of solid waste are melting. There are many factors affecting the gasification and melting process, but the main factor is the temperature of melting zone, the gasificated combustible gas goes to the secondary combustion chamber and burns out, it almost doesn't infect the process of pyrolysis and gasification, so the temperature of melting zone is only related with the feed quantity of waste. The temperature of the secondary chamber has great relations with the heat value of the waste itself, and therefore we need to build a fuzzy controller which has a good dynamic control effects. The fuzzy controller use TCP1 and DTCP1 as input variables to control the speed of waste feed. To control the secondary air, the fuzzy controller use TCP2 and DTCP2 as input variables. The fuzzy controller has four input variables and two output variables, one is the secondary air volume and the other is the waste feed time. These six variables make up of the fuzzy controller with four input/two output of the combustion process of MSW [8].

Temperature of melting zone is the main parameter to affect the effects of thermal decomposition, the generation rate of combustible gas will be increased while the temperature of melting zone rises, tar and carbon production will be reduced, the content of hydrogen and hydrocarbon in combustible gases will be increased obviously, it is helpful for the stability of the secondary combustion chamber, melting zone temperature decreases, combustible gas production rate will correspondingly decrease, tar and carbon output will rise, the decrease of hydrogen and hydrocarbon content in combustible gas will decrease the heat value of combustible gas, it will cause the temperature fluctuation. So secondary air volume is determined by temperature deviation of melting zone, temperature deviation and temperature deviation change rate of the secondary combustion chamber.

30.3 The Generating Algorithm of Fuzzy Controller Rules

A genetic algorithm (GA) is a search heuristic that mimics the process of natural evolution, which generate solutions to optimization problems using techniques inspired by natural evolution, such as inheritance, mutation, selection, and crossover.

30.3.1 Fuzzy Controller Based on GA-Fuzzy Rule Generation Algorithm

The key technologies of generation of fuzzy rule based on GA should be resolved: expression way of fuzzy rule string of controller, the determination of genetic operator, merits and demerits evaluation of generated fuzzy rules, etc.

A set of fuzzy rules can be regarded as permutations and combinations of a set of input/output variables model. When the arrangement order is certain, only need to record the fuzzy degree of output variables in the order of permutations and combinations. The fuzzy degree of output variables is very easy to express via binary numbers, so a group of fuzzy rules can be expressed by a binary number string [14].

Quantified the six variables of the combustion process of MSW to thirteen fuzzy subsets in range [−6, +6], they are related with seven linguistic variables (NB, NM, NS, ZR, PS, PM, PB), seven linguistic variables can be respectively represented by three binary codes that are used to express (001,010,011,100,101,110,111). There exists 49 fuzzy rules for controlling continuous feed waste time of the combustion process of MSW, so 147 binary strings can be used to represent the 49 fuzzy rules. In theory, there should be 343 fuzzy rules for control theory of flow volume of fuzzy controller of the combustion process of MSW, but in actual process, we only consider three cases, the temperature of melting zone is lower than the set value, higher than the set value or equal to the set value, so secondary flow volume control should have 147 fuzzy rules. The 147 fuzzy rules can be represented by 421 binary code, also an assigned 421 binary string can be converted to 147 fuzzy rules.

30.3.2 The Fitness Function Design

In the fuzzy rule generation procedure of the combustion process of MSW, we assigned a set of fuzzy rules randomly. If actual output is more less, it means the adaptive degree of this individual is more higher, predicted output is more closed to the output of fuzzy ratiocination system, in other words, it means the generated fuzzy rule is more reasonable. Fitness function was expressed by the following equation: $E(n) = \frac{1}{2} \cdot \frac{1}{N} \sum_{i=1}^{N} (y(i) - y'(i))^2$. Wherein: n act as the number of times for training; N act as the total number of samples; e act as the error; y act as the actual output value of the fuzzy controller.
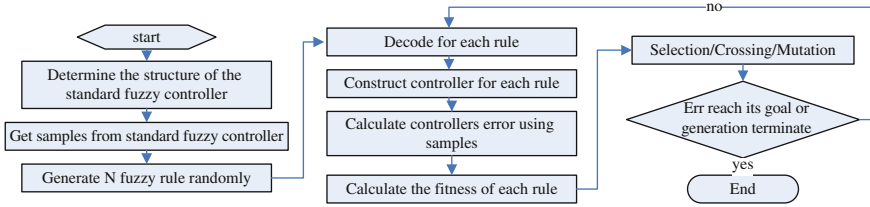
Fig. 30.1 Generation algorithm of fuzzy rules of fuzzy controller

30.3.3 The Selection of Genetic Operator to Fuzzy Rule Strings

The selection of operator means the fitness proportional method, also known as roulette laws or Monte Carlo choice, each individual's selection probability is proportional to its fitness value in this method. Setting the group size as n, its individual fitness value is f_i, then the probability that an individual is selected: $p_{si} = f_i / \sum_{i=1}^{n} f_i$, p_{si} reflects the individual's fitness in the proportion of the whole group's clearly. The larger individual fitness, the higher probability of being chosen. And vice versa [8].

30.4 Fuzzy Controller Rules for MSW Incinerator

In order to generate a set of efficient multi-objective fuzzy controller's control rules, the whole MSW incinerator will be the controller's control object according to the MSW combustion technology. The fuzzy controller's input/output variables need to be determined according to the conditions that the MSW incineration process. Once the input/output variables was determined, the linguistic variables and domain for each variable need to be set. To array input variables' binary-coded string according to certain rules in order through using the gene encoding rules for each output variable after determining the domain, then to get the gene string that we needed. According to the fitness function of GA, the algorithm carry on the selection, crossover and mutation operations to the randomly generated gene. It will get a higher fitness gene after some algebra. We can get fuzzy controller's rules which has the best control effect through decoding the final gene. We will gradually build the control rules of fuzzy controller by using GA optimization process. Such a process is an automatic way that using GA as the formation and the adjustment of fuzzy control rules. When the output of fuzzy inference was established by the weighted value of all the fuzzy control rules, fuzzy controller can achieve the requirements of the multi-objective optimization control strategy. The generation algorithm of controller's fuzzy rules was shown in Fig. 30.1 [9].
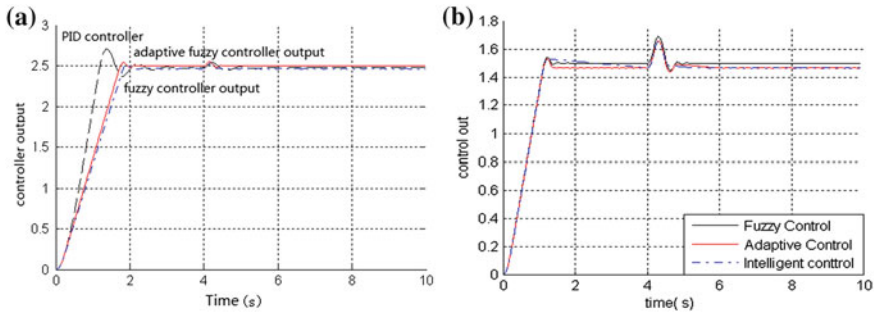
Fig. 30.2 The control effect of fuzzy controller

30.5 Simulation Results and Experimental Analysis

This section uses GA to build the fuzzy controller output control rules automatically, we select cross-parameter Pc = 0.85, variation of parameters Pm = 0.025 according to the characteristics of GA. The initial number of individuals N's values have significant impact to the GA's rapidity of convergence. We need the more numbers of fuzzy rules which will be tested and the more iteration time when N becomes greater. We first set N to 60, after 500 times iterating and optimizing, we can get the highest fitness of fuzzy rules gene string of fuzzy controller, Using temperature fuzzy controller of melting zone as input/output sample to test the fuzzy controller rules. We got the higher fitness fuzzy control rules

Automatically generated fuzzy control rules by using GA, simulation results as shown in Fig. 30.2. Its control effect is compared with the basic fuzzy controller. The fuzzy controller with the automatically generated fuzzy rules can control better than traditional PID and the basic fuzzy controller. And the control system has good dynamic, static performance, robustness and anti-jamming capability. It is an effective way to automatically build multi-input/output fuzzy controller's rule base.

30.6 Conclusion

This paper proposed a fuzzy control model and study approach of MSW incinerator's temperature which is based on GA generation fuzzy rules. The control quality of the fuzzy control model based on GA fuzzy rule generation is superior to the conventional fuzzy controller just because it combines the fuzzy reasoning process into the GA. Using GA to dynamically adjust the fuzzy control rules according to the control system's actual running state can not only make the system has a strong adaptive ability but also make the system tends towards stability as soon as possible. The next step will be combined with expert system reasoning mechanism to perfect the model's self-learning function, then the model can adapt to the more complex changes in working conditions.

References

1. Wang H (2009) MultiAgent based on-line monitoring system for MSW incinerator. ScalCom-EmbeddedCom, pp 375–380
2. Zadeh LA (1965) Fuzzy sets. Inf Control 8:339–353
3. Zadeh LA (1978) Fuzzy sets as a basis for a theory of possibility. Fuzzy Sets Sys 1:3–28
4. Wang HR, Li Y, Jin L, Liu Yp (2010) Multi-agents based fault diagnosis systems in MSW incineration process. ICMTMA, pp 721–724
5. Hanabusa G, Iwakawa Y (1989) Refuse incineration process models of shaking grate refuse incinerator [J]. Autom Meas Control Soc 25(1):62–68
6. Onishi K (1991) Fuzzy control of municipal refuse incineration plant [J]. Autom Meas Control Soc 27(3):326–332
7. Chen WC, Chang NB, Chen JC (2002) GA-based fuzzy neural controller design for municipal incinerators[J]. Fuzzy Sets Sys 129(3):343–369
8. Wang TT, Wang HR, Li Y (2010) Research on GA-fuzzy based combustion temperature model of DGM incinerators. ICEEE, pp 3721–3725
9. Wang HR, Li Y, Jiang Y (2010) Web service and multi-agent based fault diagnosis system for MSW incinerators. Adv Mater Res 179–180:580–585

Chapter 31
Hardware-in-the-Loop for On-Line Identification of SSP Driving Motor

Guichen Zhang

Abstract This paper describes a strategy for identification of Siemens-Schottel-Propulsor (SSP) driving motor which is chosen as three-phase squirrel cage induction motor (IM) in this work. The strategy is to perform on-line identification of parameters of the electrical part of IMs. The different forms of voltage and current signals are applied to the motor based on Siemens Sinamics technology, at the same time, detecting the motor voltage, current response signal, through all these signals and the relationship among them, the motor parameters can be calculated or the motor parameters can be identified using the fitting algorithm. Simulation and experimental results show advantages of the proposed strategy in the identified system, simplicity, and low cost.

Keywords Siemens-Schottel-Propulsor (SSP) · Identification · Induction motor (IM) · Hardware-in-the-loop

31.1 Introduction

Three-phase squirrel cage induction motors are the most widely used electrical drive motors on board, because of their simple structure, reliability of operation and modest cost [1]. The induction motor (IM) electrical parameters are important to achieve high performance motion for Siemens-Schottel-Propulsor (SSP) driving motor [2]. In order to obtain quick torque response, the variable V/f vector control

G. Zhang (✉)
State Laboratory of Ocean Engineering, Shanghai Jiao Tong University,
Shanghai 200030, China
e-mail: zhanggc2004@163.com

technology has been adopted with the SSP driving motor in semi-submersible vessel "Taiankou" and "Kangshengkou". However, the vector control performance is good or bad depends on the accuracy of the motor parameters, and these motor parameters change with motor temperature, skin effect and other factors during its running period [3]. When running in the weakening field, both the stator resistance and mutual inductance have an impact on control performance.

To obtain a high precision propulsion motor control, the accurate motor parameters must be in hand, therefore, before controlling unknown parameters of a motor, the required motor control parameters must be identified, hence the accurate, reliable high-performance electric motor. Parameter Identification of propulsion system is the key of corresponding design and development Guo et al. [4]. Ju and DF [5] had solved the identification problem of composite IM loads with analyzing the identifiability and using genetic algorithms. The least squares parameter identification algorithm, the real parameter complex variable error model and its parameter identification are used in [6]. The rotor resistance and load torque for vector-controlled IM are identified in [7]. Guo et al. [4] described poles designation and parameters tuning method for sensorless IM drive. Genetic algorithm, colony optimization and particle swarm optimization were applied to the IM parameter identification in [3].

In this paper, SSP driving motor use on-line identification method based on Siemens Sinamics technology. Through the different forms of voltage and current signals applied to the motor, at the same time, detecting the motor voltage, current response signal, through all these signals and the relationship among them, the motor parameters can be calculated or the motor parameters can be identified using the fitting algorithm.

31.2 Parameters Identification Method of SSP Driving Motor

Field Oriented Control (FOC) is currently the main method of high-performance IM control [8], which obtains high static and dynamic performance of AC frequency conversion velocity modulation performance by the coordinate transformation [1]. IM dynamic theory involves the rotating magnetic field and its spatial relationship depends on the motor speed and load, the motor equivalent circuit is usually obtained when the sinusoidal voltage at the steady state. But mathematical model derived from the electromagnetic theory is a high-level and parameters time-varying mathematical model, besides, there must exist certain coupling relationships between these various parameters. There are some methods, such as the least square method in practical driving system, extended Kalman filter and model reference adaptive identification are widely used in IM [3, 4]. Linear regression model has been used to approximate the nonlinear system, the system input -output data have been processed as a "black box", recursive prediction error method and adaptive observing method have been used for the motor parameter estimation, pattern recognition, such as rotor resistance, rotor inductance, stator leakage inductance of three-phase IM, rather than determine the transfer function [1].
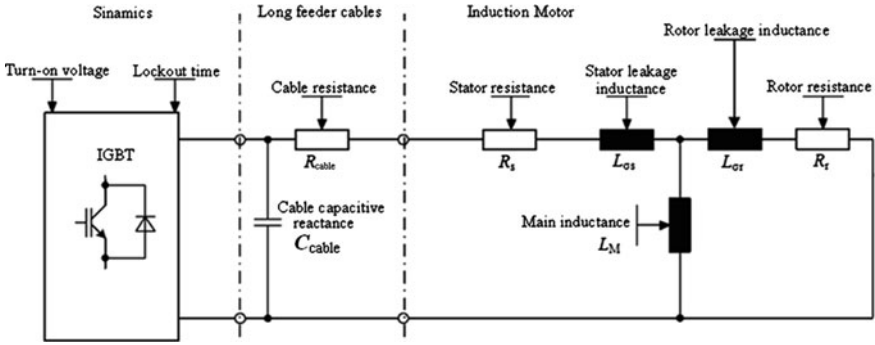
Fig. 31.1 Equivalent circuit of the IM identification

From the equivalent circuit data, motor cable resistance, IGBT turn-on voltage and IGBT lockout time compensation can be determined. Motor stator resistance value is very important for the stability of the closed-loop control and the voltage boost of V/f characteristic. Long feeder cables and the use of third-party motor, the motor data identification procedures must be performed. The equivalent circuit is shown in Fig. 31.1.

31.3 Modeling of SSP Driving Motor

Vector control performance of IM depends on motor parameters, temperature and load changes will affect IM control performance. In this paper, for uncertainty of rotor resistance variation and load torque changes, nonlinear identification algorithm of asymptotic tracking the actual value of load and rotor resistance is designed based on vector controlled IM mathematical model.

Because of mutual coupling between rotor flux ψ_r and rotor mechanical angular velocity, ω_m, the driving IM system equations are necessary to change into state equations that contains the parameter estimates. The steady state performances of the IMs are obtained using static model equations. The state-space model of IM in standard form, with respect to a static coordinates [1, 2], is as follows:

$$
\begin{bmatrix} \psi_{r\alpha} \\ \psi_{r\beta} \\ i_{s\alpha} \\ i_{s\beta} \end{bmatrix} = \begin{bmatrix} -\frac{1}{T_r} & -\omega_m & \frac{L_m}{T_r} & 0 \\ \omega_m & -\frac{1}{T_r} & 0 & \frac{L_m}{T_r} \\ \frac{L_m}{\sigma L_s L_r T_r} & \frac{L_m \omega_m}{\sigma L_s L_r} & -\frac{R_s\left(L_r^2+L_m^2\right)\omega_m}{\sigma L_s L_r^2} & 0 \\ -\frac{L_m \omega_m}{\sigma L_s L_r} & \frac{L_m}{\sigma L_s L_r} & 0 & \frac{R_s\left(L_r^2+L_m^2\right)\omega_m}{\sigma L_s L_r^2} \end{bmatrix} \times \begin{bmatrix} \psi_{r\alpha} \\ \psi_{r\beta} \\ i_{s\alpha} \\ i_{s\beta} \end{bmatrix}
$$
$$
+ \frac{1}{\sigma L_s}\begin{bmatrix} 0 \\ 0 \\ u_{1\alpha} \\ u_{2\beta} \end{bmatrix} \tag{31.1}
$$

In order to facilitate parameters identification, equation (31.1) parameters transformation is

$$R_1 = R_s, \ R_2 = \left(\frac{L_m}{L_r}\right)^2 R_r, \ L_2 = \left(\frac{L_m}{L_r}\right)^2 L_r \tag{31.2}$$

$$T_2 = \frac{L_2}{R_2} = T_r, \ \psi_{2\alpha} = \frac{L_m}{L_r}\psi_{1\alpha}, \ \psi_{2\beta} = \frac{L_m}{L_r}\psi_{1\beta} \tag{31.3}$$

Both sides of the current state by multiplying L_σ, to simplify the state equation, is as follows:

$$\begin{bmatrix} L_\sigma \dot{i}_{1\alpha} \\ L_\sigma \dot{i}_{1\beta} \\ \dot{\psi}_{2\alpha} \\ \dot{\psi}_{2\beta} \end{bmatrix} = \begin{bmatrix} -(R_1 + R_2) & 0 & \frac{1}{T_2} & \omega_m \\ 0 & -(R_1 + R_2) & -\omega_m & \frac{1}{T_2} \\ R_2 & 0 & -\frac{1}{T_2} & -\omega_m \\ 0 & R_2 & \omega_m & -\frac{1}{T_2} \end{bmatrix} \times \begin{bmatrix} i_{1\alpha} \\ i_{1\beta} \\ \psi_{2\alpha} \\ \psi_{2\beta} \end{bmatrix} + \begin{bmatrix} u_{1\alpha} \\ u_{1\beta} \\ 0 \\ 0 \end{bmatrix} \tag{31.4}$$

where R_s—stator resistance, R_1—stator resistance transform; R_r—rotor resistance, R_2—rotor resistance transform; $u_{s\alpha}(u_{1\alpha})$ and $u_{s\beta}(u_{1\beta})$ are stator voltage in $\alpha - \beta$ coordinates; $i_{s\alpha}(i_{1\alpha})$ and $i_{s\beta}(i_{1\beta})$ are stator current in $\alpha - \beta$ coordinates; ω_m-electrical angular velocity of single pole pairs; $L_\sigma(L_\sigma = \sigma L_s)$-total leakage inductance; L_r and L_2 are before and after transformation rotor inductance, respectively; T_r—rotor time constant (L_2/R_2).

Stator current state equation in static conditions ($\omega_m = 0$) is as follows:

$$\begin{bmatrix} L_\sigma \dot{i}_{1\alpha} \\ \dot{\psi}_{2\alpha} \end{bmatrix} = \begin{bmatrix} -(R_1 + R_2) & \frac{1}{T_2} \\ R_2 & -\frac{1}{T_2} \end{bmatrix} \begin{bmatrix} i_{1\alpha} \\ \psi_{2\alpha} \end{bmatrix} + \begin{bmatrix} u_{1\alpha} \\ 0 \end{bmatrix} \tag{31.5}$$

Referring to the described state-space model of IM, a hardware-in-the-loop SSP drive system was built in [9], in order to simulate the dynamic behavior of IM.

31.4 Hardware-in-the-Loop Identification of SSP Driving Motor

The stator resistance can be obtained by DC method, which UV, UW and VW conducted respectively and three sets of data measured, and finally the average of the stator resistance can be taken. Here, the accuracy of voltage detection determines the stator resistance identification accuracy. Stator resistance is small; hence, the required voltage is very small with the input rated current. The higher the voltage, the smaller proportion of the various effects, and the higher detection accuracy.

Single-phase test can be used to replace the locked rotor test to measure the rotor resistance and the leakage inductance both stator and rotor. When V phase and W-phase control signal are same, apply the voltage signal to the motor and

Table 31.1 Identification results of 120 W IM

Parameter text	Value	Unit
Motor stator resistance, cold	1.40359	Ohm
Motor rotor resistance, cold	1.69590	Ohm
Motor stator leakage inductance	9.67435	mH
Motor rotor leakage inductance	10.15039	mH
Motor magnetizing inductance	206.27832	mH
Rated motor current	6.80	Arms
Rated motor power factor	0.820	
Rated motor speed	1420.0	RPM
Motor cooling type	Non-ventilation	
Motor moment of inertia	0.013896	Kgm^2
Ratio between the total and motor moment	1.000	
Motor weight	32.5	kg
Cable resistance	0.35090	Ohm
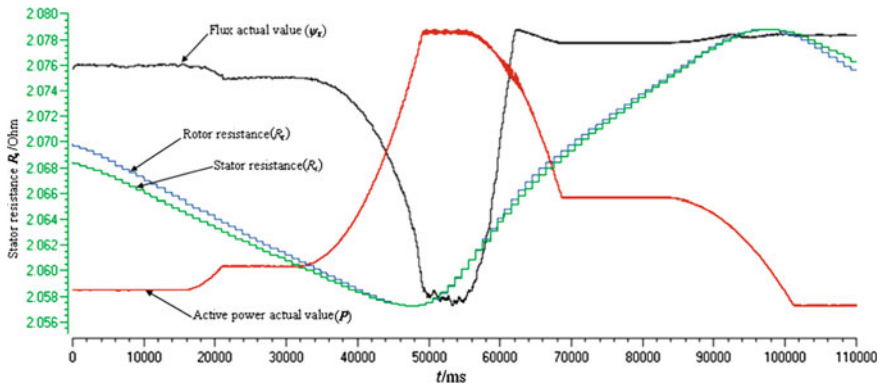
Fig. 31.2 Simulation and experimental results of IM

obtain sinusoidal current to complete the single-phase test, the equivalent circuit shown in Fig. 31.1. Usually, asynchronous motor stator and rotor leakage inductance basically is same and very small comparing to the mutual inductance.

During the operation of the SSP drive system, the parameters of the IM are changed by magnetic saturation affect the stator reactance, rotor reactance and mutual reactance to some extent. The stator resistance and rotor resistance change with temperature, this is a relatively slow process [1]. Parameter identification process is based on the actual IM output and the electrical difference between the model outputs, electrical model of IM is constantly corrected by intelligent optimization algorithms.

IM is controlled by Siemens Sinamics and applies vector control. The real parameters of the IM were used in the hardware-in-the-loop simulation SSP system and are given in Table 31.1. Table 31.1 is obtained from on-line monitoring interface of Siemens Sinamics.

The IM parameters were determined by testing the motor under load and rotor conditions, the real parameters of the IM were used in the simulated system. Simulation and experimental results is as show in Fig. 31.2:

In Fig. 31.2: 0–17,600 ms, P = 0.32 kw, ψ_r = 97.5; 21,500–32,000 ms, P = 0.58 kw, ψ_r = 97.5; 32,000–49,500 ms, P = 0.58 → 3.5 kw, ψ_r = 97.5 → 96.5; 48,500–55,900 ms, P = 3.5 kw, ψ_r = 96.5; 55,900–68,200 ms, P = 3.5 → 1.45 kw, ψ_r = 96.5 → 81.5; 68,200–84,100 ms, P = 1.45 kw, ψ_r = 81.5–81; 84, 100–101,400 ms, P = 1.45 → 0.1 kw, ψ_r = 81 → 100; 101,400–118,000 ms, P = 0.1 kw, ψ_r = 99.5, 0–48,000 ms, R_s = 2.0685 → 2.0572 Ω, R_r = 2.0015 → 1.990 Ω; 48,000–98,000 ms: R_s = 2.0572 → 2.0788 Ω, R_r = 1.99 → 2.01 Ω; 98,000–118,000 ms: R_s = 2.0788 → 2.074 Ω, R_r = 2.01 → 2.0045 Ω.

31.5 Conclusion

In this paper, a strategy for on-line identification of the electrical parameters of the electromagnetic state of SSP driving IM has been presented. Patterns of input–output signals were used in a Siemens Sinamics software environment to identify IM parameters. The stator currents, mechanical angular speed and the rotor flux are continuously monitored by Siemens Sinamics. The identified model was adopted within a hardware-in-the-loop simulation environment to test. Simulation and experimental results show the effectiveness of the proposed method.

References

1. Ashraf S, Rateb I, Tarek T (2010) Hardware-in-the-loop for on-line identification and control of three-phase squirrel cage induction motors. Simul Model Pract Theor 18:277–290
2. Paolo C, Walter G, Marcello M, Andrea T (2005) A new adaptive approach for on-line parameter and state estimation of induction motors. Control Eng Pract 13:81–94
3. Chen ZF, Zhong YR, Li J (2010) Comparison of three intelligent optimization algrithms for parameter identification of induction motors. Electr Mach Control 14:7–12 chinese
4. Guo QY, Zhou GF, Shang J et al (2010) Parameters tuning and poles designation for sensorless induction motor drive. J Tongji Univ (National Science) 38:1664–1668 Chinese
5. Ju P, Li DF (1999) Identification of composite induction motor loads. Trans Chian Electromechnical Soc 14:1–6 Chinese
6. Xia CY (2000) Some parameter identification methods of an induction motor based on its complex quantity descriptions. Proc CSEE 20:1–6 Chinese
7. Xu XZ, Qin Y (2002) Adaptive control and parameter identification for vector-controlled induction motor. Electr Mach Control 6:111–114 Chinese
8. Se S (2008) Slip energy recovery of a rotor-side field oriented controlled wound rotor induction motor fed by matrix converter. J Frankl Inst 345:419–435
9. Zhang GC, Ma J (2011) Hybrid control based on sliding mode-dynamic recursive fuzzy neural network for marine electrical propulsion. Control Theor Appl 28:625–630 Chinese

Chapter 32
Hybrid Adaptive Fuzzy Vector Control for Single-Phase Induction Motors

Ding Wang

Abstract The single-phase induction motors are the ones which have the widest applications and small power operation. The research on them mainly based on the finite model, and generally did not think of the effect of the infinite time-vary parameters. So, hybrid Adaptive fuzzy vector control for single phase induction motors is proposed to improve the system performance. At first, the indirect field oriented vector control can be obtained according to the general mathematic model of single-phase induction motor. The adaptive fuzzy controllers were constructed based on hybrid fuzzy controller after decoupling them to attain effective and easy realized control characteristics. The control schemes presented are realized by the physical prototype. The experiment results prove the total control system performance is correct. And it has the advantage of the easy realized control and the high control efficiency.

Keywords Single phase induction motor · Vector control · Adaptive control · Hybrid fuzzy control

32.1 Introduction

The single phase induction motors are the ones which have the widest applications and small power operation. It is an induction motor which has the two windings, a main one and an auxiliary one. So it has the difficult control of the dynamic and

D. Wang (✉)
Automatic Control Key Laboratory of Heilongjiang University,
Heilongjiang University, Heilongjiang, P. R. China
e-mail: climbing200310@yahoo.com.cn

nonlinear properties. The traditional control methods of the single-phase induction motors are using single-phase alternating current power which can shifted to the other phase alternating current power by the capacitor so that the one of two input power sources is applied to the main winding, and the other is applied to the auxiliary winding. It is seen perfect and developed that the most studies focus on the topologies in main loop and its control methods. With the development of control technologies, microprocessor technologies and power inverter technologies, two input independent AC power sources control are popular. So split SPWM control or the vector control be used because of the its field performances look like three-phase induction motors.

Although the vector control have the advantages of the best control method for the induction motors, their control performances are not satisfactory because of the parameter varieties and nonlinear properties of the induction motor. So, the fuzzy vector control scheme is necessary. But, a hybrid controller can provide better system performance over a simple fuzzy controller alone. And further the adaptive control is added to the fuzzy vector control scheme to improve the robust and adaptive characteristics of control system.

In this paper, hybrid Adaptive fuzzy vector control for single-phase induction motors is proposed to improve the system performance. The indirect field oriented control can be obtained according to the general mathematic model of single-phase induction motor. The speed controllers were constructed by hybrid adaptive fuzzy controller after decoupling them to attain effective and easy realized control characteristics. The paper is focus on the realizations of the control algorithms specially. The detail designs are as follows

32.2 Direct Adaptive Control

Using the synchronous rotating frame, in order to apply the indirect rotor field oriented control to the single-phase induction motor, set $\lambda'_{dr} = \lambda_r$ and set $\lambda'_{qr} = 0$, equations of the single phase induction motors in a stationary reference frame [1] can be obtained. The controller must be designed after decoupling the current components of the single-phase induction motor [2]. Therefore, the equation of plant can be described as

$$p\lambda_r = r'_{dr}L_{md}i_{ds}/(L'_{ldr} + L_{md}) - r'_{dr}\lambda_r/(L'_{ldr} + L_{md}), \tag{32.1}$$

$$p\omega_r = -B\omega_r/J + P/J\{PN_dX_{mq}\lambda_r i_{qs}/2N_q\omega_s(L'_{ldr} + L_{md}) - T_l\}. \tag{32.2}$$

where ω_r is the rotor speed, ω_s is the synchronous speed and $\omega_{sr} = \omega_s - \omega_r$, Nq and Nd are the effective numbers of winding turns along the q and d axes, P is the numbers of motor poles, Lm and L1s are the stator magnetizing and leakage inductances, respectively,

Defining the state vector $X = [x1, x2]T = [\lambda_r, \omega_r]^T$ and the control command $u = iqs$, the plant described by (32.1) and (32.2) can be expressed by the following single-input single-output continuous-time system:

$$\dot{x} = A(x) + B(x)u, \quad y = C(x), \qquad (32.3)$$

where $x \in \Re^2$ is the state vector, $u \in \Re$ is the input, $y = x_2 = \omega_r \in \Re$ is the output of the plant and the functions $A(x)$, $B(x) \in \Re^2$, and $C(x) \in \Re$ are smooth functions, which are defined as

$$A(x) = \begin{bmatrix} -r'_{dr}x_1/(L'_{ldr} + L_{md}) + r'_{dr}L_{md}i_{ds}/(L'_{ldr} + L_{md}) \\ -Bx_2/J - PT_l/J \end{bmatrix} \qquad (32.4)$$

$$B(x) = \begin{bmatrix} 0 \\ P^2 N_d X_{mq} x_1/2JN_q\omega_s(L'_{ldr} + L_{md}) \end{bmatrix} \qquad (32.5)$$

$$C(x) = x_2 \qquad (32.6)$$

Therefore, the relations between the output and input of the above system can be expressed as

$$\dot{y} = f(x) + g(x)u, \qquad (32.7)$$

which $f(x)$ and $g(x)$ represented the unknown nonlinear plant dynamics, and based on the feedback linearization there exists some ideal controller

$$u^* = (-f(x) + \mu(t))/g(x), \qquad (32.8)$$

which $\mu(t) = \dot{y}_m + \delta e_s + \bar{e}_s$, with $\bar{e}_s = \dot{e}_s - \dot{e}_o$, and $\delta > 0$, $e_o = y_m - y$, $e_s = L(s)e_o$, $L(s)$ is a multiple term differentiator which has its poles in the open left half plane.

In order to use adaptive fuzzy control, we may express u^* as [3]:

$$u^* = \theta_u^*\zeta_u(x, \mu) + d_u(x) \qquad (32.9)$$

The ideal parameter vector θ_u^* is defined as:

$$\theta_u^* = \arg\min \left[\sup_{\substack{x \in s_x, \eta \in s_m \\ \theta_u \in \Omega_u}} |\theta_u^T\zeta(x, \mu) - u^*|| \right] \qquad (32.10)$$

where Ω_u is the compact parameter set, and s_x and $s_m \subseteq \Re^n$ are defined as the spaces through which the state trajectory and the free parameter $\mu(t)$ may travel under closed-loop control. ζ_u is the partial of the approximator with respect to the parameter vector, and $d_u(x)$ is the approximation of the error which arises when u^* is represented by an approximator of finite size.

Design the direct adaptive controller based on as:

$$u_d = \hat{u}_u + u_{sd} \tag{32.11}$$

where

$$\hat{u}_u = \theta_u^T \zeta_u \tag{32.12}$$

And θ_u is updated on-line using the following gradient update law:

$$\dot{\theta}_u(t) = \rho_u^{-1} \zeta_u e_s \tag{32.13}$$

where ρ_u is a positive definite adaptation gain.

A sliding mode control term u_{sd} is defined as

$$u_{sd} = k_{sd}(t)\text{sgn}(e_s) \tag{32.14}$$

where

$$k_{sd}(t) = G(x)|e_s|/2g_0^2 + D_u(x) \tag{32.15}$$

and $D_u(x)$ is a known upper bound on the error, $|d_u(x)| \leq D_u(x)$.

32.3 Design of Hybrid Fuzzy PD Controller

In the front of adaptive controller, the fuzzy controls were used to approve the control characteristics. In order to get the easy realization, hybrid fuzzy PD controls were designed. The hybrid fuzzy PD consists of two nonlinear tracking differentiators. The nonlinear tracking differentiator TD (I) whose input ω_r^* and tracking differentiator output is r_1 and r_2 is designed as [4]

$$\dot{r}_1 = r_2 \tag{32.16}$$

$$\dot{r}_2 = -R_r sat(r_1 - \omega_r^* + \frac{r_2|r_2|}{2R_r}, \delta_r) \tag{32.17}$$

which a nonlinear saturation function $sat(A, \delta_r)$ is defined as

$$sat(A, \delta_r) = \begin{cases} \text{sgn}(A), & |A| > \delta_r \\ \frac{A}{\delta_r}, & |A| \leq \delta_r, \delta_r > 0 \end{cases} \tag{32.18}$$

in which sgn($\cdot$) is a standard sign function.

Similarly the nonlinear tracking differentiator TD (II) whose input ω_r' and tracking differentiator output is ω_{r1} and ω_{r2} can be obtained.

Using the output signal of the above speed differentiator, the fuzzy controller input signals are represented as

$$e(t) = K_e(r_1(t) - \omega_{r1}(t)), \tag{32.19}$$
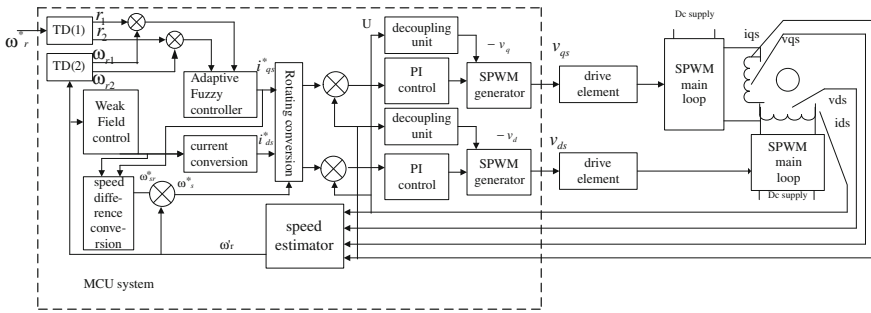
Fig. 32.1   The experiment block diagram of control system

Fig. 32.2   The step response
for system presented
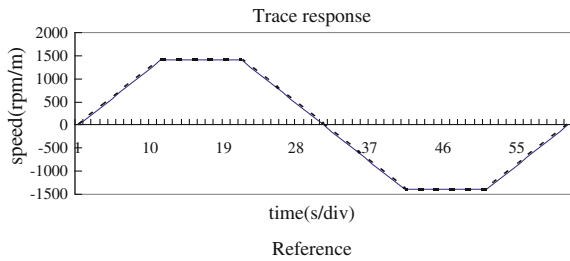
$$c(t) \;=\; K_c(r_2(t) - \omega_{r2}(t)) \tag{32.20}$$

which K_e and K_c are the scaling gains.

The membership function uses the normal distribution function, the fuzzy decision uses the approach associated with the center of gravity. All membership functions used in this PDC are triangular type with a base-width of 0.4. The basic universe of discourse for $e(t)$ and $c(t)$ are $[-1, 1]$, and have 11 fuzzy levels.

32.4 Experiment Study

The whole experiment system consists of a single-phase induction motor, some power electronic elements, some drive elements and a MCU. The MCU is the C8051F120 which has a system frequency of 100 MHz. Power electronic elements are SGB10N60A. Single phase induction motor is the YC90L-4 of 220 V and 1,100 w. The parameters on fuzzy TD controller are: R = 2.5, δ = 0.00005 R. The parameters of the SPWM inverter is T_{max} = 10 ms, N = 500. The software tasks consist of two tracking differentiator tasks, one fuzzy controller task, one adaptive control task, a speed estimator task, two current conversion tasks, a torque conversion task, a speed difference task, a weak field control task, two SPWM inverter tasks, and man–machine interface tasks. All software tasks were combined

together by the main task, realized on the embedded operation system SMALL RTOS 51. The step inputs were applied to system presented and results can be seen in Fig. 32.1. The experiment results shown in Fig. 32.2 prove the proposed control scheme is correct.

References

1. Walls TA, Sudho SD (1996) Analysis of a single-phase induction machine with a shifted auxiliary winding. IEEE Trans Energy Con 11:681–687
2. Wang D (2010) Hybrid fuzzy vector controlvector control for single phase induction motorsingle phase induction motor. 2010 Int Conf Comput Control Indust Eng 2:122–125
3. Spooner JT, Passino KM (1996) Stable adaptive control using fuzzy svstems and neural networks. IEEE Trans Fuzzy Sys 4(3):339–359
4. Su X, Yang SX, Sun D, Duan BY (2004) A simple hybrid fuzzy PD controller. Mechatronics 14:877–890

Chapter 33
Hybrid Intelligent Algorithm Based on Hierarchical Encoding for Training of RBF Neural Network

Yuan Guo She

Abstract Considering the inherent characteristics of RBF network structure, a hybrid intelligent algorithm based on hierarchical encoding strategy is proposed in this paper. This method takes LSM based on singular value decomposition to optimize the linear weights, take hierarchic genetic algorithm, which combined with Gauss–Newton descend search, immune characteristics and chaos idea, to optimize the RBF network structure and hidden layer parameters. Simulation results demonstrate it is effective and superior to some other methods.

33.1 Introduction

Since Broomhead and Lowe [1] (1988) used the radial basis functions (Radial Basis Function, RBF) for neural network design, RBF neural network with its simple structure, high non-linear approximation accuracy and fast learning ability, has been widely used in the areas such as pattern recognition, function approximation, signal processing, time series prediction, etc. [2]. But the RBF centers of hidden node and the standardization parameters are hard to find, select the appropriate radial basis function, how to determine RBF centers, widths and the number of hidden layer nodes to make the training of network meet the required accuracy, is the research hotspot in recent years [3, 4].

Y. G. She (✉)
Engineering College of Armed Police Force, 710086 Xian, China
e-mail: pwzy009@163.com

The solution achieved by the traditional method which only used the stochastic search or gradient search was always a local optimum solution. Hybrid method combining traditional optimization techniques and evolutionary algorithm can greatly enhance the possibility to locate the global optimum and obtain better results than the single use one of them [5]. For that, based on the hierarchical encoding strategy, this paper takes LSM based on singular value decomposition to optimize the linear weights, takes hierarchic genetic algorithm to optimize the RBF network structure and hidden layer parameters which combined with Gauss–Newton descend search, immune characteristics and chaos idea, so a hybrid intelligent algorithm is constructed. Simulation results show that the algorithm is effective and superior to some other methods.

33.2 RBF Network Structure and Optimization

RBF neural network is a special three-layer feed-forward network, the input to output mapping is achieved by a linear combination of nonlinear basis functions. Let $\mathbf{X} = (X_1, X_2, \ldots, X_n)^T \in R^n$ is the network input vector, n is the number of variables, $C_i, 1 \leq i \leq h$, is the centers of hidden nodes (RBF), h is the number of hidden layer nodes, $W_k, 1 \leq k \leq h$, is the weight value to connect the kth hidden nodes and output nodes, b_0 is the output unit bias. Select the most commonly used Gaussian function as radial basis function, the ith output of hidden node for input samples X is:

$$\psi_i(\mathbf{x}) = \exp\left(-\frac{\|\mathbf{x} - \mathbf{c}_i\|^2}{\sigma_i^2}\right), i = 1, 2, \ldots, h \tag{33.1}$$

Where, $\sigma_i, 1 \leq i \leq h$, is the ith width of Gaussian basis function, $\|*\|$ is the Euclidean norm. Given M pairs of training samples $(\mathbf{x}_i, d_i)$, d_i is the desired output of input sample $\mathbf{x}_i$, let the number of output nodes is 1 and the number of hidden nodes is h, the optimization problem of RBF network training is seeking the smallest h value and the corresponding network parameters $\{\mathbf{c}_i, \sigma_i, w_i\}$, that make the objective function of error

$$E(\mathbf{w}_N, \mathbf{w}_L) = [\mathbf{d} - \mathbf{R}(\mathbf{w}_N)\mathbf{w}_L]^T[\mathbf{d} - \mathbf{R}(\mathbf{w}_N)\mathbf{w}_L] \tag{33.2}$$

to meet the required accuracy. Where, $\mathbf{w}_N = (\sigma_1, \sigma_2, \ldots, \sigma_h, \mathbf{c}_1^T, \mathbf{c}_2^T, \ldots, \mathbf{c}_h^T)^T$, $\mathbf{w}_L = (w_0, w_1, \ldots, w_h)^T$, $w_0 = b_0$, $\psi_0(\mathbf{x}) = 1$, $\mathbf{d} = (d_1, d_2, \ldots, d_M)^T$, $r_{ij} = \psi_j(\mathbf{x}_i)$, $\mathbf{R}(\mathbf{w}_N) = [r_{ij}]_{M \times (h+1)}$ is the regressor matrix.

33.3 Hybrid Intelligent Algorithm

Considering the inherent characteristics of RBF network structure that the objective function for the linear parameters $\mathbf{w}_L$ is convex, based on the hierarchical encoding strategy [6], a hybrid intelligent algorithm is constructed in this paper
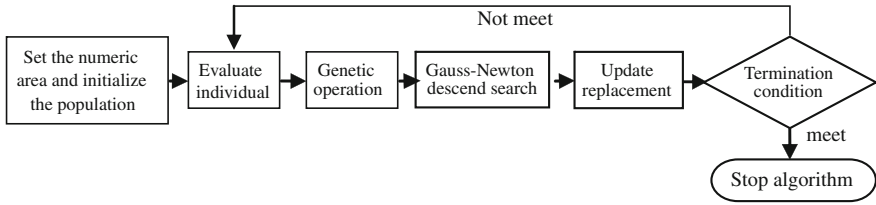
Fig. 33.1 Flowchart of the proposed algorithm

with introducing the Gauss–Newton descend search, immune characteristics and chaos idea into HGA. Flow chart of the algorithm shown in Fig. 33.1, the main steps are as follows:

33.3.1 Set the Numeric Area of Parameters and Initialize the Population

For the RBF network, the number of possible hidden nodes is $h \in [2, n_c]$, n_c is generally determined by experience. Given the appropriate δ value, this paper apply the subtractive clustering algorithm [7] to determine the maximum number of clusters as the upper limit n_c of h. The optimization search scope c_i is selected as same as the change range of input sample data, set $[a_i, b_i]$. In order to ensure the linear weight remain stable and bound, the numeric area of σ_i is determined by the formula [8]:

$$\sigma_i = \sqrt{\max_k \{\|\mathbf{x}_k - \mathbf{c}_i\|^2\} \Big/ (-\log \varepsilon_i)} \qquad (33.3)$$

where, $\varepsilon_i \in [0.0001, 0.1]$.

Adopted the general initialization method of binary genes, the initialization of control genes encodes for the 0,1 string with length n_c. The initialization of centers $\mathbf{c}_i$ encodes for the floating-point string with length n by taking the documents [9] proposed methods to generate in the interval $[a_i, b_i]$ to avoid the redundant situation. Given the values ε_i at interval $[0.0001, 0.1]$ randomly, the initialization σ_i is computed according to formula (33.3). The initialization generates a total of 3N chromosomes to form the initial population $P^{(t)}, t = 0$.

33.3.2 Chromosome Decoding and Determine the Fitness Function

When chromosome decodes, the active hidden layer nodes and their corresponding parameter values $\{\mathbf{c}_i, \sigma_i\}$ together constitute the RBF network, the optimal linear weights $\mathbf{w}_L$ is determined by the LSM based on SVD with the formula

$$\mathbf{w}_L = \left[\mathbf{R}(\mathbf{w}_N)^{\mathrm{T}} \mathbf{R}(\mathbf{w}_N) \right]^{-1} \mathbf{R}(\mathbf{w}_N)^{\mathrm{T}} \mathbf{d} \qquad (33.4)$$

Akaike information criterion (AIC) can be integrative to balance the network complexity and the goodness of fit of data, this paper takes its transform as fitness function. Specific, it is

$$fitness(v) = C_{\max} - M \log(E/M) - 2h \qquad (33.5)$$

Where, $C_{\max}$ is a larger number, M is the number of training samples, h is the number of hidden nodes, E is calculated according to Eq. (33.2).

33.3.3 Genetic Operation

(1) Select. Employing evolutionary strategy [10], the N individuals of current population with the highest fitness is chose to form parent population in accordance with the decided method in this paper.
(2) Cross. The control genes perform the crossover in accordance with double-point crossover for binary code; while real genes cross according to overall arithmetic crossover for real-coded in this paper.
(3) Mutation. With the position of mutation gene selected randomly, the mutation gene of control genes executes reverse mutation operation at a certain prob-ability. For the parameters genes $\{\mathbf{c}_i, \sigma_i\}$ with real-coded, the Gaussian mutation operator [11] is took to perform the basic bit mutation with a certain probability. The crossover probability P_c and mutation probability P_m is adjusted adaptively by use of adaptive adjusted strategies [9] in this paper.

Performed cross and mutation operations to parent population with adaptive probability, the new individuals generated by genetic operation form a new population $\mathrm{P}^{(t)}, t = t + 1$ together with the parent individuals.

33.3.4 Gauss–Newton Descend Search

Considering the inherent characteristics of RBF networks, the optimization problem (33.4) can be further reduced to least squares problem

$$\min E_h(\mathbf{w}_N) = E(\mathbf{w}_N, \mathbf{w}_L(\mathbf{w}_N)) \qquad (33.6)$$

Where $\mathbf{w}_L(\mathbf{w}_N)$ are determined by Eq. (33.4). For the solution to nonlinear least squares problem of equation (33.6), Gauss–Newton style algorithm [12] is a pragmatic solution effectively. This paper embeds one complete iteration step of Gauss–Newton descend algorithm in GA, which constitutes Gauss–Newton

descend search operator to perform the local optimum search of some excellent individuals in population. After performed the local search operation, the excellent individuals of population that performed the Gauss–Newton descend search operation are substituted with the appropriate better individuals.

33.3.5 Update Replacement Operation

Learn from the natural death and complementary mechanism of immune cells, this paper takes the initialization method of individual to produce L individuals and replace the L lower fitness individuals, which maintain the diversity of groups to improve the global convergence.

33.4 Numerical Experiments and Analysis

Consider Mackey–Glass time series

$$\frac{d_y}{d_t} = \frac{ay(t - \tau)}{1 + y^c(t - \tau)} - by(t) \tag{33.7}$$

We use the RBF network optimized by the hybrid intelligent algorithm (HIA) in this paper to prediction. Mackey–Glass time series prediction on basis of differential equation is taken as the normal test problem to verify and compare the performance of algorithms. Same as the literature [13–16], let $a = 0.2$, $b = 0.1$, $c = 10$, $l= 17$, $y(0) = 1.2$, take the fixed input vector [$y(t - 18)$, $y(t-12)$, $y(t - 6)$, $y(t)$] to prediction $y(t + 6)$. The data series produce by 4 order Runge–Kutta method, the former 500 data of the 1000 data selected in accordance with $t = 124 \sim 1123$ is used to train the RBF network, the latter 500 data is used to test the RBF network identified.

Executed the algorithm 10 times, the average value and standard deviation of prediction mean square error (MSE) for training data and test data is given in Table 33.1. For purposes of comparison, the results of hybrid algorithm 1 (HA1), hybrid algorithm 2 (HA2) and evolution algorithm (EA) in literature [13] are also listed in Table 33.1. Table 33.1 shows the network complex degrees are all general equivalent, the prediction accuracy of HIA equivalent with the above two hybrid algorithms is one order of magnitude smaller than the evolution algorithm, and MSE of test data is smaller than that of training data, as show the prediction ability of RBF network determined by HIA is good. Standard deviation reflects the robust of algorithm, Table 33.1 shows the standard deviation of test data for HIA is general equivalent with HA1, but the standard deviation of training data is one order of magnitude smaller, and the training time required is nearly one order of

Table 33.1 Comparison of the various algorithms performance

Algorithm	Number of nodes	MSE		Standard deviation		Time (min.)
		Training data	Test data	Training data	Test data	
HA1	25	2.0623E−6	1.7555E−6	9.2138E−8	1.1023E−7	89
HA2	25	2.1342E−6	1.7975E−6	2.3362E−7	2.6173E−7	29
EA	25	2.1050E−5	2.0045E−5	1.7727E−6	1.9547E−6	12
HIA	24	1.9980E−6	1.9870E−6	1.3963E−9	1.3596E−7	14.7

Table 33.2 Comparison of prediction results

Algorithm	Number of nodes	RSME	
		Training data	Test data
Literature [14]	23	0.0096	0.0114
Literature [15]	116	–	0.0015
Literature [16]	98	0.0014	0.0015
Method of this paper	24	0.0014	0.0014

magnitude smaller, general equivalent with that of EA. As it can be seen that used the RBF network optimized by this paper's method to prediction, the performance is good.

With the prediction accuracy given in the form of root mean square error (RMSE), the prediction results of Mackey–Glass time series of some other algorithm are listed in Table 33.2. Table 33.2 shows the prediction accuracy of this paper's method is the highest, and the number of nodes required is less than that of the other algorithms in the case of the similar prediction accuracy achieved. When the number of nodes is similar, the algorithm can improve prediction accuracy nearly an order of magnitude, significantly better than other algorithms.

33.5 Conclusion

Based on the hierarchical encoding strategy, this paper takes LSM based on singular value decomposition to optimize the linear weights, takes the hybrid HGA, take hierarchic genetic algorithm, which combined with Gauss–Newton descend search, immune characteristics and chaos idea, to optimize the RBF network structure and hidden layer parameters, thus constructed a hybrid intelligent algorithm. Prediction results of normal time series show that this algorithm can make full use of all the advantages of intelligent optimization technology to improve the operating efficiency and prediction accuracy, it is superior to some other methods.

References

1. Broomhead DS, Lowe D (1998) Multivariable functional interpolation and adaptive networks [J]. Complex Syst 2:321–355
2. Haykin S (2001) Neural networks. A comprehensive foundation, 2nd edn. Tsinghua University Press and Prentice Hall, Beijing, pp 298–305
3. Junfeng C, Ziwu R, Ye S (2008) A two-level learning hierarchy for the radial basis function networks. Control Theory Appl 25(4):655–660
4. Baek JY, Park BJ, Oh SK (2009) The design of polynomial RBF neural network by means of fuzzy inference system and its optimization. Trans Korean Inst Elect Eng 58(2):399–406
5. Quagliarella D, Vicini A (1998) Coupling genetic algorithms and gradient based optimization techniques. Wiley, West Sussex
6. Hongrui S, Yong L, Baokun L et al (2002) RBFNN algorithm based on hybrid hierarchy genetic algorithm and its application. Control Theory Appl 19(4):627–630
7. Pal NR, Chakraborty D (2000) Mountain and subtractive clustering method: improvements and generalizations. Int J Intell Syst 15(4):329–341
8. Peng H, Ozaki T, Haggan OV et al (2003) A parameter optimization method for the radial basis function type models. IEEE Trans Neural Netw 14(2):432–438
9. She Y, Sheng C (2009) Chaotic search-based adaptive immune genetic algorithm. In: 2009 International Conference on Business Intelligence and Financial Engineering, BIFE 2009. United States, IEEE Computer Society, pp 74–78
10. Juan G (2004) Introduction of intelligent information processing method. China Machine Press, Beijing, pp 87–90
11. Gunter R (1997) Local convergence rates of simple evolutionary algorithms with Cauchy mutations. IEEE Trans Evol Comput 4(1):249–258
12. Miaogen S, Chunli G (1999) Basis of scientific and engineering computation. Tsinghua University Press, Beijing, pp 344–356
13. Min G, Xiaoyan P, Hui P (2009) Two hybrid parameter optimization algorithms for RBF neural networks. Control Decis 24(8):1172–1176
14. Cho KB, Wang BH (1996) Radial basis function based adaptive fuzzy systems and their applications to system identification and prediction. Fuzzy Sets Syst 83(3):325–339
15. Harpham C, Dawson CW (2006) The effect of different basis functions on a radial basis function network for time series prediction: a comparative study. Neurocomputing 69(16):2161–2170
16. Du H, Zhang N (2008) Time series prediction using evolving radial basis function networks with new encoding scheme. Neurocomputing 71(729):1388–1400

Chapter 34
Improved Fuzzy Neural Network for Stock Market Prediction and Application

Xu Yi Wei and Sheng Zhong Huang

Abstract With an adaptive learning algorithm for fuzzy rules can be generated according to the needs of the specific problems a different number of fuzzy rules, and according to the fuzzy rules to determine the network structure. Determining the structure of the network, due to not randomly generated, and without trial and error, so the more scientific. Prediction in the stock, with different stocks selected, the resulting network structure are not the same, so that the trained network is more focused, be more accurate forecasts for the stock. Experiments show that the improved fuzzy neural network prediction of stock trends better stability on the future operation of the stock market has a certain significance.

Keywords Fuzzy neural network · Stock market prediction · Trend prediction

34.1 Introduction

In recent years, as people's understanding of the nonlinear characteristics of the stock market and neural network processing capabilities continue to explore non-linear problems, the neural network prediction for the stock more and more attention of researchers, there have been many such studies. As the stock market

X. Y. Wei (✉)
Department of Electric Information Engineering, Guangxi Agricultural Vocational
Technology College, 530007 Guangxi, Nanning, China
e-mail: jokerwell750918@qq.com

S. Z. Huang
Department of Mathematics and Computer Science, Liuzhou Teachers College,
545004 Guangxi, Liuzhou, China
e-mail: gxhsz@126.com

there are many fuzzy factors, such as stock prices "going up" and "down", the investment enthusiasm of the "high" and "weak" and so on, which are difficult to describe the specific data, plus the non-market Linear features just right for the nonlinear neural network capacity, based on these two reasons, makes fuzzy neural network prediction in the stock market has good prospects.

Stock forecasting using fuzzy neural network achieved good results, but there are some limitations. The more prominent of which is determining the structure of neural networks lack of scientific method, only the experience or according to the researchers repeated the test to determine, and ultimately determine whether the structure can reflect the structure of the specific issues not know the best. Therefore, it is necessary to find a way to overcome this shortcoming, this is one of this study.

Improved fuzzy neural network prediction for the stock market, the stock of historical data through time series analysis to find the law which fitted between the output and input nonlinear function, and after this function is used to forecast. Fuzzy neural network compared with the other advantages of neural networks, fuzzy neural networks can deal with fuzzy information using fuzzy logic capacity of the state of the stock with a fuzzy information as input data, to better fit the changing process of the stock market. Determining the structure of the network, due to not randomly generated, and without trial and error, so the more scientific. Prediction in the stock, with different stocks selected, the resulting network structure are not the same, so that the trained network is more focused, be more accurate forecasts for the stock.

34.2 RBF Neural Network Model

RBF neural network is essentially a two-forward network, basis functions in hidden layer of radial basis function, its input stimulus to produce a localized response, that is, when the input falls only a very small input space, designated area, the hidden unit output value of the non-zero response. The output of output layer can be used after the output of each hidden unit to obtain a weighted sum. Input to hidden unit weights set to 1, between the hidden units to output unit weights can be adjusted in real time, RBF neural network shown in Fig. 34.1.

RBF neural networks generally use Gaussian function as basis functions:

$$G(X, T_i) = G(\|X - T_i\|) = \exp\left(-\frac{\|X - T_i\|^2}{2\delta_i^2}\right) \quad i = 1, 2, \ldots, M \qquad (34.1)$$

where, $G(X, T_i)$ represents the i-unit hidden layer output, X represents a P-dimensional input vector, T_i for the i-unit hidden layer of Gaussian function center, δ_i represents the first hidden node i normalized coefficient, which is called the width of the, M said that the number of hidden nodes. Fuzzy neural network
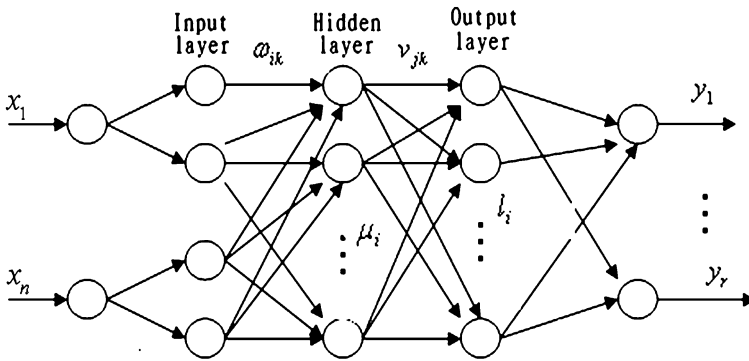
Fig. 34.1 RBF neural network map

center has three types of parameters need to be trained, that is, the center of RBF T_i, width δ_i and the connection weights $W_{i,j}$.

   Based on RBF neural network, because hidden layer and output layer nodes have different functions, the corresponding training methods can basically be divided into two categories: (a) hidden nodes with RBF function centers and width between the hidden layer and output layer connection weights of their training. (b) RBF function center, width, and the hidden layer and output layer connection weights while training. Corresponding algorithm steps [1] are:

(1) Initialization: the raw data were normalized processing. Randomly assigned values (including weight, center and width), and pre-set tolerances. Set the learning step length: η_1, η_2, η_3.

(2) Loop calculations: the results until the errors meet the pre-set or specified number of cycles. Every step of the calculation error is calculated as follows:

$$e_j = d_j - F(X_j) = d_j - \sum_{i=1}^{M} w_i G(X_j, T_i) \tag{34.2}$$

(3) to solve the output of each unit step change in the amount of weight:

$$\frac{\partial E(n)}{\partial w_i(n)} = -\frac{1}{N} \sum_{j=1}^{N} e_j \exp\left(-\frac{\|X - T_i\|^2}{2\delta_i^2}\right) \tag{34.3}$$

Weight after the changes: $w_i(n+1) = w_i(n) - \eta \dfrac{\partial E(n)}{\partial w_i(n)}$.

(4) The center of hidden units to solve a variation

$$\frac{\partial E(n)}{\partial w_i(n)} = -\frac{1}{N}\sum_{j=1}^{N} e_j \exp(-\frac{\|X - T_i\|^2}{2\delta_i^2})(\|X - T_i\|^2) \tag{34.4}$$

Width after the changes: $\delta(n+1) = \delta_i(n) - \eta_\delta \frac{\partial E(n)}{\partial \delta_i(n)}$.

(5) To solve the error is calculated as follows:

$$E = \frac{1}{2N}\sum_{j=1}^{N} e_j^2 \tag{34.5}$$

34.3 Fuzzy Neural Network Pattern Recognition Method

RBF neural network input layer has nodes l, the input feature vector with l elements; RBF neural network output layer n nodes, so the output layer pattern vectors containing n classes. RBF hidden layer neural network including the n_l nodes, output nodes and hidden layer connection weights between nodes is set to ω_{ik}, where i represents the input node number, k the output node number. Input nodes and hidden layer connection weights between nodes is set to v_{jk}, where j represents the input node number, k said the serial number of hidden nodes. Improved RBF neural network hidden layer transfer function, so that RBF neural network input–output relationship was ladder. This can make the hidden layer nodes have multiple stable states, so the input response of the sample will become more stable, and thus be able to add RBF neural network, fuzzy mechanism.

Through a set of m_t a Sigmoid function to represent the sum of RBF neural network input–output relationship of the transfer function of hidden neurons to neural network has a stable state $m_t + 1$. The more the number of Sigmoid function, RBF neural network hidden layer, the higher the degree of fuzzy. Let $X = (x_1, x_2, \cdots, x_l)^T$ for the neural network input vector, then the first i-neuron hidden layer output expression [2] is:

$$g_i = \frac{1}{m_t}\sum_{s=1}^{m_t} \tilde{g}_i^s = \frac{1}{m_t}\sum_{s=1}^{m_t} sgm(\alpha_g(\bar{g}_i - \mu_i^s)) \tag{34.6}$$

$$\bar{g}_i = \frac{1}{m_t}\sum_{k=1}^{l_t} v_{ki}x_k \tag{34.7}$$

Among them, $sgm(\varepsilon) = \frac{1}{1+\exp(\varepsilon)}$, α_g represents the smooth coefficients, μ_i^s represents the RBF neural network hidden layer transfer function of the step limit.

The objective function of fuzzy neural network expression is:

$$E = \sum_{q=1}^{N} E_q = \frac{1}{2} \sum_{q=1}^{N} \sum_{k=1}^{n} (d_{k,q} - y_{k,q})^2 \tag{34.8}$$

where, $y_{k,q}$ represents a fuzzy neural network output function, $d_{k,q}$ represents the expected results of fuzzy neural network, N represents the number of learning samples. Gradient descent on the weights of RBF neural network correction, then the minimum value of objective function can be obtained.

$$\Delta \omega_{ik} = \omega_{ik}(m) - \omega_{ik}(m-1) = -\lambda \frac{\partial E}{\partial \omega_{ik}} = -\lambda \sum_{q=1}^{N} \varsigma_{kq}^0 g_{iq} \tag{34.9}$$

where, $\varsigma_{kq}^0 = \alpha_0 y_{kq}(1 - y_{kq})(1 - d_{kq})$.

Variance within the class to a minimum of training to obtain parameters μ_i^s, l $(l = 1, 2, \cdots n)$ class of the first samples of a group of the first contacts i hidden layers corresponding to the output of the conditional variance is calculated as follows:

$$\sigma_{il}^2 = \sum_{\forall x_q \in C_l} (g_{il} - g_{iq})^2 \tag{34.10}$$

Sum of all the variance, which was expressed as follows:

$$G = \frac{1}{2} \sum_{i=1}^{m_t} \sum_{l=1}^{n} \sigma_{il}^2 \tag{34.11}$$

where, G the target function.

34.4 Stock Market Forecasting Simulation

The stock market is a complex nonlinear system, the stock price volatility is affected by many uncertainties, and these complex relationships between factors. Many facts are that volatility is not no rules to follow. The stock market as a deterministic nonlinear dynamic system, and the dynamic mechanism of the internal market is established, the stock of historical data contains information about future stock movements. The historical data as a time series $\{X_i\}$, using historical data X_n, X_{n+1},..., X_{n+m}, to predict the future. X_{m+k} $(k > 0)$ times the value, which is that the nonlinear function:

$$X_{n+m+k} = F(X_n, X_{n+1}, \ldots, X_{n+m}).$$

Since F (●) is very complicated, the traditional linear prediction method is simple observational data weighted sum, the results as a predictive value, which is clearly

Table 34.1 2008.12.31–2011.05.06 on Shanghai Composite Index closing the weekly average number of table

1728	1747	1986	1969	1871	2018	1954	2018	1851	1820
1904	1954	1990	2181	2323	2261	2082	2193	2128	2281
2374	2419	2444	2503	2448	2477	2625	2645	2597	2632
2753	2743	2880	2928	3088	3113	3189	3372	3412	3260
3046	2960	2860	2861	2989	2962	2838	2779	2911	2976
3107	2995	3164	3187	3308	3096	3317	3247	3113	3141
3277	3196	3224	3128	2989	2939	3018	3051	3031	3013
3067	3059	3157	3145	3130	2983	2870	2688	2696	2583
2655	2553	2569	2513	2552	2382	2470	2424	2572	2637
2658	2606	2642	2610	2655	2663	2598	2591	2655	2738
2971	2975	2978	3129	2985	2888	2871	2842	2841	2893
2835	2808	2838	2791	2715	2752	2798	2827	2899	2878
2842	2933	2906	2977	2967	3030	3050	3010	2911	2863

not a good complete forecast. Fuzzy logic and neural networks are nonlinear approximation tool, but both are shortcomings, such as fuzzy rules in fuzzy logic to determine the dependence on the expertise is too large, neural network "black box" issues, making the two methods There are some limitations. Neural networks and fuzzy logic combination of said fuzzy logic with neural networks, fuzzy logic, fuzzy rules to the structure by the neural network a powerful self-learning ability to achieve, not only simplifies the process of fuzzy reasoning, but also makes the results even more with the fact that Approximation. In recent years, fuzzy neural network research for many, but in most cases, the network still need to manually determine the structure, making the network effects are often affected by personal experience good or bad about the lack of scientific. Moreover, in order to find the network structure is often more appropriate to conduct repeated tests, unnecessary workload. Improved fuzzy neural network using a network structure automatically adjust the strategy. Experiment, only a few initial parameters need to be defined, when the input data into the network, the network may be under specific circumstances, automatically adjust the network structure. This not only enables researchers to work from the tedious trial and freed, and the establishment of the network structure and more scientific, to simplify the research process and the effect is more ideal for the dual function.

Using improved fuzzy neural network stock prediction is that the historical data as the research object, select the appropriate data, respectively, as the network input and output. Through the network training, network architecture to fit the internal laws of the stock price fluctuations, when the new data input, the corresponding output is the prediction.

Take 2008.12-31–2011.05.06 of the Shanghai index's weekly average for the network learning, modeling the raw data, as shown in Table 34.1.

The data is divided into two groups, first group 110, to establish a network model; the second group 20, for the simulation prediction test. Matlab compiled by improved fuzzy neural network simulation program, the establishment of forecasting model, to

Fig. 34.2 Improved fuzzy neural network prediction error curve of the stock index
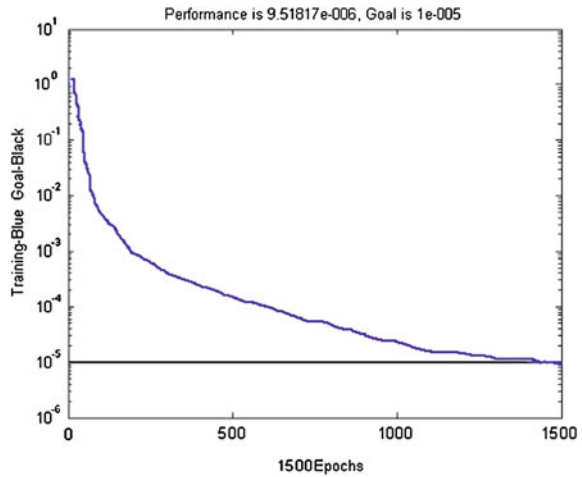
Table 34.2 Shanghai stock index average prediction week comparative table

Measured	2835	2808	2838	2791	2715	2752	2798	2827	2899	2878
Predictive	2830	2815	2810	2780	2730	2745	2790	2825	2890	2880
Measured	2842	2933	2906	2977	2967	3030	3050	3010	2911	2863
Predictive	2850	2915	2920	2960	2971	3015	3055	3025	2900	2870

Fig. 34.3 The Shanghai stock index average prediction results comparison chart week
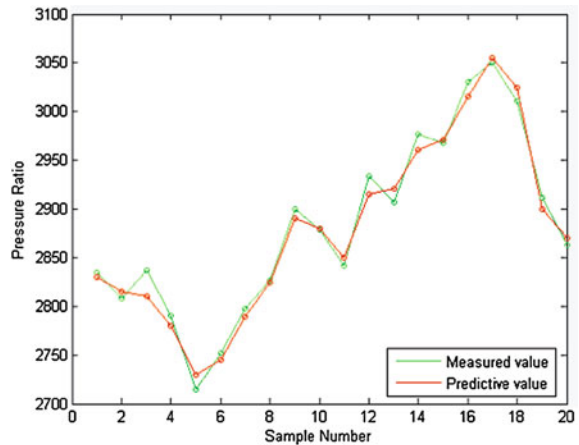
1500 when the iteration, the error of accuracy 9.51817E-6, shown in Fig. 34.2. Predicted results for the second set of data shown in Table 34.2, prediction results can be clear from Fig. 34.3, high accuracy, better fitting, to practical requirements.

34.5 Conclusion

Improved fuzzy neural network in predicting the trend of stock prices, average weekly use of the stock price of the input data as the original data to obtain better prediction results, to achieve the purpose of prediction. From the prediction results indicate that the stock market also need to continue down, through the practice observed 2011.05.06–2011.05.27 data, the Shanghai index adjusted to 2709 from 2870. Prediction results and verify the results match the actual observations show that volatility forecasts to reflect the trend of the stock operator has a certain significance.

References

1. Jing H (2007) Neural networks in stock market prediction of [D]. Shandong Normal University, Jinan
2. Bright red before, Zhao C-Y, Jiaqiu W (2007) Fuzzy neural network fuzzy neural network in the stock market prediction stock market prediction [J]. Hall University of Technology, No. 4

Chapter 35
Landslide Recognition in Mountain Image Based on Support Vector Machine

Wei Zhen-zhong, Wei Xing and Wei Xin-guo

Abstract To improve the recognition of landslides, an algorithm based on combined features and support vector machine (SVM) is proposed. The landslide image was preprocessed firstly, including size equalization and histogram equalization. Then feature extractions were done as follows: dividing the image into sub-regions vertically, extracting texture features based on gray level co-occurrence matrix (GLCM) in each sub-region, extracting segmentation feature based on RGB color space, extracting color features based on HIS color space in each sub-region, and extracting gradient features in gradient image. Based on SVM, the above extracted features were used to realize the classification as well as the disaster recognition. Experiments show that this algorithm has better recognition effect on the mountain images than the former algorithm which we have proposed before.

Keywords Landslide · Recognition · Support vector machine · Image processing

35.1 Introduction

As one of the most important transportation ways, the railway running safety situations become attracting people's much more attention, especially with the speeding up of the train velocity. For instance, along the rail-line, many mountains on which landslide disaster occurs will seriously affect the railway transportation safety. So, it is quite necessary to make fast and good recognition about mountain

Z.-z. Wei (✉) · X. Wei · X.-g. Wei
School of Instrument Science and Opto-electronics Engineering, Beihang University, 100191 Beijing, China
e-mail: zhenzhogwei@buaa.edu.cn

landslide disaster. There exist lots of researches provided in literatures which could be used to realize the recognition, including image based recognition methods. Early in this year, we had submitted a paper to a journal about mountain landslides recognition for reviews [1], in which texture features based on gray level co-occurrence matrix, segmentation feature based on RGB color space and color features based on HIS color space are used, and at the same time, literature reviews had been given in details. For the mountain landslides are various in forms, it needs to extract as many features as possible to describe the characters of the landslides. Thus, in this paper, gradient features of the mountain gradient image will be further extracted [2, 3], by combining the features used in our former submitted paper to get much better recognition results.

The support vector machine is believed to have good classification rate for high dimensional data, so we chose SVM in this paper. Finally, based on SVM and features extraction, we realize the landslide classification and recognition.

35.2 SVM Review

Assuming that the training set consists of l samples from the N-dimensional feature space $x_i \in R^{(N)}$. Each point x_i belongs to either of two classes and corresponding binary class labels $y_i \in \{+1, -1\}$. The final result is a discrimination function f conveniently expressed in original dimensional feature space X [4]:

$$f(x) = sign\left(\sum_{i,j=1}^{l} y_i \alpha_i K(x_i, x_j) + b\right) \qquad (35.1)$$

Where $\alpha = [\alpha_1, \alpha_2, \ldots \alpha_l]$ is the vector of Lagrange multipliers $K(\cdot)$ is the kernel function [5]. Some typical examples of SVM kernel functions are: linear kernel, polynomial kernel, radial basis function kernel and sigmoid kernel. The detailed expressions of these kernels can be consulted in Reference [6].

35.3 Features Extraction of the Mountain Image

35.3.1 Features Used in Our Submitted Paper

Besides adding the new feature extractions, we still need to use texture, color, segmentation features which have been stated in our submitted paper [1].
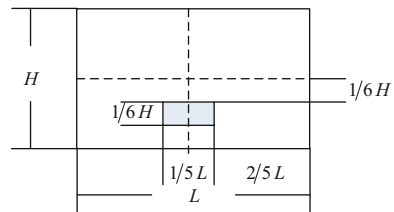
(1) Texture Features Extraction Based on GLCM.

The definition of gray level co-occurrence matrix (GLCM) can be consulted in Reference [7]. Haralick has proposed 14 statistical features extracted from the

Fig. 35.1 Sketch map of detecting windows

Fig. 35.2 Selection of color segmentation sub-region

GLCM as texture characteristics [8]. Here we select contrast, energy, entropy homogeneity and correlation.

After analyzing most landslide images, we find it is more suitable to divide the detecting windows as shown in Fig. 35.1. Then calculate the 5 texture features in each region.

(2) Segmentation Features Extraction in RGB Space

It is necessary to have a measure of similarity to perform the segmentation. One of the simplest measures is the Euclidean distance. We take the two pixels as similar if the distance between them is less than a special threshold [9].

The sub-region of color segmentation is selected as Fig. 35.2. After segmentation, the image is coded the two sets of points in the image with black and white, produces a binary segmented image.

(3) Color Features Extraction Based on Color Histogram

In this paper, we transform RGB color space to HIS color space first [9], and then quantize H, S, I in unequal interval and weighted respectively, then transform them into a one-dimension vector P. The color feature in this paper is the pixels which have maximal occurrence probability. Refer to reference paper [1] for the procedure.

The method of detecting window division in Fig. 1 is still used in color feature extraction. Calculate the color features in each region.

35.3.2 New Features Extraction Additional-Gradient Features Extraction

However, color extraction is not always working if the mountain has the similar color. For that, gradient features are extracted to improve the result. Landslide images have obvious gradient information along landslide region, while normal mountain images have the similar intensity in all directions. So, the gradient information can be used to distinguish two kinds of images.

Let c represents an arbitrary vector in RGB color space. For an image of size $M \times N$, there are MN such vectors, for $x = 1, 2, \ldots M, y = 1, 2, \ldots N$. Let r, g, and b be unit vectors along the R, G, and B axis of RGB color space, and define the vectors [9].

$$u = (\partial R/\partial x) \cdot r + (\partial G/\partial x) \cdot g + (\partial B/\partial x) \cdot b \qquad (35.2)$$

$$v = (\partial R/\partial y) \cdot r + (\partial G/\partial y) \cdot g + (\partial B/\partial y) \cdot b \qquad (35.3)$$

Let g_{xx}, g_{yy} and g_{xy} be defined in terms of the dot product of these vectors, as follows:

$$g_{xx} = u \cdot u = u^T u = \left|\frac{\partial R}{\partial x}\right|^2 + \left|\frac{\partial G}{\partial x}\right|^2 + \left|\frac{\partial B}{\partial x}\right|^2 \qquad (35.4)$$

$$g_{yy} = v \cdot v = v^T v = \left|\frac{\partial R}{\partial y}\right|^2 + \left|\frac{\partial G}{\partial y}\right|^2 + \left|\frac{\partial B}{\partial y}\right|^2 \qquad (35.5)$$

$$g_{xy} = u \cdot v = u^T v = \frac{\partial R}{\partial x}\frac{\partial R}{\partial y} + \frac{\partial G}{\partial x}\frac{\partial G}{\partial y} + \frac{\partial B}{\partial x}\frac{\partial B}{\partial y} \qquad (35.6)$$

Using this notation, it can be shown that the direction of maximum rate of change of $c(x, y)$ is given by the angle

$$\theta = \frac{1}{2}\arctan\left[2g_{xy}/(g_{xx} - g_{yy})\right] \qquad (35.7)$$

And that the value of the rate of change at $c(x, y)$ in the direction of θ, is given by

$$F(\theta) = \left\{\frac{1}{2}[(g_{xx} + g_{yy}) + (g_{xx} - g_{yy})\cos 2\theta + 2g_{xy}\sin 2\theta]\right\}^{1/2} \qquad (35.8)$$

There, $F(\theta)$ is the gradient image.

35.4 Experiments and Comparisons

In this study, MATLAB (R2007b) and "Pentium 2CPU 3.00GHz, 2.00GHz RAM" are used as software and hardware. Hundred and thirty normal mountains images and 75 landslides images were selected from internet randomly, so the conditions of them are different. We choose 60 instances including 30 normal mountains and 30 landslides as testing data, the remaining as training. Partial typical landslide images and normal mountain images are used to do experiments and shown in Figs. 35.3, 35.4.

Original image must be pre-conducted. Image preprocessing includes size equalization and histogram equalization. The purpose of histogram equalization is to reduce the influence of illumination and improve contract. The purpose of size equalization is to make feature extraction conveniently. If the length of image is bigger than the width, the size is equalized to 200×150, otherwise, 150×200.

35.4.1 Texture Feature Extractions

After times of trails, we set the parameters in this experiment as follows: the gray level i = 32, distance d = 6, direction θ is the average of texture features in the four directions of 0°, 45°, 90°, 135°. It is insensitive to the image rotation and the calculate complexity will be reduced.

The experiment results with Figs. 35.3, 35.4 have the similar results in the former study. The texture features in the normal images are stable and similar, while the values are variable between each sub-region in the landslide images. The experiment result could be referred to in paper [1].

35.4.2 Color Feature Extractions

Calculate the color features in each sub-region. Take $W_s = 3$, $W_i = 3$ when producing the one-dimension vector P. The experiment results in paper [1] show that color features in normal images are stable, and the values of mean and variance are smaller. While the values of mean and variance are bigger in landslide images.

35.4.3 Segmentation Feature Extraction

Select the measure of similarity as is shown in Fig. 35.2. Record the numbers of black points and white points in the segmentation image, and then calculate ratio of these two numbers as segmentation feature. The feature of normal mountain
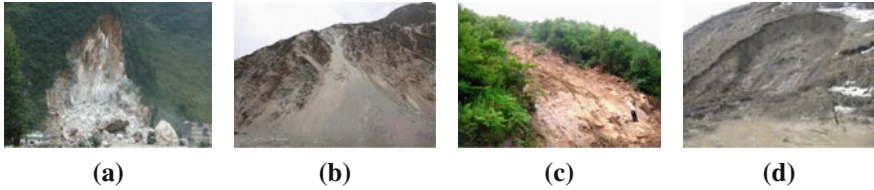
Fig. 35.3 Examples of typical landslide
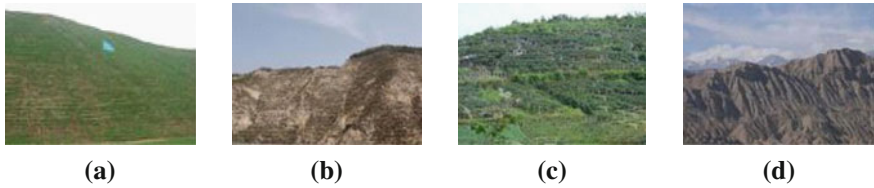
Fig. 35.4 Examples of typical normal mountain

image is bigger than landslide image. There are serious differences between two kinds of images. The experiment result could be referred to in paper [1].

35.4.4 Gradient Feature Extractions

The color extraction is not working if the mountain has the similar color, such as (b, d) in Fig. 35.3, gradient features can help to improve the result. Tables 35.1, 35.2 show the results of Figs. 35.3, 35.4.

The gradient features in the normal images are smaller than the landslide images in Tables 35.1, 35.2. These new added features make the difference between normal and landslide image when the color in the whole picture is similar. In this way, recognition rate would be improved obviously.

35.4.5 SVM Classifier Design

The experiment chooses four typical SVM kernels: linear kernel, polynomial kernel, radial basis function kernel and sigmoid kernel. The choices of each kernel are: the parameter of linear kernel $d = 3$, the parameter of RGB kernel $\sigma = 1$, the parameter of sigmoid kernel $v = 1$, $c = 0$. Penalty coefficient C = 200. Experiment selects 60 instances including 30 normal mountains and 30 landslides as testing data randomly, the remaining as training. The result is shown in Table 35.3.

Table 35.1 Comparison of gradient features of landslide images

Gradient	(a)	(b)	(c)	(d)
Percent	2.057	1.380	1.950	1.190
Variance	1.497	1.884	1.077	1.275

Table 35.2 Comparison of gradient features of normal mountain images

Gradient	(a)	(b)	(c)	(d)
Percent	0.497	0.527	0.027	0.037
Variance	0.066	0.109	0.116	0.079

Table 35.3 Recognition results with the new algorithm in this paper

	Image	Correct	Wrong	Recognition rate (%)
Normal	30	28	2	93.3
Landslide	30	26	4	86.7
All	60	54	6	90

Table 35.4 Recognition results with our former algorithm

	Image	Correct	Wrong	Recognition rate (%)
Normal	30	27	3	90
Landslide	30	24	6	80
All	60	51	9	85

Table 35.4 shows the recognition result with our former method in the paper which has been submitted [1]. By comparing of Tables, 35.3, 35.4, we can see that the new algorithm outperforms the former algorithm which do not use gradient features, and the recognition time is also acceptable to an image with the size of 150×200 (or 200×150). The recognition rate has reached 90%.

35.5 Conclusions and Future Work

Based on the combined features extraction, a new landslide recognition algorithm using SVM is proposed. This new algorithm has improved the landslide recognition rate from 85 to 90% based on SVM and gradient feature extractions combined with the other features extractions. Future researches will address issues on the landslide in different seasons, and pre-classification also should be done to improve the recognition rate under various conditions.

References

1. Wei X, Wei Z, Zhang G Landslide disaster image recognition algorithm based on SVM. J Beijing Univ Aeronaut Astronaut (in submission)
2. Sun J, Ma H, Li F (2009) Viewpoint-space partitioning based on affine invariant features. Tsinghua Univ (Sci) 49(1):53–56
3. Ding G (2009) Research on environment perception and object recognition for mobile robot based on support vector machine [D]. University of Science and Technology of China
4. Gao H, Mrinal KM, Wan J (2010) Classification of hyperspectral image with feature selection and parameter estimation. International conference on measuring technology and mechatronics automation, pp 783–786
5. Bazi Y, Melgani F Toward an optimal SVM classification system for hyperspectral remote sensing images [J]. IEEE Trans Geosci Remote Sens 44(6):1469–1478
6. Fan X (2003) Suppor vector machine and its applications [D]. Zhejiang University, Zhejiang
7. Wang HY, Dong F (2009) Image feature extraction of gas/liquid two-phase flow in horizontal pipeline by GLCM and GLGCM. International conference on electronic measurement and instruments, pp 135–139
8. Yuan H, Fu L, Yang Y et al (2009) A nalysis texture feature extracted by gray level co-occurrence matrix [J]. J Comput Appl 29(4):1018–1021
9. Rafael CG, Richard EW (2007) Digital image processing using MATLAB [M]. Beijing Publishing House of Electronics Industry, Beijing
10. Yang J (2009) Research and implementation of image retrieval based on color and texture [D]. Wuhan University of Technology, Wuhan

Chapter 36
Lecture Notes in Electrical Engineering: Magnetic Field Parameter Calculation of Permanent Magnet Reciprocating Generator

Yufeng Lu, Dawei Meng, Yongming Xu and Xifeng Wang

Abstract To calculate the electromagnetic parameter of permanent magnet reciprocating generator accurately, based on two-dimensional finite element method, in the condition of considering the end effect, the static magnetic field model is created. The method which electromagnetic parameters in a running period are calculated with is proposed, the no-load electromotive force, synchronous reactance and the no-load, loaded electromagnetic force are solved. The simulation and experiment results indicated that the error is small, and the method avoided the problem that transient analysis spending too much time.

Y. Lu (✉) · D. Meng · Y. Xu
Harbin University of Science and Technology, No.52, Xuefu Road,
Harbin, Heilongjiang, China
e-mail: luyufenghust@163.com

D. Meng
e-mail: mengdawei@hrbust.edu.cn

Y. Xu
e-mail: xuyongming@hrbust.edu.cn

X. Wang
Heilongjiang Institute of Technology, No.999, Hongqi Road, Harbin,
Heilongjiang, China
e-mail: wangxiaoxu0104@163.com

36.1 Introduction

The automobile generator adopts claw-pole alternator generally, it is actually a sort of rotational generator, connected with piston by means of driving equipment. The driving equipment transits linear motion to rotational motion, providing power for the claw-pole alternator [1]. This kind of power generation system not only takes up much space, but also increases mechanical loss, decreases the efficiency of generator.

Linear motor is a kind of equipment for converting electrical energy into linear movement directly without any in-between transferring organization, and has many advantages such as simple structure, no abrasion, low noise, high accuracy, and easy to maintain etc. After a long-term exploration and experimental stages, linear motor has entered the practical commercial stage since the 1970s. The appearing of new kinds of magnetic material, control technology, and cooling method, creates a solid condition for the economical application of linear motor with high speed and high power.

In this paper, the form of automobile generator was changed, a new kind of generator—permanent magnet reciprocating generator was raised. The new generator was connected with piston directly, the driving equipment was leaved out, and the efficiency of generator was raised. The magnetic field was analyzed aiming at 1.1 kw prototype in this paper.

36.2 The Configuration and Operation Principle of Permanent Magnet Reciprocating Generator

The new-type generator was moving magnet, two-pole, single-phase, permanent magnetic oscillating generator, the generator is much different from the former generator in configuration and operation principle, Fig. 36.1 displays the configuration section of generator.

In virtue of mover's being connected with prime mover, when the generator was operated, the rotor would be oscillating, and the frequency of rotor was the same as the prime mover's, the speed was changing on the law of sine with the time's change. From the formula of $E = Blv$, to make E varied on the law of sine, one must be sinusoidal value between magnetic flux density B and speed v. As far as we know, normal generator generates sinusoidal power by means of the sinusoidal varying of B, but the generator researched in this paper generates sinusoidal power by means of the sinusoidal speed of rotor.
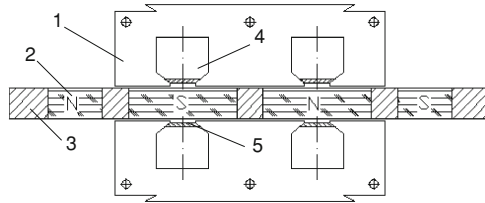
Fig. 36.1 The configuration of permanent magnet reciprocating generator In this figure, *1* represents stator of permanent magnetic oscillating generator, *2* represents permanent magnet of rotor, *3* represents aluminum rim of mover, *4* represents windings of the stator, *5* represents slot wedge of stator

## 36.3 The Magnetic Field Analysis of Reciprocating Generator

Permanent magnet reciprocating generator researched in this paper is a kind of double-side linear synchronous generator, owing to the longitudinal end effect of linear generator, the symmetry of electromagnetic field distribution in the generator was damaged, so the whole generator and the air around were taken as solution domain to solve with finite element method. According to the characteristics of generator and calculation requirement, some hypothesis were provided: (1) There is no circuit on the rotor. (2) The magnetic density along core lamination direction was constant. (3) The resistance of stator winding was ignored. (4) The load of generator was resistance. (5) The surface of stator core was smooth.

In the condition of ignoring eddy current loss, magnetic hysteresis loss in the core, the two-dimensional electromagnetic formula expressed with magnetic vector potential A as shows (Eq. 36.1):

$$\Omega : \frac{\partial}{\partial x}\left(\frac{1}{\mu}\frac{\partial A}{\partial x}\right) + \frac{\partial}{\partial y}\left(\frac{1}{\mu}\frac{\partial A}{\partial y}\right) = -J_z \quad (\forall p \in \Omega) \tag{36.1}$$

$$\Gamma : A = 0 \quad (\forall p \in \Gamma)$$

where A is magnetic vector potential, includes z component only, J_z is z component of current density J, μ is permeability, Ω is the whole solution domain, Γ is the external boundary of solution domain (AB, BC, CD, DA), p is a arbitrary point in solution domain.
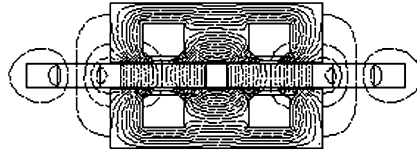
Fig. 36.2 The no-load electromagnetic field in generator is solved with FEM in this paper, so the distribution of vector potential *A* in solution domain can be obtained. When mover is at middle position, the distribution of magnetic lines in generator is illustrated in this figure

Fig. 36.3 It can be seem from the figure, the no-load EMF has dead-time at 0 and 10 ms moment, it is caused by the low speed when mover is at maximum displacement position
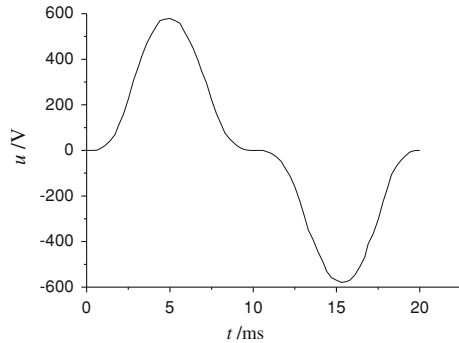
36.3.1 Calculation of No-load Electromotive Force and Synchronous Reactance

To calculate the no-load electromotive force, the flux that going through windings is solved, so according to the relationship between the no-load electromotive force *e* and linkage ψ (Eq. 36.2):

$$e = -\frac{d\psi}{dt} = -N\frac{d\phi}{dt} \qquad (36.2)$$

where N is winding turns and ϕ is the flux that going through windings.

Based on the configuration of generator, two-dimensional model is created, the vector potential is set to zero on the external boundary of the whole model assuming no flux outside the model. Then the model is solved with the finite element method (FEM), and the flux that going though windings when the mover is at any position will be calculated. Through changing the position of mover, the corresponding time is Δt, the change of the linkage when mover is at different positions can be solved [2] (Fig. 36.2).

It can be easy seem from Fig. 36.3 that the distribution of flux in stator teeth is uneven, solving the flux going through windings with air gap magnetic flux density is difficult, so the flux is solved with vector potential *A* [3]. The upper winding is

Fig. 36.4 In zone 1 of this figure, the EMF has large fluctuation, this because in the process of the generator operation, the ignition of gas engine varies the speed of mover sharply
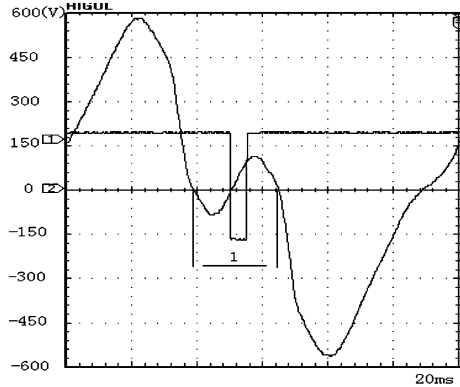
Fig. 36.5 The curve of electromagnetic force when no-load. It can be seem from the figure that the positive direction of electromagnetic force is defined to be opposite to the direction of mover speed
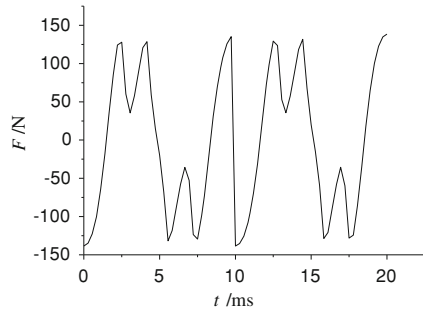
taken as an example, the average vector potential in the left and right slot is A_{z1} and A_{z2}, so the flux going through winding should be as follows (Eq. 36.3):

$$\phi = |A_{z1} - A_{z2}|l_{ef} \tag{36.3}$$

where l_{ef} is effective length of stator core in z direction.

By the analysis above, the virtual value of no-load EMF of the prototype is 334.1846 V, the result accords with design requirement. To verify the correctness of the result above, the no-load EMF curve of generator in a period is plotted according to the calculation result and compared to the curve from experiment, which are shown in Figs. 36.3 and 36.4, the wave from calculation to the wave from experiment are almost uniform except the fluctuation caused by ignition, so the accuracy of the analysis to the generator with FEM is proved.

In the process of generator running, because the mover of generator is linked with engine of automobile, if the engine rotates a period, the generator running a period ($T = 0.02\,s$) too. So the time that engine rotating 5° spends is taken as a time interval (the corresponding time is $\Delta t = T/72$) to solve the change of linkage.

Calculating stator inductance accurately is important to designing or analyzing generator. There are many methods to solve the inductance of generator, the energy method is adopted in this paper. Because the permeability of permanent-

Fig. 36.6 It is seen that the curve of electromagnetic force has large fluctuation, which could lead to quiver and yawp, affect the stability of generator. So decreasing the fluctuation of curve and making the curve smooth is important to designing generator
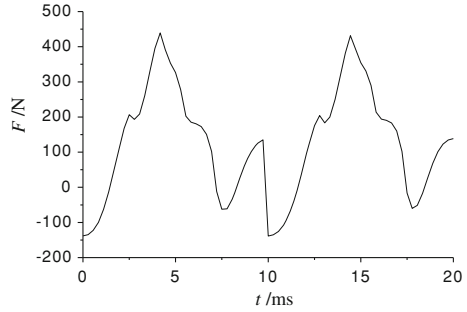
magnet and aluminum rim of mover is close to μ_0, and the aluminum rim is designed with special technology, the eddy current of rim is avoided, so the mover can be taken as air in the process of solving stator inductance. To calculate the inductance, the stator windings needs to be applied current density, after calculation, the magnetic energy W_m of the whole solution domain can be obtained (Eq. 36.4):

$$W_m = \frac{1}{2}L_1 I_1^2 + \frac{1}{2}L_2 I_2^2 + M I_1 I_2 \tag{36.4}$$

36.3.2 Electromagnetic Force

There are two methods to calculate electromagnetic force generally: Maxwell tensor method and virtual work method. The formula deduction and using of Maxwell tensor method are simple relatively, but it has larger error when adopting different element types or selecting different integral path. The virtual work method has more complex formula deduction, but it doesn't have problems of integral path and element types, so the method is adopted in this paper [4].

It is very convenient to compute electromagnetic force with virtual work method, as long as the boundary elements of solution domain are determined, the force of every element on mover can be computed in finite element program, then the electromagnetic force of mover is obtained by summing up the force of every element. The curve of no-load electromagnetic force is illustrated in Fig. 36.5.

When generator is loaded, the calculation of electromagnetic force is similar to no-load situation, the difference between them is that when generator is loaded, the magnetic field of air gap is induced by permanent magnets and stator current. So the current determined from the position of mover should be applied to winding. The curve of loaded electromagnetic force is shown in Fig. 36.6 [5].

36.4 Conclusion

The permanent magnet reciprocating generator used in automobile is designed based on the concept of thermal–mechanical-electric energy converting, owing to its special structure and operating principle, two-dimensional FEM is adopted to create the model of generator, calculate the no-load electromotive force, the inductance and electromagnetic force when generator is no-load and loaded. In the course of solving, the proper step is selected to sample time in a period, the operating parameter of generator is calculated at every step, so calculating the electromagnetic parameter in a period in static states field is realized.

The results from calculation is exactly like the data from experiment, the error is little, and avoid the problem that analyzing with transient states field costing much time. So the analysis in this paper provides available reference for latter designing, optimizing of permanent magnet linear synchronous motor.

References

1. Wang QJ, Ni YY (2007) Computation of magnetic fields and inductances of a claw-pole alternator under load conditions. Proc CSEE China 27(3):91–95
2. Tao G, Qiu A, Chai JY, Xiao X (2004) Analysis of magnetic field in permanent magnet synchronous servo motors. J Tsinghua Univ (Sci Technol) China 44(10):1317–1320
3. Sizov GY, Ionel DM, Demerdash NAO (2010) Modeling and design optimization of PM AC machines using computationally efficient-finite element analysis, Energy conversion congress and exposition, WI, USA
4. Dai W, Yu HT, Hu MQ (1996) Electromagnetic force computation of linear synchronous motor with virtual work method. Proc CSEE China 26(22):111–114
5. Lu RS, Wu WP, Ni ZH (2010) Development of permanent magnet probe for intravascular magnetic resonance imaging device. Bioinform Biomed Eng China 31(16):1–4

Chapter 37
Modeling and Vibration Control of Piezoelectric Stack Actuator in Adaptive Truss Structure

Kai Zheng, Zhiling Yang and Yiyong Yang

Abstract An adaptive truss structure with self-learning active vibration control system is developed. Some characteristics of the piezoelectric stack actuator, including displacement output and blocked force are evaluated under in-service conditions. A fuzzy-neural network (FNN) controller with adaptive membership functions is presented. Experiment of a two-bay truss structure is carried out and results show the effectiveness of the active truss structure.

Keywords Piezoelectric active member · Fuzzy neural network · Vibration control

37.1 Introduction

Piezoelectric actuators are widely used in high precision mechanical systems [1, 2], which have advanced features such as high resolution, quick response, compact size and good controllability. The adaptive truss structure integrated with piezoelectric active member is a new kind of structures and can be used in the huge spacecrafts. The technology on piezoelectric adaptive truss structure is expected to

K. Zheng (✉) · Z. Yang
School of Energy, Power and Mechanical Engineering, North China Electric Power
University (Beijing), Beijing 102206, China
e-mail: zkajiao@163.com

Z. Yang
e-mail: yzhil@ncepu.edu.cn

Y. Yang
School of Engineering and Technology, China University of Geosciences (Beijing), Beijing
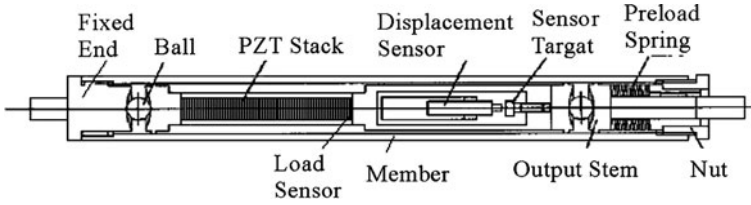100083, China
e-mail: YangYY@cugb.edu.cn

Fig. 37.1 Active member

solve the problems which are caused by space nonlinear disturbances such as vibration, precision location and shape retention [3].

In this paper, some characteristics of the piezoelectric stack are analyzed in order to determine fundamental properties important for design of the active members that incorporate the piezoelectric stacks. A fuzzy neural network (FNN) control scheme is described for the vibration suppression of adaptive truss structures.

37.2 Design of Piezoelectric Stack Actuator

Piezoelectric stack is used as an actuator to get a precision micro displacement, using converse piezoelectric effect. A typical piezoelectric stack actuator is formed by assembling several of the wafer elements in series mechanically and connecting the electrodes so that the wafers are in parallel electrically.

The output of the stack actuator is given by the following equation:

$$\delta_3 = n\left(s_{33}^E tF/A + d_{33}V\right) \tag{37.1}$$

where δ_3 is the axial strain, n is the layer number, s_{33}^E is elastic compliance matrix when subjected to a constant electrical field, t is the layer thickness of the piezoelectric ceramic, F is the applied force, A is the cross sectional area of the stack, d_{33} is the piezoelectric strain coefficient, V is the driven voltage.

Based on this equation, piezoelectric stack actuator and active member can be designed, shown in Fig. 37.1. Some parameters of the PZT stack are shown as follows: Cross sectional area of the stack, $A = 78.5$ mm^2; layer thickness, $t = 1$ mm; Number of the stack layers, $n = 108$; Material density, $\rho = 7.5 \times 10^3$ kg/m^3; Young's modulus, $E = 3.6 \times 10^{10}$ N/m^2; Piezoelectric coefficient, $d_{33} = 650 \times 10^{-12}$ m/V; Allowable applied voltage, $V_{max} = 1000$ V. The PZT stack works under conditions of the preload and cyclic electric loading, which expands and contracts with the applied voltage producing a relative motion between the two ends of the strut. A preload spring is added between the housing and the moving end of the stack to assure the ceramic never experiences tensile stresses, regardless of externally applied load. The stack is isolated from all bending moments by ball connections at both ends.

Fig. 37.2 Displacement hysteresis
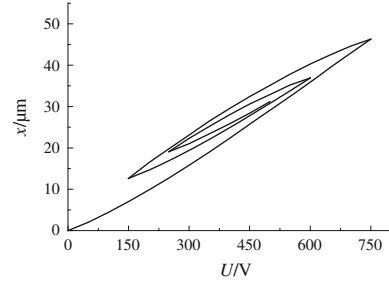
37.3 Model Formulation

To effectively incorporate piezoelectric actuators into demanding applications required of actuator systems, it's necessary to evaluate and understand the material's response under conditions simulating operating environments. The experimental set-ups are built to evaluate and understand the material's response under in-service conditions. The applied voltage is supplied by a WYG-1500 V DC high-voltage amplifier. For the dynamic tests, the drive signal is generated by a computer with a D/A, and amplified by using an HPV-3B0300A0500 piezoelectric drive power. The displacement output of the stack is obtained by a QH-8500 electric eddy sensor via a YE5937 displacement instrument, and then recorded by the computer. A PLS-S10 electro-fluid servo experimental machine is used to apply loads for the stack, and also senses output force of the stack caused by the applied voltage [4].

37.3.1 Displacement Output

For purposes of controller design, one of the most inconvenient aspects of the actuator behavior is the rate-independent hysteresis exhibited between voltage and displacement, as shown in Fig. 37.2. According to the actual design and application of the stack actuator, modified Preisach model is used to handle hysteresis. It has been shown that the classic Preisach model can be presented in the following mathematical form [5]:

$$x(t) = \iint_{\alpha \geq \beta} \mu(\alpha, \beta) \gamma_{\alpha\beta}[u(t)] \mathrm{d}\alpha \mathrm{d}\beta) \tag{37.2}$$

where $x(t)$ is the output displacement, $u(t)$ is the input driven voltage, $\mu(\alpha, \beta)$ is the Preisach weight function, α, β are the threshold of the "up" and "down" input voltage, the value of the elemental hysteresis operator $\gamma_{\alpha\beta}[u(t)]$ is between 0 and 1.

To derive the weighting function in terms of experimental data, another function $X(\alpha, \beta)$ is introduced:

$$X(\alpha, \beta) = x_\alpha - x_{\alpha\beta} \tag{37.3}$$

where $X(\alpha, \beta)$ represents the change in the output $x(t)$ as the input $u(t)$ changes from α to β.

To avoid the double numerical differentiation of the function $\mu(\alpha, \beta)$, which would amplify errors in the experimental data, two cases are needed to be considered separately.

For the case of monotonically increasing input u(t),

$$x(t) = \sum_{k=1}^{n} [X(\alpha_k, \beta_{k-1}) - X(\alpha_k, \beta_k)] + X[u(t), \beta_k] \tag{37.4}$$

For the case of monotonically decreasing input u(t),

$$x(t) = \sum_{k=1}^{n-1} [X(\alpha_k, \beta_{k-1}) - X(\alpha_k, \beta_k)] + \{X(\alpha_k, \beta_{k-1}) - X[\alpha_k, u(t)]\} \tag{37.5}$$

where $k, k - 1$ is the input history sequence.

Equations (37.4) and (37.5) provide the explicit numerical forms of the Preisach model that can be used to calculate the hysteresis response of a piezoelectric actuator $x(t)$ to an input sequence $u(t)$.

37.3.2 Blocked Force

In the design of active member, the pre-stress force F_o is applied by the internal spring K_i—the stack and the internal spring are compressed. External force F_1 is applied by compressing the series assembly—the stack is compressed and the internal spring will expand. When a positive voltage is applied, the stack will expand while still remaining in compression and the internal spring is compressed. The stress and strain in the stack under combined electro-mechanical load can be described by:

$$S_3 = \frac{(k_s + k_i)F_0 + k_sF_1}{k_s(k_s + k_i)L} + \frac{d_{33}Vk_s}{t(k_s + k_i)} \tag{37.6}$$

$$T_3 = \frac{F_0}{A} + \frac{F_1k_s}{A(k_s + k_i)} - \frac{d_{33}Vk_s}{s_{33}t(k_s + k_i)} \tag{37.7}$$

where t is the layer thickness, A and L are the cross sectional area and the initial length of the stack, k_s is the stack stiffness. Due to the presence of the internal spring, the force exerted on the actuator and read on the dial gauge F_2 will differ from the force manifested in the stack. The blocked force F_2 can be estimated by

$$F_2 = F_1 - \frac{Ad_{33}VK_s}{s_{33}t(k_s + k_i)} \tag{37.8}$$

Fig. 37.3 Comparison of experimental data and model prediction
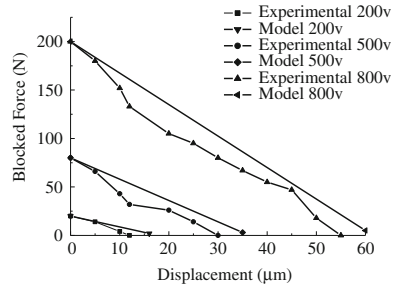
The blocked force calculated by the upper formulae shows a poor accuracy when compared with the experimental data (Fig. 37.3). The possible sources for the errors are: (1) neglecting the effects of the electrodes and resin; (2) material non-linearity properties.

37.4 Fuzzy Neural Network

Fuzzy neural networks are hybrid intelligent systems, which combine the advantages of both neural networks and fuzzy logic [6]. A five-layered fuzzy neural network (FNN) is presented to construct self-learning active vibration control system of adaptive truss structure with PZT active members. The structure diagram of the FNN with two inputs and one output is shown in Fig. 37.4.

Let x_{kj} be the ith input of the kth layer, net_{kj} and y_{kj} denote the input and the output of the jth node in the kth layer respectively, $y_{kj} = x_{(k+1)j}$. In the following, the physical meaning and the node functions of each layer will be explained.

The 1st layer is the input layer,

$$y_{1j} = net_{1j}, \ net_{1j} = x_{1i}, \ j = i \tag{37.11}$$

where x_{1i} is the ith input of the first layer, $i = 1, 2$

The 2nd layer is the fuzzification layer, which defines the fuzzy sets and membership for each of the input factors. Nodes in this layer acts as a membership function and represents linguistic term which uses Gaussian function as membership function, so these term nodes map input$x_i$onto their membership degree y_j by using the jth term node of x_i, i.e.,

$$y_{2j} = \exp\left(-\left(x_i - m_{ij}\right)^2 \big/ \sigma_{ij}\right) \tag{37.12}$$

where m_{ij} and σ_{ij} denote the mean and the width respect to the jth fuzzy set of the ith input respectively.
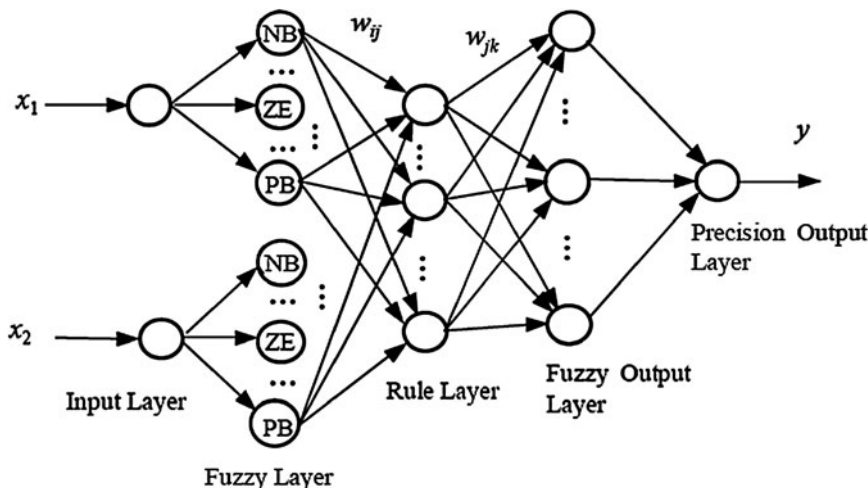
Fig. 37.4 Structure diagram of the FNN

The 3rd layer is the fuzzy rule layer that implements the related link for preconditions (term node) and consequence (output node). The jth output of the third layer is

$$y_{3j} = net_{3j} = \prod_{i=1}^{p} x_{3i} \qquad (37.13)$$

The 4th layer is the fuzzy output layer whose output is membership degree.

$$y_{4j} = \min\left(1, \sum_{l} x_{4i}\right) \qquad (37.14)$$

The 5th layer is the output layer, which performs the centroid defuzzification to get numerical output,

$$y_{5j} = net_{5j} \bigg/ \sum (\sigma_{ij} x_{5i}), net_{5j} = \sum w_{5ij} x_i = \sum (m_{ij}\sigma_{ij}) x_{5i}, \qquad (37.15)$$

where y_{5j} is the final output of the neutral net, and w_{5ij} denotes the weight value of the 5th layer, $w_{5ij} = m_{ij}\sigma_{ij}$.

An important topic in designing a fuzzy neural network is the identification of the fuzzy rules. The adjusted parameters in the FNN can be divided into two categories based on IF (premise) part and THEN (consequence) part in the fuzzy rules. The problem in designing fuzzy control systems is how to determine the free parameters of the fuzzy controller, i.e., rules and membership functions. Membership functions are used for the fuzzy input and output variables. We use the membership functions with seven linguistic variables (NB, NM, NS, ZE, PS, PM, PB),

Table 37.1 Fuzzy rules

A_i U_{ij} B_j	NB	NM	NS	ZE	PS	PM	PPB
NB	PB	PB	PB	PM	PM	ZE	ZE
NM	PB	PB	PB	PM	PM	ZE	ZE
NS	PM	PM	PM	PS	ZE	NS	NS
ZE	PM	PM	PS	ZE	NS	NS	NS
PS	PM	PS	ZE	NS	NM	NM	NM
PM	PS	ZE	ZE	NM	NM	NB	NB
PB	ZE	ZE	ZE	NM	NM	NB	NB

which represent negative big, negative medium, negative small, zero, positive small, positive medium, and positive big, respectively.

The fuzzy rules in Table 37.1 shows:

$$IF\ (x_1\ is\ A_i\ and\ x_2\ is\ B)\ then\ (y\ is\ U_{ij}), \quad i.j = 1, 2, \ldots 7 \tag{37.16}$$

where x_1 and x_2 are inputs of the controller, and y is output of the controller; A_i and B_j are the antecedent linguistic values for the ith and jth rule respectively, and U_{ij} is the consequent linguistic values.

The training set consists of input vectors and corresponding desired output vectors. The output of the as

$$E = (y_d - y_{51})^2 \big/ 2 \tag{37.17}$$

where y_d and y_{51} are the desired and actual outputs of the FNN.

The error signals are propagated backward from the 5th layer to the 1st layer in order to align themselves with the error signals. The controller weights are updated according to

$$w(t + 1) = w(t) - \eta \partial E / \partial w \tag{37.18}$$

where η is the learning rate which is generally between 0.01 and 1, and

$$\frac{\partial E}{\partial w} = \frac{\partial E}{\partial net} \cdot \frac{\partial net}{\partial y} \cdot \frac{\partial y}{\partial w} \tag{37.19}$$

The training continues until the error is within acceptable limits. After the identifier is sufficiently trained, the dynamic behavior of the identifier is close to that of the structure. They can be scaled into the range of −6 and +6 with equal span. For the vibration suppression of the truss structure, the Gaussian function is employed as initial membership function, shown in Fig. 37.5. Forty-nine fuzzy rules based on the displacement or acceleration and the difference in subsequent time are shown in Table 37.1. The training set consists of input vectors and corresponding desired output vectors. The output of the neuron is a function of the total weighted input. The membership functions are tuned by the delta rule.
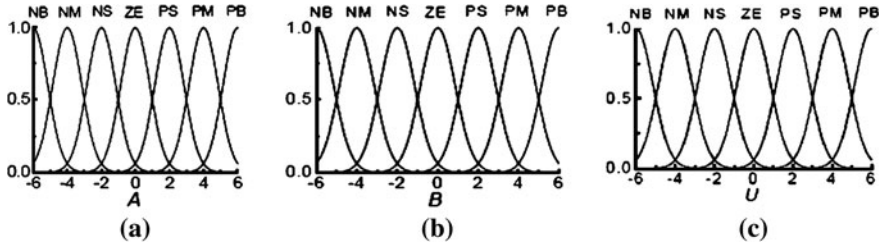
Fig. 37.5 Fuzzy input and output membership functions. **a** Input *A*. **b** Input *B*. **c** Output *U*

**Fig. 37.6** Experimental
setup

37.5 Vibration Control Experiment

The active vibration control experiment is conducted. The experimental setup and
a two-bay truss structure are shown in Fig. 37.6. Two active members are posed as
a diagonal brace of each bay truss for vibration control.

The FNN controller is applied to the truss vibration suppression. The FNN
controller first senses the output of the accelerometer as an error to activate the
adaptation of the weights of the controllers. Then a control command signal is
calculate based on the FNN inference mechanism to drive the active members.

The BP algorithm with learning rate $\alpha = 0.02$ and $\beta = 0.02$ is used to train the
FNN for obtaining weight value of the nodes. The sampling frequency is selected
as 1 kHz. An impulse force excitation is given at the node B of the truss, and two
active members are used to control vibration of the truss. Figure 37.7 shows the
acceleration responses at the node A of the truss in the time domain. As expected,
the amplitude of vibrations decreases significantly by using the closed-loop control
with the FNN. The stable times of vibration amplitudes for pen-loop (uncon-
trolled) and closed-loop control are about 0.3 s and 0.1 s respectively under an
impulse excitation. It can be seen that the controller provides excellent damping.
We have also swiped the excitation frequency to examine the adaptation capability
of this control system. The controller of the adaptive truss structure offered the
similar performance for different frequency disturbance.

Fig. 37.7 Time response.
a Open-loop. **b** Closed-loop
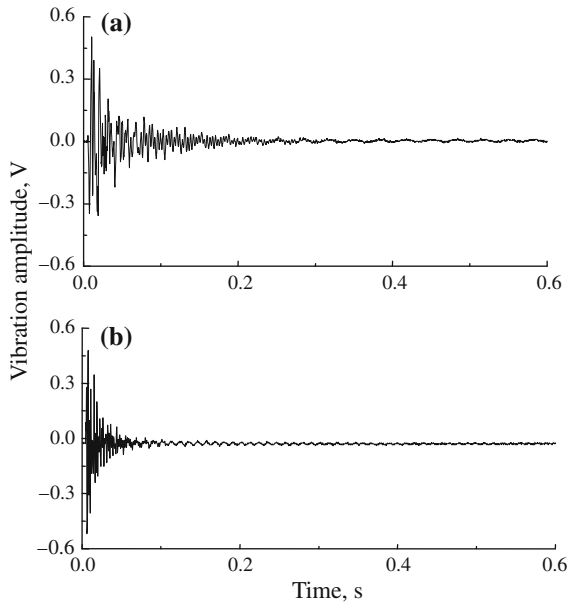
37.6 Conclusion

In this paper the design of active member used in adaptive truss structure is presented. Some characteristics, displacement output and blocked force are evaluated under in-service conditions. A modified Preisach model is presented to evaluate the displacement output of the stack actuator. A FNN controller is designed for active vibration control applications. The active vibration control experiments validated the application of the truss structure with the active members.

References

1. Mazeika D, Bansevicius R (2009) Study of resonant vibration shape of the beam type piezoelectric actuator with preloaded mass. Mechanika 2(76):33–37
2. Lucinskis R, Mazeika D, Hemsel T, Bansevicius R (2010) The experimental research of piezoelectric actuator with two vectors of polarization direction. Mechanika 2(82):50–57
3. Yan SZ, Zheng k, Xun J (2007) Mechanical properties of piezoelectric stack actuators under electro-mechanical loading. Key Eng Mater 336:331–334

4. Yan SZ, Zheng K, Li YM (2005) Vibration suppression of adaptive truss structure using fuzzy neural network. Lecture Notes in Computer Science, pp 155–160
5. Ping G, Jouaneh M (1995) Modeling hysteresis in piezoceramic actuators. Precis Eng 17: 211–221
6. Chen YJ, Teng CC (1996) Rule combination in a fuzzy neural network. Fuzzy Sets Syst 2:161–166

Chapter 38
Modeling of Human Balance Process and the Application in Evaluation

Jinzhuang Xiao, Hongrui Wang, Kun Liu and Xincai Yang

Abstract Focusing on personal balance ability evaluation, a method was developed to improve the dependency to many uncertainties, and to enhance veracity and objectivity, where impulse disturbance for human gravity center was produced by a six degree-of-freedom motion platform of 6-PSS under feet, and corresponding wave of gravity center was measured by a force plate real time. Dynamic process of overcoming this disturbance was abstracted as classic second-order linear model, where the product of damp coefficient and undammed circular frequency was estimated through recorded data based on system identification theory. By using this value, settling time was calculated and used as the balance evaluating index. Through the evaluating results of 100 students, the feasibility of this method was validated, and reference ranges of healthy persons' settling time were concluded for clinical balance evaluation.

Keywords Stroke · Balance evaluation · Passive motion · 6-DOF robot

J. Xiao (✉) · H. Wang · K. Liu
College of Electric and Information Engineering, Hebei University,
071000, Baoding, China
e-mail: robot@hbu.edu.cn

H. Wang
e-mail: hongrui@hbu.edu.cn

X. Yang
Affiliated Hospital of Hebei University, 071000, Baoding, China
e-mail: yxcyxc8866@sina.com

38.1 Introduction

Stroke is one of the most important sources leading to disability. It has the frequency of 1.75% every year, and may happen in any age including children [1, 2]. More than 70% survivals from stroke coupled with injury of sensor, motion, cognition and sentiment, which limited their activities of daily living (ADL). Loss of posture control ability influences independent living most severely [3], and it happens with the frequency of 580 times every year per 100 patients during rehabilitation after stroke. Balance ability is defined as the ability of keeping the gravity center successfully in a special supporting space [4]. In order to improve the quality of life, it is necessary to give a objective and quantitative assessment, with which better treatment options are formulated and the rehabilitation time is cut way back [5].

In clinic application, Berg Balance Scale (BBS) is treated as popular reliable method for evaluating potential fall risk [6]. However, this method was often used to measure elder's balance ability, not applied to stroke patient, and discrimination of the results is not distinct [7]. On the other hand, the valuation results mostly rely on the experience of medical doctor [8].

Force plate is deemed to be the better clinical instrument to assess balance ability [1, 9], from which little force exerted by human body could be measured and displayed real time. This measurement process depends on how much patient brings pressure to bear on force plate, and the results are often affected by many random actions of patient, for example, moving gravity center to one foot. This makes the evaluating indicators have big degree of dispersion [10].

In this paper, the thought of passive motion assessment was introduced, where a six-degree-of- freedom(6-DOF) motion platform was used as pseudo pulse excitement for human visual, proprioception and vestibular organ. System identification theory was used to build the dynamic response model. In this process, the model was approximately treated as classic linear differential equation with order two. Then the settling time could be calculated through its coefficients and regarded as the assessment of evaluation balance.

The rest of the paper is organized as follows. In Sect. 38.2, a balance assessment system is developed, and its basic principle is presented in Sect. 38.3. Detailed evaluation process and results are illuminated in Sect. 38.4. At the end of the paper, some concluding remarks are summarized in Sect. 38.5.

38.2 Construction of Modeling System

In order to get more impersonal assessment result, passive motion thought was adopted in this research; from which human balance capability was evaluated quantificationally. Its construction is presented in Fig. 38.1.

Force plate

6-DOF
motion platform
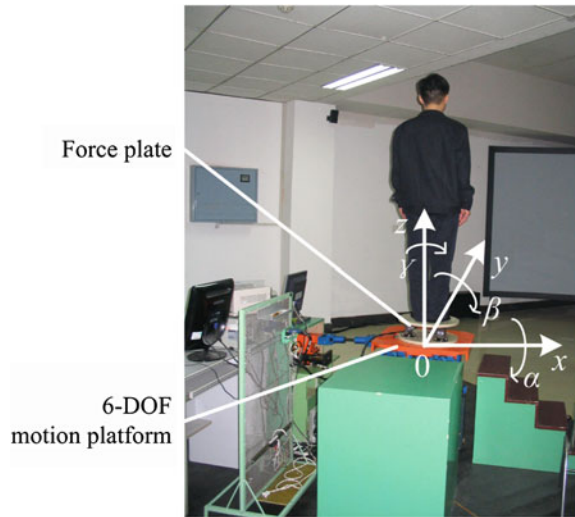
In this system, force plate is consisted of three force strain sensors, which are mounted on bottom plate, data acquisition is performed by special computer-centered software and AD card, impulse from multi different directions are carried out by a six-degree-of-freedom(6-DOF) parallel motion platform, evaluated person stands on force plate. 6-DOF platform outputs desired position steps in space. Under this impulse, person GC is disturbed suddenly because of feet friction, instinct of cerebra would try to adjust person GC to origin of force plate, and adjusting process would reflect body balance ability.

38.3 Basic Modeling Principle

Under enough high bandwidth position or angle impulse, GC is deviated suddenly, as one kind of object, human body would adjust its GC to origin. This process could be abstracted as a dynamic model which reflects body's balance ability. Profiting from the basic property, this research imposes impulse to human feet through 6-DOF motion platform. COP is transformed to voltage signals by force plate, and recorded by computer real time. Dynamic model is built through normal identification method. Then settling time is calculated basing on its coefficients, and used as the index of evaluating balance ability.

Under many times of test and analyses, the dynamic adjusting process could be concluded as a linear under damped second-order model approximately. Figure 38.2 shows an example. When a person is standing on the equipment, he/her is excited by impulse with amplitude of 15 mm; COP signal is recorded and drawn.
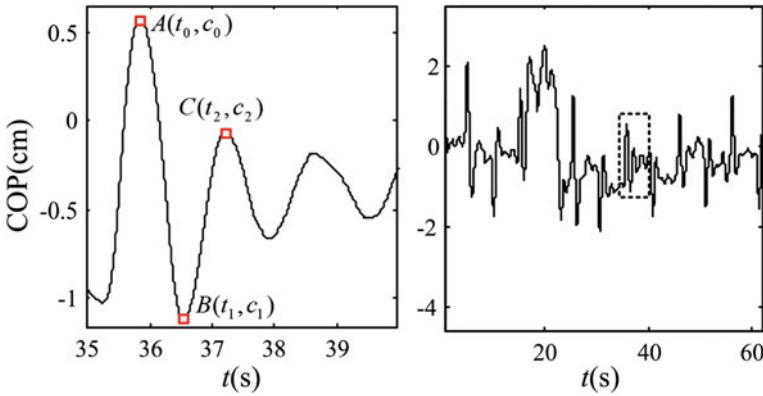
Fig. 38.2 Adjusting process of COP

With this conclusion in mind, classic response rules of second-order system could be applied to this research. By calculating the settling time of $\pm 2\%$ to steady-state, balance ability could be evaluated quantitatively. It means how long the person adjusts his gravity center to midpoint of his feet under this disturbance. Intuitively, shorter time indicates better balance ability.

Following equation is the unit impulse response function of classic second-order linear model in time domain:

$$c(t) = \frac{\omega_n}{\sqrt{1-\zeta^2}} e^{-\zeta\omega_n t} \sin(\omega_n\sqrt{1-\zeta^2}t), \tag{38.1}$$

where ω_n is undammed natural oscillation angular frequency, ζ is damping coefficient. According to systemic knowledge, settling time could be defined by the response period from start to entering the region of $\pm 2\%$ to steady-state, the approximate formula is

$$T_s = \frac{4}{\zeta\omega_n}. \tag{38.2}$$

According to formula (38.1), settling time could be calculated through typical data points in response curve. Considering the actual aspect that steady-state may deviate from the origin of COP, that is standing person transfers his origin GC to one foot, the first peak value is supposed as C_0. In Fig. 38.2, the first three poles are denoted as $A(t_0, c_0)$, $B(t_1, c_1)$ and $C(t_2, c_2)$ respectively in every curve. Then damped oscillation period is

$$T = 2 \cdot \pi \Big/ \left(\omega_n\sqrt{1-\zeta^2}\right) = t_2 - t_0. \tag{38.3}$$

So, time $t_1 = t_0 + (t_2 - t_0)/2$ and $t_2 = t_0 + (t_2 - t_0)$ could be calculated. At the three points, following three equations are satisfied

$$\frac{\omega_n}{\sqrt{1-\zeta^2}} e^{-\zeta\omega_n t_0} = (c_0 - C_0), \tag{38.4}$$

$$\frac{\omega_n}{\sqrt{1-\zeta^2}} e^{-\zeta\omega_n(t_0+(t_2-t_0)/2)} = (C_0 - c_1), \tag{38.5}$$

$$\frac{\omega_n}{\sqrt{1-\zeta^2}} e^{-\zeta\omega_n(t_0+(t_2-t_0))} = (c_2 - C_0). \tag{38.6}$$

So,

$$\zeta\omega_n = -2\ln M/(t_2 - t_0), \tag{38.7}$$

where $M = (c_2 - c_1)/(c_0 - c_1)$.

Substituting formula (38.7) to (38.2), settling time could be calculated by

$$T_s = -2(t_2 - t_0)/\ln M, \tag{38.8}$$

which is treated as the assessment formula of evaluating balance ability.

38.4 Modeling and its Application in Evaluation Balance

In order to test the feasibility of described equipment and method, 100 students were as samples participated in application process.

38.4.1 Excitement and Data Recording

They were ordered to stand on the center of force plate with two legs, close their eyes, open legs to 45° with closed heels, just as shown in Fig. 38.1. Considering the balance between affordability and better exciting results, everyone received impulse excitation from straight-line motion along axis x with the amplitude of 15 mm. The period was settled at 10 s. After measuring and storing the data of COP to hard disk real time, everyone's data is ready to be analysis off line. Just as that shown in the right half part of Fig. 38.2.

38.4.2 Settling Time Calculation and Application

In testing process, results were affected by many factors, for example, they moved their GC to one foot intentionally, or their mind strayed from this matter, which made the results show nonlinear performance occasionally. So we ordered them to keep their GC to the center of force plate at any time, excited them many periods,
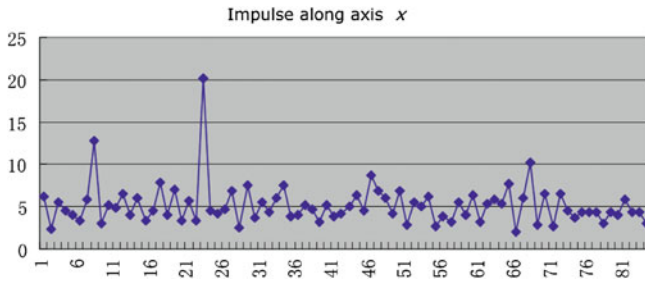
Fig. 38.3 Distribution of normal person's settling time

and looked for a graph with naked eyes which had better approximation to second-order linear response.

By using formula (38.8), settling time of different person under excitement along axis x was calculated and dotted in Fig. 38.3, where vertical axis indicates the settling time with second unit. Samples those are out of the above ranges mean abnormal or needing assessment again. The result indicates the consistence of the evaluating process, which ensures the credibility. And from it, we could conclude the normal settling time range for healthy person.

38.5 Conclusion

According to the basic response principle of person balance adjusting process, this research approximated its dynamic model as classic second-order linear one. Under impulses excitement along axis x, balance adjusting process was recorded. System identification theory was applied to calculate the settling time of dynamic process, which could be treated as the index of evaluating balance ability. Based on amount of experiments, feasibility of this method was tested and verified, normal range of healthy person was concluded at the same time.

Because excitement of the motion platform could have very high accuracy and repeatability, and it's based on passive motion, which weakens the randomness of person, this method would be more credible.

References

1. Geurts ACH, de Haart M, van Nes, IJW, Duysens J (2005) A review of standing balance recovery from stroke. Gait Posture 22:267–281
2. Warlow CP, Dennis MS, van Gijn J (2001) Stroke. Blackwell Publishers, London
3. Olsson E, Löfgren B, Gustafson Y, Nyberg L (2005) Validation of a fall risk index in stroke rehabilitation. J Stroke Cerebrovasc Dis 14:23–28
4. Matsumura BA, Ambrose AF (2006) Balance in elderly. Clin Geriatr Med 22:395–412

5. Yelnik A, Bonan I (2008) Clinical tools for assessing balance disorders. Neurophysiol Clinique/Clin Neurophysiol 38:439–445
6. Berg KO, Maki BE, Williams JI, Holliday PJ, Wood-Dauphinee SL (1992) Clinical and laboratory measures of postural balance in an elderly population. Arch Phys Med Rehabil 73:1073–1080
7. Berg K, Wood-Dauphinee S, Williams J, Maki B (1992) Measuring balance in the elderly: validation of an instrument. Can J Public Health 83:7–11
8. Fugl-Meyer A, Jaasko L, Leyman I, Olsson S, Steglind S (1975) The post-stroke hemiplegic patient. 1: a method for evaluation of physical performance. Scand J Rehabil Med 7:13–31
9. Browne JE, O'Hare NJ (2001) Review of the different methods for assessing standing balance. Physiotherapy 87:489–495
10. Jayne Garland S, Ivanova TD, Mochizuki G (2007) Recovery of standing balance and health-related quality of life after mild or moderately severe stroke. Arch Phys Med Rehabil 88:218–227

Chapter 39
Improving the Sensitivity of Winding Deformation Detection by Using Nanosecond Pulses

Xiao Lei, Jian Li, Hualin Liu and Youyuan Wang

Abstract Theoretically, the sensitivity of the transfer function (TF) method to detect transformer winding deformation is greater in the higher frequency range. Although measurement based on low voltage impulse (LVI) is definitely faster than that based on swept frequency method (SFM), the analyzable frequency band is narrow due to the typical microsecond impulse. The characteristics of the nanosecond impulse in the frequency domain were studied in this paper. A test System based on Nanosecond low voltage impulse was developed to improve the detection sensitivity. A series experiments were carried out on a 5 kV/100 kVA distribution transformer. Measurement results with two different impulses were compared and de-noising methods were studied. Besides, a destructive experiment was carried out on an special laboratory winding to verify the sensitivity of the method.

Keywords Monitoring · Winding deformation · Transfer function · Nanosecond pulses

X. Lei (✉) · J. Li · Y. Wang
State Key Laboratory of Power Transmission Equipment & System Security and New Technology, Chongqing University, Chongqing, China
e-mail: leixiao@cqu.edu.cn

J. Li
e-mail: lijian@cqu.edu.cn

H. Liu
Guizhou Electric Power Testing Research Institute, Guiyang, China

39.1 Introduction

Power transformers are supposed to be the most important and expensive equipments in power generations and transmission systems. Failures of transformers will cause catastrophic damages to power supply and significant economic loss to electric power companies. Tremendous forces generates in windings when a powerful short circuit current flows into a power transformer [1], which can cause deformation and displacement of the windings. Besides, mechanical vibrations during transport may also lead to these defects [2].

Generally, minor deformations do not destroy transformer winding immediately. But the insulation defects of the deformed parts will become more and more serious. As a consequence of ageing processes, the mechanical endurance and the insulation performance of oil-paper insulation system is considerably decreased [2]. In addition, the deformed part of winding may face asymmetric forces due to the irregular shape when the next short circuit current comes, which may make the shape more irregular. Therefore, it is greatly meaningful to develop the diagnostic technology to monitor winding deformation.

The transfer function (TF) method has been widely researched and used in many counties since Dick and Erven proposed this method in 1978 [3]. Considering the transformer winding as a two-port network, the TF can be obtained by measuring voltages and currents in time domain or frequency domain at the two ends [4–7]. Deformation and displacement can be found by comparing the TF with the reference fingerprints, since TF is mainly determined by the geometrical construction. It has been proved that the sensitivity increases in the higher frequency range [8]. Two approaches are proposed to obtain the TF: swept frequency method (SFM) and the low voltage impulse method (LVI) [9]. Compared to the SFM, the duration of measurements is much shorter for LVI, which is only a few seconds. In addition, several transfer functions can be measured simultaneously. However, the signal to noise ratio and the measurement bandwidth is limited by the typical impulse, whose parameters are front-times of 200 ns to 1μs and times to half-value of 40 to 200 μs [10].

In this paper, an improved LVI was introduced, in which nanosecond impulse generator was used to extend the frequency range. Effects of impulses with different parameters were studied, and de-noising methods were proposed. In order to verify its feasibility and sensibility, a destructive experiment was carried out on a purpose-made laboratory winding.

39.2 Theory Background

39.2.1 Principle of the Low Voltage Impulse Method (LVI)

The test winding of the transformer is excited by low impulse voltages at one of its ends. Any transient voltage and current at the two ends can be recorded. The frequency spectrum of the time domain signals is calculated by using Fast Fourier

Transform (FFT). Since the winding can be represented by a two-port network, a group of transfer functions can be calculated using the voltages and currents according to:

$$H(f) = \frac{R(f)}{V_i(f)} \tag{39.1}$$

Where $V_i(f)$ is the supply voltage, $R(f)$ can be voltage or current response at any port of transformer windings.

39.2.2 Characteristics of Impulse in Frequency Domain

Generally, the data acquired by the digitizer recorder bears the quantization error. As signals with quantization error are converted into their frequency spectrum by using FFT, the analyzable frequency band will become narrower. When signal value is smaller than the noise level in the frequency domain, information in these frequencies is lost. One method of extending the frequency range is to improve the frequency spectrum of the impulse. The shorter and sharper impulses are, the broader frequency spectrum it generates [11].

Figure 39.1(a) shows two different nanosecond impulses contaminated by noises. The parameters of impulse are front time of 5 ns and 50 ns, times to half-value of 50 ns and 200 ns. Amplitude of both impulses is about 800 V. Noise is made to be about 4 V, which simulates the situation of using an 8-bit digitizer. Figure 39.1(b) illustrates the normalized spectrum of the two impulses in the range of 0~80 MHz. Impulse a, whose rise time and duration time are shorter, has a boarder frequency spectrum. Although impulse b has sufficient energy in lower frequencies, it drops to the noise level radically.

39.3 Experiment Study

39.3.1 Experiment Setup

The end-end transfer voltage ratio is used as TF in this paper, and the measurement setup is shown in Fig. 39.2. Resister R1 and R2, which are 50 ohm, are connected at the two ends of the test winding. Voltage on R1 and voltage on R2 are used as $V_i(f)$ and $R(f)$ in the formula 1. In order to avoid oscillation, all measuring cables are terminated with matching impedance of 50 ohm.

The experiment was carried out on a 5 kV/100 kVA distribution transformer. It has a high voltage winding with 39 continuous discs and a two layer concentric low voltage winding. Two nanosecond impulse generators were made for this study. One is able to produce 5 ns rise-time, 50 ns wide, 1 kV amplitude pulses, while the other one can generate 30 ns rise-time, 150 ns wide, 1 kV amplitude
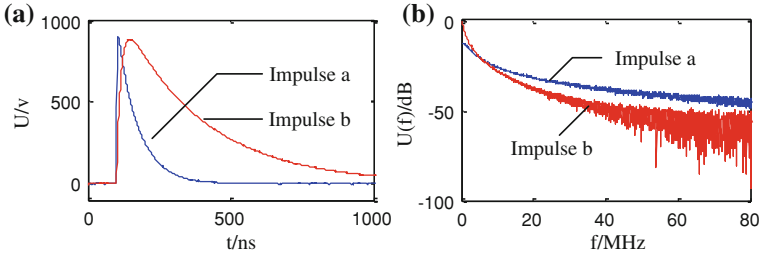
Fig. 39.1 Two nanosecond impulses made by Matlab: **a** in the time domain; **b** in the frequency domain

Fig. 39.2 Connection of measurement system
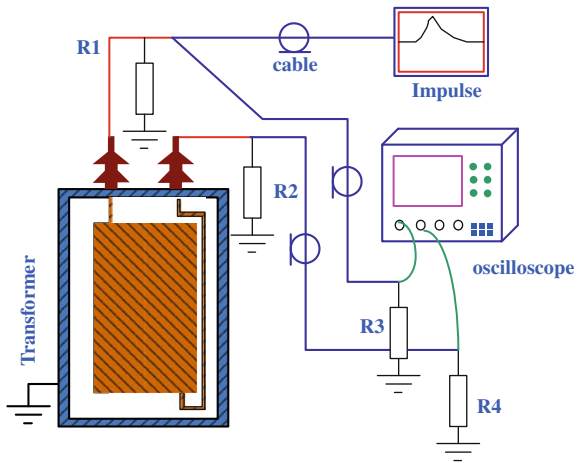
pulses. all these parameters are measured when the load is a 50 ohm resister. An 8-bit oscilloscope, LeCroy WAVERUNNER 44XI was used to record experiment data.

39.3.2 Impact of Impulses

The shape of nanosecond impulses will change when transformers are connected, since the winding of transformer is a complex load for impulse generator. The HV winding was excited and voltages at the line-end and earth-end were recorded. The parameters of the two impulse are tabulated in Table 39.1.

According to Nyquist theorem, sampling rate fs should be at least twice high as the highest frequency of the signal, which means a sampling rate of 200 MS/s is required. In this measurement sampling rate is set to 1 GS/s. As the signal length was chosen to be 1 ms, in which all useful information is contained, complicated

Table 39.1 The parameters of two impulses

Impulse	Rise time (ns)	Times to half-value (ns)	Amplitude (V)
c	10	60	450
d	50	200	450
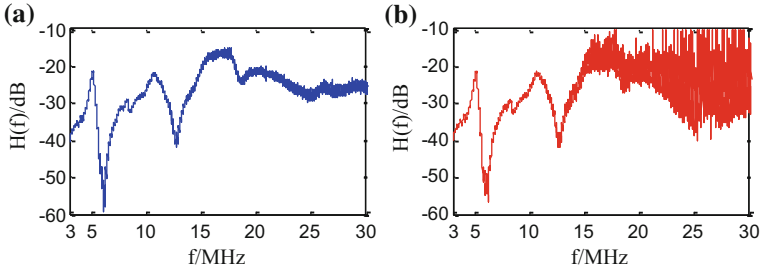
Fig. 39.3 Transfer function of the HV winding. **a** using impulse c; **b** using impulse d

windowing functions are not necessary. Besides, a simple process was done by averaging 32 measurement results. Figure 39.3 shows the results of measurement with the two impulses. It shows a good agreement in the lower range of frequencies. Performance gets worse when it comes to higher frequencies. Result of measurement with impulse d is considered to be useless beyond 15 MHz as shown in Fig. 39.3b.

39.3.3 De-noising of the Measurement

Noise not only narrow the analyzable frequency band, but also reduce the sensitivity. Thus, de-noising is one of the most important step in data processing. Noise mostly results from quantization error, and the contaminated signal can be expressed as:

$$y(t) = x(t) + e(t) \tag{39.2}$$

Where $x(t)$ is the signal and $e(t)$ is the quantization noise. According to the principle of FFT, single in frequency domain can be expressed as :

$$Y(f) = X(f) + E(f) \tag{39.3}$$

Generally, quantization noise is considered to be uniformly distributed, and its mathematical expectation is zero. Definitely, averaging multiple measurements of the same quantity is an efficient de-noising method.

The other way efficient way to increase the signal to noise ratio is to reduce the length of the digital record. The nanosecond impulse and its response only exist in a very short time, while the noise appears randomly and uniformly along the whole
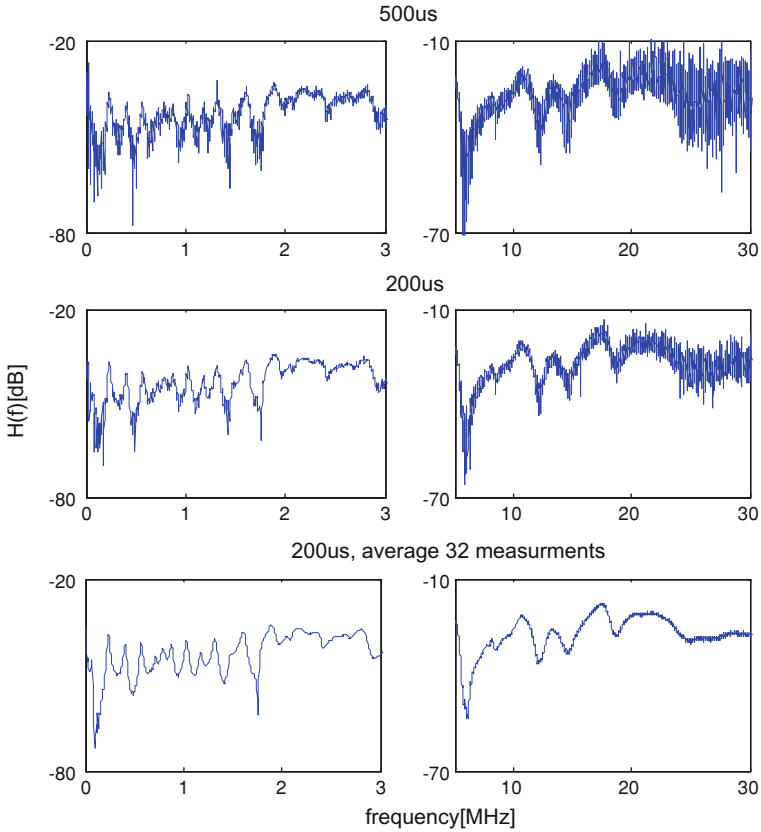
Fig. 39.4 Effects of shortening the time window and averaging 32 measurements

record. Energy of the noise will fall down when the time window become smaller. However, the length of the record can not be cut down excessively, otherwise it would create spectrum leakage.

Figure 39.4 illustrate the effects of de-noising methods while the impulse c was used in the measurement. In order to show the effects clearly, transfer function in two ranges of frequencies, 0–3 MHz and 5–30 MHz, are drawn respectively. Shortening the time window and averaging 32 measurements both have a marked effect in the whole spectrum.

39.4 Destructive Experiment

In order to verify that using the nanosecond pulse can improve the measurement sensitivity, a destructive experiment was carried out on a purpose-made laboratory winding which has 18 continuous discs, 10 turns in each disc. The winding is

Fig. 39.5 The laboratory winding and the deformed discs

Fig. 39.6 Transfer function of the original winding and the deformed winding
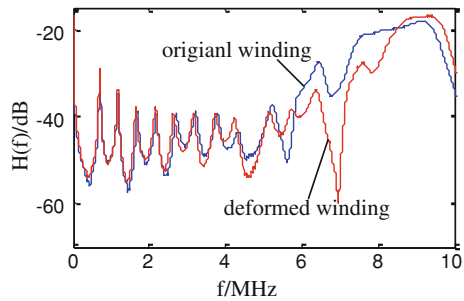
placed in a cylindrical metal tank, whose diameter is 8.5 cm bigger. The design of the test object is based on following two considerations:

- Iron core acts as an earthed boundary in the high frequencies, and have little impact on the condition of electromagnetic field. Since the distance between the tank and the winding is very short, it is not necessary to have a iron core.
- Considering the enormous cost, it is almost impossible to distort or displace windings of power transformers. This experiment aim at studying the improvement made by the nanosecond pulse, rather than interpreting the frequency response. Thus, a small winding can achieve the objective.

Since every two discs are connected by screws, it is convenient to disassemble, deform, and replace each disc of the winding. In the experiment, the 7th and the 8th discs were distorted to medal the radial deformation. Fig. 39.5 shows the winding and the deformed discs.

Impulse c was used in this measurement, and the transfer functions of original winding and deformed winding are shown in Fig. 39.6. As a single continuous winding, the transfer function is *characterized* by a series of "peaks" and "troughs" [12]. The two transfer funtions below 3 MHz are too similar that it can't diagnose the deformation. However, transfer functions above 3 MHz show a big difference from each other. The nanosecond impulse improves the sensitivity by

extending the frequency range because TF is more sensitivity to winding deformations in the high frequencies.

39.5 Conclusions

By studying the characteristics of different impulses in frequency domain, this paper develops a improved low voltage impulse method for monitoring winding deformation of power transformer. The typical microsecond impulse (0.2/40 μs) are replaced by the nanosecond impulse. This proposed measurement method is applied to a 10 kV/100 kVA distribution transformer in the laboratory. The results of measurement with two different impulses are compared. The investigation shows that a broader analyzable frequency band can be obtained by using impulses with sharper rise-time and shorter duration. Simple de-noising methods, shortening the time window and averaging multiple measurements, improve the signal to noise ratio dramatically. Besides, the destructive experiment carried out on a laboratory winding verifies that improved low voltage method has a better sensitivity.

Some factors may affect the measurement result in the high frequencies, including grounding connection, cable and bushing. These factors should be studied in the future work.

References

1. Sarkar S (2001) The performance advantages of circular windings. Electricity Today 5:33–35
2. Florkowski M, Fural J (2003) Detection of transformer winding deformations based on the transfer function-measurements and simulations. Meas Sci Technol 14:1986–1992
3. Dick EP, Erven CC (1978) Transformer diagnostic testing by frequency response analysis. IEEE Trans Power App Syst PAS-97(6):2144–2153
4. Jayasinghe JASB, Wang ZD, Jarman PN, Darwin AW (2006) Winding movement in power transformer: a comparison of FRA measurement connection methods. IEEE Trans Dielectr Electr Insul 13(6):1333–1349
5. Rahimpour E, Christian J, Feser K, Mohseni H (2003) Transfer function method to diagnose axial displacement and radial deformation of transfer windings. IEEE Trans Power Deliv 18(2):493–505
6. Abeywickrama KGNB, Serdyuk YV, Gubanski SM (2006) Exploring possibilities for characterization of power transformer insulation by frequency response analysis (FRA). IEEE Trans Power Deliv 21(3):1375–1382
7. Ragavan R, Satish L (2005) An efficient method to compute transfer function of a transformer from its equivalent circuit. IEEE Trans Power Deliv 20(2):780–788
8. Wang M, John Vandermaar A, Srivastava KD (2005) Improved detection of power transformer winding movement by extending the FRA high frequency range. IEEE Trans Power Deliv 20(3):1930–1938
9. Tenbohlen S, Ryder SA (2003) Making frequency response analysis measurements: a comparison of the swept frequency and low voltage impulse methods. In: XIIIth international symposium on high voltage engineering, The Netherlands

10. Feser K, Christian J, Neumann C, Sundermann U, Leibfried T, Kachler A, Loppacher M (2000) The transfer function method for detection of winding displacements on power transformers after transport, short circuit or 30 years of service. CIGRE paper 2000, 12/33-04
11. Hualin L, Yinbo Z, Xiao L, Youyuan W, Huarong Z, Jian L (2012) Monitoring of winding deformation of power transformer by using nanosecond pulses. In: the 4th International Conference on Measuring Technology and Mechatronics Automation, Sanya, China
12. Wang ZD, Jie Li, Dahlina M (2009) Interpretation of transformer FRA responses-part I: influence of winding structure. IEEE Trans Power Deliv 24(2):703–710

Chapter 40
Multi-Document Automatic Summarization Based on the Hierarchical Topics

Yong-Dong Xu, Fang Xu, Guang-Ri Quan and Ya-Dong Wang

Abstract A concept of is proposed for multi-document automatic summarization task, which used multi-layer topic tree structure to represent the text set. Each node in the topic tree represent specific topic and contains multiple similar sentences in the text set. The structure may describe accurately the similarity between sentences at different levels of granularity. Therefore it can reflect the real content of the text set than single layer topic set. And can be used to find the important sentences in the important topic which can compose the summary of the text set. Concretely, a series of algorithms including building tree, key sentences extraction based on tree and summarization generation are proposed. The capability of summarization system is testified by sets of experiments and shows good result.

40.1 Introduction

With the rapid growth of the Internet, the massive amounts of information make it more difficult to efficiently access the usable information. Thus, the ability to automatically compress the information covering multiple documents and present the summary to the users would help to solve this problem and in fact, has received a great deal of attention in recent research.

Y.-D. Xu (✉) · F. Xu · G.-R. Quan
Harbin Institute of Technology at WeiHai, Wei Hai, China
e-mail: ydxu@insun.hit.edu.cn

Y.-D. Wang
Harbin Institute of Technology, Harbin, China

Because the multi-document automatic summarization system should have the ability to identify the general topic of the entire set rather than the topic of each text in the set [1], thus topic identification is an important technology in multi-document automatic summarization. Some researchers used text units clustering technique, including paragraphs-level clustering [2, 3, 4], sentences-level clustering [5, 6, 7], to achieve information fusion. The idea of methods is built on the hypothesis that because these articles describe the same subject, the similar information from different articles can be regarded as the important content of set of texts [8]. In these researches, determining the range of the topic is a crucial issue: if the range is wide, two units with lower similarity could belong to the same topic, otherwise, the units with high similarity might belong to the different topics. So the traditional single layer topic partition method could hardly obtain appropriate topics set even if analysed manually by human experts. Thus we proposed the concept of : used multi-layer topic structure to take place of the traditional single layer topic structure, and proposes a sentences selection algorithm based on tree for the . The contents of this paper are as follows: Sect. 40.2 introduced the identification algorithm. Section 40.3 introduced summary sentences identification by and Sect. 40.4 showed the experimental analysis.

40.2 Hierarchical Topic Structure Identification

The task of topic identification is to divide the topic into several cohesive sub-topics which contained similar text units. In traditional single layer topic methods, the texts set can hardly be divided into appropriate sub-topics by a proper threshold in which each sub-topic was divided "big" enough to contain all sentences that describe a whole event and at the same time "small" enough not to contain any other information. Thus, this paper proposed the concept of structure and used the complete-link hierarchical agglomerative clustering algorithm to establish the tree. Firstly, each unit was an independent cluster. Then the most similar clusters were merged. This process continued until the largest similarity between two clusters was less than a threshold Φ_1 and an intermediate result in clustering tree or a proper topic division can be obtained. The algorithm restarts once more, it will obtain the upper layer of the tree by another threshold value Φ_2, …, this process continue until there is only one topic in the topic set. The formal description of Multi-threshold clustering algorithm is given as below:

1. begin
2. let Φ is the threshold vector, $\Phi = \{\Phi_1, \Phi_2, \ldots \Phi_K\}$, k is the depth of the topic tree, the initial cluster collection $S = \{s_1, s_2, \ldots, s_n\}$, n is the number of units of the text set. $l = 1$.
3. while $l \leq k$ begin
4.   while begin
5.   traverse the cluster set S, calculate the similarity between any two clusters.

6.   let $D = \max\{Sim(s_i, s_j)|s_i, s_j \in S\}$, if $D > \phi_l$, then merge s_i and s_j to
          one cluster, and update the type collection S. else break
7.   end while
8. $l = l + 1$
9. end while
10. output hierarchical topic tree.

The *Sim(s_i,s_j)* were calculated by multiple features fusion method [9]. In addition, determination of the multi-threshold value Φ of clustering is the crucial issue. The role of Φ is to suspend iterative process of clustering algorithm and generate a layer of tree. García proposed an automatic threshold identification method of the hierarchical clustering algorithm [10]. A lot of experiments had shown that the algorithm were very effective for non-convex clusters. So this paper adopted this idea and used the clustering entropy ε to determine the thresholds. ε is the square-error sum of the cluster set, and when the value of clustering entropy was minimum algorithm can get the most reasonable cluster set, the formula of the square-error sum is:

$$\varepsilon(\chi) = \Lambda + \Gamma \tag{40.1}$$

Λ and Γ separately represented the square-error sum of the internal clusters and the square-error sum between clusters. χ was the cluster set. The internal square-error sum Λ was calculated by the square-error e:

$$\Lambda = \sum_{j=1}^{k} \sum_{i=1}^{n_j} e(p_i^{(j)}, p_0^{(j)}) = \sum_{j=1}^{k} \sum_{i=1}^{n_j} d(p_i^{(j)}, p_0^{(j)})^2 \tag{40.2}$$

n_j was the size of cluster $C_j, d(p_i, p_j)$ was the distance between elements. $p_0^{(j)}$ was cluster centroid which was calculated as follow:

$$p_0^{(j)} = \frac{1}{n_j} \sum_{i=1}^{n_j} p_i^{(j)} \tag{40.3}$$

40.3 Summary Sentences Extraction

We proposed two-step sentences selection algorithm for extracting automatically summary sentences. In the first step, the initial weights of the sentences in the text set were calculated with various features. In the second step, the most important sentences were selected by a top-down reciprocal sentences weighted algorithm.

We firstly assigned an initial weight of each sentence in text set by using several metrics, including sentence position (*SP*), sentence length (*SL*) and term weight (*TW*). The score of sentence position is calculated by the equation:

$$Score_{SP}\left(s_i^{(j)}\right) = 1/(i+j) \tag{40.4}$$

which $s_i^{(j)}$ is the ith sentence in the jth paragraph. The score of sentence length is calculated by the equation:

$$Score_{SL}(s) = 0(if\ L_s > L_{min})$$
$$=(L_s - L_{min})/L_{min}(otherwise) \tag{40.5}$$

We set the score to a negative value as a penalty when a sentence is shorter than penalty threshold value L_{min} which was set 10 in this paper. The third scoring function term weight is based on term frequency (*tf*) and document frequency (*df*). The score of a sentence (S_i) is the average of the tf*idf scores of each word (w) in the sentence:

$$Score_{TW}(S_i) = \frac{1}{|S_i|}\sum\nolimits_{W \in S_i} tf \cdot idf(w) \tag{40.6}$$

DN is the number of documents in all sets. The total score for a sentence is determined using a scoring function:

$$Total - Score(s) = \sum \alpha_i\ Score_i(s) \quad \left(\sum \alpha_i = 1\right) \tag{40.7}$$

Referring to the parameter value of literature [11], each parameter α_i was set manually with $\alpha_{sp} = 0.507$, $\alpha_{SL} = 0.005$ and $\alpha_{TW} = 0.488$.

Based on the initial weight of each sentence, the top-down reciprocal sentences weighted algorithm is represented as following:

1. make the weights of all nodes zero, variable $l = 1$
2. while $l < k$, do
3. calculate the final weight of all sentences as follow:

$$W(i) = a_i + \frac{1}{n}\sum\nolimits_{j=1}^{n} (a_j + f_j) \tag{40.8}$$

Where f_j is the similarity between sentence i and j calculated by   tree: $f_j = (k-m+1)/k$, m is the depth of first layer that sentence i and j are not belonged to the same topic. a_i and a_j are initial values of sentences i and j

4. $l = l + 1$
5. end while

40.4 System Evaluation

The summarization evaluation method should have the ability of evaluating how similar automatic summaries are to the "gold standard". A problem of this method is that there may exist multiple same or similar sentences to standard summaries

Table 40.1   The result of three methods

	Method I (%)			Method II (%)			Our method (%)		
Sentences	5	10	20	5	10	20	5	10	20
Precise	10.25	25.33	58.73	54.3	50.8	65.85	70.58	75.67	67.5
Redundancy	4.37	12.68	44.15	0	8	19.33	0	10	11.33
Synthesis	5.88	12.65	14.58	54.3	42.8	46.52	70.58	65.67	56.17

and each of these can be regarded as an acceptable summary sentence. Thus, it will underestimate the quality of summarization by only matching it with the standard summary. In this paper, we resolve above problem by labeling each sentence a fuzzy value in training corpus. The sentence that can replace standard summary sentence in source text is called candidate summary sentence. Each candidate summary sentence is labeled a value ranged from 0 to 1. Standard summary sentence and related all candidate summary sentences constitute a congeneric cluster. Two sentences in congeneric clustering are named congeneric summary sentences. According to above-mentioned definitions, we can evaluate the quality of summarization system by three criterions: precise, redundancy and synthesis quality.

$$precise = (\sum_{i=1}^{k_1} \omega_i)/K$$

$$redundancy = (\sum_{i=1}^{k_1} (\sum_{j=i+1}^{k_1} \Phi(S_i, S_j)))/K \qquad (40.9)$$

$$Synthesis = precise - redundancy$$

Where K is number of all sentences in summarization. $k_1 = K \cap k_0$, k_0 is number of all sentences in standard summarization. w_i is weight of ith candidate summary sentence. $\Phi(s_i, s_j)$ is a binary discriminant function. $\phi(s_i, s_j) = 1$ if s_i, s_j are congeneric summary sentences. $\Phi(s_i, s_j) = 0$ else.

For constructing training corpus, we download 120 newswire Chinese documents from Internet and cluster them into 15 topic-relative subsets manually. For each subset, we extracted a standard summary and congeneric cluster of each summary sentence. This corpus can be obtained from our web site: http://www.hitwh.edu.cn/department/cs/sw/mds/index.asp

We carry out two baseline systems for evaluation task. The method I is the random system, which extract summary sentences randomly in the whole text set. The method II adopted single layer topic structure, not tree, to describe the similarity between two sentences for validating the effect of structure in . The result by respectively comparing the output of three summarization methods with standard summary is showed in Table 40.1.

The result of experiment shows that the quality of summary produced by our method is better than the both results produced by baseline methods for all output length of summary.
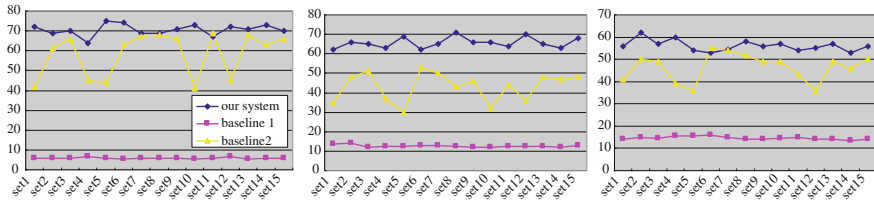
Fig. 40.1 Result of three systems with 5, 10, and 20 sentences summarization

Figure 40.1 shows the multiple Synthesis quality values of three systems in 15 text sets. The broken line of our method is stability on the whole. On the contrary, the one of baseline method II is evidently descend in text set 1, 4, 5, 10 and 12. These text sets are more complicated than other sets in contents, and the tree in our method can effectively handle these data.

40.5 Conclusion

In this paper, a hierarchical tree topic structure is proposed to address the problem of Chinese multi-document automatic summarization. This structure replaced the traditional single-layered topics set and consequently, may describe accurately the text units similarity that are completely similar or incompletely similar to each other. Thus, the wrong division of topics brought by the units clustering may be most reduced. Furthermore, we proposed summary sentences extracting and evaluating algorithms based on tree. We validated our method by comparing result to baseline method. Experimental results showed the better performance of our method in handle different kind of data.

References

1. Dragomir RR, Hongyan J, Malgorzata B (2000) Centroid-based summarization of multiple documents: sentence extraction, utility-based evaluation, and user studies. In: ANLP/NAACL Workshop on summarization, Seattle, WA, Apr 2000
2. Hilda H (2001) Cross-document summarization by concept classification. Workshop on text summarization (DUC 2001). New Orleans, 2001
3. Boros E, Kantor PB, Neu DJ (2001) A clustering based approach to creating multi-document summaries. In: Proceedings of the 24th annual international ACM SIGIR conference on research and development in information retrieval, New Orleans,

4. Guo Y, Stylios G (2003) A new system. In: Proceedings of the document understanding conference
5. Carenini G, Ng R, Pauls A (2006) Multi-Document summarization of evaluative text. In: Proceedings of the conference of the european chapter of the association for computational linguistics (EACL), Trento
6. Hu M, Liu B. (2004) Mining and summarizing customer reviews. In: Proceedings of the Tenth ACM SIGKDD international conference on knowledge discovery and data mining, Seattle, WA, pp 168–177
7. Titov I, McDonald R (2008) A joint model of text and aspect ratings for sentiment summarization. 46th meeting of association for computational linguistics(ACL), Ohio, USA, pp 308–316
8. Ku W, Liang YT, Chen HH (2006) Opinion extraction,summarization and tracking in news and blog cor pora. In: Proceedings of the AAAI-2006 spring symposium on computational approaches to analyzing weblogs (AAAI-CAAW), pp 100-107
9. Xu YD et al (2005) Using multiple features and statistical model to calculate text units similarity, In: Proceedings of the 4th international conference on machine learning and cybernetics IEEE, Guangzhou, pp 19–21 Aug 2005
10. García JA, Fdez-Valdivia J, Cortijo FJ, Molina R (1994) A dynamic approach for clustering data. Signal Process 44(2):181–196
11. Nobata C, Sekine S (2003) Results of CRL/NYU system at DUC-2003 and an experiment on division of document Sets. In: 2003 document understanding conference draft papers, pp 79–85

Chapter 41
Observer-Based Feedback Control for Networked Control Systems With Quantisation and Packet Dropouts

Dajun Du, Haoliang Bai and Xue Li

Abstract The paper investigates Networked Control Systems (NCSs) with quantisation and packet dropouts both the sensor-to-controller (S/C) and controller-to-actuator (C/A). Firstly, the signals both the S/C and C/A are quantised using a logarithmic quantiser while the packet dropouts are modeled as two Bernoulli distributed white sequences. Then, an augmented model is proposed based on an observer, and a sufficient condition is derived for NCSs to be the exponentially mean-square stable. Finally, simulation results confirm the effectiveness of the proposed method.

Keywords Networked control systems · Quantisation · Packet dropouts · Observer-based feedback

41.1 Introduction

Network control systems (NCSs) is composed of a controller and a remote system containing the physical plant, sensors and actuators, which have attracted significant amount of interests from the industry and academics due to its various advantages such as low cost of installation and great flexibility [1, 2]. However, network is introduced in the feedback control loops, which inevitably results in the

D. Du · H. Bai · X. Li (✉)
School of Mechatronical Engineering and Automation, Shanghai University,
Shanghai 200072, China
e-mail: lixue@shu.edu.cn

D. Du
e-mail: ddj@shu.edu.cn

packet dropouts due to the limited bandwidth or signal disturbance. This can affect stability and performance of NCSs. Therefore, stability analysis and control strategy for NCSs with packet dropouts and quantisation will be investigated in this paper.

With respect to the quantisation for NCSs, some recent research results have been reported. The problem of quantised stage feedback H_∞ stabilization for LTI systems over data networks with limited network QoS was studied, and a quantised state feedback strategy was developed for global and asymptotical stabilization [3]. The state feedback stabilization problem for a class of NCSs with nonlinear perturbation and state quantisation was investigated, and a quantised asymptotically stabilizing sufficient condition was proposed [4]. A unified framework for controller design for control system with quantisation and time scheduling via an emulation-like approach was developed [5]. Considering the S/C quantisation and data dropout, an output-feedback control for NCSs was designed, which guaranteed the exponentially mean-square stable [6]. Recently, the quantisation between the C/A without network was studied, and full and reduced-order observer-based quantised feedback controller was designed to guarantee the asymptotic stability of the closed-loop system [7]. However, quantiser between the S/C and C/A was not considered simultaneously.

Motivated from the above observations, this paper investigates the stability of NCSs with quantisation and data dropouts both the S/C and C/A. The signals both the S/C and C/A are quantised using a logarithmic quantiser while the packet dropouts are modeled as two Bernoulli distributed white sequences. An augmented model is then proposed based on an observer to estimate the system state, and a sufficient condition is derived for NCSs to be the exponentially mean-square stable.

41.2 Problem Formulation and Modeling

The configuration of NCSs with the quantisation and packet dropouts both the S/C and C/A is shown as Fig. 41.1. Consider the following discrete linear time-invariant (LTI) system:

$$
\begin{aligned}
x(k+1) &= Ax(k) + Bu_s(k) \\
y(k) &= Cx(k)
\end{aligned}
\tag{41.1}
$$

where $u_s(k), y(k), x(k)$ are the plant's input, output and state, A, B, C is the relevant known matrices.

Since quantisation is required before signals are transmitted through network, the output signals y(k) and the control signals v(k) are firstly quantised by the logarithmic quantiser [7]. The quantiser is denoted as $q[\cdot] = [q_1[\cdot], \ldots, q_m[\cdot]]^T$, which is assumed to be symmetric. For each $q_j[\cdot]$, the quantisation levels expressed by: $Y_i = \{\pm y_i : y_i = \rho^i \mu_0, i = 0, \pm 1, \pm 2 \ldots\} \cup \{0\}, 0 < \rho < 1, \mu_0 > 0$.
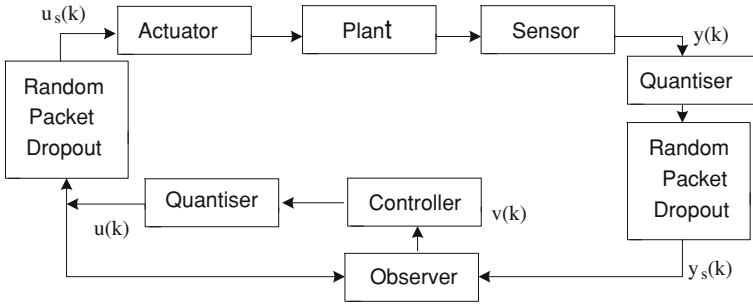
Fig. 41.1 Structure of observer-based NCSs with packet dropouts and quantisation

As the density of logarithmic quantiser is proportional to ρ, we take ρ as the density of logarithmic quantiser. Thus, the associated quantiser is described as follow:

$$q(y) = \begin{cases} y_i & \text{if } y_i/(1+\delta) < y \le y_i/(1-\delta) \\ 0 & \text{if } y = 0 \\ -q(-y) & \text{if } y < 0 \end{cases} \tag{41.2}$$

where $\delta = (1-\rho)/(1+\rho)$, it is observed that the quantiser is symmetric and time-invariant.

When the quantized signals are transmitted to the controller through network, data packet dropouts are inevitably introduced. We model the packet dropouts as the Bernoulli process θ with the probability distribution as follow:

$$\Pr\{\theta = 1\} = E\{\theta\} = \overline{\theta}, \ \Pr\{\theta = 0\} = 1 - E\{\theta\} = 1 - \overline{\theta},$$
$$\text{Var}\{\theta\} = E\{(\theta - \overline{\theta})^2\} = \overline{\theta}(1 - \overline{\theta}) = a^2 \tag{41.3}$$

where $\theta = 1$ denotes the packet transmits normally, $\theta = 0$ denotes the packet losses. Moreover, the known positive constant $0 < \overline{\theta} < 1$ indicates the probability that the packet will be transmitted successfully while a denotes the variance of θ. Thus, at the kth sampling time, the measured output signals that the controller receives can be described as $y_s(k) = \theta q[y(k)]$. Using the sector bound method [3], the quantization error for a given quantization density ρ_1 can be expressed as:

$$q[y(k)] - y(k) = \Delta(y(k))y(k), \quad \|\Delta(y(k))\| \le \delta_1 \tag{41.4}$$

Similarly, the control signals v(k) are quantized: $u(k) = f[v(k)]$. Packet dropouts modeled as:

$$\Pr\{\alpha = 1\} = E\{\alpha\} = \overline{\alpha}, \ \Pr\{\alpha = 0\} = 1 - E\{\alpha\} = 1 - \overline{\alpha}, \ \text{Var}\{\alpha\}$$
$$= E\{(\alpha - \overline{\alpha})^2\} = \overline{\alpha}(1 - \overline{\alpha}) = b^2 \tag{41.5}$$

The control signals that the actuator actually receives can be defined as: $u_s(k) = \alpha f[v(k)]$, and the quantization error for a given quantization density ρ_2 is expressed as:

$$f[v(k)] - v(k) = \Delta(v(k))v(k), \quad \|\Delta(v(k))\| \le \delta_2 \tag{41.6}$$

Next, we will consider the system with the state unmeasured (as is often the case), an observer is designed to estimate the system state using the available output information. The observer-based feedback controller is introduced as follows:

$$\hat{x}(k+1) = A\hat{x}(k) + Bu(k) + L(y_s(k) - C\hat{x}(k)) \tag{41.7}$$

where $u(k) = f[v(k)]$, $v(k) = K\hat{x}(k)$, K and L are feedback and observer gain, respectively.

Defining $e(k) = x(k) - \hat{x}(k)$ and $Z(k) = [e(k)^T, x(k)^T]^T$, the augmented model with the packet dropouts and quantization error can be expressed by:

$$Z(k+1) = A_0 Z(k) + A_1 Z(k) + A_2 Z(k) \tag{41.8}$$

$$\Pi_1 = A - LC, \ \Pi_2 = BK, \Pi_3 = BK(1 + \Delta(v(k)))$$

where $\quad \Pi_4 = (1 - \overline{\alpha})BK(1 + \Delta(v(k))), \ \Pi_5 = \overline{\alpha}BK(1 + \Delta(v(k))), \ \Pi_6 = LC,$

$$\Pi_7 = LC(1 + \Delta(y(k))), \ \Pi_8 = \overline{\theta}LC(1 + \Delta(y(k)))$$

$$A_0 = \begin{bmatrix} \Pi_1 + \Pi_4 & \Pi_6 - \Pi_8 - \Pi_4 \\ -\Pi_5 & A + \Pi_5 \end{bmatrix},$$

$$A_1 = \begin{bmatrix} -(\alpha - \overline{\alpha})\Pi_3 & (\alpha - \overline{\alpha})\Pi_3 \\ -(\alpha - \overline{\alpha})\Pi_3 & (\alpha - \overline{\alpha})\Pi_3 \end{bmatrix}, \ A_2 = \begin{bmatrix} 0 & -(\theta - \overline{\theta})\Pi_7 \\ 0 & 0 \end{bmatrix}$$

41.3 Main Results

It is obvious that the system is actually an uncertain stochastic system. To analyze stochastic stability in the means-square sense, a notion is given firstly.

Definition 1 The closed-loop system (41.8) is said to be exponentially mean-square stable if there exist constant $\omega > 0$ and $\tau \in (0, 1)$ such that $E\{\|Z(k)\|^2\} \le \omega\tau^k E\{\|Z(0)\|^2\}$.

Lemma 1 Let $V(Z(k))$ to be a Lyapunov functional. If there exist real scalars, $\lambda \ge 0$, $\kappa > 0$, $\gamma > 0$ and $0 < \varphi < 1$ such that $\kappa\|Z(k)\|^2 \le V(Z(k)) \le \gamma\|Z(k)\|^2$ and $E\{V(Z(k+1)|Z(k))\} - V(Z(k)) \le \gamma - \varphi V(Z(k))$, then the sequence $Z(k)$ satisfies: $E\{\|Z(k)\|^2\} \le \frac{\gamma}{\kappa}\lambda\|Z(0)\|^2(1 - \varphi)^k + \frac{\lambda}{\kappa\varphi}$.

Theorem 1 For the given quantization density $\rho_1 > 0$, $\rho_2 > 0$ and packet dropout rate $\overline{\theta}$, $\overline{\alpha}$, if there exist symmetric positive-definite matrices P, real matrices K, L

and a scalar $\varepsilon > 0$, such that (41.9) *hold, then the closed system* (41.8) *is exponentially mean-square stable.*

$$
\begin{bmatrix}
-P+\Sigma_2 & * & * & * & * & * & * & * \\
-\Sigma_2 & -P+\Sigma_1+\Sigma_2 & * & * & * & * & * & * \\
\Pi_1+\Sigma_4 & \Pi_6-\Sigma_4-\Sigma_5 & -P^{-1} & * & * & * & * & * \\
-\Sigma_3 & A+\Sigma_3 & 0 & -P^{-1} & * & * & * & * \\
-\Pi_2 & \Pi_2 & 0 & 0 & -2a^{-2}P^{-1} & * & * & * \\
0 & -\Pi_6 & 0 & 0 & 0 & -b^{-2}P^{-1} & * & * \\
0 & 0 & \Sigma_4^T & -\Sigma_3^T & -\Pi_2^T & 0 & -\varepsilon I & * \\
0 & 0 & -\Sigma_5^T & 0 & 0 & -\Pi_6^T & 0 & -\varepsilon I
\end{bmatrix} < 0
$$

$$(41.9)$$

where $\Sigma_1=\delta_1^2\varepsilon I,\ \Sigma_2=\delta_2^2\varepsilon I,\ \Sigma_3=\overline{\alpha}BK,\ \Sigma_4=(1-\overline{\alpha})BK,\ \Sigma_5=\overline{\theta}LC.$

Proof Choosing a Lyapunov functional as follow:

$V(Z(k)) = e(k)^T Pe(k) + x(k)^T Px(k)$, where P is symmetric positive-definite matrices.

Using the above formula and noting $E[(\alpha-\overline{\alpha})^2]=a^2,\ E[(\theta-\overline{\theta})^2]=b^2$, we have:

$$E\{V(Z(k+1)|Z(k))\} - V(Z(k)) = Z(k)^T\Psi Z(k) \tag{41.10}$$

where

$$
\Psi =
\begin{bmatrix}
\Pi_1+\Pi_4 & \Pi_6-\Pi_8-\Pi_4 \\
-\Pi_5 & A+\Pi_5 \\
-\Pi_3 & \Pi_3 \\
0 & -\Pi_7
\end{bmatrix}^T
\begin{bmatrix}
P & * & * & * \\
0 & P & * & * \\
0 & 0 & 2a^2P & * \\
0 & 0 & 0 & b^2P
\end{bmatrix}
\begin{bmatrix}
\Pi_1+\Pi_4 & \Pi_6-\Pi_8-\Pi_4 \\
-\Pi_5 & A+\Pi_5 \\
-\Pi_3 & \Pi_3 \\
0 & -\Pi_7
\end{bmatrix}
$$
$$
-\begin{bmatrix} P & * \\ 0 & P \end{bmatrix}
$$

According to Schur's complment, $\Psi < 0$ is equivalent to

$$
\begin{bmatrix}
-P & * & * & * & * & * \\
0 & -P & * & * & * & * \\
\Pi_1+\Pi_4 & \Pi_6-\Pi_8-\Pi_4 & -P^{-1} & * & * & * \\
-\Pi_5 & A+\Pi_5 & 0 & -P^{-1} & * & * \\
-\Pi_3 & \Pi_3 & 0 & 0 & -2a^{-2}P^{-1} & * \\
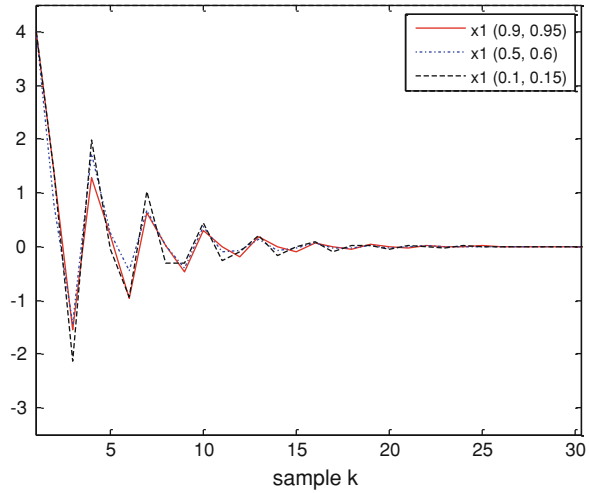0 & -\Pi_7 & 0 & 0 & 0 & -b^{-2}P^{-1}
\end{bmatrix} < 0
$$

The above inequality can be re-written and finally is equivalent to (41.9) for any scalar $\varepsilon > 0$.

Furthermore, we will proof the closed-loop system (41.8) is exponentially mean-square stable. According to (41.10), we have:

$$E\{V(Z(k+1)|Z(k))\} - V(Z(k)) = Z(k)^T \Psi Z(k) \leq - \lambda_{\min}(-\Psi)Z(k)^T Z(k) < - \eta Z(k)^T Z(k)$$

$$(41.11)$$

where $0 < \eta < \min(\lambda_{\min}(-\Psi), \chi)$, $\chi = \lambda_{\max}(P)$, and (41.11) can be re-written as:

$$E\{V(Z(k+1)|Z(k))\} - V(Z(k)) < - \eta Z(k)^T Z(k) < \frac{\eta}{\chi} V(Z(k)) = -\nu V(Z(k))$$

where $\nu = \eta/\chi \in (0, 1)$, using the Definition 1 and Lemma 1, it is obviously found that (41.8) is exponentially mean-square stable. This completes the proof.

The above matrices inequality is not a linear matrices inequality (LMI), and can hardly be solved by the matlab LMI toolbox. Next, we will make some improvement to the inequality to get it easily solved by the toolbox. Without lose of generality, matrix B is assumed to be of full-column rank.

Theorem 2: Under the assumptions as in Theorem 1, if there exist symmetric positive-definite matrices P, real matrices M, N, and a scalar $\varepsilon > 0$, such that (41.12) hold, then (41.8) is exponentially mean-square stable.

$$\begin{bmatrix} -P + \Sigma_2 & & & & & & & \\ -\Sigma_2 & -P + \Sigma_1 + \Sigma_2 & & & & & & \\ \Xi_6 + \Xi_4 & \Xi_5 - \Xi_4 - \Xi_7 & -P & & & & & \\ -\Xi_3 & PA + \Xi_3 & 0 & -P & & & & \\ -a\Xi_8 & a\Xi_8 & 0 & 0 & -2P & & & \\ 0 & -b\Xi_5 & 0 & 0 & 0 & -P & & \\ 0 & 0 & \Xi_4^T & -\Xi_3^T & -a\Xi_8^T & 0 & -\varepsilon I & \\ 0 & 0 & -\Xi_7^T & 0 & 0 & -b\Xi_5^T & 0 & -\varepsilon I \end{bmatrix} < 0$$

$$(41.12)$$

$$PB = BP_0 \qquad (41.13)$$

where

$$\Xi_3 = \overline{\alpha}BM, \ \Xi_4 = (1 - \overline{\alpha})BM, \ \Xi_5 = NC, \ \Xi_6 = PA - NC, \ \Xi_7 = \overline{\theta}NC, \ \Xi_8 = BM, \ K = P_0^{-1}M, \ L = P^{-1}N$$

Proof Pre- and post-multiplying both sides of (41.9) by diag(I, I, P, P, P, P, I, I), using (41.13) and $P_0K=M$, $PL=N$, (41.12) is obtained. This completes the proof.

Finally, (41.13) can be converted to the following LMI:

$$\begin{pmatrix} -rI & B^T P - P_0 B^T \\ PB - BP_0 & -I \end{pmatrix} < 0 \qquad (41.14)$$

Thus, the stability problem of the closed-loop system (41.9) can be solved by searching the global solution of the following problem:

Fig. 41.2 The trajectory of state ×1 under different packet transmission rates $(\overline{\theta}, \overline{\alpha})$

$$\begin{aligned} min \ \ & r \\ s.t. \ (12) \ \ & and \ \ (14) \end{aligned} \qquad (41.15)$$

41.4 Simulation Examples

Considering the following discrete system:

$$A = \begin{bmatrix} 0.3 & 0.4 & 0.7 \\ 0.3 & 0 & -0.8 \\ -0.2 & 0.4 & -0.7 \end{bmatrix} \quad B = \begin{bmatrix} 1 & 0.4 & -0.5 \end{bmatrix}^T \quad C = \begin{bmatrix} 0.2 & 0.3 & 0.4 \end{bmatrix}$$

The initial state of the system is assumed as $x = \begin{bmatrix} 4 & -3 & 2 \end{bmatrix}^T$, $\hat{x} = \begin{bmatrix} 4 & -3 & 2 \end{bmatrix}^T$, the packet normal transmission probability and quantization density are set as $\overline{\theta} = 0.8$, $\overline{\alpha} = 0.9$, $\rho_1 = 0.5$, $\rho_2 = 0.6$. By solving (41.15), $K = [-0.0625 \ -0.1170 - 0.2540]$, $L = [0.4473 \ -0.3383 \ -0.1008]$.

To demonstrate the effectiveness of the proposed method, comparison experiments were performed. Quantization density is fixed, simulations were done under different packet transmission rates ($(i.e., (\overline{\theta}, \overline{\alpha}) = \{(0.9, 0.95), (0.5, 0.6), (0.1, 0.15)\})$). Figure 41.2 shows the trajectory of state x_1 under different packet transmission rates. The trajectory of state x_2 and x_3 are similar to that of x_1, and thus is omitted. It is clearly seen from Fig. 41.2 that the system is stable under the proposed control strategy.

41.5 Conclusions

In this paper, an observer-based feedback control scheme is developed for NCSs with quantization and data packet dropouts both the S/C and C/A. The signals are quantized using a logarithmic quantiser, while the packet dropouts are modeled as two Bernoulli distributed white sequences. An augmented model is then proposed, and a sufficient condition is derived for NCSs to be the exponentially mean-square stable. Simulation results show the feasibility of our control scheme.

References

1. Wang X, Lemmon MD (2011) Event-triggering in distributed networked control systems. IEEE Trans Aut Cont 56(3):586–601
2. Du D, Fei M (2008) A two-layer networked learning control system using actor-critic neural network. Appl Math Comput 205(1):26–36
3. Peng C, Tian Y (2007) Networked H_∞ control of linear systems with state quantization. Inf Sci 177:5763–5774
4. Zhou L, Lu G (2010) Quantized feedback stabilization for networked control systems with nonlinear perturbation. Int J Innov Comput Inf Cont 6(6):2485–2495
5. Nesic D, Liberzon D (2009) A unified framework for design and analysis of networked and quantized control systems. IEEE Trans Aut Cont 54(4):732–747
6. Niu Y, Jia T et al (2009) Output-feedback control design for NCSs subject to quantization and dropout. Inf Sci 179(21):3804–3813
7. Zhang J, Lam J, Xia Y (2010) Observer-based output feedback control for discrete systems with quantised inputs. IET Cont Theory Appl 3(5):478–485

Chapter 42
Optimization and Design of Key Structure for Electric Equipment Based on MDO

Honggen Zhou, Xuwen Jing and Xiaojun Zhang

Abstract This paper attempted to introduction the method into design process of electronic devices structure optimization, and carried out an experiment on a specific object to verify the feasibility and effectiveness of the method that used in electronic equipments structure design. An integrated system for and synthetically optimizing key structure was built which was based on and VC ++, and the whole optimum process was carried out. The model was built with weight lighting, heat dissipating and vibration performance, coupling effect was considered, the SQP algorithm was used and the global optimal solution was gotten at last. As the results shown, applying method to optimization of the electronic equipment structure is effective, and also can provide reference for subsequent optimization and design of the whole machine.

Keywords Electric equipment · MDO · Parametric Modeling · iSIGHT · Ontology

42.1 Introduction

Recent years, the architecture of electronic devices has developed from independent and separated into modular and integrated, which made the devices smaller and lighter. And some multidisciplinary problems, such as thermal design, vibration design, EMC design and so on, in developing devices become more

H. Zhou (✉) · X. Jing · X. Zhang
School of Mechanical Engineering, Jiangsu University of Science
and Technology, Zhenjiang 212003, China
e-mail: hgzhou205@gmail.com

H. Zhou
School of Mechanical Engineering, Southeast University,
Nanjing 211189, China

**Fig. 42.1** Structural model of a certain type of airborne electronic equipments
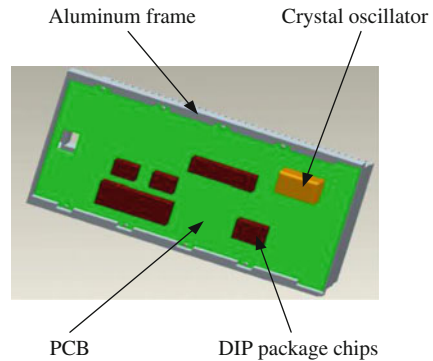
prominent [1]. Traditional serial design not only ignores the synergy caused by Mutual coupling in each disciplines but also separates the interaction in different disciplines. So traditional serial can only get partial optimal solution and is likely to lose the global optimal solution. Besides, for traditional serial, design cycle is longer and costs are higher. Obviously, these features can't adapt to the more and more stringent design requirements [2]. Multidisciplinary design optimization (), which is proposed for this problem, is developed in aviation and aerospace fields in recent years and become one of the widely used and most dynamic and latest research area, also play an important role in promoting the performance of corresponding products [3–6]. This paper attempts to introduce the method into optimization design process of electronic devices structure, and carries out an experiment on specific objects to verify the feasibility and effectiveness of the method that used in electronic equipments structure design.

42.2 Multidisciplinary Design Optimization Problems of Airborne Electronic Equipment

42.2.1 The Multidisciplinary Design Optimization Model of A Certain Type of Airborne Electronic Equipment

This paper describes the method of multidisciplinary design optimization through a certain type of airborne electronic equipments. Structure model is shown in Fig. 42.1, outer structure of the electronic equipment is aluminum frame, and internal structure installed printed circuit board (PCB) according to function design. Some components with different functions is installed in PCB by welding or other methods, the main components include crystal oscillator, dual in-line chip and other important ones. This type of airborne electronic equipments has not only

Fig. 42.2 The key size of radiator for a certain type of airborne electronic equipment
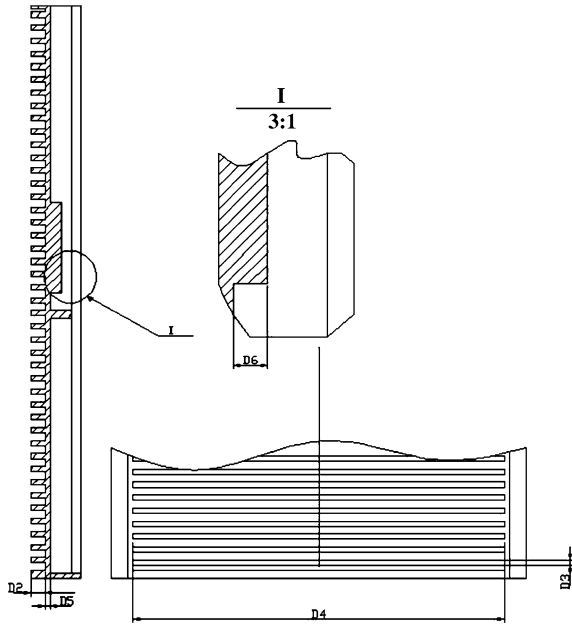
the typical structure of airborne electronic equipment but also the actual research value.

This type of electronic equipment works in a poor environment, and suffers large shock and vibration. In order to avoid resonance, the natural frequency and vibration excitation frequency should be different and the ratio between the two should be greater than 2.5 [7]. Simultaneously, high temperature of the component will leads to thermal failure, so the cooling requirements are relatively high. This paper researches how to improve the overall performance of the part after considering its resonant and cooling performance. In part design, in order to strengthen the cooling capacity of electronic components, flat radiator is used to increase heat radiating area of electronic components. The layout of the components in this part has been fixed, so the structure design of the part is the only way to improve the overall performance. Related design variables of this structure are listed as follows: number of cooling fins, height of cooling fins, thickness of cooling fins, length of cooling fins, thickness of heat extended surface and thickness of heat pedestal. The sizes represented by each design variable are shown in Fig. 42.2, the initial values and the range of parameters are shown in Table 42.1.

In summary, this paper takes minimize the maximum temperature in steady-state and maximize the natural frequency of first-order in modal analysis as objective functions to optimize component. At the same time, it also takes the design criteria ofstructure lightweight of airborne electronic equipment into account. The optimization model is defined as follows.

Table 42.1 The selected design variables

No	Design Variables(mm)	Initial value	Range
1	Number of colling fins (D1)	38	[35, 40]
2	Height of cooling fins(D2)	5.5	[4, 6]
3	Thickness of cooling fins (D3)	2	[1, 3, 5]
4	Length of cooling fins(D4)	143	[140, 145]
5	Thickness of heat extended surface(D5)	2	[1, 3, 5]
6	Thickness of heat sink of pedestal (D6)	4.3	[3, 5]

$$
\begin{cases}
\text{Design variables :} & \bar{X}=[D_1,D_2,D_3,D_4,D_5,D_6] \\
\text{Objective function :} & MinTemperature=f_1(\bar{X}) \\
& MaxFirstFreq=f_2(\bar{X}) \\
\text{Constraint function :} & Mass=f_3(\bar{X}) \leq 0.5Kg \\
& Temperature=f_1(\bar{X}) \leq 60°C \\
& FirstFreq=f_2(\bar{X}) \geq 40Hz \\
& \bar{X}_{i\min} \leq \bar{X}_i \leq \bar{X}_{i\max}(i=1,2L,6)
\end{cases}
\tag{42.1}
$$

$\bar{X}$ is a column vector formed by optimal design variables, which is composed of the six independent variables, as is shown in Table 42.1. Values will be selected from the lower and upper bound of $[\bar{X}_{i\min}, \bar{X}_{i\max}]$.In order to meet the heat dissipation of the structure, the maximum temperature in steady state should be lower than 60° C. Considering the actual requirements of vibration performance, the first order natural frequency should be lower than 40 Hz; and considering the demand for structures lightweight, the overall weight of structure should be less than 0.5 kg after optimizing.

42.2.2 The Strategy and Process of Multidisciplinary Optimization

As known from the design optimization model, the structure optimization is a multi-dimensional coupling optimization problem including steady state heat-vibration-lightweight-structure. Structural design variables span two disciplines-thermal and kinetic, the key point to simplify the complex design of optimal process is to weak the coupling relationship between this two disciplines and give the two disciplines certain autonomy. Because only two disciplines are related in the structural design, so design variables are limited and the calculation in each disciplines is not complex. Therefore, MDF method in the optimization strategy is used [8, 9]. According to MDF optimization strategy and based on the finite element method (FEM), this paper comprehensively considers some important factors of the structure, such as heat dissipation, vibration performance, and light weight and so on. At last, the multidisciplinary design optimization process is proposed, as is shown in Fig. 42.3.
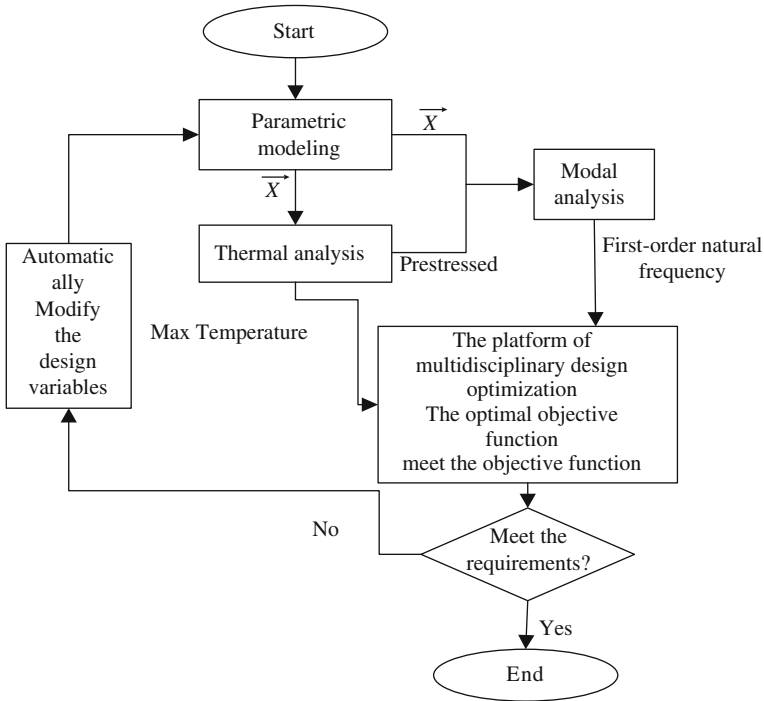
Fig. 42.3 Process of multi-disciplinary design optimization

42.2.3 Selection of Optimization Algorithms

This paper uses , integrated with thermal in steady state-Modal analysis-structure lightweight, to optimize comprehensively. As the relationship between design variables and optimization goals is highly non-linear, SQP (Sequential quadratic programming algorithm) is selected to optimize. SQP is an effective numerical schemes based on gradient information, and also be regarded as one of the best algorithms in solving nonlinear programming problems [10].

The basic idea of sequential quadratic programming algorithm is as follows: constructing a quadratic programming sub problem at every iterative point, regarding the solution that belongs to sub problem as iterative search directions, making one dimensional along the direction and finally approaching to the solution of constrained optimization problem.

Constrained nonlinear programming problem can be described as follows:

$$\begin{cases} \min f(x)\, x \in R^n \\ s\ell.c_i(x) \le 0 (i = 1, 2, \mathrm{L}, m) \end{cases} \tag{42.2}$$

x is a independent variable, $x = (x_1, x_2, \cdots, x_n)^T$, $f(x)$, is objective function, $c_i(x)$ is the constraint.

The optimization problem above can be summed up as a quadratic programming sub problem:

$$\begin{cases} \min QP(s) = \left[\nabla f\left(x^{(k)}\right)\right]^T + \frac{1}{2}s^T B^{(k)} \\ ss.t. c_i\left(x^{(k)}\right) + \left[\nabla c_i\left(x^{(k)}\right)\right]^T s = 0 \; i = 1, 2, L, m \end{cases} \tag{42.3}$$

S is search direction, $\alpha_k s^{(k)} = x^{(k+1)} - x^{(k)}$, $B^{(k)}$, is the approximation of the Hesse matrix.

Therefore, the solving steps of sequential quadratic programming algorithm can be summarized as follows:

Step①: select the initial point $x^{(0)} \in R^n$, $\alpha_0 x^{(0)}$, and positive definite symmetric matrix $B^{(0)}$, allowed tolerance ε_1 (or ε_2 or ε_3);

Step②: solve quadratic programming sub problem QP, determine the new vector of Lagrange multipliers $\lambda^{(k+1)}$ and search direction $s^{(k)}$;

Step③: determine the step factor α_k, get new iterative point $x^{(k+1)} = x^{(k)} + \alpha_k s^{(k)}$;

Step④: test the criterion which meet the convergence, if it satisfies $\left\|\nabla_x L\left(x^{(k+1)}, \lambda^{(k+1)}\right)\right\| < \varepsilon_1$ or satisfies both $c_i\left(x^{(k+1)}\right) < \varepsilon_2 (i = 1, 2, \cdots, P)$ and $\left|f\left(x^{(k+1)}\right) - f\left(x^{(k)}\right)\right| / \left|f\left(x^{(k)}\right)\right| < \varepsilon_3$, stop iterating, else go to step ⑤;

Step ⑤: Amend approximation matrix $B^{(k)}$ of $H^{(k)}$, then make $k = k + 1$, return to step ②.

42.3 The Process of Structure Multidisciplinary Design Optimization for a Certain Type of Airborne Electronic Device

This paper uses platform to integrate the thermal-modal model parameters according to the process of multi-disciplinary optimization.

As an integrated framework of multi-disciplinary design optimization, abstracts maximum temperature from thermal analysis results file and first-order natural frequency from modal analysis results file as the objective function value. It also takes the structural weight and other design variables as constraints to realize the modification and automatically re-analysis of the model and finally completes the optimization of design variables in optimization process according to the configured SQP optimization algorithm.

A relatively satisfactory result can be obtained after eighty-six times iterative optimization according to the calculation steps of SQP algorithm. Objective function value in iterative process and convergent curve of constraint function are shown in Fig. 42.4 the lateral axis represents the number of optimization calculation, and the vertical axis represents the value of objective function (the

MaxT-Run Counter   FirstFreq-RunCounter   Mass-RunCounter
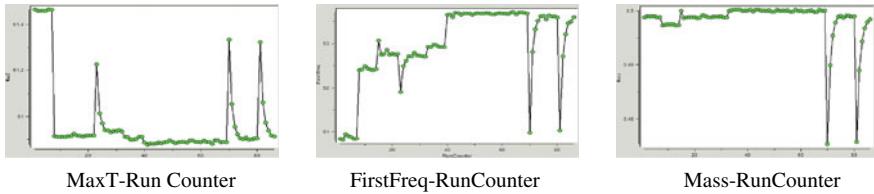
Fig. 42.4 The curve convergence of the process of optimization. **a** MaxT-RunCounter; **b** FirstFreq-RunCounter; **c** Mass-RunCounter

Table 42.2 Comparison of design variables before and after optimization

Design variables	Initial value	Results after optimization
D1	38	38
D2	5.5	5.9939
D3	2	1.5
D4	143	145
D5	2	2.2464
D6	4.3	4.7080

Table 42.3 Comparison of the objective function before and after optimization

Names of variables	Initial value	Results after optimization	Degree of improvement
The maximum temperature	40.1194°C	39.9316°C	−0.4681%
First-order natural frequency	50.8442 Hz	53.7123 Hz	5.6410%
Quality	0.4988 kg	0.4998 kg	0.2005%

maximum temperature and the first-order frequency) and the constraint function (weight).

Table 42.2 represent the contrast of the design variables and function value before and after optimization. As is shown in Table 42.3, after multidisciplinary design optimization, the maximum temperature of the structure in steady state decreased from 40.1194 to 39.9316° C, reduced 0.4681%; first-order natural frequency increased from 50.8442 to 53.7123 Hz t, increased 5.6410%; total mass increased from 0.4988 to 0.4998 kg, increased 0.001 kg. Obviously, it is effective to apply multidisciplinary design optimization to the design of key structures for electronic devices, performance of heat dissipation and vibration are improved, and the overall weight is increased, but changes a little. In short, implementation of multidisciplinary design optimization is meaningful to airborne equipments.

42.4 Conclusions

This paper integrates CAE software by using   method.   and self-composed platform are used to optimize key structures of the electronic device. As the results shown, applying method to optimization of the electronic equipment structure is

effective.A multidisciplinary design optimization model is established, MDF optimization strategy and SQP optimization algorithm in multi-disciplinary design optimization are used according to the performance indicators of key components of a certain type of electronic equipment, such as cooling performance, vibration performance and lightweight of the structure. This paper adopts a multidisciplinary design optimization method to design and optimize the electronic equipments structure by fully considering the coupling effect in various disciplines. Heat dissipation performance and vibration performance of the structure are improve while the increasing of design weight are avoided, which provides a new way to design this kind of electronic equipments structure.

References

1 Lu L, Feng G, Fang W (2009) Application of technology in avionics [J]. Telecommun Technol 12(4):20–23
2 Han M, Deng J (2004) Research on multidisciplinary design optimization of integrated environment in complex engineering systems [J]. J Mech Eng 40(9):100–105
3 Bojun C (2009) New ideas of mechanics design in flight [J]. Sci Sinica, 39(3):575–578
4 Yu Xiongqing (2008) Status Quo and development trend of multidisciplinary design optimization for aircraft [J]. J Nanjing Univ Aeronaut Astronaut 40(4):417–426
5 Kesseler E, Vankan WJ (2006) Multidisciplinary design Analysis and multi-objective optimization applied to aircraft wing [J]. WSEAS transaction on systems and control 1(2): 221–227
6 Li X (2003) Multidisciplinary design optimization and its application in aircraft design [D]. Xi'an, Northwestern Polytechnical University
7 Yu J et al. (2008) Thermal design and analysis for electronic equipments [M]. Xi'an: Beihang University Press
8 Jiang Z, Cui W (2009) Comparison of multidisciplinary design optimization and its application in ships and ocean platforms [J]. Ship Mech 13(1):150–160
9 Gu L, Gong C (2005) Comparison of multidisciplinary design optimization [J]. J Navig Guid 25(1):60–62
10 Xue W Qin J Jia C Xue G (2009) Optimization of the mechanical structure parameters based on virtual prototypes and SQP [J]. Comput Meas Cont 17(10):2042–2044

Chapter 43
Optimized Assignment of Airport Gate Configuration Based on Immune Genetic Algorithm

Wang Li and Xiaofang Xu

Abstract Airport gate assignment is to appoint an appropriate gate for the arrival or departure flight and to ensure the flights are on schedule. A key task of airport ground operations is assigning the airport gate with high efficiency and reasonable arrangement. This paper establishes optimized model based on the characteristics of flight and the characteristics of airport gate(the flight type, flight down time and the number of passengers are considered as the characteristics of flight. the ease of airport gate is considered as the characteristics airport gate),and a space representation of solutions and direct graph model of airport gate configuration based on the dynamic scheduling parallel machines are given, and the solving method of airport gate configuration based on the immune genetic algorithm is designed. The simulation result shows the effectiveness of this model and algorithm.

Keywords Airport gate assignment · The characteristic of flight · Immune genetic algorithm

43.1 Introduction

Considering the flight and airport gate, the airport gate assignment is to appoint an appropriate gate for every arrival or departure flight during a period of future time and to ensure the flights are on schedule and to provide gates for the passengers to

W. Li (✉) · X. Xu
College of Aeronautical Automation Civil, Aviation University of China,
300300 Tianjin, China
e-mail: lwang@cauc.edu.cn

board or get off the airplanes. The reasonable assignment of the gates is a key task of airport ground operations. Nowadays, though the civil aviation develops rapidly, the facilities have many shortcomings and these shortcomings limit the size of the airport operations, so optimized assignment of airport gate becomes an important problem.

To the problem, the scientists at home and broad propose several analysis methods. The literature [1] provides the sorting algorithm. The literature [2] provides the expert system. The literature [3–8] provides the method of mathematical programming. These literatures just only optimize the airport gate from the perspective of passengers without considering the characteristic of gate. With the description of the gate assignment by literature [8], this paper designs a method based on the immune genetic algorithm. The simulation result shows the effectiveness of this model and algorithm.

43.2 The Description of the Airport Gate Assignment

The gate optimized assignment is to get the largest satisfaction of the passengers and the high efficient airport ground operations and the effective airport benefit according to optimized assignment. The literature [8] gives a description about the gate assignment: setting a possible distributed assignment A_{SS} to make the sum of the product of flight characteristics σ_i and the distributed airport gate characteristics biggest. The objective function of this method is $\max \pi(A_{ss}) = \sum_{i \in \underline{l}} \gamma_i * \sigma(A_{SS_i})$. The optimized assignment of flight collection A is named: $A_{SS}^*(A)$. The literature [8] gives a model of optimized assignment of gate based on the dynamic scheduling parallel machines. The model is $\overline{A} = \{\overline{A_1}, \overline{A_2}, \cdots, \overline{A_k}\}$, the set makes up of all the scheduling in the set of the airport gate P has the following ordered product of limited:

$$_C\Omega_l^n = {}_{C_1}\Omega_l^{n_1} \times {}_{C_2}\Omega_l^{n_2} \times \cdots \times {}_{C_k}\Omega_l^{n_k} = \prod_{i-1}^{k} {}_{C_i}\Omega_l^{n_i}.$$

And any scheduling is named that:

$$\omega = \omega_1 \times \omega_2 \times \cdots \times \omega_k = \left(\begin{pmatrix} \omega_{11} \\ \omega_{21} \\ \vdots \\ \omega_{k1} \end{pmatrix} \begin{pmatrix} \omega_{12} \\ \omega_{22} \\ \vdots \\ \omega_{k2} \end{pmatrix} \cdots \begin{pmatrix} \omega_{1l} \\ \omega_{2l} \\ \vdots \\ \omega_{kl} \end{pmatrix} \right) \in {}_C\Omega_i^n \quad (43.1)$$

where $\omega_i \in {}_{C_i^{\omega^{i-1}}}\Omega_l^{n_i}, i \in \underline{k}$. Or the form of matrix: $\omega = (\omega_{ij}), i \in \underline{k}, j \in \underline{l}$.

43.3 Optimized Assignment of Airport Gate Configuration Based on Immune Genetic Algorithm

In the Eq. 43.1, every possible distributed assignmentω of the space of solution is an individual. ω is made up of k genes $(\omega_1, \omega_2, \cdots, \omega_k)$ by the characteristics of the space structure of solution. The following is the immune genetic algorithm based on the model of solution space.

43.3.1 Individual Code

According to the model characteristics by Eq. 43.1, we identified a two-dimensional array as encoding:

$$\omega = \begin{pmatrix} \omega_1 \\ \omega_2 \\ \vdots \\ \omega_k \end{pmatrix} = \begin{pmatrix} \omega_{11} & \omega_{12} & \cdots & \omega_{1l} \\ \omega_{21} & \omega_{22} & \cdots & \omega_{2l} \\ \vdots & \vdots & \vdots & \vdots \\ \omega_{k1} & \omega_{k2} & \cdots & \omega_{kl} \end{pmatrix} = (\omega_{ij}), i \in \underline{k}, j \in \underline{l} \qquad (43.2)$$

where $\omega_i \in {}_{C_i^{\omega_{i-1}}}\Omega_l^{n_i}, i \in \underline{k}$.

Every line of array represents a gene, and an individual is made up of k genes. Every gene ω_i includes l information. The range of information is $\{0. \cdots, n\}$. If $\omega_{ij} = x, x \in \underline{n}$, it describes flight x is parking in the gate j. If $\omega_{ij} = 0$, there is not flights in the gate j.

43.3.2 Fitness Function

We directly use the objective function: $\pi(\omega) = \sum_{i=1}^{k} \sum_{j=1}^{l} c(\omega_{ij}) * \gamma_j$, where $c(\omega_{ij})$ describes the characteristic of the flight ω_{ij}, $c(0) = 0$; γ_j describes the characteristic of gate j. According to the objective function, we define the function $\pi(\omega_i) = \sum_{j=1}^{l} c(\omega_{ij}) * \gamma_j$ reflecting the good quality of gene ω_i.

Definition 1 if $\pi(\omega_i^*) = \max\limits_{\omega_i \in {}_{C_i^{\omega_{i-1}}}\Omega_l^{n_i}} \pi(\omega_i), i \in \underline{k}$, we consider ω_i^* as a good gene of $\omega_i \in {}_{C_i^{\omega_{i-1}}}\Omega_l^{n_i}$.

43.3.3 Population Initialization

Assume the initial population is composed by s individuals, which includes s_1 satisfactory solution using heuristic algorithms and s_2 individuals selected in the solution space.

The following will discuss how to select randomly s_2 individuals in the solution space. Selecting s_2 individuals $\omega_1^i \in {}_{C_1}\Omega_l^{n_1}, i \in \underline{s_2}$ and form the first gene. To the conflict flights set $\overline{A_1} = \{{}_1\overline{a_1}, \cdots {}_1\overline{a_{m_1}}\}$ that contains a set of extended flights, then randomly ordering gates for each flight. As to flight ${}_1\overline{a_1}$, we distribute randomly a gate $P({}_1\overline{a_1})$ from the gate set P. As to flight ${}_1\overline{a_2}$, we distribute randomly a gate $P({}_1\overline{a_2})$ from the rest of gate set $P({}_1\overline{a_1})$ that remove from gate set. Like that, we identify randomly a distributed method $\{P({}_1\overline{a_1}), P({}_1\overline{a_2}), \cdots, P({}_1\overline{a_{m_1}})\}$ for the flight set $\overline{A_1}$. As to flights not being assigned gates, we assume that the flight number is 0, that is $\{P({}_1\overline{a_1}), P({}_1\overline{a_2}), \cdots, P({}_1\overline{a_{m_1}}), P(0), \cdots P(0)\}$. Consequently, all flights are allocated gates. According to ascending order of numbers of airport gate and with the flight number as the element, we will regard the flight number being allocated in the first gate as the first element and in the second gate as the second element, and until all the gates are completed. Then we describe it with this set $\left\{{}_1\widetilde{a_1}, {}_1\widetilde{a_2}, \cdots, {}_1\widetilde{a_l}\right\}$, where $P\left({}_1\widetilde{a_i}\right) = i, i \in \underline{l}$. Then we get the first gene: $\omega_1^1 = (\omega_{11}^1, \cdots \omega_{1l}^1), \omega_{1j}^1 = {}_1\widetilde{a}_j$ of the first individual, and we can get the first gene of all individuals with the same method.

Then we need identify the second gene. We select randomly $\omega_2^i \in {}_{C_2^{\omega_1^i}}\Omega_l^{n_2}$ as the second gene of the individual i. Continuing to do so, all the genes are identified and s_2 individuals will be also identified. Combining s_1 satisfactory solution of the problem by the heuristic with s_2 solutions got randomly from the solution space as the initial population. The initial population is designed:

$\widetilde{\Omega}_0 = \{{}_1\omega_0, {}_2\omega_0, \cdots, {}_s\omega_0\}$, The population of the j generation is denoted:

$$\widetilde{\Omega}_j = \left\{{}_1\omega_j, {}_2\omega_j, \cdots, {}_s\omega_j\right\} \tag{43.3}$$

Where, ${}_i\omega_j = \left\{{}_i\omega_j^1, {}_i\omega_j^2, \cdots, {}_i\omega_j^k\right\}, i \in \underline{s}, {}_i\omega_q^j$ represents the q gene of the i individual in the initial population.

43.3.4 Genetic Operator

43.3.4.1 Selection Operator

The size s of population is given by Eq. 43.2, where each individual is represented as a two-dimensional array with $k \times l$. The following individuals are given some definitions, such as the similarity, concentration, expected reproductive rate, selection probability.

(1) Similarity taking any two individuals,

$$_{i_1}\omega_{j_1} = \left\{_{i_1}\omega_{j_1}^1, _{i_1}\omega_{j_1}^2, \cdots, _{i_1}\omega_{j_1}^k\right\}, _{i_2}\omega_{j_1} = \left\{_{i_2}\omega_{j_1}^1, _{i_2}\omega_{j_1}^2, \cdots, _{i_2}\omega_{j_1}^k\right\}$$

Where, $i_1, i_2 \in \underline{s}, i_1 \neq i_2$, j_1 represents the number of evolution generation. We assume that the adaptation of individual $_{i_1}\omega_{j_1}$ is $\pi\left(_{i_1}\omega_{j_1}\right)$ and the other $_{i_2}\omega_{j_1}$ is $\pi\left(_{i_2}\omega_{j_1}\right)$, then assuming ε is a normal appropriate small number ($\varepsilon > 0$), if $1 - \varepsilon \leq Q\left(_{i_1}\omega_{j_1}, _{i_2}\omega_{j_1}\right) = \dfrac{\pi\left(_{i_1}\omega_{j_1}\right)}{\pi\left(_{i_2}\omega_{j_1}\right)} \leq 1 + \varepsilon$ is right, we call the two individuals $_{i_1}\omega_{j_1}$ and $i_2\omega_{j_1}$ are similar. Where $Q\left(_{i_1}\omega_{j_1}, _{i_2}\omega_{j_1}\right)$ reflects the indicators of the quality of similarity of the individuals $_{i_1}\omega_{j_1}$ and $_{i_2}\omega_{j_1}$; ε is defined similarity threshold of individual. If $\varepsilon = 0.02$, the last type holds on, then we say the two individuals have 98% similarity in the quality. Comparing with similarity definition of individual based on information entropy and Euclidean distance, the definition has two advantages: the definition of percentage similarity of the two individuals described more intuitive has a smaller amount of computation.

(2) Concentration During individuals with the particular and the scale for s , the number of individuals being similar to the individual $q \in \underline{s}$ (including individual q itself) is called the concentration of individual q, and denoted c_q.

(3) Expected rate of reproduction As to the individuals of particular and the scale for s , the expected rate e_q of reproduction of the individual $q \in \underline{s}$ is defined as $e_q = \dfrac{\pi\left(q\omega_j\right)}{\left(c_q\right)^\beta}$, Where $\pi\left(q\omega_j\right)$ is the fitness of the individual q ; c_q is the concentration of individual q ; β is a relatively important parameter that reflects the concentration and fitness of the reproductive rates.

(4) Copy (clone) the probability As to the individuals with particular and the scale for s , we assume the expected rate of reproduction of individual $q \in \underline{s}$ is e_q , then the probability P_q of individual q that is chosen to be copied (clone) is:

$$P_q = e_q \bigg/ \sum_{t=1}^{s} e_t \qquad (43.4)$$

For the selected individuals, the crossover and mutation operations need to implement.

43.3.4.2 Crossover Operator

During the cross operation, the individual is divided into several groups, and each part is composed of a group of two individuals to complete the single point crossover and multipoint crossover operation with the cross probability.

Single point crossover randomly selects two individuals:

$_{i_1}\omega_{j_1} = \left\{ _{i_1}\omega_{j_1}^1, _{i_1}\omega_{j_1}^2, \cdots, _{i_1}\omega_{j_1}^k \right\}$ And $_{i_2}\omega_{j_1} = \left\{ _{i_2}\omega_{j_1}^1, _{i_2}\omega_{j_1}^2, \cdots, _{i_2}\omega_{j_1}^k \right\}$, Where $i_1, i_2 \in \underline{s}, i_1 \neq i_2$. Then we randomly select a point $r \in \underline{k}, r \geq 2$. If $_{i_1}\omega_{j_1}^r \in {}_{c_r^{i_2}\omega_{j_1}^{r-1}}\Omega_l^{n_\gamma}, _{i_2}\omega_{j_1}^\gamma \in {}_{c_r^{i_1}\omega_{j_1}^{r-1}}\Omega_l^{n_\gamma}$, that is to meet the restriction of optimized assignment. Then we perform the crossover operation to generate two offspring individuals:

$_{i_1}\omega_{j_1} = \left\{ _{i_1}\omega_{j_1}^1, _{i_1}\omega_{j_1}^2, \cdots, _{i_1}\omega_{j_1}^{r-1}, _{i_2}\omega_{j_1}^{r'}, _{i_2}\omega_{j_1}^{r+1}, \cdots, _{i_2}\omega_{j_1}^k \right\}$,

$_{i_2}\omega_{j_1} = \left\{ _{i_2}\omega_{j_1}^1, _{i_2}\omega_{j_1}^2, \cdots, _{i_{21}}\omega_{j_1}^{r-1}, _{i_1}\omega_{j_1}^{r'}, _{i_1}\omega_{j_1}^{r+1}, \cdots, _{i_1}\omega_{j_1}^k \right\}$. If they do not meet the compatibility condition, crossover operation is not performed. Similarly, multipoint crossover is also treated.

43.3.4.3 Mutation Operator

Mutation can help to increase the diversity of the population. As to the parent individual $_i\omega_j = \left\{ _i\omega_j^1, _i\omega_j^2, \cdots, _i\omega_j^k, \right\}$, we need to implement single point mutation and multipoint mutation with the rate of the variation.

Single point: randomly selecting a point $q \in \underline{k}$, if $_i\omega_j^{q'} \in {}_{c_q^i \omega_j^{q-1}}\Omega_l^{n_q}, _i\omega_j^{q+1} \in {}_{c_{q+1}^i \omega_j^{q'}}\Omega_l^{n_{q+1}}$ that is meeting to the restriction of optimized assignment. Then we replace $_i\omega_j^q$ with $_i\omega_j^{q'}$, and we get the offspring individual

$_{i'}\omega_j = \left\{ _i\omega_j^1, _i\omega_j^2, \cdots, _i\omega_j^{q-1}, _i\omega_j^{q'}, _i\omega_j^{q+1}, \cdots, _i\omega_j^k \right\}$ Similarly, multipoint mutation is also treated.

43.3.4.4 Immune Operator

As to an individual, vaccination is to modify some of its locus on the gene in accordance with its prior knowledge, so that individuals with higher income have a higher probability of fitness.

Assuming population $\widetilde{\Omega}_j = \left\{ _1\omega_j, _2\omega_j, \cdots, _s\omega_j \right\}$ (Eq. 43.2), vaccinated the population refers to an operation that we operate the randomly selected individuals $s_\alpha = \alpha s$ from the population in accordance the ratio of $\alpha(0 < \alpha \leq 1)$. To an extracted individual $_i\omega_j = \left\{ _i\omega_j^1, _i\omega_j^2, \cdots, _i\omega_j^k, \right\}$ we need vaccinate each locus, and to the $q \in \underline{k}$ gene locus:

By the Definition 2.1, we assume the good gene on the gene locus is $_i\omega_j^*$. If $_i\omega_j^* \in {}_{c_q^i \omega_j^{q-1}}\Omega_l^{n_q}, _i\omega_j^{q+1} \in {}_{c_{q+1}^i \omega_j^*}\Omega_l^{n_{q+1}}$ then instead the $q \in \underline{k}$ gene of the individual,

we used the good gene $_i\omega_j^*$ to generate the new individual: $_{i'}\omega_{j=}\{_i\omega_j^1,_i$
$\omega_j^2,\cdots,_i\omega_j^{q-1},_i\omega_j^*,_i\omega_j^{q+1},\cdots,_i\omega_j^k\}$. If they don't meet the compatibility condition, then the vaccination is not carried. Obviously, the new individual has bigger fitness function than the original individual, so it is the best individual.

As to the current parent population $\widetilde{\Omega}_j = \{_i\omega_{j,2}\,\omega_j,\cdots,_s\omega_j\}$, after the selection operator, crossover, mutation operator and vaccination, it results in a number of offspring individual group, denoted: $\widetilde{\Omega}_{j+1}$. And we copy an individual of parent population by selection operator to the offspring of individuals, still denoted: $\widetilde{\Omega}_{j+1}$. To maintain the population size is still s, if the number of the individual is more than s during the offspring population, then selecting s individuals of the parent population as a collection; if the number is less than s, then from the not selected individual with selection operator of the original parent population, we need select the individual with the maximum value of fitness function, and add it to the offspring population, so that the size of the offspring population is still s.

43.3.5 The Elite Retention Policy

Assuming that when the genetic algorithm evolutes the t generation, the group ω_t^* is the best individual. And suppose $\widetilde{\Omega}_{t+1}$ is a new generation of groups, if ω_t^* does not exist in $\widetilde{\Omega}_{t+1}$, then put ω_t^* to $\widetilde{\Omega}_{t+1}$ as the $s + 1$ individual of $\widetilde{\Omega}_{t+1}$, where s is the size of the group. To maintain constant population size, if the individual is added to the new generation of elite groups, then the individual with the smallest fitness off the new generation is out. Elite individual is the highest fitness individual tat can be selected in the evolutionary of population genetic algorithm to the current date.

The advantage of using elitist: so far, the best individuals can not loss and be damaged by the selection, crossover and mutation in the evolutionary process of genetic algorithm. Elitist strategy for improving the global convergence of the standard genetic algorithm has a significant role, the standard genetic algorithm with elitist is global convergence.

43.3.6 The Selection and Termination Conditions of Algorithm Parameter

43.3.6.1 Algorithm Parameter Selection

The number of population is one of factors effecting optimizing performance and efficiency of algorithm. Typically, the population is too small to provide sufficient sampling points resulting in poor performance of the algorithm, even not a feasible solution of the problem; despite the population is so large that it can increase the optimize information to prevent the occurrence of premature convergence, it will

Table 43.1 An example: Evolution generation

Evolution generation	0	20	40	60	80	90
Objective function value	5930492	6030222	6096818	6163414	6220870	6220870
The error rate comparing with the objective function upper bound (6,529,041)	9.17%	7.64%	6.62%	5.60%	4.72%	4.72%
Computing time [min]	0	11	20	27	34	40

undoubtedly increase the computational so that the convergence time is too long. Of course, the number of species in the optimization process is to allow the change.

Crossover probability is used to control the frequency of crossover operation. Probability is so large and the string of the population update quickly that it can make the high-fit value of the individual destroyed quickly. When the probability is too small, the crossover operation is rarely implemented, which will make search stagnation.

Mutation probability is an important factor to increase population diversity. In the genetic algorithm based on binary encoding, a lower mutation rate is enough to prevent the entire group of genes in any position to change. However, the rate is too small to produce new individuals, and too large probability makes the genetic algorithm a random search algorithm.

43.3.6.2 Algorithm Termination Condition

The convergence theory of genetic algorithm describe the limit properties of genetic algorithm with probability 1 convergence, so what we have to purse is to improve the convergence rate, which effects the design and parameter selection of the algorithm operation.

The most common termination condition is to be given one of the biggest evolutionary steps, or determine whether the cadres of the best optimal value do not change significantly and continuously.

43.4 An Example and Results Analysis

We Choose 20 gates from one gate of a busy domestic airport and 120 flights in the peak hours (6 h) in one day as test objects. Writing a program using MATLAB and calculating it with an ordinary desktop computer(performance: the speed of CPU is 2.98 GHZ, the lenovo brand with 2G memory machine, the operating system is Windows x-p), taking one hour 10 min, the rate of crossover is $P_c = 0.6$, the rate of mutation is $P_m = 0.2$, $\beta = 1.5$, $\varepsilon = 0.02$, $m = 30$, If the 10 consecutive generation of the best individual fitness does not change, stop the calculation, and the calculation results and the evolution of the convergence process is shown in Table 43.1.

43.5 Conclusion

With the description of the gate assignment by literature [8], this paper designs a method based on the immune genetic algorithm. The simulation result shows the effectiveness of this model and algorithm. It should be noted that the assignment of the gate is a complex issue, this paper considers optimization method of the gate assignment based on the immune genetic algorithm, and there is a certain practicality. The article assumes that the gate is always more than enough, as to not having enough stands, the problem that some of flights need to stop in the far flight needs further study, and considering the dynamic allocation of flight delays and other problems requires further study.

References

1. Wen J, Sun H, Xu J, Liang ZJ (2004) The distribution of airport gate based on sorting algorithm [J](In Chinese). Syst Eng 22(7):102–106
2. Su YY, Srihari K (2001) A knowledge-based aircraft-gate assignment advisor [J]. Comput Ind Eng 25(2):123–126
3. Ding H, Lim A, Rodrigues B, Zhu Y (2005) The over-constrained airport gate assignment problem. Comput Oper Res 32:1867–1880
4. Hu XB, Di Paolo E (2008) An efficient genetic algorithm with uniform crossover for the multi-objective airport gate assignment problem. In: IEEE congress on evolutionary computation, pp 55–62
5. Drexl A, Nikulin Y (2008) Multicriteria airport gate assignment and Pareto simulated annealing. IIE Trans (Institute of Industrial Engineers) 40(4):385–397
6. Yan S, Tang C-H (2007) A heuristic approach for airport gate assignments for stochastic flight delays. Eur J Oper Res 180(2):547–567
7. Ju S-M, Xu Li (2008) Airport gate assignment problems based on GSAA. J Transp Syst Eng Inf Technol 8(1):138–143
8. Wang L (2010) Optimized assignment of civil airport gate. In: 2010 international conference on intelligent system design and engineering application, pp 33–38

Chapter 44
Output Feedback Adaptive Dynamic Surface Control for a Class of Nonlinear Systems With Input Saturation

Xiu-Duan Yu, Xiu-Xia Sun and Wen-Han Dong

Abstract An output feedback adaptive tracking scheme is proposed for a class of nonlinear systems with parameter uncertainty and input saturation. The unmeasured states are estimated by constructing filters, then dynamic surface control system is designed, which avoids explosion complexity of backstepping control. The effect of actuator saturation on system performance is compensated by neural network. It is shown that the proposed scheme can guarantee semi-global stability of the closed-loop system and the tracking error can be made arbitrarily small.

Keywords Output feedback · Dynamic surface control · Input saturation · Neural networks · Adaptive control

44.1 Introduction

Controller design for nonlinear systems with input saturation offers both practical significance and theoretical challenges. Over the last decades there have been various kinds of approaches which account for the capacity of actuator saturation. In [1], observer-based anti-windup was developed for a class of nonlinear systems, in which state observer was applied to monitor and regulate the state when actuator saturation occurred. In [2], input constraints were incorporated into unified framework for linear time-invariant systems, the framework was based on two-step design: design the linear controller ignoring control input nonlinearities and then

X.-D. Yu (✉) · X.-X. Sun · W.-H. Dong
The Engineering Institute, Air Force Engineering University,
Xi'an 710038, Shaanxi, China
e-mail: yuxiuduan2003@yahoo.com.cn

add anti-windup bumpless transfer (AWBT) compensation to minimize the adverse effects of input saturation. In [3], backstepping control was proposed to cope with input saturation, in which saturation nonlinearity is compensated by using neural network, and the transient performance is also established by tuning several design parameters.

Backstepping control mentioned above suffers from "explosion of complexity", which is caused by repeated differentiation of nonlinear functions. In [4], a new technique named dynamic surface control (DSC) was applied to tracking controller design, where low pass filters were utilized to prevent direct derivative of the control signal, thus drawback of backstepping control is well eliminated. However, most of the current adaptive DSC schemes for nonlinear systems are focused on full-state feedbacks, it is difficult to be applied to the case where only system output is available.

In this paper, an output feedback adaptive control scheme using DSC technique is proposed for a class of nonlinear systems with input saturation. By utilizing K-filters the system state is estimated with only system output signal, then a DSC controller is designed which employs neural network to compensate the effect of input saturation on system performance. We show that the control law can be greatly simplified, and good tracking performance can be achieved.

The rest of the paper is organized as follows. In Sect. 44.2, the control problem is formulated. In Sect. 44.3, the design procedure of output feedback adaptive DSC controller is presented. Section 44.4 gives the stability analysis for the proposed scheme. The tracking performance is validated by simulation study in Sect. 44.5. Some conclusions are made in Sect. 44.6.

44.2 System Problem Presentation

Consider a class of nonlinear systems with input saturation in the following output feedback form [5]:

$$\dot{x}_1 = x_2 + f_{0,1}(y) + \sum_{i=1}^{p} a_i f_{i,1}(y)$$

$$\dot{x}_{\rho-1} = x_\rho + f_{0,\rho-1}(y) + \sum_{i=1}^{p} a_i f_{i,\rho-1}(y)$$

$$\dot{x}_\rho = x_{\rho+1} + f_{0,\rho}(y) + \sum_{i=1}^{p} a_i f_{i,\rho}(y) + b_{n-\rho} g(y)\tau(u) \qquad (44.1)$$

$$\dot{x}_n = f_{0,n}(y) + \sum_{i=1}^{p} a_i f_{i,n}(y) + b_0 g(y)\tau(u)$$

$$y = x_1,$$

where $x \in \Re^n$ is the state, $y \in \Re$ is output; $f_i(y) = [f_{i,1}(y), \cdots, f_{i,n}(y)]^T$, $i = 0, \cdots, p$ and $g(y) \neq 0$ are known smooth functions; $a_1, \cdots, a_n$ and $b_0, \cdots, b_{n-\rho}$ are uncertain constant parameters; ρ is the relative degree of the system; $\tau(u)$ is a saturation function with regard to control input $u(t)$ and can be expressed as

$$\tau(u) = \begin{cases} \tau_{\max}, & u(t) < \tau_{\max}, \\ u, & \tau_{\min} \leq u(t) \leq \tau_{\max}, \\ \tau_{\min}, & u(t) < \tau_{\min}, \end{cases} \tag{44.2}$$

where $\tau_{\max}$ and $\tau_{\min}$ are known saturation bounds. Only system output y is available for measurement.

It is clear that if control signal $u(t)$ falls outside the range $[\tau_{\min}, \tau_{\max}]$, saturation of actuator occurs, therefore control signal $u(t)$ can not be fully implemented. Similar to the method in [6], we define non-implemented control as $\delta = \tau - u$, which is an unknown nonlinear function as viewed from control.

Many results show that unknown smooth functions can be approximated well by using radial basis function neural network (RBFNN), therefore it can be employed to approximate δ.

Lemma 1 [7] *RBFNN is universal approximator in the sense that given any real continuous function $f(\cdot) : \Re^m \to \Re$ over a compact set $\Omega_Z \subset \Re^m$, for any $\varepsilon^* > 0$, there exists RBFNN such that*

$$f(Z) = W^* R(Z) + \varepsilon^*, \quad \forall Z \in \Omega_Z, \tag{44.3}$$

where $W^* \in \Re^N$ is constant weight in the output layer, N is neurons number in hidden layer, $R(Z) = [R_1(Z), \cdots, R_N(Z)]^T$ is a vector of radial basis function often adopted as Gaussian function.

Generally, W^* is unknown and need to be replaced by its estimation $\hat{W}$, hence, the optimal weight of RBFNNs can be defined as $W^* = \arg_{\hat{W} \in \Omega_f} \min |\hat{W}^T R(Z) - f(Z)|$, in which $\Omega_f = \{\hat{W}| \, ||\hat{W}|| \leq \iota\}$ is a valid field of the weight with ι being a design parameter.

For developing an adaptive controller, we make the following assumptions on (44.1):

Assumption 1 The polynomial $B(s) = b_{n-\rho} s^{n-\rho} + \cdots + b_1 s + b_0$ is Hurwitz, where the sign of $b_{n-\rho}$ is known. Without loss of generality, suppose that $0 < b_{n-\rho} < b_{n-\rho}^M$ with $b_{n-\rho}^M$ being a known bound.

Assumption 2 The reference signal y_r and its first two derivatives are continuous, and they belong to a known compact set $\Pi = \{(y_r, \dot{y}_r, \ddot{y}_r) | y_r^2 + \dot{y}_r^2 + \ddot{y}_r^2 \leq \kappa\}$ with κ being a known constant.

The control objective is to design an adaptive controller such that system output y asymptotically tracks a given reference signal y_r while keeping all signals of the closed-loop system bounded.

44.3 Output Feedback DSC Controller Design

To begin with, we rewrite (44.1) in the following compact form:

$$\dot{x} = Ax + f_0(y) + \sum_{i=1}^{p} a_i f_i(y) + \bar{b}g(y)\tau(u),$$

$$y = c^T x, \tag{44.4}$$

where

$$A = \begin{bmatrix} 0 & I_{n-1} \\ 0 & 0 \end{bmatrix}, \; \bar{b} = [\underbrace{0 \cdots 0}_{\rho-1} b_{n-\rho} \cdots b_1 b_0]^T, \; c = [1 \underbrace{0 \cdots 0}_{n-1}]^T.$$

Since only output y is available, we employ the following K-filters in [5] to estimate the state:

$$\begin{aligned}
\dot{\xi}_0 &= A_o \xi_0 + Ky + f_0(y), \\
\dot{\xi}_i &= A_o \xi_i + f_i(y), \; 1 \le i \le p, \\
\dot{v}_j &= A_o v_j + e_{n-j} g(y)\tau, \; 0 \le j \le n - \rho,
\end{aligned} \tag{44.5}$$

where e_i is ith coordinate vector in $\Re^n$ and K is a vector which is appropriately chosen such that $A_o = A - Kc^T$ is a Hurwitz matrix. In view of (44.4) and (44.5), x can be expressed as

$$x = (\xi_0 + \sum_{i=1}^{p} a_i \xi_i + \sum_{j=0}^{n-\rho} b_j v_j) + \mu \tag{44.6}$$

where μ is observation error satisfying $\dot{\mu} = A_o \mu$.

The procedure of our output feedback DSC design is given below.

Step 1: Define the first surface error $S_1 = y - y_r$. From (44.1), we can see that

$$\dot{S}_1 = \dot{x}_1 - \dot{y}_r = x_2 + f_{0,1}(y) + \sum_{i=1}^{p} a_i f_{i,1}(y) - \dot{y}_r. \tag{44.7}$$

Since x_2 is unmeasurable, from (44.6) we have:

$$x_2 = (\xi_{0,2} + \sum_{i=1}^{p} a_i \xi_{i,2} + \sum_{j=0}^{n-\rho} b_j v_{j,2}) + \mu_2,$$

where μ_2 is the second entry of μ. Thus we have

$$\dot{S}_1 = \xi_{0,2} + f_{0,1}(y) - \dot{y}_r + \sum_{i=1}^{p} a_i (\xi_{i,2} + f_{i,1}(y)) + \sum_{j=0}^{n-\rho} b_j v_{j,2} + \mu_2 \tag{44.8}$$

Note from (44.5) that u will first appear in the ρth derivative of $v_{n-\rho,2}$. Define

$$\theta = \left[\frac{1}{b_{n-\rho}}, \frac{a_1}{b_{n-\rho}}, \cdots \frac{a_p}{b_{n-\rho}}, \frac{b_0}{b_{n-\rho}}, \cdots, \frac{b_{n-\rho-1}}{b_{n-\rho}} \right]^T \qquad (44.9)$$

$$\phi = \left[l_1 S_1 + \xi_{0,2} + f_{0,1}(y) - \dot{y}_r, \xi_{1,2} + f_{1,1}(y), \cdots, \xi_{p,2} + f_{p,1}(y), v_{0,2}, \cdots, v_{n-\rho-1,2} \right]^T \qquad (44.10)$$

where l_1 is a design parameter.[1]

If θ were known, taking $v_{n-\rho,2}$ as virtual control, choosing $v_{n-\rho,2} = -\theta^{*T}\phi$ would make $\dot{S}_1 = -l_1 S_1 + \varepsilon_2$. However, since θ is unknown, we let $\hat{\theta}$ be the estimate of θ which is updated by

$$\dot{\hat{\theta}} = -\eta_1 \Gamma_1 \hat{\theta} + S_1 \Gamma_1 \phi, \qquad (44.11)$$

where $\eta_1 > 0$ is design parameter and $\Gamma_1 = \Gamma_1^T > 0$. Then the desired virtual control can be chosen as

$$\bar{v}_{n-\rho,2} = -\hat{\theta}^T \phi. \qquad (44.12)$$

Let $\bar{v}_{n-\rho,2}$ pass through a first-order filter with time constant τ_2 to obtain a new state variable z_2:

$$\tau_2 \dot{z}_2 + z_2 = \bar{v}_{n-\rho,2}, \quad z_2(0) = \bar{v}_{n-\rho,2}(0). \qquad (44.13)$$

Step i ($2 \le i \le \rho - 1$): Define the ith surface error $S_i = \bar{v}_{n-\rho,i} - z_i$. By (44.5), the derivative of S_i is

$$\dot{S}_i = -k_i v_{n-\rho,1} + v_{n-\rho,i+1} - \dot{z}_i \qquad (44.14)$$

Viewing $v_{n-\rho,i+1}$ as virtual control, its desired signal $\bar{v}_{n-\rho,i+1}$ is chosen as follows

$$\bar{v}_{n-\rho,i+1} = -l_1 S_i + k_i v_{n-\rho,1} + \dot{z}_i \qquad (44.15)$$

Similarly, we let $\bar{v}_{n-\rho,i+1}$ pass through the following filter with time constant τ_{i+1} to obtain z_{i+1}:

$$\tau_{i+1} \dot{z}_{i+1} + z_{i+1} = \bar{v}_{n-\rho,i+1}, \quad z_{i+1}(0) = \bar{v}_{n-\rho,i+1}(0) \qquad (44.16)$$

Step ρ: Define the last surface error $S_\rho = v_{n-\rho,\rho} - z_\rho$, whose time derivative is

$$\dot{S}_\rho = -k_\rho v_{n-\rho,1} + v_{n-\rho,\rho+1} + g(y)(u + \delta) - \dot{z}_\rho. \qquad (44.17)$$

Since δ is unknown, inspired by NN saturation compensator in [6], we use RBFNN to approximate $g(y)\delta$ on a given compact set Ω_z as follows

---

[1] All the design parameters l_i in the next steps are assumed to be positive numbers.

$$g(y)\delta = W^T R(Z) + \varepsilon \tag{44.18}$$

where $Z = \left[S_\rho, v_{n-\rho,1}, v_{n-\rho,\rho+1}, \dot{z}_\rho, y\right]^T$ is the network input, $W \in \Re^N$ is the constant weight, ε is the approximation error which is taken as a small constant. We use $\hat{W}$ to replace W, which is updated by

$$\dot{\hat{W}} = -\eta_2 \Gamma_2 \hat{W} + S_\rho R(Z) \tag{44.19}$$

where η_2 is a positive constant and $\Gamma_2 = \Gamma_2^T > 0$. Now, the control law u can be designed as

$$u = \frac{1}{g(y)}\left[-l_\rho S_\rho + k_\rho v_{n-\rho,1} - v_{n-\rho,\rho+1} + \dot{z}_\rho - \hat{W}^T R(Z)\right] \tag{44.20}$$

44.4 Stability Analysis

Stability analysis for the developed control system is complicated due to the derivation of the low pass filters. For convenience, define filter error $y_i = z_i - \bar{v}_{n-\rho,i}$, $i = 2, \cdots, \rho$, then we can rewrite (44.8) as

$$\dot{S}_1 = -l_1 S_1 + b_{n-\rho} S_2 + b_{n-\rho} y_2 - b_{n-\rho} \tilde{\theta}^T \phi + \mu_2 \tag{44.21}$$

where $\tilde{\theta} = \hat{\theta} - \theta^*$. In the same way, we have

$$\dot{S}_i = -l_i S_i + S_{i+1} + y_{i+1}, \quad i = 2, \cdots, \rho - 1 \tag{44.22}$$

Substituting (44.18), (44.19) and (44.20) into (44.17) yields

$$\dot{S}_\rho = -l_\rho S_\rho - \tilde{W}^T R(Z) + \varepsilon \tag{44.23}$$

where $\tilde{W} = \hat{W} - W^*$ is parameter error.

On the other hand, considering (44.12), (44.15), we obtain

$$\dot{y}_2 = \dot{z}_2 - \dot{\bar{v}}_{n-\rho,2} = -\frac{y_2}{\tau_2} + \dot{\hat{\theta}}^T \phi + \hat{\theta}^T \dot{\phi}$$

and

$$\dot{y}_{i+1} = \dot{z}_{i+1} - \dot{\bar{v}}_{n-\rho,i+1} = -\frac{y_{i+1}}{\tau_{i+1}} + l_i \dot{S}_i - k_i \dot{v}_{n-\rho,1} + \frac{\dot{y}_i}{\tau_i},$$

$$i = 2, \cdots, \rho - 1,$$

from which we have

$$\left|\dot{y}_2 + \frac{y_2}{\tau_2}\right| \leq B_2(S_1, S_2, \tilde{\theta}, y_2, y_r, \dot{y}_r, \ddot{y}_r, \mu) \tag{44.24}$$

$$\left| \dot{y}_{i+1} + \frac{y_{i+1}}{\tau_{i+1}} \right| \leq B_{i+1}(S_1, \cdots, S_{i+1}, \tilde{\theta}, \tilde{W}, y_2, \cdots, y_{i+1}, y_r, \dot{y}_r, \ddot{y}_r, \mu) \tag{44.25}$$
$$i = 2, \cdots, \rho - 1,$$

where B_2 and B_{i+1} are some continuous functions. In what follows, a theorem will be established.

Theorem 1 *Define Lyapunov function* candidate $V = \sum_{i=1}^{\rho} V_i$ with

$$V_1 = \frac{1}{2}S_1^2 + \frac{1}{2}b_{n-\rho}\tilde{\theta}^T\Gamma_1^{-1}\tilde{\theta} + \frac{1}{2}y_2^2 + \mu^T P\mu,$$
$$V_i = \frac{1}{2}S_i^2 + \frac{1}{2}y_{i+1}^2, \quad i = 2, \cdots, \rho - 1, \tag{44.26}$$
$$V_\rho = \frac{1}{2}S_\rho^2 + \frac{1}{2}\tilde{W}^T\Gamma_2^{-1}\tilde{W}$$

in which P is the solution of $PA_0 + A_0^T P = -I$. For any $\gamma > 0$, if $\sum_{i=1}^{\rho} V_i(0) \leq \gamma$, there exist $l_i(i = 1, \cdots, \rho)$, $\tau_j(j = 2, \cdots, \rho)$, η_1, η_2 such that all signals of the closed-loop system are semi-global ultimately bounded, in addition, the tracking error converges to a residual set that can be made arbitrarily small.

Proof The time derivative of V_1 is

$$\dot{V}_1 \leq -l_1 S_1^2 + b_{n-\rho}S_1 S_2 + b_{n-\rho}S_1 y_2 + S_1\mu_2 - b_{n-\rho}\eta_1\tilde{\theta}^T\hat{\theta} + y_2\dot{y}_2 - \mu^T\mu \tag{44.27}$$

Define the following compact sets:

$$\Omega_i = \left\{ (S_1, \cdots, S_i, y_2, \cdots, y_i, \tilde{\theta}, \tilde{W}) \middle| \sum_{j=1}^{i} S_j^2 + b_{n-\rho}\tilde{\theta}^T\Gamma_1^{-1}\tilde{\theta} + \sum_{j=2}^{i} y_j^2 + 2\mu^T P\mu + \tilde{W}^T\Gamma_2^{-1}\tilde{W} \leq 2\gamma \right\},$$
$$i = 2, \cdots, \rho. \tag{44.28}$$

Note that $\Pi \times \Omega_i$ are also compact sets. Thus continuous functions B_i in (44.24) and (44.25) have maximums, say, M_i, on $\Pi \times \Omega_i$. Therefore $y_i\dot{y}_i \leq -y_i^2/\tau_i + |B_i y_i| \leq -y_i^2/\tau_i + y_i^2/2 + M_i^2/2$, $i = 2, \cdots, \rho$. Using inequalities $\tilde{\theta}^T\hat{\theta} \geq \frac{1}{2}(||\tilde{\theta}||^2 - ||\theta||^2)$, $\tilde{W}^T\tilde{W} \geq \frac{1}{2}(||\tilde{W}||^2 - ||W||^2)$, $B_i|y_i| \leq \frac{\lambda}{2}M_i^2 y_i^2 + \frac{1}{2\lambda}$, $\lambda > 0$, we have

$$\dot{V}_1 \leq -\left(l_1 - \frac{1}{2} - b_{n-\rho}^M\right)S_1^2 - \left(\frac{1}{\tau_2} - \frac{b_{n-\rho}^M}{2} - \frac{\lambda M_2^2}{2}\right)y_2^2 - \frac{b_{n-\rho}^M\eta_1}{2\lambda_{\max}(\Gamma_1^{-1})}\tilde{\theta}^T\Gamma_1^{-1}\tilde{\theta}$$

$$+ \frac{b_{n-\rho}^M\eta_1}{2}||\theta||^2 + \frac{1}{2\lambda} + \frac{b_{n-\rho}^M}{2}S_2^2 \tag{44.29}$$

where $\lambda_{\max}(\Gamma_1^{-1})$ is the maximum eigenvalue of Γ_1^{-1}.

From (44.22) and (44.26), the time derivative of V_2 satisfies

$$\dot{V}_2 \leq -\left(l_2 - 1 - \frac{b_{n-\rho}^M}{2}\right)S_2^2 - \left(\frac{1}{\tau_3} - \frac{1}{2} - \frac{\lambda M_3^2}{2}\right)y_3^2 + \frac{1}{2\lambda} - \frac{b_{n-\rho}^M}{2}S_2^2 + \frac{1}{2}S_3^2$$

(44.30)

Similarly, for $i = 3, \cdots, \rho - 1$, we have

$$\dot{V}_i \leq -\left(l_i - \frac{3}{2}\right)S_i^2 - \left(\frac{1}{\tau_{i+1}} - \frac{1}{2} - \frac{\lambda M_{i+1}^2}{2}\right)y_{i+1}^2 + \frac{1}{2\lambda} - \frac{1}{2}S_i^2 + \frac{1}{2}S_{i+1}^2 \quad (44.31)$$

In the end, considering (44.19) and (44.23), the time derivative of V_ρ is

$$\dot{V}_\rho \leq -\left(l_\rho - 1\right)S_\rho^2 - \frac{\eta_2}{2\lambda_{\max}(\Gamma_2^{-1})}\tilde{W}^T\Gamma_2^{-1}\hat{W} + \frac{\eta_2}{2}\|W\|^2 + \frac{\mu^2}{2} - \frac{1}{2}S_\rho^2 \quad (44.32)$$

If we choose $r = \min\left(\frac{\eta_1}{2\lambda_{\max}(\Gamma_1^{-1})}, \frac{\eta_2}{2\lambda_{\max}(\Gamma_2^{-1})}\right)$, which meanwhile satisfies

$$r = \min_{\substack{i=3,\cdots,\rho-1 \\ j=3,\cdots,\rho}}\left\{l_1 - \frac{1}{2} - b_{n-\rho}^M, l_2 - 1 - \frac{b_{n-\rho}^M}{2}, l_i - \frac{3}{2}, l_\rho - 1, \frac{1}{\tau_2} - \frac{b_{n-\rho}^M}{2} - \frac{\lambda M_2^2}{2}, \frac{1}{\tau_j} - \frac{1}{2} - \frac{\lambda M_j^2}{2}\right\}$$

(44.33)

then along the trajectories of (44.29)–(44.32), the time derivative of V is

$$\dot{V} = \sum_{i=1}^{\rho}\dot{V}_i \leq -2rV + C + 2r\mu^T P\mu \quad (44.34)$$

where $C = b_{n-\rho}^M\eta_1\|W\|^2/2 + \eta_2\|W\|^2/2 + (\rho - 1)/2\lambda + \mu^2/2$.

Since μ exponentially decays, it can be verified that $\mu^T P\mu \leq \mu^T(0)P\mu(0)$. If $r > C/(2(\gamma - \mu^T(0)P\mu(0)))$, then $\dot{V} < 0$ on $V = \gamma$. In other words, V is an invariant set. By Lasalle invariant set theorem, the inequality (44.34) implies that all signals included in V, i.e. $S_1, \cdots, S_\rho$ $y_2, \cdots, y_\rho$, $\tilde{\theta}$, $\tilde{W}$, ε are bounded.

Since both S_1 and y_r are bounded, it follows that y is bounded, which implies that the smooth functions $f_i(y)$ and $g(y)$ are bounded as well. Because A_0 is a Hurwitz matrix, from (44.5) we obtain that $\xi_0, \cdots, \xi_p$ are also bounded. Note that (44.1) is equivalent to differential equation $\frac{d^n y}{dt^n} = \sum_{i=1}^{n} \frac{d^{n-i}}{dt^{n-i}}\left[f_{0,i}(y) + \sum_{j=1}^{p}a_jf_{j,i}(y)\right] + \sum_{i=\rho}^{n}b_{n-i}\frac{d^{n-i}}{dt^{n-i}}[g(y)\tau]$. Using the deduction similar to [5, pp 342], the bound of y, the smoothness of $f_i(y)$ and $g(y)$, Assumption 1 implies that $v_j, j = 0, \cdots, n - \rho$, are bounded. Therefore, $\hat{x}$ and x are bounded due to the boundedness of $\xi_0, \cdots, \xi_p$ and v_j. Since $g(y)$ is bounded away from zero, u is bounded. Hence, all signals of the closed-loop system are bounded.

Furthermore, integrating (44.34) on time interval [0, t], we have $\lim_{t\to\infty} V(t) \leq \frac{c}{2r}$, which implies that $S_1 \leq \sqrt{\frac{c}{r}}$. Thus the tracking error S_1 can be made arbitrarily small by choosing r sufficiently large.

44.5 Simulation Results

In this section, the tracking control for a second-order spring, mass and damper system with input saturation is considered (Details of modeling procedure and characteristics are given in [3]):

$$
\begin{aligned}
\dot{\zeta}_1 &= \zeta_2 \\
\dot{\zeta}_2 &= -\frac{k}{m}\zeta_1 - \frac{k}{m}\zeta_2 + -\frac{1}{m}\tau(u)
\end{aligned}
\tag{44.35}
$$

where ζ_1, ζ_2 are the position, velocity, respectively, m is the mass of object, k is the stiffness constant of the spring, c is the damping, $\tau(u)$ is the actuator saturation nonlinearity. Only position ζ_1 is the measurable variable. The real values of the system parameter are $m = 1.25\,\text{kg}$, $k = 8\,\text{N/m}$ and $c = 2\,\text{N}\cdot\text{s/m}$, $\tau_{\max} = 13\,\text{N}$, $\tau_{\min} = -13\,\text{N}$. Control objective is to design an output feedback adaptive controller, so that the position can track the reference signal $y_r = -0.2\cos(2\pi t) + 0.2$.

Define a change of variables $x_1 = \zeta_1$, $x_2 = \zeta_2 + \frac{c}{m}\zeta_1$, then (44.35) can be converted to the form of (44.1):

$$
\begin{aligned}
\dot{x}_1 &= x_2 - \frac{c}{m}y, \\
\dot{x}_2 &= -\frac{k}{m}y + \frac{1}{m}\tau(u), \\
y &= x_1,
\end{aligned}
\tag{44.36}
$$

Construct the K-filters as follows: $\dot{\xi}_0 = A_0\xi_0 + Ky$, $\xi_0(0) = 0$; $\dot{\xi}_1 = A_0\xi_1 + f_{1(y)}$, $\xi_1(0) = 0$; $\dot{\xi}_2 = A_0\xi_2 + f_{2(y)}$, $\xi_2(0) = 0$; $\dot{v}_0 = A_0 v_0 + e_2\tau(u)$, $v_0(0) = 0$, where $A_0 = A - Kc^T = \begin{bmatrix} -5 & 1 \\ -1 & 0 \end{bmatrix}$, $K = [5\ \ 1]^T$, $f_1(y) = [y\ \ 0]^T$, $f_2(y) = [0\ \ y]^T$. In simulation, the initial conditions are set as $x_1(0) = 0.6$, $x_2(0) = 0.8$. Let $\theta = [m\ \ -c\ \ -k]^T$ with $\hat{\theta}(0) = [1\ \ -1\ \ -1]^T$, parameter update law (44.11) and RBFNNs weight tuning law (44.19) are employed, in which the neurons number in hidden layer is chosen as $N = 61$, the centers of Gaussian function are distributed between -3 and $+3$, and the initial weights $\hat{W}(0)$ are set to be zero. The related design parameters are set as $l_1 = 10$, $l_2 = 80$, $\tau_2 = 0.08$, $\Gamma_1 = 20I_2$, $\Gamma_2 = 20I_{61}$, $\eta_1 = 0.0001$, $\eta_2 = 0.01$. Simulation results are shown in Fig. 44.1.
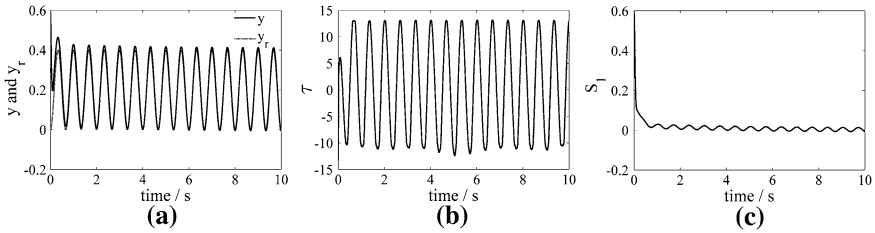
Fig. 44.1 Simulation results of the proposed DSC scheme. **a** System output (*solid line*) and reference signal (*dot line*), **b** Control signal τ, **c** Tracking error
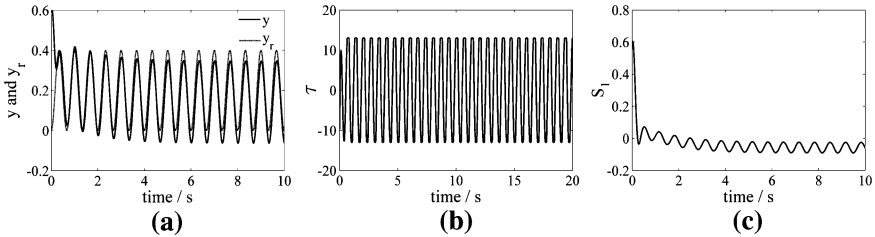
Fig. 44.2 Simulation results without considering input saturation. **a** System output (*solid line*) and reference signal (*dot line*), **b** Control signal τ, **c** Tracking error

In order to compare the effectiveness of control performance, using the same design parameters, the simulation results of (44.1) without considering input saturation are given in Fig. 44.2. It can be clearly observed that the desired tracking capacity is obtained by our proposed control scheme.

44.6 Conclusion

We have shown that the developed controller does not require the full availability of the system state, by using DSC technique the control law becomes quite simple, and the effect of actuator saturation on system performance is compensated by RBFNN, thus desired tracking performance is achieved.

References

1. Astrom KJ, Rundqwist L (1989) Integrator windup and how to avoid it [C]. In: Proceedings of the 1989 American control conference, Pittsburgh, PA, U S A
2. Kothare MV, Campo PJ, Morari M (1994) An unified framework for the study of anti-windup designs [J]. Automatic 30(12):1869–1883

3. Zhou J (2009) Adaptive neural network control of uncertain nonlinear plants with input saturation [C]. In: 2009 Chinese control and decision conference, Shanghai, pp 23–28
4. Swaroop D, Hedrick JK, Yip PP et al (2000) Dynamic surface control for a class of nonlinear systems [J]. IEEE Trans Autom Control 45(10):1893–1899
5. Kristic M, Kanellakopoulos I, Kokotovic PV (1995) Nonlinear and adaptive control design [M]. Wiley, New York
6. Gao W, Selmic RR (2006) Neural network control of a class of nonlinear systems with actuator saturation [J]. IEEE Trans Neural Netw 17(1):147–156
7. Chen T, Chen R (1995) Approximation capability to functions of several variables, nonlinear functionals, and operators by radial basis function networks [J]. IEEE Trans Neural Netw 6(4):904–910

Chapter 45
PID Tuning of Networked Feedforward-Feedback Control Systems

Congzhi Huang and Yan Bai

Abstract The issue of PID controller tuning for a typical class of networked feedforward-feedback control systems with constant network-induced delays is addressed. Feedforward-feedback control system, wherein the control loops are closed via a real-time network, is called a networked feedforward-feedback control system (NFCS for short). A typical configuration of NFCS is proposed and the locations of networks are explicitly pointed out. With the process given as first order plus time delay (FOPTD), as well as the desired closed-loop response, the PID tuning parameters of the feedback controller are proposed in the form of analytical expressions by approximating pure delays with first order Páde expression. Finally, the effectiveness of the proposed approach is validated by the simulation results.

Keywords Networked feedforward-feedback control system · Network-induced delay · PID · Tune

45.1 Introduction

Feedback control system, wherein the control loops are closed via real-time networks, is called networked control system [1] (NCS for short hereinafter). The introduction of real-time networks into the control loops brings in a lot of

C. Huang (✉) · Y. Bai
School of Control and Computer Engineering, North China Electric Power University,
Beijing 102206, People's Republic of China
e-mail: hcz190@ncepu.edu.cn

Y. Bai
e-mail: by@ncepu.edu.cn

advantages in an NCS, such as largely reduced wiring cost, greatly improved system flexibility, as well as facility of system maintenance and diagnostics. However, it also has many fundamental issues, such as network-induced delay, data packet dropout, and so on, which may degrade the system performance or even destabilize the system. As a result, the traditional control theory has to be reevaluated before applied to the NCS. At present, NCS has become a hot topic in the domestic and foreign control theory academia and industrial control field, see some recent special issues [2–6] and surveys in [7–10].

However, the feedforward control method has been widely used in practical process control [11–16], since it can compensate the effect of disturbance variables on the controlled variable. In order to improve system performance, feedforward control is often combined with feedback control to form feedforward-feedback control system. Feedforward-feedback control system, wherein the control loops are closed via real-time networks, is called networked feedforward-feedback control system (NFCS for short hereinafter).

In practical industrial process control, the PID controller is still the most widely used controller, for its explicit and obvious physical meaning, facilitate tuning and robustness. The PID controller design methods for time-delay process were reviewed in [17], and the applications of PID in NCS were studied in [18–20]. A simultaneous PID tuning method was proposed for a cascade control system based on desired closed-loop system response in [21], which was implemented by approximating pure delay with Maclaurin series. A PID tuning algorithm based on IMC was proposed in [22] for single loop control system. However, none of them have studied the tuning of PID controllers in an NFCS. This paper focuses on the PID tuning method of NFCS with constant network-induced delays.

The issue of PID controller design for a typical class of NFCSs is studied in this paper, and it's arranged as follows. In Sect. 45.2, the system configuration is presented and the locations of network-induced delays are explicitly pointed out. Motivated by [21] and based on desired closed-loop system responses, the PID tuning parameters for the kind of NFCSs with constant network-induced delays are proposed in Sect. 45.3 in the form of expressions by approximating the pure delay with Páde expression. With the proposed PID control method in the NFCS, the simulation examples are given in Sect. 45.4. Finally, conclusions are given in Sect. 45.5.

45.2 Configuration of NFCS

In an NFCS, different configurations lead to different locations of networks, and thus the analysis and synthesis of an NFCS are quite different. In practical industrial process control, there may be several kinds of NFCSs. The general configuration diagram for the typical kind of NFCS is presented in Fig. 45.1.

As can be seen from Fig. 45.1, the sensor S_1 samples the process variable y, and sends the sampling data to the feedback controller C_{fb} through a network, and the

Fig. 45.1 Configuration diagram of NFCS
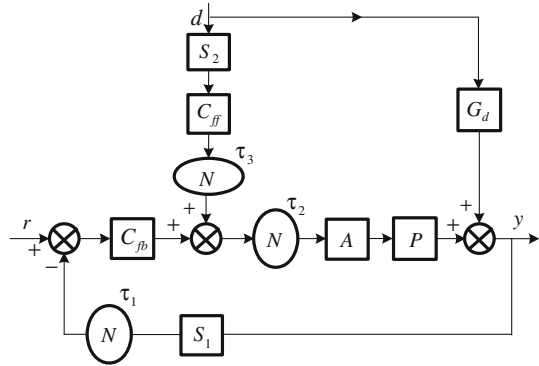
Fig. 45.2 Block diagram of NFCS equivalent to Fig. 45.1
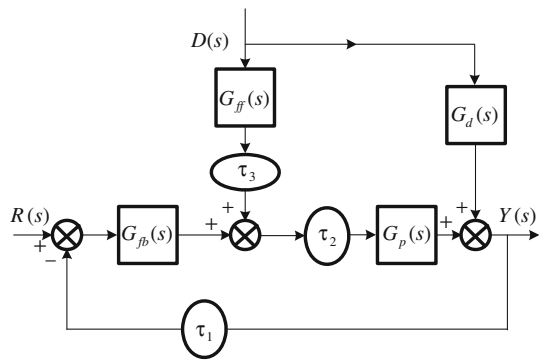
corresponding network-induced delay is τ_1. In order to compensate for the effect of the disturbance on the process variable, the disturbance variable d is sampled by the sensor S_2 and sent to the feedforward controller C_{ff}. Then, the feedforward control output is added into the output of the feedback controller through a network, and the corresponding network-induced delay is τ_3. Then, the control output is sent to the actuator A after experiencing a delay τ_2. The network-induced delays τ_1, τ_2, τ_3 may be constant, time-variable, or even random. However, by using a buffer with a certain capacity at the receiving nodes, the time-varying delays can be transformed into constant delays.

45.3 PID Tuning of NFCS

The block diagram of NFCS equivalent to Fig. 45.1 is shown in Fig. 45.2, where $R(s)$, $D(s)$, and $Y(s)$ are the reference input, disturbance input, and process variable, respectively. $G_p(s)$ represent the transfer function of the controlled process, while $G_d(s)$ is the transfer function of the disturbance input channel. $G_{fb}(s)$, and $G_{ff}(s)$ indicate the feedback controller, and the feedforward controller,

respectively. The delays of the forward and feedback channels are denoted by τ_1, and τ_2, respectively, and the feedforward channel delay is expressed as τ_3. Here, τ_1, τ_2, τ_3 are all assumed to be known constant values.

Assume the controlled process is a first order plus pure delay time (FOPDT), and its transfer function is given as $G_p(s) = \frac{K}{Ts+1} e^{-\theta s}$, where K is the gain, T is the time constant, θ is the delay time of the process, respectively.

Despite of so many sophisticated control algorithms, the PID controller is still the dominant control strategy widely used in practical process control. The typical expression of PID controller usually used in practical engineering is shown as follows:

$$G_{fb}(s) = \frac{1}{(T_f s + 1)} K_p (1 + \frac{1}{T_i s} + T_d s) \tag{45.1}$$

Where K_p is the proportional gain, T_i is the integral time, T_d is the derivative time, T_f is the time coefficient of the filter, respectively.

Assume the desired closed-loop transfer function of the NFCS as shown in Fig. 45.2 is:

$$G_{cl}(s) = \frac{e^{-ds}}{\lambda s + 1} \tag{45.2}$$

where $d = \theta + \tau_2$, and λ is the only parameter to be tuned.

It's easy to follow from Fig. 45.1 that the closed-loop transfer function of the NFCS is:

$$G_{cl}(s) = \frac{G_{fb}(s) G_p(s) e^{-\tau_2 s}}{1 + G_{fb}(s) G_p(s) e^{-\tau s}} \tag{45.3}$$

where τ is a summation of τ_1 and τ_2, i.e., $\tau = \tau_1 + \tau_2$. By comparing Eqs. (45.2) and (45.3), we can obtain the ideal transfer function of the feedback controller as follows:

$$G_{fb}(s) = \frac{Ts + 1}{K(\lambda s + 1 - e^{-\alpha s})} \tag{45.4}$$

Where $\alpha = \theta + \tau = \theta + \tau_1 + \tau_2$. Then, by approximating the pure delay with first order Páde expression, we can rewrite Eq. (45.4) as follows:

$$G_{fb}(s) = \frac{(T + \alpha/2)[1 + \frac{1}{(T+\alpha/2)s} + \frac{2T}{2T+\alpha} s]}{K(\lambda + \alpha)[\frac{\lambda \alpha}{2(\lambda+\alpha)} s + 1]} \tag{45.5}$$

By comparing Equation (45.5) with the standard form as shown in Equation (45.1), the tuning parameters can be obtained:

$$K_p = \frac{T + \alpha/2}{K(\lambda + \alpha)}, \ T_i = T + \alpha/2, \ T_d = \frac{\alpha T}{2T + \alpha}, \ T_f = \frac{\lambda \alpha}{2(\lambda + \alpha)} \tag{45.6}$$

The transfer function of the disturbance channel is given as: $G_d(s) = \frac{K_d}{T_d s + 1} e^{-\theta_d s}$, where K_d is the gain, T_d is the time constant, θ_d is the delay time of the disturbance channel, respectively.

To fully compensate for the effect of the disturbance on the process variable, it's easy to obtain that

$$G_{ff}(s)e^{-(\tau_2+\tau_3)s}G_p(s) + G_d(s) = 0 \tag{45.7}$$

It's easy to follow from Eq. (45.6) that the feedforward controller can be obtained as follows:

$$G_{ff}(s) = -\frac{K_d(Ts+1)}{K(T_ds+1)}e^{-(\theta_d-\theta-\tau_2-\tau_3)s} \tag{45.8}$$

45.4 Simulation Examples

Assume the transfer functions of the process and the disturbance channel in Fig. 45.2 are given as: $G_p(s) = \frac{1}{100s+1}e^{-s}$, and $G_d(s) = \frac{1}{20s+1}e^{-4s}$, respectively. Assume the network-induced delays are the same constant, and are equal to τ, i.e., $\tau_1 = \tau_2 = \tau_3 = \tau$. For the NFCS shown in Fig. 45.2 without any network-induced delays, the PID tuning parameters of the feedback controller can be obtained by Eq. (45.6): $K_p = 67$, $T_i = 100.5$, $T_d = 0.4975$, $T_f = 0.1667$. It's easy to follow from Equation (45.8) that the transfer function of the feedforward controller is: $G_{ff}(s) = -\frac{(100s+1)}{(20s+1)}e^{-3s}$. In addition, the parameters of the feedforward controller are nearly the same except that the time delay value varies according to the value of the network-induced delays.

In the NFCS as shown in Fig. 45.2, the reference input rises to a unit at time 1 s, and at time 20 s, the disturbance input steps to 1. By using the PID tuning parameters of the feedback controller obtained without taking into account the network-induced delays and taking the sampling period as 0.25 s, the responses of the NFCS with different delays are shown in Fig. 45.3.

As can be seen from Fig. 45.3, the performance of the NFCS degrades with the presence of the network-induced delay. In addition, with the increasing of the network-induced delay, the performance of the NFCS becomes worse. The system is unstable while the network-induced delay rises to 1 s. The disturbance is quickly attenuated by the feedforward controller, which fully compensates the effect of the disturbance on the controlled process variable.

For the NFCS, the PID tuning parameters of the feedback controller in the NFCS with different network-induced delays are shown in Table 45.1.

By using the feedback controllers with PID parameters as shown in Table 45.1, the responses of the NFCS with different delays are shown in Fig. 45.4.

As can be seen from Fig. 45.4, the performance of the NFCS with feedback controller compensating for the delays remains satisfied, even in the presence of network-induced delay as large as 1 s. However, with the increasing of the network-induced delay, the performance of the NFCS becomes worse: the rising time

Fig. 45.3 Responses of
NFCS without compensating
delays
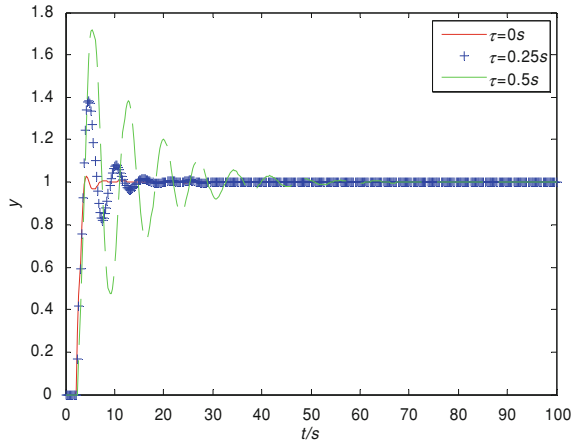
Table 45.1 PID tuning
parameters of NFCS with
different delays

τ	K_p	T_i	T_d	T_f
0.25	47.4118	100.75	0.7444	0.2206
0.5	36.7273	101	0.9901	0.2727
1	25.375	101.5	1.4778	0.375

Fig. 45.4 Responses of
NFCS compensating delays
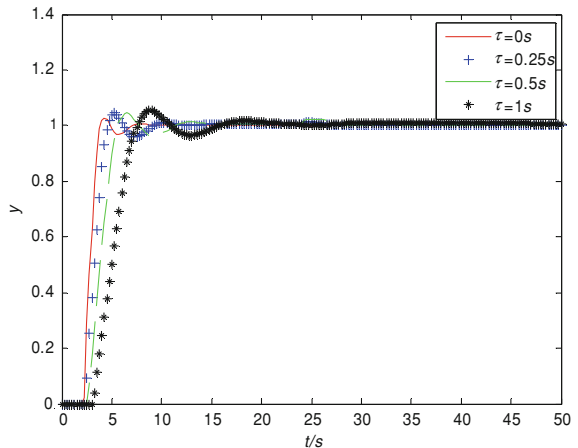
and settling time become more and more larger, the overshoot becomes more and
more greater. The disturbance in the NFCS can also be quickly attenuated by the
feedforward controller, which fully compensates the effect of the disturbance on
the controlled process variable.

By comparing Figs. 45.3 and 45.4, it's easy to follow that with the proposed
PID tuning approach, the performance of the NFCS with feedback controller

compensating the delays is better than the NFCS with feedback controller not compensating the delays.

45.5 Conclusions

The concept of networked feedforward-feedback control system (NFCS) is proposed based on practical control engineering, and the PID parameter tuning method is proposed. The effectiveness of the proposed method of the feedback controller is validated by the simulation results. However, the network-induced delays in the NFCS are often not constant but usually time-varying, how to tune the PID parameters of the NFCS with time-varying delays is a much more challenging issue, which is also the next research direction.

References

1. Zhang W, Branicky MS, Phillips SM (2001) Stability of networked control system [J]. IEEE Control Syst Mag 21(1):84–99
2. Bushnell LG (2001) Networks and control [J]. IEEE Control Syst Mag 21(1):21–22
3. Antsaklis P, Baillieul J (2004) Guest editorial special issue on networked control systems [J]. IEEE Trans Autom Control 49(9):1421–1423
4. Antsaklis P, Bailliful J (2007) Special issue on technology of networked control systems. Proc IEEE 95(1): 5–8
5. Koo TJ, Sastry S (2008) Special issue on networked embedded hybrid control systems [J]. Asian J Control 10(1):1–2
6. El-Farra NH, Mhaskar P (2008) Special issue on control of networked and complex process systems [J]. Comput Chem Eng 32(9):1963
7. Hespanha JP, Naghshtabrizi P, Xu Y (2007) A survey of recent results in networked control systems [J]. Proc IEEE 95(1):138–162
8. Yang TC (2006) Networked control system: a brief survey. In: IEE proceedings on control theory and applications vol 153, no 4, pp 403–412
9. Ge Y, Tian L, Liu Z (2007) Survey on the stability of networked control systems [J]. J Control Theory Appl 5(4):374–379
10. Tang X, Yu J (2007) Networked control system: survey and directions [J]. Lect Notes Comput Sci 4688:473–481
11. Metzger AJ, Dromerick AW, Schabowsky CN (2010) Feedforward control strategies of subjects with transradial amputation in planar reaching [J]. J Rehabil Res Dev 47(3):201–212
12. Jain N, Otten RJ, Alleyne AG (2010) Decoupled feedforward control for an air-conditioning and refrigeration system [C]. In: Proceedings of the 2010 American control conference: pp 5904–5909
13. Marchetti G, Barolo M, Jovanovic L (2008) A feedforward-feedback glucose control strategy for type 1 diabetes mellitus [J]. J Process Control 18(2):149–162
14. Zhao DY, Li SY, Gao F (2007) Fully adaptive feedforward feedback synchronized tracking control for stewart platform systems [J]. Int J Control Autom Syst 6(5):689–701

15. Chiu CS (2006) Mixed feedforward/feedback based adaptive fuzzy control for a class of MIMO nonlinear systems [J]. IEEE Trans Fuzzy Syst 14(6):716–727

16. Mendez-Acosta HO, Campos-Delgado DU, Femat R (2005) A robust feedforward/feedback control for an anaerobic digester [J]. Comput Chem Eng 29(7):1613–1623

17. Nag KH, Chon G (2005) PID control system analysis, design, and technology [J]. IEEE Trans Control Syst Technol 13(4):559–576

18. Okano R, Ohtani T, Nagashima A (2008) Networked control systems by PID controller [J]. In: Proceeding of the IEEE international conference on industrial informatics, Daejeon, Korean, pp 1126–1132

19. Pohjola M (2006) PID controller design in networked control systems [D]. Helsinki University of Technology

20. Quevedo DE, Welsh JS, Goodwin GC, McLeod M (2006) Networked PID control [C]. In: Proceeding of the IEEE international conference on control applications, Munich, Germany, pp 1695–1700

21. Lee Y, Park S (1998) PID controller tuning to obtain desired closed loop response for cascade control systems [J]. Ind Eng Chem Res 37(5):1859–1865

22. Panda RC (2008) Synthesis of PID tuning rule using the desired closed-loop response [J]. Ind Eng Chem Res 47(22):8684–8692

Chapter 46
Plume Source Localization Based on Multi-AUV System

Hongli Xu and Xiaodong Kang

Abstract Multi-AUV system has advantages in high-accuracy localization with cooperative navigation and adaptive sampling with space–time distribution. It is expected to be a valuable platform in searching for hydrothermal vents, unexploded ordnances, and sources of hazardous chemicals or pollutants. This paper studies how to use multiple AUVs to locate these interesting sources, named the plume source localization problem. Two localization algorithms are proposed respectively based on time priority and distance priority. Simulation tests demonstrate that they are feasible and effective, and the distance priority based algorithm is better than the other with the higher localization accuracy and the shorter exploration time.

Keywords Multi-AUV system · Plume exploration · Plume source localization · Plume tracing

46.1 Introduction

With the progress of multi-AUV coordination control technology, multi-AUV system is expected as a valuable platform in searching for hydrothermal vents, unexploded ordnances, and sources of hazardous chemicals or pollutants. Especially it is a very interesting research field to how to apply multiple AUVs to locate these interesting sources. These sources have a common characteristic: some materials,

H. Xu (✉)
State Key Laboratory of Robotics, Shenyang Institute of Automation, CAS,
Shenyang 110016, China
e-mail: xhl@sia.cn

X. Kang
SANY Group Co., Ltd, Changsha 410100, China
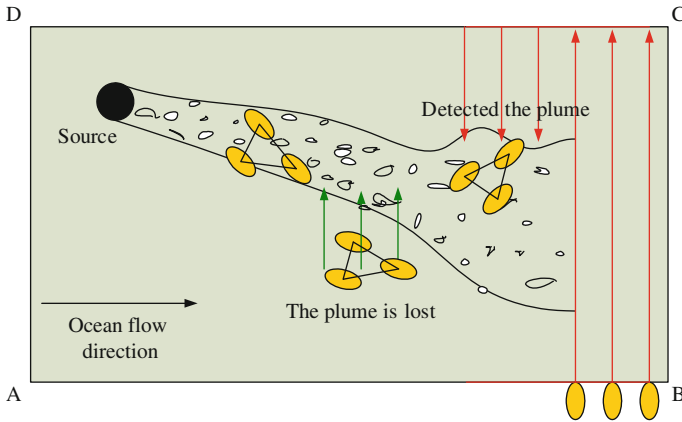
Fig. 46.1 The sketch map of the plume exploration process with multi-AUV system

emitted from the sources, disperse downstream and form a plume which is both physically and chemically different from the surrounding seawater. Through detecting these physical or chemical anomalies AUV can autonomously identify a plume and trace it to its source. We call this progress as the plume exploration.

The plume exploration can be divided into two steps, the plume tracing and the source localization. This paper will be focus on the latter. Now the main methods for plume source localization include particle swarm optimization algorithms [1–3], reinforcement learning algorithms [4], ant colony algorithms [5], evolutionary-based approach [6] and so on. These algorithms firstly translate the problem of plume source localization into the problem of multi-objective optimization by the mathematical model of the plume in time–space distribution, and then try to find the optimization solutions to calculate the plume source localization. But in real ocean environment the plume distribution is discontinuous and irregular under the influence of turbulence and vortex. It's very difficult to describe all the characteristics of the plume by an ideal model. The plume location may be not corresponding to the optimization solution. So this paper presents two autonomous localization algorithms based on multi-AUV system, which declare the plume source through sharing information among AUVs.

This paper is organized as follows. Section 46.2 provides the process of the plume exploration with multi-AUV system. Section 46.3 presents the two localization algorithms respectively based on time priority and distance priority. Section 46.4 presents some simulation results. Finally, Sect. 46.5 gives some concluding remarks.

46.2 Plume Exploration Based on Multi-AUV System

As shown in Fig. 46.1, ABCD is assumed as an anomaly area. When the mission starts, multiple AUVs form a formation with a defined horizontal spacing and

Table 46.1 The strategies of declaring the plume source based on multi-AUV system

Leader AUV	Slave AUV	Strategies
0	0	Perform the reacquire-plume behavior
0	1	Transform the roles between the leader and the slaver
1	0	Continue the maintain-plume behavior
1	1	Continue the maintain-plume behavior

search for the plume along the tangent direction of ocean flow. There are two searching results. One is that mission time has been depleted or the whole area has been explored completely, so the mission will be ended. The other is that the plume is detected, so multi-AUV system will change formation to trace the plume.

During the process of tracing the plume and sailing upstream to its source, sometimes all the AUVs can not detect the plume, in other words, the plume is "lost". At this time, we need to analyze the reason. Maybe it is oriented from some uncertain factors, like turbulence, ocean flow and seafloor terrain, or multi-AUV system has arrived at the source. If the plume source has been declared, there need some algorithms to estimate the source location. This is the problem that will be solved in next section.

46.3 Plume Source Localization

Wei Li presented the strategies inspired by insect orientation to pheromone for the plume source localization with an AUV in [7]. This paper improved these strategies and designed two new methods for plume source localization with multi-AUV system.

Assume that there is an AUV is the leader in multi-AUV system, the others are slavers. So at one time the four contact states between multi-AUV system and the plume are shown in Table 46.1. In this table 0 denotes that AUV can't detect the plume, and it isn't within the plume; 1 denotes that AUV can detect the plume, and it is within the plume. Correspondingly multi-AUV system may response to them with three strategies, performing the reacquire-plume behavior, transforming roles between the leader and the slaver which detected the plume, continuing the maintain-plume behavior. The design and parameters selection of these behaviors may refer to the Ref. [8]. When multi-AUV system can not detect the plume information and are ready to perform the reacquire plume behavior, we record the location of the leader AUV where it detected the plume last time. The last location is denoted by Plcdp. According to the difference of ordering rules of a list of Plcdp points, we propose a time priority based algorithm and a distance priority based algorithm.

46.3.1 The Localization Algorithm Based on Time Priority

Multi-AUV system will repeat constantly to perform the reacquire-plume behavior near the plume source. So we can acquire a list of Plcdp points. The time priority
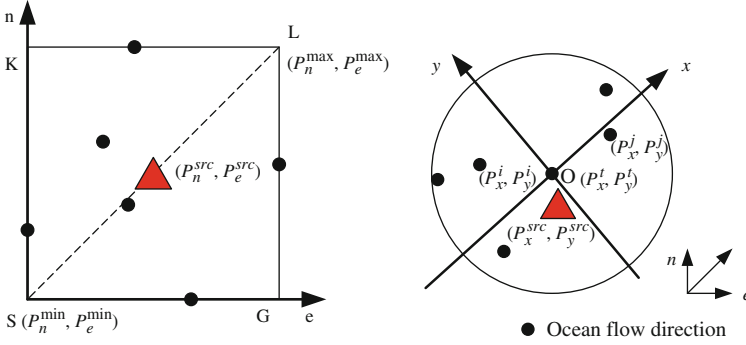
Fig. 46. 2 The sketch maps of the two localization algorithms

indicates that the list L is updated by the rule that the newer Plcdp point always has the higher priority.

$$L[(P_n^t, P_e^t), (P_n^{t-1}, P_e^{t-1}), \cdots (P_n^1, P_e^1)] \qquad (46.1)$$

Nc is defined as the least numbers of Plcdp points to declare the plume source. ε_T is the permitted localization error. Obviously when t < Nc, multi-AUV system is not near the plume source. And when t = Nc, the following strategies will be applied to judge whether multi-AUV system is right within the plume source or not.

Shown in left Fig. 46.2, the rectangle KSGL contains all the Plcdp points in the global coordinate system. We define the following formulas:

$$\begin{cases} P_n^{\min} = \min\{P_n^{N_c}, P_n^{t-1}, \ldots P_n^1\} \\ P_e^{\min} = \min\{P_e^{N_c}, P_e^{t-1}, \ldots P_e^1\} \end{cases} \qquad (46.2)$$

$$\begin{cases} P_n^{\max} = \max\{P_n^{N_c}, P_n^{t-1}, \ldots P_n^1\} \\ P_e^{\max} = \max\{P_e^{N_c}, P_e^{t-1}, \ldots P_e^1\} \end{cases} \qquad (46.3)$$

If $|SL| = \sqrt{(P_n^{\max} - P_n^{\min})^2 + (P_e^{\max} - P_e^{\min})^2} \leq \varepsilon_T$ is satisfied, we determine that the plume source can be declared and the source location is estimated according to the formula:

$$\begin{cases} P_n^{src} = \sum\limits_{i=1}^{N_c} P_n^i \Big/ N_c \\ P_e^{src} = \sum\limits_{i=1}^{N_c} P_e^i \Big/ N_c \end{cases} \qquad (46.4)$$

46.3.2 The Localization Algorithm Based on Distance Priority

The *O-xyz* reference coordinate system is shown in right Fig. 46.2. The current P_{lcdp} point is the origin, the ocean flow direction is the x-axis direction and its vertical line is y-axis direction. All the P_{lcdp} points are projected to this coordinate system. The current flow direction is denoted as C_{dir}. So the translation matrix is:

$$T_{ne}^{xy} = \begin{bmatrix} \cos(C_{dir} + 180°) & -\sin(C_{dir} + 180°) \\ \sin(C_{dir} + 180°) & \cos(C_{dir} + 180°) \end{bmatrix} \tag{46.5}$$

The distance priority based algorithm orders the Plcdp points according to the absolution of their x coordinates, namely that the nearer to the origin, the higher priority in the list. Suppose $|P_x^t| \leq \cdots |P_x^i| \leq |P_x^j|$, the list is denoted as:

$$L\left[(P_x^t, P_y^t), \cdots (P_x^i, P_y^i), (P_x^j, P_y^j) \cdots \right] \tag{46.6}$$

When the number of the Plcdp points is smaller than Nc, it can be immediately concluded that the multi-AUV system is not near the plume source and continue performing the reacquire plume behavior. Otherwise, when Plcdp number is equal or larger than Nc, the following strategies will be applied.
(Pxm, Pym) denotes the average of all the Plcdp points. The distances of all the Plcdp points to the point can be calculated and the max distance is denoted by Pmax. It is calculated by the formula:

$$D_{\max} = \max\left\{ \sqrt{(P_x^i - P_x^m)^2 + (P_y^i - P_y^m)^2} \right\}, \quad i = 1, 2, \ldots N \tag{46.7}$$

There are two possibilities:
① If $D_{\max} > \varepsilon_F$ (where ε_F denotes the localization error), the $P^{\max}$ point will be removed from the L list, and we conclude that multi-AUV system has not arrived in the plume source and carry on the reacquire plume behavior.
② If $D_{\max} \leq \varepsilon_F$, the plume source will be declared, and the plume source location is regarded as the first point in the L list (P_x^t, P_y^t).

46.4 Simulation Tests

We built a plume exploration simulation system by C++ programming language and the OpenGL library. The system comprises three parts: vehicle dynamics, flow field and plume model, which are introduced in [9]. The simulation parameters are followed. The exploration area is specified in [0,100] along x-axis and [−50,50] along y-axis. The plume source is located at (10,0) and emits 5 particles randomly every second. The flow velocity is 1.0 m/s. The multi-AUV system is compose of three AUVs. Their mission-start positions and mission-end positions are all on the
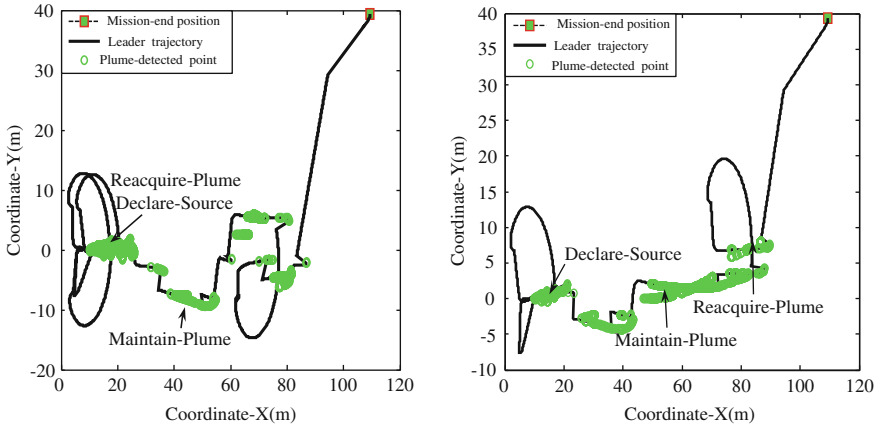
Fig. 46.3 The trajectory of the leader AUV during the plume exploration

Table 46.2 The performance comparison of the two localization algorithms

Localization algorithm	Time priority	Distance priority
Average error(m)	0.11	1.58
Errors in 0∼0.5m	921/1000 (92.1%)	25/1000 (2.5%)
Average PET(s)	195.11	230.49
PET in 150∼200s	645/1000 (64.5%)	185/1000 (18.5%)

locations (100,40), (105,42) and (115,41). In each plume exploration mission they sail from their mission-start positions, perform a series of behaviors for tracing and declaring the plume, and return to the mission-end positions.

In this simulation system the two localization algorithms are respectively demonstrated for 1,000 times. We evaluate their performances using the average localization error and the average plume exploration time (PET, it is the period from the mission starts to the mission ends). Their comparisons are shown in Fig. 46.3 and Table 46.2. In Fig. 46.3 the left is based on the time priority based algorithm and the right is based on the distance priority algorithm. It can be concluded that the two algorithms are all feasible and effective, and the distance priority based algorithm is better that the other with the higher localization accuracy and the shorter exploration time.

46.5 Conclusion

This paper has presented two localization algorithms respectively based on time priority and distance priority for declaring the plume source with multi-AUV system. The simulation tests demonstrate that the distance priority based algorithm

can acquire the higher source localization accuracy and the shorter plume exploration time. These algorithms have the guiding significance for the application of multi-AUV system in the hydrothermal exploration in the future. But some uncertain influences, such as the interruption of acoustic communication, need to be considered in the following work.

References

1. Marques L, Nunes U et al (2006) Particle swarm-based olfactory guided search [J]. Auton Robot 20(3):277–287
2. Jatmiko W, Sekiyama K et al (2006) A mobile robots PSO-based for odor source localization in dynamic advection-diffusion environment. In: Proceedings of the 2006 IEEE/RSJ international conference on intelligent robots and systems
3. Jatmiko W, Mursanto P et al (2008) Modified PSO algorithm based on flow of wind for odor source localization problem in dynamic environments [J]. WSEAS Trans Syst 7(3):106–113
4. Bai S (2009) Research on active olfaction based on reinforcement learning algorithm. The master's degree paper of Tianjin University
5. Zou Y, Luo D (2008) A modified ant colony algorithm used for multi-robot odor source localization. In: Proceedings of the 4th international conference on intelligent computing: advanced intelligent computing theories and applications-with aspects of artificial intelligent, pp 502–509
6. Marques L, Nunes U et al (2003) Odour searching with autonomous mobile robots: an evolutionary-based approach. In: Proceedings of IEEE international conference on advanced robotics, pp 494–500
7. Li W, Farrell JA et al (2001) Tracking of fluid-advected odor plumes: strategies inspired by insect orientation to pheromone [J]. Adapt Behav 9(3–4):143–169
8. Kang X (2010) Research on chemical plume exploration via multiple AUVs with formation-keeping, The doctoral dissertation, Shenyang Institute of Automation CAS
9. Yu T, Zhang A (2010) Simulation environment and guidance system for AUV tracing chemical plume in 3-dimensions. In: The 2nd international Asia conference on informatics in control, automation and robotics, pp 407–411

Chapter 47
Preliminary Risk Assessment of Metal Pollution in Source Water of Huaihe River

Zhi-feng Wang and Zhong-xing Guo

Abstract This study investigated the levels of eight metallic elements (Cr, Fe, Mn, Cu, Zn, Cd, Pb, Hg) in source water of 30 tap water treatment plants (TWTPs) located along Huaihe River in the section of Jiangsu Province, China during 2007–2009 and assessed the preliminary risk assessment induced by metals. Among all the metals, Fe was found to have the highest concentration (107.7 µg L^{-1}), and Hg had the lowest (0.027 µg L^{-1}). A preliminary risk assessment was then carried out to determine the human health risk by calculating Hazard Quotient (HQ) and carcinogenic risk of the metals. Both HQs of individual metals in each TWTP were lower than unity. The carcinogenic risk of both Pb and Fe was higher than 10^{-6}, suggesting that the two metals may pose potential adverse effects to local residents.

Keywords Preliminary risk assessment · Metal · Source water · Huaihe river

47.1 Introduction

Jiangsu Province is one of the most developed economic regions of China. Huaihe River, located in North Jiangsu, is the main sources of drinking water for the local residents. However, the region is suffering enormous environmental deterioration

Z.-f. Wang (✉) · Z.-x. Guo
College of Pubic Administration, Nanjing Agricultural University,
Nanjing 210095, China
e-mail: njwzf@yahoo.cn

Z.-f. Wang
Jiangsu Institute of Economic and Trade Technology,
Nanjing 210007, China

from industrialization. Various pollutants, including heavy metals, have been detected in the surface water of Huaihe River [1, 2]. These pollutants with high toxicities even at trace level may pose potential health risk on the water-consuming population [3].

As a generally accepted method of heath risk assessment, carcinogenic risk assessment model recommended by Environmental Protection Agency of the United Nations (USEPA) has been widely used to assess the potential risks induced by the metals in various environments. Currently, concerns mainly focus upon the quantitative detection of heavy metals in water and sediments of Huaihe River [1, 2]. To our best knowledge, limited information is available about the carcinogenic risk posed by the metals in the source water in China.

In this study, we carried out a preliminary assessment on non-carcinogenic risk induced by the metals of Cr, Fe, Mn, Zn, Cd, Pb, Hg and Cu in source water of 30 tap water treatment plants (TWTPs) in Jiangsu Province, China based on the chemical detections during 2007–2009. The approach used might provide a reference for future studies.

47.2 Materials and Methods

47.2.1 Water Sampling

Source water samples were collected from a total of 30 TWTPs located along Huaihe River (33° 53.4′N, 118° 12.6′E–32° 37.2′N, 119° 28.2′E) at the section of Jiangsu Province of China (Fig. 47.1). Source water (1 L) was sampled once every 3 months from February 2007 to August 2009, and each sampling was performed in triplicate. The samples were collected in pre-cleaned polyethylene bottles and transported in an ice bath to the laboratory after acidification with HCl. The samples were kept at $-20°C$ until analysis

47.2.2 Measurement of Metals

Water samples (10 ml each) were filtered through a cellulose acetate membrane filter (0.2-μm pore size) and acidified with 30 μl of HNO^3 before analysis of dissolved trace elements, including Cr, Fe, Mn, Zn, Cd, Pb, Hg and Cu. Metallic elements were analyzed using high-resolution inductively coupled plasma–mass spectrometry (HRICP-MS; Agilent 7500, USA) and inductively coupled plasma–atomic emission spectroscopy (ICP-AES; Jarrell-Ash 1100, USA). The robustness of the measurements was assured by cross-evaluation between different methods, e.g. ICP-AES versus HRICP-MS. The results of cross-checking agreed within $\pm5\%$. Calibration curves had R2 of over 0.999 and standard deviations (SD) of
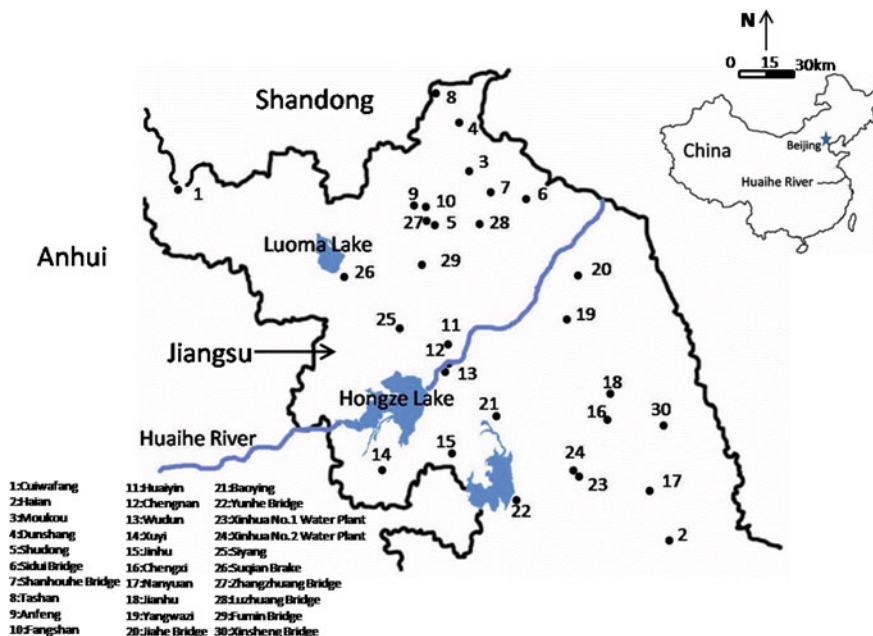
Fig. 47.1 Source water sampling locations of 30 drinking water treatment plants along Huaihe River, China

triplicates were below 5%. The detection limit of the measurements was defined as the concentration value which numerically equals to three times the SD of 10 replicate blank measurements.

47.2.3 Carcinogenic Risk Assessment

The potential exposure pathways of the metals included: (1) direct ingestion, (2) inhalation through the mouth and nose, (3) dermal absorption. For metals in water environment, ingestion and dermal absorption play the most important role [4]. Considering that above pathways, the exposure doses were calculated by Eqs. 47.1 and 47.2 adapted from the US Environmental Protection Agency [5, 6]:

$$\mathrm{CD_{Iingestion}} = \frac{C_w \times IR \times ABS_g \times EF \times ED}{BW \times AT} \tag{47.1}$$

$$\mathrm{CD_{Idermal}} = \frac{C_w \times SA \times K_p \times ABS_d \times ET \times EF \times ED \times CF}{BW \times AT} \tag{47.2}$$

Where CDI is the exposure dose contacted through ingestion of water (CDIingestion) and dermal absorption (CDIdermal), $\mu g kg^{-1} day^{-1}$; Cw is the concentration of

metals in drinking water, $\mu g\ L^{-1}$; IR is the ingestion rate, 2.2 L day^{-1}; SA is the exposed skin area (in this study, 2,800 cm^2); Kp is the skin adherence factor, cm h^{-1}; ABSg is the gastrointestinal absorption factor; ABSd is the dermal absorption factor; ET is the exposure time, in this study, 0.6 h day^{-1}; EF is the exposure frequency, in this study, 365 day year^{-1}; ED is exposure duration in this study, 70 years; CF is the unit conversion factor; BW is average body weight, in this study, 60 kg; AT is averaging time, for non-carcinogens and carcinogens, 25,550 days; The human health risk assessment was performed by calculating the Hazard Quotients and carcinogenic risk for metals using Eqs. 47.3, 47.4:

$$Hazard\ Quotient = \frac{CDI}{RFD} \tag{47.3}$$

$$Carcinogenic\ Risk = 1 - \exp(-CDI \times SF) \tag{47.4}$$

where CDI ($\mu g\ kg^{-1}\ day^{-1}$) is the exposure dose obtained from Eqs. (47.1) and (47.2) and RfD ($\mu g\ kg^{-1}\ day^{-1}$) is the reference dose of the contaminant. The values of ingestion reference dose (RfDi) were obtained from USEPA [4, 7]. RfDi was multiplied by a gastrointestinal absorption factor to yield the corresponding dermal absorption reference dose, RfDd [8]

According to Eq. (47.4), Risk-based concentration table (US EPA 2006), except Pb, which is derived from the World Health Organization's Guidelines (2006). SF is the slope factor of a carcinogen, expressed in $(\mu g\ kg^{-1}\ day^{-1})^{-1}$, which is based on USA. Risk-based concentration table [9]. Toxicity values for dermal absorption have been calculated: oral reference doses are multiplied, and slope factors divided, by an ABSg to yield the corresponding dermal values [6].

47.2.4 Statistical Analysis

Experimental results were statistically analyzed using Excel 2007 (Microsoft Excel, Washington, USA). All values were expressed as the mean $\pm$ SD. The significance of the difference among the concentrations of the metals in different TWTPs was assessed with independent samples t test. A $p < 0.05$ was considered statistically significant.

47.3 Results and Discussion

47.3.1 Concentration of Metals in Source Waters

This study investigated the concentrations of eight metals in the source water of 30 TWTPs in Jiangsu Province, China during 2007–2009. The concentrations of both

Table 47.1 Summary statistics of the analytical results of metals in the source water of 30 drinking water treatment plants along Huaihe River of China ($\mu g\ L^{-1}$)

Elements	Limit of detection	Range	Mean	SD
Cr	0.002	1−90	4	5.9
Fe	0.002	10−400	107.7	77.5
Mn	0.002	2−155	19.6	19
Cu	0.005	1−90	10.2	11
Zn	0.01	1−100	19.6	10.6
Cd	0.005	0.02−15	0.8	1
Pb	0.002	0.137−16.7	4.5	2.5
Hg	0.002	0.003−0.1	0.027	0.02
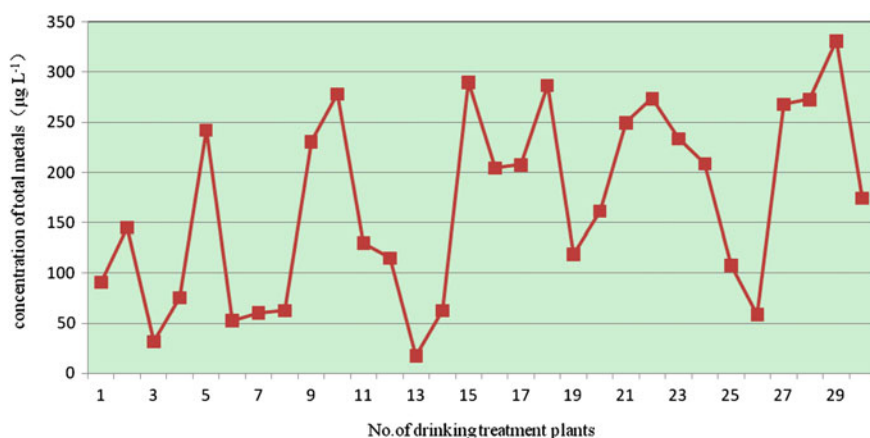
Fig. 47.2 Total concentrations of metals in different drinking water treatment plants each year ($\mu g\ L^{-1}$)

individual and total metals fluctuated greatly (Table 47.1). The total concentrations of metals in different drinking water treatment plants each year ranged from 17.4 $\mu g\ L^{-1}$ (TWTP. 13) to 331.5 $\mu g\ L^{-1}$ (TWTP. 29) with the mean value of 168.2 $\mu g\ L^{-1}$ (Table 47.1 and Fig. 47.2).

All metals were detectable at each site, in terms of individual metal composition in surface water. Fe was found to have the highest concentration, followed by Mn and Zn (Table 47.1). These three metals contributed nearly 85% to the total concentrations.

Few studies have been carried out to detect the level of metals in the surface waters of Huaihe River, but it was previously indicated that a rapid increase of the contents of heavy metals in the sediments resulted from urbanization and industrialization [11] and extensive use of fertilizers on farmlands [2] during the past several decades. Levels of eight metals determined in this study ware below the

Table 47.2 Reference dose and Hazard Quotient for each element

Elements	RfDingestion($\mu g\ kg^{-1}\ day^{-1}$)	RfDdermal($\mu g\ kg^{-1}\ day^{-1}$)	
Cr	3	0.015	5.98×10^{-4}
Fe	700	105	1.71×10^{-3}
Mn	24	0.96	9.33×10^{-3}
Cu	40	12	2.74×10^{-3}
Zn	300	60	7.26×10^{-5}
Cd	0.5	0.005	4.58×10^{-4}
Pb	2	0.6	2.49×10^{-3}
Hg	0.3	0.003	1.15×10^{-4}

Table 47.3 Carcinogenic risk of each metallic element in Huaihe River

Elements	Carcinogenic risk
Cr	1.12×10^{-7}
Fe	3.01×10^{-6}
Mn	5.47×10^{-7}
Cu	2.91×10^{-7}
Zn	5.48×10^{-7}
Cd	2.3×10^{-8}
Pb	1.23×10^{-6}
Hg	7.5×10^{-9}

permissible limit of China [12], but the concentration of Pb in most of sampling sites exceeded the standards of USEPA [4]. The health risk problem has potentially arisen with lead pollution recorded in water and sediments of the Huaihe River Basin, China [12].

47.3.2 Carcinogenic Risk Induced by the Metals

A preliminary carcinogenic risk assessment was carried out for the metals in the source waters of the 30 TWTPs based on the results of chemical detections. Table 47.2 summarizes Hazard Quotients (HQs) of each metal according to the oral consumption (HQi) and dermal absorption (HQd) of water. Both HQs (the sum of HQi and HQd) of the individual metals were smaller than unity, demonstrating that these pollutants could pose negligible hazards to public health of local residents. The HQdermal (hazard quotient of dermal absorption) were all lower than the HQingestion, which suggests that the concentrations of these metals may pose little or no health threat via dermal adsorption.

Carcinogenic risk is defined as the incremental probability that an individual will develop cancer during ones lifetime due to chemical exposure under specific scenarios [13, 14]. Under most regulatory program, carcinogenic risk between 10^{-6} and 10^{-4} suggests potential risk [13, 15].

The mean carcinogenic risks of eight metals by ingestion and dermal exposure are shown in Table 47.3. The risk of Pb was about 1.23×10^{-6} which was higher than 10^{-6}, while the risk of Fe was over twofold higher than that of Pb. The results of carcinogenic risk suggest that the Pb and Fe in Huaihe River pose potential health risk to the residents.

47.4 Conclusions

In this study, we investigated the carcinogenic risks posed by eight metallic elements in source water of 30 TWTPs located along Huaihe River in the section of Jiangsu Province, China. Among the metals analyzed, Fe had the highest concentration in each of the source waters during 2007–2009, while Hg had the lowest level. Both HQs of individual metals in each TWTP were below carcinogenic risk level, suggesting that these pollutants caused negligible hazard to the public health of local residents. The results of carcinogenic risk suggest that the Pb and Fe in Huaihe River pose potential health risk to the residents.

However, this study contained some possible uncertainties. For example, different exposure conditions might also contribute to different risks. The RfD and SF obtained from US EPA and WHO might not be specific to Chinese [16]. Therefore, this study only presents a preliminary assessment of the carcinogenetic risks induced by the metals in Huaihe River. In subsequent investigations, a more precise assessment for heavy metals should be carried out to measure the risk levels, and some efforts should be exerted on the control of heavy metal pollution in the river.

References

1. Huang H, Ou WH, Wang LS (2006) Semivolatile organic compounds, organochlorine pesticides and heavy metals in sediments and risk assessment in Huaihe RiverHuaihe River of China [J]. J Env Sci 18(2):236–241
2. Zhang H, Shan B (2008) Historical records of heavy metal accumulation in sediments and the relationship with agricultural intensification in the Yangtze–Huaihe region, China [J]. Sci Total Env 399(1–3):113–120
3. Fu C, Guo JS, Pan J, Qi JS, Zhou WS (2009) Potential ecological risk assessment of heavy metal pollution in sediments of the Yangtze River within the Wanzhou Section, China [J]. Biol Trace Elem Res 129(1–3):270–277
4. Kim EY, Little JC, Chiu N (2004) Estimating exposure to chemical contaminants in drinking water [J]. Environ Sci Technol 38:1799–1806
5. US EPA (US Environmental Protection Agency) (1989) Risk Assessment Guidance for Superfund Volume I Human Health Evaluation Manual (Part A) [M]
6. De Miguel E, Iribarren I, Chacon E, Ordonez A, Charlesworth S (2007) Risk-based evaluation of the exposure of children to trace elements in playgrounds in Madrid (Spain) [J]. Chemosphere 66:505–513

7. USEPA (U. S. Environmental Protection Agency) (2010) Residential tapwater supporting table. http://www.epa-prgs.ornl.gov/chemicals/index.shtml. Accessed 11 Dec 2010

8. USEPA (U.S. Environmental Protection Agency (2010) Risk assessment guidance for superfund volume I human health evaluation manual. http://www.epa.gov/oswer/riskassessment/ragsa/pdf/rags-vol1-pta_complete.pdf. Accessed 5 Nov 2010

9. USEPA (U.S. Environmental Protection Agency) (2007) Risk-basedconcentrationtable. http://www.epa.gov/reg3hwmd/risk/human/rb-concentration_table/Generic_Tables/index.htm. Accessed 5 Nov 2010

10. Xue B, Yao SC and Xia WL (2007) Environmental changes in Lake Taihu during the past century as recorded in sediment cores [J]. Hydrobiologia 581:117–123

11. SEPAC (State Environmental Protection Administration of China) (2002) Monitoring and analysis method of water and wastewater [M] 4th ed, China Environmental Science Press, Beijing

12. Yao SC, Xue B, Xia WL, Zhu YX, Li SJ (2009) Lead pollution recorded in sediments of three lakes located at the middle and lower Yangtze River Basin, China [J]. Quaternary Int 208:145–150

13. Chen SC, Liao CM (2006) Health risk assessment on human exposed to environmental polycyclic aromatic hydrocarbons pollution sources[J]. Sci Total Env 366:112–123

14. Obiri S, Dodoo DK, Okai-Sam F, Essumang DK (2006) Cancer health risk assessment of exposure to arsenic by workers of AngloGold Ashanti–Obuasi Gold Mine [J]. Bull Environ Contam Toxicol 76:195–201

15. Liao CM, Chiang KC (2006) Probabilistic risk assessment for personal exposure to carcinogenic polycyclic aromatic hydrocarbons in Taiwanese temples [J]. Chemosphere 63:1610–1619

16. Wei S, Lau RKF, Fung CN, Zheng GJ, Lam JCW, Connell DW, Fang Z, Richardson BJ, Lam PKS (2006) Trace organic contamination in biota collected from the Pearl River Estuary, China: Apreliminary risk assessment [J]. Mar Pollut Bull 52:1682–1694

Chapter 48
Properties of Degree Induced Covering Rough Set

Dingjun Chen and Kaiteng Wu

Abstract The concept of positive field, negative field, boundary regions in induced covering rough set are proposed based on the degree induced covering rough sets. The related properties of degree induced covering rough sets approximation operators are discussed. The useful results which are got in the paper have greatly extended the covering rough set theory.

Keywords Degree · Induced · Covering · Approximation operator

48.1 Introduction

Rough set theory (RST), proposed by Pawlak [1, 2], is an extension of set theory for the study of intelligent systems characterized by insufficient and incomplete information. It provides a systematic approach for classification of objects through an indiscernibility relation. Many examples of applications of the rough set method to process control, economics, medical diagnosis, biochemistry, environmental science, biology, chemistry psychology, conflict analysis and other fields can be found in [3–5].

A lot of meaningful extensions of pawlak rough set are proposed by scholars. For example, variable precision rough set model was proposed by Ziarko [6] in

D. Chen (✉) · K. Wu
Key Laboratory of Numerical Simulation of Sichuan Province,
Neijiang Normal University, Neijiang 641112, China
e-mail: chen-dingjun@163.com

K. Wu
e-mail: wukaiteng@263.net

order to deal with a certain degree of "inclusion" and "belong to". Zakowski [7, 8] extended to the covering rough set by the covering in division. Dai [9] induced the error of classification on the base of the model of rough set based on covering, construct the degree rough set model based on covering, discusses several relevant properties of this model. Zhang [10] proposed the concept of induced covering rough set and research the properties of the model. Chen [11] constructs the degree induced covering rough set model by the error of classification on the base of the model of induced rough set based on covering and discusses several relevant properties. Now we further discussed the problem with the concept of positive field, negative field, boundary regions in degree induced covering rough set.

48.2 Preliminaries

Definition 1 [12] Let U be a universe of discourse, C a family of subsets of U. If none subsets in C is empty, and $\cup C = U$, C is called a covering of U.

Definition 2 [10] Let U be a non-empty set, $C = \{C_1, C_2, \ldots, C_n\}$ a covering of U. $\forall x \in U$, $C_x = \cap\{C_j | C_j \subseteq C, x \in C_j\}$, then $Cov(C) = \{C_x | x \in U\}$ is also a covering of U, which is called a induced covering by C.

Definition 3 [10] Let $\Delta = \{C_i | i = 1, 2, \ldots, m\}$ a covering of U. $\forall x \in U$, $\Delta_x = \cap\{C_{ix} | C_{ix} \subseteq Cov(C_i)\}$, then $Cov(\Delta) = \{\Delta_x | x \in U\}$ is also a covering of U, which is called a induced covering by Δ.

Definition 4 [10] Let (U, C) be a covering approximation space. For each $X \subseteq U$,

Set $\underline{\Delta}(X) = \cup\{\Delta_x | \Delta_x \subseteq X\}$ is called the induced covering lower approximation of X.

Set $\bar{\Delta}(X) = \cup\{\Delta_x | \Delta_x \cap X \neq \varnothing\}$ is called the induced covering upper approximation of X.

Definition 5 Let (U, C) be a covering approximation space. For each $X \subseteq U, k \in Z^+$,

Set $\underline{\Delta}_k X = \cup\{\Delta_x | |\Delta_x| - |\Delta_x \cap X| \leq k\}$ is called the k degree induced covering lower approximation of X.

Set $\bar{\Delta}_k X = \{\Delta_x | |\Delta_x \cap X| > k\}$ is called the k degree induced covering upper approximation of X.

If $\underline{\Delta}_k X = \bar{\Delta}_k X$, it is called definable. Otherwise, we call $(\underline{\Delta}_k X, \bar{\Delta}_k X)$ rough set.

When $k = 0$, the model be the induced covering rough set.

Set $pos_{\Delta k} X = \underline{\Delta}_k X \cap \bar{\Delta}_k X$ is called the k degree induced covering positive region of X.

Set $neg_{\Delta k} X = \neg(\underline{\Delta}_k X \cup \bar{\Delta}_k X)$ is called the k degree induced covering negative region of X.

Set $Ubn_{\Delta k}X = \bar{\Delta}_kX - \underline{\Delta}_kX$ is called the k degree induced covering upper boundary region of X.

Set $Lbn_{\Delta k}X = \underline{\Delta}_kX - \bar{\Delta}_kX$ is called the k degree induced covering lower boundary region of X.

Set $bn_{\Delta k}X = \neg(pos_{\Delta k}X \cup neg_{\Delta k})X$ is called the k degree induced covering boundary region of X.

Obviously, $bn_{\Delta k}X = Ubn_{\Delta k}X \cup Lbn_{\Delta k}X$.

48.3 The Properties of Degree Induced Covering Rough Set

Theorem 1 [11] *Let* (U,C) *be a covering approximation space. For each* $X, Y \subseteq U, k \in Z^+$, *then*

(1) $\underline{\Delta}_k(U) = U,$ $\qquad\qquad\qquad$ $\bar{\Delta}_k(\varnothing) = \varnothing;$
(2) $\underline{\Delta}_k(X) = \neg\bar{\Delta}_k(\neg X),$ $\qquad$ $\bar{\Delta}_k(X) = \neg\underline{\Delta}_k(\neg X);$
(3) $\underline{\Delta}_k(X \cap Y) \subseteq \underline{\Delta}_k(X) \cap \underline{\Delta}_k(Y),$ $\quad$ $\bar{\Delta}_k(X \cup Y) \supseteq \bar{\Delta}_k(X) \cup \bar{\Delta}_k(Y);$
(4) $\underline{\Delta}(X) = \underline{\Delta}_0(X),$ $\qquad\qquad\qquad$ $\bar{\Delta}(X) = \bar{\Delta}_0(X);$
(5) *if* $X \subseteq Y$, *then*
$\qquad$ $\underline{\Delta}_k(X) \subseteq \underline{\Delta}_k(Y),$ $\qquad\qquad$ $\bar{\Delta}_k(X) \subseteq \bar{\Delta}_k(Y);$
(6) *if* $k \geq l$, *then*
$\qquad$ $\underline{\Delta}_k(X) \supseteq \underline{\Delta}_l(X),$ $\qquad\qquad$ $\bar{\Delta}_k(X) \subseteq \bar{\Delta}_l(X).$

Theorem 2 *Let* (U,C) *be a covering approximation space. For each* $X \subseteq U, k \in N$, $|\Delta_x| > 2k$,

(1) *if* $|\Delta_x \cap X| \geq |\Delta_x| - k$, *then* $\Delta_x \subseteq pos_{\Delta k}X$;
(2) *if* $|\Delta_x \cap X| \leq k$, *then* $\Delta_x \subseteq U - \bar{\Delta}_kX$ *and* $\Delta_x \subseteq neg_{\Delta k}X$;
(3) *if* $|\Delta_x \cap X| \in (k, |\Delta_x| - k)$, *then* $\Delta_x \subseteq Ubn_{\Delta k}X$.

Proof (1) For $|\Delta_x \cap X| \geq |\Delta_x| - k$ i.e. $|\Delta_x| - |\Delta_x \cap X| \leq k$, we can easily get $\Delta_x \subseteq \underline{\Delta}_kX$. And $|\Delta_x| > 2k$, that means $|\Delta_x| - k > k$, there exists $|\Delta_x \cap X| \geq |\Delta_x| - k > k$, which means $\Delta_x \subseteq \bar{\Delta}_kX$. Therefore, $\Delta_x \subseteq pos_{\Delta k}X$.

Similarly, we can prove (2) and (3).

Theorem 3 *Let* (U,C) *be a covering approximation space. For each* $X \subseteq U$, $k \in N, |\Delta_x| \in (k, 2k]$,

(1) *if* $|\Delta_x \cap X| > k$, *then* $\Delta_x \subseteq pos_{\Delta k}X$;
(2) *if* $|\Delta_x \cap X| < |\Delta_x| - k$, *then* $\Delta_x \subseteq neg_{\Delta k}X$;
(3) *if* $|\Delta_x \cap X| \in [|\Delta_x| - k, k]$, *then* $\Delta_x \subseteq Lbn_{\Delta k}X$;

Proof (1) To $|\Delta_x| \in (k, 2k]$, we have $k < |\Delta_x| \leq 2k$, i.e. $0 < |\Delta_x| - k \leq k$. And $|\Delta_x \cap X| > k$, that $|\Delta_x \cap X| > k \geq |\Delta_x| - k$. Which means $\Delta_x \subseteq \underline{\Delta}_k X$. Another $\Delta_x \subseteq \bar{\Delta}_k X$ because of $|\Delta_x \cap X| > k$. Therefore $\Delta_x \subseteq pos_{\Delta k} X$.

Similarly, we can prove (2) and (3).

Theorem 4 *Let (U, C) be a covering approximation space. For each $X \subseteq U$, $k \in N$, if $|\Delta_x| \in [1, k]$, then $\Delta_x \subseteq Lbn_{\Delta k} X$.*

Proof Thanks to $|\Delta_x| \in [1, k]$, we have $1 \leq |\Delta_x| \leq k$ i.e. $|\Delta_x| - k \leq 0 \leq |\Delta_x \cap X|$, there have $\Delta_x \subseteq \underline{\Delta}_k X$. Another $|\Delta_x \cap X| \leq k$, then $\Delta_x \not\subset \bar{\Delta}_k X$. Therefore, $\Delta_x \subseteq Lbn_{\Delta k} X$.

Theorem 5 *Let (U, C) be a covering approximation space. For each $X \subseteq U$, $k \in N$, when Δ_x formation a division of U, then*

$$\bar{\Delta}_k(\bar{\Delta}_k X) = \bar{\Delta}_k X \subseteq \underline{\Delta}_k(\bar{\Delta}_k X).$$

Proof For $\Delta_x \subseteq \bar{\Delta}_k(\bar{\Delta}_k X)$, then $|\Delta_x \cap \bar{\Delta}_k X| > k$, which means $\Delta_x \subseteq \bar{\Delta}_k X$. Otherwise, if $\Delta_x \not\subset \bar{\Delta}_k X$ and Δ_x formation a division of U, which with $|\Delta_x \cap \bar{\Delta}_k X| = 0$. So $\bar{\Delta}_k(\bar{\Delta}_k X) \subseteq \bar{\Delta}_k X$. To $\Delta_x \subseteq \bar{\Delta}_k X$, according to the definition, we have $|\Delta_x \cap X| > k$, then $|\Delta_x \cap \bar{\Delta}_k X| = |\Delta_x| \geq |\Delta_x \cap X| > k$ and $|\Delta_x \cap \bar{\Delta}_k X| = |\Delta_x| \geq |\Delta_x| - k$, so we have $\Delta_x \subseteq \underline{\Delta}_k(\bar{\Delta}_k X)$ and $\Delta_x \subseteq \bar{\Delta}_k(\bar{\Delta}_k X)$.

Therefore $\bar{\Delta}_k X \subseteq \underline{\Delta}_k(\bar{\Delta}_k X)$ and $\bar{\Delta}_k X \subseteq \bar{\Delta}_k(\bar{\Delta}_k X)$ hold. Now we have proved $\bar{\Delta}_k(\bar{\Delta}_k X) = \bar{\Delta}_k X \subseteq \underline{\Delta}_k(\bar{\Delta}_k X)$.

Theorem 6 *Let (U, C) be a covering approximation space. For each $X \subseteq U$, $k \in N$, when Δ_x formation a division of U, then*

$$\underline{\Delta}_k(\bar{\Delta}_k X) = \bar{\Delta}_k X \cup (\cup\{\Delta_x | |\Delta_x| \leq k\}).$$

Proof If $|\Delta_x| \leq k$, then $|\Delta_x| - k \leq 0$. So $|\Delta_x \cap \bar{\Delta}_k X| = |\Delta_x| - k$ which means $\Delta_x \subseteq \underline{\Delta}_k(\bar{\Delta}_k X)$. There also have $\bar{\Delta}_k X \subseteq \underline{\Delta}_k(\bar{\Delta}_k X)$, so $\underline{\Delta}_k(\bar{\Delta}_k X) \supseteq \bar{\Delta}_k X \cup (\cup\{\Delta_x | |\Delta_x| \leq k\})$. If $\Delta_x \subseteq \underline{\Delta}_k(\bar{\Delta}_k X)$, according to the definition, we have $|\Delta_x \cap \bar{\Delta}_k X| \geq |\Delta_x| - k$. if $|\Delta_x| - k > 0$, i.e. $|\Delta_x| > k$, when Δ_x formation a division of U, then $\Delta_x \subseteq \bar{\Delta}_k X$. If $|\Delta_x| - k \leq 0$ i.e. $|\Delta_x| \leq k$, when Δ_x formation a division of U, then $\Delta_x \notin \bar{\Delta}_k X$ and $\Delta_x \subseteq \cup\{\Delta_x | |\Delta_x| \leq k\}$. Therefore $\underline{\Delta}_k(\bar{\Delta}_k X) \subseteq \bar{\Delta}_k X \cup (\cup\{\Delta_x | |\Delta_x| \leq k\})$.

Theorem 7 *Let (U, C) be a covering approximation space. For each $X \subseteq U$, $k \in N$, when Δ_x formation a division of U, then*

$$\bar{\Delta}_k(\underline{\Delta}_k X) \subseteq \underline{\Delta}_k X = \underline{\Delta}_k(\underline{\Delta}_k X).$$

Proof Let $\Delta_x \subseteq \bar{\Delta}_k(\underline{\Delta}_k X)$, according to the definition, we have $|\Delta_x \cap \underline{\Delta}_k X| > k$, if $\Delta_x \not\subset \underline{\Delta}_k X$ and Δ_x formation a division of U, that in coincide with $|\Delta_x \cap \underline{\Delta}_k X| = 0$. So $\Delta_x \subseteq \underline{\Delta}_k X$ i.e. $\bar{C}_k(\underline{\Delta}_k X) \subseteq \underline{\Delta}_k X$. If $\Delta_x \subseteq \underline{\Delta}_k X$, according to the definition, we have $|\Delta_x \cap \underline{\Delta}_k X| > |\Delta_x| - k$, then $|\Delta_x \cap \underline{\Delta}_k X| = |\Delta_x| \geq |\Delta_x| - k$, which means

$\Delta_x \subseteq \underline{\Delta}_k(\underline{\Delta}_k X)$. Otherwise, if $\Delta_x \subseteq \underline{C}_k(\underline{C}_k X)$, then $|\Delta_x \cap \underline{\Delta}_k X| \geq |\Delta_x| - k$. If $\Delta_x \not\subseteq \underline{\Delta}_k X$, we have $|\Delta_x \cap \underline{\Delta}_k X| = 0$ and $0 \leq |\Delta_x \cap X| < |\Delta_x| - k$, which in coincide with $|\Delta_x| - k \leq 0$. So $\Delta_x \subseteq \underline{\Delta}_k X$ i.e. $\underline{\Delta}_k(\underline{\Delta}_k X) \subseteq \underline{\Delta}_k X$. Therefore $\underline{\Delta}_k X = \underline{\Delta}_k(\underline{\Delta}_k X)$.

Theorem 8 *Let (U, C) be a covering approximation space. For each $X \subseteq U$, $k \in N$, when Δ_x formation a division of U, then*

$$\underline{\Delta}_k X = \bar{C}_k(\underline{\Delta}_k X) \cup (\cup\{\Delta_x | |\Delta_x| \leq k\}).$$

Proof If $|\Delta_x| \leq k$, then $\Delta_x \subseteq \underline{C}_k X$, another that $\bar{C}_k(\underline{\Delta}_k X) \subseteq \underline{\Delta}_k X$, so $\underline{\Delta}_k X \supseteq \bar{C}_k(\underline{\Delta}_k X) \cup (\cup\{\Delta_x | |\Delta_x| \leq k\})$. Otherwise, if $\Delta_x \subseteq \underline{\Delta}_k X$, when Δ_x formation a division of U, then $|\Delta_x \cap \underline{\Delta}_k X| = |\Delta_x|$. If $|\Delta_x| > k$, we have $\Delta_x \subseteq \bar{C}_k(\underline{\Delta}_k X)$. Otherwise $|\Delta_x| \leq k$. So $\underline{\Delta}_k X \subseteq \bar{C}_k(\underline{\Delta}_k X) \cup (\cup\{\Delta_x | |\Delta_x| \leq k\})$. Therefore, $\underline{\Delta}_k X = \bar{C}_k(\underline{\Delta}_k X) \cup (\cup\{\Delta_x | |\Delta_x| \leq k\})$.

References

1. Pawlak Z (1982) Rough sets. Int J Comput Inf Sci 11:341–356
2. Pawlak Z (1991) Rough sets: theoretical aspects of reasoning about data. Kluwer Academic Publishers, Boston
3. Angiulli F, Pizzuti C (2005) Outlier mining in large high-dimensional data sets. IEEE Trans Knowl Data Eng 17(2):203–215
4. Polkowski L, Skowron A (eds) (1998) Rough sets and current trends in computing, vol 1424. Springer, Heidelberg
5. Zhong N, Yao Y, Ohshima M (2003) Peculiarity oriented multidatabase mining. IEEE Trans Knowl Data Eng 15(4):952–960
6. Ziarko W (1993) Variable precision rough set model. J Comput Syst Sci 46(1):39–59
7. Zakowski W (1983) Approximations in the space (u, π). Demonstratio Mathematica 16: 761–769
8. Bonikowski Z, Bryniarski E, Wybraniec U (1998) Extensions and intentions in the rough set theory. Inf Sci 107:149–167
9. Dai D, Wang J-P, Xue H-F (2008) Degree rough set model based on covering. J Jianghan University (Nat Sci) 36(1):13–17
10. Zhang G, Huo Y (2010) The concept and property of induced covering rough set. China New Technol Prod 12:237
11. Chen D, Li L, Wu K (2010) Degree induced covering rough set model [C]. ETT2010 346–348
12. Zhu W, Wang F-Y (2006) Relations among three types of covering rough sets. In: IEEE GrC 2006, Atlanta, GA, USA. pp 3–48

Chapter 49
Real-Time Setting and Processing on LCD Touch Panel for Electronic Handwriting Exercising to Chinese Character

Ding Wang

Abstract The LCD touch panels have become the basic parts of most products as the human–machine interfaces. The LCD touch panels can become the main parts since their working areas become the bigger, and their real-time properties become the better. That is to say, we can immediately use of the LCD touch panels as the key operating parts of some system for some picture information. It has been known the handwriting touch traces on the LCD touch panel can be displayed immediately on the liquid crystal display, which has the properties like the paper. Therefore, we can use the LCD touch panels as the tool of the handwriting exercising as the paper did. So, we present and study the electronic handwriting exercising technologies (EHET) for Chinese character. The technologies presented consisted of the hardware design, the software design, and the algorithms of the function which were the key of the system designs. Its fundamental operation frames were the page structure. It became a kind of two-part architecture which included a MCU and an integrated operation parts. Its characteristics come from permitting of LCD touch panel and need of the operation task, and made the application wider. The physical prototype implemented proved the above studies mentioned were practical and effective.

Keywords Multiple man–machine interfaces · Feature extraction · Handwriting exercise · Chinese character

D. Wang (✉)
Key Laboratory of Electronics Engineering of College of Heilongjiang Province,
Heilongjiang University, Harbin, People's Republic of China
e-mail: climbing200310@yahoo.com.cn

49.1 Introduction

The LCD touch panels in which a liquid crystal display and a touch panel are integrated into an organic whole, appeared in the end of 1980s to reduce the area of a display panel and a input panel, and which were also called as a touch display panel or an integrated touch panel LCD device, or LCD touchscreen panel. Since then, they had many developments. The main characteristics of them are to display the information and to allow a user to interact with them by touching on or near the displayed information. Therefore, the LCD touch panels have become the basic parts of most products as the human–machine interfaces, such as Portable computer, Cellular phone, and Multi-window type NC apparatus. The LCD touch panels were in the case of auxiliary roles.

The handwriting is a fundamental skill of learning and using the language for humans. The development of writing ability is not only important in building a child's self-esteem, but is considered an essential ingredient for success in school. In our society, handwriting is both a means of communication and a necessary life skill, as in writing a letter or telephone message, completing an application form, or writing a check. Handwriting is still the most immediate form of graphic communication [1]. Handwriting exercising is related with the handwriting ability of language, is a main method of the development of writing ability. For the structures of the Chinese character are complicated, their handwriting is very difficult so that their handwriting exercising is a more important.

The two kinds of the traditional handwriting exercising methods for the Chinese character were the copying from the calligraphy (CC) and facsimileing the calligraphy (FC) on paper, which was formed thousands of years ago. The CC was generally making the handwriting exercising to refer to the calligraphy usually written by calligraphy artists on front of paper of the handwriting exercising. And the FC is making the handwriting exercising to trace the strobes of the calligraphy beneath the paper of the handwriting exercising. But traditional handwriting exercise to Chinese character had several shortcomings which are to need lots of calligraphy works to copy from, not to feedback the guiding and evaluation to the handwriting exercising results in time, and to waste a plenty of paper. So, the new handwriting exercise method is very necessary.

The LCD touch panels can become the main parts since their working areas become the bigger, and their real-time properties become the better. That is to say, we can immediately use of the LCD touch panels as the key operating parts of some system for some picture information. It has been known the handwriting touch traces on the LCD touch panel can be displayed immediately on the liquid crystal display, which has the properties like the paper. Therefore, we can use the LCD touch panels as the tool of the handwriting exercising as the paper did. The electronic handwriting exercising technologies (EHET) for Chinese character which has been invented by author. In order to attain the above goal, we must use and build two relative areas on the LCD touch panel. The both of them can be to

Fig. 49.1 Scheme of handwriting exercising

Display position of the template Chinese character to exercise

Position of Chinese character for the FC

Position of Chinese character for the CC

liquid crystal touch screen
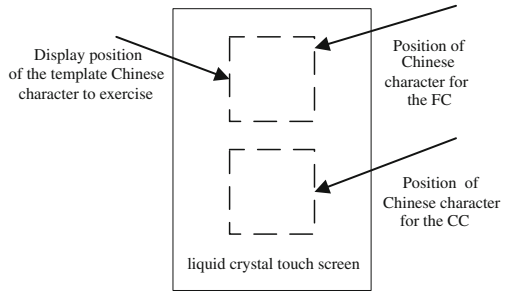
display the template character of the Chinese character to exercise, one of them can be allowed to input and display the relative Chinese character to exercise. It is had better that the EHET had the real-time properties. The EHET had the some advantages: to save paper which handwriting exercising use, the high efficiency of handwriting exercising, and the additional function to other consumer apparatus such as mobile phones.

In this paper, we studied several main technologies of EHET: the scheme of system, hardware design, software design, and its function algorithms which were the key of the system designs. The example of the EHET was made. And the detail of the EHET presented by the paper is discussed as follows.

49.2 Basics of the EHET

49.2.1 Structure

Based on the requirements of the EHET, the structure was presented, shown in Fig. 49.1: Display the template character of the Chinese character to exercise on the upper part of the liquid crystal screen, then input the relative Chinese character to exercise with handwriting by the touch panel; during the CC, the position of the Chinese character to exercise by touch panel is on the lower part of the liquid crystal screen which was different from that of the Chinese character; During the FC, the position of them were both the same. The evaluation of performance for the EHET was made by comparing the Chinese character on the liquid crystal screen with the Chinese character to exercise by touch panel. In some sense, the practical application of the EHET had the structure of three layers of the system, hardware, software and its functional algorithms. Their functional algorithms divided three aspects: the man–machine interface (page controls) which controlled the conversion each other between the operation pages, system setting which made the LCD touch panel operated correctly and handwriting exercising operation which organized the template character library and displayed the character to exercise and processed handwriting input data.

Fig. 49.2 Block diagram
of system hardware
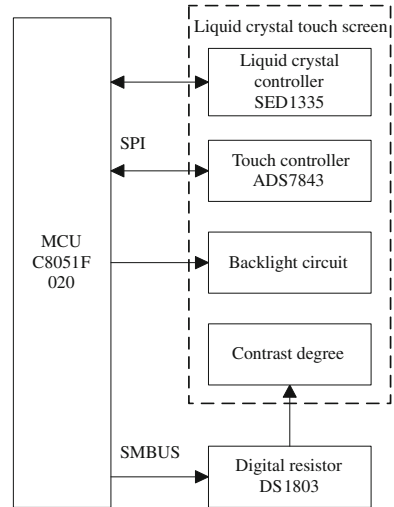
49.2.2 Hardware Design

The hardware is the base of system. The hardware platform for the EHET
consisted of the liquid crystal screen for displaying the Chinese character to
exercise, the touch panel to input the Chinese character for exercising and the
control circuit board. The liquid crystal and touch integrated screen of bigger
320*240 size is chosen. Its liquid crystal controller is SED1335 and its touch
controller is ADS7843. The operation conditions of liquid crystal screen are the
adjustable contrast degree control and the adjustable back light. System hardware
block diagram is shown in Fig. 49.2.

49.2.3 Design of Software

The tasks of the system software consisted of chip driving task programs and
information task programs. The requirements of driving task programs were
determined by the configuration of the hardware. The information task programs
were determined by the functions of system. The chip driving task programs were
MCU initialization program, the liquid crystal screen controller SED 1335 chip
driving task program, the SPI bus chip driving task program and the SMBUS bus
driving task program. The information tasks were divided three parts, human–
machine interface parts, system setting and handwriting data processing which
were discussed in the last section.

The operation processes of the system software were: After the initial setting
mentioned above in terms of chip driving task programs was operated, the initial

picture was displayed, then the main picture of the operation menu is displayed waiting the touch operation of the operator. As soon as the touch signals are detected, the detail setting functions are completed. Finally the page processing was entered.

49.2.4 Multiple Man–Machine Interface for EHET

The man–machine interface was the base on which the some functions were realized. We used a Graphic User Interface (GUI) which was to build the main program into the internal ROM of the controller chip so it did not need to use extra internal RAM to store the main program externally. A General single page interface based on a LCD touch panel was programmed easily: The operation sign of the function keys were transform by the special character model generation tools into the code which can be displayed on LCD; the software delivered the code on the LCD to display when necessary; and the function of relative touch judgments were set to recognize the touch actions of the function keys. But for the EHET, it's necessary to use multiple page interfaces because there were the data of multiple layers and to switch repeatedly each other between multiple pages. We could specify the only page flag for the every page to recognize the different page first. Set its page flag as one when it's used, the other ones is zero. And display program only displayed the page which has the relative page flag of one. According to the function of the system, there were handwriting functions and touch keys function on some pages. Hence there were two kinds of pages, touch pages and handwriting excising page. Set the handwriting flag and touch keys flag. We used the touch keys as the input condition and exit condition, and specified the touch flag for the pages with the touch keys, specified the handwriting flag for a handwriting exercise page. The relative page programs had two parts, page picture on LCD and touch input data process on the touch panel.

49.2.5 Data acquisition and Processing for Handwriting on LCD Touch Panel

The handwriting data were acquired from the touch panel. And external interruption INT0 of the MCU was set as the mode of interruption for monitoring the state of handwriting assigning the global valuable pen_down with the zero for the no handwriting or one for the handwritingnd entered into the corresponding the subprogram in which the transferring commend for x or y were sent to ADS7843 and the returning value of ADS7843 were fetched and processed to save in the save16_x[ ] and save16_y[ ]. The handwriting data were stored respectively as the save_x[ ] save_xx and save_y[ ] save_yy[ ] because of the data formulas of 8 bit of
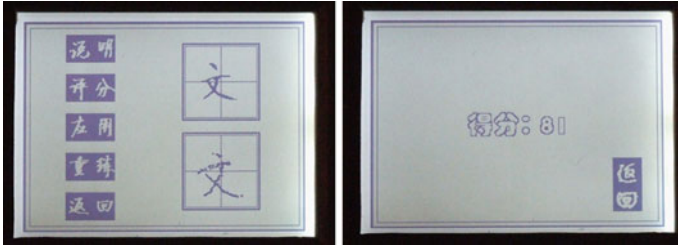
Fig. 49.3 The case of the hardwiring character

the MCU, finally were stored as the integer valuable save16_x[ ] and save16_y[ ] of the 12 bits to process.

The handwriting data processing from the touch panel is a pattern recognition problem with known template: Input and process the handwritings to Chinese character from the touch panel, compare the feature to Chinese character extracted with that of template character on the LCD, so the distances between the feature of handwriting to Chinese character and the that of relative template character are measured to present in the form of performance index on the LCD. The drawbacks of projection characteristic [2, 3] are short of detail characteristic which are affected by the type and size of characters, so that the feature to Chinese character is made by applying discrete time wavelet transformation (DTMT) to projection characteristic to obtain wavelet coefficients as the feature.

49.3 Results and Discussion

When the Chinese character to exercise was displayed on the upper part of the liquid crystal screen of the left picture shown in Fig. 49.3, the hardwiring character was inputted and displayed on the lower part of the liquid crystal screen of the left picture shown in Fig. 49.3, obtaining the exercising marks on the right picture shown in Fig. 49.3.

Compared with the methods of traditional handwriting exercise to Chinese character, the EHET had the following characteristics. There were the differences between the material to write on during the hardwiring exercising because the EHET used a LCD touch panel and the methods of traditional handwriting exercise used a piece of paper. Another difference was that the number of template characters was only one with the methods traditional handwriting exercise and many ones to choose during the EHET. The analysis of the handwriting character written for exercising was important to improve handwriting ability. The handwriting exerciser did it oneself for the methods of traditional handwriting exercise, but the professional unit in the handwriting exercise system built with the EHET gave it for the EHET.

References

1. Feder KP, Majnemer A (2007) Handwriting development, competency, and intervention. Dev Med Child Neurol 49:312–317
2. Verma B, Blumenstein M, Ghosh M (2004) A novel approach for structural feature extraction: contour versus direction. Pattern Recognit Lett 25:975–988
3. Blumensteina M, Liua XY, Vermab B (2007) An investigation of the modified direction feature for cursive character recognition. Pattern Recognit 40:376–388

Chapter 50
Research and Construction of a Sensing Forest System based on the Internet of Things

Junguo Zhang, Wenbin Li and Zheng Fu

Abstract Forest information collection plays an important role in the process of building modern forestry. This paper proposes a monitoring system—Sensing Forest System, based on the Internet of Things, 3G and 3D GIS, to make up for the shortcomings of traditional monitoring methods. Key issues, such as system architecture, design of wireless multimedia sensor nodes and data transfer process in the network, have been studied and presented, for obtaining real-time comprehensive forestry information, accurately, automatically and remotely, to lay foundations for applications of the Internet of Things in forestry.

Keywords Sensing forest system · The internet of things · System architecture · Sensor nodes · Data transfer

50.1 Introduction

Forest information collection plays an important role for improving the level of production, operation, management and protection in modern forestry. Traditional forestry information collection methods include manual samplings and satellite remote sensing. In manual samplings, it's incapable of monitoring environment parameters remotely, and scope-limited, labor-intensive, target-poor, and not

J. Zhang (✉) · W. Li
Beijing Forestry University, 35 Haidian District, qinghua East Road,
Beijing 100083, P.R. China
e-mail: zhangjunguo@bjfu.edu.cn

Z. Fu
Graduate University of Chinese Academy of Sciences,
3 Nanyitiao Alley, Zhongguancun, Haidian District,
Beijing 100049, P.R. China

real-time. There are also many disadvantages in satellite remote monitoring, such as, not very high accuracy and incomplete parameters [1]. Therefore, modern forestry needs advanced information access technologies as a complement. The Internet of Things provides a brand new insight of information obtaining and processing, and environmental monitoring system based on it is becoming a research focus. This paper proposes a monitoring system—Sensing Forest System, based on the Internet of Things, 3G and 3D GIS, to make up for the shortcomings of traditional monitoring methods. Key issues, such as system architecture, design of wireless multimedia sensor nodes and data transfer process in the network, have been studied and presented, for obtaining real-time comprehensive forestry information, accurately, automatically and remotely, to lay foundations for applications of the Internet of Things in forestry.

50.2 Introduction to the Internet of Things

The Internet of Things is a new dynamic network that connects everything, by embedding short-range mobile transceivers into a wide array of additional gadgets and everyday items, enabling new forms of communication between people and things, and between things themselves. A new dimension has been added to the world of information and communication technologies: from anytime, anyplace connectivity for anyone, we will now have connectivity for anything [2]. As shown in Fig. 50.1, the Internet of Things is composed of three layers.

The bottom layer is sensing layer, mainly including wireless sensor networks, RFID and other information sensing devices. The middle layer is network access layer, including 3G telecommunication network and so on. The top layer is application layer, running different applications and providing interfaces for humans. And among them the sensing layer is fundamental core.

50.3 The Sensing Forest System Based on the Internet of Things

50.3.1 The Content of Sensing Forest System

Sensing Forest System applies kinds of sensing methods including wireless sensor networks and RFID, providing a visualized, digital, intelligent picture of the whole forest. That is, a network connects people and things in forests, by integrating sensing technology, communication technology, information technology, control technology and information management with modern forestry, to obtain infor-mation of climate, soil, hydrology, wild animals and trees in forests. As a result, we can describe and control the monitoring process real-time and in detail, to ensure the ecological stability of forest environment.
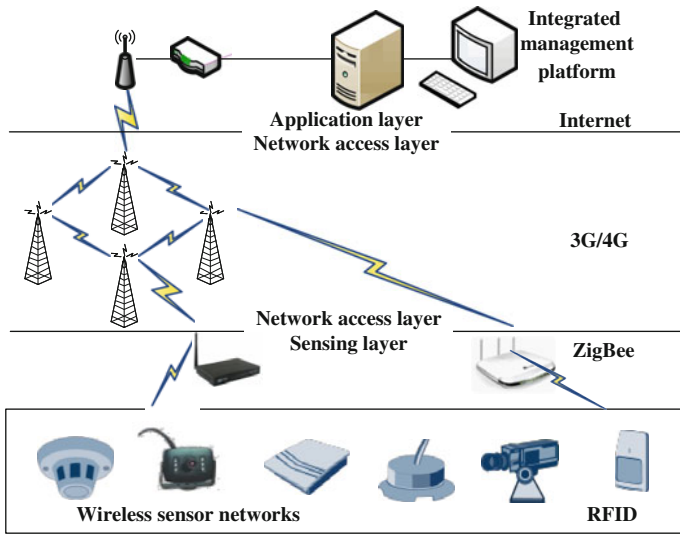
Fig. 50.1 System architecture of the internet of thing
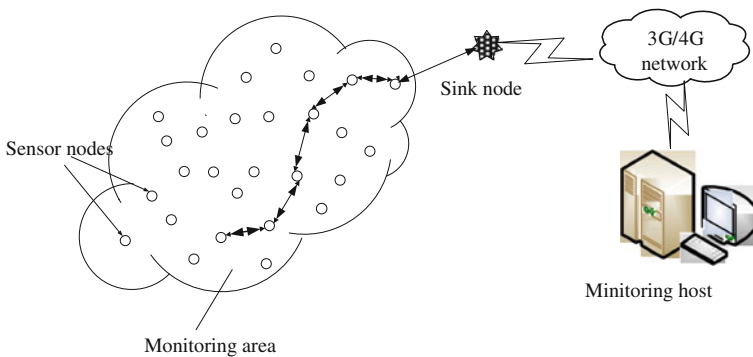
Fig. 50.2 System architecture of sensing forest system

50.3.2 System architecture of Sensing Forest System

The system architecture of Sensing Forest System is shown in Fig. 50.2.

As with the Internet of Things, Sensing Forest System is composed of 3 layers: sensing layer, network access layer, application layer. The sensing layer is mainly based on wireless multimedia sensor networks, which is composed of a lot of sensor nodes. Sensor nodes with processing unit are deployed in forests, form self-organized network. They are also equipped with a variety of sensors, such as temperature, illumination, smog, tree diameter, CMOS image sensor, microphone and so on, to obtain information of climate, soil, hydrology, wild animals and trees

in forests, and process the information locally to transfer the processed information to the sink node one by one [3]. Network access network includes 3G telecommunication network and so on, to transfer the data to Internet, finally to the control center. The control center in application layer is integrated with 3S (GPS, RS, GIS) systems, achieving a multiple forestry monitoring system, including forest-fire monitoring system, environmental monitoring system, wild animals monitoring system, accurate forestry and so on. So researchers can monitor the whole forest real-time in a control room with the information of the forest in detail.

50.4 Hardware Design

50.4.1 Design of Sensor Node with Solar Energy Supply

Sensing Forest System mainly depends on wireless multimedia sensor networks, which consist of lots of sensor nodes as a basis [4–6]. Therefore, the most important work is focused on the development of low-cost wireless multimedia sensor nodes used to forest environment [7]. Taken the characteristics of multimedia data processing and energy consumption into account, sensor nodes based on ARM7 are designed in the paper, including ARM7 processing unit, ZigBee transceiver, CMOS image sensor module, microphone, other sensors, and solar energy supply module. The specific hardware architecture is shown in Fig. 50.3.

The processor that we propose to be included in our sensor nodes is Atmel AT91SAM7X512, which is based on ARM7TDMI, 32-bit RISC architecture. It operates at a maximum speed of 55 MHz and features 512 KB of flash and 128 KB of SRAM. Typical core supply is 1.8 V, I/Os are supplied at 1.8 V or 3.3 V and are 5 V tolerant. It can set the parameters of the imager, instruct the imager to capture a frame and run local computation on the image to produce an inference. We adopt TI CC2520 as the ZigBee transceiver. The CC2520 is TI's second generation ZigBee/ IEEE 802.15.4 RF transceiver for the 2.4 GHz unlicensed ISM band. This chip enables industrial grade applications by offering state-of-the-art selectivity/co-existence, excellent link budget, hardware support for frame handling and low voltage operation, thus reducing the load on the host controller. And it connects with the processor through SPI. The image sensor module for our platform is OmniVision OV7670 combined with embedded DSP OV529. The OV7670 image sensor is a low voltage CMOS sensor that provides the full functionality of a single-chip VGA camera and image processor. The OV7670 provides full-frame, sub-sampled or windowed 8-bit images in a wide range of formats, operating at up to 30 frames per second (fps), controlled through the Serial Camera Control Bus (SCCB) interface. The OV529 Serial bridge contains an Embedded JPEC CODEC and controller chip that can compress and transfer image data from the Camera Sensor to an external device. The OV529 performs all imaging function like white balance, downsizing and compressed image to JPEG format. And the image sensor module connects with the processor through UART. We choose SiSonic SP0103NC3 as the microphone,
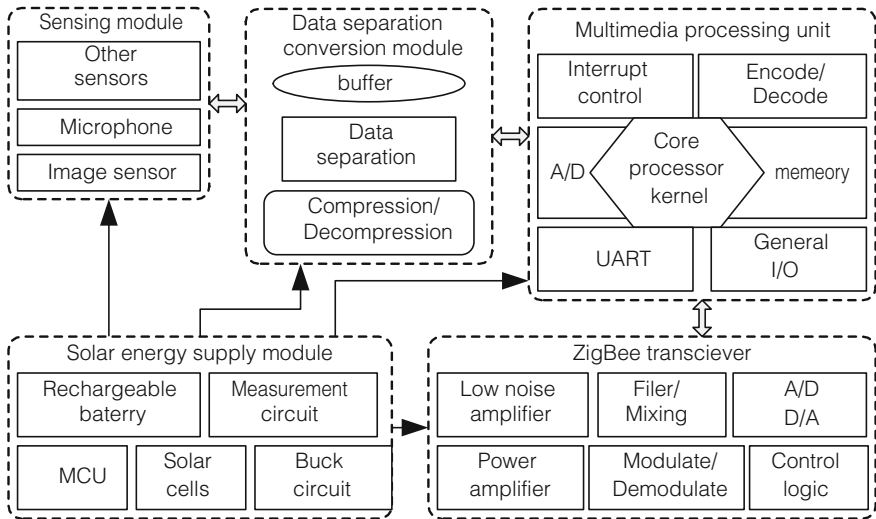
Fig. 50.3 Specific hardware architecture of sensor node/module block diagram

connecting to the AD pin of the processor. In addition, a solar energy module is developed, which consists of a microcontroller MSP430, solar cells, rechargeable battery, measurement circuits, BUCK circuits and so on, to supply power to the node with it efficiently.

50.4.2 Design of Sink Node

The sink node aims at connecting the wireless multimedia sensor networks with 3G telecommunication networks, establishing a reliable connection and two-way data transmission between remote server, mobile users and wireless sensor networks, to meet the practical needs. The specific hardware architecture is shown in Fig. 50.4.

The sink node consists of processor, memory, ZIgBee transceiver, 3G communication module and other expanded interfaces. Considering the dramatic amount of data of the sink node, PXA270 from Marvell has been chosen as the core processor module. It incorporates the Intel XScale technology which complies with the ARM* version 5TE instruction set (excluding floating-point instructions) and works at 520 MHz. To work with the PXA270, two chips of HY57V561620 from Hynix have been selected as 64 MB SDRAM, and two chips of TE28F128J3C-150 from Intel have been selected as 64 MB Flash. CC2520 has been adopted as ZigBee transceiver as described above. We choose SIMCom SIM5218 as the 3G module. The SIM5218 series is a Tri-Band/Single-Band HSPA/WCDMA and Quad-Band GSM/GPRS/EDGE module solution which supports up to 7.2Mbps downlink speed and 5.76Mbps uplink speed services. And it connects to the processor through UART.
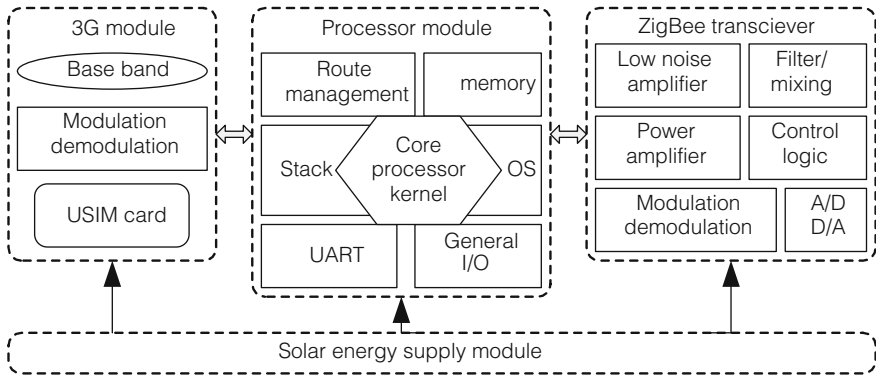
Fig. 50.4 specific hardware architecture of sink node
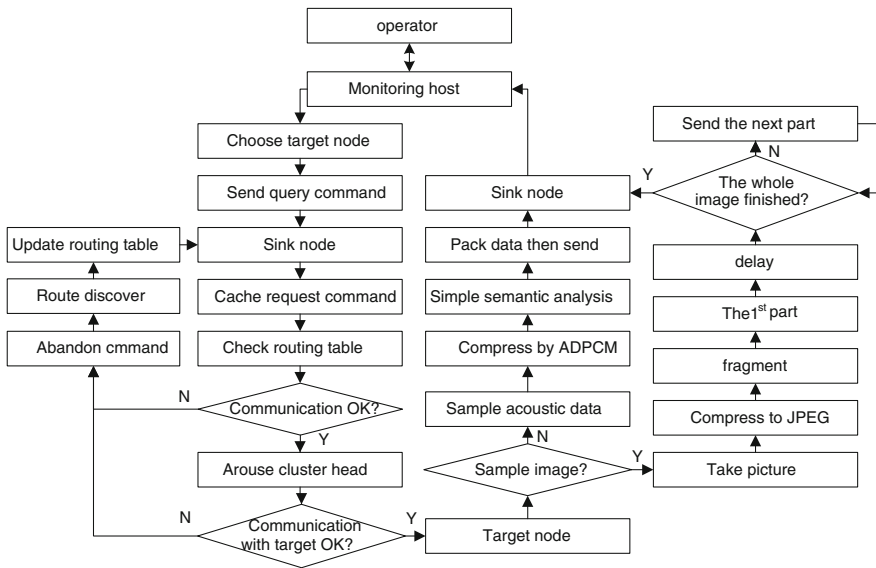
Fig. 50.5 Data transfer scheme in the networks

50.5 Data Transfer Scheme in the Networks

Overall, the control center requests actively, and then the nodes response passively to achieve the data transmission in the networks. Specifically, operators send query commands for information on the forest environment with control center, and then this command goes to the sink node via Internet and 3G network. The sink node then checks its routing table in its memory and select a route record. Then the cluster head in this route is aroused to receive the command, and according to the route record, the appropriate enddevice is also aroused to sample the information.

If none of routes is found in the original table, the nodes open route search function to discover a new route and update their routing tables. The captured JPEG file by the camera module is fragmented into 64 bytes units, and acoustic data is compressed by ADPCM method [8–10]. Then these data is sent back the same way to the control center. The data transfer scheme is shown in Fig. 50.5.

50.6 Conclusion

To make up for the shortcomings of traditional monitoring methods and remote sensing, this paper proposes a monitoring system –Sensing Forest System, based on the Internet of Things, 3G and 3D GIS. The monitoring system helps researchers with the detailed information of forest environment, trees, wild animals, etc. provides a visualized information map of the whole forest by the ubiquitous network. And researchers can control the whole forest in a control room remotely. The proposed system will push forward the application of the Internet of Things in forestry, and make it possible to obtain real-time comprehensive forestry information, accurately, automatically and remotely. It is undeniable that there are some key issues to solve before its practical application, for example, the multimedia processing and data fusion, which are also the scholars' main research interests in the future.

References

1. Zhang J, Li W, Han N, Kan J (2007) Forest fire detection system based on ZigBee wireless sensor network. J Beijing For Univ 29(4):41–45
2. Liu Q, Cui L, Chen H (2010) Key technologies and applications of internet of things. Comput Sci 37(6):1–4
3. Ma H-D, Tao D (2006) Multimedia sensor network and its research progresses. J Softw 17(9):2013–2028
4. Akyildiz IF, Melodia T, Chowdhury KR (2007) A survey on wireless multimedia sensor networks. Comput Netw 51(4):921–960
5. Akyildiz IF, Melodia T, Chowdhury KR (2008) Wireless multimedia sensor networks: applications and testbeds, 08855-1331. Institute of Electrical and Electronics Engineers Inc, Piscataway, pp 1588–1605
6. Sharif A, Potdar V, Chang E (2009) Wireless multimedia sensor network technology: a survey. Institute of Electrical and Electronics Engineers Inc, Cardiff, pp 606–613
7. Seema A, Reisslein M (2010) Towards efficient wireless video sensor networks: a survey of existing node architectures and proposal for a flexi-WVSNP design. IEEE Commun Surv Tutor 13(3):462–486

8. Mangharam R, Rowe A, Rajkumar R, Suzuki R (2006) Voice over sensor networks, 27th IEEE international real-time systems symposium, RTSS, Rio de Janeiro, Brazil, pp 291–302, 5–8 Dec 2006
9. Wu H, Abouzeid A (2005) Energy efficient distributed image compression in resource-constrained multihop wireless networks. Comput Commun 28(14):1658–1668
10. Luo W-S, Zhai Y-P, Lu Q (2008) Study on wireless multimedia sensor networks. J Electron Inf Technol 30(6):1511–1516

Chapter 51
Research and Simulation of Variable Step-Size Uncorrelated Adaptive Volterra Filter Algorithm on Anti-Vibration and De-Noising

Xinling Wen and Xiaowen Zhang

Abstract In order to realize anti-vibration and de-noising on the aircraft main wing through the active control, the research of non-linear adaptive control algorithm is particularly important. Based on the study of the Volterra LMS algorithm, we improved a kind of variable step-size uncorrelated algorithm with better convergence speed and precision under the strong correlation input signal. Through the simulation, the new algorithm can realize faster convergence under strong correlation input signal of 500 times iterative computation, the weight coefficient mean-square error norm (*NSWE*) can achieve -30 dB, which verifying the accuracy of improved algorithm.

Keywords Volterra series · Improved LMS algorithm · Non-linear adaptive filter · Convergence character · Anti-vibration

51.1 Introduction

With the increasingly deep research of the non-linear theory and application, people have grown more and more interest in non-linear filters. Because Volterra series is a kind of functional, under satisfying the input signal energy limited conditions, most non-linear system can use Volterra series approximation to the arbitrary accurate degree. Therefore, Volterra filter is one kind of non-linear filters

X. Wen (✉)
Zhengzhou Institute of Aeronautical Industry Management,
Zhengzhou 450015, China
e-mail: wenxinling@zzia.eud.cn

X. Zhang
Interactive Media, Computer Science Department, University College Cork,
Cork, Ireland
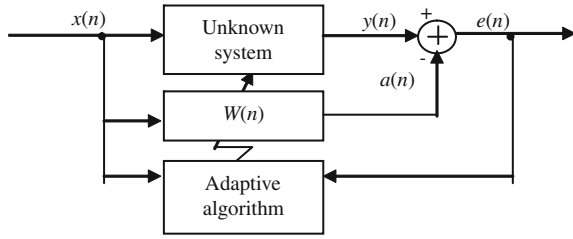
with the widely application prospects. In recent years, Volterra filters adaptive
filter algorithm and the applied research has caught people's attention. Among
them, variable step-size Volterra LMS filtering algorithm has many advanced
characters such as mall amount of calculation, easy to realize, and stability, which
has widely used, but, the constant step-size LMS adaptive algorithm in conver-
gence speed, tracking speed and power between the requirement is maladjusted
noise contradictory. In order to overcome these inherent contradictions, people
developed various variable step-size LMS algorithm of adaptive filter [1, 2].
Especially in variable step-size iteration, we introduce error autocorrelation
method, which can effectively eliminate the noise interference. In previous sim-
ulation, we have obtained the good convergence speed and the accuracy of con-
vergence, but these algorithm is based on the independence of the assumptions in
the weak-related input signal or moderate related input signal, we can able to get
better convergence effect.

But when the input signal is strongly related, the conditions are not statistically
independent LMS algorithm, which can cause the performance dramatically
reduction, and even cause algorithm un-convergence. Therefore, because the
introduction of solution related principles can remove the correlation in every
moment between the input vectors, which is the key of speeding up the conver-
gence rate of LMS algorithm. [3]

51.2 Volterra Filter of Non-Linear System

The principle structure diagram based on Volterra LMS adaptive identification
model of nonlinear system is shown as Fig. 51.1; [4].

The Volterra kernel of non-linear system is infinite, but, in practical appli-
cation, it must be truncated. Truncation processing contains order number
p and memory depth N. but, how to realize truncation is related to N, the
specific research system of non-linear type and the performance of the
requirements. For convenience, only consider the second order truncation,
namely order number $p = 2$, and hypothesis $h_0 = 0$, memory depth for
N. From Fig. 51.1, $w(n)$ is a Volterra filter coefficient vector with length of

$M = N(N + 3)/2$. Definition coefficient vector of the Volterra filter $w(n)$ is shown as formula (51.1).

$$w(n) = [w_0(n), w_1(n), \ldots, w_{M-1}(n)]^T \tag{51.1}$$

Then, output $a(n)$ of Volterra filter is shown as formula (51.2).

$$a(n) = W^T X(n) \tag{51.2}$$

Among formula (51.2), $X(n)$ is the input vector.

The purpose of the system identification is to change the filter coefficient vector $W(n)$ through some kind of adaptive algorithm, and makes the error signal $e(n)$ in a sense for minimum, that is to say, makes a cost function $J(n)$ of $e(n)$ to a minimum. When cost function $J(n)$ reach the minimum, we can think kernel vector $H(n) \approx W(n)$.

51.3 LMS Algorithm

If defining cost function $J(n)$ is shown as formula (51.3).

$$J(n) = e^2(n) = [y(n) - W^T(n)X(n)]^2 \tag{51.3}$$

Calculating the derivative of $J(n)$ about $W(n)$, and make $W(n)$ to change in opposite direction of the derivative, we can get pursuit of the best $W(n)$ of recursion algorithm, namely LMS algorithm. LMS algorithm process can be summarized as formula (51.4).

$$e(n) = y(n) - W^T(n)X(n), \quad W(n + 1) = W(n) + \mu X(n)e(n) \tag{51.4}$$

Among formula (51.4), the initial value $W(0)$ of $W(n)$ can be define by prior knowledge, or we can simply select $W(0) = [0\ 0\ \ldots 0]$. u is step factor, and it is a certain value, which value is selected by the convergence speed, tracking performance and stability of LMS algorithm. $X(n)e(n)$ is the iterative update direction vector.

Because the convergence speed of Volterra LMS algorithm is generally slow. In order to accelerate the convergence, we can adopt different step-size. The adjustment of variable step-size adaptive filter algorithm should meet step-size is long when initial convergence stage or unknown system parameter changes, in order to have a bigger fast convergence rate and the tracking speed of time-varying systems.

51.4 Improved Variable Step-Size Uncorrelated Algorithm

In order to solve the convergence speed and stable error, the literature [1] present a kind of variable step LMS algorithm (VSSLMS), which using the change step $u(n)$ instead of fixed step length u, its step iteration formula is shown as formula (51.5):

$$u(n + 1) = au(n) + \gamma e^2(n) \qquad (51.5)$$

VSSLMS algorithm better solved the conflict between convergence speed and steady-state error, but easy to be influenced by the independent noise. In Volterra LMS filter algorithm, we can define correlation coefficient $a(n)$ of $X(n)$ and $X(n-1)$ similar to projection coefficient, which is shown as formula (51.6):

$$a(n) = \frac{X^T(n)X(n-1)}{X^T(n-1)X(n-1)} \qquad (51.6)$$

$a(n)$ is the association degree between $X(n)$ and $X(n-1)$, and $a(n)$ is larger, the connections between them are stronger. Therefore, we can write the improved update orientation vector, such as below formula (51.7).

$$b(n) = X(n) - a(n)X(n-1) \qquad (51.7)$$

Clearly, $a(n)X(n-1)$ is the relevant part between $X(n)$ and $X(n-1)$, Subtracting a part from $X(n)$, which is equivalent to decorrelation operations. We can use adjusting weight coefficient of $c(n)$ can achieve more accurately and more quickly value. Therefore, formula (51.2) can be amended as formula (51.8).

$$W(n + 1) = W(n) + \mu e(n)b(n) \qquad (51.8)$$

In order to solve the contradiction between the steady-state error and the convergent speed, we will modify the constant step factor μ of formula (51.8) to variable step by step length factor, which is shown as formula (51.9) [2]. In literature [2], MVSSLMS algorithm introduced $p(n)$ to estimate $e(n)$ and $e(n-1)$. It controls step length refresh by self correlation time estimate $p(n)$, which making algorithm have not influence of the relevant noise. The iteration step formula is shown as formula (51.9).

$$p(n) = \beta p(n-1) + (1-\beta)e(n)e(n-1), \ u(n+1) = au(n) + \gamma p^2(n) \quad (51.9)$$

However, in the actual adaptive process, error signal $e(n)$ is smaller in convergence process stages, using $e(n)e(n-1)$ to control step-size can lead to step-size factor small, and causing algorithm quickly reduced to minimum before the step-size convergence. So, this algorithm largely improves the performance of the algorithm. But they are based on the input signal independent theory. Research shows that, when the input signal is highly related, the performance of the

algorithm greatly affected. [8] Therefore, we adopt the related principle, with the input signal of orthogonal component to update the adaptive filter weight vector, and realize the signal de-correlation processing. Therefore, we can introduce memory factor γ and $\gamma(i) = \exp(-2i)$ $(i = 0, 1, 2 \ldots n - 1)$ [9]. Its purpose is to overcome the convergence process correlation smaller deficiency of $e(n)$, in order to get new variable step-size Volterra LMS adaptive algorithm, the formula is shown as formula (51.10).

$$p(n) = \chi p(n - 1) + [(1 - \chi)e(n)e(n - 1) + \sum_{i=0}^{n-1} \gamma(i)e^2(n - i)] \qquad (51.10)$$

Weight coefficient mean-square error (NSWE) is shown as formula (51.11).

$$NSWE = \frac{10 \log 10 \sum_{i=0}^{N-1} \left| h_i(n) - h_i^* \right|^2}{\sum_{i=0}^{N-1} h_i^*} \qquad (51.11)$$

51.5 Algorithm Simulation and Performance Analysis

Assuming identifies various orders non-linear system kernel coefficient of the expected output signal for a (n) is: $a(n) = -0.75x(n) + 0.42x(n - 1) - 0.34x(n - 2) + 0.5x^2(n) + 0.23x^2(n - 1) - 1.51x^2(n - 2) - 0.54x(n)x(n - 1) + 1.74x(n - 1)x(n - 2) - 0.9x(n)x(n - 2) + v2(n)$, and input signal is $x(n) = ax(n - 1) + v1(n)$, among them, $v1$ and $v2$ are all mean for 0, variance 1 gaussian white noise, and mutual independence. Adaptive Volterra filter order is 2, member length N is 3, and we select $\mu_{\max} = 0.5$, $\mu_{\min} = 0.001$, $L = 12$, $\sigma = 0.95$, $\alpha = 0.95$, $\beta = 0.000001$, $c = 0.000001$ and input signal is strong correlated, it is $x(n) = 0.9x(n - 1) + v1(n)$. Literature 2 algorithm can not achieve rapid convergence. This paper presents improved Volterra LMS adaptive filter algorithm obtain each kernel coefficient convergence curve is shown as Fig. 51.2.

From Fig. 51.2 we can see, in strong correlation input condition, this paper uses the variable step-size uncorrelated algorithm can achieve convergence, and has fast convergence speed, quantity of steady-state disorders is much low.

From Fig. 51.2 simulation results we can see, the convergence speed or steady mismatch of the Volterra LMS algorithm are better than literature. After algorithm 500 times iterations, all can achieve convergence, and to achieve the desired effect with high convergence precision. But literature Volterra LMS algorithm cannot achieve the convergence. In Fig. 51.3, weight coefficient error norm can achieve -30 dB after the iterative 500 times, convergence speed is fast and has high accuracy. In aircraft main wing complex non-linear vibration damping and
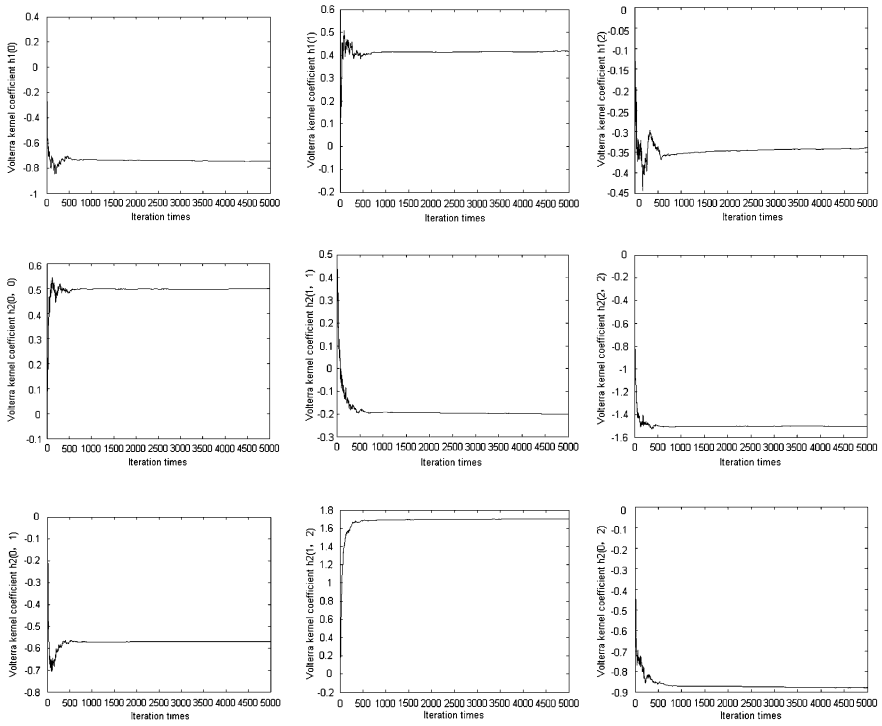
Fig. 51.2 Identification result in strong correlation input signal

Fig. 51.3 Weight coefficient
mean-square error (*NSWE*)
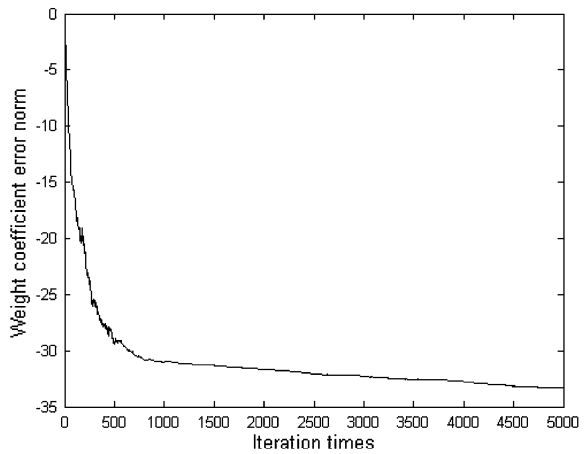
de-noising, input signal may be strong correlation, so, study the algorithms in strong correlated is very important.

51.6 Conclusions

This paper studied a kind of variable step-size uncorrelated LMS improved algorithm. Algorithm largely improved the performance, especially when the input signal is in strong correlation, this algorithm can still achieve faster convergence speed and higher precision. Therefore, the research of variable step-size uncorrelated LMS Volterra algorithm has significance, and is important process to realize anti-vibration and de-noising of vibration in aircraft motor and aircraft wing, etc.

References

1. Kwong RH, Johnston EW (1992) A variable step size LMS algorithm. IEEE Trans Signal Process 40:1633–1642
2. Aboulnasr T, Mayas K (1997) A robust variable step-size LMS-type algorithm: analysis and simulation. IEEE Trans Signal Process 45:631–639
3. Jianyou L, Zizhan W, Shunhui X, Zhenghua D (2006) An uncorrelated variable step-size normalized LMS adaptive algorithm. Comput Eng Sci 4:60–62
4. Guangsen W, Cheng W (2005) Nonlinear systems identification based on adaptive Volterra filter. Electr Opt Control 4:42–43
5. Feuer A, Weinstein E (1985) Convergence analysis of LMS filters with uncorrelated Gaussian data. IEEE Trans Acoust Speech Signal Process 33:222–229
6. MATHEWS VJ (1991) Adaptive polynomial filters. IEEE Signal Process Mag 8:10–26
7. Jie JIN, Donghui LI, Yinhao XU (2008) New uncorrelated variable step LMS algorithm and its application. Comput Eng Appl 44:57
8. Jianyou Long, Zizhan Wang, Shunhui Xia, Zhenghua Duan (2006) An uncorrelated variable step-size normalized LMS adaptive algorithm. Comput Eng Sci 28:60–61
9. Fangwei Li, Hao Zhang (2009) A new variable step size LMS adaptive filtering algorithm and its simulation. J Chongqing University Posts Telecomm (Natural Science Edition) 10:593

Chapter 52
Research on and Applications of Product Development Chain Modeling Technology Based on Semantic Web

Honggen Zhou, Xuwen Jing and Xiaojun Zhang

Abstract During each period of modern complex electronic products development, product is the core when the development actions are organized. Product development is completed through coordination of different enterprise or department and the complex electronic products development chain is built. This paper focuses on the basic principle of complex electronic products semantic develop chain, definites its base elements and substantive characteristics, and established its work pattern, discussed its major function. Finally, the method and process of realizing semantic development chain model on the basis of the system structure of complex electronic products semantic development chain is discussed, then a logical foundation for the semantization integration and reusing of complex electronic products is provided.

Keywords Ontology · Semantic web · Development chain · Complex electronic equipments

52.1 Introduction

Judging from the characteristics of the product development, as complex electronic products related to a complex discipline field and an increasingly fierce competition in technology, the development process is not only a product design problem,

H. Zhou (✉) · X. Jing · X. Zhang
School of Mechanical Engineering, Jiangsu University of Science and Technology,
Zhenjiang 212003, China
e-mail: hgzhou205@gmail.com

H. Zhou
School of Mechanical Engineering, Southeast University,
Nanjing 211189, China

butalso a comprehensive system engineering involving knowledge, process, resources and personnel. Complex electronic products development requires not only innovation, responsive agility but also systematicness, integration, isomerism, distributivity and collaboration. As the complexity and technical content of complex electronic products increase, single enterprise is often restricted by technology and resources, which can't be qualified the whole development process. So enterprises or departments, composed of multi-fields and constraints without time and space limited, cooperate with each other to complete product development has become a common requirement in products design unit. Traditional design theory and methodology have already been unable to meet the requirement for guiding this product development activity, at the same time, changes in market, external environment and resources structure also put forward new propositions to the development theory and methods of modern complex electronic products. The concept of development chain of complex electronic products and related researches are proposed under the requirements.

At present researches on the product development management and organization are mostly focused on a certain aspect, but the systematicness and operability is weak [1]. The development chain links each stage of the product development and the develop personnel closely by development target. And complete the whole product development process supported by computer hardware and software tools and network communication environment. With the help of product development chain, according to the user needs, developers can analysis and optimize the product development process, drive software and hardware tools and resources, develop high-quality products efficiently. However, this process is based on accurately organizing, obtaining, sharing and reusing of product development dates and knowledge, so suitable theory and methods are needed to manage and organize the product development chain.

It is evident that product information distributed in different department are not existing alone but link to each other more or less, this semantic link make it possible for the realization of the sharing of product information. The semantic development chain offers the theory and realization tools. That is, by constructing semantic ontology system in each fields and departments to put up a semantic sharing platform for their information exchanging, and through this platform realize highly sharing and integration of information, avoid problems of providing wrong information to users or omitting important information in some degree.

52.2 Structure and Frame of the Semantic Development Chain

The semantic development chain of complex electronic products is a dynamic system composed of many elements, which mainly includes six basic elements, personnel organization structure, development resources, product dates, development tasks or activities, semantic support and synergy. Personnel organization is the executive

body of development task and they are divided into different roles according to the division of work in the development chain. Product date object is the carrier of the development object and its date, with the continuous extension of development chain, product objects are constantly divided into sub-goals and sub-objects, the development tasks will be done by the next-level members in the development chain, so the products data will be flowing orderly and forming the data stream. Development task is the key element of the product development chain, which is a collection of a series of development activities carried out by developers focus on product objects. Software resources in development chain are used to realize the development process of complex electronic products. Semantic mechanism is the semantic coordination and management of the development process.

Based on the analysis above, the structure of the semantic development chain of the complex electronic products can be defined as follows: ESDC = $\{O,D,T,R,S,C\}$, in which O represents organizational structure of the development chain; D represents product data; T represents development task or activity; R represents development resource; S represents semantic mechanism of the development chain; C represents coordination mechanism of the development chain.

Semantic Web provides a common understanding pattern for the development activities and resources of the development chain, establishes a collaborative relationship-an informal relationship-for the developers. Cooperation is achieved through the integration of external resources or enterprises, which is also an information creation and transfer process. In order to improve the development efficiency and technological competitiveness, each development activity/input, output, constraints and knowledge of tasks must be analyzed at first, so as to identify how the related development activities/tasks interact in development chain, pave the way for the semantic cooperation. Based on the analysis above, referring to the experience of previous studies, this paper put forwards the frame of the semantic development chain of the complex electronic products, as is shown in Fig. 52.1.

52.3 Building Process of ESDCM Ontology

Product modeling technology plays a key role in product development and process management. Although the development costs account for only 5% of the entire product costs according to the traditional calculation method, it can determine the 70% of total cost [2, 3]. Capturing information of product development process has become a hotspot of product design, and several models and theories are formed. Previous studies show that there is not a universal theory and model at present, so researchers are hoping to build engineering activities ontology, which can capture and manage the development knowledge, to describe the product development process. And the present researches provide a rich application background for the ontology development, viewing from public literature, some ontology have already been used in industry, at the same time, the importance of ontology has been
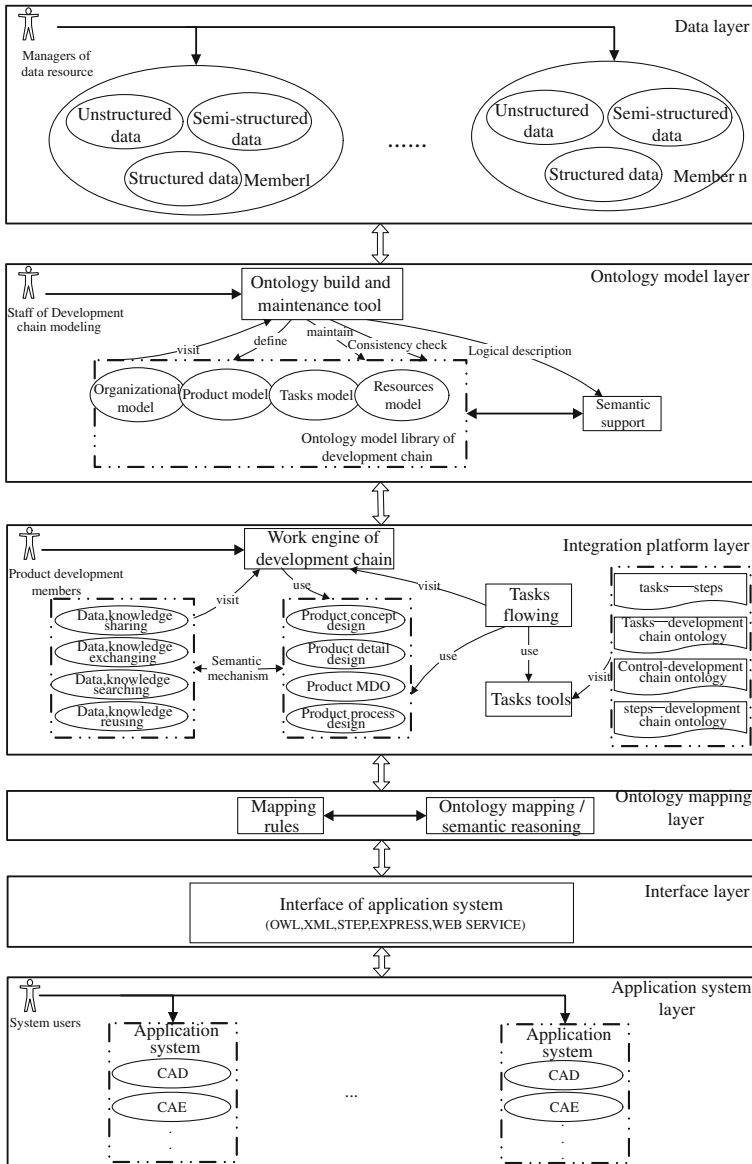
Fig. 52.1 Frame of the semantic development chain of the complex electronic products

recognized by different fields including cognition psychology, artificial intelligence design, lifelike design, design cognition theory, plan and knowledge engineering and so on [4–6]. As structured knowledge and organizational model of digital resources, ontology clearing the concepts relationship and concepts (classes) implicit in information resources under the premise of guaranteeing semantic

consistency. Clearing the mutual relations between development resources and objects according to the semantic of ontology, to establish a more universal and regulatory classification model of product development resources and improving the effectiveness of the development chain management.

Ontology building method Multidisciplinary Domain Ontology Building (MDOB) for Multidisciplinary fields is adopted according to the characteristics of ESDCM model of radar product under the coordination environment, building process as follows.

(1) *Choosing a domain-dependent ontology as the dependent ontology*. The multidisciplinary characteristics in ESDCM are reflected by some domain-dependent ontology;

(2) *Divided the target ontology into static and derived ontology*. Static ontology is shared ontology, which is efficient when the whole ontology is meaningful;

(3) *Choosing elements to build the ESDCM ontology*. Choosing the elements and listing the important terms and concepts to form a term list of development resources;

(4) *Choosing the theory to build the ESDCM ontology*. The set theory is the basic theory of the electronic ontology and provides terminology and relation for each kind of ontology, which can be used in the radar product and development resources ontology;

(5) *Choosing a language to describe the ontology*. According to the requirements of integrating and sharing under product development network environment, choosing OWL of the W3C to describe the ESDCM ontology;

(6) *Building the ESDCM examples*. At first choosing the development resources and process class which is needed to instantiated from class hierarchy, then creating objects for the class and assigning value for each property;

(7) *Evaluating the ESDCM ontology*. The ESDCM ontology should satisfy not only the universal principles but also the sharing of product development resource under network environment, if the conditions mentioned above are satisfied, the ontology is complete, or else editing and operating the concepts and their relationship is needed to make the ontology move towards maturity gradually.

52.4 Building ESDCM Concepts Set

The purpose of ontology is to capture knowledge in related fields, provide a common understanding in this field knowledge, confirm mutually accepted concepts in this field, and give a clear definition of these concepts and the relationships among concepts from different levels of formal models, therefore, the definition of the concept set is the key part of ontology modeling [4–6].

Table 52.1 Construction operator and semantics of OWL classes

OWL abstract	DLSyntax	Semantic interpretation	Instances
A (URI reference)	A	$A^I \subseteq \Delta^I$	Product model
OWL: Thing	$\top$	$OWL:Thing^I = \Delta^I$	Product development knowledge = product model $\cap$ development knowledge
OWL: Nothing	$\bot$	$OWL:Nothing^I = \phi$	
Intersection of (C$_1$, C$_2$)	$C_1 \cap C_2$	$(C_1 \cap C_2)^I = C_1^I \cap C_2^I$	Product model = CAD model $\cup$ CAE model $\cup \cdots$
Union of (C$_1$,C$_2$)	$C_1 \cup C_2$	$(C_1 \cup C_2)^I = C_1^I \cup C_2^I$	Thing = ¬Nothing
Complement of (C)	$\neg C$	$(\neg C)^I = \Delta^I \backslash C^I$	
One of (O1…)	$\{o_{1,\ldots}\}^I$	$\{o_{1,\ldots}\}^I = \{o_{1,\ldots}^I\}$	CAD tools = {Pro/E, UG,…}
Restriction (R. some Values Form (C))	$\exists R \cdot C$	$(\exists R \cdot C)^I = \{x \mid \exists_y \cdot <x,y> \in R^I\, and\, y \in C^I\}$	Tactical indicators. flexibility
Restriction (R. all Values Form (C))	$\forall R \cdot C$	$(\forall R \cdot C)^I = \{x \mid \forall_y \cdot <x,y> \in R^I\, and\, y \in C^I\}$	$\vee$ Multidisciplinary optimization capability. Isight
Restriction (R.h as values (o))	$\ni R : C$	$(\ni R : C)^I = \{x \mid <x,o^I> \in R^I$	$\ni$ optimization project.isolator weight
Restriction (R. Cardinality (n))	$\equiv nR$	$(\equiv nR)^I = \{x \mid \#(\{y \cdot <x,y> \in R^I\}) = n\}$	$\equiv$ Aluminum cooling plate.material
Restriction (R. minCardinality (n))	$\geq nR$	$(\geq nR)^I = \{x \mid \#(\{y \cdot <x,y> \in R^I\}) \geq n\}$	$\geq$ 3 cooling plate.thickness
Restriction (R. maxCardinality (n))	$\leq nR$	$(\leq nR)^I = \{x \mid \#(\{y \cdot <x,y> \in R^I\}) \leq n\}$	$\leq$ 52 cooling plate.weight

Concepts are basis for ontology building. Object-oriented abstract methods are in line with the way people understanding the world, the establishment of concepts and relationship class hierarchy, object-oriented method can be used to identify objects, by abstracting specific object to find class, mark the classification and assembly structure of class. Clustering, generalization, classification, inheritance and other methods can be used to abstract space concept from the complex development chain data resources, and reflect the product development entities in real-world. The specific procedures are as follows:

(1) Determining the original concept and original relationship, this can be used to build other concepts and relationships;
(2) Defining new concepts by using the original concept and original relationship, and classifying the new concepts;
(3) Finding out objects properties in each class and establishing relationships between objects and properties;
(4) Determining the semantic relationships among classes, further marking the basic types of every relationship and their mutual relationship, such as the inverse relationship, passing relations, and reflexive relationship;
(5) Defining the concepts and properties in detail, such as whether the property value is restricted or has a default value;

ESDCM is conceptualizing the related information and knowledge of the complex electronic product development chain by analyzing the field and knowledge, according to the building process above between concept and relationship, the set related to development organization, products, development activities and development resources and their concepts, semantic description, properties and instances in these four fields. ESDCM contains a total of 322 concept classes (under four categories), nine base class relationships (extended to 35 class relations) and 532 class instances.

52.5 Ontology Analysis of ESDCM

The semantics in the semantic development chain model refers to the physical meaning of the model content, which is an interpretation of information for the model element. In development chain model, development chain model is composed of models from different product development stages, and heterogeneous nature of this model has greatly influenced the interactions among sub-models of development chain [7], main reason for the model isomerism is the inconsistency of the model description in grammar, structure and the semantics, of which semantic knowledge is the most important.

As ESDCM ontology is described by OWL DL language, OWL DL is based on the description logic (Description Logic, DL), description logic is a formalized tool on the bases of object-oriented knowledge representation, a decidable subset

of first-order predicate logic and can offer reasoning services. Looking from the demand of mark language of semantic Web knowledge representation, it is appropriate to regard the description logic as the formalized foundation [8]. In description logic, semantics is defined through mapping $(\Delta', ')$, Δ' means domain of discourse. Mapping function $'$map a concept into a subset of Δ' and a relationship into a subset of $\Delta' \times \Delta'$. For example, semantic of the concept A is defined as: $A' \in \Delta'$, semantics of relationship R is defined as: $R \in \Delta' \times \Delta'$. The analysis and description of the OWL class based on the DL and axiom are shown in Table 52.1.

52.6 Building Example of ESDCM

After building the semantic development chain description model of the complex electronic products, the product development chain description based on the model can be done. As mentioned above, this paper uses OWL language to describe the building process of the development chain model on the basis of ESDCM ontology, semantic development chain model building by this method is a strictly formalized model that can be processed by computer.

ESDCM ontology model of radar is build in this paper according to special functions and multidisciplinary nature of the development process of radar products, through the general terms offered by this model, the cognitive consistency in the development process can be achieved, semantic heterogeneity problem can be solved and the constraints in concept can be defined, formalized expressing the recessive knowledge exists in fact. This paper uses the Protégé-4.1, developed by Stanford University, as tool to build the radar ESDCM ontology. Edit and increase the development chain class, subclass, properties, instances, and the namespace ontology elements by human-computer interaction, design the information model based on the OWL in the conceptual level. Due to limited space, this section discusses the semantic description of ESDCM through examples on the basis the description frame. First, use the OWL clause <rdf:RDF … xmlns=" http://www.owl-ontologies.com/Products.owl#" … />, quote the product ontology to describe the domain space, then use the sentences <owl:Class>, <rdtfs:subClassOf> to describe the conceptional structure of the ESDCM class and properties; At last use the OWL sentences <owl:DatatypeProperty>, <owl:ObjectProperty>, <rdfs:range>, <rdfs:domain> to describe Data type Property (minimum value, maximum value, default value, data type and so on) and Object Property (Property, property units and so on).

References

1. Zha XFDH (2006) Knowledge-intensive collaborative design modeling and support: part I: review, distributed models and framework [J]. Comput Ind 57(1):39–55
2. Marcela Vegetti LL, Silvio Gonnet HL (2008) A semantic Web based architecture to support product data management systems [M]. Latin American Web Conference. 2008 IEEE. pp 91–100
3. Kumar PP (2008) Design process modeling towards an ontology of engineering design activities [D]. Clemson University
4. Zhan P (2007) An ontology-based approach for semantic level information exchange and integration in applications for product lifecycle management[D]. Washington State University
5. Tonci Grubic I-SF (2009) Integrating process, ontology for supply chain modeling [M]. 2009 International conference on interoperability for enterprise software and applications China. pp 228–35
6. Chi Y-L (2010) Rule-based ontological knowledge base for monitoring partners across supply networks [J]. Expert Syst Appl 37:1400–1407
7. Lin HK, Harding JA (2007) A manufacturing system engineering ontology model on the semantic web for inter-enterprise collaboration [J]. Comput Ind 58(2007):428–437
8. Sarder MB (2006) The development of a design ontology for products and process [D]. The University of Texas at Arlington

Chapter 53
Research on Cycling Policies in the UK White Paper

Sui Chao and Liwei Chen

Abstract This paper aims to evaluate an improvement–tripling the number of cycling in the UK by 2010, which may contribute to environment and urban road congestion. Then the related cycling policies will be reviewed and discussed in this essay. After that, the achievement in the 'Ten Year Plan' since 2000 and prospects will be given in the following text. Finally, some possible improving measures will be presented as a conclusion.

Keywords British transport policies · Cycling · White paper · Ten year plan

53.1 Introduction

In recent decades, the state of tense traffic in Britain is aggravated with the progress of economy and society. To provide a convenient and smooth transport service, British government set out many policy-based measures. From 1998 White Paper, a series of transport policies with a conception of integrated transport were implemented, while all the previous transport policies focused efforts on de-regulation and franchising. This white paper identified some key issues in transport system and proposed a set of improving objectives, which have to be

S. Chao (✉)
Department of Transportation Engineering,
Research Institute of Highway Ministry of Transport,
100088, Beijing, China
e-mail: z.chao@rioh.cn

L. Chen
School of Highway, Chang'an University,
710064, Xi'an, Shanxi, China
e-mail: Liviachen2009@hotmail.com

achieved by 2010, on road congestion, passenger and freight rail transport, passenger bus ride, walking and cycling trips as well as land use planning. This essay aims to evaluate one of these improvements—tripling the number of cycling by 2010, which takes small parts in these documents, but may bring considerable benefits on environment and urban road congestion. In doing so, it will begin by reviewing the process of policy advance from 1998 to 2010 and examining to what extend has this ideal realised, then go on to discuss how to encourage bicycle using in the future. Finally, a conclusion of some feasible strategies will be presented.

53.2 The Progress of Cycling Policy and Its Achievements

With the increasing requirement of new residents, many British cities have experienced a high speed urban sprawl in the past several decades. New roads and transport facilities have established to adapt the travel demand. However, someone claimed that it is the road-building itself which takes up most of the place of housing and green field, leading to urban expansion [1]. To alleviate this contradiction, people try to seek new solutions, of which increasing cycling trips might be a much greener and healthier one. The set of transport policy carried out by United Kingdom from 1998 to 2010, all made efforts on cycling growth and safety.

53.2.1 1998 White Paper

In this paper, the British government has realised that as a way to reduce traffic and environment pressure, the status of cycling is not so satisfactory, when compared with some other European countries. However, although the total cycling trip had been turned down, it is believed that if 'easier and safer' cycling could be provided, the prospect of cycling trip would be much brighter [2]. The new ideal of cycling is in accord with the National Cycling Strategy (NCS)—double cycling by 2002 and be quadrupled by 2012, on the basis of 1996 [2]. To achieve this, the government would like to support the initiatives of local authorities, which can be concluded in two aspects. One is policy and management method, such as setting out 'local transport plans', founding 'cycle review' and 'cycle audits', offering provisions about speed restraint and secure parking and applying planning influence to encourage cycling; The other one is based on infrastructure and facilities, including sharing road space for cyclists, giving them priority in junctions and keeping cyclist lanes in good condition [2]. As safety issue is considered the key factor affecting the use of cycle, it received particular attention and many researches and promotions were promised to be done. What's more, it also agreed on setting up National Cycle Network by connecting 'traffic-free paths' and 'traffic-calmed roads' to about 8,000 miles 'safe and attractive routes' by 2005 [2].

Fig. 53.1 Trends in walking and cycling stages: 1990/00 (in England). *Source* DfT National Travel Survey [8]
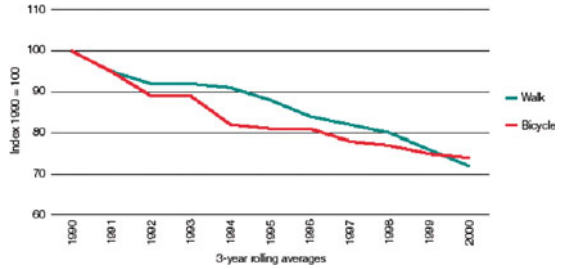
53.2.2 2000 The 10 Year Plan and Related Documents

Transport 2010: The 10 Year Plan carried out in 2000, continuing to be steadfast in the pursuit of 1998 White Paper goals and putting forward some related implementations. It pointed out definitely the target of trebling the cycling trips by 2010 from 2000 level [3]. This is assumed to be achieved by provision progress and integrating the National Cycle Network. In addition, another target with safety concern—cut casualties of children by 50% in road accidents by 2010 based on average 1994–1998, will be accomplished by generating 20 mph traffic-calmed zones and assessing numerous 'Home Zones' [3].

After 2000, several assessment reports on the 10 year plan were issued. In February 2001, the first analysis, Running to Stand Still, pointed out the cycling together with buses and walking is like the 'Cinderella of transport policy', which was not treat as important as promised, lacking investment and indications on interaction with vehicles [4]. The CfIT's initial assessment report on the Ten Year Plan published in May 2002, believing the target of cycling would be challenging; the Transport Select Committee Report, which set in the same month, claimed that the cycling had been under invested and failed to meet the 2002 interim Target [5, 6]. In July of the same year, Department for Transport presented a progress report on Ten Year Plan; it accepted the fact that the declining situation of cycling was not reversed yet (shown in Fig. 53.1), but also affirmed some important building blocks had been established. Moreover, this report emphasized on two new national initiatives—foundation of National Cycling Strategy Board and the £2 million Cycling Projects Fund. According to the second assessment of the Ten Years Plan by CfIT [7], cycling trip felt 17% nationally in 2001, on a 2000 base, but rose on London strategic road network.

53.2.3 2004 White Paper and Related Documents

In 2004 White Paper, the target for cycling is more general than 1998s—in future 20 or 30 years increasing cycling by attracting more short journeys especially those related to work and school. It concluded the achievements since 2000 as: manifold small-scale schemes on cyclist facilities and road safety but the facilities

Fig. 53.2 Average annual
trips made by mode:
1995/97–2008, Great
Britain. *Source* National
travel survey, department
for transport [9]
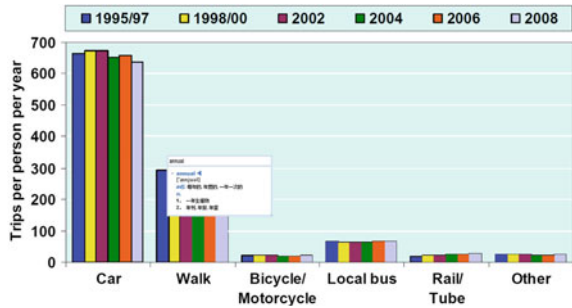
are imbalanced and promotions lag behind; a new action plan, Walking and
Cycling, was issued to push the growth of cycling. Besides, it proposed some
workable solutions, like delegating the management to local authorities, support-
ing voluntary sector, setting up model projects, improving road design and
assisting children to use bicycles as well as protecting their safety [10]. One thing
to be mentioned in this paper is they had chosen Worcester, Darlington, and
Peterborough as sustainable travel demonstration towns and they were expected to
reduce traffic level by 7–10% over 5 years [10].

A report sponsored by DfT [11] about changing personal attitude and behaviour
offering a number of 'soft' measures to advance the usage of cycle. The workplace
travel and school travel plans, personal travel planning, travel awareness
campaigns as well as public transport information and marketing all improved the
chance of adopting cycling as an alternative mean of travel. Since 2004, numerous
review reports towards this White Paper had emerged. Some of these studies
did excellent job, for example the Eddington Transport Study. Although they
mentioned little about cycling, some findings and recommends are valuable to
its development, such as the small-scale investment and independent planning
commission, which have already used on cycling [12].

However, the performance of cycling trip was disappointing. The following
two charts are trends of average annual trips and distance made by mode from
1995/1997 to 2008. It can be seen that the trips by bicycle or motorcycle varied
only slightly across the years at around 20 and the distance travelled by bicycle or
motorcycle grew a little from 78 to 80 miles per year. These results are far from
the target set by 2010 Ten Year Plan (Figs. 53.2, 53.3).

53.2.4 2010 Active Travel Strategy and Business
Plan 2011–2015

In February 2010, DfT [13] published the Active Travel Strategy, focusing on
walking and cycling development. It introduced the National Cycle Plan—the
Decade of Cycling, which aims to make cycling a preferable mode of travelling in

Fig. 53.3 Average annual distance travelled by mode: 1995/97–2008, Great Britain. *Source* National travel survey, department for transport [9]
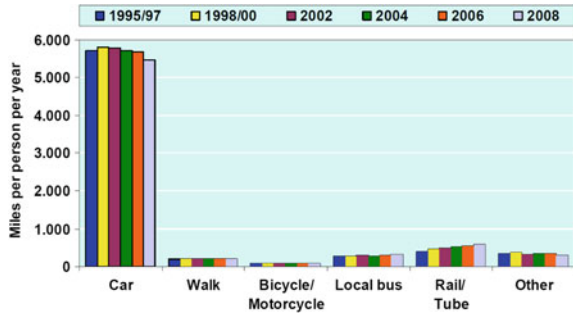
England. This plan anticipates a pack of improvements: 20 mph zones into more residential streets, new generation with well bike abilities, public sector employer cycling to work and safety cycle parking in public building and rail station. Additionally, this report also underlined the environmental and society effects of cycling, while admitted the failure in popularizing it.

In October, Spending Review 2010 assessed and predicted the expenditure on transportation system but most of the budget will be spend on railways while little on local authorities in future 5 years [14]. And in November, The Business Plan 2011–2015 assured to make structure reforms to encourage cycling travel and provide impact indicator of urban trips proportion under 5 miles taken by walking or cycling by April 2011 [15].

53.3 Discussion

During the last decades, it was witnessed a boom in car sales and a sustained growth in car mileage and rail travel. On the contrary, trip by cycling has been in long-term decline, only 2% of trips now [13]. Nevertheless, there is still a great potential of increasing cycling trip. Some towns and cities, enjoyed a high percentage of cycling for a long time, take Cambridge an instance, the mode share of cycling was estimated 18% [13]. Moreover, in accordance with a summary report of DfT [16], the sustainable travel demonstration projects turned out to have been successful. As showed in Table 53.1, people in these towns took more trips as well as travelling longer distance by bicycle. Then how to make cycling more welcome by British nationwide? There is no denying that, the government and people working on this issue have made many efforts. The remedy of reversing the cycling decline, however, leaves a lot to be desired.

Since the Ten Years Plan, quite a few cyclist-friendly facilities have been set up, not only the traffic-calm zones, but also infrastructures on reducing the disturbance of vehicles. Nonetheless, these facilities need to go with land use planning and be well maintained and assessed. Due to the high expenditures, the advisability and feasibility of infrastructure construction should be considered

Table 53.1 Evidence on cycling

	Household surveys ##		Manual/automatic counts	
	Trips per person (%)	Distance per person (%)	Change in counts	Timing of change
National trend	−9*	−17*		
Sustainable travel towns	+26 to +30	+28 to +32		
Darlington	+89 to +113	+76 to +112	+51 to +57% (town wide automatic counts) +84% to +116% (manual counts at town centre cordon)	Cycle flow stable from 2001 to 2005. Steady growth thereafter, but two main surges in Spring 2006 and Spring 2008
Peterborough	+10 to +17	+23 to +38	Broadly stable cycle level town wide (following previous decline of 20–30%). +11% in the central part of the town**	Decline in cycling between 1998 and 2002–2004; levels broadly stable from then onwards
Worcester	+11 to +23	−14 to +2	+16% (town wide automatic counts)	Cycle flow stable prior to STT work. Increase mainly between Summer 2004 and Summer 2005, subseqently sustained

Source DfT [16]

*This was the change between 2004 and 2006 (not 2008), as there are concerns that short trips were under-recorded in NTS data in 2007 and 2008. Reductions between 2004 and 2008 were greater for cycle trips (-34%) and cycle distance (-28%). The small sample sizes for cycle trips in the NTS make these data vulnerable to year-to-year fluctuation. Use of three year bands still suggests a fall in the number of cycle trips nationally (-6% between 2002–2004 and 2004–2006), whilst it is possible that distance cycled nationally was roughly constant over this period. From the period 2002–2004 to 2006–2008, both cycle trip numbers and distances decline, though this may be due to the under-recording in 2007 and 2008

** Pre-Sustainable Travel Town trend is from two different sets of manual counts. Growth in central part of town is from manual counts. Stable town-wide cycle levels are from automatic counter data

carefully. And some further measures can be taken on ensuring the facilities used fully.

Government also applied various active policies and promotions, some of which were proved quite effective, such as smart choice and sustainable travel towns. What can be done in the future might be bring commercial competition into cycling travel. This has been implemented in rail and bus industry for many years, though was considered as a failure. Quite different from rail or bus, cycling is not as a integrate system, but more individual and flexible. One possible business is bicycle-rent service. For the low ownership of bicycles, this service has a broad developing space. The leased place can be a chain, locating in populous and traffic busy areas; therefore, people can rent and return bike conveniently and it offers an alternative of cars and buses, when the street is congested. In addition, people do not have to worry the bicycle being stolen or destroyed, if they returned it to the owner. Another commercial uses might be bicycle parking as well as remunerative bicycle keeping service, cycling delivery and cycling journey, some of which have been employed in the UK.

53.4 Conclusion

To sum up, this essay reviewed the progress of cycling since 1998 white paper and assessed how much of the target—trebling the number of cycling trip by 2010—has been realised. As a supporting role in transport system, cycling did not arouse enough attention at the beginning, but improved gradually after 2004 White Paper. Unfortunately, the cycling trip even did not rise, far lower than the initial target of increasing threefold. Thus this essay attempted to explore some possible improving measures, which can be concluded as follows: most of the cycling facilities are helpful, but it should follow careful plan, be maintained in time and be assessed regularly; some of the policies and promotions work well, especially the smart choice and sustainable travel projects, which have to be applied nationwide; explore more commercial use of cycling, such as bicycle-rent, adding an active force into this traditional mode of travel. The possibilities to extend this research are almost endless due to the lack of current investigation and the partial understanding of this issue. Much deeper research is needed to understand the problems exiting in raising cycling trips. More feasible solutions and advanced policies will be provided. For the hydraulic variable pitch object, the paper has analyzed the reason of the fault by adopting fault diagnosis method of bond graph model. In this paper, it has established bond graph model of the pitch angle. As the example of the piston rod response inadequate fault, the fault tree of system is established by using causal theory based on bond graph. Through the qualitative value assigned for parameters in the fault tree, the fault source was detected. Comparing with quantitative fault diagnosis, qualitative fault diagnosis based on bond graph has less calculation and doesn't need accurate mathematical model. It also has the advantage of good completeness and strong flexibility.

References

1. BBC News (1998) UK battlelines drawn in fight against urban sprawl [Online] Available at: http://news.bbc.co.uk/1/hi/uk/48182.stm. Accessed 8 Dec 2010
2. Department for Transport (DfT), (1998) A new deal for transport: better for everyone (1998 White Paper). HMSO, London
3. Department of the Environment, Transport, the Regions (DETR) (2000) Transport 2010: the 10 year plan. HMSO, London
4. Council for the Protection of Rural England (CPRE) (2001) Running to stand still? An analysis of the ten years plan for transport. HMSO, London
5. Commission for Integrate Transport (2002) CfIT's initial assessment report on the ten year plan. HMSO, London
6. Transport, Local Government and the Regions Select Committee (2002) Transport, Local Government and the Regions—Eighth Report [Online] Available at: http://www.publications.parliament.uk/pa/cm200102/cmselect/cmtlgr/558/55802.htm. Accessed 8 Dec 2010
7. Commission for Integrate Transport (2003) 10 Year Plan-Second Assessment Report. HMSO, London
8. Department for Transport (DfT) (2002) Ten year plan progress report. HMSO, London
9. Department for Transport (DfT) (2009) National travel survey. Section 2: personal travel by mode. HMSO, London
10. Department for Transport (DfT) (2004) The future of transportation network for 2030 (2004 White Paper). HMSO, London
11. Department for Transport (DfT) (2004). Smarter choices—changing the way we travel. [Online] Available at http://www.dft.gov.uk/pgr/sustainable/smarterchoices/ctwwt/. Accessed 10 Dec 2010
12. Cherrett DT (2010) UK Transport Policy 2004 onwards: The 2004 Transport White Paper… and beyond. Transportation planning: Policies and methods. School of Civil Engineering and Environment. University of Southampton
13. Department for Transport (DfT) (2010) Active travel strategy. HMSO, London
14. HM Treasury (2010) Spending review 2010. HMSO, London
15. Department for Transport (DfT) (2010) Business plan 2011–2015. HMSO, London
16. Department for Transport (DfT) (2010) The effects of smarter choice programmes in the sustainable travel towns: summary report. HMSO, London

Chapter 54
Robot Simultaneous Localization and Mapping Based on Non-Linear Interacting Multiple Model Concerning Statistical Property Mutation

Yingmin Yi and Liu Ding

Abstract To investigate robot Simultaneous Localization and Mapping (SLAM) in the unknown environment, the non-linear Interacting Multiple Model (IMM) SLAM algorithm is applied to solve the problem concerning the statistical property mutation of a system. The key point of this algorithm is to use non-linear Gaussian model to approximate non-linear and non-Gaussian model so that robot Simultaneous Localization and Mapping can be achieved. Each model employs the Extended Kalman Filter (EKF) algorithm to linearize the non-linear system and uses the non-linear Interacting Multiple Model algorithm in each step to get fusion estimated value. The Monte Carlo simulation results show that the proposed algorithm has better estimate precision.

Keywords Automatic control system · Nonlinear · Interacting multiple model · Statistical property mutation · Simultaneous localization and mapping

54.1 Introduction

Robot Simultaneous Localization and Mapping (SLAM) in the unknown environment is a hot issue in the field of robot research. In structured environment, system noise is Gaussian so the traditional EKF-SLAM algorithm can be successfully adopted [1–4]. When the probability distribution is non-Gaussian, the

Y. Yi (✉) · L. Ding
Faculty of Automation and Information Engineering, Xi'an University of Technology, Xi'an, China
e-mail: yiym@xaut.edu.cn

Fast-SLAM algorithm can be successfully applied as suggested in [3]. But in the unknown environment, the statistical properties of a system mutate with the change of the environment. The linearization of the non-linear model and the filter method of Gaussian assumption may lead to significant errors in estimating the system state, and they are likely to diverge. Therefore, the EKF-SLAM algorithm can not be used here. It is suggested in [3] that by using the Fast-SLAM algorithm, there exist significant errors between the sample obtained from importance functions and that from real posterior distribution, especially when the likelihood function is the tail or the peak value of the system state transfer probability density function. Besides, many samples become invalid and then lead to the system divergence due to the small normalized weight. And how to converge the filtering algorithm when parameters mutate is a new problem in Simultaneous Localization and Mapping (SLAM).

To solve the above-mentioned problems, this paper introduces Interacting Multiple Model into SLAM research and applies the non-linear IMM-SLAM algorithm. The EFK algorithm is used to linearize the non-linear model and multiple linear Gaussian models are built for interaction. In this way, the latest observation value can be drawn on, which makes the estimate of the system closer to the posterior probability distribution. Besides, the problem about the non-linear and non-Gaussian properties of a system can also be solved so that the suggested algorithm can be used for robot SLAM in the changeable natural environment.

54.2 System Description

The described SLAM system state is formed by the robot's pose and the observed coordinates of the landmarks in the static environments. The joint state vector at the k moment is shown as:

$$\mathbf{x}_k = [x_{vk}, y_{vk}, \theta_{rk}, x_1, y_1, \ldots, x_N, y_N]^{\mathrm{T}} = \begin{bmatrix} \mathrm{x}_{vk} \\ \mathrm{n} \end{bmatrix} \tag{54.1}$$

In (54.1), $x_{vk}, y_{vk}, \varphi_{vk}$ stand for the position and heading of the robot in two-dimensional space respectively. The map is static. Notice that the map parameters $\mathrm{n} = [x_1, y_1, \ldots, x_N, y_N]^{\mathrm{T}}$ do not have a time subscript as they are modeled as stationary. The robot's movement model is rolling motion constraints [1].

$$\mathbf{x}_k = f_v(\mathbf{x}_{vk-1}, \mathbf{u}_k) = \begin{bmatrix} x_{vk-1} + v_k \Delta T \cos(\theta_{rk-1} + G_k) \\ y_{vk-1} + v_k \Delta T \sin(\theta_{rk-1} + G_k) \\ \theta_{rk-1} + \frac{v_k \Delta T}{B} \sin(G_k) \end{bmatrix} \tag{54.2}$$

In (54.2), the time interval between $k - 1$ and k is ΔT, the velocity v_k and the steering angle G_k are constants and they consist of the controlled vector $\mathbf{u}_k = [v_k, G_k]^{\mathrm{T}}$, The wheelbase between the front and rear axles is B.

The observation model is given by

$$z_{ik} = h_i(\mathbf{x}_k) = \begin{bmatrix} \sqrt{(x_i - x_{vk})^2 + (y_i - y_{vk})^2} \\ \arctan \frac{y_i - y_{vk}}{x_i - x_{vk}} - \theta_{rk} \end{bmatrix} \tag{54.3}$$

54.3 The Non-Linear IMM Algorithm for SLAM

The traditional Interacting Multiple Model algorithm applies Kalman Filter to the filtering of each model. All of these models are linear. The non-linear Interacting Multiple Model algorithm for SLAM put forward in this paper employs the Extended Kalman Filter algorithm to first filter each model and then integrate the estimated values of the filtering for each model, and finally to get an overall estimated value.

54.3.1 The Interacting Multiple Model Algorithm

The Interacting Multiple Model algorithm is an effective hybrid estimate formula. Each cycle of IMM algorithm includes four steps: model condition reinitialization; filtering calculation; model probability update and estimate fusion. The system discussed in this paper is composed of the process model in (54.2) and the observation model in (54.3). For IMM algorithm, see [5].

54.3.2 The Non-Linear Interacting Multiple Model Algorithm for SLAM

The non-linear Interacting Multiple Model algorithm [6] for SLAM includes five steps: model condition reinitialization; model condition filtering and data association; model probability update; estimate fusion; state augmentation and map building. For the algorithm, see Fig. 54.1.

Step 1 Model condition reinitialization.

(1) Hybrid probability

$$\mu_{k-1|k-1}^{i,j} \overset{\text{def}}{=} p(m_{k-1}^{(i)}|m_k^{(j)}, Z^{k-1}) = \frac{1}{\bar{c}_j}\pi_{ij}\mu_{k-1}^{(i)} \tag{54.4}$$

In (54.4), $\bar{c}_j = \sum_{i=1}^{r} \pi_{ij}\mu_{k-1}^{(i)}$.
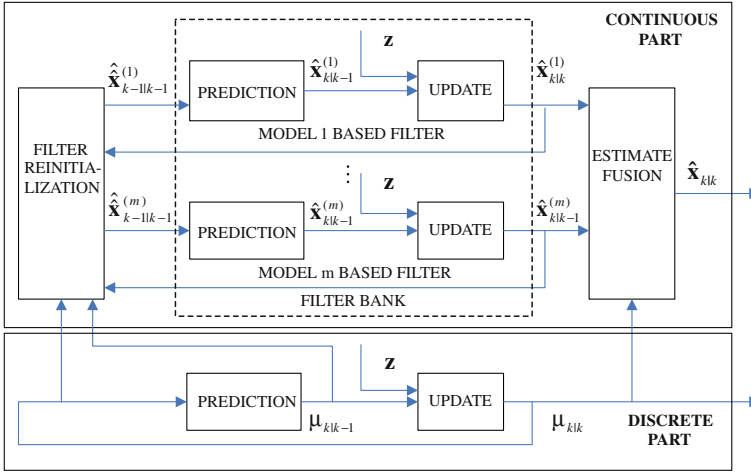
Fig. 54.1 Non-linear interacting multiple model algorithm scheme

(2) Hybrid estimate

$$\hat{\mathbf{x}}_{k-1|k-1}^{(j)} \overset{def}{=} E(\mathbf{x}_{k-1}|m_k^{(j)}, Z^{k-1}) = \sum_{i=1}^{r} \hat{\mathbf{x}}_{k-1|k-1}^{(i)} \mu_{k-1|k-1}^{(i,j)}$$

$$\hat{\mathbf{P}}_{k-1|k-1}^{(j)} = \sum_{i=1}^{r} \left[\mathbf{P}_{k-1|k-1}^{(i)} + (\hat{\mathbf{x}}_{k-1|k-1}^{(i)} - \hat{\mathbf{x}}_{k-1|k-1}^{(j)})(\hat{\mathbf{x}}_{k-1|k-1}^{(i)} - \hat{\mathbf{x}}_{k-1|k-1}^{(j)})^T \right] \mu_{k-1|k-1}^{(i,j)}$$

$$(54.5)$$

Step 2 Model condition filtering.

(1) State predication

$$\hat{\mathbf{x}}_{k|k-1}^{(i)} = \mathbf{F}_{k-1}^{(i)} \hat{\mathbf{x}}_{k-1|k-1}^{(i)} + \mathbf{\Gamma}_{k-1}^{(i)} \bar{\omega}_{k-1}^{(i)}$$

$$\mathbf{P}_{k|k-1}^{(i)} = \mathbf{F}_{k-1}^{(i)} \hat{\mathbf{P}}_{k-1|k-1}^{(i)} (\mathbf{F}_{k-1}^{(i)})^T + \mathbf{\Gamma}_{k-1}^{(i)} \mathbf{Q}_{k-1}^{(i)} (\mathbf{\Gamma}_{k-1}^{(i)})^T$$

$$(54.6)$$

(2) Data association

Data association applies the Nearest-Neighbor approach put forward by Singer [7], and divides observation $\mathbf{z}$ into associated observation $\mathbf{z}_k$ and the observation of new landmark $\mathbf{z}_{nk}$.

$$z^{(i)} = \begin{bmatrix} z_k^{(i)} & z_{nk}^{(i)} \end{bmatrix}^{\mathrm{T}} \tag{54.7}$$

(3) Residuals and covariance matrix predication

$$\begin{aligned}
\tilde{z}_k^{(i)} &= z_k - H_k^{(i)} \hat{x}_{k|k-1}^{(i)} - \bar{v}_k^{(i)} \\
S_k^{(i)} &= H_k^{(i)} P_{k|k-1}^{(i)} (H_k^{(i)})^{\mathcal{T}} + R_k^{(i)}
\end{aligned} \tag{54.8}$$

Likelihood function

$$\Lambda_k^{(i)} = p(z_k|m_k^{(i)}, Z^{k-1}) \approx p\left[z_k|m_k^{(i)}, \hat{x}_{k-1|k-1}^{(i)}, S_k^{(i)}(P_{k-1|k-1}^{(i)})\right] \tag{54.9}$$

Under the assumption of Gaussian conditions

$$\Lambda_k^{(i)} = p(z_k|m_k^{(i)}, Z^{k-1}) \overset{\text{Gauss}}{=} \left|2\pi S_k^{(i)}\right|^{-1/2} \exp\left\{-\frac{1}{2}(\tilde{z}_k^{(i)})^{\mathcal{T}}(S_k^{(i)})^{-1}\tilde{z}_k^{(i)}\right\} \tag{54.10}$$

Filter update

$$\begin{aligned}
\mathbf{K}_k^{(i)} &= \mathbf{P}_{k|k-1}^{(i)}(\mathbf{H}_k^{(i)})^{\mathcal{T}}(\mathbf{S}_k^{(i)})^{-1} \\
\hat{\mathbf{x}}_{k|k}^{(i)} &= \hat{\mathbf{x}}_{k|k-1}^{(i)} + \mathbf{K}_k^{(i)}\tilde{\mathbf{z}}_k^{(i)} \\
\mathbf{P}_{k|k}^{(i)} &= \mathbf{P}_{k|k-1}^{(i)} - \mathbf{K}_k^{(i)}\mathbf{S}_k^{(i)}(\mathbf{K}_k^{(i)})^{\mathcal{T}}
\end{aligned} \tag{54.11}$$

Step 3 Model probability update.

$$\mu_k^{(i)} = p(m_k^{(i)}|Z^k) = \frac{1}{c}\Lambda_k^{(i)}\bar{c}_i \tag{54.12}$$

In (54.12), $\bar{c}_i = \sum_{j=1}^{r} \pi_{ji}\mu_{k-1}^{(j)}$.

Step 4 Estimate fusion.

$$\begin{aligned}
\hat{x}_{k|k} &= \sum_{i=1}^{r} \hat{x}_{k|k}^{(i)}\mu_k^{(i)} \\
P_{k|k} &= \sum_{i=1}^{r} \left[P_{k|k}^{(i)} + (\hat{x}_{k|k} - x_{k|k}^{(i)})(\hat{x}_{k|k} - x_{k|k}^{(i)})^{\mathcal{T}}\right]\mu_k^{(i)}
\end{aligned} \tag{54.13}$$

Step 5 Map building.

$$\begin{aligned}
\mathbf{x}_k^{\text{new},i} &= h^{-1}(\mathbf{z}_{nk}^{(i)}, \mathbf{x}_{vk}^{(i)}) \\
\mathbf{x}_k^{(i)} &= \begin{bmatrix} \mathbf{x}_k^{(i)} & \mathbf{x}_k^{\text{new},i} \end{bmatrix}^{\mathrm{T}}
\end{aligned} \tag{54.14}$$
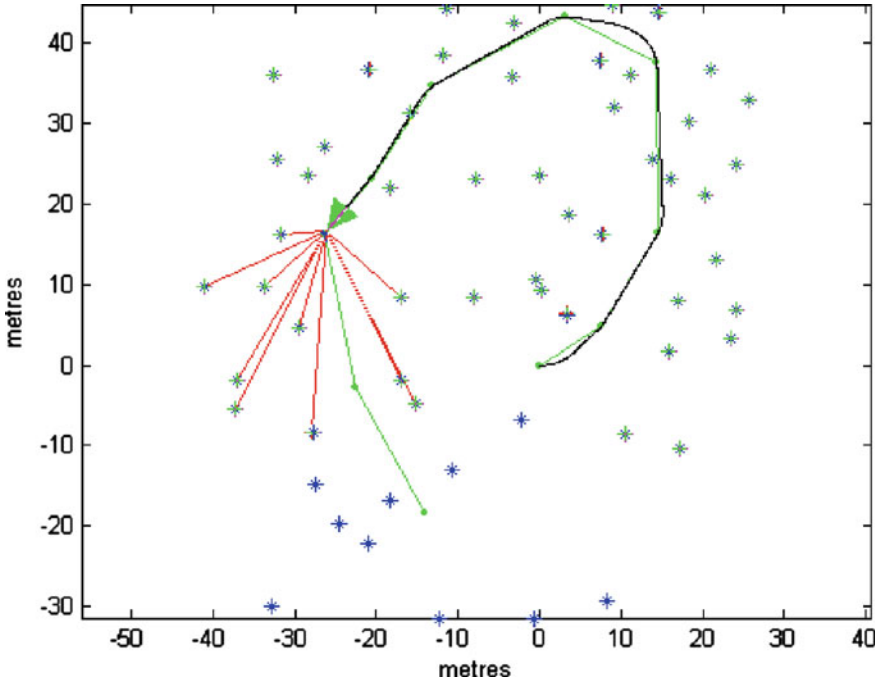
Fig. 54.2 The simulation of the robot SLAM

The suggested algorithm uses EKF algorithm to linearize the non-linear model and adopts Interacting Multiple Model (IMM) to integrate the estimated value. This approach has solved the problem of non-Gaussian statistical properties caused by the parameter mutation.

54.4 Simulation and Analysis

The simulation environment is composed of randomly-generated landmarks. The moving direction of the robot is controlled by 10 direction landmarks. The experimental simulation uses the model in Eq. 54.2, with the process noise $Q_0 = \text{diag}(\sigma_V, \sigma_\gamma) = \text{diag}(0.015, 0.15 * 180/\text{pi})$, the observation noise $R_0 = \text{diag}(\sigma_r, \sigma_\theta) = \text{diag}(0.005, 0.05 * 180/\text{pi})$ and the velocity of the robot $V = 3\,\text{m/s}$, $T = 0.025\,\text{s}$. Data association adopts the Nearest-Neighbor approach, with the maximal associated distance of 4 m, and the minimal of 25 m regarding the new landmarks. This paper uses the robot pose root mean square (RMS) errors [8] as the standard to judge the advantages and disadvantages of algorithms. The simulation of the robot SLAM is shown in Fig. 54.2.

Fig. 54.3 The robot pose
RMS as process noise
mutation occurs
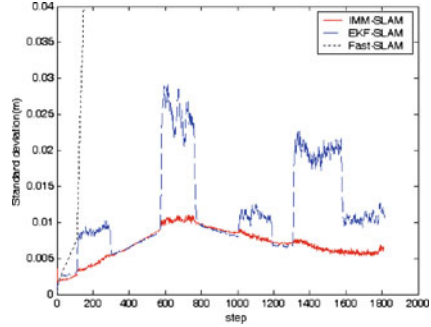
Table 54.1 The comparison of RMS errors when process noise mutation occurs

Items/algorithms	EKF–SLAM algorithm	Non-linear IMM–SLAM algorithm	RMS ratio = non-linear IMM–SLAM/ EKF–SLAM (%)
RMS peak value	0.028	0.011	39.3
RMS mean value	0.014	0.0075	53.6

(1) Simulation of the process noise mutation

There are three model sets [9], and the process noises are $Q_0, 100Q_0, 500Q_0$. The paths of the robot are divided into nine sections and are numbered from 1 to 10 according to the time. The changes of process noises are as follows: in the range of 1–2, 2–3, 4–5, 6–7, and 8–9 the process noise is Q_0; in the range of 3–4 and 7–8, the process noise is $100Q_0$; in the range of 5–6 and 9–10 the process noise is $500Q_0$. When process noise mutation occurs, the robot pose RMS is shown in Fig. 54.3.

Analysis: 200 Monte Carlo simulations were conducted respectively in the experiment. From Fig. 54.3, it can be seen that with the increase of process noise covariance, the robot pose RMS also increases. But in the range of 2–3, 4–5, 6–7, and 8–9, when the statistical property of process noises mutates, RMS, according to the EKF-SLAM algorithm, increases dramatically. When suggested algorithm is used, the curve of robot pose RMS is smoother than that of the EKF-SLAM algorithm, and does not diverge as a result of the process noise mutation. When process noise mutates, the comparison of RMS errors shows that the suggested algorithm is robust than EKF-SLAM algorithm and Fast-SLAM algorithm. See Table 54.1:

(2) Simulation of the observation noise mutation

There are three model sets [9], and the observation noises are $R_0, 100R_0, 400R_0$. The changes of observation noises are as follows: in the range of 1–2, 3–4, 5–6, 7–8 and 9–10, the observation noise is R_0; in the range of 2–3, 6–7, and 8–9,

Fig. 54.4 The robot pose
RMS as observation noise
mutation occurs
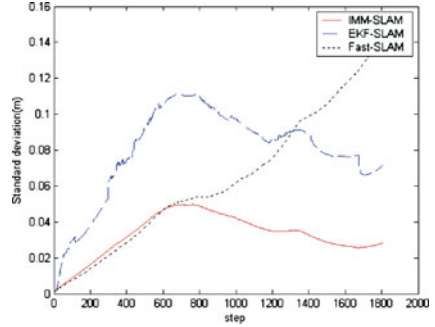
Table 54.2 The comparison of RMS errors when observation noise mutation occurs

Items/ algorithms	EKF–SLAM algorithm	Non-linear IMM– SLAM algorithm	RMS ratio = non-linear IMM–SLAM/ EKF–SLAM (%)
RMS peak value	0.11	0.05	45.5
RMS mean value	0.078	0.033	42.3

the observation noise is $100R_0$; in the range of 4–5, the observation noise is $400R_0$. When observation noise mutation occurs, the robot pose RMS is shown in Fig. 54.4.

Analysis: 200 Monte Carlo simulations were conducted respectively in the experiment. When statistical properties of the observation noise mutate, the robot pose RMS, according to the EKF–SLAM algorithm, increases dramatically and its curve is not smooth. The Fast-SLAM algorithm diverges due to the statistical property mutation. But when the suggested algorithm is used, the curve of robot pose RMS is smooth and below the curve of the EKF–SLAM algorithm. When observation noise mutates, the comparison of RMS errors shows that the suggested algorithm is robust than EKF–SLAM algorithm and Fast-SLAM algorithm. See Table 54.2:

(3) Simulation of process noise mutation and observation noise mutation at different periods of time

In the unknown environment, the statistical properties of both process noise and observation noise are likely to mutate. According to the suggested algorithm, there are five model sets [9]. Model 1: the process noise is Q_0 and the observation noise is R_0; model 2: the process noise is Q_0 and the observation noise is $100R_0$; model 3: the process noise is $500Q_0$ and the observation noise is R_0; model 4: the process noise is Q_0 and the observation noise is $400R_0$; model 5: the process noise is $100Q_0$ and the observation noise is R_0. Then the simulation of robot SLAM can be conducted according to those five models.

Fig. 54.5 The robot RMS as process noise and observation noise mutate at the same time
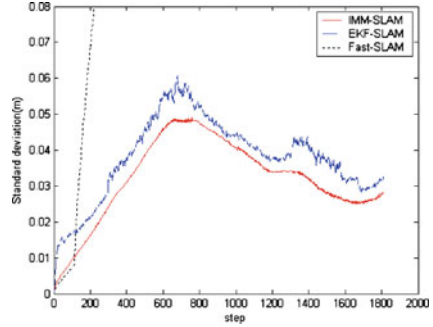
Table 54.3 The comparison of RMS errors when both process noise mutation and observation noise mutation occur

Items/ algorithms	EKF–SLAM algorithm	Non-linear IMM– SLAM algorithm	RMS ratio = non-linear IMM–SLAM/ EKF–SLAM (%)
RMS peak value	0.061	0.048	78.7
RMS mean value	0.038	0.031	81.6

In the process of simulation, the changes of the assumption of process noise and observation noise are as follows:

$$Q(k_w) = \begin{cases} Q_0 : k_w = \{(1-3), (4-5), (6-7), (8-9)\} \\ 100Q_0 : k_w = \{(3-4), (7-8)\} \\ 500Q_0 : k_w = \{(5-6), (9-10)\} \end{cases}$$

$$R(k_w) = \begin{cases} R_0 : k_w = \{(1-2), (3-4), (5-6), (7-8), (9-10)\} \\ 100R_0 : k_w = \{(2-3), (6-7), (8-9)\} \\ 400R_0 : k_w = \{(4-5)\} \end{cases}$$

Here k_w is the subscript of the path the robot took. When process noise and observation noise mutate at the same time, the robot RMS is shown in Fig. 54.5.

Analysis: 200 Monte Carlo simulations were conducted respectively in the experiment. As is shown in Fig. 54.5, when process noise mutation and observation noise mutation occur at the same time, the Fast-SLAM algorithm diverges due to the statistical property mutation. When non-linear IMM-SLAM algorithm is used, the curve of robot pose RMS is smoother than that of the EKF-SLAM algorithm, and is completely below the curve of the EKF-SLAM algorithm. When the process noise and observation noise mutate at the same time, the comparison of RMS errors shows that the suggested algorithm is robust than EKF-SLAM algorithm and Fast-SLAM algorithm. See Table 54.3:

The simulation results shows that the filtering effect of a single model Kalman filter is not good and even cause the system to diverge for fixed model. The system

state estimation by IMM filter is more accurate than a single model Kalman filter. The best simulation results will occur only if the system model parameters are consistent with the real model parameters.

54.5 Conclusion

The non-linear IMM-SLAM algorithm was put forward in this paper to solve the problem of statistical property mutation of the system. This algorithm linearizes the SLAM non-linear model and uses IMM algorithm of multiple EKF-SLAM model to make predication, observation, data association, update, estimate fusion and map building concerning robot pose. The suggested algorithm can still be used for precise localization and mapping when system parameters mutate and thus expands the scope of robot simultaneous localization and mapping. The Monte Carlo simulations were conducted when process noise mutation and observation mutation occur respectively or they occur at the same time. The analyses of the simulation results show that the suggested algorithm is better than EKF-SLAM algorithm and Fast-SLAM algorithm.

References

1. Smith R, Self M, Cheeseman P (1987) A stochastic map for uncertain spatial relationships. In: International symposium of robotics research pp 467–474
2. Csorba M (1997) Simultaneous localisation and map building. Ph.D. Thesis, University of Oxford, Robotics Research Group
3. Montemerlo M (2003) FastSLAM: a factored solution to the simultaneous localization and mapping simultaneous localization and mapping problem with unknown data association. Carnegie Mellon University, Pittsburgh
4. Bailey T, Durrant-Whyte H (2006) Simultaneous localization and mapping simultaneous localization and mapping (SLAM): part II. IEEE Robotics Autom Mag 13(3):108–117
5. Rong Li X, Jilkov VP (2003) A survey of maneuvering target tracking—part V, multiple-model methods. In: Proceeding of SPIE conference on signal and data processing of small targets, San Diego, CA
6. Bailey T, Nieto J, Guivant J, Stevens M, Nebot E (2006) Consistency of the EKF-SLAM algorithm. In: IEEE/RSJ international conference on intelligent robots and systems
7. Liu J, Li R, Zhang Z, Liu Y (2007) Model set design for interacting multiple model interacting multiple model algorithm. Control Decis 22(3):326–332
8. Lv N, Feng Z (2007) Nonlinear interacting particle filter algorithm. Control Decis 22(4): 378–383
9. Singer RA, Sea RG (1971) A new filter for optimal tracking in dense multi target environment. In: Proceedings of the ninth Allerton conference circuit and system theory. University of Illinois, Urbana-Champaign, U S A pp 201–211

Chapter 55
Scalable Stereo Video Coding Scheme Based on H.264/MPEG-4 MVC

Kexin Zhang, Zongze Wu, Shengli Xie and Rong Wu

Abstract Traditional stereo video coding scheme can not adapt to different net conditions and terminals for the single layer coding method, in this paper, a scalable stereo video coding scheme based on H.264/MPEG-4 MVC was proposed. The proposed scheme which takes full consideration of binocular suppression theory, encodes stereo video in multi-layers with good stereoscopic perception, so the stereo video application can adapt to various networks and terminals. Experimental results show that the proposed scheme achieves better scalability and maintains stereoscopic perception as good as possible.

Keywords Stereo video · H.264/MPEG-4 MVC · Binocular suppression · Scalable coding

55.1 Introduction

Stereo video applications have achieved great development in recent years, this is mainly due to the push from two factors. The first one is the development of technology, with the development of display technology, signal processing, transmission technology, and circuit design, three-dimensional video is being introduced to home through various channels, including Blu-Ray, disc, cable and satellite transmission, terrestrial broadcast, and streaming and download through the Internet. The other one is the notable increase in the production of 3D content,

K. Zhang (✉) · Z. Wu · S. Xie · R. Wu
School of Electronic and Information Engineering,
South China University of Technology, 510640 Guangzhou, China
e-mail: zhang.kexin@mail.scut.edu.cn

more and more films will have 3D feature releases is a good proof. At the present stage stereo video is consist of two or more views, which means the video contains more data than traditional single view video, so efficient video compression scheme becomes more and more important. Compare to independent coding of each view, multiview video coding (MVC) [1, 2] exploits not only the redundancies that exist temporally between the frames within a given view, but also the similarities between frames of neighboring views, so a reduction in bit rate can be achieved without sacrificing the reconstructed video quality, which means MVC gets a much higher compression ratio than encode each view independently. In consideration of the high compression ratio, MVC has become the first choice in stereo video coding. In 1996, the international video coding standard H.262/MPEG-2 Video was amended to support the coding of multiview video [3], however the multiview extension of H.262/MPEG-2 Video was never deployed in actual products due to the limitation of technology at that time. And later international video coding standard H.264/MPEG-4 AVC [4] also introduced its MVC design [5, 6] as an extension. As the most recent stereo video coding standard, H.264/MVC adopts inter-view prediction and keeps compatible with the key technique in H.264/AVC, by doing this, H.264/MVC achieved good compression performance, which means up to 50% savings in bit rate.

In addition to MVC, more and more researchers began to study asymmetric coding scheme which is based on the binocular suppression theory [7]. Binocular suppression theory derives from Lew Stelmach and Wa James Ta's research in literature [7], they studied the response of human visual system to mixed-resolution stereo video. In the study, one eye view was spatially or temporally low-pass filtered, the other view remained unchanged, then the tests on overall quality, sharpness, and sensation of depth were given, compared to the case where both views remained unchanged, it was found that spatial filtering produced better results: the overall sensation of depth was unaffected by low-pass filtering, while ratings of quality and of sharpness were strongly weighted towards the eye with the greater spatial resolution. By comparison, temporal filtering produced unacceptable results: field averaging and drop-and-repeat frame conditions yielded images with poor quality and sharpness, even though perceived depth was relatively unaffected. That is the binocular suppression theory, based on the theory, Heribert Brust and Alijoscha Smolic pointed out that in a stereo sequence, where the quality of left eye and right eye view differ, the perceived binocular quality was rated close to the better one [8]. Taking full consideration of the theory, asymmetric coding scheme encode one view of the stereoscopic pair with lower quality to obtain high compression efficiency, while the perceptual quality degradation for the stereoscopic display can be negligible by human eyes.

Even so, the schemes above still didn't change the status that stereo video contains too many data and has high requirements for network and terminals. So we propose a scalable stereo video coding scheme, by which stereo video application can adapt to different networks and terminals. The proposed scheme is based on H.264/MVC, takes full consideration of the binocular suppression theory, and generates scalable stereoscopic bit stream, meanwhile maintains stereoscopic

perception as good as possible. The generated bit stream can be divided into a base layer and multiple enhancement layers, so the decoder can select part of the bit stream to decode as needed, that is to say when the terminal capacity is poor or the available bandwidth is not enough, select less bit stream to transfer and display, otherwise, select more bit stream to transfer and display. By scalable coding, the generated stereo video bit stream can be adjusted to different terminals and networks.

The paper is organized as follows. Section 55.1 gives the encoding structure. Section 55.2 explains the hierarchical coding strategies adopted by this scheme. Section 55.3 describes the experimental results in detail. Concluding remarks are given in Sect. 55.4.

55.2 Encoding Structure

Based on the binocular suppression theory, more and more scholars began to study stereo video asymmetric coding in order to improve coding efficiency. In literature [9], a spatially down sampling process is directly performed for right view before inter-view prediction. In Ref. [10], regionally adaptive filtering had been proposed to obtain low-resolution right view. In Ref. [11], full-resolution left images and down-sampled right images are encoded to improve the coding efficiency with low computational complexity. However, none of these methods considered encoding stereoscopic video hierarchically based on the theory to get the adaptation to network and terminal. Based on the research of Stelmach and Wa James, this paper presents a scalable stereo video coding scheme. The scheme encodes the left view of a stereoscopic video in single-layer, and the right view in multi-layers, to provide scalable features, meanwhile maintains stereoscopic perception as good as possible. In consideration of Stelmach and Wa James Ta's research, we just hierarchically encode the right view in quality domain, and not do this in temporal domain.

This scheme is based on H.264/MVC stereo high profile, but the hierarchical idea also applies to H.264/MVC multiview high profile. The scheme keeps the bit stream format and encoding methods of left view unchanged, encodes the right view in quality domain hierarchically, and generates scalable video bit stream to support the various network and terminals. The encoding structure is shown in Fig. 55.1.

As the Figure shown, the data of left view is decomposed in temporal domain and then encoded by traditional single-layer coding method, while the right view data is transformed, gradually quantized, then the generated DCT (Discrete Cosine Transform) coefficients are divided into several parts, at last the generated bit stream is grouped into luma bit stream and chroma bit stream in order to achieve more truncation points in the bit stream. The generated bit stream by this scheme can be arbitrarily truncated, so we can select appropriate bit stream to transmit and decode according to the specific application.
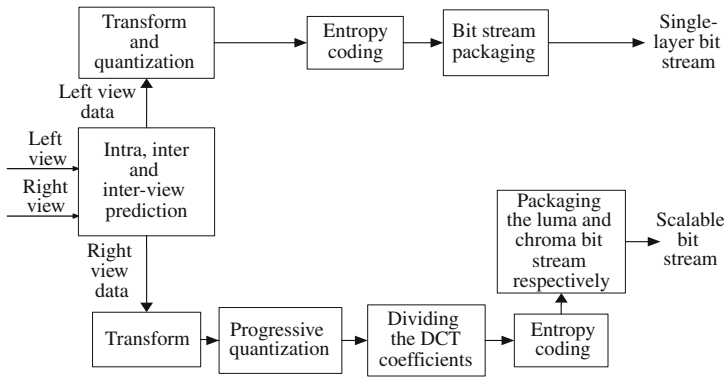
Fig. 55.1 Encoding structure

55.3 Strategies for Scalable Codingscalable coding

The proposed scheme adopts four strategies for scalable coding, including progressive quantization, writing DCT coefficients into several slices, abandoning the chroma components, discarding the right view. All the four strategies will be explained in detail in the following subsections.

55.3.1 Progressive Quantization

The difference between progressive quantization and traditional quantization is that we would have just one quantization coefficient with the traditional quantization, while as to the progressive quantization, we firstly quantize the transform coefficient with a large quantization step to get a coarse coefficient, and then quantize the residuals formed by the last quantification with a smaller quantization step. By repeating the above steps we finally get more than one coefficient. In the process of progressive quantization, the transform coefficient before quantization is gradually approximated, the process is given by Formula 55.1:

$$D = \pm(a_1 Q_1 + a_2 Q_2 + \cdots + a_n Q_n) \tag{55.1}$$

In the formula, D is the DCT coefficient, Q_n is the nth quantizer's quantization step and a_n is the generated quantization coefficient. By the way of progressive quantization, we can encode the DCT coefficients hierarchically. For instance, when we just get Q_1 and a_1, then the reconstructed value D_r from inverse quantization is a rough value of the DCT coefficient D, but when get more quantization coefficients, the reconstructed value D_r could be a approximate value of D, that is to say the more quantization coefficients we get, the closer the reconstructed value D_r is to the original DCT coefficient D. So the quantization coefficients
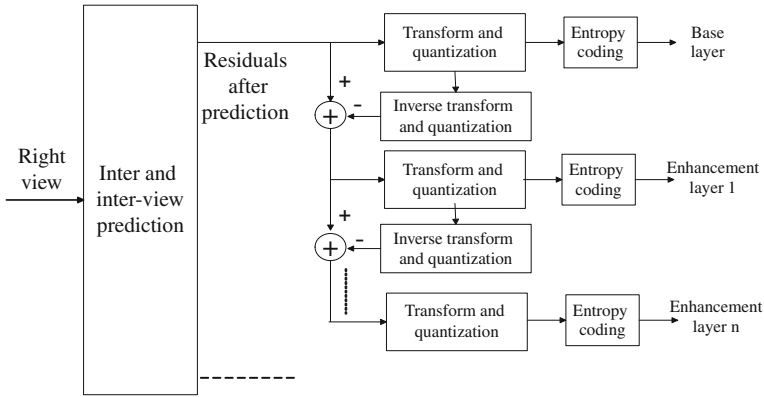
Fig. 55.2 Gradually quantization of *right* view

$\{a_1, a_2, \ldots, a_n\}$ can be encoded respectively to generate different bit stream layers, the bit stream generated by a_1 works as the basic layer, and the other bit stream work as enhancement layers. According to the idea of progressive quantization, this paper quantizes the DCT coefficients by an N-order quantizer, where the N can be changed as needed, and the process of progressive quantization is shown in Fig. 55.2.

55.3.2 Encoding DCT Coefficient Slices

Discrete Cosine Transform has always been the important technique in video and image compression. In the latest international video coding standard H.264/AVC, integer transform based on DCT has be adopted as the key module. The DCT of a two-dimensional N × N matrix f (x, y) is defined as Formula 55.2:

$$F(u,v) = \frac{2}{N} \sum_{x=0}^{N-1} \sum_{y=0}^{N-1} f(x,y) \cdot \cos[\frac{\pi}{2N}(2x+1)u] \cdot \cos[\frac{\pi}{2N}(2y+1)v]$$

$$u, v = 0, 1, 2 \ldots, N-1$$

According to the formula, we can see that the DCT coefficients correspond to different frequency respectively, and can be generally divide into low frequency, medium frequency and high frequency coefficients. As the low-frequency coefficients contain more information of original signal, so the corresponding reconstructed image is similar to the original image, while high-frequency coefficients represent the details of original image. According to this feature of DCT, we can divide the DCT coefficients into several slices, each slice contains some specific frequency coefficients, and then the slices are encoded into different layers. By this way, the generated bit stream can be divided into several layers,

Fig. 55.3 Dividing DCT
coefficients into three slices
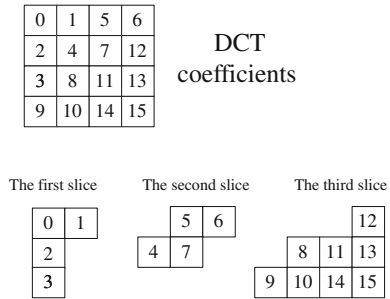
so the decoder can reconstruct the video according to the layers obtained. That is to say, when we get the layer that just contains low-frequency coefficients, the medium-frequency and high-frequency coefficients will be set to zero in the process of decoding; and when we get layers that contain low-frequency and medium-frequency coefficients, the high-frequency coefficients will be set to zero. In conclusion, the missing coefficients will be set to zero before inverse DCT in decoding process. A typical partitioning strategy [12] of DCT coefficients is shown in Fig. 55.3.

The method shown in Fig. 55.3, divides the DCT coefficients which are zigzag scanned into three slices as {0,1,2,3}, {4,5,6,7}, and {8,9,10,11,12,13,14,15}, then the slices are encoded into three layers. If some of the layers are missing, the missing part will be set to zero in decoding process. In the practical system, DCT coefficients can be divided into 1–16 slices, not limited to the three slices shown in the figure.

55.3.3 Abandoning Chroma Components

The raw video for compression is generally in the format of YUV (4:2:0), in this format the video is consist of three components, Y (luma component), U, V (chroma components), where the Y component represents the video's luma information, and U, V components contain the chroma information. The proposed scheme in this paper packages the bit stream of luma component and chroma components separately, so the generated bit stream can be divided into different layers, which makes it possible to abandon the chroma components if necessary. Taking full consideration of the binocular suppression theory, this scheme abandons the chroma components of right view in the case that the storage space or available bandwidth is not enough, and then the decoded right view will be gray image. The reconstructed right views before and after abandoning chroma components are shown in Fig. 55.4.

Before abandoning chroma
components

After abandoning chroma
components

Fig. 55.4 Reconstruct video before and after abandoning chroma component

Fig. 55.5 Inter-view
prediction
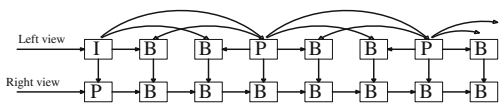
55.3.4 Discarding Right View

The stereo video at this stage is generally consisted of two views, the right view
and the left view, when one of the views is missing, the stereo video will degrade
into 2-D video. The scheme proposed in this paper is based on H.264/MVC, and
the inter-view prediction process is shown in Fig. 55.5:

From the Figure we can see that the left view is selected as references by the
right view at a particular time, while the right view is never selected by left view,
so discarding the right view will not influence the left view in decoding process.
Based on this, the proposed scheme discards the right view in the case that the
storage space or available bandwidth is so limited, and then the 3-D video will
degrade into 2-D video.

55.4 Experimental Results

The proposed scheme which is based on H.264/MVC realizes the scalable coding of
stereo video by adopting the strategies explained in Sect. 55.3, meanwhile the
scheme keeps stereoscopic perception as good as possible by taking full consider-
ation of the binocular suppression theory. The experimental results are given in this
section in the case of six layers quantization, dividing the DCT coefficients into three
slices, packaging the bit stream of luma and chroma component separately, and
discarding the right view if necessary. However the number of quantization layers
and DCT coefficients slices can be changed as needed, the experimental results are
similar, so we just give the experimental results in the case above.
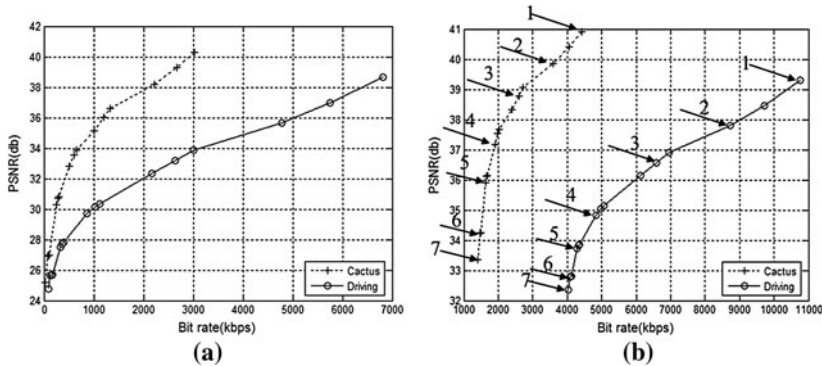
Fig. 55.6 Rate-distortion curve. **a** R–D curve of *right* view; **b** R-D curve of the stereo video(adding *left* view)

In the experiment, the six quantization steps correspond to the steps in H.264/AVC when quantization parameters are 51, 48, 42, 36, 30, 24 respectively. The DCT coefficients are written into three slices as shown in Fig. 55.3. The raw videos for encoded are cactus.yuv and car.yuv. The resolutions of left and right views are both 600×480. The R–D (rate-distortion) curve based on the truncation points' bit rates and PSNR is shown in Fig. 55.6. Since the PSNR parameter makes no sense in the case of discarding chroma components or right view, so the two truncation points whose scalable performance will be evaluated in the subjective tests were not shown in the R–D curve.

In Fig. 55.6,' + ' and 'o' represent the truncation points. From the truncation points' bit rates and PSNR, we can see that the proposed scheme realizes the scalable coding of stereo video, the generated bit stream has many truncation points which correspond to different bit rates and PNSR. The quality of reconstructed video is proportional to the obtained bit stream, which means the more bit stream we get the better video we reconstruct. Considering the subjective perceived feature of 3D video, besides the rate-distortion experiment above, we will give the subjective evaluation experiment in the following part.

In the subjective evaluation experiment, part of the generated bit stream was selected to reconstruct the videos (Car and cactus), and then the quality, depth and sharpness of the reconstructed videos were evaluated by three groups of viewers severally. The evaluation standard was based on ITU-R Recommendation BT.500-11[13], and had five levels, excellent, good, fair, poor and bad which corresponded to [8, 10], [6, 8], [4, 6], [2, 4], [2, 0] on a scale of 0–10. In the experiment we selected nine pieces of bit stream which was respectively corresponding to the truncation points 1–7 in the R-D curve, abandoning the chroma components (named as 8) and discarding the right view (named as 9). The three groups were all consisted of 20 viewers: ten males and ten females, all the viewers should have normal visual sensitivity and language skills. The evaluation results (average value) given by the three groups were shown in Tables 55.1 and 55.2.

Table 55.1 Subjective evaluation results (Car)

Truncation points	Bit rate	Depth	Quality	Sharpness
1	10768	9.83	9.76	9.50
2	8732.3	9.59	9.01	9.21
3	6590.8	8.79	8.56	8.46
4	4828.1	8.68	7.65	7.10
5	4326.2	8.60	6.56	6.30
6	4104.4	8.41	5.68	5.25
7	4039.9	8.32	4.86	4.12
8	4006.8	8.18	3.12	3.56
9	3957.6	2-D video	9.75	9.63

Table 55.2 Subjective evaluation results (Cactus)

Truncation points	Bit rate	Depth	Quality	Sharpness
1	4410.7	9.85	9.89	9.84
2	3599.9	9.45	9.40	8.96
3	2592.2	8.86	8.79	8.51
4	1900.8	8.43	7.95	7.62
5	1664.1	8.39	6.98	6.10
6	1479.7	8.24	6.01	5.11
7	1409	8.18	5.89	4.16
8	1399.8	8.08	3.10	3.46
9	1384.7	2-D video	9.85	9.79

From Table 55.1 and Table 55.2 we can see that, along with the decrease of the bit rate from truncation point 1 to 8, the depth information of the video got a little loss, and the evaluations of quality and sharpness information declined from excellent to poor. The evaluation results prove that the proposed scheme realizes the scalable coding of stereo video, and meanwhile keeps stereoscopic perception as good as possible. As for truncation point 9, the stereo video degraded into 2-D video for the reason of discarding the right view. All in all, from the tables, we can see that the more bit stream we get the better video we reconstruct.

From the results of the rate-distortion experiment and subjective evaluation experiment, it can be found that the proposed scheme realizes the scalable coding of stereo video, and maintains good stereoscopic perception, the generated bit stream can be truncated as needed to adapt to different networks and terminals.

55.5 Conclusions

For the large data quantity, stereo video occupies too many resources (available bandwidth and computation capacity) when transmitted and displayed, so encode the stereo video hierarchically to adapt to various networks and terminals is very important. Based on H.264/MVC, the proposed scheme takes full consideration of

the binocular suppression theory, just encodes the right view of stereo video hierarchically. By doing this, the scheme realizes the scalable coding of stereo video, and maintains stereoscopic perception as good as possible, the stereo video encoded by this scheme can adapt to various application environment.

References

1. Lukacs ME (1986) Predictive coding of multi-viewpoint image sets. In: Proceedings of IEEE international conference on acoust, speech signal process, Tokyo, vol 1, pp 521–524
2. Perkins MG (1992) Data compression of stereo pairs. IEEE Trans Commun 40(4):684–696
3. ITU-T and ISO/IEC JTC 1 (1996) Final draft amendment 3, amendment 3 to ITU-T recommendation H.262 and ISO/IEC13818-2 (MPEG-2 Video), ISO/IEC JTC 1/SC29/WG 11 (MPEG) Doc. N1366
4. Wiegand T, Sullivan GJ, Bjontegaard G (2003) Overview of the H.264/AVC video coding standard. IEEE Trans Circuits Syst Video Technol 13(7):560–576
5. ITU-T and ISO/IEC JTC 1 (2010) Advanced video coding for generic audiovisual services, ITU-T Recommendation H.264 and ISO/IEC 14496-10 (MPEG-4 AVC)
6. Vetro T, Wiegand GJ, Sullivan X (2011) Overview of the stereo and multiview video coding extensions of the H.264/MPEG-4 AVC standard. Proc IEEE 99(4):626–642
7. Stelmach L, Tam WJ, Meegan D (2000) Stereo image quality: effects of mixed spatio-temporal resolution. IEEE Trans Circuits and Sys Video Technol 10(2):188–193
8. Brust H, Smolic A, Mueller K (2009) Mixed resolution coding of stereoscopic video for mobile devices, the 3rd 3DTV-conference: the true vision-capture, transmission and display of 3d video, 3DTV-CON, pp 1–4
9. Fehn C, Kauff P, Cho S (2007) Asymmetric coding of stereoscopic video for transmission over T-DMB, the 1st international conference on 3DTV, 3DTV-CON, pp 1–4
10. Chen Y, Wang YK, Gabbouj M (2009) Regionally adaptive filtering for asymmetric stereoscopic video coding, IEEE international symposium on circuits and systems, ISCAS 2009, Taipei, vol 2, pp 585–588
11. Park SN, Sim DG (2009) View-dependency video coding for asymmetric resolution stereoscopic views. Optical Eng 48(7):077009–0770098
12. Joint Video Team (JVT) (2007) ISO-IEC MPEG & ITU-T VCEG, JVT-W090, CE1: simplified FGS, April 2007
13. ITU-R BT.500-11 (2000) Methodology for the subjective assessment of the quality of television pictures<!Query ID="Q1" Text="Reference [5] has been split into two different references. Please check and confirm."–>

Chapter 56
Study About the Influence on the Numerical Analysis of Pump Restoration Scheme to the Saline Groundwater by Water Sensitivity

Zhi-Yong Han, Wei Li, Feng-lin Tang and Ling Lu

Abstract Based on analyzing and approximating the graphic and hydrogeology conditions of the saline water distribution area, a quantity and quality solute numerical model is set up by generalizing the hydrogeology conditions of the study area. Then numerical analysis of different pumping restoration schemes ignoring and considering the water sensitivity of aquifers are put forward to simulate and analyze for the saline groundwater at upper reach of the impenetrable wall by groundwater simulation software-Visual-MODFLOW 4.1. The results indicate that the pumping scheme is very efficient to remove the high concentration saline groundwater; for the schemes ignoring water sensitivity of aquifers, the saline groundwater body fall back to the shallow aquifer at upper reach of the impenetrable wall after 36 months pumping with 3073.40×10^4 m^3 saline groundwater is pumped, the remaining saline groundwater area with concentration of Cl- over 450 mg/l is 5.85 km^2; but for the schemes considering water sensitivity of aquifers, the saline groundwater body fall back to the edge of the impenetrable wall after 24 months pumping with 2342.11×10^4 m^3 saline groundwater is pumped, the remaining saline groundwater area with concentration of Cl- below 450 mg/l is 1.07 km^2.

Keywords Water sensitivity · Saline groundwater · Restoration schemes · Numerical analysis

Z.-Y. Han (✉) · W. Li · F. Tang · L. Lu
College of Petrochemical Technology, Lanzhou University of Technology,
730050, Lanzhou, China
e-mail: hanzhy_009@sina.com

W. Li
e-mail: liwei_609@163.com

56.1 Introduction

The shortage of fresh water resource caused by seawater intrusion had become an important constraining factor for the development of coastal cities. Seawater intrusion occurs in more than 200 km^2 of freshwater aquifers in Shandong coastal area, with more than 4.5 million acres of farmland were affected [1]. The lower reaches area of Dagu River was the most important water supply sources for Qingdao area with 60–70% fresh water supply for Qingdao, Jiaozhou and Lancun cities. But, accompanied with the exhaustive exploitation since 1980–1998, seawater intrusion phenomenon had been the most serious threat for the water resource this region and the distribution of saline groundwater had been over 70 km^2 today. It resulted in the exhaustion of freshwater resource in the south and southeast of this area and the increase of the cost of industrial water. For example, the cost for water desalination in Jiaozhou Power Plant was over RMB1.6 million/a. Meanwhile, large areas of agricultural land barren and the local agriculture had been seriously affected because there was no fresh water for irrigation [2].

There were many project examples for the the recovery and management of underground water. As in the early 1970s, the United States (Coe, 1972) of Oxnard Valley pumping systems was succeed in removing the saline of underground water after 7 months of operation, with the pumping distance of 200 m and single-well out of water 5,700 m^3/d. In addition, the pumping regions—water injection system in Palo Alto, California, United States, was a successful example with water curtain (adding the treated wastewater, 2,500 m^3/d) was established in downstream of the salt water body in order to cut off the source of salt water. Saline groundwater was pumped out (4,500 m^3/d), and the water which contains less chlorides was recycled [3]. Besides, seawater desalination technology, such as reverse osmosis technology, was employed by the United States and Israel to deal with saline groundwater, and turned the salt water into usable water and even potable water [4]. In China, research about this issue remained mostly in idealized mathematical modeling or in creating small projects to prevent the expansion of saline water in the aquifer. For example, Li and Mao [5] carried out mathematical simulation of the salt water recovery and improvement for single-well injection, the saline water body was characterized by homogeny, isotropic homogeneity and single aquifer. The water injection rate of single-well injection is 1.4 m^3/s. After the operation for 4 months, underground saline water was forced back to the impenetrable wall in the vicinity. Furthermore, Zhuyou Town in Laizhou City, water drainage along the coast was excavated to prevent the further expansion of saline water by underground fresh water curtain which was formed during rainwater infiltration [6]. But these programes, both in engineering practice and numerical analysis, did not consider water sensitivity caused by fresh water when it flowed into aquifer to replace the original saline water. Water sensitivity, which was a complicated hydro-geochemical phenomenon, had been discovered for more than 70 years. It could be described that when the low concentration saline water or fresh water flowed into the aquifer to replace the high concentrations one, the

permeability of aquifers declined quickly and abruptly and even made some of the aquifers became an impermeable one. Based on the studies of the water sensitivity [7–10], considered the water sensitivity characteristic of different aquifers at the downstream of Dagu River, a mathematical simulation model for the saline water pumping restoration scheme was founded and simulated by the Visual MOD-FLOW-4.1 in this paper.

56.2 Natural Geographical and Hydro-Geochemical Conditions

56.2.1 Natural Geography

Dagu River, which was one of the major rivers in Shandong Peninsula, running out of the Fushan Mountain in Zhaoyuan city, flowed through Zhaoyuan, Yexian, Laixi, Pingdu, Jimo and Jiaozhou, eastwards into Jiaodong Bay. The annual average temperature was 12.5°C, annual average precipitation was 687.5 mm, and average annual evaporation was 600 mm. The saline ground water area was 14.96 km^2, and it located in the downstream of Dagu River, 12 km north of Jiaozhou Bay.

56.2.2 Hydrological and Geological Conditions

Hydro-geological conditions, including the occurrence, recharge, discharge and water chemistry characteristics of groundwater, are the most important controlling factors of the ground water movement.

56.2.2.1 Occurrence of Groundwater

The ground water of the study area mainly located in the loose ancient river sediments of the Quaternary (Q), and the aquifer was the alluvial–alluvial type with the significant double-layer structure. The upper formation of the aquifer mainly was clay sand (part was sandy clay and clunch) and the thickness of which was 2–5 m with many skylights; the lower one was sand and sand gravel, and the thickness of which was 5–8 m which had strong permeability and water yield property. At the edge of the ancient riverbed, sand and gravel aquifer became gradually to thin even pinching out, meanwhile, the property of water yield weakened to disappear (Fig. 56.1).
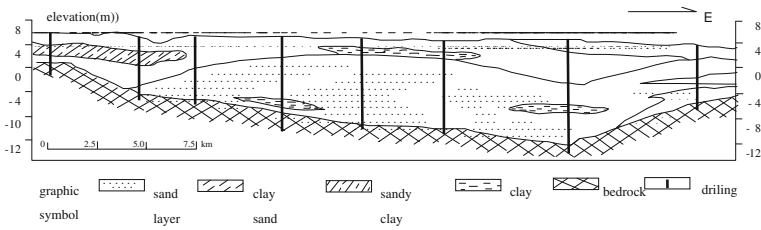
Fig. 56.1 Typical geological section of the study area (impenetrable wall)

56.2.2.2 Recharge and Discharge of Groundwater

Atmospheric precipitation and river infiltration were the main recharging sources of the ground water in this region, and the industrial, agricultural and domestic water explorations were the major discharging pathways of groundwater. The hydraulic relationship between the river and the ground water was very close-knit of recharging and discharging each other. Limited by the impact of groundwater hydraulic gradient (about 1/2,000), the seepage velocity of ground water was very low which resulted in the recharging and discharging quantity was very limited.

56.2.2.3 Chemical Characteristics of the Ground Water

Ground water within the study area was terrestrial lixiviation phreatic water. HCO_3- and $Cl-$ were the main anion, Ca_2+ and $Na+$ were the main cations. The concentration of chloride in the ground water was less than 100 mg/l, and mineralization of the ground water was 0.3–0.5 g/l; after the saline water intrusion, the chemistry ion characteristic of anions and cations in groundwater changed to chloride and sodium respectively. The concentration of chloride in the ground water increased by 600–800 mg/l and the mineralization of the water increased greater than 2.0 g/l. The concentration of chloride in the ground water increased with the depth above 2.5 m, and there was almost no change below the depth of 2.5 m.

56.3 Mathematical Model and Calibration on Saline Groundwater Restoration Scheme

56.3.1 Generalized Boundary Conditions

According to the current situation of the exploitation, the sea water intrusion area, the location of impenetrable wall and the distribution of observation wells group(water level and quality observation), the study area was demarcated, and the

north boundary was Zhangjia Village to Xibeitun Village line, the south one reached the impenetrable wall, the east and west one reached the edge of Dagu River ancient valley. The total area was 95.74 Km^2. The east and west boundary was defined as the impervious boundary for the fact that the aquifer gradually got thinner and pinched out. The impenetrable wall, with the depth 4–12 m and top height 0 m above sea level, was built on the bedrock, and it was defined as the constant head boundary because the water would pass though its top from its upstream or downstream. The aquifer in the northern border was steady and uniform and it connected with the upstream groundwater as a whole, which was defined as fixed water quantity boundary.

56.3.2 Mathematical Modelling

According to the hydro-geological conditions of the study area, the transportation of the solute in this phreatic aquifer matched to the following definite equation.

$$\begin{cases} \mu \frac{\partial h}{\partial t} = div\left[K(h-b)\right] gradh - W^2, (x,y) \in G, T > 0 \\ Initial \cdot condition : h|_{t=0} = h_0(x,y), (x,y) \in G \\ Boundary \cdot condition : h(x,y,t)|\Gamma_1 = g_1(x,y,t), (x,y) \in \Gamma_1, t > 0 \\ [K(h-b)gradh] \bullet \overrightarrow{n}|\Gamma_2 = -g(x,y,t), (x,y) \in \Gamma_2, t > 0 \end{cases} \quad (56.1)$$

$$\begin{cases} \frac{\partial}{\partial t}[(h-b) \bullet C] = \frac{1}{nR_\alpha} div[(h-b)DgradC] - \frac{1}{R_\alpha} div[(h-b)V_c] - W, \\ (x,y) \in G, t > 0 \\ Initial \cdot condition : C(x,y,t)|_{t=0} = C_0(x,y), (x,y) \in G \\ Boundary \cdot condition : C(x,y,t)|\Gamma_1 = f_1(x,y,t), (x,y) \in \Gamma_1, t > 0 \\ (h-b)(V_c - DgradC)\overrightarrow{n}|\Gamma_2 = f_2(x,y,t), (x,y) \in \Gamma_2, t > 0 \end{cases} \quad (56.2)$$

In the formula:

C0/C—the initial density and density ratio; n—porosity; W/W′—source/sink (m^3); h/b—top and bottom elevation (m); Rα—Reynolds number; D—coefficient of hydrodynamic diffusion (m^2/s); Vc—velocity of solute transportation (m/s).

56.3.3 Determination of Hydro-Geological Parameters

Hydro-geological parameters are the key factors of hydro-geological model. The correctness and reasonableness of those parameters were directly related to the accuracy of the model and credibility. Parameters used in the model included diffusion coefficient, hydraulic conductivity, specific yield, coefficient of recharge from precipitation, limited depth of evaporation. The data were from indoor and field trials and showed in the Table 56.1.

Table 56.1 Hydrogeology parameters

Soil/parameter	Hydraulic conductivity (m/d)	Degree of water supply	Oozing factor of rain	(Limited depth of evaporation) (m)	(Longitudinal/lateral diffusion degree) (m)
Clay	0.01–0.05	0.002–0.05	0.1–0.15	6.21	–
Sandy clay	0.03–0.5	0.03–0.06	0.15–0.2	5.69	–
Clay sand	0.5–1.0	0.04–0.07	0.2–0.25	4.1	–
Slity sand	1.0–5.0	0.05–0.11	0.25–0.3	3.56	0.0856–0.8558/0.0086–0.0171
Medium sand	8.0–25.0	0.09–0.20	0.25–0.3	2.42	0.3423–1.7117/0.0859–0.1712
Coarse sand	20.0–25.0	0.15–0.25	0.25–0.3	2.42	0.3423–1.7117/0.0859–0.1712
Grail	≥50.0	0.20–0.35	≥0.5	–	1.7117–8.5586/0.3424–1.7117

56.3.4 Initial Condition and Equilibrium

56.3.4.1 Initial Condition

Initial conditions mean the initial water level and chloride ion concentration of the saline ground water. According to the observation material of the water level and water quality, the saline water distribution area remained unchanged since the second half of 1999 (after the impenetrable wall was accomplished). But the chloride ion concentration of the surface saline water was in fluctuation influenced by precipitation infiltration and molecular diffusion. In addition, the level of groundwater in the saline water district was remained stable, and the water level fluctuation which was generally less than 2 m was mainly caused by precipitation. Therefore, the water level and chloride ion concentration of groundwater on September 27, 1999 were taken as initial conditions in the study area.

56.3.4.2 Equilibrium

(1) Rainfall discharge

The precipitation information which was collected during 1976–2010 at Nancun Station indicated that the average annual precipitation in the study area was 603.68 mm (Table 56.2).

(2) Agricultural extraction

According to the current level of agricultural production, during the restoration of the saline water, the agriculture extraction was about 17.1 million m^3/a in the study area, including water for domestic water and township and village enterprises (Table 56.2).

Table 56.2 Average rainfall and groundwater exploitation quantity every month at downstream area of Dagu River

Month	1	2	3	4	5	6	7	8	9	10	11	12
Precipitation (mm)	10.93	10.82	18.27	30.23	35.97	82.73	158.55	139.22	50.87	37.26	18.18	10.65
Agriculture (10^4 m³)	0.0	0.0	205.2	307.8	136.8	188.1	34.2	17.1	171	376.2	273.6	34.2
Idustry (10^4 m³)	32	33	100	92	136	122	124	117	106	29	58	43

Fig. 56.2 Distribution of lithology and reckoning area
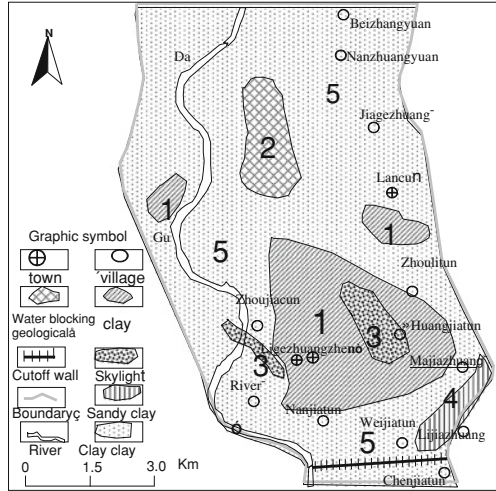
(3) Industrial extraction

According to the industrial extraction in Dagu River in Jiaozhou city 1999, the industrial exploitation quantity was determined as 9.93 million m^3/a, monthly distribution was showed in Table 56.2.

(4) River recharge

According to the actual measured information about the typical year of Dagu River-1982 and 1985, we took 20,680 m^3/d·km as river infiltration rate of Dagu River in unit time and unit length in this study. In the study area, runoff length of Dagu River was 21 km. In addition, according to the runoff conditions of Dagu River during the calculation time, the recharge capacity of the river was 3.04 million m^3/a in the simulation context.

56.3.5 Model Calculations and Calibration

According to the different lithology, the study region was subdivided into different computational domain in the model (Fig. 56.2). By the calculation of the groundwater simulation software-Visual-MODFLOW4.1, the study area was divided into 7,344 units, and 4,259 units was the effective unit. The calibration period of this model was from September 27, 1999 to September 27, 2010, with the time step of 2 months and total calculation interval of 12 months. In this calibration process, data on water quality obtained in the long-term observation hole (Huang Jiatun and Wei Jiatun) at the depth of 2.5 m (water quality changed little or remained unchanged below this depth) was fitted with the concentration values obtained by the model data, and the results matched perfectly (Fig. 56.3).

Fig. 56.3 Distribution of lithology and reckoning area
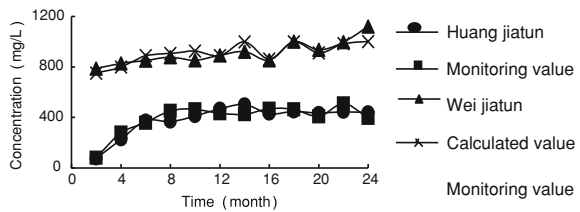
56.4 Numerical Analysis of Pumping Restoration Scheme

56.4.1 Normal Pumping Scheme

Pumping scheme referred to pump the saline groundwater out of the aquifer and drained it away. The basic idea was using the most reasonable exploitation layout, the least extraction wells quantity and the shortest time, avoiding causing adverse consequences of the geological environment phenomenon (land subsidence, ground subsidence, etc.) to achieve the purpose of pumping out the saline water. The impact of bottom topography was considered first of all when determined the treatment schemes. It should made full use of terrain factors to pump the highest concentration saline water in priority, and reduce the pollution scope of saline water bodies.

In addition, considering the water level downstream the impenetrable wall generally maintained at 1.5–2.0 m above the sea level, while the elevation of the impenetrable wall roof was 0 m, there was a hydraulic connection between the sea water and the saline water body. In the case of drainage, if there was excessive pumping at the upstream of the impenetrable wall, it would result in large quantity seawater flowing back again from the downstream and it was not conducive to the implementation of restoration schemes. At the same time, the interference between pumping wells should be reduced in order to improve the pumping efficiency.

The pumping wells were laid on the saline water aquifers (thickness $\geq$5 m) in the form of rectangular grid.

56.4.1.1 Single Well Pump Output and Well Spacing

According to the mining practices of the study area since 1981 and the pumping and injection tests in this area, the initial pumping capacity of pumping wells were desired as 1500 m^3/d (during the pumping process, with the water head reducing, it gradually reduced to 1000 m^3/d and 500 m m^3/d), single-well pump output in the fringe of aquifer desired as 1000 and 500 m^3/d, and the well spacing as 300 m.

56.4.2 Results Analysis

(1) Change of the saline water and mount of pumping

After 6 months, the area shrank by 0.76 km^2; from the first 12 month to the 30 month, the average shrinking rate of the saline water body area was 3.81 km^2/a; at the 18 months the area of the saline water body reduced to 6.59 km^2, and the 36 months, 5.85 km^2, the chloride ion concentration most of the remaining saline water in the aquifer was below 450 mg/l. At the end of this scheme, the shrinking speed of the saline water body became very slowly (1.47 km^2/a), and most of it distributed in the thin edge of the study area which was not conductive to concentrated to be extracted (Fig. 56.4F).

(2) The cone of depression

The change of the distribution area of the cone of depression during the pumping process was showed in the Table 56.4. In the 36 months of pumping process, the scope of the cone remained expanding and the water level in funnel center remained declining. However, the water level of the cone center in vertical changed abruptly in the first 6 months (1.383 m). Subsequently, the lowest water level of the cone was stabled at 14 m. At the end of the third year, the area of the cone (−2 m water line) had spread to 24.21 km^2 (Tables 56.3 and 56.4).

56.4.3 Pumping Scheme Considering the Water Sensitivity

Because of extracting the ground saline water can cause the later be recharged by the fresh water, resulting in the typical lithology of the aquifer to produce water-sensitive, dramatic changes in its permeability. At this point the sensitive data of the model will use the data which has been tested and after the occurrence of the sensitivity of water (Table 56.5).

56.4.3.1 The Pumping Capacity of Single Well and the Amount of Well Spacing

The same as the 4.1.1.

56.4.3.2 The Analysis of the Results

(1) The dynamics change of saline water distribution area

After pumping for 6 and 12 months, the area change of the saline water was as same as the scheme one, because the funnel has not yet reached the interface of saline and fresh water, and the water sensitivity did not happened at the transition zone aquifer. At the later of the 12 months, the funnel range expanded to the west
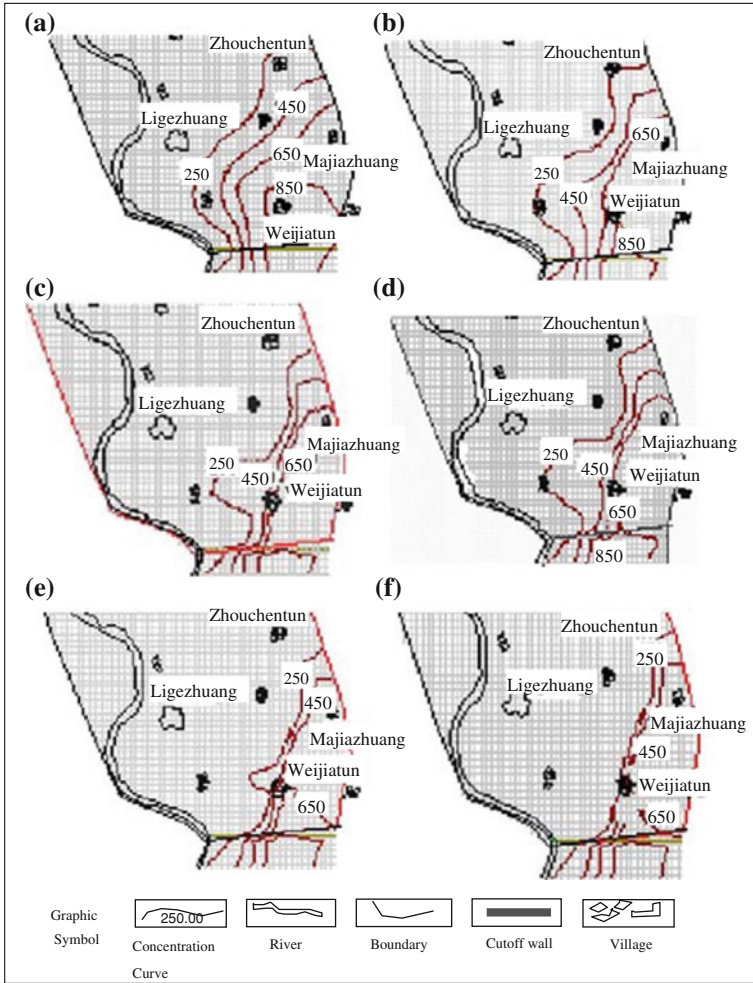
Fig. 56.4 Changes of the saline-water scope in the scheme ignoring the water sensitivity after 6, 12, 18, 24, 30 and 36 months

Table 56.3 Statistics of salinewater scope and total pumping quantity

Time	0	6 months	12 months	18 months	24 months	30 months	36 months
Distribution area of the saltwat (km^2)	14.96	14.21	12.39	10.51	8.49	6.59	5.85
Shrinking speed (km^2/a)	–	1.51	3.63	3.76	4.04	3.81	1.47
Total pumping capacity (10^4 m^3)	–	1028.30	1963.90	2356.20	2632.11	2871.94	3073.40

Table 56.4 Scope statistics cone of depression

Time	Hopper center		−2 water line	
	Elevation (m)	Buried depth (m)	Long-axis	Area (km^2)
6 months	−6.6	10.1	NE-SW	7.964344
12 months	−12.2	15.7	NE-SW	13.610536
18 months	−10.7	14.2	NE-SW	16.961528
24 months	−10.9	14.4	NE-SW	18.269792
30 months	−11.4	14.9	NE-SW	21.988016
36 months	−9.9	13.4	NE-SW	24.21436

Table 56.5 Hydraulic conductivities after water sensitivity (m/d)

Lithological character	Clay	Sandy clay	Clay sand	Slity sand	Medium sand	Coarse sand	Grial
Coefficient permeability	0	10.9	10.4–10.7	0.001–0.05	4–12.5	18–22.5	≥50

Table 56.6 Statistics of salinewater scope and total pumping quantity

Time	0	6 months	12 months	18 months	24 months
Distribution area of the saltwater (km^2)	14.96	14.21	12.39	6.32	1.07
Shrinking speed (km^2/a)	–	1.51	3.63	12.14	10.5
Total pumping capacity (10^4 m^3)	–	1028.30	1963.90	2207.30	2432.11

and the northern border and reached the freshwater zone. Then, under pressure of the water head, the fresh ground water started flooding into the saline water aquifer to replace the latter which resulted in the occurring of the water sensitivity phenomenon, and the permeability of the aquifer decreased sharply and abruptly in a short time and the quantity of the fresh water flowing into the aquifer was reduced abruptly. It could be described as a low permeability curtain built between fresh groundwater and saline water body which greatly reduced the recharging quantity and accelerated the extraction rate of the saline water body. After 18 months, the area of chloride concentration line of 250 mg/l had reduced to 6.32 km^2; at the en of the 24 month, the saline water body had returned to the shallow aquifer near the impenetrable wall and the area was reduced to 1.07 km^2, and the chloride concentration of the remaining saline water was less than 450 mg/l (Table 56.6 and Fig. 56.5).

(2) The cone of depression

The change of the distribution area of the cone of depression during the pumping process was showed in the Table 56.7. In the 24 months of pumping process, the scope of the cone remained expanding and the water level in funnel center remained declining. However, the water level of the cone center in vertical changed abruptly in the first 12 months (1.310 m). Subsequently, the lowest water level of the cone was stabled at 14 m. At the end of the second year, the area of the cone (−2 m water line) had spread to 28.98 km^2 (Table 56.7).
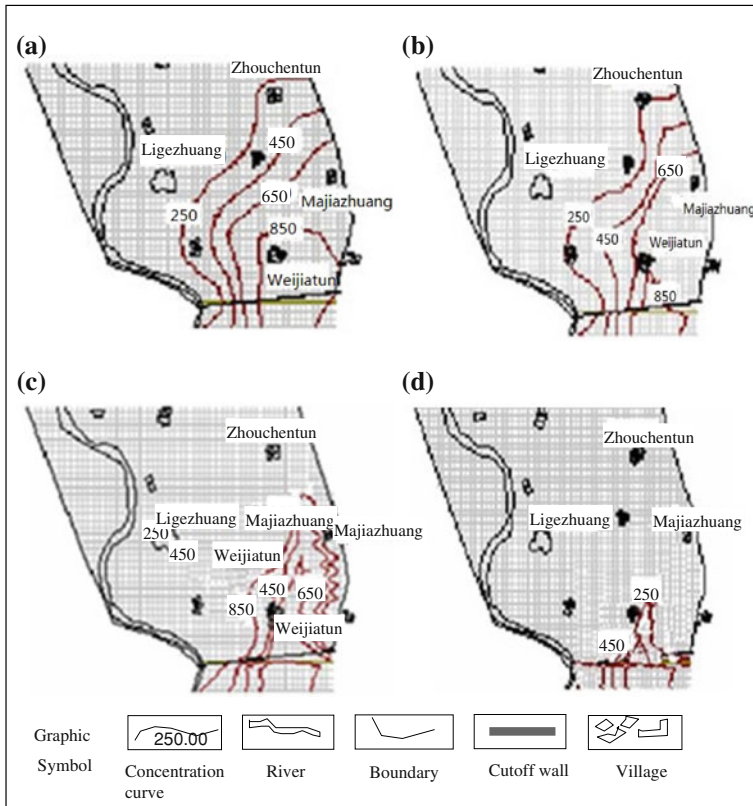
Fig. 56.5 The changes of the saline-water scope in the scheme considering the water sensitivity after 6, 12, D 18 and 24 months

Table 56.7 The scope statistics of the funnel area

Time	Hopper center		−2 water line	
	Elevation (m)	Buried depth (m)	Long-axis	Area (km²)
6 months	−6.6	10.1	NE-SW	7.964344
12 months	−12.2	15.7	NE-SW	13.610536
18 months	−10.7	14.2	NE-SW	22.476528
24 months	−10.9	14.4	NE-SW	28.981550

56.4.4 Impact Analysis of the Sea Water Reflux From Downstream of the Impenetrable Wall

The impact of the reflux quantity from downstream of the impenetrable wall was analyzed in the two schemes, and the curves were drawn between the water reflux quantity and time (Fig. 56.6). In the initial pumping period, the

Fig. 56.6 Curves between
water reflux quantity and time
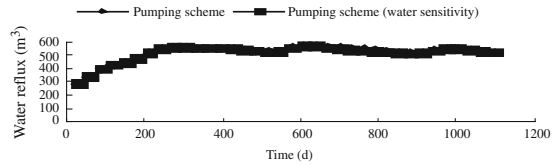
water reflux quantity of sea water increased rapidly, after 12 months, water reflux quantity from the downstream of the impenetrable wall was stable (550 m^3/d). However, some small cyclical fluctuations may happened due to the cyclical rainfall. In the whole restoration process, the total water reflux quantity was about 1.8% of the total pumping quantity, and two schemes are almost the same. It indicated that the impenetrable wall could cut off the connection of upstream and downstream of the saline water. What's more, the sea water reflux from the downstream of the impenetrable wall had little effect on the restoration schemes.

56.5 Conclusions

The numerical simulation and analysis of the pumping schemes considering the water sensitivity of the aquifer or not was studied. The results showed that the presence of water sensitivity had very important impact on the pumping restoration schemes.

(1) For the pumping scheme which did not consider the water sensitivity of the aquifer, the saline water body returned to the shallow aquifer near impenetrable wall after 36 months, the area of the remaining saline water body was l 5.85 km^2 and most of the chloride ion content of it was higher than 450 mg/l. So, it still needed further treatment.

(2) For the pumping scheme which considered the water sensitivity of the aquifer, the saline water body was removed very quickly. Just after 24 months, the saline water body had returned to the impenetrable wall edge with the remaining area only 1.07 km^2. All the chloride ion content of the remaining saline water was lower than 450 mg/l.

(3) For the first pumping scheme, 30.734 million m^3 saline water was pumped out in 36 months, it was much greater than the second one, which pumped out 24.321 million m^3 in 24 months.

(4) The pumping water quantity of the first scheme was much greater than the second one, but the saline water treatment effect was much lower than the latter, it indicated that much more high chloride ion concentration saline water was pumped out in the second scheme.

References

1. Han Z, Zheng X, Lin G (2004) Dagu River downstream of saline groundwater restoration program numerical analysis [J]. Eng Investig 24(6):81–85 (in Chinese)
2. Chen H et al (2002) Coastal groundwater system dynamics method [M]. Geological Publishing House, Beijing, pp 20–41 (in Chinese)
3. Jin X, Hao Z, Zhang J (2006) Hydrological model of research and development. Sichuan Environ 13(4):197–199 (in Chinese)
4. Wang B (2005) The Chinese city of Geology. China Geological Publishing House, Beijing (in Chinese)
5. Li B, Mao C (1992) Seawater intrusion of groundwater research. Nanjing Hydraulic Res Inst (2):145–155 (in Chinese)
6. Qin H, Liu G (1995) White River plain groundwater system simulation. Ocean Univ China (2):206–212 (in Chinese)
7. Han Z, Zheng X, Chen J (2007) Brackish water interface affect the water sensitivity of several factors. Hydrogeol Eng Geol 34(6):24–27 (in Chinese)
8. Han Z, Zheng X, Chen J et al (2008) Experimental study on the water sensitivity of the powder-silver sand. Adv Water Sci 19(5):630–634 (in Chinese)
9. Han Z, Zheng X, Chen J (2009) Applications of water sensitivity in situ remediation at saltwater-freshwater interface. Trans Tianjin Univ 15(2):150–155 (in English)
10. Han Z, Li K, Feng X et al (2009) Influence factors on the water sensitivity of the sand media. Prog Environ Sci Technol II(B):1301–1305 (in English)

Chapter 57
The Antenna Up-To-Down Gain Ratio Design for Multipath Mitigation of GNSS Reference Station Receivers

Geshi Tang, Huicui Liu, Xiao Cheng, Lv Zhou and Feixue Wang

Abstract Multipath is one of the dominant causes of error in pseudorange observations for GNSS (Global Navigation Satellite Systems) reference station receivers whose multipath mitigation performances are related to four factors: the receiving scenario, the antenna height, the antenna gain pattern (up-to-down gain ratio) and the receiver-internal multipath mitigation technique. However, quantitative analysis of relations between the code tracking multipath error and the antenna parameters (including the height and up-to-down ration) is still absent. With two assumptions that the reflectors in the typical GNSS reference station receiving scenario are horizontal planes and the receiver-internal technique is Double-delta technique, the paper derives the functional relations between the code tracking multipath error and the antenna parameters. Based on these functions, this paper proposes theoretical formulae for the antenna up-to-down gain ratio design given the upper limit of the code tracking multipath error and antenna height. The quantitative and exercisable results presented in this paper are significant and instructive in the multipath-rejecting antenna design for GNSS reference station receivers.

Keywords Antenna · GNSS · Multipath · Up-to-down gain ratio · Height

G. Tang (✉)
Beijing University of Aeronautics and Astronautics, Beijing, China
e-mail: tanggeshi@bacc.org.cn

G. Tang · H. Liu · Lv. Zhou
Science and Technology on Aerospace Flight Dynamics Laboratory, Beijing, China
e-mail: vlcx26@gmail.com

X. Cheng
Beijing Aerospace Control Center, Beijing, China

F. Wang
School of Electronic Science and Engineering, National University of Defense
Technology, Changsha, China

57.1 Introduction

Multipath is the primary error source constraining the accuracy of GNSS (Global navigation satellite systems). It distorts the signal modulation and can lead to meters of error to the pseudo-range measurements [1]. Lots of receiver-internal multipath mitigation techniques [2, 3] are investigated and widely applied in the receiver signal-processing phase; nevertheless those techniques are not effective to all kinds of multipath. For example, the short delay multipath which has the time delay less than 0.1 chips compared with the direct signal can hardly be distinguished by most of the receiver-internal techniques [4]. For the GNSS reference station which is generally located in the open area where the ground near the receiving antenna acts as the reflector, the received signal is mainly influenced by strong short delay multipath. Several meters of multipath error degrades the measurements accuracy and burdens the succedent data processing. In this case, it is important for improving the multipath mitigation capacity of the receiver that the antenna is carefully designed to adjust to the receiving scenario and cooperate with the receiver-internal technique.

A lot of multipath-rejecting antennas are developed with different manufacture techniques, such as the choke ring antenna [5] and the pinwheel antenna [6]. Those antennas are all designed to achieve low gains below the horizon in order to reject the multipath signals arriving from these directions whereas maintain high gains above the horizon in order to enhance the power of the direct signal. Theoretically the multipath signals can be totally eliminated if the antenna gains below the horizon are zeros. But in practice, the antenna gains below the horizon can not be reduced to zeros; furthermore the antenna gains both below and above the horizon are interactional so the latter are affected if the former are reduced arbitrarily. In addition, the phrase "below the horizon" indicates an angel range up to π and so far there has been a lack of quantitative theories for the antenna gain patter designing to show that how low the antenna gain of a certain angle below the horizon should be to fulfill a given demand when the receiver-internal technique is fixed.

In this paper, given the upper limit of the multipath tracking error and antenna height, theoretical formulae for antenna up-to-down gain ratio design are proposed based on the integration of the typical GNSS reference station receiving scenario and the multipath tracking error model of Double-delta technique.

57.2 The Effects of Antenna Parameters on Multipath Tracking Error

57.2.1 The Multipath Signal Model of GNSS Reference Stations

There are two types of multipath signals: one is the diffuse scattering multipath signal which generally behaves as an additional noise channel and has little effects

Fig. 57.1 The typical
reflecting geometry of GNSS
reference stations
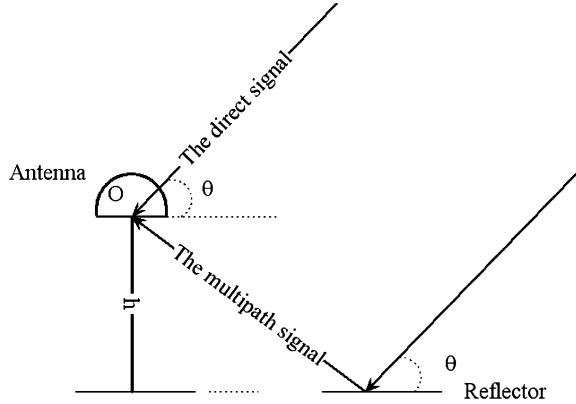
on the code tracking; the other is the specular multipath signal which can be
modeled as a replica of the direct signal with a certain power damping factor,
additional time delay, and carrier phase shift. In the presence of a single specular
multipath signal, the composite signal received by the antenna can be written as
follows:

$$r(t) = p(t - \tau_0) \cos(2\pi ft + \phi_0) + \alpha p(t - \tau_0 - \Delta\tau_m) \cos(2\pi ft + \phi_0 - \Delta\phi_m)$$

(57.1)

where $p(t)$ is the spread-spectrum code; f is the carrier frequency; τ_0 and ϕ_0 are
respectively the arrive time (delay) and the carrier phase of the direct signal; α,
$\Delta\tau_m$ and $\Delta\phi_m$ are separately the power damping factor, time delay, and carrier
phase shift of the multipath signal relative to the direct signal.

The following part of this research analyzes the specular multipath signal only
for it affects more greatly than the diffuse scattering multipath signal. In addition,
the reflector is considered as a horizontal plane for the GNSS reference stations are
usually sited in open areas and the antennas are generally fixed on the building
roof or the ground higher than any other surrounding reflectors. The geometry of
the reflector and the receiving antenna is shown in Fig. 57.1.

Suppose that the reflecting plane extends into infinity; the antenna height is
h meters and O denotes the antenna phase center. Then the multipath signal travels
D meters longer than the direct signal and D can be written as [7]:

$$D = 2h \sin(\theta), \quad 0 \leq \theta \leq \pi$$

(57.2)

where θ is the elevation of the satellite. So the relative time delay of the multipath
signal can be expressed as:

$$\Delta\tau_m = \frac{D}{c} = \frac{2h \sin(\theta)}{c}$$

(57.3)

where c is the light speed. The corresponding relative carrier phase shift of the
multipath signal is:

$$\Delta\phi_m = 2\pi f \Delta\tau_m + \sigma = \frac{4\pi h f \sin(\theta)}{c} + \sigma \qquad (57.4)$$

where σ is the phase jump caused by the reflector, which can hardly be modeled [8]. So the multipath phase shift is considered as random instead of correlated with $\Delta\tau_m$ in this paper.

When the received signal arrives at the input port of the receiver code tracking loop, the power damping factor α of the multipath signal contains three parts:

The power attenuation caused during the distance D. But compared with the distance from the satellite to the antenna, D is much smaller. So this part of power attenuation is usually ignored.

The power attenuation caused during the reflection. It is related to the characteristics of the reflectors. If the reflector is concrete building roof or ground, this part of power attenuation can be considered as zero [7].

The power attenuation caused by the difference between the antenna gain for the direct signal and the antenna gain for the multipath signal. It is shown from Fig. 57.1 that for a horizontal reflector the incident directions of the direct signal and the multipath signal are symmetrical relative to the horizon line. So this part of power attenuation is related with the antenna up-to-down gain ratio $GR(\theta)$(in dB) which is defined as the difference between the antenna gain at the positive elevation angle θ and the antenna gain at the negative elevation angle $-\theta$.

With the assumption that the first two parts of the power attenuation be ignored, α can be expressed as:

$$\alpha = 10^{-GR(\theta)/20} \qquad (57.5)$$

The antenna gains above the horizon are usually larger than those below the horizon for a representative GNSS antenna, so $GR(\theta) > 0$ and then $0 < \alpha < 1$. Additionally the satellite elevation can be limited to $0 \leq \theta \leq \frac{\pi}{2}$ if the antenna gain pattern is supposed to have good spherical symmetry.

According to the analysis in this section, the functional relations are established between the multipath signal parameters $(\alpha, \Delta\tau_m \text{ and } \Delta\phi_m)$ and the antenna parameters.

57.2.2 Code Tracking Multipath Error Model

Different receiver-internal techniques have different multipath error models. In this paper, two popular multipath mitigation solutions, the Narrow-correlator technique and the Double-delta technique, are analyzed to obtain the functional relations between the code tracking multipath error and the multipath signal parameters.

Suppose the bandwidth of the receiver's front-end filter be infinite and the side-lobes of the code correlation function be ignored. The basic concept of Double-delta code tracking loop is described in detail in [9]. Compared with the

two correlators code tracking loop such as that of the Narrow-correlator technique, there is one more pair of correlators in the Double-delta code tracking loop. The four correlators' spacing is $\left[\frac{d}{2}, d, \frac{d}{2}\right]$ in turn. The code tracking multipath error for the Double-delta technique can be written as Eq. 57.6 where T is the chip width of the spread-spectrum code; $\tau_A = \dfrac{1 + \alpha\cos(\Delta\phi_m - \Delta\phi)}{2}d$, $\tau_B = \frac{\alpha d\cos(\Delta\phi_m - \Delta\phi)}{4} + T - \frac{d}{2}$, $\tau_C = -\frac{\alpha d\cos(\Delta\phi_m - \Delta\phi)}{4} + T + \frac{d}{2}$.

$$\varepsilon(\alpha, \Delta\tau_m, (\Delta\phi_m - \Delta\phi)) = \begin{cases} \frac{\alpha\Delta\tau_m\cos(\Delta\varphi_m - \Delta\varphi)}{1 + \alpha\cos(\Delta\phi_m - \Delta\phi)}, & 0 < \Delta\tau_m \leq \tau_A \\ \frac{\alpha(d - \Delta\tau_m)\cos(\Delta\phi_m - \Delta\phi)}{1 - \alpha\cos(\Delta\phi_m - \Delta\phi)}, & \tau_A < \Delta\tau_m \leq d \\ \frac{\alpha\cos(\Delta\phi_m - \Delta\phi)}{2 + \alpha\cos(\Delta\phi_m - \Delta\phi)}(d - T + \Delta\tau_m), & T - d \leq \Delta\tau_m \leq \tau_B \\ \frac{\alpha\cos(\Delta\phi_m - \Delta\phi)}{2 - \alpha\cos(\Delta\phi_m - \Delta\phi)}(T - \Delta\tau_m), & \tau_B < \Delta\tau_m \leq \tau_C \\ \frac{\alpha\cos(\Delta\phi_m - \Delta\phi)}{2 + \alpha\cos(\Delta\phi_m - \Delta\phi)}(-d - T + \Delta\tau_m), & \tau_C < \Delta\tau_m \leq T + d \\ 0, & otherwise \end{cases}$$

$$(57.6)$$

Based on Eq. 57.6, the multipath signals can be divided into four categories according to the value of $\Delta\tau_m$, which are:

Short delay multipath signals $(0 \leq \Delta\tau_m < d)$. In this region, the multipath can hardly be distinguished by most of the receiver-internal techniques [4]. Especially it is interesting to be noticed that the multipath error function when $0 < \Delta\tau_m \leq \tau_L = \tau_A$ is only correlated with the parameters of the multipath signals. Therefore Double-delta technique is unable to mitigate the effects of short delay multipath signals and then the performance of the receiving antenna is crucial.

Medium delay multipath signals $(d \leq \Delta\tau_m < T - d)$. The multipath error is linear with d, the Double-delta technique can eliminate this kind of multipath completely, so there is no restriction on the antenna.

Long delay multipath signals $(T - d \leq \Delta\tau_m \leq T + d)$. Only few of the receiver-internal techniques are effective to this kind of multipath signals [9, 10], so the receiving antenna plays an important role for mitigating this kind of multipath signals is using Double-delta technique.

Non-correlated multipath signals $(T + d \leq \Delta\tau_m)$. This kind of multipath signal is not correlated with the direct signal so the tracking error is 0. Then there is no restriction on the antenna.

57.2.3 Peak Multipath Error Envelope

From Eq. 57.6 it can be seen that the code tracking multipath error reaches its positive or negative peak when $\Delta\phi_m - \Delta\phi = 0$ or π. So for a fixed α and $\Delta\tau_m \geq 0$, $\varepsilon(\alpha, \Delta\tau_m, 0)$ and $\varepsilon(\alpha, \Delta\tau_m, \pi)$ compose the multipath error envelope. Furthermore the peak multipath error envelope can be defined as:

$$\varepsilon_{\max}(\alpha, \Delta\tau_m) = \max[\,|\varepsilon(\alpha, \Delta\tau_m, 0)|, \quad |\varepsilon(\alpha, \Delta\tau_m, \pi)|\,] \tag{57.7}$$

By replacing α and $\Delta\tau_m$ with Eqs. 57.3 and 57.5, the peak multipath error envelope for Double-delta technique, as functions of h and $GR(\theta)$, can be written respectively as Eq. 57.8 where $\rho_{A1} = \dfrac{cd}{4}\left(1 - \dfrac{1}{10^{GR(\theta)/20}}\right)$, $\rho_{A2} = \dfrac{cd}{4}\left(1 + \dfrac{1}{10^{GR(\theta)/20}}\right)$, $\rho_{B1} = \dfrac{cT}{2} - \dfrac{cd}{8}\cdot\left(2 + \dfrac{1}{10^{GR(\theta)/20}}\right)$, $\rho_{B2} = \dfrac{cT}{2} - \dfrac{cd}{8}\cdot\left(2 - \dfrac{1}{10^{GR(\theta)/20}}\right)$, $\rho_{C1} = \dfrac{cT}{2} + \dfrac{cd}{8}\cdot\left(2 - \dfrac{1}{10^{GR(\theta)/20}}\right)$, $\rho_{C1} = \dfrac{cT}{2} + \dfrac{cd}{8}\cdot\left(2 + \dfrac{1}{10^{GR(\theta)/20}}\right)$.

$$\varepsilon_{\max}(G(\theta), h, \theta) = \begin{cases} \dfrac{1}{10^{GR(\theta)/20}-1}\cdot\dfrac{2h\sin(\theta)}{c}, & 0 < h\sin(\theta) \le \rho_{A1} \\[2mm] \dfrac{1}{10^{GR(\theta)/20}+1}\left(d - \dfrac{2h\sin(\theta)}{c}\right), & \rho_{A1} < h\sin(\theta) \le \dfrac{cd}{4} \\[2mm] \dfrac{1}{10^{GR(\theta)/20}+1}\cdot\dfrac{2h\sin(\theta)}{c}, & \dfrac{cd}{4} < h\sin(\theta) \le \rho_{A2} \\[2mm] \dfrac{1}{10^{GR(\theta)/20}-1}\left(d - \dfrac{2h\sin(\theta)}{c}\right), & \rho_{A2} < h\sin(\theta) \le \dfrac{cd}{2} \\[2mm] \dfrac{1}{2\cdot10^{GR(\theta)/20}-1}\left(d - T + \dfrac{2h\sin(\theta)}{c}\right), & \dfrac{c(T-d)}{2} \le h\sin(\theta) \le \rho_{B1} \\[2mm] \dfrac{1}{2\cdot10^{GR(\theta)/20}+1}\left(T - \dfrac{2h\sin(\theta)}{c}\right), & \rho_{B1} < h\sin(\theta) \le \dfrac{c(T-d/2)}{2} \\[2mm] \dfrac{1}{2\cdot10^{GR(\theta)/20}+1}\left(d - T + \dfrac{2h\sin(\theta)}{c}\right), & \dfrac{c(T-d/2)}{2} \le h\sin(\theta) \le \rho_{B2} \\[2mm] \dfrac{1}{2\cdot10^{GR(\theta)/20}-1}\left|T - \dfrac{2h\sin(\theta)}{c}\right|, & \rho_{B2} < h\sin(\theta) \le \rho_{C1} \\[2mm] \dfrac{1}{2\cdot10^{GR(\theta)/20}+1}\left(d + T - \dfrac{2h\sin(\theta)}{c}\right), & \rho_{C1} < h\sin(\theta) \le \dfrac{c(T+d/2)}{2} \\[2mm] \dfrac{1}{2\cdot10^{GR(\theta)/20}+1}\left(-T + \dfrac{2h\sin(\theta)}{c}\right), & \dfrac{c(T+d/2)}{2} \le h\sin(\theta) \le \rho_{C2} \\[2mm] \dfrac{1}{2\cdot10^{GR(\theta)/20}-1}\left(T + d - \dfrac{2h\sin(\theta)}{c}\right), & \rho_{C2} < h\sin(\theta) \le \dfrac{c(T+d)}{2} \\[2mm] 0, & otherwise \end{cases} \tag{57.8}$$

Now the functional relations between the peak multipath error and the antenna parameters are established.

57.3 The Design of Antenna Up-To-Down Gain Ratio with a Fixed Antenna Height

The multipath mitigation ability of a receiver is fixed if its' code tracking loop configuration and the corresponding algorithm are fixed. If the upper limit of the peak multipath error is given and it can not be fulfilled by the receiver processing only, carefully designing antenna up-to-down gain ratio and can be of help according to the analysis of last section.

According to Eq. 57.8, for a fixed h, the smaller the peak multipath error is demanded to be, the larger $GR(\theta)$ should be. Therefore with a given upper limit of the peak multipath error, denoted by $\bar{\varepsilon}$, the following equation should be satisfied:

$$\varepsilon_{\max}(GR_{\min}(\theta), h, \theta) = \bar{\varepsilon} \tag{57.9}$$

where $GR_{\min}(\theta)$ is the required minimum up-to-down gain ratio at the angle θ. Referring to Eq. 57.8, the expression of $GR_{\min}(\theta)$ for Double-delta technique can be derived as Eq. 57.10 where $\rho'_{A1} = \dfrac{c(d - 2\bar{\varepsilon})}{4}$, $\rho'_{A2} = \frac{c(d+2\bar{\varepsilon})}{4}$, $\rho'_{B1} = \frac{c(2T-d-2\bar{\varepsilon})}{4}$, $\rho'_{B2} = \frac{c(2T-d+2\bar{\varepsilon})}{4}$, $\rho'_{C1} = \frac{c(2T+d-2\bar{\varepsilon})}{4}$, $\rho'_{C2} = \frac{c(2T+d+2\bar{\varepsilon})}{4}$.

$$GR_{\min}(\theta) = \begin{cases} 10\log_{10}\left(1 + \frac{2h\sin(\theta)}{c\bar{\varepsilon}}\right)^2, & 0 < h\sin(\theta) \leq \rho'_{A1} \\ 10\log_{10}\left(\frac{cd-2h\sin(\theta)}{c\bar{\varepsilon}} - 1\right)^2, & \rho'_{A1} < h\sin(\theta) \leq \frac{cd}{4} \\ 10\log_{10}\left(\frac{2h\sin(\theta)}{c\bar{\varepsilon}} - 1\right)^2, & \frac{cd}{4} < h\sin(\theta) \leq \rho'_{A2} \\ 10\log_{10}\left(\frac{cd-2h\sin(\theta)}{c\bar{\varepsilon}} + 1\right)^2, & \rho'_{A2} < h\sin(\theta) \leq \frac{cd}{2} \\ 10\log_{10}\left(\frac{c(d-T)+2h\sin(\theta)}{2c\bar{\varepsilon}} + \frac{1}{2}\right)^2, & \frac{c(T-d)}{2} \leq h\sin(\theta) \leq \rho'_{B1} \\ 10\log_{10}\left(\frac{cT-2h\sin(\theta)}{2c\bar{\varepsilon}} - \frac{1}{2}\right)^2, & \rho'_{B1} < h\sin(\theta) \leq \frac{c(T-d/2)}{2} \\ 10\log_{10}\left(\frac{c(d-T)+2h\sin(\theta)}{2c\bar{\varepsilon}} - \frac{1}{2}\right)^2, & \frac{c(T-d/2)}{2} < h\sin(\theta) \leq \rho'_{B2} \\ 10\log_{10}\left(\left|\frac{cT-2h\sin(\theta)}{2c\bar{\varepsilon}}\right| + \frac{1}{2}\right)^2, & \rho'_{B2} < h\sin(\theta) \leq \rho'_{C1} \\ 10\log_{10}\left(\frac{c(T+d)-2h\sin(\theta)}{2c\bar{\varepsilon}} - \frac{1}{2}\right)^2, & \rho'_{C1} < h\sin(\theta) \leq \frac{c(T+d/2)}{2} \\ 10\log_{10}\left(\frac{-cT+2h\sin(\theta)}{2c\bar{\varepsilon}} - \frac{1}{2}\right)^2, & \frac{c(T+d/2)}{2} < h\sin(\theta) \leq \rho'_{C2} \\ 10\log_{10}\left(\frac{c(T+d)-2h\sin(\theta)}{2c\bar{\varepsilon}} + \frac{1}{2}\right)^2, & \rho'_{C2} < h\sin(\theta) \leq \frac{c(T+d)}{2} \end{cases} \tag{57.10}$$

Hence for an antenna with a given height, the peak multipath error of the receiver is less than $\bar{\varepsilon}$ if the up-to-down gain ratio is larger than the minimum calculated from Eq. 57.10.

57.4 Summary

With the development of GNSS, the multipath error is the last obstacle to improving the performance of high accuracy applications, especially GNSS reference station receivers. By integrating the typical GNSS reference station receiving scenario and one widely-used receiver-internal multipath mitigation technique (Double-delta technique), this paper proposes theoretical formula for antenna up-to-down gain ratio design given the upper limit of receiver's peak multipath error and antenna height. It can be concluded based on the analysis in this paper that:

With a given upper limit of the peak multipath error $\bar{\varepsilon}$ and a fixed receiver-internal multipath mitigation technique, the receiver's multipath mitigation ability can be improved by carefully designing the antenna up-to-down gain ratio and selecting the appropriate antenna height.

With a given $\bar{\varepsilon}$ and a certain antenna height, the antenna's up-to-down gain ratio can be designed according to Eq. 57.10 for Double-delta technique.

In order to make the antenna and the receiver-internal technique cooperate with each other in an unchanged receiving scenario, the antenna design should be in accord with the receiver-internal technique. Only Double-delta technique are analyzed in this paper but the analytical method can be applied to other techniques. The details of this method applying into Narrow-correlator technique can be found in [11].

The formula for antenna up-to-down gain ratio design proposed in this paper are quantitative and exercisable. This research is substantial to the multipath-rejecting antenna design for GNSS reference station receivers.

References

1. Braasch M (1994) Optimum antenna design for DGNSS ground reference stations [C]. In: Proceedings of ION GPS, pp 1291–1297
2. Townsend B, Fenton P (1994) A practical approach to the reduction of pseudorange multipath errors in a L1 GNSS receiver [C]. In: Proceedings of ION GPS, pp 143–148
3. Garin L, van Diggelen F, Rousseau JM (1996) Strobe & Edge correlator multipath mitigation for code [C]. In: Proceedings of ION GPS, pp 657–664
4. Braasch M (1996) GNSS multipath model validation [C]. In: Proceedings of IEEE Position location and navigation symposium, pp 672–678
5. Tranquilla JM, Carr JP, Al-Rizzo HM (1994) Analysis of a choke ring ground-plane for multipath control in global positioning system applications [J]. IEEE Trans Antennas Propag 42(7):905–911
6. Kunysz W (2000) High performance GNSS pinwheel antenna. In: Proceedings of ION GPS, pp 2500–2511
7. Counselman CC (1999) Multipath-rejecting GNSS antenna [J]. IEEE Proc 87(1):86–91
8. Van Nee RDJ (1992) Multipath effects on GPS code phase measurement [J]. Navigation 39(2):177–190
9. Lee YC (2002) Compatibility of the new military GPS signals with non-aviation receivers [C]. In: Proceedings of the institute of navigation 58th annual meeting/cigtf 21st guidance test symposium, pp 581–597
10. Van Nee RDJ (1992) The multipath estimating delay lock loop [C]. In: Proceedings of IEEE 2nd internal symposium on spread spectrum techniques and applications, pp 39–42
11. Liu H, Cheng X, Wang F (2011) An Investigation on the optimum height and up-to-down gain ratio for multipath-rejecting antennas of gnss reference station receivers [C]. In: Proceedings of CSNC, pp 913–919 (In Chinese)

Chapter 58
The Difference Method of 2-Dimensional Euler Equations With Flux Vector Splitting

Zhifeng Yin and Xinfeng Ge

Abstract It is important to find an effective method of capturing shock waves in computational fluid dynamics (CFD) field,in this paper the basic properties of the 2-D Euler equations are learned by studying hyperbolic PDEs, the Steger-Warming flux vector splitting method and the NND scheme are given. The NND scheme is used for solving 2-D Euler equations by improved Steger-Warming flux vector splitting and it shows that the numerical oscillation is restrained. The finite difference method has higher order of accuracy and better efficiency.

58.1 Introduction

Building an effective method to capture shock waves that has been an important part of the study in computational fluid dynamics (CFD) field [1]. John Von Neumann first proposed the use of artificial viscosity method to capture shock,and the method of artificial viscosity is still one of the core in the CFD. The emergence of artificial viscosity means losing the part of information, and lowering the computational accuracy. For the non-physical oscillations problems generated near the shock wave, Harten [2–4] proposed the total variation difference scheme- the concept of TVD scheme, which the total variation is decreasing,and constructed the specific TVD scheme with second order accuracy. meanwhile, Steger and Warming [5] proposed a new class of upwind scheme—vector splitting scheme (FVS scheme). Steger-Warming splitting method are often used by other schemes to better capture the shock wave for its characteristics of high efficiency and easy to program. The difference

Z. Yin (✉) · X. Ge
College of Electrical and Information Engineering, Xuchang University,
461000 Xuchang, China
e-mail: yinzhifeng11@126.com

method that can automatically capture the shock wave is proposed based on the combination of improved Steger-Warming splitting method and NND scheme. The algorithm maintained the characteristics of high efficiency and easy to program that Steger-Warming splitting method have had, and overcomed the numerical oscillation near the shock wave that in Steger-Warming splitting method, and had accuracy and maneuverability. Method proposed in this paper have some reference value to the calculation of vector splitting.

58.2 The FVS Split of Euler Equations

58.2.1 Euler Equations

Conservation form of two-dimensional Euler equations [6] are:

$$\frac{\partial U}{\partial t} + \frac{\partial F}{\partial x} + \frac{\partial G}{\partial y} = 0 \tag{58.1}$$

Which $U = \begin{pmatrix} \rho \\ \rho u \\ \rho u \\ E \end{pmatrix}, F = \begin{pmatrix} \rho u \\ \rho u^2 + p \\ \rho uv \\ (E+p)u \end{pmatrix}, G = \begin{pmatrix} \rho v \\ \rho vu \\ \rho v^2 + p \\ (E+p)v \end{pmatrix}$, Therein

$$E = \frac{p}{\gamma - 1} + \frac{1}{2}\rho(u^2 + v^2), a = \sqrt{\frac{\gamma p}{\rho}}, H = \frac{E+p}{\rho} = \frac{1}{2}(u^2 + v^2) + \frac{a^2}{\gamma - 1} = \frac{1}{2}(u^2 + v^2) + \frac{\gamma p}{(\gamma - 1)\rho}$$

58.2.2 Flux Vector Splitting Technique

Jacobian matrix is

$$A = \frac{\partial F}{\partial U} = \begin{pmatrix} 0 & 1 & 0 & 0 \\ \frac{1}{2}(\gamma - 3)u^2 + \frac{1}{2}(\gamma - 1)v^2 & (3 - \gamma)u & (1 - \gamma)v & \gamma - 1 \\ -uv & v & u & 0 \\ \frac{1}{2}(\gamma - 2)(u^3 + uv^2) - \frac{a^2 u}{(\gamma - 1)} & \frac{1}{2}(3 - 2\gamma)u^2 + \frac{1}{2}v^2 + \frac{a^2}{(\gamma - 1)} & (1 - \gamma)uv & \gamma u \end{pmatrix},$$

$$B = \frac{\partial G}{\partial U} = \begin{pmatrix} 0 & 0 & 1 & 0 \\ uv & v & u & 0 \\ \frac{1}{2}(\gamma - 1)u^2 - \frac{1}{2}(\gamma - 3)v^2 & (1 - \gamma)u & (3 - \gamma)v & \gamma - 1 \\ \frac{1}{2}(\gamma - 2)(v^3 + u^2 v) - \frac{a^2 v}{(\gamma - 1)} & (1 - \gamma)uv & \frac{1}{2}(3 - 2\gamma)v^2 + \frac{1}{2}u^2 + \frac{a^2}{(\gamma - 1)} & \gamma v \end{pmatrix}$$

$$\tag{58.4}$$

Matrix A and B were similarly transformed respectively as follows:

$$A = M\Lambda_1 M^{-1}, B = N\Lambda_2 N^{-1} \tag{58.5}$$

Therein, the expressions of eigenvalues matrices is respectively:

$$\Lambda_1 = diag[u,\ u,\ \mathrm{u} + \mathrm{a},\ \mathrm{ua} - \mathrm{a}],\ \Lambda_2 = diag[v,\ \mathrm{v},\ \mathrm{v} + \mathrm{a},\ \mathrm{v} - \mathrm{a}] \tag{58.6}$$

Therein $\lambda_1^{(1)} = \lambda_1^{(2)} = u, \lambda_1^{(3)} = u + a, \lambda_1^{(4)} = u - a;\ \lambda_2^{(1)} = \lambda_2^{(2)} = v, \lambda_2^{(3)} = v + a, \lambda_2^{(4)} = v - a$

The left and right eigenvector matrices of A and B are respectively:

$$M = \begin{pmatrix} 1 & 0 & \frac{\rho}{\sqrt{2}a} & \frac{\rho}{\sqrt{2}a} \\ u & 0 & \frac{\rho}{\sqrt{2}a}(u+a) & \frac{\rho}{\sqrt{2}a}(u-a) \\ v & -\rho & \frac{\rho v}{\sqrt{2}a} & \frac{\rho v}{\sqrt{2}a} \\ \frac{1}{2}(u^2+v^2) & -\rho v & \frac{\rho}{2\sqrt{2}a}(u^2+v^2) + \frac{\rho a + \rho u(\gamma-1)}{\sqrt{2}(\gamma-1)} & \frac{\rho}{2\sqrt{2}a}(u^2+v^2) + \frac{\rho a - \rho u(\gamma-1)}{\sqrt{2}(\gamma-1)} \end{pmatrix}$$

$$M^{-1} = \begin{pmatrix} 1 - \frac{(\gamma-1)}{2a^2}(u^2+v^2) & \frac{(\gamma-1)u}{a^2} & \frac{(\gamma-1)v}{a^2} & \frac{(1-\gamma)}{a^2} \\ \frac{v}{\rho} & 0 & -\frac{1}{\rho} & 0 \\ \frac{(\gamma-1)}{2\sqrt{2}\rho a}(u^2+v^2) - \frac{u}{\sqrt{2}\rho} & \frac{1}{\sqrt{2}\rho} - \frac{(\gamma-1)u}{\sqrt{2}\rho a} & -\frac{(\gamma-1)v}{\sqrt{2}\rho a} & \frac{(\gamma-1)}{\sqrt{2}\rho a} \\ \frac{(\gamma-1)}{2\sqrt{2}\rho a}(u^2+v^2) + \frac{u}{\sqrt{2}\rho} & -\frac{1}{\sqrt{2}\rho} - \frac{(\gamma-1)u}{\sqrt{2}\rho a} & -\frac{(\gamma-1)v}{\sqrt{2}\rho a} & \frac{(\gamma-1)}{\sqrt{2}\rho a} \end{pmatrix}$$

$$\tag{58.7}$$

$$N^{-1} = \begin{pmatrix} 1 - \frac{(\gamma-1)}{2a^2}(u^2+v^2) & \frac{(\gamma-1)u}{a^2} & \frac{(\gamma-1)v}{a^2} & \frac{(1-\gamma)}{a^2} \\ -\frac{u}{\rho} & \frac{1}{\rho} & 0 & 0 \\ \frac{(\gamma-1)}{2\sqrt{2}\rho a}(u^2+v^2) - \frac{v}{\sqrt{2}\rho} & \frac{(1-\gamma)u}{\sqrt{2}\rho a} & \frac{1}{\sqrt{2}\rho} - \frac{(\gamma-1)v}{\sqrt{2}\rho a} & \frac{(\gamma-1)}{\sqrt{2}\rho a} \\ \frac{(\gamma-1)}{2\sqrt{2}\rho a}(u^2+v^2) + \frac{v}{\sqrt{2}\rho} & \frac{(1-\gamma)u}{\sqrt{2}\rho a} & -\frac{1}{\sqrt{2}\rho} - \frac{(\gamma-1)v}{\sqrt{2}\rho a} & \frac{(\gamma-1)}{\sqrt{2}\rho a} \end{pmatrix}$$

$$N = \begin{pmatrix} 1 & 0 & \frac{\rho}{\sqrt{2}a} & \frac{\rho}{\sqrt{2}a} \\ u & \rho & \frac{\rho}{\sqrt{2}a}u & \frac{\rho}{\sqrt{2}a}u \\ v & 0 & \frac{\rho}{\sqrt{2}a}(v+a) & \frac{\rho}{\sqrt{2}a}(v-a) \\ \frac{1}{2}(u^2+v^2) & \rho u & \frac{\rho}{2\sqrt{2}a}(u^2+v^2) + \frac{\rho a + \rho v(\gamma-1)}{\sqrt{2}(\gamma-1)} & \frac{\rho}{2\sqrt{2}a}(u^2+v^2) + \frac{\rho a - \rho v(\gamma-1)}{\sqrt{2}(\gamma-1)} \end{pmatrix}$$

$$\tag{58.8}$$

There are the following relationships between the matrix M and N

$$C = M^{-1}N = \begin{pmatrix} 1 & 0 & 0 & 0 \\ 0 & 0 & -1/\sqrt{2} & 1/\sqrt{2} \\ 0 & 1/\sqrt{2} & 1/2 & 1/2 \\ 0 & -1/\sqrt{2} & 1/2 & 1/2 \end{pmatrix},$$

$$C^{-1} = N^{-1}M = \begin{pmatrix} 1 & 0 & 0 & 0 \\ 0 & 0 & 1/\sqrt{2} & -1/\sqrt{2} \\ 0 & -1/\sqrt{2} & 1/2 & 1/2 \\ 0 & 1/\sqrt{2} & 1/2 & 1/2 \end{pmatrix}$$

(58.9)

From formular (58.12) a can be seen that matrix C and C^{-1} has nothing to do with flow variables.

Now splitting the flux vector,and first, the eigenvalues of Jacobian matrix,that are $\lambda_1^{(l)}$, $\lambda_2^{(l)}$, split the sum form of two:

$$\lambda_1^{(l)} = \lambda_1^{(l)+} + \lambda_1^{(l)-}; \lambda_1^{(l)+} \geq 0, \lambda_1^{(l)-} \leq 0; \lambda_2^{(l)} = \lambda_2^{(l)+} + \lambda_2^{(l)-}; \lambda_2^{(l)+} \geq 0, \lambda_2^{(l)-} \leq 0$$
$$l = 1, 2, 3, 4$$

(58.10)

According to flux vector splitting method

$$\lambda_1^{(l)\pm} = (\lambda_1^{(l)} \pm |\lambda_1^{(l)}|)/2; \lambda_2^{(l)\pm} = (\lambda_2^{(l)} \pm |\lambda_2^{(l)}|)/2$$ (58.11)

Thus, the eigenvalues matrix after splitting are respectively:

$$\Lambda_1^{\pm} = diag[\lambda_1^{(1)\pm}, \lambda_1^{(2)\pm}, \lambda_1^{(3)\pm}, \lambda_1^{(4)\pm}]; \Lambda_2^{\pm} = diag[\lambda_2^{(1)\pm}, \lambda_2^{(2)\pm}, \lambda_2^{(3)\pm}, \lambda_2^{(4)\pm}]$$

(58.12)

And the corresponding Jacobian matrices after splitting are respectively:

$$A^{\pm} = M\Lambda_1^{\pm}M^{-1}, B^{\pm} = N\Lambda_2^{\pm}N^{-1}$$ (58.13)

The corresponding flux vector can be obstained in the end after splitting

$$F^{\pm} = A^{\pm}U, G^{\pm} = B^{\pm}U$$ (58.14)

The expressions as follows:

$$F^+ = \frac{\rho}{2\gamma} \begin{pmatrix} \lambda_1^{(4)+} + 2(\gamma-1)\lambda_1^{(2)+} + \lambda_1^{(3)+} \\ (u-a)\lambda_1^{(4)+} + 2(\gamma-1)u\lambda_1^{(2)+} + (u+a)\lambda_1^{(3)+} \\ v\lambda_1^{(4)+} + 2(\gamma-1)v\lambda_1^{(2)+} + v\lambda_1^{(3)+} \\ (H-ua)\lambda_1^{(4)+} + (\gamma-1)(u^2+v^2)\lambda_1^{(2)+} + (H+ua)\lambda_1^{(3)+} \end{pmatrix}$$

$$F^- = \frac{\rho}{2\gamma} \begin{pmatrix} \lambda_1^{(4)-} + 2(\gamma-1)\lambda_1^{(2)-} + \lambda_1^{(3)-} \\ (u-a)\lambda_1^{(4)-} + 2(\gamma-1)u\lambda_1^{(2)-} + (u+a)\lambda_1^{(3)-} \\ v\lambda_1^{(4)-} + 2(\gamma-1)v\lambda_1^{(2)-} + v\lambda_1^{(3)-} \\ (H-ua)\lambda_1^{(4)-} + (\gamma-1)(u^2+v^2)\lambda_1^{(2)-} + (H+ua)\lambda_1^{(3)-} \end{pmatrix} \qquad (58.15)$$

$$G^+ = \frac{\rho}{2\gamma} \begin{pmatrix} \lambda_2^{(4)+} + 2(\gamma-1)\lambda_2^{(2)+} + \lambda_2^{(3)+} \\ u\lambda_2^{(4)+} + 2(\gamma-1)u\lambda_2^{(2)+} + u\lambda_2^{(3)+} \\ (v-a)\lambda_2^{(4)+} + 2(\gamma-1)v\lambda_2^{(2)+} + (v+a)\lambda_2^{(3)+} \\ (H-va)\lambda_2^{(4)+} + (\gamma-1)(u^2+v^2)\lambda_2^{(2)+} + (H+va)\lambda_2^{(3)+} \end{pmatrix}$$

$$G^- = \frac{\rho}{2\gamma} \begin{pmatrix} \lambda_2^{(4)-} + 2(\gamma-1)\lambda_2^{(2)-} + \lambda_2^{(3)-} \\ u\lambda_2^{(4)-} + 2(\gamma-1)u\lambda_2^{(2)-} + u\lambda_2^{(3)-} \\ (v-a)\lambda_2^{(4)-} + 2(\gamma-1)v\lambda_2^{(2)-} + (v+a)\lambda_2^{(3)-} \\ (H-va)\lambda_2^{(4)-} + (\gamma-1)(u^2+v^2)\lambda_2^{(2)-} + (H+va)\lambda_2^{(3)-} \end{pmatrix} \qquad (58.16)$$

The derivative of positive and negative flux is noncontinuous near the sign reversal point of Eigenvalue [5], and leading the flux vector splitting methods not to be transited smoothly. Therefore, turn flux F, G into continuous function of $\lambda_1^{(3)}$, $\lambda_1^{(4)}$, $\lambda_1^{(3)}$ and $\lambda_2^{(4)}$.

Assumed $\lambda_1^{(2)\pm} = (\lambda_1^{(3)\pm} + \lambda_1^{(4)\pm})/2$; $\lambda_2^{(2)\pm} = (\lambda_2^{(3)\pm} + \lambda_2^{(4)\pm})/2$ $\qquad$ (58.17)

So far, we have been completed splitting the flux F, G.

58.3 NND Scheme in Two-Demensional and New Scheme

The NND scheme [7] is a computational scheme that has a non-volatile, no free parameters characeristics, and can effectively suppress numerical calculation oscillation. From the modified equation in the scheme, different schemes were used according to the location of relative break points, and physical meaning is clear. For Eq. (58.1), Explicit scheme of NND scheme can be expressed as follows:

Fig. 1 The pressure distribution of $y = 0.5$
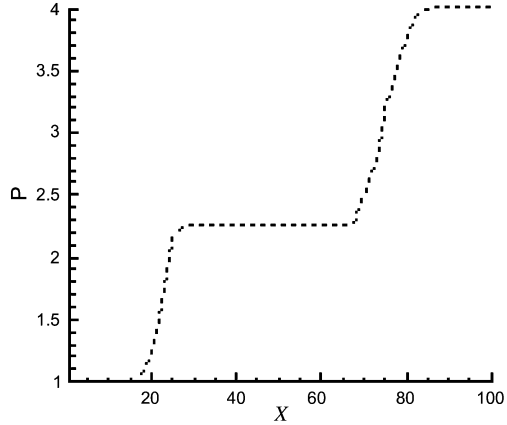
$$U_{i,j}^{n+1} = U_{i,j}^{n} - \frac{\Delta t}{\Delta x}(\overline{F}_{i+1/2}^{n} - \overline{F}_{i-1/2}^{n}) - \frac{\Delta t}{\Delta y}(\overline{G}_{j+1/2}^{n} - \overline{G}_{j-1/2}^{n}) \qquad (58.18)$$

Therein

$$\overline{F}_{i+1/2} = F_{i+1/2,L}^{+} + F_{i+1/2,R}^{-}, F_{i+1/2,L}^{+} = F_{i,j}^{+} + \frac{1}{2}\mathrm{min\,mod}(\Delta F_{i-1/2,j}^{+}, \Delta F_{i+1/2,j}^{+})$$

$$F_{i+1/2,R}^{-} = F_{i+1,j}^{-} - \frac{1}{2}\mathrm{min\,mod}(\Delta F_{i+1/2,j}^{-}, \Delta F_{i+3/2,j}^{-}), \Delta F_{i+1/2,j}^{+} = F_{i+1,j}^{+} - F_{i,j}^{+}, \Delta F_{i+1/2,j}^{-} = F_{i+1,j}^{-} - F_{i,j}^{-}$$

$$\overline{G}_{j+1/2} = G_{L,j+1/2}^{+} + G_{R,j+1/2}^{-}, G_{L,j+1/2}^{+} = G_{i,j}^{+} + \frac{1}{2}\mathrm{min\,mod}(\Delta G_{i,j-1/2}^{+}, \Delta G_{i,j+1/2}^{+}), G_{R,j+1/2}^{-}$$

$$= G_{i,j+1}^{-} - \frac{1}{2}\mathrm{min\,mod}(\Delta G_{i,j+1/2}^{-}, \Delta G_{i,j+3/2}^{-})$$

$$\Delta G_{i,j+1/2}^{+} = G_{i,j+1}^{+} - G_{i,j}^{+}, \Delta G_{i,j+1/2}^{-} = G_{i,j+1}^{-} - G_{i,j}^{-}$$

$$\mathrm{min\,mod}(x, y) = \begin{cases} 0 & x \cdot y \leq 0 \\ \mathrm{sign}(x) \cdot \mathrm{min}(|x|, |y|) & x \cdot y > 0 \end{cases}$$

In summary, formular (58.15, 58.16) and (58.18) are the difference method combining the improved Steger-Warming flux vector splitting.

58.4 Numerical Experiments

The calculation of the flow field in shock wave Pipe is the common example to test ability in capturing the shock wave. The answer to this problem can compare to the Riemann's analytical solution [8]. The initial equation is 2-dimensional unconstant Euler equations (58.1), the initial conditions are uniform flow field.

Inlet conditions: the inlet density $\rho = 1.0$, mach number $Ma = 2.9$, inlet angle $\beta_1 = 29$, inlet total pressure $p = 1.0$, air specific heat ratio $\gamma = 1.4$. Outlet condition:

$$\frac{\partial p}{\partial x} = \frac{\partial \rho}{\partial x} = \frac{\partial u}{\partial x} = \frac{\partial v}{\partial x} = 0$$

The pressure distribution of $y = 0.5$ is shown in Fig. 58.1. From Fig. 58.1 can be seen that: The computational scheme that constructed by combination of Steger-Warming splitting vector method and the NND scheme has good ability in capturing shock wave,the calculated results and the theoretical values are in good agreement, and there is no calculated value oscillation appeared near shock wave.

58.5 Conclusion

Steger-Warming flux vector splitting scheme is becoming the first choice in CFD calculations because of its high precision and efficiency in for numerical calculation of Euler equations, the Steger-Warming flux vector splitting scheme is improved in this paper and make the scheme transit smoothly near the sign reversal point of Eigenvalue. A differential algorithm is constituted by combined the improved Steger-Warming flux vector splitting scheme and the NND scheme, the flux decomposition term in NND scheme is processed by Steger-Warming flux vector splitting method,so that algorithm has higher efficiency. By solving the two-dimensional Euler equations, numerical experiment results can be verified that differentiate scheme can inhibit oscillations and maintain precision and stability, ensure that the shock wave in flow field is captured effectively. Method used in this paper has some reference value about the calculation of flux vector splitting.

References

1. Su MD, Huang SY (1997) The computational fluid dynamic basis. Tsinghua University Press,
2. Harten A, Hyman JM, Lax PD (1976) On finite difference approximations and entropy condition for shocks. Commun Pure Appl Math 29:297–322
3. Harten A (1983) High resolution schemes for hyperbolic conservation laws. J Comput Phys 49:357–393
4. Harten A, Engquist B, Osher S et al (1987) Uniformly high order essentially non-oscillatory schemes. J Comput Phys 71:231–303
5. Steger JL, Warming RF (1981) Flux vector splittingflux vector splitting of the inviscid gasdynamic equations with application to finite difference method. J Comput Phys 40:263–293
6. Zhang HX (1988) Non-oscillatory and non-free-parameter dissipation difference scheme. Acta Aerodynamica Sinica 6:143–165
7. Zhang HX, Zhuang FG (1992) NND scheme and their application to numerical simulation of two and three dimensional flows. Adv Appl Mech 29:193–256
8. Yahiaoui T, Adjlout L, Imine O (2010) Experimental investigation of in-line tube bundles. Mechanika 5:37−43

Chapter 59
The Information Key Technologies for Quality and Safety Monitor and Management of Agricultural Products

Ying Yu, Jin Li and Xiangyang Qin

Abstract This paper studied on the information key technologies which were applied in quality and safety monitor and management of agricultural products and pointed out that the important role of the information technologies. The rapid detection technology included of three aspects: quality inspection (machine vision, near infrared spectroscopy, electronic nose etc.), pesticide residue detection (ELISA, biosensor and Raman spectra etc.), and producing environmental monitoring (mainly used X-ray rapid measurement of soil heavy metals etc.), using of these technologies, some advanced new detection systems and devices to be developed gradually. Referred to auto identification technology, the common technologies of bar codes and RFID were introduced. They were widely used in the building of an agricultural products quality and safety traceability management system, which could cover production, processing, circulation and consumption etc. whole process, and is helpful in agricultural products recall. In the system or platform of quality and safety agricultural products, network technology and database technology were applied to supply and demand inquiry, tracking and other function.

Y. Yu (✉) · J. Li · X. Qin
National Engineering Research Center for Information Technology in Agriculture,
Beijing Academy of Agriculture and Forestry Sciences, Beijing Agriculture Building A819,
Shuguang Huayuan Middle Road 11#, Haidian district, 100097 Beijing,
People's Republic of China
e-mail: yuy@nercita.org.cn

59.1 Introduction

Quality and safety of agriculture products is currently a hot topic, but also present must be solved problem of implementation agricultural and rural economic restructuring, improving the competitiveness of agricultural products. As in China, the quality and safety of agricultural products started late, the foundation is poor, the technology is weak, and its overall level cannot meet the current demand of agriculture development. Especially with the agricultural development, for pursuit of increased output, the pesticide, fertilizer and plant growth regulator is heavily used. Meanwhile, the agriculture market in China is a discrete market which is composed of many small producers and operators, the supply chain of agriculture is long, and many other factors have led to excessive pesticide residues in agricultural products, environmental degradation etc. a series of events to occur, so it is difficult to manage and monitor the agricultural products quality and safety. The traditional monitoring methods cannot meet the social demand for quality and safety of agricultural products [1]. Information technology was applied to monitoring quality and safety of agricultural products, which could timely, accurately, efficiently acquire and process all relevant information of agricultural products quality and safety, and connect with the existing monitoring technology; to dramatically improve the level of monitoring quality and safety of agricultural products, ensure food safety [2].

Quality and safety issues can be analyzed from various angles. Food from farm to table, to go through the production, processing, distribution and many other aspects, the food supply systems become more complex and international [3].

Information systems are concerned with data capture, storage, analysis and retrieval. In the context of food safety management they are vital to assist decision making in a short time frame, potentially allowing decisions to be made and practices to be acted in real time. Databases with information on microorganisms pertinent to the identification of food borne pathogens, response of microbial populations to the environment and characteristics of foods and processing conditions are the cornerstone of food safety management systems. The computer software packages to aid the practical application of HACCP and risk assessment and decision trees to bring logical sequences to establishing and modifying food safety management practices [4].

There is an urgent need to develop automated inspection systems that can operate on-line in real-time in the poultry slaughter plant environment. These systems should be able to accurately detect and identify carcasses unfit for human consumption. The study of Benhai Xiong etc. adopted animal identification, intelligent personal digital assistant (PDA) reading and writing, general packet radio service (GPRS), and other information technologies, proposed a pork tracking and traceability infrastructure based on pork production substrate flow and data flow, designs the metadata structure and related databases for farming, slaughtering, and retailing sector based on intensive pig farming and small hold pig farming, developed three different data-recording systems, and finally

established a public network platform for the information inquiry in light of "the administrative rules on identification and rearing files for animal and poultry" in China [5].

Many applications using machine vision technology have been developed in agricultural sectors, such as land-based and aerial-based remote sensing for natural resources assessments, precision farming, postharvest product quality and safety detection, classification and sorting, and process automation. Based on an early study using industrial machine frames, a transportable dual-camera system for separating wholesome and unwholesome chicken carcasses on-line was assembled [6].

Chenglong Chuang' research integrated mechanical design, mechatronics instrumentation, X-ray and charge-coupled device (CCD) image acquisition devices, LabVIEW-based analysis and control software, and image diagnosis algorithm into the automatic X-ray quarantine scanner system which presented a new automatic and effective quarantine system for detecting pest infestation sites in agricultural products [7].

In the agricultural products and food supply chain there are increased demands for traceability. The outbreak of recent food safety incidents has highlighted the importance of being able to track forward and trace back product information throughout the supply chain with the purpose of decreasing product risk and enabling recalls. Polymeros Chrysochou indicated that technologies with the ability to track forward and trace back product-related information in the food supply chain. The description of the results is organized around the four trace-ability information carriers (the RFIDs, fish label, barcodes on fruit and fruits edible label) used in the study protocol. For each carrier, the benefits and drawbacks as evaluated by the participants are discussed [8].

In this paper, the representative information technologies in the control and management of agricultural products quality and safety are introduced: rapid detection, automatic identification, network technology, database technology and the internet of things [9]. It can achieved the whole production process (before the production, production process, and after production) information collection and services sharing, improve the logistics of agricultural products efficiency and service quality, complete a intact network monitoring and management system of quality and safety of agricultural products.

59.2 Rapid Detection Technology

The rapid detection technology of agricultural products mainly included of three aspects: quality inspection (machine vision, near infrared spectroscopy, electronic nose etc.), pesticide residue detection (ELISA, biosensor and Raman spectra etc.), and agricultural environmental monitoring (mainly used X-ray rapid measurement of soil heavy metals).

59.2.1 Quality Inspection

Increasing safety events caused by food and agricultural products quality problems has caught more and more attention; therefore nondestructive fast detection of food and agricultural products quality becomes necessary. At present, fast detection methods commonly used include chemical colorimetric method, near infrared spectroscopy (NIRS) technique, machine vision, electronic nose, bio-sensor technique, biochip detection method, bioluminescence method, and so on. NIRS technique has found wide application in food and agricultural products quality detection because of its characteristics such as very high speed, no sample preparation, non-destruction, no pollution, low cost etc. [10].

At present, NIRS technique had applied in online quality detection and control of fruit, fish, meat, milk, grain, fermentation of cheese and alcohol etc. Fat, protein and water were determined by visible and NIR transmittance spectroscopy in chilled pork [11]. Jingzhu Wu etc. built NIR models for a sample set composed of different types of milk powder. With 70 samples provided by one manufacturer, 6 NIR models including acidity, fat, lactose, sucrose, protein and ash, were built by optimizing algorithms [12]. In order to investigate the stability and application range of near infrared spectroscopy (NIR) models, four calibration models (local model, transferred local model, global model, and optimized global model) were constructed [13]. In the present study, improved laser-induced light backscattering imaging was studied regarding its potential for analyzing apple SSC and fruit flesh firmness [14]. In university of California, Davis, a new test scanner was developed which used in testing the wine whether deterioration without opening the packaging. The development of the scanner referred to the magnetic resonance imaging (MRI) technology which is widely used in the field of medicine; it can detect acetic acid in wine [15]. In Germany, there was a light, rapid and effective PEN2 electronic nose system, it was used in inspecting and testing gaseous matter and steamy, now all the scent of meat, fruit, yogurt, milk, alcohol and coffee etc. could be tested by it [16].

59.2.2 Pesticide Residue Test Technology

Currently, pesticide residue test technologies mainly include of enzyme-linked immune sorbent assay (ELISA), bio-sensor and Raman spectroscopy etc. Using of these technologies, some advanced new detection systems and devices to be developed gradually.

Beijing CapitalBio Corporation and Beijing Entry-Exit Inspection and Quarantine Bureau cooperated to develop "Protein Chip Veterinary drug residues in protein microarray platform", multiple samples in a variety of veterinary drug residues could be detect on the same chip [17]. Changchun Jilin University Instrument Co., Ltd developed a serial of measuring instruments, one of them is

"Pesticide Residues in Food Supplies fast detector", it can be applied to flour, rice, soybeans, green beans surface-site rapid detection of pesticide residues [18]. Chinese Military Academy of Medical Sciences used indicator paper and the light reflection sensors to develop equipment: "portable multi-function devices for food safety rapid testing". It was the first time to blend the following technologies together, such as electro-optical technology, sensor technology, microelectronics, micro-mechanical technology, computer technology and food safety testing technology, the testing covered all kinds of food daily, each sample test only 15 s–30 min [19].

59.2.3 Agricultural Environmental Monitoring

Near infrared spectroscopy in the soil inspection has a good application, to determine soil moisture, organic matter, total nitrogen and available nitrogen, organic carbon and total carbon [20]. Laser-induced breakdown spectroscopy (LIBS) has emerged in the past 10 years as a promising technique for analysis and measure [21]. A Laser induced breakdown spectroscopy (LIBS) system used for detecting heavy metals in polluted soil was established. Samples containing various heavy metals such as Cd, Cu, Pb, Cr, Zn, Ni and soil sample were analyzed by this system, and main spectral lines of heavy metals and main elements were recognized [22].

59.3 Automatic Identification

Auto identification refers to the methods of automatically identifying objects, collecting data about them, and entering that data directly into computer systems (i.e. without human involvement). Technologies typically considered as part of auto identification include bar codes, Radio Frequency Identification (RFID), biometrics, magnetic stripes, Optical Character Recognition (OCR), smart cards, and voice recognition. At present, the main auto identification technologies which are applied in agricultural products' monitoring and management are bar code and RFID.

59.3.1 Bar Code

Bar code is the method of automatic identification and data collection. The technology was invented by inventors Joseph Woodland and Bernard Silver in 1949 [23]. The Woodland and Silver bar code can be described as a "bull's eye" symbol, made up of a series of concentric circles.

The bar code is applied in many systems such as "The Food Sentinel System", which used a bar code to help detect pathogens. This bar code traveled with the product from processing to retail, and a colored bar appears if there was contaminating bacteria present. Unlike other system, it involved the collection of a sample at a given time and place and subsequent sample preparation and analysis, the Food Sentinel System remained with the product and performed a continuous tracking for product safety. This helped alert food processors, distributors, public health officials and consumers of the presence of pathogenic bacteria of human health concern in fish, poultry, meat and other agricultural products.

The European Article Numbering (EAN) association had made some effort towards standardization by introducing several codes: the best known was the EAN/UCC Global Location Numbers (GLN) in the EAN/UCC-13 version. EAN/UCC system could identify each node of the whole process of the supply chain effectively, establish information management, transfer and exchange scheme, and thus tracking and tracing in the food supply chain from material collection, processing, packaging, storage, transportation, marketing and other aspects, timely detected problems and properly treated [24]. At present, there are more than 20 countries and regions adopt EAN/UCC system for tracing food production process, and it has got good results in application. With regard to food industry in China, because of concept, capital and technology etc., EAN/UCC system was mainly used in retail settlement, in the whole process of food supply chain there is only a few application.

59.3.2 RFID Technology

RFID is a technology that uses radio waves to communicate between an electronic tag and a reader, to track and identify an object. Earlier, RFID tags were used to keep track of cattle and are now focused more towards tracking consumer products. In recent years, Radio Frequency Identification (RFID) has received significant coverage by many interested parties [25]. One of the main uses has been in supply chain management as a way of controlling transportation costs and to make it easier to track shipments. If a truck which is equipped with one of these systems, when it is delivering items and it is possible to tell where that vehicle is and when the package or item will be delivered. RFID for animals, food and farming will become the largest RFID market of all because it will benefit the food supply chain in a huge number of ways including livestock disease control and merchandising prepared food.

Use of the technology in building of an agricultural products quality and safety traceability management system, it could cover production, processing, circulation and consumption etc. every phases (Fig. 59.1), which is helpful in quality control and product recall.
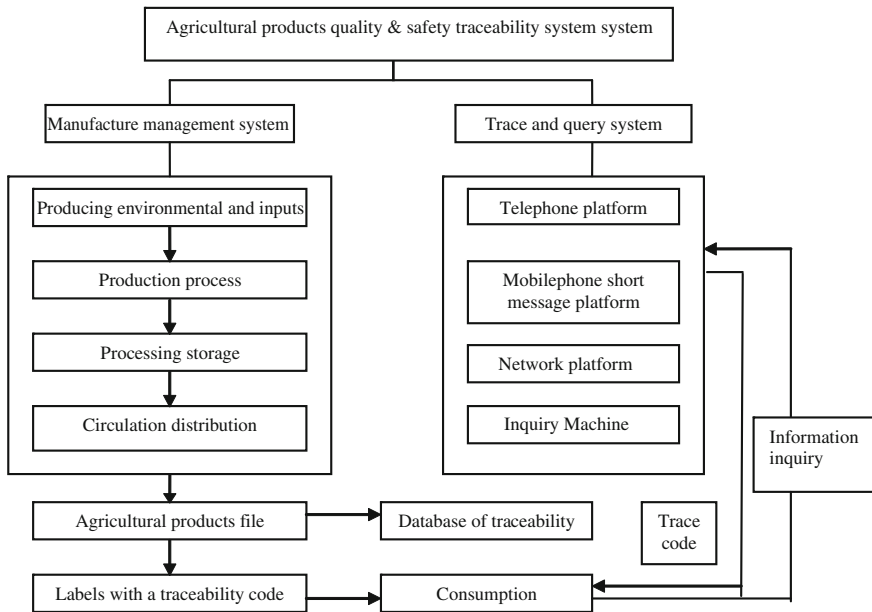
Fig. 59.1 Framework for agricultural products quality and safety traceability system

59.4 Network Technology

Network technology was applied in the traceability system for quality and safety agricultural products, the information collected was stored in the network database with web dynamic interaction technologies and Browser/Server (B/S) mode, achieved the information access and sharing, for all levels of producers and consumers to query and trace.

Guanglei Shen etc. designed and developed a beef quality and safety traceability system via internet technology. The system adopted JSP to design the Object-Oriented dynamic pages and adopted the MySQL to design the database. The B/S (Browser/Server) structure was used to put the management system on the internet, which implemented the management of beef traceability system via internet and made the beef traceability system be more networking and popularizing [26].

59.5 Database Technology

A database is a collection of information that is organized so that it can easily be accessed, managed, and updated, as an electronic filing system.

Based on analyzing agricultural products traceability and investigating the producing enterprises of agricultural products, agricultural products archive management system (FPAMS) with B/S (Browser/Server) structure was founded by using database technology [27]. In FPAMS, there were 17 datasheets such as field information, farmers' information, environment information and sales information etc. FPAMS had characteristics of reasonable structure, high security and handy manipulation, so it will be applied widely.

59.6 Conclusions

For the monitor and management in quality and safety of agricultural products, the paper has analyzed the key information technologies which applied in the field. In this paper, it has introduced rapid detection technology, automatic identification, network technology and database technology. As the example of the automatic identification technology, the framework of agricultural products quality and safety traceability system is established by using the RFID technology. Through some application of the information key technologies in the detection and traceability of agricultural products, the quality and safety was controlled. There are still many integrated and advanced information technologies which be applied in agricultural products' management, such as the internet of things, they also have the great advantage and the role of controlling the quality and safety of agricultural products.

References

1. Wang J, Lu A, Ma Z (2007) Research on agricultural products quality and safety traceability and environmental monitoring of farmland. Agric Qual Stand S1:26–28
2. Zhao C, Wang J, Zhu D et al (2002) Rural information technology. China Agricultural Science and Technology Press, Beijing
3. Zhou Y, Geng X (2002) Application of traceability in food safety. Res Agric Mod 23(6): 451–454
4. McMeekin TA, Baranyi J, Bowman J, Dalgaard P, Kirk M, Ross T, Schmid S, Zwietering MH (2006) Information systems in food safety management. Int J Food Microbiol 112: 181–194
5. Xiong B, Fu R, Lin Z, Qing Y, Yang L, Pan J (2010) A solution on pork quality traceability from farm to dinner table in Tianjin city China. Agric Sci China 9:147–156
6. Chen Y, Chao K, Kim MS (2002) Machine vision technology for agricultural applications. Comput Electron Agric 36:173–191
7. Chuang C, Ouyang C, Lin T, Yang M, Yang E, Huang T, Kuei C, Luke A, Jiang J (2011) Automatic X-ray quarantine scanner and pest infestation detector for agricultural products. Comput Electron Agric 77(1):41–59

8. Chrysochou P, Chryssochoidis G, Kehagia O (2009) Traceability information carriers. Technol Backgr Consumers Percept Technol Solut Appetite 53:322–331

9. Ma M, Qin X, Li J (2009) Review and application prospects of information technology for agricultural products safety. Chinese Agric Sci Bull 25(2):258–262

10. Sun T, Xu H, Ying Y (2009) Progress in application of near infrared spectroscopy to nondestructive on-line detection of products/food quality. Spectrosc Spectr Anal 29(1): 122–126

11. Liu K, Cheng F, Lin H, Sun T, Xu K, Hu L, Ying Y, Xu H (2009) Visible/NIR analysis of fat, protein and water in chilled pork. Spectrosc Spectr Anal 29(1):102–105

12. Wu J, Wang Y, Zhang X, Xu Y (2007) Study on quality detection of milk powder based on near infrared spectroscopy(NIR). Spectrosc Spectr Anal 27(9):1735–1738

13. Zhu D, Meng C, Tu Z, Qing Z, Ji B, Yan Y, Pan L (2009) Application of different of models near infrared spectroscopy in detection of apple juice. Transact Chinese Soc Agric Eng 25(S2):325–329

14. Qing Z, Ji B, Shi B, Zhu D, Tu Z, Zude M (2008) Improving apple fruit quality predictions by effective correction of vis-NIR laser diffuse reflecting images. Spectrosc Spectr Anal 28(6):1273–1277

15. Ya A (2006) The United States developed a wine quality detection scanner. Food Sci 27(10):563

16. Wang X, Cao Y, Jun Ma, Huang Feng, Yu A (2006) New advances in fast detection techniques for quality and security control of farm produce. Mod Scientific Instrum 1:121–123

17. Wu L, Dong J (2005) Simultaneous detection of a variety of veterinary drug residues, "protein chip for detection of veterinary drug residues platform". Jiangxi Feed 3:41

18. Feng G, Wang X, Xie F, Yu A (2005) The in Situ detection of residual pesticide in rice, flour, fruit and vegetable. Mod Sci Instr 1:86–88

19. Wang X, Wu Z (2005) Food safety on-site rapid detection equipment comes out. Fam Tradit Chinese Med 12:13

20. Chen P, Liu L, Wang J, Shen T, Lu A, Zhao C (2008) Real-time analysis of soil n and p with near infrared diffuse reflectance spectroscopy. Spectrosc Spectr Anal 28(12):295–298

21. Wang J, Zhang N, Hou K, Li H (2008) Application of LIBS technology to the rapid measure of heavy metal contamination in soils. Progr Chem 20(7/8):1165–1171

22. Le Yu, Zhao H, Ma X, Liu Y, Zhang M, Liao Y (2008) Research of LIBS method for detection of heavy metals in polluted soil. Laser J 5:66–67

23. Fei Z (1992) Bar code technology and application. Shanghai Science and Technology Literature Publishing House, Shanghai

24. Yang X, Sun C, Qian J, Chen L, Liu X (2006) Design and implementation of quality traceable label for farm products based on UCC/EAN-128 bar code. Packag Eng 27(6):113–114

25. McMeekin TA, Baranyi J, Bowman J, Dalgaard P, Kirk M, Ross T, Schmid S, Zwietering MH (2006) Information systems in food safety management. Int J Food Microbiol 112:181–194

26. Shen G, Zan L, Duan J, Wang L, Zheng T (2007) Implementation of beef quality and safety traceability system via internet. Transac Chinese Soc Agric Eng 23(7):170–173

27. Yang X, Qian J, Sun C, Liu X, Han X (2006) Implement of farm product archives management system based on traceability system. Chinese Agric Sci Bull 22(6):441

Chapter 60
The Research of the Systematical Construction Method of Chinese Conventional Road Guide Signs Based on the Characteristic of Chinese Drivers

Ming Jiang and Rui Zhou

Abstract Guide sign is an important traffic management facility and informs the drivers of road network information. It also has great impact on the smooth flow and traffic safety. This article draws on the construction method of conventional roads guide signs system from Manual on Uniform Traffic Control Devices (MUTCD). Based on the recognizing characteristic and the information retrieval model of Chinese drivers, this research provides the construction method of Chinese conventional roads guide signs system combined with the feathers of the Chinese road network structure. Using this method to the typical road network, the comparison and analysis of vehicle road experiments before and after reconstruction shows this method can effectively direct the drivers to improve the efficiency of arriving at the destination and reduce the probability of taking the wrong path. Based on this effect, it can be considered the effectiveness of guide signs designing is improved. (Programme No: 2009BAG13A02)

M. Jiang (✉)
Key Laboratory of Road Safety, Department of Traffic Engineering, Road Safety Research Center, Research Institute of Highway, M.O.C, 100088 Beijing, China
e-mail: m.jiangg@rioh.cn

R. Zhou
Beijing University of Technology, 100124 Beijing, China

60.1 Introduction

Traffic guide signs play very important role on the traffic management, applying the information of direction, location and distance for the participants in order to lead them to the destinations. Due to the direct relationship to the traffic safety and road network line efficiency, many countries pay attention to the research of road guide signs and take the establishment of a complete road guide system, improvement of the rationality of designing and enhancement of the effectiveness of guide signs as important goals.

According to the conventional roads, roads connect to each other through the junctions and form a integrated road network to achieve the various functions of transport. Drivers need to select the correct route to the final destination in every junction on the ground of effective and correct information on the guide sign. In the past, Chinese guide signs design only considered the point and provided the guide from point to point. In the case of the high density of the road network, this guidance method can hardly meet the actual demand of the drivers and is unable to play the role of road network. This research provides the construction method of Chinese conventional roads guide signs system combined with the feathers of the Chinese road network structure and makes reference to the relevant setting method and rule of the conventional roads that proposed by Manual on Uniform Traffic Control Devices (MUTCD). Based on the recognizing characteristic and the information retrieval model of Chinese drivers, the author provided the intersection guide system contains Advanced Inform signs-Guide signs-Confirm signs three type of signs and guide sign construction method of this system. The vehicle road experiments testified that this method is significant to improve the effectiveness of guide signs.

60.2 Conventional Roads Guide Signs Systemic Design Method of MUTCD

60.2.1 Guide System Components

MUTCD [1] established the system construction method for the conventional roads guide signs. According to the functions and the location, in this method system, the guide signs are divided into three types: Advance Route Turn Assembly, directional signs and confirming signs.

60.2.2 Guidance of the Component Guide Signs

Advance Route Turn Assembly includes the notice of intersection information and the route information. The notice of intersection information is usually erected at

400 ft (120 m) before the intersection; the notice of the route information is erected at 200 ft (60 m) before the intersection.

Directional signs include the guide for the direction and the guide of the route information. In these the guide sign for the direction is placed at 200 ft (60 m) before intersection; the guide sign of the route information should be located on the near right corner of the intersection.

Confirming signs include the confirmation of the route information as well as confirming information of the destination and the distance. Confirmation of the route information is generally erected at 25–200 ft (8–60 m) after the intersection, confirming information of the anterior place and distance is usually set at 300 ft (90 m) after the intersection.

The illustration of the guide system of the MUTCD sees Fig. 60.1.

60.3 The Constitute of Chinese Conventional roads Guide System

60.3.1 Guide Information Search Model of the Chinese Drivers

The investigation of a wide range of drivers found that Chinese drivers usually search relevant information to do the operation such as looking for destination, turning or confirming the route while driving through the intersection. The process generally consists of three stages, stage I: discovering the intersection and begin to slow down, consciously determining the shape of the intersection and being desirous to get the information of all of the route information and preparing for the next determination. Stage II: before reaching the intersection the driver needs to decide how to turn towards the destination. Stage III: after passing the intersection, normally the driver hope to determine whether he is driving the expected route. At the same time he needs to know the distance to the destination in order to arranging the travel plan.

60.3.2 System Constitution

According to the Chinese driver information search process, it embodies three stages, the "pre-estimation, turning operation, the confirmation of direction ". The guide system given by MUTCD meets the demand of the Chinese drivers. Draws on the relevant provisions of the MUTCD, the author integrated the characteristics of Chinese guide sign design and established the Chinese conventional Road guide system [2]. Comparison between the Chinese guide signs and MUTCD related signs are shown in Table 60.1.
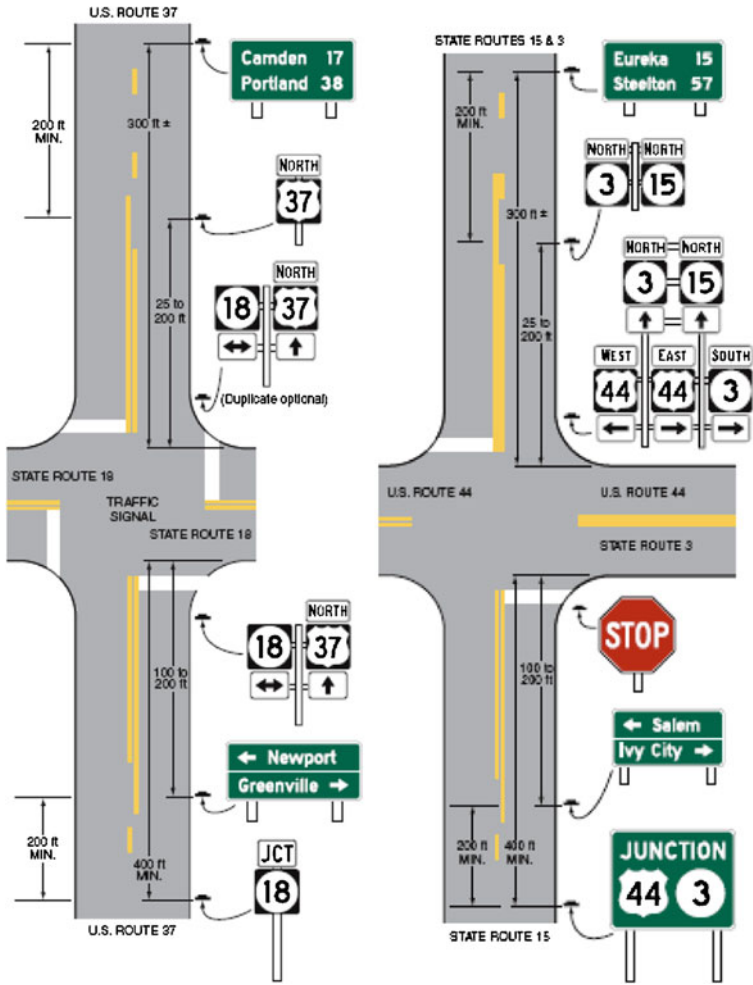
Fig. 60.1 The illustration of the guide system of the MUTCD

60.3.3 The Content of Guide Signs and the Relationship Between Each Signs

The content of guide signs and the relationship between each signs are showed in Fig. 60.2.

Table 60.1 Comparison between the Chinese guide signs and MUTCD related signs

Type	Standard	Function	Example
Advance guide signs	MUTCD	Notice the intersection information	
		Notice route information	
	CHINA	Notice the intersection. Using for the multi-lane highway	
		Notice route information. Using for two-lane highway	
	Comparison	For the multi-lane highway, on the advance guide signs route information is placed on the arrow and show the distance to the next intersection in China for the multi-lane highway, advance guide signs of MUTCD and CHINA are similar.	
Directional signs	MUTCD	Direct the destination	

60.3.4 Guide Sign Configuration Method

According to the Chinese road network features, it is impossible to set advance guide signs, directional signs, confirming signs [3] around each intersection. The first reason is the lack of the funds. The second reason is there are several low

Table 60.1 Comparison between the Chinese guide signs and MUTCD related signs

Type	Standard	Function	Example
		Route information signs	
CHINA	Direct the destination and route information		
Comparison	Combined the guide of destination and route information on one guide signs. The route number is placed on the arrow.		
Confirming signs	MUTCD	Routing confirming information	
		Destination and distance information	
	CHINA	Routing confirming information	
		Distance information	
	Comparison	Similar	

design level roads, the vehicles speed are slow so it is useless to erect the advance guide sign.

Based on the actual situation in China, guide sign configuration may refer to the Table 60.2 according to the class of the cross-highway:
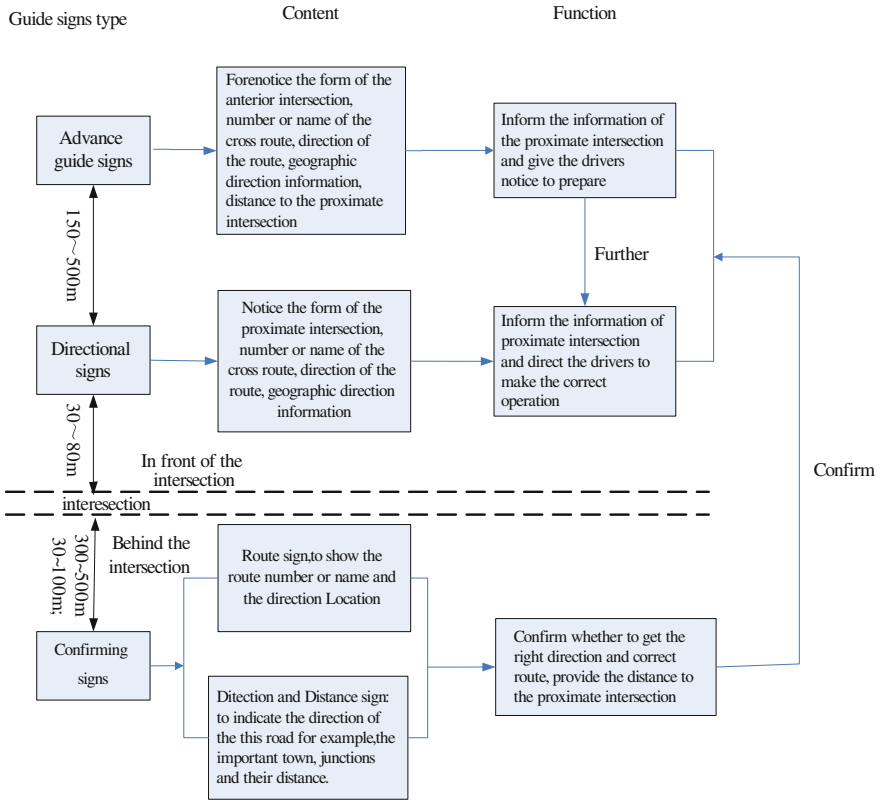
Fig. 60.2 Implication and location of the guide signs

60.3.5 Setting Example

According to the above rules, the setting example of the conventional road guide sign design is made as Fig. 60.3.

60.4 Vehicle Road Experiments

The method proposed in this paper was applied to Beijing guide signs reconstruction project, the comparison and analysis of vehicle road experiments was taken to judge the effectiveness of the method.

Table 60.2 Guide sign configuration according to the class of the cross-highway

Cross highway current highway	National road	Provincial road	County road	Village road
National road	A,D,C	A,D,C	A,D,C	(D)
Provincial road	A,D,C	A,D,C	(A),D,C	(D)
County road	(A),D,C	(A),D,(C)	(A),D,(C)	(D)
Village road	(A),(D),(C)	(A),(D),(C)	(D)	(D)

A—Advance guide signs; C—Confirming signs; D—Directional signs; ()—guide sign as the de

Fig. 60.3 Guide sign setting example in the general road
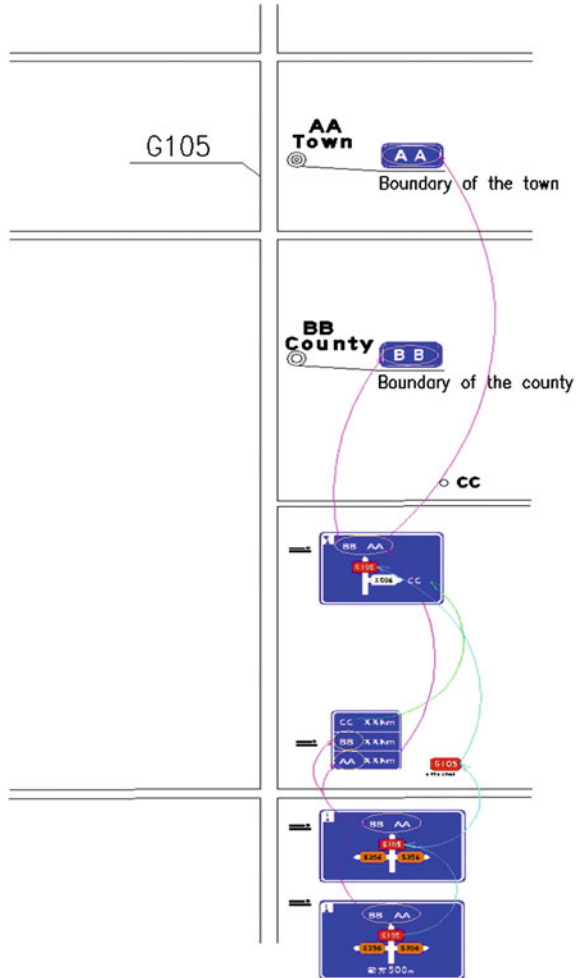
Fig.60.4 Experimental map

60.4.1 Experimental Design

This project is in Mentougou a district of Beijing. Twenty three drivers who have never been to Mentougou was taken as the test driver, including ten non-professional drivers and 20 professional drivers, all male.

Before the experiment the test member would provided a map (see Fig. 60.4) to the driver and asked him to complete the route with stated speed.

60.4.2 Experimental Route

In order to fully verify the effect of guide signs reconstruction, this test selected the route from LuGu besides lianshi west road to the Mentougou government, totally 40 km. The route is divided into two parts due to the different design speed. The first part is from LuGu to ShiMenYing Roundabout and the design speed is 80 km/h, as well as the drivers were asked to drive at 70 km/h. The second part is from ShiMenYing Roundabout to Mentougou government and the design speed is 60 km/h as well as the drivers were asked to drive at 50 km/h. The experimental route is shown in Fig. 60.5.

60.4.3 Evaluation Criterion

The recorder noted the following data during the experiment:

Driving time: totally driving time (except the traffic signal);

Information of the driver's taking the wrong way, amount and location, the method to get the right way, how long to get the right way back.

Fig. 60.5 Comparison of actual driving time before and after reconstruction
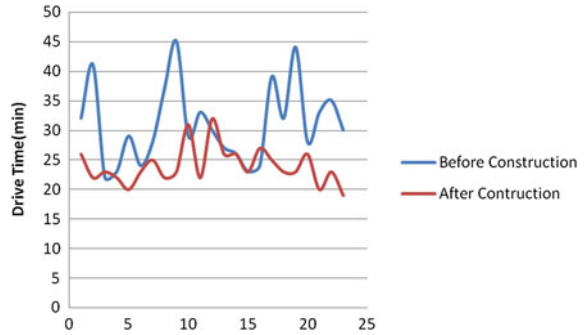
60.4.4 Analysis

The comparison of actual driving time and the amount of taking the wrong way before and after reconstruction with the certain speed and same route was shown as follow:

The comparison of actual driving time and the number of taking the wrong way was shown in Figs. 60.5, 60.6.

Statistics shows that before the reconstruction the drivers took mean average 30.1 min to arrive the destination and the variance was 6.6 min. However, the average time is short to 23 min and the time variance is 3.9 min after the reconstruction. It shows that scientific and reasonable guide signs plays very positive effect. It improves the operational Efficiency while eliminating the difference of driving time caused by the drivers' experience. Before reconstruction, the amount of the drivers reaching the destination directly without taking the wrong way accounted for 58% of the total, while the proportion is raised to 70% after the reconstruction. It also illustrated that the effectiveness of guide signs is improved.

60.5 Conclusion

This paper made a reference to the setting method of the conventional road guide signs that was proposed by MUTCD. Based on characteristics of Chinese road network and combined information search methods of Chinese drivers, Chinese general guidance system is established. This research determined the composition of guidance system, the configuration of guidance system, guide sign setting methods and corresponding information methods.

The real vehicle experiments show that the method of guidance system for improving the effectiveness and reducing the probability of wrong way plays a very positive effect.

Fig. 60.6 Comparison the number of taking wrong way before and after transformation **a** The number of taking the wrong way before reconstruction **b** The number of taking the wrong way after reconstruction
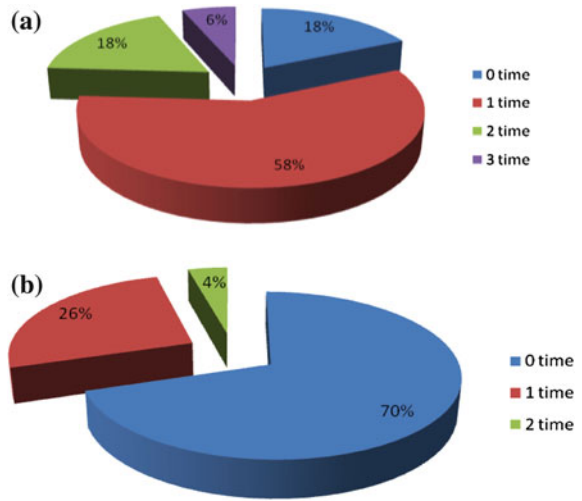
References

1. Manual on uniform traffic control devices (2009)
2. He Y, Tang C-C, Jiang M (2009) Road traffic signs. Standards Press, Beijing
3. Du Z, Pan X, Guo X (2008) Relationship between information quantity and visual cognition of traffic guide sign. J Traffic Transp Eng 2:118–122

Chapter 61
Voltage Sag Detection Algorithm Based on Dual DQ Decoupling Transformation

Wei Chen, Jun Xiao and Weizhou Wang

Abstract Conventional DQ transformation method and the PLL technology can detect the amplitude and phase of voltage sag accurately, but the method is only applicable to the case of symmetrical three-phase voltage. When three-phase voltage unbalance, there is a certain bias in the results by use of this detection method. A new detection method of improved PLL based on dual DQ decoupling transformation is proposed in this paper, it removed the coupling relationship of output voltages by setting the positive and negative sequence voltages reference, so this method can accurately detect the amplitude and phase information of the voltage sag. Simulation results validate that the proposed method is effective and feasible.

Keywords Dynamic voltage restorer · Voltage sag · Voltage asymmetry · Dual DQ decoupling transformation

61.1 Introduction

According to statistics of scholars and power departments in various countries, voltage sag's probability is the highest in many kinds of power quality problems of the power system [1, 2]. Therefore, people concerned voltage sag more than the

W. Chen (✉)
College of Electrical and Information Engineering, Lanzhou University of Technology, 730050 Lanzhou, China
e-mail: chenlin@lut.cn

J. Xiao · W. Wang
Gansu Electric Power Research Institute, 730050 Lanzhou, China
e-mail: gschenwei@lut.cn

other power quality problems. Ideal three-phase power supply voltage is symmetrical, both of voltage amplitude and frequency are constant, and waveform is sine without distortion. However, in actual power distribution system, due to the impact of system failure, three-phase voltage is not always symmetrical. Dynamic voltage restorer is usually designed according to three-phase symmetry condition, if the degree of asymmetry is too large, it will seriously affect the accuracy of dynamic voltage restorer detection algorithm [3, 4].

DQ transformation method based on instantaneous reactive power theory can detect system voltage sag and harmonic nicely, but which is only applicable to the case of symmetrical three-phase voltage. When the system occurs short circuit caused by fault of three-phase voltage unbalance, voltage in positive and negative sequence DQ transformation, there are certain coupling relationship between the output voltages. A new detection method of improved PLL based on dual DQ decoupling transformation is proposed in this paper, it removed the coupling relationship of output voltages by setting the positive and negative sequence voltage reference, then accurately extract the positive and negative sequence voltage components and introduce the phase deviation value into the transformation matrix, so this method can accurately detect the amplitude and phase information of the voltage sag.

61.2 Voltage Sag Detection with Improved PLL Based on Dual DQ Decoupling Transformation

Since 1983 three-phase instantaneous reactive power theory was proposed by the Japanese Hirofumi Akagi have been successful applications in many fields [5]. Voltage instantaneous detection principle based on DQ transformation is that the ABC of three-phase system voltage is transformed to DQ coordinates by transformation matrix Three-phase voltage could express as following:

$$\begin{cases} u_a = \sqrt{2}U\sin(\omega_1 t + \varphi) \\ u_b = \sqrt{2}U\sin(\omega_1 t + \varphi - 2\pi/3) \\ u_c = \sqrt{2}U\sin(\omega_1 t + \varphi + 2\pi/3) \end{cases} \tag{61.1}$$

as we know, the transformation relationship is:

$$\begin{bmatrix} u_d \\ u_q \end{bmatrix} = C \begin{bmatrix} u_a \\ u_b \\ u_c \end{bmatrix} \tag{61.2}$$

where, $C = \sqrt{\frac{2}{3}} \begin{bmatrix} \sin \omega t & \sin(\omega t - 2\pi/3) & \sin(\omega t + 2\pi/3) \\ -\cos \omega t & -\cos(\omega t - 2\pi/3) & -\cos(\omega t + 2\pi/3) \end{bmatrix}$

In transformation matrix C, $\sin \omega t$ and $\cos \omega t$ can be obtained by PLL and sine/cosine generator. The results through Park transformation as following:

$$
\begin{cases}
u_d = \sqrt{3/2}\,U[\cos((\omega_1 - \omega) + \varphi)] \\
u_q = -\sqrt{3/2}\,U[\sin((\omega_1 - \omega) + \varphi)]
\end{cases}
\tag{61.3}
$$

which amplitude and phase angle is:

$$
U = \frac{\sqrt{3}}{3}\sqrt{u_d^2 + u_q^2}
\tag{61.4}
$$

$$
\varphi = \arctan \frac{u_q}{u_d}
\tag{61.5}
$$

Through the theory analysis above, it shown that DQ transformation method in three-phase voltage symmetrical situation could accurately detect voltage sag of system, there is a phase angle difference between the voltage and the sequence voltage at the initial phase angle when the system occurs short circuit caused by fault of three-phase voltage unbalance, thus it will be a certain bias in the results by use of this detection method. As long as the power grid distorts, in spite of three-phase voltage symmetrical or asymmetrical, the results must have an error by using DQ transformation method. When system occur short circuit fault and causes three-phase voltage unbalance, due to symmetrical component method, the three-phase voltage is the sum of positive, negative and zeros sequence voltages, the same as following:

$$
\begin{cases}
U_a = \sqrt{2}U_s^+ \cos(\omega t + \varphi_1) + \sqrt{2}U_s^- \cos(\omega t + \varphi_2) + \sqrt{2}U_s^0 \cos(\omega t + \varphi_3) \\
U_b = \sqrt{2}U_s^+ \cos(\omega t + \varphi_1 - \frac{2\pi}{3}) + \sqrt{2}U_s^- \cos(\omega t + \varphi_2 - \frac{2\pi}{3}) + \sqrt{2}U_s^0 \cos(\omega t + \varphi_3 - \frac{2\pi}{3}) \\
U_c = \sqrt{2}U_s^+ \cos(\omega t + \varphi_1 + \frac{2\pi}{3}) + \sqrt{2}U_s^- \cos(\omega t + \varphi_2 + \frac{2\pi}{3}) + \sqrt{2}U_s^0 \cos(\omega t + \varphi_3 + \frac{2\pi}{3})
\end{cases}
$$

where U_s^+, U_s^- and U_s^0 is effective value of fundamental positive, negative and zeros sequence component respectively. ω is angular frequency of workers. φ_1, φ_2, and φ_3 is initial phase angle of fundamental positive, negative and zeros sequence component respectively.

Dual DQ transformation includes positive and negative sequence DQ transformations, which is respectively used to detect fundamental positive and negative sequence component. Considering positive sequence component as:

$$
U_s^+(dq) = C^+ \begin{pmatrix} U_a \\ U_b \\ U_c \end{pmatrix}
\tag{61.6}
$$

where, $C^+ = \sqrt{\frac{2}{3}} \begin{bmatrix} \cos(\omega t) & \cos(\omega t - \frac{2\pi}{3}) & \cos(\omega t + \frac{2\pi}{3}) \\ -\sin(\omega t) & -\sin(\omega t - \frac{2\pi}{3}) & -\sin(\omega t + \frac{2\pi}{3}) \end{bmatrix}$

So,

$$U_s^+(dq) = \begin{pmatrix} U_d^+ \\ U_q^+ \end{pmatrix} = \sqrt{3}\begin{pmatrix} U_s^+\cos\varphi_1 \\ U_s^+\sin\varphi_1 \end{pmatrix} + \sqrt{3}\begin{pmatrix} U_s^-\cos(2\omega t+\varphi_2) \\ U_s^-\sin(2\omega t+\varphi_2) \end{pmatrix} \quad (61.7)$$

Similarly negative sequence component as:

$$U_s^-(dq) = \begin{pmatrix} U_d^- \\ U_q^- \end{pmatrix} = \sqrt{3}\begin{pmatrix} U_s^-\cos\varphi_2 \\ U_s^-\sin\varphi_2 \end{pmatrix} + \sqrt{3}\begin{pmatrix} U_s^+\cos(2\omega t+\varphi_1) \\ U_s^+\sin(2\omega t+\varphi_1) \end{pmatrix} \quad (61.8)$$

Through the analysis above, it shown that the positive sequence component of output voltage changes into a DC component and the negative sequence component changes into a AC component with 2ω frequency in positive sequence DQ transformation; Similarly, in negative sequence DQ transformation, the negative sequence component of output voltage changes into a DC component and the positive sequence component changes into a AC component with 2ω frequency.

Therefore, under the condition of unbalanced grid voltage, positive sequence in DQ transformation U_q^+ not only contains DC part, but also generates secondary harmonic due to negative sequence component. That is, unbalanced voltage through positive and negative sequence in DQ transformations, there is a certain coupling relationship between the output voltages, we can extract positive and negative sequence components by way of decoupling.

Due to positive and negative sequence DQ transformations, we can know as following:

$$\begin{pmatrix} U_d^{+*} \\ U_q^{+*} \end{pmatrix} = \begin{pmatrix} U_d^+ \\ u_q^+ \end{pmatrix} - \sqrt{3}U_s^-\begin{pmatrix} \cos(2\omega t+\phi_2) \\ \sin(2\omega t+\phi_2) \end{pmatrix} \quad (61.9)$$

$$\begin{pmatrix} U_d^{-*} \\ U_q^{-*} \end{pmatrix} = \begin{pmatrix} U_d^- \\ u_q^- \end{pmatrix} - \sqrt{3}U_s^-\begin{pmatrix} \cos(2\omega t+\phi_1) \\ \sin(2\omega t+\phi_1) \end{pmatrix} \quad (61.10)$$

When three-phase voltage unbalanced, for example phase-A, there is a phase-difference of initial phase angle between voltage of phase-A and positive sequence voltage of phase-A. Traditional PLL can only extract voltage of phase-A, and could not fetch positive sequence voltage of phase-A. Now assuming the phase-difference of initial phase angle is θ between the voltage of phase-A and the positive sequence voltage of phase-A, and then making a error analysis to this.

Due to the existence of θ, the transformation matrix C^+ changes into C_1^+:

$$C_1^+ = \sqrt{\frac{2}{3}}\begin{bmatrix} \cos(\omega t+\theta) & \cos(\omega t-\frac{2\pi}{3}+\theta) & \cos(\omega t+\frac{2\pi}{3}+\theta) \\ -\sin(\omega t+\theta) & -\sin(\omega t-\frac{2\pi}{3}+\theta) & -\sin(\omega t+\frac{2\pi}{3}+\theta) \end{bmatrix} \quad (61.11)$$

By the principle of dual DQ transformation, we can know as following:

$$U_{s1}^+(dq) = \begin{pmatrix} U_{d1}^+ \\ U_{q1}^+ \end{pmatrix} = \sqrt{3}\begin{pmatrix} U_s^+\cos(\varphi_1+\theta) \\ U_s^+\sin(\varphi_1+\theta) \end{pmatrix} + \sqrt{3}\begin{pmatrix} U_s^-\cos(2\omega t+\varphi_2+\theta) \\ U_s^-\sin(2\omega t+\varphi_2+\theta) \end{pmatrix}$$

(61.12)

$$U_{s1}^-(dq) = \begin{pmatrix} U_{d1}^- \\ U_{q1}^- \end{pmatrix} = \sqrt{3}\begin{pmatrix} U_s^-\cos(\varphi_2+\theta) \\ U_s^-\sin(\varphi_2+\theta) \end{pmatrix} + \sqrt{3}\begin{pmatrix} U_s^+\cos(2\omega t+\varphi_1+\theta) \\ U_s^+\sin(2\omega t+\varphi_1+\theta) \end{pmatrix}$$

(61.13)

Because of the presence of phase-difference θ, allowing the detection results of positive and negative sequence voltage amplitudes and phases deviation [6]. This paper makes the following improvements to detect the positive and negative sequence components of voltage sag when grid voltage unbalanced.

$$U_s = \begin{pmatrix} U_a \\ U_b \\ U_c \end{pmatrix}$$

(61.14)

$$U_{dq} = C_s \begin{pmatrix} U_a \\ U_b \\ U_c \end{pmatrix}$$

(61.15)

where, $C_s = \sqrt{\frac{2}{3}}\begin{bmatrix} \cos(\omega t+\theta) & \cos(\omega t-\frac{2\pi}{3}+\theta) & \cos(\omega t+\frac{2\pi}{3}+\theta) \\ -\sin(\omega t+\theta) & -\sin(\omega t-\frac{2\pi}{3}+\theta) & -\sin(\omega t+\frac{2\pi}{3}+\theta) \end{bmatrix}$

Produced phase deviation value by power frequency signal generator, its value does not affect the accuracy of positive sequence voltage detection at last to grid voltage. This latched phase could provide sine and cosine signals for detection system, both of the signals have the same phase with positive sequence voltage. Consequently, the method could detect the amplitude and phase of voltage sag accurately.

61.3 Simulation

Building simulation models in Matlab/Simulink software environment and setting input voltage imbalance caused by single phase fault, where frequency is 50 Hz, $\omega_{ff} = 314\,rad/s$, $t_s = 0.045\,s$, $k_p = 0.5$, $k_i = 0.1$. Simulation results of Improved PLL based on dual DQ decoupling transformation are shown as Fig. 61.1.

From Fig. 61.1, it shows that the method of improved PLL based on dual DQ decoupling transformation could isolate voltage by decoupling calculation, so it can accurately detect amplitude and phase information of voltage sag.

Fig. 61.1 Simulation results
of improved PLL based on
dual dq decoupling
transformation. **a** Positive
sequence voltage dq
transformation. **b** Voltage
bias value. **c** Output phase.
d Phase deviation value
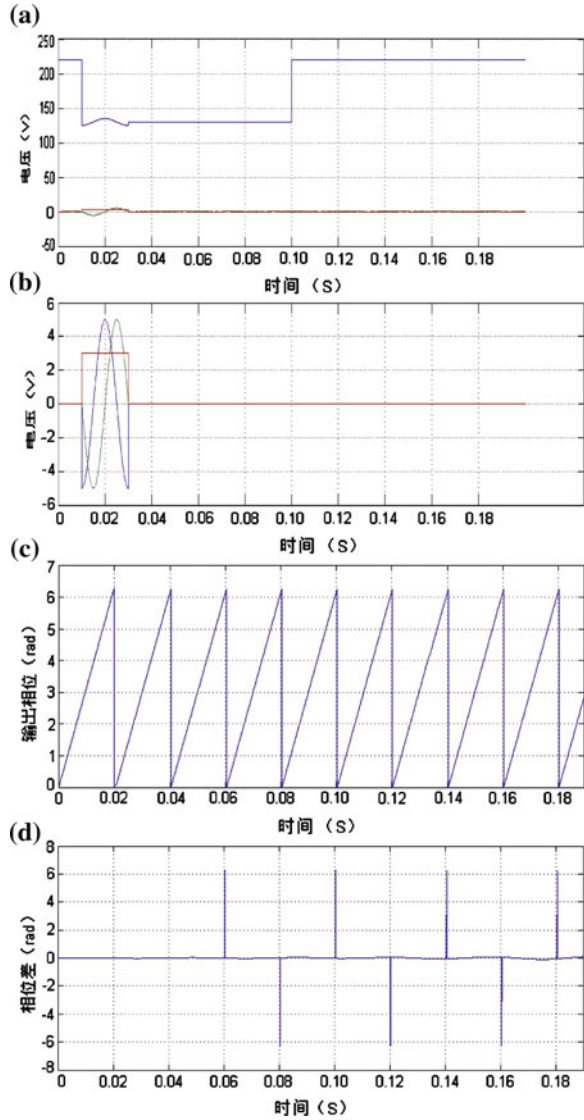
61.4 Conclusion

DQ transformation which is now commonly used in DVR will have biases under
grid voltage asymmetric. For this issue, a new detection algorithm of improved
PLL based on dual DQ decoupling transformation is proposed, it removed the
coupling relationship of output voltage by setting the positive and negative
sequence voltages reference, then accurately extract the positive and negative

sequence voltage components and introduce the phase deviation value into the transformation matrix, so this method can accurately detect the amplitude and phase information of the voltage sag.

References

1. Hao X, Du X, Chen W (2008) Survey on research dynamic voltage restorer. Sci Technol Eng 5:1259–1264
2. Park C, Gilsoo J (2007) Stochastic estimation of voltage sags in a large meshed network. IEEE Trans Power Deliv 3:1655–1664
3. Singh B, Al-Haddad K, Chandra A (1998) Three-Phase compensator for load balancing and reactive power Compensation in three-phase four wire electric power distribution systems. Electr Mach pow sys 26:27–37
4. Ding H, Duan X, He Y (2000) A novel dynamic voltage restorer for unbalanced distribution systems. In: Proc CSEE 11:46–50
5. Akagi H, Kanazawa Y, Nabe A (1984) Instantaneous reactive power compensators comprising switching devices without energy storage compensators. IEEE Trans Ind Appl 3:625–630
6. Yang J (2003) The research on long-distance power quality monitoring and active power filter. South China University of Technology, Guangzhou

Index